I. R. IRAN

ISSN: 1728-144X
e-ISSN: 1735-9244

# International Journal of Engineering

Journal Homepage: www.ije.ir

MERC

## TRANSACTIONS B: APPLICATIONS

Volume 35, Number 11, November 2022

*Materials and Energy Research Center*

**In the Name of God**

# *INTERNATIONAL JOURNAL OF ENGINEERING*
# *Transactions B: Applications*



**DISCLAIMER**

The publication of papers in International Journal of Engineering does not imply that the editorial board, reviewers or publisher accept, approve or endorse the data and conclusions of authors.


**I**nternational **J**ournal of **E**ngineering *Transactions A: Basics* (ISSN 1728-1431) (EISSN 1735-9244)
**I**nternational **J**ournal of **E**ngineering *Transactions B: Applications* (ISSN 1728-144X) (EISSN 1735-9244)
**I**nternational **J**ournal of **E**ngineering *Transactions C: Aspects* (ISSN 2423-7167) (EISSN 1735-9244)
Web Sites: www.ije.ir & www.ijeir.info E-mails: ije.editor8@gmail.com, Tel: (+9821) 88771578, Fax: (+9821) 88773352
Materials and Energy Research Center (MERC)

ISSN: 1728-144X, e-ISSN: 1735-9244

International Journal of Engineering, Volume 35, Number 11, November 2022

## CONTENTS

### Transactions B: Applications

ISSN: 1728-144X, e-ISSN: 1735-9244

**International Journal of Engineering, Volume 35, Number 11, November 2022**

International Journal of Engineering

Journal Homepage: www.ije.ir

# Ensemble of Log-Euclidean Kernel SVM based on Covariance Descriptors of Multiscale Gabor Features for Face Recognition

B. Asghari Beirami*, M. Mokhtarzade

*Department of Photogrammetry and Remote Sensing, Faculty of Geodesy and Geomatics, K. N. Toosi University of Technology, Tehran, Iran*

*PAPER INFO*

*Paper history:*
Received 14 March 2022
Received in revised form 8 July 2022
Accepted 20 July 2022

*Keywords*:
*Face Recognition*
*Covariance Descriptors*
*Gabor Features*
*Log-Euclidean Kernel SVM*
*Voting*

*ABSTRACT*

Face recognition (FR) is a challenging computer vision task due to various adverse conditions. Local features play an important role in increasing the recognition rate of an FR method. In this direction, the covariance descriptors of Gabor wavelet features have been one of the most prominent methods for accurate FR. Most existing methods rely on covariance descriptors of Gabor magnitude features extracted from single-scale face images. This study proposes a new method named multiscale Gabor covariance-based ensemble Log-euclidean SVM (MGcov-ELSVM) for FR that uses the covariance descriptors of Gabor magnitude and phase features derived from multiscale face representations. MGcov-ELSVM begins by producing multiscale face representations. Gabor magnitude and phase features are derived from the multiscale face images in the second stage. After that, the Gabor magnitude and phase features are used to generate covariance descriptors. Finally, Covariance descriptors are classified via a log-Euclidean SVM classifier, and a majority voting technique determines the final recognition results. The experimental results from two face databases, ORL and Yale, indicate that the MGcov-ELSVM outperforms some recent FR methods.

***doi***: *10.5829/ije.2022.35.11b.01*

## 1. INTRODUCTION

Face recognition (FR) is the process of recognizing an unknown face from a set of labeled face samples. FR has various applications in criminal screening, surveillance, military, mobile telephone, computer unlocking, and social media monitoring. As technology advances and data volumes increase, artificial intelligence techniques play an increasingly important role in automatic face recognition. Recognition of faces with machine learning techniques is challenging due to the various complex factors such as facial expression, image noise, head poses and illumination conditions, sensitivity to geometrical variations such as scale, rotation, and translation, the large volume of data, and small training sample size [1, 2].

The performance of the FR method depends on its robustness against the mentioned adverse conditions. Gabor textural filters inspired by the functioning of the mammalian visual cortices are robust under some adverse conditions [2]. Gabor textural features are usually generated by convolving the Gabor filters in the different scales and orientations with the original face image. Although resultant Gabor features vectors are discriminative, managing the high dimensionality of these vectors is challenging.

Tuzel et al. [3] proposed the covariance matrix as a novel image region descriptor and used it to detect objects and classify textures. The covariance matrix is a powerful image descriptor, with each diagonal element representing variance and each non-diagonal member representing covariance between two features. The rotation invariance is the most critical advantage of the covariance descriptor. In addition, covariance descriptor is the natural way to transform the high dimensional data to the new low dimensional matrix-based features, which contain discriminative second-order statistics.

*Corresponding Author: b_asghari@email.kntu.ac.ir
(B. Asghari Beirami)

Please cite this article as: B. Asghari Beirami, M. Mokhtarzade, Ensemble of Log-Euclidean Kernel SVM based on Covariance Descriptors of Multiscale Gabor Features for Face Recognition, ***International Journal of Engineering, Transactions B: Applications***, Vol. 35, No. 11, (2022) 2065-2071

Most of the existing FR techniques rely on the single-scale representation of the faces; however, recently, different studies have shown that multiscale facial representation can increase the FR approach's performance [4]. In this work, motivated by the effectiveness of covariance descriptors and Gabor features in FR, we proposed a novel ensemble FR approach based on covariance descriptors of multiscale Gabor features. It seems that by using the ability of Gabor features and covariance descriptors, the proposed FR method can become more robust to adverse conditions such as illumination conditions and geometric variations. In addition, the proposed FR method can better manage the high dimensionality of Gabor features, leading to appropriate recognition rates in small sample size situations. The following is a summary of this study's contributions:

- We introduce a novel effective FR system that uses covariance descriptors of Gabor magnitude and covariance descriptors of Gabor phase information. It should be noted that the combined Gabor textural features gained a powerful tool for modeling the local characteristics of face images.
- We offer a novel ensemble FR system that integrates covariance descriptors of the Gabor feature generated from the multiscale face representation.
- The study demonstrated the efficacy of the proposed method over several new FR methods using two well-known face databases.

The organization of the study is as follows. Section 2 delves into the related works. section 3 introduces the proposed FR method. The benchmark FR databases are introduced in section 4. Section 5 contains an analysis of the experimental results. In section 6, we conclude this study.

## 2. RELATED WORKS

Generally, FR methods can be categorized into two major groups, holistic and local approaches. This section reviews some important recent approaches of mentioned two groups of FR.

The use of holistic methods has a long literature. The most well-known methods in this group are eigenface (based on principal component analysis) and fisherface (based on Linear Discriminant Analysis). Aliyu et al. [5] compared the performance of eigenface and fisherface for FR on the LFW dataset and proved that the FR with fisherface technique outperformed the eigenface technique. Other recent classifiers, such as extreme learning machines (ELMs), have lately been employed for FR in addition to traditionally used nearest neighbor and support vector classifiers. ELMs can handle the high dimensional data and commonly perform better than SVM for FR. In this direction, Abd Shehab and Kahraman [6] proposed an ensemble version of ELM for FR to address the problem of its randomization nature In another study, Dalal and Vishwakarma [7] used the optimized extreme learning machines with PCA transform for FR. Their results on various face datasets proved some merits of the proposed method against the standard extreme learning machines. As stated earlier, FR is a complex task due to the various adverse conditions. In addition, the high dimensionality of face feature vectors is another issue that leads to the poor performance of the traditional FR methods. To address this problem, Khalili Mobarakeh et al. [8] proposed a new method named supervised kernel locality-based discriminant neighborhood embedding. Using nonlinear kernel mapping, this method effectively represents the nonlinear and complex variations of face images while simultaneously preserving the local structure information of data from the same class as well as discriminant information from other classes. Although their method can achieve appropriate recognition results on some FR dataset such as ORL, their results on complex face databases such as Yale is not better than the recent state-of-the-art methods. In another study, Gao et al. [9] proposed the new FR method, named extendface, that uses the complex number data augmentation and collaborative representation to address the problem of the high dimensionality of face images. Like the previous method, their results on the complex Yale face dataset do not reach a high level of recognition according to the state-of-the-art methods.

Holistic methods do not consider local characteristics of the face image, so they do not lead to optimal accuracy. Different Recent researches suggest that incorporating local features can improve recognition rates of the FR [2]. In this direction, Zaaraoui et al. [10] proposed the new local descriptor for face recognition by dividing the face image into some regions and calculating the histogram of dictionary words in each region. Their final results show an average accuracy of about 91% on two ORL and Yale face databases. Although their proposed method outperformed other FR methods, such as PCA, it seems that the use of the histogram method to generate the final local features reduced the performance of the proposed method, especially in small training samples size. In another recent study, Asadi Amiri and Rajabinasab [11] used the local features of color and edge orientation difference histogram in the conjugation with Canberra measure for FR. Their final results demonstrated a recognition rate of below 80% on the Yale database in the situation of the limited training sample size, which is not in comparison to recent state-of-the-art methods. In another recent study, Zhang and Yan [12] proposed a new local FR method that uses the histogram of local image gradient feature compensation as the feature descriptors of the face. Although their experiment reported the appropriate results on the ORL

face database, their recognition accuracy is commonly below 80% on the challenging Yale database.

Among all the mentioned methods, Gabor features have received the most attention from researchers [2, 13]. Gabor features can model facial texture using filters at different scales and directions. Although using Gabor features for FR can improve recognition rate, it is challenging to manage the high dimensionality of the generated features. Covariance descriptors can effectively solve this problem by compressing the high-dimensional Gabor data cube into a matrix. In addition, covariance descriptors contain information about second-order statistics that are useful in face recognition. In recent years, several studies, such as Pang et al. [14, 15], used the covariance descriptors of Gabor features for FR. Although Gabor feature covariance descriptors have been used in several studies for FR, it seems that the capabilities of these descriptors for FR have not been fully exploited due to the following points:

- The proposed covariance-based methods usually use only Gabor magnitude features and do not consider the valuable information of the Gabor phase features.
- Previous works have usually used a single-scale representation of faces, discarding the valuable information contained in different scales of face representation.
- The ability of some advanced matrix-based classification methods such as SVM with Log-Eclidean SVM for FR is less exploited. Log-Eclidean SVM is a powerful machine learning technique that can handle matrix-based descriptors such as covariances.

According to the mentioned points, this study proposes a new ensemble-based FR method that uses covariance descriptors obtained from multiscale Gabor magnitude and phase. In addition, this study's new ensemble-based FR method can effectively exploit the underlying information of multiple covariance descriptors.

## 3. METHODOLOGY

In this section, at first, Gabor features, covariance descriptors, and log-Euclidean kernel SVMs are reviewed, and finally, the proposed FR method is introduced.

### 3. 1. Feature Extraction with Gabor Filters

Gabor functions can accurately model a cell in the human visual brain. Gabor filters are commonly employed in image processing to extract texture information. Many FR approaches are based on Gabor features, which can describe the frequency content of images in different orientations. Gabor representation ($G_{\mu,v}$) of a face image ($I$) at each pixel ($z$= ($x$, $y$), $x$ and $y$ are the coordinates of the pixel $z$) are produced by convolving the face image with the Gabor kernel ($\psi_{\mu,v}$) as following [16]:

$$G_{\mu,v}(z) = I(z) * \psi_{\mu,v}(z) \quad (1)$$

$$\psi_{\mu,v}(z) = \frac{||k_{\mu,v}||^2}{\sigma^2} e^{(-||k_{\mu,v}||^2||z||^2/2\sigma^2)}[e^{ik_{\mu,v}z} - e^{-\sigma^2/2}] \quad (2)$$

In which the parameters of the above equations are as follows [16, 17]:

- $\mu, v$: are the orientation and scale
- $k_{\mu,v} = k_v e^{i\phi_\mu}$, $k_v = {k_{max}}/{f^v}$ , $\phi = \mu \cdot \pi/8$
- $f$ is the spacing between kernels in the frequency domain set to $\sqrt{2}$.
- $k_{max}$ is the max frequency, commonly set to 0.25
- $\sigma$ is commonly set to $\pi$.

The solution to Equation (1) for each pixel is a complex number with two parts: real (Re(z)) and imagery (Img(z)). From them, Gabor magnitude (mag) and phase features are defined as follows [16]:

$$Mag(z) = \sqrt{Re(z)^2 + Img(z)^2} \quad (3)$$

$$phase(z) = arctan\left({Img(z)}/{Re(z)}\right) \quad (4)$$

This work created Gabor magnitude and phase textural features using the MATLAB 2020b image processing toolbox. Eight orientations [0, 22.5, 45, 67.5, 90, 112.5, 135, 157.5] and nine wavelengths [from 2:1:10] are used to create these features. As a result, at each scale of the face representation, the numbers of Gabor magnitude and phase features are both equal to 72.

**3. 2. Covariance Descriptors** Here, we calculate the covariance descriptors of the Gabor magnitude and phase features derived from each scale of faces. Each created Gabor feature has the same size as a single-scale face image with $m \times m$ pixels. We produced 72 Gabor magnitude and phase features for each facial image. As a result, the final feature vector of each Gabor feature for the $i^{th}$ pixel is a (72+2)-dimensional feature vector ($z_i$), which is composed of two coordinate features ($x_i$, $y_i$) and 72 Gabor features [14]:

$$z_i^{mag} = [x_i, y_i, mag_i^1, mag_i^2 ..., mag_i^{72}] \quad (5)$$

$$z_i^{phase} = [x_i, y_i, phase_i^1, phase_i^2 ..., phase_i^{72}] \quad (6)$$

Covariance descriptors ($C$) of each Gabor feature with the size (72+2)×(72+2), which are symmetric, are computed by Pang et al. [14]:

$$C_{mag} = \frac{1}{(m\times m)-1}\sum_{i=1}^{m\times m}(z_i^{mag} - \mu^{mag})^T(z_i^{mag} - \mu^{mag}) \quad (7)$$

$$C_{phase} = \frac{1}{(m\times m)-1}\sum_{i=1}^{m\times m}(z_i^{phase} - \mu^{phase})^T(z_i^{phase} - \mu^{phase}) \quad (8)$$

where $\mu$ is the mean vector and T is the transposition operator. A regularization approach is used to make the covariance matrix strictly positively defined.

**3. 3. Log-Euclidean Kernel SVM** Covariance descriptors of Gabor features ($C$) are on a Riemannian manifold; therefore, the logarithm of matrix operator ($logm$) is used to $C$ to transfer them from Riemannian to Euclidean space. The Log-Euclidean-based kernel function is then defined as follows [18]:

$$k_{logm}(C_i, C_j) = trace[logm(C_i) \cdot logm(C_j)] \quad (9)$$

In which $C_i$ and $C_j$ are the covariance descriptors of $i^{th}$ and $j^{th}$ face images. Since the Log-euclidean kernel of Equation (9) is symmetric and a positive defined function, it meets mercer's conditions; therefore, it can be applied to categorize data using SVM [19].

**3. 4. Proposed FR System** Figure 1 depicts a flowchart of the proposed multiscale Gabor covariance-based ensemble Log-euclidean SVM (MGcov-ELSVM) method. According to Figure 1, this method has five stages:

1) In the first stage, to incorporate information from the multiscale representation of faces, each original face image is resized to 30×30, 60×60, and 90×90 pixels using the bicubic interpolation method.
2) In the second stage, the magnitude and phase of the Gabor filter are calculated using Equations (3) and (4) for each face scale from the previous stage.
3) In stage 3, the covariance matrices of features are extracted for each obtained group of Gabor features from each scale of faces using Equations (6) and (7).
4) In stage 4, log-Euclidean kernel SVM is used to classify covariance matrices, and the recognition results of each branch in Figure 1 are obtained.
5) In the end, majority voting between the obtained results of each classifier determines the final recognition result.

## 4. FACE DATABASES

The proposed MGcov-ELSVM method was tested on the two challenging Face databases, ORL and Yale. The ORL face database contains ten separate image samples from 40 different people taken under various conditions such as illumination and lighting, facial emotions (natural and smiling), and head attitude. All of the images have dark backgrounds and are viewed from the front, and their original size is 92×112 pixels. Prior to further processing, a pre-processing stage based on median filtering with a kernel size of 5×5 is used to decrease noise and increase the accuracy of the proposed technique. Figure 2 illustrates several samples of the ORL face database.

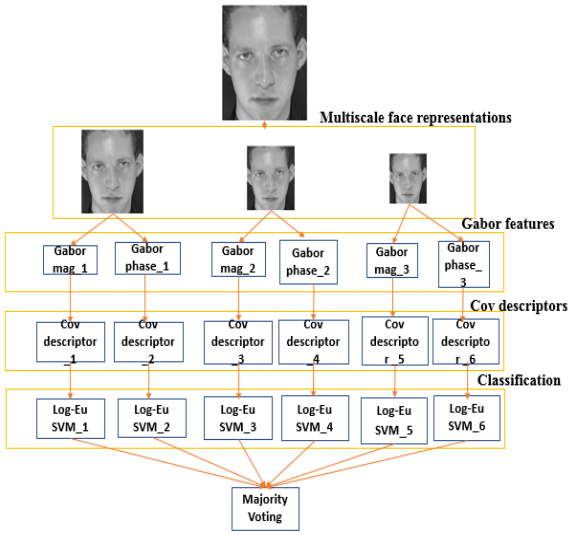


**Figure 1.** Flowchart of proposed MGcov-ELSVM method

**Figure 2.** ORL face database

The Yale database has 165 images at a resolution of 320 ×243 pixels from 15 different subjects, each with 11 images. These images display variations in lighting and emotions. To eliminate noise, a median filter with a kernel size of 5×5 is applied to each image. Figure 3 depicts several images from this database.

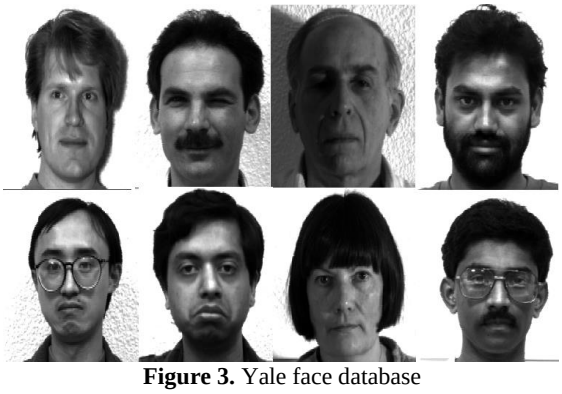

**Figure 3.** Yale face database

## 5. EXPERIMENTAL RESULTS

This section has the four subsection. First subsecrion analyzes the efficacy of the suggested ensemble technique. In the second subsection, the performance of the suggested method is compared with various existing cutting-edge FR approaches. Third subsection investigates the computational complexity of proposed method. Finaly in fourth subsection named, discussion, most important findings are presented along with some advantages and disadvantages of proposed method.

In the following experiments, for each face database, different sizes of training samples (T4=4, T5=5, and T6=6) are selected at random for each individual, and reminders are used as test samples for the method assessment. The experiment is repeated fifty times with different sets of training and test samples, and the mean recognition rate is reported.

**5. 1. Efficacy of the Ensemble Strategy** In the first experiment, we investigate the efficacy of the ensemble strategy used in the proposed method on both face databases. Figures 4 and 5 compare the recognition results of each branch of figure 1 based on the covariances of Gabor features and Log-Euclidean SVM from each scale of face images to the ensemble of results with the majority voting for both datasets. As a result, the proposed ensemble strategy can improve recognition rates. The superiority of the ensemble method is thought to lie in the integration of contextual information from multiple scales of faces.

**5. 2. Comparison to Other Methods** In this subsection, we compare the recognition results of our MGcov-ELSVM method with some recent FR methods on two face databases, ORL and Yale. We compare our proposed method to the following seven recent methodologies on both face databases: Mobarakeh et al. [8], Gao et al. [9], Zaaraoui et al. [10], Abd Shehab and Kahraman [6], Dalal and Vishwakarma. [7], Asadi Amiri and Rajabinasab [11] and Zhang and Yan [12]. The results of various comparing methods are all provided based on their original articles. In order to provide a fair comparison, all techniques use the same sample sizes during training and testing. Tables 1 and 2 summarise the mean recognition rate of each method on the ORL and Yale face databases, respectively.

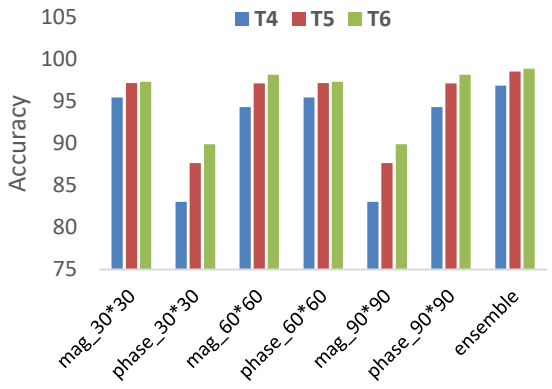


**Figure 4.** Recognition results for ORL database

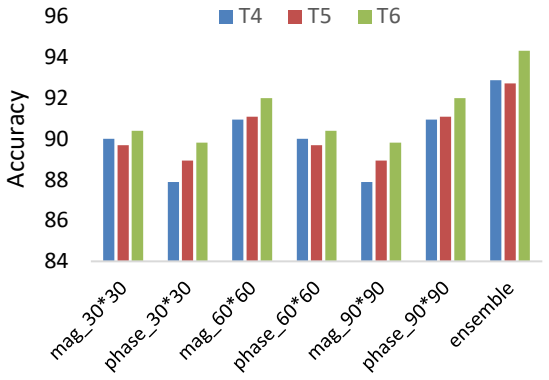


**Figure 5.** Recognition results for Yale database

Table 1 shows that for the ORL face database, MGcov-ELSVM achieves the average recognition accuracy of 98.04 on all sizes of training samples which is 1% higher than the recognition results of the very recent Zhang and Yan [12] method. Also proposed method performed 1.78% better than the new ensemble-based FR technique of Abd Shehab and Kahraman [6]. Table 2 shows that comparing methods can hardly achieve recognition accuracy higher than 90% in almost all cases on challenging the Yale face database. Whereas, the proposed MGcov-ELSVM has excellent performance (above 90%) on Yale databased, even when small numbers of training samples are provided (T4). Proposed MGcov-ELSVM achieves the best classification results

**TABLE 1.** Recognition results of different methods on the ORL face database

| Methods | Ref/ year | Training size | | |
|---|---|---|---|---|
| | | T4 | T5 | T6 |
| Mobarakeh et al | [8]/2019 | 93.33 | 94 | 96.87 |
| Gao et al. | [9]/2020 | --- | 92 | --- |
| Zaaraoui et al. | [10]/2020 | --- | 92.5 | --- |
| Abd Shehab and Kahraman | [6]/2020 | 94.81 | 96.93 | --- |
| *Dalal* and Vishwakarma | [7]/2021 | 85.83 | 88.5 | 89.37 |
| Asadi Amiri and Rajabinasab | [11]/2021 | 79.58 | 89 | 95.62 |
| *Zhang and Yan* | [20]/2022 | 93.75 | 98 | **99.38** |
| *MGcov-ELSVM* | | **96.82** | **98.49** | 98.83 |

***Result is not reported in the original paper**

**TABLE 2.** Recognition results of different methods on the Yale face database

| Methods | Ref/ year | Training size | | |
|---|---|---|---|---|
| | | T4 | T5 | T6 |
| Mobarakeh et al | [8]/2019 | ---* | --- | 85 |
| Gao et al. | [9]/2020 | --- | 88.89 | --- |
| Zaaraoui et al. | [10]/2020 | --- | 90.66 | --- |
| Abd Shehab and Kahraman | [6]/2020 | 81.49 | 84.92 | --- |
| Dalal and Vishwakarma | [7]/2021 | 73.33 | 80 | 86.67 |
| Asadi Amiri and Rajabinasab | [11]/2021 | 72.38 | 74.44 | 81.33 |
| Zhang and Yan | [12]/2022 | 75.24 | 77.78 | 78.67 |
| *MGcov-ELSVM* | | **92.78** | **92.71** | **94.32** |

***Result is not reported in the original paper**

for the Yale face database, with a 9.54% higher recognition rate than the ensemble approach of Abd Shehab and Kahraman [6]. Also, compared to the recent FR approach of Zhang and Yan proposed MGcov-ELSVM method achieved about 16% higher recognition accuracy.

In conclusion, the recognition rates can be improved by incorporating the local characteristics of the face. The performance of the proposed method on a complex Yale database can reveal that the proposed method is more robust than other recent methods under complex adverse conditions. In our view, the superiority of the proposed method can be explained by the ability of Gabor features to extract contextual information from multiscale face representations and the ability of covariance descriptors to model the relationship between Gabor features.

**5. 3. Time Complexity** All experiments in this study are implemented in MATLAB 2020a on a computer with a Core i5 4590 CPU with 8 GB of RAM. Due to the unavailability of codes for almost all competing FR methods, in this experiment, we only report the execution time of our proposed method. In general, the proposed method has three steps: preprocessing (Pre), feature generation (FG), and classification (CL). The time complexity of each step of the proposed method on ORL and Yale face databases is shown in Table 3.

According to Table 3, it is obvious that most of the execution time of the proposed method is related to the feature generation stage. It is worth noting that the parallel processing technique can reduce the execution time of the proposed method in such a way that the processing of each scale is executed on a separate system and then the final results are combined.

**TABLE 3.** Running time (in second) of the proposed method

| Dataset | Pre | FG | CL | Total |
|---|---|---|---|---|
| ORL | 1.3 | 150 | 0.29 | **151.59** |
| Yale | 0.6 | 62 | 0.09 | **62.69** |

**5. 4. Discussion** This study proposes a new ensemble strategy based on covariance descriptors of multiscale Gabor magnitude and phase feature for FR. We assess the proposed method in the three experiments. The first experiment proved that the decision fusion of covariance descriptors, derived from multiscale Gabor magnitude and phase features, can improve the recognition accuracy compared to the single-scale approach. In the second experiment, we compared the proposed method with seven states of FR methods. This experiment reveals that some recent competitor methods, such as Zhang and Yan [12], have a challenging performance on the complex Yale face database. This also shows that even recent approaches may not be invariant enough to FR under adverse conditions. The final results demonstrate that the proposed method outperformed the competitor methods in almost all experiments. Also, it can be concluded that the proposed method is more robust to the different challenges since it can achieve appropriate performance even when four samples are available for training. In the last experiment, we assess the performance of the proposed method in terms of computational cost. Final computational cost analysis shows that the feature generation stage consumes most of the time of the proposed method. Most advantages and disadvantages of the proposed method are listed as follows:

*Advantages:*

- The proposed method of this study has a simple but efficient structure that does not need expensive hardware to run, in contrast to many recent FR methods.
- The recognition rate of the proposed method is commonly above 92%, even when few training samples are available.

*Disadvantages:*

- The computational time of the proposed method is not as fast as some recent FR techniques. This issue should be solved in future studies.
- The performance of the proposed method degraded when only one training sample was available for each person. In future studies, we should propose an improved version of the proposed method, which is more robust to the training sample size.

## 6. CONCLUSIONS

We present a new ensemble classification approach for the FR in this study. This technique utilizes an ensemble

of log-Euclidean kernel SVMs to recognize faces based on the covariance descriptors of Gabor magnitude and phase features obtained from the multiscale representation of faces. Experiments on the two well-known face databases, ORL and Yale, reveal that the suggested technique outperforms some current state-of-the-art FR methods. In the future study, we will combine covariance descriptors of various textual features for accurate FR.

## 7. REFERENCES


1. Hassanpour, H. and Ghasemi, M., "A three-stage filtering approach for face recognition", ***International Journal of Engineering, Transactions B: Applications,*** Vol. 34, No. 8, (2021), 1856-1864. https://doi.org/10.5829/IJE.2021.34.08B.06
2. Li, C., Huang, Y., Huang, W. and Qin, F., "Learning features from covariance matrix of gabor wavelet for face recognition under adverse conditions", ***Pattern Recognition***, Vol. 119, (2021), 108085. https://doi.org/10.1016/j.patcog.2021.108085
3. Tuzel, O., Porikli, F. and Meer, P., "Region covariance: A fast descriptor for detection and classification", in European conference on computer vision, Springer., (2006), 589-600.
4. Moujahid, A. and Dornaika, F., "Multi-scale multi-block covariance descriptor with feature selection", ***Neural Computing and Applications***, Vol. 32, No. 10, (2020), 6283-6294. https://doi.org/10.1007/s00521-019-04135-7
5. Aliyu, I., Bomoi, M.A. and Maishanu, M., "A comparative study of eigenface and fisherface algorithms based on opencv and sci-kit libraries implementations", ***International Journal of Information Engineering & Electronic Business***, Vol. 14, No. 3, (2022). https://doi.org/10.5815/ijieeb.2022.03.04
6. Abd Shehab, M. and Kahraman, N., "A weighted voting ensemble of efficient regularized extreme learning machine", ***Computers & Electrical Engineering***, Vol. 85, (2020), 106639. https://doi.org/10.1016/j.compeleceng.2020.106639
7. Dalal, S. and Vishwakarma, V.P., "Optimization of weights in elm for face recognition", ***Journal of Information and Optimization Sciences***, Vol. 42, No. 6, (2021), 1337-1352. https://doi.org/10.1080/02522667.2021.1893473
8. Khalili Mobarakeh, A., Cabrera Carrillo, J.A. and Castillo Aguilar, J.J., "Robust face recognition based on a new supervised kernel subspace learning method", ***Sensors***, Vol. 19, No. 7, (2019), 1643. https://doi.org/10.3390/s19071643
9. Gao, J., Li, L. and Guo, B., "A new extendface representation method for face recognition", ***Neural Processing Letters***, Vol. 51, No. 1, (2020), 473-486. https://doi.org/10.1007/s11063-019-10100-1
10. Zaaraoui, H., Saaidi, A., El Alami, R. and Abarkan, M., "A new local descriptor based on strings for face recognition", ***Journal of Electrical and Computer Engineering***, Vol. 2020, (2020). https://doi.org/10.1155/2020/3451808
11. Asadi Amiri, S. and Rajabinasab, M., "Face recognition using color and edge orientation difference histogram", ***Journal of AI and Data Mining***, Vol. 9, No. 1, (2021), 31-38. https://doi.org/10.22044/JADM.2020.9376.2072
12. Zhang, Y. and Yan, L., "A fast face recognition based on image gradient compensation for feature description", ***Multimedia Tools and Applications***, (2022), 1-20. https://doi.org/10.1007/s11042-022-12804-4
13. Hammouche, R., Attia, A., Akhrouf, S. and Akhtar, Z., "Gabor filter bank with deep autoencoder based face recognition system", ***Expert Systems with Applications***, (2022), 116743. doi. https://doi.org/10.1016/j.eswa.2022.116743
14. Pang, Y., Yuan, Y. and Li, X., "Gabor-based region covariance matrices for face recognition", ***IEEE Transactions on Circuits and Systems for Video Technology***, Vol. 18, No. 7, (2008), 989-993. https://doi.org/10.1109/TCSVT.2008.924108
15. Pang, Y., Yuan, Y. and Li, X., "Effective feature extraction in high-dimensional space", ***IEEE Transactions on Systems, Man, and Cybernetics, Part B (Cybernetics)***, Vol. 38, No. 6, (2008), 1652-1656. https://doi.org/10.1109/TSMCB.2008.927276
16. Xie, S., Shan, S., Chen, X. and Chen, J., "Fusing local patterns of gabor magnitude and phase for face recognition", ***IEEE Transactions on Image Processing***, Vol. 19, No. 5, (2010), 1349-1361. https://doi.org/10.1109/TIP.2010.2041397
17. Dong, B. and Ren, G., "A new scene classification method based on local gabor features", ***Mathematical Problems in Engineering***, Vol. 2015, (2015). https://doi.org/10.1155/2015/109718
18. Fang, L., He, N., Li, S., Plaza, A.J. and Plaza, J., "A new spatial–spectral feature extraction method for hyperspectral images using local covariance matrix representation", ***IEEE Transactions on Geoscience and Remote Sensing***, Vol. 56, No. 6, (2018), 3534-3546. https://doi.org/10.1109/TGRS.2018.2801387
19. Wang, R., Guo, H., Davis, L.S. and Dai, Q., "Covariance discriminative learning: A natural and efficient approach to image set classification", in 2012 IEEE conference on computer vision and pattern recognition, IEEE., (2012), 2496-2503.
20. Wang, G. and Shi, N., "Collaborative representation-based discriminant neighborhood projections for face recognition", ***Neural Computing and Applications***, (2019), 1-18.


## Persian Abstract


**چکیده**

تشخیص چهره به دلیل عوامل مختلفی مانند نویز، میزان روشنایی و شرایط محیطی یک کار چالش برانگیز در حوزه بینایی ماشین است. ویژگی‌های محلی تصویر نقش مهمی را در افزایش دقت شناسایی روش‌های تشخیص چهره ایفا می‌کنند. در این راستا، توصیفگرهای کوواریانس ویژگی‌های موجک گابور یکی از برجسته‌ترین روش‌ها برای تشخیص دقیق چهره بوده است. بیشتر روش‌های موجود در این دسته بر توصیف‌گرهای کوواریانس ویژگی‌های بزرگی گابور استخراج‌شده از تصاویر تک‌مقیاس چهره تکیه می‌کنند. در این مقاله یک سیستم طبقه‌بندی چندگانه جدید (به نام MGcov-ELSVM ) برای تشخیص چهره پیشنهاد شده است که بر اساس توصیف‌گرهای کوواریانس به دست آمده از ویژگی‌های بزرگی و فاز گابور در مقیاس‌های گوناگون است. MGcov-ELSVM با تولید نمایش‌های چند مقیاسی چهره آغاز می‌شود. ویژگی‌های اندازه و فاز گابور از تصاویر چند مقیاسی چهره در مرحله دوم استخراج می‌شوند. پس از آن، ویژگی‌های بزرگی و فاز گابور برای تولید توصیفگرهای کوواریانس استفاده می‌شود. در نهایت، توصیفگرهای کوواریانس از طریق طبقه‌بندی‌کننده ماشین بردار پشتیبان با کرنل لگاریتم اقلیدسی طبقه‌بندی می‌شوند و رای‌گیری اکثریت نتیجه نهایی شناسایی چهره را تعیین می‌کند. نتایج تجربی بر روی دو پایگاه داده چهره، ORL و Yale، نشان می‌دهد که MGcov-ELSVM از برخی روش‌های اخیر تشخیص چهره بهتر عمل می‌کند.

International Journal of Engineering

Journal Homepage: www.ije.ir

RESEARCH NOTE

# Influence of Frequency of Wave Action on Oil Production

V. V. Poplygin*[a], C. Qi[b], M. A. Guzev[a], E. P. Riabokon[a], M. S. Turbakov[a], E. V. Kozhevnikov[a]

[a] *Department of Oil and Gas Technologies, Perm National Research Polytechnic University (PNRPU), Perm, Russian Federation*
[b] *Beijing University of Civil Engineering and Architecture, Beijing, China*

*PAPER INFO*

*Paper history:*
Received 17 April 2022
Received in revised form 22 July 2022
Accepted 24 July 2022

*Keywords*:
*Elastic Wave*
*Frequency*
*Oil Viscosity*
*Permeability*

*ABSTRACT*

When elastic waves act on rocks, the structure of the void space changes. The nucleation and formation of new cracks is possible. Wave action technologies are divided into two groups: with a frequency of less than 100 Hz and a frequency of more than 1 kHz. In the intermediate zone, no completed works and studies of wave action were found. The paper studies the results of the impact of elastic waves with different frequencies and amplitudes on oil production. With low-frequency exposure, an increase in permeability values is noted to a greater extent due to the appearance of new and an increase in the size of existing cracks. With high-frequency exposure, the viscosity of reservoir oil is greatly reduced. The greater the value of the initial viscosity, the more intense it decreases when exposed to high-frequency waves. For the Perm Territory, a comparison was made of the results of wave processing of production wells depending on the frequency of exposure. As the impact frequency increases, the average oil recovery after wave treatment decreases. With an increase in the frequency of exposure, the duration of operation of a well with increased oil production after wave treatment decreases. Models have been obtained to predict the time of operation of wells with additional oil production, additional oil production and an increase in oil production rate of wells after wave action. As a result, it can be noted that the most effective technologies are those with a lower frequency, but a large amplitude of exposure.

***doi**: 10.5829/ije.2022.35.11b.02*

**NOMENCLATURE**

| | | | |
|---|---|---|---|
| $f_{mid}$ | average frequency of wave action, Hz | f | frequency of wave action, Hz |
| Q | oil production after a wave action | T | well operation time with additional production |
| ΔQ | the average increase in well production rate after a wave impact | | |

## 1. INTRODUCTION

Wave action is one of the common methods for increasing the permeability of rocks and extracting oil from wells. Under wave action on rocks, their mechanical and filtration properties change significantly. New faults and cracks appear in the rocks. Existing fractures increase in size, and the rheological characteristics of the oil also change. There are several wave action technologies that differ in frequency and amplitude. Depending on the type of rock, the effectiveness of wave action varies.

*Corresponding Author Institutional Email: poplygin@bk.ru
(V. V. Poplygin)

At present, many studies have been carried out on the non-linear impact on rocks. Poplygin and Wiercigroch [1] studied on a low-frequency impact on the formation with an amplitude of up to 10 MPa. Long-term non-stationary water injection leads to a redistribution of the injected agent in the rocks and an increase in oil displacement from the pore matrix. The values of porosity and permeability of rocks have a strong influence on oil recovery. The results of studies conducted by Poplygin and Pavlovskaia [2] showed an intense change in permeability with a change in effective pressure. The results reported by Kozhevnikov et al. [3] and Guzev et al. [4] indicated an increase in the Young's modulus of sandstone with increasing values of dynamic load and frequency. Accordingly, an increase

Please cite this article as: V. V. Poplygin, C. Qi, M. A. Guzev, E. P. Riabokon, M. S. Turbakov, E. V. Kozhevnikov, Influence of Frequency of Wave Action on Oil Production, ***International Journal of Engineering, Transactions B: Applications***, Vol. 35, No. 11, (2022) 2072-2076

in the frequency of impact leads to the strengthening of rocks and a decrease in the likelihood of the formation of new cracks and voids [5, 6].

Depending on the method of oil production, various methods of wave stimulation of rocks are used. An elastic wave has a different amplitude and frequency For example, dilatation action is used in wells with rod pumps, and with acoustic action, the device is fixed under the pump. During the dialatation action, elastic waves with a low frequency and large amplitude are created, and vice versa during the acoustic action. In the work it is planned to study the change in the parameters of rocks at different frequencies of wave action and develop a model for predicting the results of wave action depending on the frequency of the action.

## 2. ELASTIC WAVE

A search was made for the results of using elastic waves on reservoir permeability and oil production. At the same time, the type of wave action technology was not taken into account. Elastic wave technology is divided into two parts: low frequency and high frequency.

**2. 1. Low-frequency** Lo et al. [7], investigaed based on Biot equation for a low-frequency dilatation wave propagating through a completely saturated porous medium, a relation was obtained according to which the permeability of the rock and the viscosity of the liquid will affect the damping of the elastic wave. The inclusion of these parameters leads to the appearance of opposite effects: a more permeable medium containing less viscous oil will show less wave attenuation and vice versa.

Guzev et al. [6] and Zheng et al. [8] noted an increase in porosity by 40–45% in the frequency range of 8–20 Hz. Increasing the frequency to 20 Hz leads to a decrease in the effect of wave action.

Sun et al. [9] showed the effect of vibration on fluid filtration during wave stimulation. It is reported that the combination of a low frequency wave and surfactant injection with a frequency between 15 and 25 Hz accelerates the penetration of the injected agent into the formation. However, when the gel is pumped and simultaneous wave stimulation with a frequency of 12 Hz - 30 Hz, the gelation process worsens.

Ariadji [10] studied wave stimulation on sandstone samples. Optimal frequencies of 10 Hz and 15 Hz have been identified. At this optimal frequency, residual oil saturation decreases, porosity and permeability increase, oil viscosity and capillary pressure decrease.

Louhenapessy and Ariadji [11] presented the results of studies of wave action with a low frequency and their effect on oil recovery. It has been established that with longitudinal vibrations up to 10 Hz, oil recovery increases by 8.58%. An increase in the frequency of forced longitudinal waves to 20 Hz leads to a decrease in oil recovery from the base value by 2.98 Hz. A further increase in frequency leads to an increase in oil recovery. When exposed to circular waves from 35 Hz to 45 Hz, oil recovery increases, and with a subsequent increase in frequency, it decreases (Figure 1).

**2. 2. Ultrasound** Under the ultrasonic action of waves, a synergy was observed Li et al. [12]; they obtained from a change in the viscosity of oil and modification of the microstructure of rocks. In oil-wetted cores, ultrasonic waves with high frequency (25 kHz and 28 kHz) showed the greatest increase in oil recovery.

During core flooding accompanied by ultrasonic treatment with a frequency of 40 kHz, an increase in oil recovery by 11% was observed [13].

In another work conducted by Mohammadian et al. [14], when filtering through samples saturated with kerosene with a wave action frequency of 40 kHz, oil recovery increased by 15–21%, and with a frequency of 65 kHz, by 15%–20%.

Wang et al. [15] studied the dependence of the decrease in oil viscosity on the frequency of wave action. At a frequency of 18 kHz, the decrease in viscosity for high-viscosity oil was 62%, at 20 kHz -

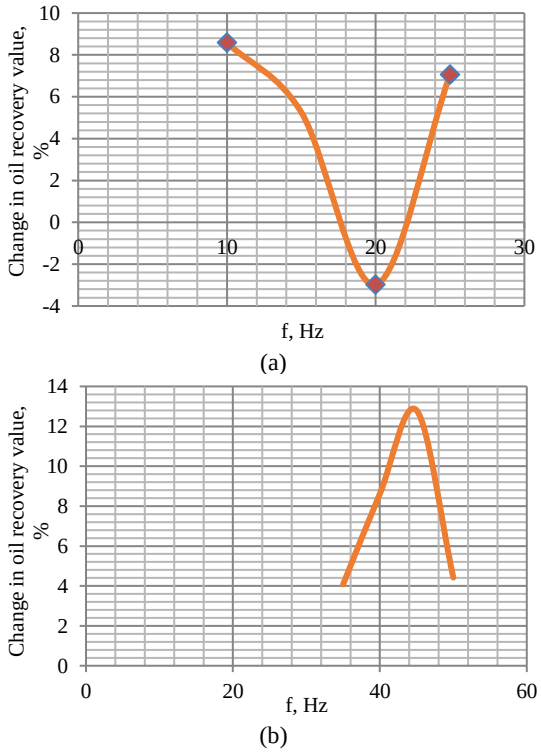


**Figure 1.** Change in oil recovery under wave action compared to stationary production: (a) longitudinal wave; (b) circular wave

28.9%, at 25 kHz - 26.5%. Hamidi et al. [16] have noted for synthetic oil and kerosene, the greatest decrease in oil viscosity when exposed to a frequency of 25-30 kHz. With a higher frequency of wave action, the effect decreased.

Hamidi et al. [17] investigated the results of applying acoustic exposure with a frequency of 20 kHz in Western China. After treatment, the reservoir permeability increased from 11.4 mD to 22 mD, and the oil viscosity decreased from 63.5 mPa·s to 37 mPa·s.

When exposed to acoustic waves in wells in Western Siberia with a frequency of 25 kHz, the effect increases oil recovery by 30–50% or more in wells with a permeability of more than 20 mD and a porosity of more than 15%. The effect of ultrasonic treatment lasts from 3 to 12 months or longer. The method increases the permeability of the bottomhole zone and can reduce clogging due to the presence of mineral particles. On reservoirs with lower permeability and porosity, ultrasonic treatment turned out to be ineffective [18].

Ultrasonic treatment (25 kHz) leads to an increase in the productivity of oil wells by 33%, and the well flow rate increased by 40%-100% as noted by Abramova et al. [19].

Ultrasonic treatment of oil from the fields of Tatarstan made it possible to reduce its viscosity by 19.2% [20].

It was noted by Khan et al. [21] that the maximum extraction up to 22.3% is achieved at an ultrasonic wave frequency of 20 kHz. At a frequency of 50 kHz, the reservoir permeability and oil recovery will increase by only 11%.

## 3. EXPERIENCE IN THE USE OF WAVE ACTION IN THE PERM REGION

In the Perm Territory (Russia), testing of wave stimulation technologies was carried out. Research was carried out on deposits of limestone and sandstone. The impact was carried out through the device under acoustic influence, water was introduced through special devices to create an amplitude and frequency in a wide range, as well as a dilatation effect with a low frequency and a large amplitude. The main results of testing technologies are presented in this paper.

The average frequencies of exposure varied from 9 Hz to 25 kHz.

The dependence of additional oil production on the frequency of wave action is shown in Figure 2. According to the dependence, the frequency is the determining factor in the wave action.

The dynamics of changes in additional oil production from frequency coincides with the dynamics of changes in porosity from frequency reported by Guzev et al. [6] and Zheng et al. [8]. Researchers have noted an increase in porosity of 40-45% in the frequency range 8-20 Hz. An increase in the frequency of 20 Hz leads to a decrease in the effect of the wave action.

An equation is proposed for predicting additional oil production after a wave action (the area of use of the equation varies from 10 to 25000 Hz):

$$Q = 1191\, e^{-0{,}611\log(f/fmid)} \quad (1)$$

Figure 3 shows dependence of the well operation time with additional production on the logarithm of the frequency. With an increase in the logarithm from frequency from 1 to 4.3, the value of the duration increased in production rate for wells decreases from 1800 to 250 days.

An equation is obtained for the dependence of the well operation time with additional production on the logarithm of the impact frequency (the area of use of the equation varies from 10 to 25000 Hz):

$$T = 331{,}9\, e^{-0{,}597\log(f/fmid)} \quad (2)$$

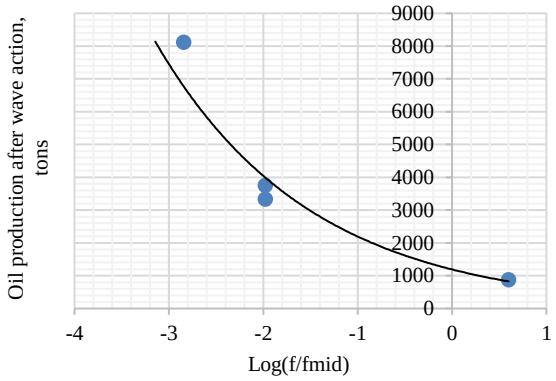


**Figure 2.** Dependence of additional oil production after wave action on relative frequency

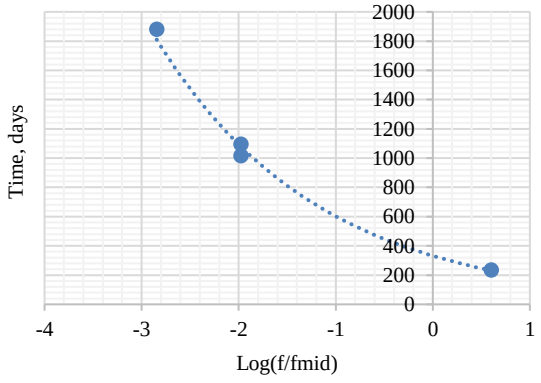


**Figure 3.** Dependence of the well operation time with additional production on the logarithm of the relative frequency

Figure 4 shows the dependence of the average increase in well production rates on the logarithm of the frequency of vibration exposure. The increase in well flow rate is obtained as the difference between the flow rate after wave action and the flow rate before wave action. For each technology, these values are averaged. An increase in the value of log ($f/f_{mid}$) from -3 to 1 leads to decrease in the indicator.

An equation is proposed for predicting the average increase in well production rate after a wave impact on the impact frequency (the area of use of the equation varies from 10 to 25000 Hz):

$$\Delta Q = -0{,}45 \text{ Log}(f/f_{mid})+2{,}05 \quad (3)$$

With low-frequency processing of rocks near the bottoms of wells, their flow rates according to Equation (4) increase more than with high-frequency acoustic exposure. This effect may be due to the fact that the oil of the fields under consideration has a low viscosity. With high-frequency exposure, the main change occurs in the viscosity of the oil, and not in the permeability. Therefore, for low-viscosity oil conditions, the resulting equations can be used.

The decrease in the effectiveness of high-frequency wave action in wells can be associated with a decrease in the amplitude of the action with increasing frequency. At exposure frequencies over 20 kHz, the amplitude does not exceed 0.3 MPa; when using DWA technology, the amplitude is up to 10 MPa. With a large amplitude, stresses arise in rocks, at which new faults and cracks are formed. Also, high-amplitude vibrations penetrate a greater distance into the formation. The results obtained are consistent with the studies reviewed earlier in the paper. As already noted, low-frequency impact leads to an increase in porosity up to 45%, which entails a proportional increase in permeability and oil production. With high-frequency exposure, the change in permeability and porosity is significantly lower, which explains the lower efficiency of high-frequency exposure. The flow rates of production wells increased due to changes in the permeability of rocks [22, 23].

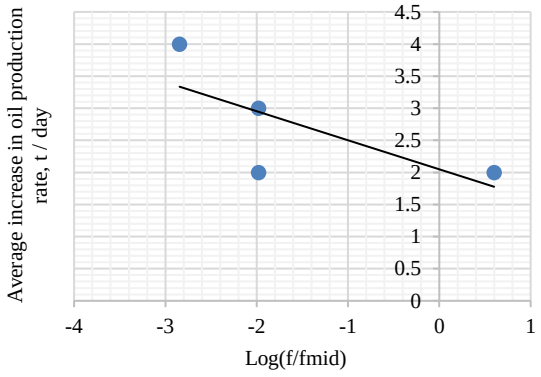


**Figure 4.** Dependence of the **a**verage increase in oil production rate on the logarithm of the relative frequency

## 4. CONCLUSIONS

A review of the known studies reveals the dependences of permeability and porosity on frequency, as well as a possible increase in oil production. On the basis of data from oil fields, the dependences of the actual change in well parameters after wave action are constructed and compared with the results. A good correlation is noted between studies in the laboratory and the results of wave action on wells.

The article summarizes the materials on the results of the use of wave action on wells and core samples. It is noted that low-frequency exposure leads to a change in permeability, and high-frequency exposure primarily affects the decrease in oil viscosity. The greatest change in reservoir and well parameters occurred during low-frequency impact with a frequency of up to 20 Hz and high-frequency impact with a frequency of 20 kHz.

Analysis done of the results of wave action in the production wells of the Perm region. An increase in the frequency of exposure leads to a decrease in the technological efficiency of exposure. The results of the authors of the work coincide with the results of studying the change in the permeability and porosity of rocks from the frequency of exposure. An equation for predicting cumulative oil production from wave action in wells is obtained in this work. The accumulated production is reduced by 8 times with an increase in the frequency of exposure from 10 Hz to 25000 Hz. The duration of wells operation with increased production rates also decreases. It is recommended to use wave action technologies with frequencies up to 100 Hz in the Perm region.

## 5. FUNDING STATEMENT

The reported study was supported by the Government of Perm Krai, research project No. C-26/628 dated 05.04.2021.

## 6. REFERENCES

1. Poplygin, V. and Wiercigroch, M., "Research of efficiency of complex non-stationary impact on layer with high-quality oil", ***Bulletin of Tomsk Polytechnic University. Geo Assets Engineering***, Vol. 331, No. 3, (2020), 7-12.
2. Poplygin, V. and Pavlovskaia, E., "Investigation of the influence of pressures and proppant mass on the well parameters after hydraulic fracturing", ***International Journal of Engineering, Transactions A: Basic***, Vol. 34, No. 4, (2021), 1066-1073.
3. Kozhevnikov, E.V., Turbakov, M.S., Riabokon, E.P. and Poplygin, V.V., "Effect of effective pressure on the permeability

of rocks based on well testing results", ***Energies***, Vol. 14, No. 8, (2021), 2306. https://doi.org/10.3390/en14082306

4. Guzev, M., Kozhevnikov, E., Turbakov, M., Riabokon, E. and Poplygin, V., "Experimental investigation of the change of elastic moduli of clastic rocks under nonlinear loading", ***International Journal of Engineering, Transactions C: Aspects***, Vol. 34, No. 3, (2021), 750-755.
5. Guzev, M., Kozhevnikov, E., Turbakov, M., Riabokon, E. and Poplygin, V., "Experimental studies of the influence of dynamic loading on the elastic properties of sandstone", ***Energies***, Vol. 13, No. 23, (2020), 6195.
6. Guzev, M., Riabokon, E., Turbakov, M., Kozhevnikov, E. and Poplygin, V., "Modelling of the dynamic young's modulus of a sedimentary rock subjected to nonstationary loading", ***Energies***, Vol. 13, No. 23, (2020), 6461.
7. Lo, W.-C., Sposito, G. and Majer, E., "Low-frequency dilatational wave propagation through fully-saturated poroelastic media", ***Advances in Water Resources***, Vol. 29, No. 3, (2006), 408-416.
8. Zheng, L., Pu, C., Xu, J., Liu, J. and Zhao, X., "Modified model of porosity variation in seepage fluid-saturated porous media under elastic wave", ***Journal of Petroleum Exploration and Production Technology***, Vol. 6, No. 4, (2016), 569-575. doi: 10.1007/s13202-015-0217-3.
9. Sun, Q., Retnanto, A. and Amani, M., "Seismic vibration for improved oil recovery: A comprehensive review of literature", ***International Journal of Hydrogen Energy***, Vol. 45, No. 29, (2020), 14756-14778.oi.
10. Ariadji, T., "Effect of vibration on rock and fluid properties: On seeking the vibroseismic technology mechanisms", in SPE Asia Pacific Oil and Gas Conference and Exhibition, OnePetro., (2005).
11. Louhenapessy, S.C. and Ariadji, T., "The effect of type waves on vibroseismic implementation of changes properties of rock, oil viscosity, oil compound composition, and enhanced oil recovery", ***Petroleum Research***, Vol. 5, No. 4, (2020), 304-314.
12. Li, X., Pu, C., Chen, X., Huang, F. and Zheng, H., "Study on frequency optimization and mechanism of ultrasonic waves assisting water flooding in low-permeability reservoirs", ***Ultrasonics Sonochemistry***, Vol. 70, (2021), 105291. https://doi.org/10.1016/j.ultsonch.2020.105291
13. Agi, A., Junin, R., Shirazi, R., Afeez, G. and Yekeen, N., "Comparative study of ultrasound assisted water and surfactant flooding", ***Journal of King Saud University-Engineering Sciences***, Vol. 31, No. 3, (2019), 296-303. https://doi.org/10.1016/j.jksues.2018.01.002
14. Mohammadian, E., Parak, M. and Babakhani, P., "The effects of properties of waves on the recovery of ultrasonic stimulated waterflooding", ***Petroleum Science and Technology***, Vol. 32, No. 8, (2014), 1000-1008. https://doi.org/10.1080/10916466.2011.611564
15. Wang, Z., Xu, Y. and Gu, Y., "Lithium niobate ultrasonic transducer design for enhanced oil recovery", ***Ultrasonics Sonochemistry***, Vol. 27, (2015), 171-177. https://doi.org/10.1016/j.ultsonch.2015.05.017
16. Hamidi, H., Mohammadian, E., Junin, R., Rafati, R., Manan, M., Azdarpour, A. and Junid, M., "A technique for evaluating the oil/heavy-oil viscosity changes under ultrasound in a simulated porous medium", ***Ultrasonics***, Vol. 54, No. 2, (2014), 655-662. https://doi.org/10.1016/j.ultras.2013.09.006
17. Hamidi, H., Haddad, A.S., Otumudia, E.W., Rafati, R., Mohammadian, E., Azdarpour, A., Pilcher, W.G., Fuehrmann, P.W., Sosa, L.R. and Cota, N., "Recent applications of ultrasonic waves in improved oil recovery: A review of techniques and results", ***Ultrasonics***, Vol. 110, (2021), 106288. https://doi.org/10.1016/j.ultras.2020.106288
18. Abramov, V.O., Mullakaev, M.S., Abramova, A.V., Esipov, I.B. and Mason, T.J., "Ultrasonic technology for enhanced oil recovery from failing oil wells and the equipment for its implemention", ***Ultrasonics Sonochemistry***, Vol. 20, No. 5, (2013), 1289-1295. https://doi.org/10.1016/j.ultsonch.2013.03.004
19. Abramova, A., Abramov, V., Bayazitov, V., Gerasin, A. and Pashin, D., "Ultrasonic technology for enhanced oil recovery", ***Engineering***, Vol. 2014, (2014). doi: 10.4236/eng.2014.64021.
20. Abramov, V.O., Abramova, A.V., Bayazitov, V.M., Mullakaev, M.S., Marnosov, A.V. and Ildiyakov, A.V., "Acoustic and sonochemical methods for altering the viscosity of oil during recovery and pipeline transportation", ***Ultrasonics Sonochemistry***, Vol. 35, (2017), 389-396. https://doi.org/10.1016/j.ultsonch.2016.10.017
21. Khan, N., Pu, C., Li, X., He, Y., Zhang, L. and Jing, C., "Permeability recovery of damaged water sensitive core using ultrasonic waves", ***Ultrasonics Sonochemistry***, Vol. 38, (2017), 381-389. https://doi.org/10.1016/j.ultsonch.2017.03.034
22. Mekaideche, K., Derfouf, F.M., Laimeche, A. and Abou-Bekr, N., "Influence of the hydric state and lime treatment on the thermal conductivity of a calcareous tufa", ***Civil Engineering Journal***, Vol. 7, No. 3, (2021), 419-430. https://doi.org/10.28991/cej-2021-03091663
23. Vali, R., "Water table effects on the behaviors of the reinforced marine soil-footing system", ***Journal of Human, Earth, and Future***, Vol. 2, No. 3, (2021), 296-305. http://dx.doi.org/10.28991/HEF-2021-02-03-09

## Persian Abstract

**چکیده**

هنگامی که امواج الاستیک بر روی سنگ ها اثر می کنند، ساختار فضای خالی تغییر می کند. هسته زایی و تشکیل ترک های جدید امکان پذیر است. فناوری های عمل موج به دو گروه تقسیم می شوند: با فرکانس کمتر از ۱۰۰ هرتز و فرکانس بیش از ۱ کیلوهرتز. در ناحیه میانی، هیچ کار تکمیل شده و مطالعات عمل موج یافت نگردید. این مقاله نتایج تاثیر امواج الاستیک با فرکانس‌ها و دامنه‌های مختلف بر تولید نفت را بررسی می‌کند. با قرار گرفتن در معرض فرکانس پایین، افزایش مقادیر نفوذپذیری به دلیل ظهور ترک‌های جدید و افزایش اندازه ترک‌های موجود، به میزان بیشتری مشاهده می‌شود. با قرار گرفتن در معرض فرکانس بالا، ویسکوزیته روغن مخزن تا حد زیادی کاهش می یابد. هر چه مقدار ویسکوزیته اولیه بیشتر باشد، هنگام قرار گرفتن در معرض امواج با فرکانس بالا، شدت آن کاهش می یابد. برای منطقه پرم، مقایسه ای از نتایج پردازش موجی چاه های تولید بسته به فرکانس قرار گرفتن در معرض انجام می شود. با افزایش فرکانس ضربه، میانگین بازیافت روغن پس از عملیات موجی کاهش می یابد. با افزایش فرکانس قرار گرفتن در معرض، مدت زمان بهره برداری از یک چاه با افزایش تولید نفت پس از درمان موج کاهش می یابد. مدل‌هایی برای پیش‌بینی زمان بهره‌برداری چاه‌ها با تولید نفت اضافی، و افزایش نرخ تولید نفت چاه‌ها پس از تاثیر موج به‌دست آمده‌اند. در نتیجه، می توان اشاره کرد که موثرترین فناوری ها آنهایی هستند که فرکانس کمتر، اما دامنه نوردهی بیشتری دارند.

IJE TRANSACTIONS B: Applications Vol. 35, No. 11, (November 2022) 2077-2091

International Journal of Engineering

Journal Homepage: www.ije.ir

# A Bi-objective Model of Research and Development in Battery Manufacturing Industry to Improve Customer Satisfaction

M. Latifian[a], M. A. Keramati[a,*], R. Tavakkoli-Moghaddam[b]

[a] *Department of Technology Management, Central Tehran Branch, Islamic Azad University, Tehran, Iran*
[b] *School of Industrial Engineering, College of Engineering, University of Tehran, Tehran, Iran*

*PAPER INFO*

*Paper history:*
Received: 07 April 2022
Received in revised form: 30 June 2022
Accepted: 04 July 2022

*Keywords*:
*Research and Development*
*Bi-objective Mathematical Model*
*Fuzzy Multi-criteria Decision Making*
*Battery Industry*
*Uncertainty*

*ABSTRACT*

Reviewing the efficiency of Research and Development (R&D) by giving an equal amount of importance to different R&D actions can make the measuring process too simple, which may cause an inaccurate interpretation of the R&D function and lead to an imprecise interpretation of R&D models. R&D comprises the creative work undertaken on a systematic basis to increase the stock of knowledge, including knowledge of man, culture, and society, and the use of this stock of knowledge to devise new applications. This research provides a two-phase approach to designing an R&D model in the auto battery manufacturing industry based on customer satisfaction. Due to the important role of R&D in customer satisfaction, no study has been conducted in this field and industry. In the first phase, the effective models for R&D management and the indices influencing customer satisfaction in R&D models are identified. In the second phase, the significance coefficients related to the customer satisfaction indices are obtained by using the fuzzy SWARA (Stepwise Weight Assessment Ratio Analysis) as a multi-criteria decision-making method. Furthermore, each model's importance and final priority are calculated by the fuzzy COPRAS (Complex Proportional Assessment) method. Finally, to apply the proposed framework in the battery manufacturing industry, a bi-objective R&D model is presented. The coefficients obtained by the fuzzy COPRAS method are utilized as the input for the proposed model. Therefore, policy-makers and managers can perform their activities based on this method. The obtained results showed that the proposed framework is effective in the case under study.

***doi:*** *10.5829/ije.2022.35.11b.03*

**NOMENCLATURE**

| | | | |
|---|---|---|---|
| $V_m$ | Significance coefficient of model $m$ | $P_{mn}$ | Probability of risk due to customer dissatisfaction with the implementation of model $m$ in manufacturer $n$ (loss of customer) |
| $W_{mn}$ | Capital required to select model $m$ in manufacturer $n$ | $B_n$ | The amount of budget available to manufacturer $n$ |
| $L_{mn}$ | Expected sales through the introduction of a new product by model $m$ in manufacturer $n$ | $x_{mn}$ | Is equal to one if method m is assigned to producer n otherwise it is zero |
| $D_n$ | Number of models allowed to assign to manufacturer $n$ | $R_{mn}$ | Risk due to customer dissatisfaction with the implementation of model $m$ in manufacturer $n$ |

## 1. INTRODUCTION

The role of knowledge in industrial economics has enhanced in recent decades; thus, industrial economics were named Knowledge-Based Economies (KBE) since the continuation of the growth of these economies relies on speeding up developments in technology and innovation. Hence, Research and Development (R&D) is an important category of a knowledge-based economy that explains part of the technological revolution's factors [1]. Moreover, many researchers have reported R&D as an important factor in supporting the company's competitiveness and its influence on the competitiveness of the country [2]. Overall, government financial support could be frequently seen in industrialized countries. Indeed, it is argued that government grants will result in

* Corresponding Author's Email: moh.keramati@iauctb.ac.ir
(M. A. Keramati)

Please cite this article as: M. Latifian, M. A. Keramati, R. Tavakkoli-Moghaddam, A Bi-objective Model of Research and Development in Battery Manufacturing Industry to Improve Customer Satisfaction, ***International Journal of Engineering, Transactions B: Applications***, Vol. 35, No. 11, (2022) 2077-2091

additional private investment [3]. R&D activities are taken into account as determining factors of productivity, growth, and competitiveness of firms [4].

Generally, R&D in companies embraces numerous activities and resources. These items contain basic research, applied research, development, and support activities like technology intelligence, technology forecasting, and market analysis [5].

The significance of R&D activities makes measuring R&D performance as a principal concern for companies [5-7]. As the complexity and diversity of technical and scientific knowledge have made R&D activities costly and risky, R&D performance measurement has become an essential issue for companies [8]. Overall, R&D managers have numerous reasons for measuring R&D performance: 1) The market is becoming more dynamic, customer needs are changing quickly, and the number of competitors is increasing; 2) Knowledge could be produced very rapidly, and thus the variety of products and services is greater, and 3) The complexity of knowledge in products and services is rising [5].

Employing structures and techniques to measure R&D performance upgrades a company's performance [9]. Nevertheless, uncontrollable factors turn R&D performance measurement into a challenging problem for managers [5]. In a survey in 1999, quantitative indices for assessing R&D in four perspectives on R&D performance, i.e., financial, customer, innovative and learning, and internal business processes were identified [6].

Nowadays, all industrialized or developing countries strive to elevate the volume of their research investments. In the meantime, industrialized countries invest in research for maintaining their position or increasing their superiority in international competition arenas. Developing countries have also understood that they have no choice but to invest in research to accomplish real growth and development and systematic resolving of their economic and social problems. Among the critical factors, which have led to the creation of a gap between countries, is the difference in their capability to carry out continuous innovation in all political, economic, cultural, and social aspects. Concerning the rapid growth of technology in the past two decades and the prediction of this process in the future, the scope of this gap will be undoubtedly aggravated over time in a case that proper measures are not taken. One of the approaches to deal with this challenge is to enhance innovation capability in the country via increasing R&D activities in various economic units [10].

Today, batteries are used in a variety of devices, including cell phones, laptops, and even cars. Just look around to see that almost all homes, work, and public places are filled with all kinds of large and small electronic devices and equipment that work with batteries. The number of batteries has increased so much that they are considered an invisible part of various devices. The point is that despite the widespread use of batteries and easy access to them in various stores, there are signs that innovation in this area will be extremely exciting in the future. According to the International Energy Agency's Sustainable Development Scenario, batteries with a capacity of nearly 10,000 MWh will be needed annually by 2040. This is while about 200 GWh are needed today. This issue can be studied from the two following aspects:

- An extensive and immediate demand can be a great opportunity for the development of innovations.
- A great need for technological advances is required to find new solutions for energy storage in large quantities and at an affordable price.

The European Patent Office (EPO) and the International Energy Agency (IEA) have conducted a joint study analyzing patents in the field of batteries and electricity storage from 2005 to 2018. According to this report, the patent activity in this area has experienced annual growth of 12%, which is four times faster than the average growth rate in all technology areas [11].

Therefore, about the listed descriptions, the objective of this study was to propose a two-step decision-making approach for evaluating R&D models in the automotive battery industry emphasizing customer satisfaction. In the first section, the models influencing the R&D management and the indicators affecting customer satisfaction on R&D models are detected. In the second section, the weighting coefficients associated with customer satisfaction indices are achieved using the fuzzy Stepwise Weight Assessment Ratio Analysis (SWARA) technique. Additionally, the weight of each model and their ultimate prioritization are calculated using the fuzzy Complex Proportional Assessment (COPRAS) method. In the second step, a Bi-Objective Mathematical Programming (BOMP) model is offered to allocate optimal models to the automotive battery industry. Eventually, due to the bi-objective nature of the proposed model, the Augmented Epsilon Constraint Method will be exploited to solve the mathematical model. Subsequently, the structure of the research is broken down as follows.

The second section deals with the research literature. The third section explains the research methodology. The fourth section provides the case study and the framework of the proposed indexes. The fifth section addresses the discussion on the results of calculations. Finally, an overall conclusion and some recommendations for further studies are presented in the sixth section.

## 2. THEORETICAL BASIS AND LITERATURE REVIEW

In this section, investigating the theoretical basis, literature review, and the research gap will be addressed.

**2. 1. Research and Development (R&D)** R&D is referred to as a set of novel, creative, innovative, systematic, and planned activities, which generally is carried out to spread the boundaries of scientific cognition and the treasure of human knowledge and human society and the application of this knowledge in various domains to promote human life, briefly for the innovation and establishment of new products, processes, equipment, tools, systems, services, and approaches [12]. At present, R&D activities are recognized as the driving and central factor for all firms' industrial and economic development and are considered among the most crucial agents in strengthening countries' technological potential and economic growth. There are various techniques and mechanisms for technology development through R&D, such as Internal R&D, Joint R&D, R&D Contract, and R&D outsourcing [13].

Similar to R&D units, functional units need a specific model to advance their unit's objectives. These models should be designed in a coordinated and synchronized manner with the models of a company. R&D models comprise the definition of the set of R&D projects needed to accomplish the specified goals in the sphere of technology acquisition set in the framework of a company's overall model. Among the essential R&D models that could be pointed out are the implementation models of R&D. Domestic execution of R&D projects, cooperation, or outsourcing projects are the approaches addressed in various references.

Assessing the success of organizations in the exploitation of the domestic R&D spillover or buying it from foreign companies and the linkage of these two items with the absorptive capacity of organizations demonstrate that organizations with the same absorption capacity placed in more advanced economic conditions and settings are more successful in exploiting R&D spillovers [14]. R&D outsourcing causes an enhancement in the knowledge of organizations. That is, what these organizations can do (competencies) will be upgraded; however, what they should avoid (costs) will be transparent to organizations. Furthermore, conducting R&D in developed countries leads to promoting the level of R&D [15]. There are two primary models in the acquisition and use of knowledge for R&D, one is to limit the scope of knowledge, and the other is its diversity. The results gained from investigations reveal that control on the scope of knowledge flow in particular fields has overall a more significant influence on the sale of new products. Internal and external R&D outsourcing will differently affect innovation performance, and the number of these contracts is impressive on the mode of transfer and the achieved results [16].

**2. 2. Customer Satisfaction** Customers are people or processes that buy the product or result from a performance that they need and benefit from. Since any performance in an organization is undoubtedly done with a purpose, so it has customers as well. Customer orientation is taken into account as a critical factor in the success of organizations. One of the most important theoretical and experimental matters for many marketers and marketing researchers is customer satisfaction [17]. Customer satisfaction is regarded as a condition that a person has experienced, which is associated with assessing the hypothetical characteristics of products and expectations of that person about those features. Besides, customer satisfaction is defined as service quality performance levels that meet users' expectations. Assessing customer satisfaction offers a salient and objective view of their choices and beliefs. Customer surveys can contribute to resolving the discrepancy between expectations and satisfaction. The current competition worldwide persuades R&D organizations to maximize customer satisfaction and decipher quality management concepts in the standardization of measures and, consequently, enhancing the quality of services [18].

**2. 3. Literature Review** Soltanzadeh et al. [19] assessed the impact of government intervention on a company's innovation activities. This paper offers a framework to elaborate on the behavioral changes in the company resulting from government intervention. This investigation intends to estimate the influence of R&D subsidies on Iranian companies (small-, medium-, and large-sized companies) using the Propensity Score Matching (PMS) technique. This article found that R&D subsidies have a substantial impact on the innovation process.

In an investigation, Liu et al. [20] examined the R&D performance of industrial companies in China based on a two-stage data envelopment analysis (DEA) by data from 2009 to 2014. Based on the results gained in this study, several policy proposals for the R&D activities of Chinese industrial companies were provided. Sinimole and Saini [21] in a study, evaluated and compared the R&D performance of Asian countries divided into two groups based on a threshold expenditure of 1% of GDP on R&D. In this study, they exploited an output-oriented DEA model.

Chachuli et al. [22] explored the performance of R&D activities in five renewable energy resources, namely, solar, wind, biomass, biogas, and mini-hydro. The case study is Malaysia and considers the data from 2012 to 2017 concerning two policy thrusts, namely, systematic R&D program and human capital development towards the renewable energy deployment in Malaysia. This research uses the DEA method to evaluate the efficiency of the R&D activities of renewable energy resources considering the variables in the government's renewable energy policy. In a study, Koçak et al. [23] used a data envelopment analysis (DEA) and bootstrap DEA to study the environmental efficiency of R&D expenditures for energy efficiency, renewable energy, hydro and fuel cells, fossil energy,

nuclear energy, and other power and storage technologies in OECD countries. In their study, Matte and Belgin [24] examined the impact of knowledge management (KM) performance on the efficiency of 20 companies operating in R&D in the production of parts and accessories for the motor vehicle industry in Turkey. In their investigation, they employed conventional data envelopment analysis (DEA) and DEA based on weight restrictions for the analysis of data. Based on the results, there is a significant difference between companies' efficiency in R&D with high performance and low performance in terms of knowledge management (KM) dimensions, namely, knowledge creation, information system infrastructure, knowledge culture, and knowledge worker productivity.

Dai et al. [25] reviewed the development of battery management systems in the past and presented a multilayer design architecture for advanced battery management. They also discussed future trends in research and battery management development for future generations. Valacuse [26] examined R&D models for pharmaceutical products following the coronavirus epidemic in the first quarter of 2020. The results of his research show that the COVID -19 crisis highlights the urgent need to reshape global public health for health R&D. Amaskra et al. [27] studied the role of investment in R&D and economic policy uncertainty in Sri Lanka's economic growth. The results of their study show that R&D is crucial to increasing the productivity of all factors in the country. Also, through R&D, EPUs have a significant detrimental effect on the TFP growth, although only in the short run. In 2022, Belderbos et al. [28] studied the international diversity of top management teams and the effectiveness of R&D strategies to increase innovation performance. Their study analyzed the innovation performance of 165 companies in Europe, Japan, and the USA.

Karamasa [29] established the service quality criteria in three-star hotels in Erzurum and ranked the importance levels of the determining criteria. The SWARA method was used to weight the determining criteria. The results of this method show that "Price Availability" was the most important service quality criterion in three-star hotels. This was followed by "Courtesy and Respect Level", "Reliability", "Service and Process Flexibility", "Restaurant Service Quality" and "Cleanliness", respectively. The criteria considered the least important include "Quality of Housekeeping" and "Front Office Service Quality".

Bac [30] proposed a framework to evaluate different smart card systems to determine the best one and additionally validate their benefits while comparing with the traditional fare payment system. For this purpose, an integrated Multi-Criteria Decision-Making (MCDM) framework was used that combines two recent and popular methodologies. The proposed methodology used the SWARA method for determining the criteria weights in the decision model and the Weighted Additive Sum Product Assessment (WASPAS) method for comparing alternatives. Research results revealed that all smart card systems show improvements in performance, reliability, and user satisfaction-related criteria.

Khalili and Alinezhad [31] evaluated the performance of Aggregate Production Planning (APP). In this regard, the optimal values were determined by the multi-objective Grey Aggregate Production Planning (GAPP) model, and the weights of the input and output indicators for the performance evaluation were characterized by the SWARA method. Further, the efficiency of Decision-Making Units (DMUs) was determined by the Ratio Efficiency Dominance (RED) mode, and then, DMUs were ranked. As a result, the efficiency and resource loss increased and decreased, respectively.

**2. 4. Research Gap** As seen from the literature review, the problem of research and development (R&D) is still among the most critical scientific challenges and especially a vital matter in Iran. Therefore, in this study, we intend to design an R&D model in the automotive battery industry by proposing a new framework based on the SWARA method, the fuzzy COPRAS method, and a BOMP model, taking into account the dimensions of customer satisfaction.

## 3. FRAMEWORK OF THE PROPOSED ASSESSMENT APPROACH

In this section, the basic definitions associated with the suggested decision-making approach are briefly expressed. Besides, a bi-objective mixed-integer linear programming (MILP) model is formulated. By these core concepts, a new hybrid approach of fuzzy multi-criteria decision making (MCDM) - mathematical optimization (mathematical programming) is proposed.

**3. 1. Fuzzy Set Theory** The triangular fuzzy number is defined as a triple ($a_1$, $a_2$, $a_3$), which its membership function is equal to [32]:

$$\mu_{\tilde{a}}(x)=\begin{cases}(x-a_1)/(a_2-a_1), & \&if\ a_1\le x\le a_2\\ 1 \quad (a_3-x)/(a_3-a_2), & \&if\ a_2\le x\le a_3\\ 0, & \text{Otherwise}\end{cases} \tag{1}$$

So, $a_1$, $a_2$, and $a_3$ are the minimum possible, the highest, and the maximum possible values, respectively.

If $\tilde{A}=(a_1,a_2,a_3)$ and $\tilde{B}=(b_1,b_2,b_3)$ are two fuzzy triangular numbers so that $a_1\le a_2\le a_3$ and $b_1\le b_2\le b_3$, and $\beta$ is also $a$ number greater than zero, then the basic operations of fuzzy triangular numbers will be [33]:

$$\tilde{A}\oplus\tilde{B}=(a_1+b_1,a_2+b_2,a_3+b_3) \tag{2}$$

$$\tilde{A}\otimes\tilde{B}=(a_1b_1,a_2b_2,a_3b_3) \tag{3}$$

$$\tilde{A} \ominus \tilde{B}=(a_1-b_3,a_2-b_2,a_3-b_1) \quad (4)$$

$$\tilde{A} \oslash \tilde{B}=(a_1/b_3,a_2/b_2,a_3/b_1) \quad (5)$$

$$\beta\tilde{A}=(\beta a_1,\beta a_2,\beta a_3) \quad (6)$$

If $\tilde{A}=(a_1,a_2,a_3)$ is a triangular fuzzy number, then the best non-fuzzy performance is calculated by [34, 35]:

$$R(\tilde{A})=\frac{1}{6}(a_1+4a_2+a_3) \quad (7)$$

**3. 2. Fuzzy SWARA Method** Overall, the procedure for achieving the relative weights of the criteria using the fuzzy SWARA technique is as follows:

**Step 1:** The criteria are arranged in a sequence from the highest degree of importance (priority) to the lowest degree of importance (priority) according to experts' opinions and based on the purpose of the decision. As decision-making about real-world problems is always associated with uncertainties, the language scale provides more freedom to experts. These linguistic scales can be provided by Triangular Fuzzy Numbers (TFNs) according to Table 1.

**Step 2:** This process starts from the second criterion where the experts allocate a linguistic variable for each criterion to criterion $j$ with the previous criterion ($j-1$). This ratio is recognized as the comparative importance of the average value [36].

**Step 3:** Calculate the fuzzy coefficient $\tilde{k}_j$ by:

$$\tilde{k}_j=\begin{cases}1, & j=1\\ \tilde{S}_j+1, & \&j>1\end{cases} \quad (8)$$

**Step 4:** Calculate the fuzzy weight ($\tilde{q}_j$) by:

$$\tilde{q}_j=\begin{cases}1, & j=1\\ \frac{\tilde{q}_{j-1}}{\tilde{k}_j}, & \&j>1\end{cases} \quad (9)$$

**Step 5:** Calculate the fuzzy relative weights of evaluation criteria by:

$$\tilde{w}_j=\frac{\tilde{q}_j}{\sum_{k=1}^{n}\tilde{q}_k} \quad (10)$$

where $\tilde{w}_j$ represents the relative weights of criteria $j$ and $n$ represents the total number of criteria.

**Step 6:** Defascularization of fuzzy relative weights of criterion $j$ that results from Equation (7).

**3. 3. Fuzzy COPRAS Method** The steps of the COPRAS technique are as follows:

**Step 1:** Creating a fuzzy decision matrix using the fuzzy membership functions presented in Table 2 based on the following equation.

$$\tilde{X}=\begin{bmatrix}(x_{11}^l,x_{11}^m,x_{11}^u) & \cdots & (x_{1n}^l,x_{1n}^m,x_{1n}^u)\\ \vdots & \ddots & \vdots\\ (x_{m1}^l,x_{m1}^m,x_{m1}^u) & \cdots & (x_{mn}^l,x_{mn}^m,x_{mn}^u)\end{bmatrix} \quad (11)$$

where $m$ is the number of options, $n$ is the number of criteria, and $x_{mn}$ represents the performance of option $i$ in relation to criterion $j$. Conversion instructions for fuzzy membership functions are indicated in Table 2 [37].

**Step 2:** Normalize the fuzzy decision matrix using Equations (12) – (14) to enhance its comparability. The normalized value of the fuzzy decision matrix is calculated using the procedure adopted in the research [38]. This normalization approach of the initial fuzzy decision matrix improves the computational process and upgrades the accuracy of numbers [39].

*As*: $\tilde{s}_{ij}=(s_{ij}^l,x_{ij}^m,x_{ij}^u)$ , $\forall ij$

$$s_{ij}^l=x_{ij}^l/\sqrt{\sum_{i=1}^{m}\left[\left(x_{ij}^l\right)^2+\left(x_{ij}^m\right)^2+\left(x_{ij}^u\right)^2\right]} \quad (12)$$

$$s_{ij}^m=x_{ij}^m/\sqrt{\sum_{i=1}^{m}\left[\left(x_{ij}^l\right)^2+\left(x_{ij}^m\right)^2+\left(x_{ij}^u\right)^2\right]} \quad (13)$$

$$s_{ij}^u=x_{ij}^u/\sqrt{\sum_{i=1}^{m}\left[\left(x_{ij}^l\right)^2+\left(x_{ij}^m\right)^2+\left(x_{ij}^u\right)^2\right]} \quad (14)$$

**Step 3:** Calculate the weighted normalized fuzzy decision matrix. This matrix is obtained by multiplying the weights gained for each criterion by the cumulative weighted method in the normal fuzzy decision matrix.

Fuzzy multiplication is illustrated as Equation (2).

**TABLE 1.** Verbal phrase for pairwise comparison of criteria

| Verbal phase | Fuzzy scale |
|---|---|
| No matter (EU) | (0.0,0.0,0.1) |
| Importance is very weak (NVI) | (0.0,0.1,0.3) |
| Poor importance (NI) | (0.1,0.3,0.5) |
| Relative importance (F) | (0.3,0.5,0.7) |
| Important (I) | (0.5,0.7,0.9) |
| Very important (VI) | (0.7,0.9,1.0) |
| Absolute importance (EI) | (0.9,1.0,1.0) |

**TABLE 2.** Verbal phrase to evaluate the R&D models

| Verbal phase | Fuzzy scale |
|---|---|
| Very poor (VP) | (0.0,0.0,1.0) |
| Poor (P) | (0.5,1.0,2.5) |
| Medium poor (MP) | (1.5,3.0,4.5) |
| Medium (M) | (3.5,5.0,6.5) |
| Medium important (MG) | (5.5,7.0,8.0) |
| Important (G) | (7.5,9.0,9.5) |
| Very important (VG) | (9.5,10,10) |

**Step 4:** Calculate the sum of all the criteria according to Equation (15) so that their maximum value is preferred for each further option.

$$\widetilde{P}_i=\sum_{j=1}^{k}\tilde{x}_{ij} \qquad i=1,2,\ldots,m; j=1,2,\ldots,n \tag{15}$$

**Step 5:** Calculate the sum of all the criteria based on Equation (16) so that the minimum value is preferred for each further option.

$$\widetilde{R}_i=\sum_{j=k+1}^{n}\tilde{x}_{ij} \qquad \begin{matrix} i=1,2,\ldots,m; \\ j=k+1,k+2,\ldots,n \end{matrix} \tag{16}$$

where in the above equations, $k$ is equal to the number of criteria of utility, and $n$-$k$ is the number of criteria of cost.

**Step 6:** Non-Fuzzy values of $\widetilde{P}_i$ and $\widetilde{R}_i$ are calculated by utilizing equation 7.

**Step 7:** Calculate the minimum value of $R_i$ through Equation (17).

$$R_{min}=\min_i R_i;\ i=1,\ldots,m \tag{17}$$

**Step 8:** Calculate the options' relative importance values through Equation (18).

$$Q_i=P_i+\frac{R_{min}\sum_{i=1}^{m}R_i}{R_i\sum_{i=1}^{m}\frac{R_{min}}{R_i}};\ i=1,\ldots,m \tag{18}$$

**Step 9:** Calculate the degree of each option. The utility of desirability of each option is calculated by comparing it with the ideal option based on the following equations.

$$Q_{max}=\max_i Q_i;\ i=1,\ldots,m \tag{19}$$

$$N_i=\frac{Q_i}{Q_{max}}\times 100 \tag{20}$$

where $Q_i$ is the non-fuzzy relative weight for each option, and $Q_{max}$ is the ideal option value. Eventually, the options are ranked based on the value $N_i$ so that the option with a high value of $N_i$ is optimal and is placed in the first rank.

**3. 4. Suggested Mathematical Model** In this section, a bi-objective mathematical model is proposed to assign R&D models to automobile battery manufacturing companies, taking profit and risk objectives into account. To model the problem, like other mathematical models, hypotheses need to be considered. The assumptions employed in this study are as follows:

- The number of R&D models is specific and limited.
- The number of battery manufacturing factories is specified and limited
- The expenditure for executing each model, the degree of customer satisfaction with each model and the total budget considered for the models are different and specific values.
- There is the possibility of choosing several models for each manufacturer.
- The values associated with the model parameters are certain.
- Each model has a coefficient of importance in the model, the value of which is a definite number between zero and one, which results from the characteristic of the fuzzy COPRAS method.

### 3. 4. 1. Mathematical Modeling

$$\text{Max } Z_1=\sum_{m=1}^{p}\sum_{n=1}^{q}V_mL_{mn}x_{mn} \tag{21}$$

$$\text{Min } Z_2=\sum_{m=1}^{p}\sum_{n=1}^{q}P_{mn}R_{mn}x_{mn} \tag{22}$$

s.t.

$$\sum_{m=1}^{p}W_{mn}x_{mn}\le B_n \qquad \forall\ n \tag{23}$$

$$\sum_{m=1}^{p}x_{mn}\le D_n \qquad \forall\ n \tag{24}$$

$$\sum_{m=1}^{p}x_{mn}\ge 1 \qquad \forall\ n \tag{25}$$

$$x_{mn}\in\{0,1\} \qquad \forall\ m,n \tag{26}$$

The offered model has two objective functions that will be elaborated below. The first objective function (21) maximizes the expected sales of the new product from the execution of R&D models in battery manufacturers. The second objective function (22) addresses minimizing the risk of customer loss via implementing R&D models in battery manufacturers. Also, the model has four constraints. Phrase (23) estimates the constraint associated with the budget. Phrase (24) ensures that the number of models assigned to each manufacturer does not exceed the allowable limit. Constraint (25) ensures that each manufacturer is allocated at least one model. Ultimately, Constraint (26) specifies the type of variables applied to the problem.

**3. 4. 2. Constraint Method** The constraint ε method formula is as follows: The first objective is introduced as the main objective [40, 41].

$$\text{Min } f_1(X) \tag{27}$$

$$x\in X \tag{28}$$

$$\begin{matrix} f_2(X)\le\varepsilon_2 \\ f_n(X)\le\varepsilon_n \end{matrix} \tag{29}$$

In the proposed query of this study, the initial objective is considered the primary objective, and other objectives are viewed as secondary objectives. Hence, according to the constraintε method, the new formula of the proposed model culminates in the following optimization problem.

$$\text{Min } Obj_1 \tag{30}$$

$$Obj_2\ge\varepsilon_2 \tag{31}$$

Equation (29) represents the main objective function of the problem, and Equation 30 adds to the problem's set of constraints. The constraint ε method's steps/stages are as follows:

- Select one of the objective functions as the primary objective function.
- Solve the problem each time according to one of the selected objective functions, and obtain the optimal values of each objective function.
- Divide the interval between the two optimal values of the sub-objective functions into a predetermined number and obtain a table of values for $\varepsilon\_2, \ldots, \varepsilon\_n$
- Solve the problem with the main objective function with each of the values of each time $\varepsilon\_2, \ldots, \varepsilon\_n$
- Report the Pareto findings.

We calculate the size of the objective function 2, …, $p$ for each objective function, and then, we divide the limit $k$ of the objective function into equal distances $q_k$. $r_k$ of the scope becomes the objective function of $k$ ($k$=2, …, $p$). The decoupling step for this objective function is defined by:

$$step_k = {}^{r_k}/_{q_k} \quad (32)$$

The values on the right-hand side for the corresponding constraint on $t$ iterations in a given objective function correspond to Equation (33).

$$e_{kt=fmin_k+t\times step_k} \quad (33)$$

where $fmin_k$ is a half function and t counter is a specific objective function. After optimization, the excess variable is obtained and the passage coefficient is calculated so that $int()$ is a function of the integer Component (34).

$$b=int(s_2/step_2) \quad (34)$$

In the proposed constraint $\varepsilon$ method, as mentioned, the initial objective function is presumed as the primary objective function and the second objective function as the sub-objective function; Thereafter, the n number of failures is presumed for each objective, and a total of 2$n$ Pareto points are generated for each problem. Next, the best answer for the objective functions is presented between the Pareto points of the ε-constraint method.

## 4. CASE STUDY

In this survey, the population under study included experts from battery companies (i.e., $a$-1). There are numerous indices and criteria in conjunction with the assessment of R&D models. The classification provided in this study has put together the indicators that are closer to the intended problem by the concept. Therefore, in this phase, a list of relevant criteria to assess R&D models (Figure 1) is initially detected in Table 3 through the revision and literature review, and in-person interviews with experts.

## 5. RESULTS

This section describes the result of implementing the proposed approach.

**5. 1. Determining the Weights of Criteria: Fuzzy SWARA Technique** As previously mentioned, the final list of criteria and sub-criteria relating to the assessment of R&D models in the automotive battery industry for the decision-making board (experts) is offered. This committee includes experts from the most important manufacturers in the country's battery industry. In the next step, the experts determine the relative weight of the main criteria and the relevant sub-criteria.

After several rounds of discussion, the board of experts formed a common consensus and arranged the main criteria from the most important criteria to the least important criteria, respectively. Next, the relative importance of the mean value ($\tilde{S}_j$) for each of the criteria of quality, market, technical, and process is assessed by experts using the fuzzy verbal scale presented in Table 1.

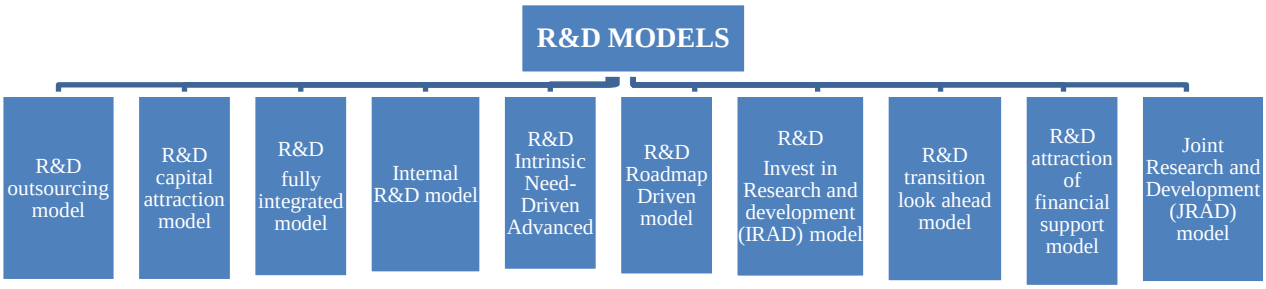


**Figure 1.** Conceptual model of the R&D models in the battery industry

Next, the fuzzy coefficient $\tilde{k}_j$ for each criterion is calculated using Equation (8). After that, the calculated fuzzy weight $\tilde{q}_j$ and the relative fuzzy weight $\tilde{w}_j$ for the main criteria are specified by employing Equations (9) and (10), respectively.

The results associated with these steps are given in Table 3. As can be inferred from the results, the order of importance (priority) of the main criteria in the experts' opinion is so that the most important criterion belongs to the criterion of Technical. Then, the criteria of Market, Process, and Quality are placed, respectively. Similarly, a pairwise comparison of the sub-criteria of each of the four main criteria, the defuzzified local weight, is provided in Table 4. Eventually, the optimized overall weights for the indicators affecting the R&D models in the automotive battery industry are achieved, as demonstrated in Table 5.

**TABLE 3.** Evaluation framework for the R&D models

| Criterion /index | Main dimensions |
|---|---|
| Durability and longevity ($R_{11}$) | Quality ( $R_1$) |
| Weight and dimensions ($R_{12}$) | |
| Service & product innovation ($R_{13}$) | |
| Market share ($R_{21}$) | Market ($R_2$) |
| Price ($R_{22}$) | |
| Brand ($R_{23}$) | |
| Amount of combination with other operations ($R_{31}$) | Technical ($R_3$) |
| Compatibility with technology ($R_{32}$) | |
| Safety ($R_{33}$) | |
| Warranty ($R_{41}$) | Process ($R_4$) |
| Ease of access to sales centers ($R_{42}$) | |
| Cooperation with car assistance ($R_{43}$) | |

**5. 2. Assessment of R&D models: a Fuzzy COPRAS Method** In the previous steps, the weights of evaluation indicators of R&D models in the automotive battery industry were determined. In this section, the performance characteristic of each model could be measured by converting verbal variables into quantitative values using the fuzzy COPRAS technique. For this purpose, by distributing and collecting the relevant questionnaires and implementing them step by step, the proposed method of ranking 10 models identified as:

1- R&D outsourcing model (A1);
2- R&D capital attraction model (A2);
3- R&D fully integrated model (A3);
4- Internal R&D model (A4);
5- R&D intrinsic need-driven advanced (A5);
6- R&D roadmap driven model (A6);

**TABLE 4.** Results related to local optimal weights of the main criteria

| | $\tilde{S}_j$ | $\tilde{k}_j$ | $\tilde{q}_j$ | $\tilde{w}_j$ | $w_j^{Crisp}$ |
|---|---|---|---|---|---|
| Technical ($R_3$) | | (1,1,1) | (1,1,1) | (0.328,0.335,0.404) | 0.335 |
| Market ($R_2$) | (0.283,0.333,0.408) | (1.283,1.333,1.408) | (0.710,0.750,0.779) | (0.254,0.325,0.345) | 0.325 |
| Process ($R_4$) | (0.377,0.467,0.613) | (1.377,1.467,1.613) | (0.440,0.511,0.566) | (0.158,0.208,0.229) | 0.208 |
| Quality( $R_1$) | (0.260,0.300,0.354) | (1.260,1.1300,1.354) | (0.325,0.393,0.449) | (0.116,0.132,0.181) | 0.132 |

**TABLE 5.** Optimal global weights indicators evaluation models

| Main dimensions | Local weight main dimensions | Under the criteria | Local weight of each sub-criterion | $w_j^{Final}$ | Rank |
|---|---|---|---|---|---|
| | | Durability and longevity ($R_{11}$) | 0.589 | 0.078 | 6 |
| Quality ($R_1$) | 0.132 | Weight and dimensions ($R_{12}$) | 0.167 | 0.022 | 12 |
| | | Service & product innovation ($R_{13}$) | 0.224 | 0.032 | 11 |
| | | Market share ($R_{21}$) | 0.167 | 0.054 | 8 |
| Market ($R_2$) | 0.325 | Price ($R_{22}$) | 0.461 | 0.150 | 2 |
| | | Brand ($R_{23}$) | 0.372 | 0.121 | 3 |
| | | Amount of combination with other operations ($R_{31}$) | 0.567 | 0.190 | 1 |
| Technical ($R_3$) | 0.335 | Compatibility with technology ($R_{32}$) | 0.290 | 0.097 | 4 |
| | | Safety ($R_{33}$) | 0.144 | 0.048 | 9 |
| | | Warranty ($R_{41}$) | 0.461 | 0.096 | 5 |
| Process ($R_4$) | 0.208 | Ease of access to sales centers ($R_{42}$) | 0.372 | 0.077 | 7 |
| | | Cooperation with car assistance ($R_{43}$) | 0.167 | 0.035 | 10 |

7- Invest in R&D (IRAD) model (A7);
8- R&D transition look ahead model (A8);
9- R&D attraction of financial support model (A9);
10- Joint R&D (JRAD) model (A10).

After achieving the priority of each expert, in the next step, the average of the degrees is calculated, and the average fuzzy decision matrix is obtained according to Table 6. The initial gray decision matrix needs to be converted to a comparable scale to ensure consistency between the evaluation criteria.

Therefore, the normal weighted fuzzy decision matrix is obtained by using Equations (12)-(14) as shown in Table 7. Ultimately, following Table 8, the performance values $\tilde{R}_i$, $\tilde{P}_i$ and the features $Q_i$ and $N_i$ are calculated employing Equations (15), (16), (18), and (20), respectively.

As is deducted from the results, the "joint R&D model (JRAD)" is chosen as the optimal model because of enjoying the highest degree of desirability (utility).

**5. 3. Optimal Allocation of Models: Solving Mathematical Model** In this part, a set of R&D models will be allocated to each manufacturer via solving a mathematical programming model. It is worth mentioning that the collection of manufacturers includes the companies, namely Saba battery, Faraz battery, Pasargad battery, Durna Aras battery, Aco battery, Azar battery, Niru Gostaran battery, and Vaya battery.

The input parameters of the examined problem can be observed in Tables 9-14. Subsequently, the results of how to allocate R&D models to each manufacturer are provided after solving the problem.

The $\varepsilon$-constraint method is exploited in GAMS software version 24.3 and the CPLEX solver to solve the suggested mathematical model. To solve the problem and reach the ideal positive and negative values, each time one of the objective functions is used as the basis, and the next objective function is inserted into the bounds with the limit $\varepsilon$. After solving the model based on the described method, the upper bound is determined by the basis of the first objective function (*i.e.*, maximization) and the lower bound by the basis of the second objective function (*i.e.*, minimization).

**TABLE 6.** Fuzzy initial decision matrix option-criterion

| | $R_{11}$ | $R_{12}$ | $R_{13}$ | $R_{21}$ | $R_{22}$ | $R_{23}$ |
|---|---|---|---|---|---|---|
| $A_1$ | (10,16,22) | (18,23,27.5) | (19,26,30) | (14,20,26) | (14,20,26) | (10,16,22) |
| $A_2$ | (20,26,32) | (16,22,28) | (12,16,21) | (18,24,30) | (30,35,37.5) | (32,37,38.5) |
| $A_3$ | (12,18,24) | (26,31,35.5) | (24,30,35) | (26,32,35) | (22,28,32) | (20,26,30) |
| $A_4$ | (16,22,28) | (18,24,30) | (7,12,18) | (12,18,24) | (18,23,27.5) | (24,30,35) |
| $A_5$ | (24,30,33) | (24,30,35) | (16,22,27) | (22,28,33) | (22,28,32) | (22,28,33) |
| $A_6$ | (26,30,33) | (10,16,22) | (18,24,30) | (20,26,31) | (24,30,34) | (26,31,34.5) |
| $A_7$ | (20,26,31) | (16,22,27) | (14,20,26) | (14,20,25) | (18,24,29) | (24,30,35) |
| $A_8$ | (14,20,26) | (16,22,28) | (18,24,30) | (20,26,31) | (24,30,35) | (24,29,33.5) |
| $A_9$ | (20,26,31) | (20,26,31) | (24,29,32.5) | (22,27,31.5) | (28,34,37) | (36,39,39.5) |
| $A_{10}$ | (14,20,25) | (22,28,33) | (26,31,35.5) | (30,35,37.5) | (26,32,35) | (30,35,37.5) |
| | $R_{31}$ | $R_{32}$ | $R_{33}$ | $R_{41}$ | $R_{42}$ | $R_{43}$ |
| $A_1$ | (10,16,22) | (20,25,28.5) | (18,24,29) | (16,22,28) | (14,20,25) | (10,16,22) |
| $A_2$ | (20,26,31) | (15,20,26) | (16,20,24) | (13,18,24) | (34,37,38.5) | (30,36,38) |
| $A_3$ | (14,20,25) | (24,30,34) | (24,30,34) | (20,26,30) | (20,26,30) | (18,24,29) |
| $A_4$ | (16,22,28) | (10,14,20) | (15,20,26) | (16,22,28) | (22,27,31.5) | (32,36,38) |
| $A_5$ | (14,20,26) | (24,30,34) | (14,18,23) | (18,24,28) | (30,34,36) | (28,33,35.5) |
| $A_6$ | (20,25,29.5) | (17,22,27) | (19,24,28) | (24,30,34) | (18,23,27.5) | (10,16,22) |
| $A_7$ | (22,28,32) | (26,32,35) | (20,26,31) | (22,28,32) | (16,22,28) | (18,23,27.5) |
| $A_8$ | (24,29,32.5) | (17,21,25.5) | (11,16,22) | (18,24,30) | (20,25,28.5) | (14,20,26) |
| $A_9$ | (28,32,34) | (10,14,20) | (16,20,24) | (15,20,26) | (26,30,33) | (14,20,25) |
| $A_{10}$ | (28,34,37) | (24,30,34) | (23,28,31) | (26,32,35) | (6,12,18) | (20,26,32) |

**TABLE 7.** Normalized decision matrix option-criterion

| | $R_{11}$ | $R_{12}$ | $R_{13}$ | $R_{21}$ | $R_{22}$ | $R_{23}$ |
|---|---|---|---|---|---|---|
| $A_1$ | (0.005,0.008,0.011) | (0.004,0.005,0.006) | (0.007,0.01,0.011) | (0.006,0.009,0.011) | (0.011,0.016,0.021) | (0.006,0.009,0.012) |
| $A_2$ | (0.01,0.013,0.016) | (0.004,0.005,0.007) | (0.005,0.006,0.008) | (0.008,0.011,0.013) | (0.025,0.029,0.031) | (0.018,0.02,0.021) |
| $A_3$ | (0.006,0.009,0.012) | (0.006,0.007,0.008) | (0.009,0.011,0.013) | (0.011,0.014,0.015) | (0.018,0.023,0.026) | (0.011,0.014,0.017) |
| $A_4$ | (0.008,0.011,0.014) | (0.004,0.006,0.007) | (0.003,0.005,0.007) | (0.005,0.008,0.011) | (0.015,0.019,0.023) | (0.013,0.017,0.019) |
| $A_5$ | (0.012,0.015,0.017) | (0.006,0.007,0.008) | (0.006,0.008,0.01) | (0.01,0.012,0.015) | (0.018,0.023,0.026) | (0.012,0.015,0.018) |
| $A_6$ | (0.013,0.015,0.017) | (0.002,0.004,0.005) | (0.007,0.009,0.011) | (0.009,0.011,0.014) | (0.02,0.025,0.028) | (0.014,0.017,0.019) |
| $A_7$ | (0.01,0.013,0.016) | (0.004,0.005,0.006) | (0.005,0.008,0.01) | (0.006,0.009,0.011) | (0.015,0.02,0.024) | (0.013,0.017,0.019) |
| $A_8$ | (0.007,0.01,0.013) | (0.004,0.005,0.007) | (0.007,0.009,0.011) | (0.009,0.011,0.014) | (0.02,0.025,0.029) | (0.013,0.016,0.019) |
| $A_9$ | (0.01,0.013,0.016) | (0.005,0.006,0.007) | (0.009,0.011,0.012) | (0.01,0.012,0.014) | (0.023,0.028,0.03) | (0.02,0.022,0.022) |
| $A_{10}$ | (0.007,0.01,0.013) | (0.005,0.007,0.008) | (0.01,0.012,0.013) | (0.013,0.015,0.017) | (0.021,0.026,0.029) | (0.017,0.019,0.021) |
| | $R_{31}$ | $R_{32}$ | $R_{33}$ | $R_{41}$ | $R_{42}$ | $R_{43}$ |
| $A_1$ | (0.012,0.019,0.026) | (0.018,0.023,0.026) | (0.013,0.017,0.021) | (0.01,0.014,0.018) | (0.006,0.008,0.011) | (0.003,0.005,0.007) |
| $A_2$ | (0.023,0.03,0.036) | (0.014,0.018,0.024) | (0.011,0.014,0.017) | (0.008,0.011,0.015) | (0.014,0.016,0.016) | (0.01,0.011,0.012) |
| $A_3$ | (0.016,0.023,0.029) | (0.022,0.027,0.031) | (0.017,0.021,0.024) | (0.013,0.017,0.019) | (0.008,0.011,0.013) | (0.006,0.008,0.009) |
| $A_4$ | (0.019,0.026,0.033) | (0.009,0.013,0.018) | (0.011,0.014,0.018) | (0.01,0.014,0.018) | (0.009,0.011,0.013) | (0.01,0.011,0.012) |
| $A_5$ | (0.016,0.023,0.03) | (0.022,0.027,0.031) | (0.01,0.013,0.016) | (0.011,0.015,0.018) | (0.013,0.014,0.015) | (0.009,0.01,0.011) |
| $A_6$ | (0.023,0.029,0.035) | (0.015,0.02,0.025) | (0.013,0.017,0.02) | (0.015,0.019,0.022) | (0.008,0.01,0.012) | (0.003,0.005,0.007) |
| $A_7$ | (0.026,0.033,0.037) | (0.024,0.029,0.032) | (0.014,0.018,0.022) | (0.014,0.018,0.02) | (0.007,0.009,0.012) | (0.006,0.007,0.009) |
| $A_8$ | (0.028,0.034,0.038) | (0.015,0.019,0.023) | (0.008,0.011,0.016) | (0.011,0.015,0.019) | (0.008,0.011,0.012) | (0.004,0.006,0.008) |
| $A_9$ | (0.033,0.037,0.04) | (0.009,0.013,0.018) | (0.011,0.014,0.017) | (0.01,0.013,0.017) | (0.011,0.013,0.014) | (0.004,0.006,0.008) |
| $A_{10}$ | (0.033,0.04,0.043) | (0.022,0.027,0.031) | (0.016,0.02,0.022) | (0.017,0.02,0.022) | (0.003,0.005,0.008) | (0.006,0.008,0.01) |

**TABLE 8.** Degree of the desirability of the R&D models

| | $P_i^{Crisp}$ | $R_i^{Crisp}$ | $Q_i$ | $N_i$ | Rank |
|---|---|---|---|---|---|
| $A_1$ | 0.135 | 0.008 | 0.151 | 72% | 10 |
| $A_2$ | 0.171 | 0.013 | 0.181 | 86% | 4 |
| $A_3$ | 0.175 | 0.009 | 0.190 | 90% | 2 |
| $A_4$ | 0.143 | 0.011 | 0.155 | 74% | 9 |
| $A_5$ | 0.168 | 0.015 | 0.177 | 84% | 6 |
| $A_6$ | 0.165 | 0.015 | 0.174 | 83% | 8 |
| $A_7$ | 0.171 | 0.013 | 0.181 | 86% | 5 |
| $A_8$ | 0.162 | 0.010 | 0.175 | 83% | 7 |
| $A_9$ | 0.174 | 0.013 | 0.184 | 87% | 3 |
| $A_{10}$ | 0.198 | 0.010 | 0.211 | 100% | 1 |

As previously described, the ε-constraint method solves the evolved constraint by considering one of the objective functions as the main objective function and the other objective functions in the constraint problem, and it remains to be seen what effect this approach will have on the objective function values. Based on this information, the mathematical problem designed by the 200 iterations of the Epsilon constraint method is solved, and the Pareto front gained from the two objective functions is shown in Figure 2. The number of cuts is assumed to be 100 and considering that the problem model is zero and one, each cut is a single step.

**TABLE 9.** Capital required to implement the model in the manufacturer

| $W_{mn}$ | $M_1$ | $M_2$ | $M_3$ | $M_4$ | $M_5$ | $M_6$ | $M_7$ | $M_8$ |
|---|---|---|---|---|---|---|---|---|
| $A_1$ | 17,600 | 27,164 | 13,306 | 13,252 | 16,736 | 23,504 | 12,202 | 28,340 |
| $A_2$ | 20,676 | 15,645 | 13,168 | 19,956 | 20,727 | 24,689 | 14,196 | 18,205 |
| $A_3$ | 10,159 | 17,964 | 14,547 | 10,868 | 14,699 | 11,146 | 16,226 | 20,011 |
| $A_4$ | 14,727 | 24,801 | 19,047 | 26,852 | 11,867 | 25,400 | 23,871 | 25,711 |
| $A_5$ | 24,102 | 19,156 | 24,945 | 27,905 | 26,957 | 22,437 | 23,582 | 26,316 |
| $A_6$ | 28,810 | 20,392 | 13,714 | 15,729 | 11,999 | 15,339 | 23,180 | 14,405 |
| $A_7$ | 25,074 | 11,448 | 12,084 | 27,917 | 29,406 | 11,837 | 29,109 | 21,003 |
| $A_8$ | 26,402 | 14,550 | 25,184 | 21,199 | 28,946 | 23,065 | 20,320 | 27,216 |
| $A_9$ | 16,582 | 26,763 | 17,841 | 28,148 | 13,177 | 11,488 | 27,798 | 16,569 |
| $A_{10}$ | 27,853 | 16,767 | 20,497 | 20,556 | 12,048 | 26,560 | 14,700 | 21,890 |

**TABLE 10.** Number of sales expected from the implementation of the model in the manufacturer

| $L_{mn}$ | $M_1$ | $M_2$ | $M_3$ | $M_4$ | $M_5$ | $M_6$ | $M_7$ | $M_8$ |
|---|---|---|---|---|---|---|---|---|
| $A_1$ | 26,524 | 13,452 | 25,167 | 20,354 | 27,523 | 19,318 | 23,197 | 12,360 |
| $A_2$ | 10,076 | 29,112 | 28,759 | 25,523 | 11,988 | 10,441 | 18,194 | 23,524 |
| $A_3$ | 13,573 | 16,586 | 22,882 | 19,472 | 13,072 | 19,130 | 14,054 | 15,423 |
| $A_4$ | 24,086 | 25,912 | 21,147 | 12,677 | 13,210 | 11,601 | 20,172 | 14,555 |
| $A_5$ | 16,678 | 23,654 | 17,300 | 28,989 | 25,848 | 27,050 | 16,793 | 25,229 |
| $A_6$ | 16,844 | 12,169 | 25,134 | 13,251 | 18,991 | 20,231 | 29,227 | 12,477 |
| $A_7$ | 27,421 | 25,603 | 10,631 | 26,478 | 12,407 | 15,761 | 17,100 | 26,314 |
| $A_8$ | 29,638 | 19,141 | 17,526 | 16,826 | 23,851 | 12,286 | 23,949 | 10,879 |
| $A_9$ | 17,497 | 26,385 | 11,393 | 29,989 | 13,550 | 19,292 | 29,060 | 29,258 |
| $A_{10}$ | 21,585 | 22,801 | 21,506 | 11,317 | 28,285 | 13,383 | 27,172 | 17,623 |

**TABLE 11.** Risk of customer dissatisfaction with the implementation of the model in the manufacturer

| $R_{mn}$ | $M_1$ | $M_2$ | $M_3$ | $M_4$ | $M_5$ | $M_6$ | $M_7$ | $M_8$ |
|---|---|---|---|---|---|---|---|---|
| $A_1$ | 0.6138 | 0.6552 | 0.8635 | 0.8012 | 0.6844 | 0.7898 | 0.9141 | 0.7500 |
| $A_2$ | 0.6477 | 0.8741 | 0.8118 | 0.8142 | 0.6281 | 0.6075 | 0.7765 | 0.6699 |
| $A_3$ | 0.9338 | 0.6784 | 0.6071 | 0.8645 | 0.8791 | 0.6446 | 0.8580 | 0.6914 |
| $A_4$ | 0.6951 | 0.7340 | 0.9102 | 0.8676 | 0.6427 | 0.6479 | 0.6218 | 0.9456 |
| $A_5$ | 0.9335 | 0.6649 | 0.8782 | 0.8792 | 0.8157 | 0.7533 | 0.8530 | 0.6573 |
| $A_6$ | 0.8844 | 0.7209 | 0.6821 | 0.6310 | 0.9265 | 0.7555 | 0.7558 | 0.6090 |
| $A_7$ | 0.6811 | 0.8733 | 0.6550 | 0.6304 | 0.8265 | 0.7831 | 0.9216 | 0.6468 |
| $A_8$ | 0.8621 | 0.6728 | 0.7405 | 0.8698 | 0.6108 | 0.8620 | 0.9243 | 0.6613 |
| $A_9$ | 0.9474 | 0.6862 | 0.8123 | 0.8310 | 0.6622 | 0.7302 | 0.9451 | 0.7605 |
| $A_{10}$ | 0.6543 | 0.7919 | 0.8437 | 0.8247 | 0.7586 | 0.8954 | 0.7200 | 0.8787 |

**TABLE 12.** Probability of risk of customer dissatisfaction with the implementation of the model in the manufacturer

| $P_{mn}$ | $M_1$ | $M_2$ | $M_3$ | $M_4$ | $M_5$ | $M_6$ | $M_7$ | $M_8$ |
|---|---|---|---|---|---|---|---|---|
| $A_1$ | 0.7191 | 0.6575 | 0.7187 | 0.7307 | 0.5926 | 0.7009 | 0.6343 | 0.6820 |
| $A_2$ | 0.6617 | 0.6193 | 0.5592 | 0.7039 | 0.5601 | 0.6493 | 0.5510 | 0.7464 |
| $A_3$ | 0.6558 | 0.6399 | 0.5606 | 0.7121 | 0.6431 | 0.5896 | 0.6673 | 0.7159 |
| $A_4$ | 0.6702 | 0.5623 | 0.7335 | 0.6111 | 0.7437 | 0.7492 | 0.7297 | 0.6910 |
| $A_5$ | 0.6622 | 0.7261 | 0.7040 | 0.5975 | 0.6245 | 0.6327 | 0.6135 | 0.6132 |
| $A_6$ | 0.6814 | 0.5840 | 0.6105 | 0.6115 | 0.6088 | 0.5943 | 0.5868 | 0.7411 |
| $A_7$ | 0.6679 | 0.6919 | 0.5618 | 0.6721 | 0.5500 | 0.7058 | 0.6524 | 0.5532 |
| $A_8$ | 0.6807 | 0.6324 | 0.7237 | 0.7113 | 0.5798 | 0.6130 | 0.7477 | 0.6353 |
| $A_9$ | 0.5849 | 0.6254 | 0.6812 | 0.6379 | 0.6439 | 0.6722 | 0.6005 | 0.5782 |
| $A_{10}$ | 0.7239 | 0.7389 | 0.7026 | 0.5758 | 0.6298 | 0.7077 | 0.6757 | 0.5702 |

**TABLE 13.** Number of models allowed to be assigned to each manufacturer

| | $M_1$ | $M_2$ | $M_3$ | $M_4$ | $M_5$ | $M_6$ | $M_7$ | $M_8$ |
|---|---|---|---|---|---|---|---|---|
| $D_n$ | 2 | 3 | 1 | 2 | 3 | 3 | 2 | 1 |

**TABLE 14.** Budget available to any manufacturer

| $M_1$ | $M_2$ | $M_3$ | $M_4$ |
|---|---|---|---|
| 68,000 | 73,250 | 51,050 | 65,500 |
| **$M_5$** | **$M_6$** | **$M_7$** | **$M_8$** |
| 49,500 | 56,850 | 63,250 | 65,250 |

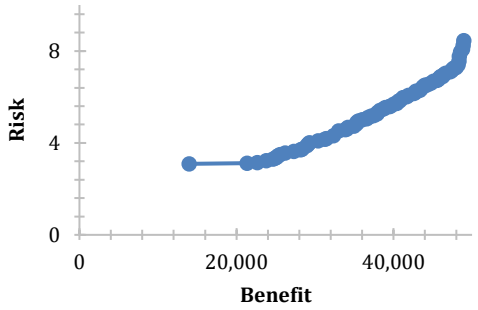


**Figure 2.** Pareto chart created based on benefit and risk goals

After presenting the results to the experts and considering the values obtained for the objective functions, the experts found consensus on choosing the best answer from the 76 points on the Pareto front, presented in Table 15. Also, the mode of allocation of models to each manufacturer will be described in Table 16.

**TABLE 15.** Optimal value of the objective function based on the common opinion of experts

| Benefit ($Z_1$) | Risk( $Z_2$) |
|---|---|
| 37,152 | 5.17 |

**TABLE 16.** Assigning the R&D models to each manufacture

| Model | Manufacturer | | | | | | | |
|---|---|---|---|---|---|---|---|---|
| | 1 | 2 | 3 | 4 | 5 | 6 | 7 | 8 |
| $A_1$ | | | | | | | | |
| $A_2$ | ✓ | | | | ✓ | | | |
| $A_3$ | | | | | | | | |
| $A_4$ | | ✓ | | | | ✓ | | |
| $A_5$ | | | | | | | | |
| $A_6$ | | | ✓ | | | | ✓ | |
| $A_7$ | | | | ✓ | | | | ✓ |
| $A_8$ | | | | | | ✓ | | |
| $A_9$ | | ✓ | | | | | | |
| $A_{10}$ | ✓ | ✓ | | | ✓ | | | |

## 6. CONCLUSION AND FURTHER SUGGESTIONS

Nowadays, numerous firms have encountered challenges in strengthening and enhancing their competitiveness to survive in a competitive business environment. In the meantime, only companies that take advantage of key capabilities and comparative advantages have achieved sustainable success. In creating competitive advantages, R&D model formulation activities play a very important

role. Because the model planning process of R&D must be done before product design and development, so far limited structured methodologies have been used in this field. therefore, Therefore, in this study, a new fuzzy model for evaluating and selecting R&D models in the automotive battery industry is proposed. First, expert and research committees were selected. According to the previous literature as well as the opinion of experts, the final indicators for evaluating R&D models using the Delphi technique and brainstorming in four categories of quality, market, technical and process were identified and finalized.

In the second stage, after allocating the experts' subjective preferences to the criteria, the final weight of the criteria was calculated through the fuzzy SWARA (Stepwise Weight Assessment Ratio Analysis) technique. In addition, the weight of each model and their final prioritization were determined using the fuzzy Complex Proportional Assessment (COPRAS) method. Based on the results obtained from the fuzzy SWARA method, the three influential factors in evaluating R&D models in the automotive battery industry include the following items, respectively: "The amount of combination with other operations", "Price", and "Brand". Furthermore, the "joint R&D model" was recognized as the superior model because of the optimal level of the optimal membership. Also, the "R&D outsourcing model" gained the least importance among R&D models in the automotive battery industry. Eventually, Zero-One Goal Programming (ZOGP) in an assignment of each model to the manufacturers of the country's battery industry was obtained by presenting and solving a bi-objective mathematical model. Accordingly, the "joint R&D model" in companies 1, 2 and 5 enjoys the highest numbers of frequency.

Some other Multi-Criteria Decision-Making (MCDM) approaches in other uncertainty environments, such as fuzzy intuitions, Z numbers, etc., could be employed in further studies and compared the obtained results with each other. Besides, some inputs of the proposed mathematical model (e.g., the parameter of cost) in uncertainty conditions could be considered. Fuzzy Goal Programming (FGP) or robust Programming could be exploited to fix this problem.

## 7. REFERENCES


1. Azoulay, P., Graff Zivin, J.S., Li, D. and Sampat, B.N., "Public r&d investments and private-sector patenting: Evidence from nih funding rules", ***The Review of Economic Studies***, Vol. 86, No. 1, (2019), 117-152. doi: 10.1093/restud/rdy034.
2. Kayserili ,A. and Kiyak, M., "Evaluation of r&d activities and the perspectives of the participants of pharmaceutical companies on r&d in turkey", ***Hacettepe University Journal of the Faculty of Pharmacy***, Vol. 39, No. 2, (2019), 65-80. https://dergipark.org.tr/en/download/article-file/1102229
3. Carboni, O.A., "The effect of public support on investment and r&d: An empirical evaluation on european manufacturing firms", ***Technological Forecasting and Social Change***, Vol. 117, (2017), 282-295. doi: 10.1016/j.techfore.2016.11.017.
4. Salimi, N. and Rezaei, J., "Evaluating firms' r&d performance using best worst method", ***Evaluation and Program Planning***, Vol. 66, (2018), 147-155. doi: 10.1016/j.evalprogplan.2017.10.002 .
5. Lazzarotti, V., Manzini, R. and Mari, L., "A model for r&d performance measurement", ***International Journal of Production Economics***, Vol. 134, No. 1, (2011), 212-223. doi: 10.1016/j.ijpe.2011.06.018 .
6. Kerssens-van Drongelen, I.c. and Bilderbeek, J., "R&d performance measurement: More than choosing a set of metrics", ***R&D Management***, Vol. 29, No. 1, (1999), 35-46. doi: 10.1111/1467-9310.00115 .
7. Moncada-Paternò-Castello, P., Ciupagea, C., Smith, K., Tübke, A. and Tubbs, M., "Does europe perform too little corporate r&d? A comparison of eu and non-eu corporate r&d performance", ***Research Policy***, Vol. 39, No. 4, (2010), 523-536. doi: 10.1016/j.respol.2010.02.012 .
8. Tidd, J. and Bessant, J.R., "Managing innovation: Integrating technological, market and organizational change, John Wiley & Sons.(2020) ,
9. Griffin, A., "Pdma research on new product development practices: Updating trends and benchmarking best practices", ***Journal of Product Innovation Management: An International Publication of The Product Development & Management Association***, Vol. 14, No. 6, (1997), 429-458. doi: 10.1016/S0737-6782(97)00061-1 .
10. Simao, L. and Franco, M., Understanding the influence of r&d collaboration on organizational innovation: Empirical evidences, in Disruptive technology: Concepts, methodologies, tools, and applications. 2020, IGI Global.1983-2005.
11. IAE, E., *Innovation in batteries and electricity storage, a global analysis based on patent data*. 2020, septembre.
12. Lukach, R., Kort, P.M. and Plasmans, J., "Optimal r&d investment strategies under the threat of new technology entry", ***International Journal of Industrial Organization***, Vol. 25, No. 1, (2007), 103-119. doi: 10.1016/j.ijindorg.2006.02.002 .
13. Penan, H., "R & d strategy in a techno-economic network: Alzheimer's disease therapeutic strategies", ***Research Policy***, Vol. 25, No. 3, (1996), 337-358. doi: 10.1016/0048-7333(95)00833-0 .
14. Aldieri, L., Sena, V. and Vinci, C.P., "Domestic r&d spillovers and absorptive capacity: Some evidence for us, europe and japan", ***International Journal of Production Economics***, Vol. 198, (2018), 38-49. doi: 10.1016/j.ijpe.2018.01.015.
15. Lampert, C.M. and Kim, M., "Going far to go further: Offshoring, exploration, and r&d performance", ***Journal of Business Research***, Vol. 103, (2019), doi: 10.1016/j.jbusres.2018.01.007.
16. Steinberg, P.J., Procher, V.D. and Urbig, D., "Too much or too little of r&d offshoring: The impact of captive offshoring and contract offshoring on innovation performance", ***Research Policy***, Vol. 46, No. 10, (2017), 1810-1823, doi: 10.1016/j.respol.2017.08.008 .
17. Brady, M.K. and Cronin Jr, J.J., "Customer orientation: Effects on customer service perceptions and outcome behaviors", ***Journal of Service Research***, Vol. 3, No. 3, (2001), 241-251. doi: 10/1016.S0148-2963(00)00171-5.
18. Ritu, S., Jatinder, K., Jaspreet, S. and Niraj, S., Effect of internal customer satisfaction index on revamping of iso implementation structure in a r&d organization, in Decision analytics applications in industry. 2020, Springer.13-20.

19. Soltanzadeh, J., Elyasi, M., Ghaderifar, E., Soufi, H.R. and Khoshsirat, M., "Evaluation of the effect of r&d subsidies on iranian firms' innovative behavior: Reconceptualizing behavioral additionality", ***Journal of Science and Technology Policy Management***, (2019). doi: 10.1108/JSTPM-11-2018-0109.
20. Liu, H.-h., Yang, G.-l., Liu, X.-x. and Song, Y.-y., "R&d performance assessment of industrial enterprises in china: A two-stage dea approach", ***Socio-Economic Planning Sciences*** ,Vol. 71, (2020), 100753. doi: 10.1016/j.seps.2019.100753.
21. Sinimole, K. and Saini, K.M., "Performance evaluation of r&d organisations: An asian perspective", ***International Journal of the Economics of Business***, Vol. 28, No. 2, (2021), 179-196, doi: 10.1080/13571516.2020.1858703.
22. Chachuli, F.S.M., Mat, S., Ludin, N.A. and Sopian, K., "Performance evaluation of renewable energy r&d activities in malaysia", ***Renewable Energy***, Vol. 163, (2021), 544-560. doi: 10.1016/j.renene.2020.08.160.
23. Koçak, E., Kınacı, H. and Shehzad, K., "Environmental efficiency of disaggregated energy r&d expenditures in oecd: A bootstrap dea approach", ***Environmental Science and Pollution Research***, Vol. 28, No. 15, (2021), 19381-19390. doi: 10.1007/s11356-02-0-12132w.
24. Mete, M.H. and Belgin, O., "Impact of knowledge management performance on the efficiency of r&d active firms: Evidence from turkey", ***Journal of the Knowledge Economy***, Vol. 13, No. 2, (2022), 830-848. doi: 10.1007/s13132-021-00758-1.
25. Dai, H., Jiang, B., Hu, X., Lin, X., Wei, X. and Pecht, M., "Advanced battery management strategies for a sustainable energy future: Multilayer design concepts and research trends", ***Renewable and Sustainable Energy Reviews***, Vol. 138, (2021), 110480, doi: 10.1016/j.rser.2020.110480.
26. Velásquez, G., Rethinking r&d for pharmaceutical products after the novel coronavirus covid-19 shock, in Vaccines, medicines and covid-19. 2022, Springer.59-72.
27. Amarasekara, C., Iyke, B.N. and Narayan, P.K., "The role of r&d and economic policy uncertainty in sri lanka's economic growth", ***Financial Innovation***, Vol. 8, No. 1, (2022), 1-19. doi: 10.1186/s40854-021-00322-5.
28. Belderbos, R., Lokshin, B., Boone, C. and Jacob, J., "Top management team international diversity and the performance of international r&d", ***Global Strategy Journal***, Vol. 12, No. 1, (2022), 108-133. doi: 10.1002/gsj.1395 .
29. Karamaşa, Ç., "Ranking service quality using multi-criteria decision-making methods: Example of erzurum province ," ***Journal of Process Management and New Technologies***, Vol. 9, No. 3-4, (2021), 1-12. doi: 10.5937/jpmnt9-33449.
30. Baç, U., "An integrated swara-waspas group decision making framework to evaluate smart card systems for public transportation", ***Mathematics***, Vol. 8, No. 10, (2020), 1723. doi: 10.3390/math8101723.
31. Khalili, J. and Alinezhad, A., "Performance evaluation in aggregate production planning using integrated red-swara method under uncertain condition", ***Scientia Iranica***, Vol. 28, No. 2, (2021), 912-926, doi: 10.24200/sci.2020.50202.1584.
32. Fenton, N. and Wang, W., "Risk and confidence analysis for fuzzy multicriteria decision making", ***Knowledge-Based Systems***, Vol. 19, No. 6, (2006), 430-437. doi: 10.1016/j.knosys.2006.03.002.
33. Vincent ,F.Y. and Hu, K.-J., "An integrated fuzzy multi-criteria approach for the performance evaluation of multiple manufacturing plants", ***Computers & Industrial Engineering***, Vol. 58, No. 2, (2010), 269-277. doi: 10.1016/j.cie.2009.10.005.
34. Liao, M.-S., Liang, G.-S. and Chen, C.-Y., "Fuzzy grey relation method for multiple criteria decision-making problems", ***Quality & Quantity***, Vol. 47, No. 6, (2013), 3065-3077. doi: 10.1007/s11135-012-9704-5.
35. Zhao, H. and Guo, S., "Selecting green supplier of thermal power equipment by using a hybrid mcdm method for sustainability", ***Sustainability***, Vol. 6, No. 1, (2014), 217-235. doi: 10.3390/su6010217.
36. Keršuliene, V., Zavadskas, E.K. and Turskis, Z., "Selection of rational dispute resolution method by applying new step-wise weight assessment ratio analysis (SWARA)", ***Journal of Business Economics and Management***, Vol. 11, No. 2, (2010), 243-258. doi: 10.3846/jbem.2010.12.
37. Mavi, R.K., Goh, M. and Zarbakhshnia, N., "Sustainable third-party reverse logistic provider selection with fuzzy swara and fuzzy moora in plastic industry", ***The International Journal of Advanced Manufacturing Technology***, Vol. 91, No. 5, (2017), 2401-2418. doi: 10.1007/s00170-016-9880-x.
38. Kaklauskas, A., Zavadskas, E.K., Raslanas, S ,.Ginevicius, R., Komka, A. and Malinauskas, P., "Selection of low-e windows in retrofit of public buildings by applying multiple criteria method copras: A lithuanian case", ***Energy and Buildings***, Vol. 38, No. 5, (2006), 454-462. doi: 10.1016/j.enbuild.2005.08.005.
39. Zarbakhshnia, N., Soleimani, H. and Ghaderi, H., "Sustainable third-party reverse logistics provider evaluation and selection using fuzzy swara and developed fuzzy copras in the presence of risk criteria", ***Applied Soft Computing***, Vol. 65, (2018), 307-319. doi: 10.1016/j.asoc.2018.01.023.
40. Collette, Y. and Siarry, P., "Multiobjective optimization: Principles and case studies, Springer Science & Business Media, (2004).
41. Babbar, C. and Amin, S.H., "A multi-objective mathematical model integrating environmental concerns for supplier selection and order allocation based on fuzzy qfd in beverages industry", ***Expert Systems with Applications***, Vol. 92, (2018), 27-38. doi: 10.1016/j.eswa.2017.09.041.

## Persian Abstract

**چکیده**

اندازه گیری عملکرد تحقیق و توسعه و تخصیص میزان اهمیت یکسان به اقدامات مختلف تحقیق و توسعه می تواند فرآیند اندازه گیری آن را بیش از حد ساده کند، که ممکن است منجر به تفسیر نادرست از عملکرد و در نتیجه منجر به تفسیر اشتباه مدل های تحقیق و توسعه شود. تحقیق و توسعه شامل کار های خلاقانه ای است که به صورت سیستماتیک به منظور افزایش ذخایر دانش از جمله دانش انسان، فرهنگ و جامعه و استفاده از این انبار دانش برای ابداع برنامه های کاربردی جدید انجام می شود. هدف از این پژوهش ارائه رویکردی دو مرحله‌ای جهت طراحی مدل تحقیق و توسعه در صنایع باتری‌سازی خودرو با تأکید بر رضایت مشتریان است. با توجه به نقش مهم تحقیق و توسعه در رضایت مشتری، مطالعه ای در این زمینه و صنعت انجام نشده است. در بخش نخست ابتدا مدل های مؤثر بر مدیریت تحقیق و توسعه و شاخص های اثرگذار رضایت‌مندی مشتریان بر مدل های تحقیق و توسعه شناسایی می‌شوند. در بخش دوم ضرایب معنی داری مربوط به شاخص های رضایت‌مندی مشتریان از طریق به کارگیری روش تصمیم‌گیری چند معیاره سوارا فازی نتیجه می‌گردد. علاوه بر این اهمیت و اولویت نهایی هر مدل با استفاده از روش کوپراس فازی محاسبه می‌شوند. در نهایت، برای اعمال چارچوب پیشنهادی در صنعت تولید باتری، یک مدل تحقیق و توسعه دو هدفه ارائه شده است. ضرایب به دست آمده با روش کوپراس فازی به عنوان ورودی برای مدل پیشنهادی استفاده می شود. بنابراین، سیاست‌گذاران و مدیران می‌توانند فعالیت های خود را براساس این روش انجام دهند. نتایج به دست آمده نشان داد چارچوب پیشنهادی کارایی مؤثری در مسئله مورد بررسی را دارد.

International Journal of Engineering

Journal Homepage: www.ije.ir

# Natural frequency of Sandwich Beam Structures with Two Dimensional Functionally Graded Porous Layers Based on Novel Formulations

P. Mehdianfar, Y. Shabani, K. Khorshidi*

*Department of Mechanical Engineering, Arak University, Arak, Iran*

*PAPER INFO*

*Paper history:*
Received 04 February 2022
Received in revised form 16 July 2022
Accepted 24 July 2022

*Keywords*:
*Vibration Analysis*
*Porous*
*Two-dimensional Functionally Graded Materials*
*Galerkin Method*
*Sandwich Beam*

*ABSTRACT*

This study presents an analytical solution for free vibration analysis of two-dimensional functionally graded (2D-FG) porous sandwich beams. The equations of motion for the beam were derived using Hamilton's principle, and then the Galerkin method was employed to solve the equations. The material properties of the sandwich beams vary with the thickness and length of each layer according to the power-law function. The mechanical properties gradually changed from aluminum to alumina as the metal and ceramic, respectively. The vibration analysis was investigated based on two new higher-order shear deformation beam theories (NHSDBTs). These two new theories do not need any shear correction factor and have fewer unknown variables than other higher order shear beam theories. The obtained natural frequencies for the three types of beams were compared with the results of the Timoshenko, first-order , and parabolic shear deformation beam theories. In addition, the effects of porosity, L/h, and FG power indexes along the thickness and length on the non-dimensional frequency of three special types of beams are presented and discussed. Furthermore, the mode shapes of the beam are depicted for various FG power indexes based on these new theories. By comparing the results of the two proposed theories with those of existing studies, the accuracy of the proposed theories was validated. Power-law indexes shifted the node point to the left and resonance will be accrued sooner than the non-FGM beam.

***doi***: *10.5829/ije.2022.35.11b.04*

## 1. INTRODUCTION

Functionally graded (FG) materials are usually formed by combining a certain volume ratio with ceramics and metals materials. These materials have been highly discussed among researchers because they include characteristics such as: heat-resistance, toughness, low volumetric mass and high strength. Sandwich structures are widely used in the aerospace, space, shipbuilding and construction industries due to their excellent electrical, thermal and mechanical properties. Research on the different aspects of FG beams has been conducted extensively in recent years [1-3]. Typically, functionally graded material is a compositional gradient but it can also be a microstructural gradient, for instance, porosity gradients. As far as the search for literature goes, a few studies were carried out on the mechanical actions of porous structures [4, 5].

The higher shear deformation theories (HSDT) support transverse shear effects, hence is appropriate for analysis of both moderately thick and thin plates and beams. Vibration behaviours of FG structures have been investigated in many studies. For example, in a study, the free vibration of simply supported functionally graded beams (FGs) whose material properties may be arbitrarily altered in thickness direction has been undertaken by Celebi et al. [6]. In a different work, Lei et al. [7]. examined a size-dependent model of beam to study vibration and bending of FG microbeams with simply supported boundary conditions based on the strain gradient elasticity theory and sinusoidal shear deformation theory. Ke et al. [8]. considered the non-linear free vibration of FG nanotube-reinforced composite beams by employing direct iterative and Ritz method based on the TBT and using von Karman type strain-displacement relationships. Researchers have used various numerical methods to analyze FG beam

*Corresponding Author Institutional Email: k-khorshidi@araku.ac.ir (K. Khorshidi)

Please cite this article as: P. Mehdianfar, Y. Shabani, K. Khorshidi, Natural frequency of Sandwich Beam Structures with 2D-FG Porous Layers Based on Novel Formulations, ***International Journal of Engineering, Transactions B: Applications***, Vol. 35, No. 11, (2022) 2092-2101

vibrations. Free vibration of FGM layered beams under various boundary conditions through the use of finite element method were analyzed by Mashat et al. [9]. Recently, Faghidian [11-13] developed size-dependent elasticity theories such as the nonlocal modified gradient theory [10], the higher-order nonlocal gradient theory for analyzing the mechanical behavior of nanostructures. Shahba and Rajasekaran [14] calculate the longitudinal transverse frequencies of FGM beams applied the differential transform element method (DTEM) and differential quadrature element method (DQEM) of lower order. The vibrational analysis of composite beams is carried out in different studies [15, 16]. Shafiei et al. [17] employed the DQM to investigate vibration of 2D FG Timoshenko nano and micro beams with porosity. Kandil et al. [18] studied sandwich panels with various properties of face and core. They found decreasing thickness of concrete face wythes had a positive effect on strength/weight ratio. Singh and Sangle [19] were studied nonlinear static response of vertically oriented coupled wall with finite element method.

Based on the studies mentioned above, it can be noted that the studies vibration of two-dimensional functionally graded sandwich beams with porosity are very limited. For the first time, natural frequency analysis of the 2D-FG sandwich beams investigated based on two new higher order theories. Vibration analysis of two-dimensional functionally graded beams by considering the porosities that might occur inside the materials with gradient properties during manufacturing process is presented. Three types of sandwich beams were investigated in second section. In the first type, a single-layer 2D-FG porous beam is assumed. The second type is sandwich beam with 2D-FG core and pure metal/ceramic face sheet. FG layers have a smooth and gradual change in mechanical behaviour throughout their length and thickness. On the other hands, the third type we have two 2D-FG layers with porosity as faces and pure ceramic core. In present research, Alumina ($Al_2O_3$) and Aluminium (Al) are considered as ceramic and metal, respectively. Two new beam theories are introduced. results obtained with new higher shear deformation beam theories (NHSDBT1 and 2) show great convergence with Timoshenko (TBT), first-order (FSDBT), and parabolic (PSDBT) shear deformation beam theories. In this paper at first, formulations and types of beams, governing equation of motion and solving method are presented at end of section two. Then, accuracy of our two new higher order formulations is confirmed and the influence of porosity, L/h, shapes, and FG power indexes along thickness and length on non-dimensional natural frequencies on the beams are discussed in the last section. Also, natural frequencies with various beam theories are calculated and results are concluded. Both novels introduced theories are simple than some other higher beam theories because of fewer unknown variables as a result it helps to reduce the time of calculating. Also, one of the other advantages of these two new proposed distributions is that they don't need any shear correction factor and they satisfy free stress conditions at the top and bottom surfaces of the structure.

## 2. PROBLEM AND FORMULATION

**2. 1. Numerical Simulation Procedure** Consider a beam, as shown in Figure 1 with length L, width b, and thickness h, with the Cartesian coordinate system O (x y z), where the origin of coordinate system O is chosen at the left of the beam. The mechanical properties of the beam, such as Young's modulus E (x, z), shear modulus G (x, z), Poisson's modulus υ (x, z), and mass density ρ (x, z), with the material properties can vary along the length and thickness, as shown in Figure 1. In this study, three different types of 2D-FG beam models were considered: isotropic 2D-FG beam (Model I), sandwich beam with homogeneous faces and 2D-FG core (Model II), and sandwich beam with 2D-FG faces and homogeneous ceramic core (Model III).

The effective material properties (P) can be expressed using the rule of mixtures as follows:

$$P(x,z)=P_cR_c(x,z)+P_mR_m(x,z) \tag{1}$$

$$R_c(x,z)+R_m(x,z)=1 \tag{2}$$

where $P_c$ and $P_m$ are the epitomes of the mechanical properties. In addition, $R_c$ and $R_m$ are the volume fractions of ceramic and metal. The effective material properties of the porosity are defined as follows [20]:

$$P(x,z)=(P_c-P_m)R_c+P_m-\left(\frac{\eta}{2}(P_c+P_m)\right) \tag{3}$$

where $\eta$ is porosity volume fraction.

**2. 1. 1. Model Ⅰ: Isotropic 2D-FG Beam** The first beam Model was graded from the metal at the lower left corner edge to the ceramic at the top right corner edge (Figure 2). The volume fraction of the ceramic material is given by Şimşek [21]:

$$R_c(x,z)=\left(\frac{x}{L}\right)^{k_x}\left(\frac{z}{h}+\frac{1}{2}\right)^{k_z} \tag{4}$$

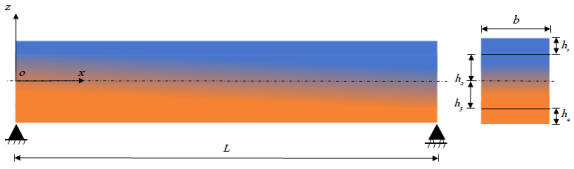


**Figure 1.** Geometry of 2D-FG beam and cross section

**Figure 2.** Isotropic 2D-FG beam, Model I

$k_x$ and $k_z$ are the power laws of the beam, which have certain properties in the length and thickness directions.

**2. 1. 2. Model Ⅱ: Homogeneous Faces and 2D-FG Core** In this Model, the core layer of the sandwich beam is similar to that of Model I, and the bottom and top faces are made of pure metal and pure ceramic as shown in Figure 3. The volume fraction of the ceramic for the second Model is given by the following expression:

$$R_c(x,z)=\begin{Bmatrix} 1 & h_2<z<\dfrac{h}{2} \\ \left(\dfrac{x}{L}\right)^{k_x}\left(\dfrac{h_2-z}{h_2-h_3}\right)^{k_z} & h_3<z<h_2 \\ 0 & -\dfrac{h}{2}<z<h_3 \end{Bmatrix} \quad (5)$$

**2. 1. 3. Model Ⅲ: 2D-FG Faces and Ceramic Core** In Model III, the two 2D-FG skins covered a homogeneous pure ceramic layer (Figure 4). In this case, the volume fraction of the ceramic constituent $R_c(x, z)$ is given as follows:

$$R_c(x,z)=\begin{Bmatrix} \left(\dfrac{x}{L}\right)^{k_x}\left(\dfrac{(h_2+h_1)-z}{h_1}\right)^{k_z} & h_2<z<\dfrac{h}{2} \\ 1 & h_3<z<h_2 \\ \left(\dfrac{x}{L}\right)^{k_x}\left(\dfrac{(h_3+h_4)-z}{h_4}\right)^{k_z} & -\dfrac{h}{2}<z<h_3 \end{Bmatrix} \quad (6)$$

The variation of the volume fraction of the ceramic ($R_c$) through the beam thickness and length for all three Models with respect to $k_x$ and $k_z$ is plotted in Figure 5.

**2. 2. Numerical Simulation Procedure** The displacement field for the present shear deformation beam theories, are given by Equation (7):

**Figure 3.** Sandwich beam with homogeneous faces and a 2D-FG core, Model II

**Figure 4.** Sandwich beam with 2D-FG faces and homogeneous ceramic core, Model III

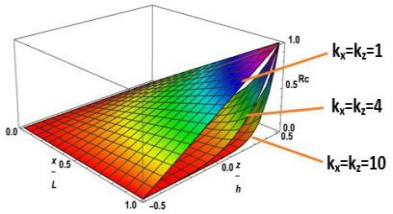


(a) Model I

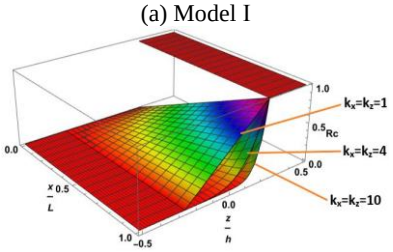


(b) Model II

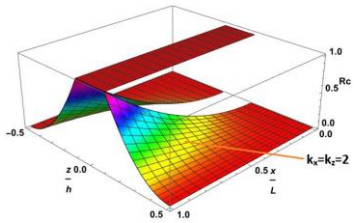


(c) Model Ⅲ

**Figure 5.** Variation of volume fraction of the ceramic ($R_c$) through the beam thickness and length according to power-law indexes

$$u_x(x,z)=u(x)-g(z)\frac{\partial w(x)}{\partial x}+f(z)\varphi(x) \quad (7a)$$

$$u_z(x,z)=w(x) \quad (7b)$$

where u(x) and w(x) represent the axial and transverse displacements for the mid access, respectively, and φ is the rotation of the cross sections. g(z) and f(z) are shape functions that differ based on the theory under consideration, as listed in Table 1. In this study, two new

**TABLE 1.** Various theories for Modelling the structure

| Theories | g(z) | f(z) |
|---|---|---|
| TBT [22] | 0 | $z$ |
| FSDBT [23] | $z$ | $z$ |
| PSDBT [24] | $z$ | $z\left(1-\dfrac{4z^2}{3h^2}\right)$ |
| NHSDBT1 | $z$ | $z\left(\dfrac{4}{h}-\dfrac{16z^2}{3h^3}\right)$ |
| NHSDBT2 | $z$ | $z\left(\dfrac{1}{h}-\dfrac{2z^2}{h^3}+\dfrac{8z^4}{5h^5}\right)$ |

higher-order shear deformation theories, NHSDBT1 and NHSDBT2, were introduced for the first time.

By assuming infinitesimal deformations, strain-displacement relations are [25]:

$$\varepsilon_{xx} = \frac{\partial u(x)}{\partial x} - g(z)\frac{\partial^2 w(x)}{\partial x^2} + f(z)\frac{\partial \varphi(x)}{\partial x} \tag{8a}$$

$$\gamma_{xz} = -\frac{\partial g(z)}{\partial z}\frac{\partial w(x)}{\partial x} + \frac{\partial f(z)}{\partial z}\varphi(x) + \frac{\partial w(x)}{\partial x} \tag{8b}$$

The stress-strain relations by using Hook's law defined. The Hamilton's principle is employed to extract equations of motion [26]:

$$\int_0^t (\delta U - \delta T)dt = 0 \tag{9}$$

where U and T are the strain and kinetic energies of the beam, respectively. δ denotes the variation operator. The strain energy of the beam (U) is calculated as follows [27]:

$$U = \frac{1}{2}\int_V \sigma_{ij}\varepsilon_{ij}dV = \frac{1}{2}\int_V (\sigma_{xx}\varepsilon_{xx} + \tau_{xz}\gamma_{xx})dV \tag{10}$$

Finally, the variation of strain energy with respect to u(x), w(x) and $\varphi(x)$ is shown as follows:

$$\delta U = \frac{1}{2}\int_A \left[-\delta u\frac{\partial A_{xx}}{\partial x} - \delta w\left(\frac{\partial^2 B_{xx}}{\partial x^2} - \frac{\partial S_{xz}}{\partial x} + \frac{\partial A_{xz}}{\partial x}\right) - \delta\varphi\left(\frac{\partial D_{xx}}{\partial x} - T_{xz}\right)\right]dA \tag{11}$$

Where $A_{xx}$, $A_{xz}$, $B_{xx}$, $D_{xx}$, $S_{xz}$ and $T_{xz}$ are defined by:

$$(A_{xx}, A_{xz}) = -\int_{-h/2}^{h/2}(\sigma_{xx}, \tau_{xz})\,dz \tag{12a}$$

$$(B_{xx}, D_{xx}) = \int_{-h/2}^{h/2}(g(z), f(z))\,\sigma_{xx}\,dz \tag{12b}$$

$$(S_{xz}, T_{xz}) = \int_{-h/2}^{h/2}\left(\frac{\partial g(z)}{\partial z}, \frac{\partial f(z)}{\partial z}\right)\tau_{xz}\,dz \tag{12c}$$

The kinetic energy is obtained as follows [28]:

$$T = \frac{1}{2}\int_V \rho\left[\dot{u}_x^2 + \dot{u}_z^2\right]dV \tag{13}$$

The inertia coefficients are defined as Equation (14) [25]

$$(I_1, I_2, I_3, I_4, I_5, I_6) = -\int_{-h/2}^{h/2}\rho(1, g(z), f(z), g(z)f(z), g(z)^2, f(z)^2)dz \tag{14}$$

Finally, the total variation of the kinetic energy associated with the sandwich beam in the integral form is:

$$\delta T = \frac{1}{2}\int_A \left[\left(-I_1\ddot{u} + I_2\frac{\partial \ddot{w}}{\partial x} - I_3\ddot{\varphi}\right)\delta u + \left(-I_3\ddot{u} + I_4\frac{\partial \ddot{w}}{\partial x} - I_6\ddot{\varphi}\right)\delta\varphi - \left(I_2\frac{\partial \ddot{u}}{\partial x} - I_5\frac{\partial^2 \ddot{w}}{\partial x^2} + I_4\frac{\partial \ddot{\varphi}}{\partial x} - I_1\ddot{w}\right)\delta w\right]dA \tag{15}$$

By substituting the strain energy Equation (11) and kinetic energy Equation (15) into Hamilton's principal, Equation (9), equations of motion may be expressed as Equation (16).

$$\delta u: \frac{\partial A_{xx}}{\partial x} = I_1\ddot{u} - I_2\frac{\partial \ddot{w}}{\partial x} + I_3\ddot{\varphi} \tag{16a}$$

$$\delta w: \frac{\partial^2 B_{xx}}{\partial x^2} - \frac{\partial S_{xz}}{\partial x} + \frac{\partial A_{xz}}{\partial x} = I_2\frac{\partial \ddot{u}}{\partial x} - I_5\frac{\partial^2 \ddot{w}}{\partial x^2} + I_4\frac{\partial \ddot{\varphi}}{\partial x} + I_1\ddot{w} \tag{16b}$$

$$\delta\varphi: \frac{\partial D_{xx}}{\partial x} - T_{xz} = I_3\ddot{u} - I_4\frac{\partial \ddot{w}}{\partial x} + I_6\ddot{\varphi} \tag{16c}$$

**2. 3. Analytical Solution** To obtain the theoretical solution, the Galerkin method is considered. According to this method, the displacements functions u(x, t), w(x, t) and $\varphi(x,t)$ are assumed as follows [28, 29]:

$$u(x,t) = \sum_{m=1}^{K}\left[(L-x)^{q_0}x^{p_0}x^{m-1}\bar{u}_m\right]e^{iwt} \tag{17a}$$

$$w(x,t) = \sum_{n=1}^{K}\left[(L-x)^{q_0}x^{p_0}x^{n-1}\bar{w}_n\right]e^{iwt} \tag{17b}$$

$$\varphi(x,t) = \sum_{j=1}^{K}\left[(L-x)^{q_0}x^{p_0}x^{j-1}\bar{\varphi}_j\right]e^{iwt} \tag{17c}$$

where $\bar{u}_m$, $\bar{w}_n$ and $\bar{\varphi}_j$ are unknown coefficients which will be determine. i = $\sqrt{-1}$, K denote the order of series and $\omega$ is the natural frequency. These functions satisfy the fully clamped boundary conditions. Free vibration analysis of the bi-dimensional functionally graded sandwich beam can be computed from Equation (18) [30]:

$$\{[K] - \omega^2[M]\}\{\lambda\} = 0 \tag{18}$$

where, [M] and [K] are global mass and stiffness matrix, also $\omega$ and $\{\lambda\}$ are natural frequency of the beam and unknown coefficients, respectively.

## 3. NUMERICAL RESULTS AND DISCUSSION

In this section, the free vibration of three types of 2D-FG porous sandwich beam concerning porosity coefficients ($\eta$) for clamped-clamped boundary condition are studied and discussed. 2D-FG sandwich beam has various shapes, including (1-8-1), (1-1-1), (2-1-2) and (1-2-1). The first, second and third element indicates the thickness ratio of the top, core and bottom layer,

respectively. Functionally graded material composed of mixture of alumina and aluminum as ceramic and metal, respectively with the material. Their properties are given in Table 2. The influence of different slenderness ratios, L/h = 5, 10, 15 and 20 for various theories, contains two new theories on the non-dimensional natural frequency are investigated. The shear correction factor for TBT and FSDBT theories is considered as $k_s$ = 5/6 and for other theories are taken as $k_s$ = 1.

The dimensionless fundamental frequency is defined as Equation (19) [31]:

$$\bar{\omega} = \omega \frac{L^2}{h}\sqrt{\frac{12\rho_c}{E_c}} \tag{19}$$

where L, h are total length and thickness of the sandwich beam, moreover $\rho_C$, $E_C$ are density and Young's modulus of the middle layer of the sandwich beam. In this research, the results are calculated for different power-law indexes between 0 to 10 and porosity coefficients are taken as $\eta$ = 0, 0.1, and 0.2 in various displacements theories. The total thickness of beam (h) is constant and it is 0.1 m in all third Models I, II and III. The width of beam (b) considers as 0.1 m and the function indexes ($p_0$ and $q_0$), are taken as 2 to satisfy the clamped-clamped boundary condition. Validation of our formulation and the results are obtained and compared with the results reported in literature [25]. The material properties in Table 3 are used for this purpose. A flowchart of the configuration of the research paper is presented in Figure 6.

The distribution of transverse shear stress along the thickness of the structure for FSDBT, PSDBT, and two present introduced theories are illustrated in Figure 7. The modified shear deformation theory satisfies free stress conditions at z = -h/2 and the z = h/2 surfaces of the beam. In Table 4, the first frequency of FG porous-less beam with L/h = 10 for Model I based on the Galerkin method and clamped-clamped support condition for three different power-law indexes are

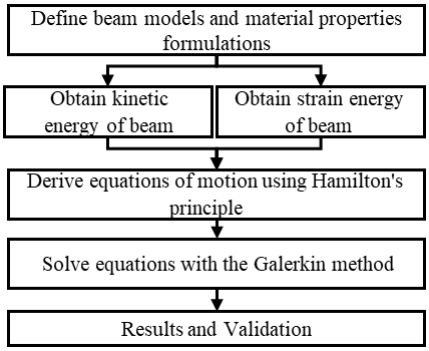


**Figure 6.** Research methodology flowchart

calculated. It is clear the present non-dimensional frequency values are in good agreement with the reference.

Moreover, the accuracy of our results and our new formulation is verified by comparison with the exact solution study for the non-dimensional frequencies of the FG beams [32]. The results are presented in Table 5 by assuming Bouamama et.al. material properties with L/h = 10, results show that our theories have high accuracy as proven by the good agreement between the results in all three first frequencies. The percentage below each value in Tables 4 and 5 represents the difference with the corresponding results obtained from references.

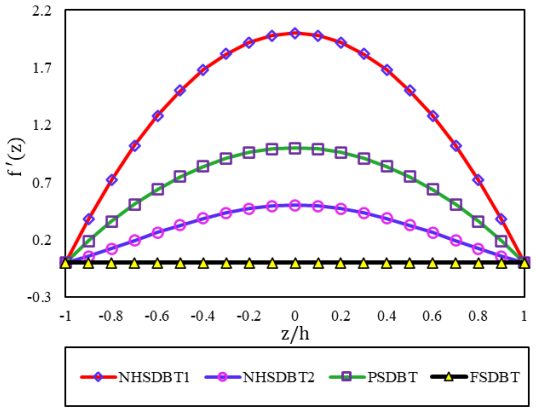


**Figure 7.** A comparison of transverse shear stress distributions of the beam based on various theories

**TABLE 2.** Properties of materials

| Materials | Elasticity module (E) | Mass density ($\rho$) | Poisson's ratio ($\upsilon$) |
|---|---|---|---|
| Alumina | 380 | 3965 | 0.23 |
| Aluminium | 70 | 2700 | 0.23 |

**TABLE 3.** Properties of materials reported by Elmeiche et al. [25]

| Materials | Elasticity module (E) | Mass density ($\rho$) | Poisson's ratio ($\upsilon$) |
|---|---|---|---|
| Alumina | 380 | 3800 | 0.23 |
| Aluminium | 70 | 2700 | 0.23 |

**TABLE 4.** Comparison of the results of $\bar{\omega}$ with Elmeiche et al. [25]

| | $k_w$ = 5 | | $k_w$ = 10 | |
|---|---|---|---|---|
| | FSDBT | PSDBT | FSDBT | PSDBT |
| Elmeiche et al [25] | 14.2348 | 14.0866 | 13.6883 | 13.5237 |
| Present | 14.2380 | 14.1021 | 13.6966 | 13.5534 |
| | -0.02% | -0.1% | -0.06% | -0.2% |

**TABLE 5.** Comparison of the results with Mohamed et al. [32]

| | $\omega_1$ | $\omega_2$ |
|---|---|---|
| NHSDBT1 | 21.3931 (4.3%) | 58.3604 (5.37%) |
| NHSDBT2 | 21.4001 (4.3%) | 58.3877 (5.32%) |
| Mohamed et al.[32] | 22.3730 | 61.6730 |

In Table 6 natural frequencies of first type 2D-FG considered beam are calculated for all FSDBT, PSDBT, NHSDBT1 and NHSDBT2.

To show the accuracy of results of our two new theories for thick beam, we investigate natural frequencies of the 2D-FG beam in Table 7.

Fixed coefficients and their reduction rates in these two theories are different from other theories, hence this difference causes a change in the transverse shear strain. The results express a convergent by using these two new theories. According to this table, there is a bit different among the results obtained from various shear deformation theories. These differences are due to the fact that, function f(z) have different expansions through the thickness in various theories. It is worth to mention that every extra power in the expansion of function f(z) through the thickness of the structure includes additional unknown variables in those theories. Additionally, physical interpretation of these unknown variables are difficult [33]. Thus, it is better to use such distributions that are simpler with acceptable accuracy. Although two new proposed theories are simpler than other modified shear deformation theory, they are nearly identical in accuracy.

Figure 8, display the non-dimensional frequency (ω) of the 2D-FG porous beam of Model I for various values of power-law indexes ($k_x$ and $k_z$). These figures are calculated based on new higher shear deformation theory (NHSDBT2) by assuming porosity volume fraction (η) and slenderness ratios (L/h) as 0.1 and 10. It is clear from the figure that the value of natural frequency decreases with increasing FG power-law indexes ($k_x$ and $k_z$). This is because of the decrease in modulus of elasticity. Also, the flexibility of the sandwich beam increases while the power-law indexes increase. The first line ($k_x$=0) shows dimensionless frequencies for the one-dimensional FG beams, whereas other lines show the natural frequencies of the 2D-FG beams. It is clear that when the beam change to 2D-FG, the amount of non-dimensional frequencies will decrease.

In Figure 9, the effect of porosity on the natural frequency for NHSDBT1 and NHSDBT2 are illustrated. It is clear that porosity is not a significant parameter for frequency in the low amount of power-law index ($k_z < 2$). As the porosity increases, the rigidity of the beam decreases, which reduces the stiffness. Decreasing the stiffness, reduces the natural frequency value. In Figure. 10, two first modes of the natural frequency of 2D-FG sandwich beam respected to different slenderness ratios (L/h = 5, 10, 15 and 20) are compared. As the numerical value of the porosity parameter increases, we see more effectiveness of graded parameters

**TABLE 6.** Comparison of the results of $\bar{\omega}$ based on various theories for type 1, L/h = 10, $k_x$ = 0 and $\eta$ = 0

| Theories | $k_z = 0$ | $k_z = 1$ | $k_z = 5$ | $k_z = 10$ |
|---|---|---|---|---|
| FSDBT | 21.1695 | 16.5043 | 14.2380 | 13.6966 |
| PSDBT | 21.1690 | 16.5042 | 14.1021 | 13.5534 |
| NHSDBT1 | 21.1618 | 16.5051 | 14.1027 | 13.5504 |
| NHSDBT2 | 21.1791 | 16.5150 | 14.0906 | 13.5551 |

**TABLE 7.** Comparison of the results of $\bar{\omega}$ based on various theories for type 1, L/h = 5, $k_x$ = 0 and $\eta$ = 0

| Theories | $k_z = 0$ | $k_z = 1$ | $k_z = 2$ | $k_z = 6$ | $k_z = 10$ |
|---|---|---|---|---|---|
| FSDBT | 18.538 | 14.665 | 13.380 | 12.250 | 11.800 |
| PSDBT | 18.559 | 14.680 | 13.297 | 11.899 | 11.468 |
| NHSDBT1 | 18.559 | 14.677 | 13.297 | 11.898 | 11.470 |
| NHSDBT2 | 18.590 | 14.703 | 13.309 | 11.888 | 11.480 |

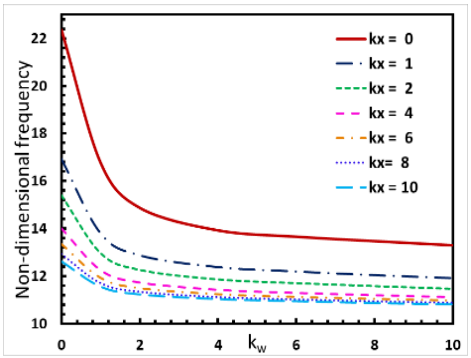


**Figure 8.** $\bar{\omega}$ of 2D-FG porous beam for various $k_x$ and $k_z$ based on NHSDBT2 theory (L/h = 10, η = 0.1 and Model I)

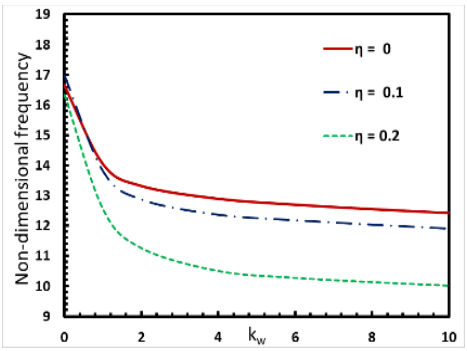


**Figure 9.** $\bar{\omega}$ of 2D-FG porous beam for various $k_z$ and η, based on NHSDBT1 (L/h = 10, $k_x$ = 1 and Model I)

As shown in Figure 10, L/h = 5 has more effect on frequencies in comparison with other slenderness ratios. In another word, free vibration frequencies decrease with decreasing value of L/h. Reducing the length to a constant thickness reduces the bending moment, which reduces the strain energy, which in turn reduces the natural frequency value. It is good to mention that, the decrement is higher for the second mode. It can be pointed out that slenderness ratios (L/h) effects become more prominent in smaller values on the natural frequencies of the beam.

To verify the accuracy of the two newly presented theories (NHSDBT1 and NHSDBT2), Figure 11 is plotted. A good agreement can be observed between the reported results. Our two new theories and parabolic shear deformation formulation come up with close results for Model I.

Figure 12 indicates that non-dimensional natural frequencies for Model II of the 2D-FG porous sandwich beam have good agreement with different theories. The effect of core thickness on the natural frequency for Model II is illustrated. In this figure, it can be observed 1-8-1 shape determine a larger range of natural frequency than other shapes. This is due to the ratio of the thickness of the core layer, which has no dependency on FG is larger than other shapes. In this Model specially, results of PSDBT always coincide with our two new higher shear deformation beam theories. Due to the graded properties of the beam, the natural frequencies change gradually, which starts from the metal phase and leads to the ceramic. For this reason, the values of the frequencies in the presented graphs have a downward trend.

Like Model II, results in Figure 13 shows great accuracy between theories for Model III, which demonstrates the validity of the new theories. On the other hand, in this figure, the 1-8-1 shape has the smallest range of natural frequencies variation and the 2-1-2 shape has the largest variation range among shapes. This is because FG face sheets are thicker in the 2-1-2 shapes compared to other shapes and the variation in the properties of FG material, affects the frequencies. Generally, amount of frequencies in 1-8-1 shape are higher than the others.

In Figure 14, dimensionless frequencies of the beam are graphed for assumptions of L/h = 10, $\eta = 0.1$ and $k_x = 1$ based on NHSDBT2. It is noteworthy that, the effect of FG layers on the natural frequencies of the 2D-FG beam is significant for variable $k_z$. Consequently, the 1-8-1 shape in Model II (Figure. 14(a)) and the 2-1-2 shape in Model III (Figure 14(b)) had most affected by the power-law index of functionally graded material, compared to the other shapes in each Model. The stiffness of FG beams will decrease as the power-law index is increased for all shapes types because FG material went to have more ceramic volume. Also, by

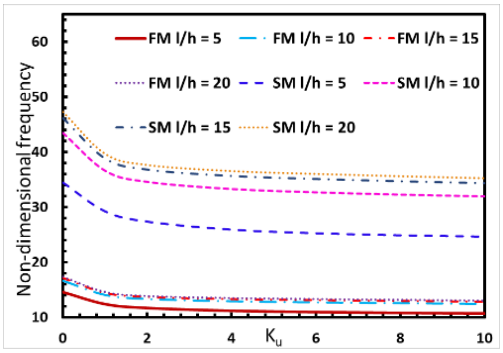


**Figure 10.** First and Second modes of $\bar{\omega}$ of 2D-FG porous beam respected to L/h, based on NHSDBT1 ($\eta = 0$, $k_x = 1$ and Model I)

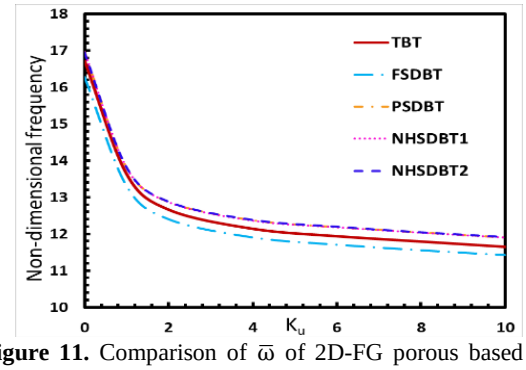


**Figure 11.** Comparison of $\bar{\omega}$ of 2D-FG porous based on different theories ($\eta = 0.1$, $k_x = 1$ and Model I)

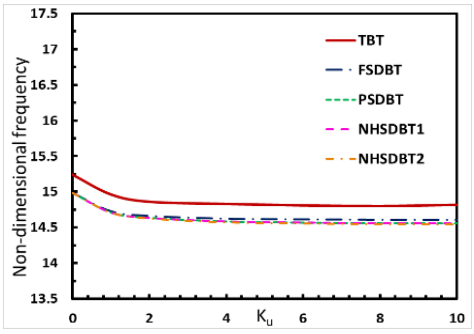


(a) 2-1-2

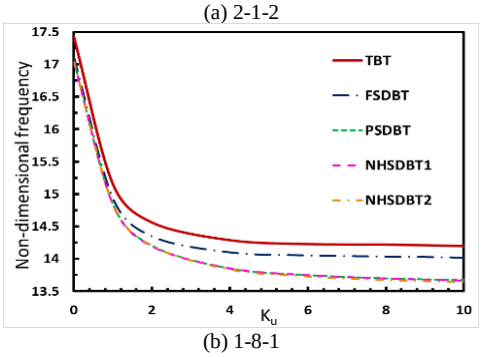


(b) 1-8-1

**Figure 12.** Comparison of $\bar{\omega}$ for various $k_z$ and theories (L/h = 10, $k_x = 1$, $\eta = 0.1$ and Model II)

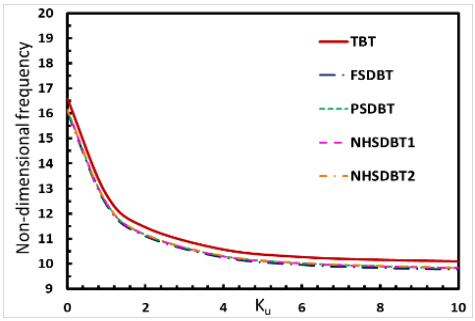


(a) 2-1-2

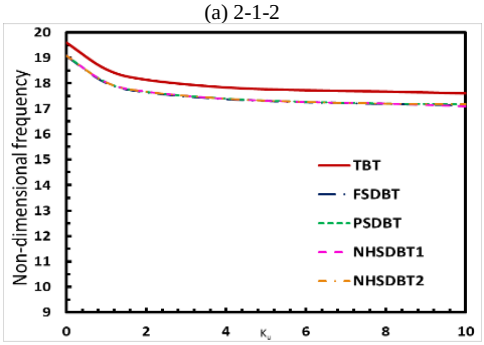


(b) 1-8-1

**Figure 13.** Comparison of $\bar{\omega}$ for various $k_z$ and theories (L/h = 10, $k_x$ = 1, $\eta$ = 0.1 and Model III)

checking the results in model two, it is possible to achieve a unique natural frequency with various shapes. this phenomenon provides a state to use in reality. In Figure 15, based on our new theory (NHSDBT1) the first and second mode shapes of two dimensional functionally

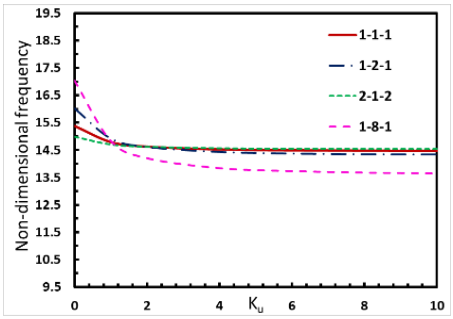


(a) Model II

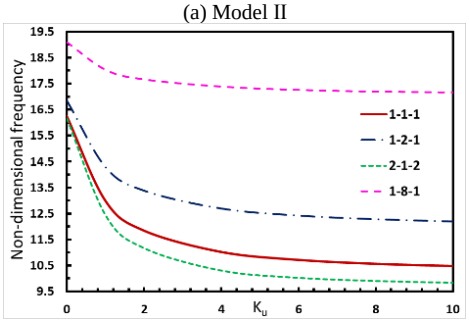


(b) Model III

**Figure 14.** $\bar{\omega}$ of 2D-FG porous beam for various $k_z$ and shapes, based on NHSDBT2 (L/h = 10, $k_x$ = 1, and $\eta$ = 0.1)

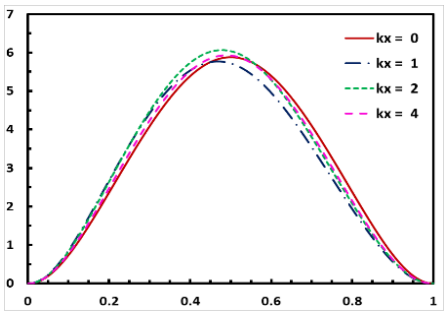


(a) First mode shape ($\times 10^{-5}$)

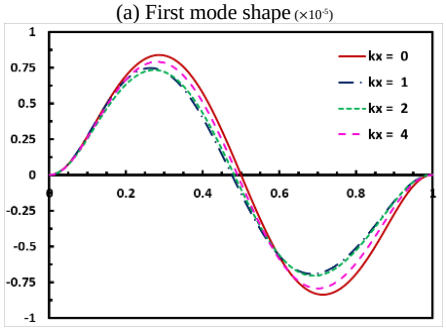


(b) Second mode shape ($\times 10^{-5}$)

**Figure 15.** The first two mode shape of 2D-FG beam for Model I, based on NHSDBT1 (L/h = 10 and $k_z$ = 1)

graded beam investigated. A fully clamped beam with L/h = 10 and $k_z$ = 1 for various $k_x$ based on Model I is chosen.

## 4. CONCLUSION

In this paper, two new higher order shear deformation beam theories (NHSDBT 1 and 2) to obtain non-dimensional frequencies of 2D-FG porous sandwich beams are introduced. Effect of different shapes, porosity ($\eta$), slenderness ratios (L/h) and power-law indexes in both axial and thickness directions ($k_x$ and $k_z$) on natural frequencies of the 2D-FG porous beam in three different beam Models, based on various theories (TBT, FSDBT, PSDBT, NHSDBT 1 and 2) for clamped-clamped boundary condition are investigated. The higher order governing equations are derived by using Hamilton's principle. In the following, the Galerkin method is employed to solve them. The effect of power-law indexes on shape modes is illustrated. The presented theories are validated for the free vibration of beams. The major results of this paper are briefly explained below:

- By implementing the presented two new theories, a good agreement was obtained. The results indicate that the accuracy of the NHSDBT1 and NHSDBT2 are close to other order shear deformation beam theories although using the presented theories are easier than them.
- There are some parameters that will rise the amounts of natural frequencies by increasing them.

The slenderness ratio (L/h) is one of them, whereas the power-law indexes ($k_x$ and $k_z$) and porosity volume fraction (η) show an indirect relation with frequencies. Frequencies are more sensitive to porosity in high-value power-law indexes.

- It is noteworthy that, the effect of FG layers on the natural frequencies of the 2D-FG beam is significant for variables $k_x$ and $k_z$. Consequently, by increasing thickness of the functionally graded layer in each shape
- Generally, power-law indexes shifted the node point to the left and resonance will be accrued sooner than the non-FGM beam.

## 5. REFERENCES


1. Bakhshi Khaniki, H., Hosseini Hashemi, S. and Bakhshi Khaniki, H., "Free vibration analysis of functionally graded materials non-uniform beams", ***International Journal of Engineering, Transactions C: Aspects***, Vol. 29, No. 12, (2016), 1734-1740. doi: 10.5829/idosi.ije.2016.29.12c.12.
2. Sherafatnia, K., Farrahi, G.H. and Faghidian, S.A., "Analytic approach to free vibration and buckling analysis of functionally graded beams with edge cracks using four engineering beam theories", ***International Journal of Engineering, Transactions C: Aspects***, Vol. 27, No. 6, (2014), 979-990. doi: 10.5829/idosi.ije.2014.27.06c.17.
3. El Khouddar, Y., Adri, A., Outassafte, O., Rifai, S. and Benamer, R., "Non-linear forced vibration analysis of piezoelectric functionally graded beams in thermal environment", ***International Journal of Engineering, Transactions B: Applications***, Vol. 34, No. 11, (2021), 2387-2397. doi: 10.5829/ije.2021.34.11b.02.
4. Amoozgar, M. and Gelman, L., "Vibration analysis of rotating porous functionally graded material beams using exact formulation", ***Journal of Vibration and Control***, (2019), 10775463211027883. doi: 10.1177/10775463211027883.
5. Hadji, L., Bernard, F., Safa, A. and Tounsi, A., "Bending and free vibration analysis for fgm plates containing various distribution shape of porosity", ***Advances in Materials Research***, Vol. 10, No. 2, (2021), 115-135. doi: 10.12989/AMR.2021.10.2.115.
6. Celebi, K., Yarimpabuc, D. and Tutuncu, N., "Free vibration analysis of functionally graded beams using complementary functions method", ***Archive of Applied Mechanics***, Vol. 88, No. 5, (2018), 729-739. doi: 10.1007/s00419-017-1338-6.
7. Lei, J., He, Y., bo, Z., Gan, Z. and Zeng, P., "Bending and vibration of functionally graded sinusoidal microbeams based on the strain gradient elasticity theory", ***International Journal of Engineering Science***, Vol. 72, (2013), 36–52. doi: 10.1016/j.ijengsci.2013.06.012.
8. Ke, L.-L., Yang, J. and Kitipornchai, S., "Nonlinear free vibration of functionally graded carbon nanotube-reinforced composite beams", ***Composite Structures***, Vol. 92, (2010), 676-683. doi: 10.1016/j.compstruct.2009.09.024.
9. Mashat, D.S., Carrera, E., Zenkour, A.M., Al Khateeb, S.A. and Filippi, M., "Free vibration of fgm layered beams by various theories and finite elements", ***Composites Part B: Engineering***, Vol. 59, (2014), 269-278. doi: 10.1016/j.compositesb.2013.12.008.
10. Faghidian, S.A., "Flexure mechanics of nonlocal modified gradient nano-beams", ***Journal of Computational Design and Engineering***, Vol. 8, No. 3, (2021), 949-959. doi: 10.1093/jcde/qwab027.
11. Faghidian, S.A., Żur, K.K. and Reddy, J.N., "A mixed variational framework for higher-order unified gradient elasticity", ***International Journal of Engineering Science***, Vol. 170, (2022), 103603. doi: 10.1016/j.ijengsci.2021.103603.
12. Faghidian, S.A., "Higher order mixture nonlocal gradient theory of wave propagation", ***Mathematical Methods in the Applied Sciences***, (2020). doi: 10.1002/mma.6885.
13. Faghidian, S.A., "Two-phase local/nonlocal gradient mechanics of elastic torsion", ***Mathematical Methods in the Applied Sciences***, Vol. n/a, No. n/a, (2020). doi: 10.1002/mma.6877.
14. Shahba, A. and Rajasekaran, S., "Free vibration and stability of tapered euler–bernoulli beams made of axially functionally graded materials", ***Applied Mathematical Modelling***, Vol. 36, No. 7, (2012), 3094-3111. doi: 10.1016/j.apm.2011.09.073.
15. Wang, Y., Xie, K.-j., Fu, T. and Shi, C., "Vibration response of a functionally graded graphene nanoplatelet reinforced composite beam under two successive moving masses", ***Composite Structures***, (2019). doi: 10.1016/j.compstruct.2018.11.014.
16. Xu, J., Yang, Z., Yang, J. and Li, Y., "Free vibration analysis of rotating fg-cnt reinforced composite beams in thermal environments with general boundary conditions", ***Aerospace Science and Technology***, Vol. 118, (2021), 107030. doi: 10.1016/j.ast.2021.107030.
17. Shafiei, N., Mirjavadi, S.S., MohaselAfshari, B., Rabby, S. and Kazemi, M., "Vibration of two-dimensional imperfect functionally graded (2d-fg) porous nano-/micro-beams", ***Computer Methods in Applied Mechanics and Engineering***, Vol. 322, (2017), 615-632. doi: 10.1016/j.cma.2017.05.007.
18. Kandil, M., Abdelraheem, A., Mahdy, M. and Tahwia, A., "Effect of changing properties of wythes in precast structural sandwich panels", ***Civil Engineering Journal***, Vol. 6, (2020), 1765-1778. doi: 10.28991/cej-2020-03091581.
19. Singh, V. and Sangle, K., "Analysis of vertically oriented coupled shear wall interconnected with coupling beams", ***HighTech and Innovation Journal***, Vol. 3, No. 2, (2022), 230-242. doi: 10.28991/HIJ-2022-03-02-010.
20. Mirjavadi, S.S., Mohasel Afshari, B., Shafiei, N., Rabby, S. and Kazemi, M., "Effect of temperature and porosity on the vibration behavior of two-dimensional functionally graded micro-scale timoshenko beam", ***Journal of Vibration and Control***, Vol. 24, No. 18, (2018), 4211-4225. doi: 10.1177/1077546317721871.
21. Şimşek, M., "Buckling of timoshenko beams composed of two-dimensional functionally graded material (2d-fgm) having different boundary conditions", ***Composite Structures***, Vol. 149, (2016), 304-314. doi: 10.1016/j.compstruct.2016.04.034.
22. Timoshenko, S.P., "X. On the transverse vibrations of bars of uniform cross-section", ***The London, Edinburgh, and Dublin Philosophical Magazine and Journal of Science***, Vol. 43, No. 253, (1922), 125-131. doi: 10.1080/14786442208633855.
23. Aydogdu, M. and Taskin, V., "Free vibration analysis of functionally graded beams with simply supported edges", ***Materials & Design***, Vol. 28, No. 5, (2007), 1651-1656. doi: 10.1016/j.matdes.2006.02.007.
24. Simsek, M., "Fundamental frequency analysis of functionally graded beams by using different higher-order beam theories", ***Nuclear Engineering and Design***, Vol. 240, (2010), 697-705. doi: 10.1016/j.nucengdes.2009.12.013.
25. Elmeiche, A., Megueni, A. and Lousdad, A., "Free vibration analysis of functionally graded nanobeams based on different order beam theories using ritz method", ***Periodica Polytechnica Mechanical Engineering***, Vol. 60, No. 4, (2016), 209-219. doi: 10.3311/PPme.8707.

26. Khorshidi, K. and Shabani, Y., "Free vibration analysis of sandwich plates with magnetorheological smart fluid core by using modified shear deformation theory", ***Journal of Science and Technology of Composites***, (2022), doi: 10.22068/jstc.2022.552957.1782.

27. Khorshidi, K., Taheri, M. and Ghasemi, M., "Sensitivity analysis of vibrating laminated composite rec-tangular plates in interaction with inviscid fluid using efast method", ***Mechanics of Advanced Composite Structures***, Vol. 7, No. 2, (2020), 219-231. doi: 10.22075/macs.2020.18605.1224.

28. Khorshidi, K. and Karimi, M., "Analytical approach for thermo-electro-mechanical vibration of piezoelectric nanoplates resting on elastic foundations based on nonlocal theory", ***Mechanics of Advanced Composite Structures***, Vol. 6, No. 2, (2019), 117-129. doi: 10.22075/macs.2019.15518.1156.

29. Ghayesh, M.H., Amabili, M. and Farokhi, H., "Nonlinear forced vibrations of a microbeam based on the strain gradient elasticity theory", ***International Journal of Engineering Science***, Vol. 63, (2013), 52-60. doi: 10.1016/j.ijengsci.2012.12.001.

30. Shabani, Y. and Khorshidi, K., "Free vibration analysis of rectangular doubly curved auxetic-core sandwich panels integrated with cnt-reinforced composite layers using galerkin method", ***Journal of Science and Technology of Composites***, Vol. 8, No. 3, (2022), 1686-1677. doi: 10.22068/jstc.2022.545477.1762.

31. Khorshidi, K. and Fallah, A., "Free vibration analysis of size-dependent, functionally graded, rectangular nano/micro-plates based on modified nonlinear couple stress shear deformation plate theories", ***Mechanics of Advanced Composite Structures***, Vol. 4, No. 2, (2017), doi: 10.22075/MACS.2017.1800.1094.

32. Mohamed, B., Elmeiche, A., Elhennani, A., Kebir, T., El, Z. and zine el abidine, H., "Exact solution for free vibration analysis of fgm beams", ***Revue des Composites et des Matériaux Avancés***, Vol. 30, (2020). doi: 10.18280/rcma.300201.

33. Reddy, J.N. and Robbins, D.H., Jr, "Theories and computational models for composite laminates", ***Applied Mechanics Reviews***, Vol. 47, No. 6, (1994), 147-169. doi: 10.1115/1.3111076.

## Persian Abstract

**چکیده**

در این پژوهش ارتعاش آزاد تیرهای ساندویچی مدرج تابعی دو جهته متخلخل ارائه شده‌است. معادلات حاکم بر تیر به کمک اصل همیلتون استخراج شده و با استفاده از روش گلرکین حل شده‌اند. خواص مواد تیر ساندویچی در راستای ضخامت و طول هر لایه از تیر، با توجه به نسبت‌های حجمی مدرج متغییر می‌باشند. خواص مکانیکی تیر بین آلومینیوم و آلومینیا ،به عنوان فلز و سرامیک، به صورت تدریجی تغییر می‌کنند. ارتعاش آزاد براساس دو تئوری مرتبه بالای برشی جدید که در این پژوهش برای اولین بار ارائه شده‌اند، برای سه مدل متفاوت تیر محاسبه گردیده‌است. نتایج حاصل با تئوری‌های تغییر شکل برشی تیموشنکو، مرتبه اول و پارابولیکی قیاس شده‌اند. علاوه بر این، تاثیر تخلخل، نسبت طول به ضخامت تیر و نسبت‌های حجمی مدرجی در راستای طول و ضخامت برروی فرکانس‌ها بررسی شده‌اند. همچنین، شکل مودهای تیر تحت نسبت‌های حجمی متفاوت براساس تئوری جدید ترسیم گردید. صحت نتایج حاصل از دو تئوری جدید با نتایج دو مقاله با روش‌های حل دقیق و تحلیلی مقایسه گردیده‌است.

International Journal of Engineering

Journal Homepage: www.ije.ir

# Comprehensive Analysis of Stress-strain Relationships for Recycled Aggregate Concrete

A. J. Pawar*[a], S. R. Suryawanshi[b]

*Department of Civil Engineering, S. V. National Institute of Technology, Surat, India*

*PAPER INFO*

*Paper history:*
Received 17 June 2022
Received in revised form 20 July 2022
Accepted 21 July 2022

*Keywords*:
*Stress-strain Relationship*
*Recycled Aggregate Concrete*
*Normalised Toughness*
*Ductility Index*
*Root Mean Square Error*

*ABSTRACT*

There is a growing demand of suitable substitute materials of concrete ingredients especially fine and coarse aggregates in order to achieve sustainable development in the era of rapid urbanisation. Therefore, the concrete making process by utilisation of aggregates that recycled from construction and demolition (C&D) debris has emerged as a primary objective for many government agencies. Consequently, the utilisation of recycled aggregate concrete (RAC) in structural applications become essential aspect. However, RAC can be employed in structural applications only if effective stress-strain relationship is available. The stress-strain models developed for natural aggregate concrete (NAC) are not fully suitable for RAC. Hence, the selection of good model which has precise prediction capacity plays a crucial role. Moreover, the stress-strain models provide the basis for the analysis and modern design procedures especially in FEA packages. In the present study, the stress-strain models for RAC have been selected from the literature and critically reviewed in order to evaluate their predictive efficacy. The test samples in the form of measured stress-strain relations–hips derived from literature have been compared with the predictions of each selected model. Besides the comparison of measured and predicted stress-strain profiles, the output of selected models in terms of normalized toughness and ductility index was assessed. The consistency of output of models are further evaluated by employing statistical tools such as coefficient of variance and root mean square error. The outcomes of the model in the form of polynomial expression was relatively more accurate to that of other counterparts.

***doi***: *10.5829/ije.2022.35.11b.05*

**NOMENCLATURE**

| | | | |
|---|---|---|---|
| $\sigma$ | Stress in concrete corresponding to specified strain level $\varepsilon$ | $\varepsilon$ | Strain in concrete corresponding to specified stress level $\sigma$ |
| $\sigma_{max}$ | Peak stress of concrete | $n, k$ | Coefficients |
| $f_c$ | the prism compressive strength | $f_{cm}$ | Average cylinder compressive strength at 28 days |
| $\sigma_c$ | Compressive stress | *FEA* | Finite Element Analysis |

## 1. INTRODUCTION

Since the beginning of the urbanisation, there has been rapid growth in the building industry, and as a result, the amount of construction waste produced has increased year by year [1, 2]. Every year, around 2.01 billion tonnes of municipal debris are produced across the globe [3]. Due to rapid urbanization, the appropriate utilization of C&D waste has become very important. The demand of coarse and fine aggregate has been in an ever increasing rate, but as they are natural resources, their supply is limited [4]. On one side, there is exploitation of the natural resources, on the other hand, debris produced by demolition and other construction activities is increasing. A process to extract fine and the coarse aggregate from C&D waste that could be replaced with the natural aggregates in construction is very crucial as it would relieve the pressure on natural resources. It is high time that the entire C&D waste is properly recycled and utilized as the natural building materials are becoming scarce. In the recent decade, due to the rapid population growth there has been a big boom in the construction industry as the expansion of cities and redevelopment of the existing cities have gained a big momentum. Due to

*Corresponding Author Email: akshay4592@gmail.com (A. J. Pawar)

Please cite this article as: A. J. Pawar, S. R. Suryawanshi, Comprehensive Analysis of Stress-strain Relationships for Recycled Aggregate Concrete, ***International Journal of Engineering, Transactions B: Applications***, Vol. 35, No. 11, (2022) 2102-2110

this rapid development, there have been a massive increase in C&D waste generation. In order to promote sustainability and alleviate the stress on the environment from the excessive use of natural aggregates, recycled aggregates are increasingly used in concrete manufacturing [5].

Plenty of studies [6-8] on the utilisation of recycled aggregate from C&D waste are available in the literature, but the studies on structural application of RAC are comparatively limited in their number. Emphasis on the utilization of recycled concrete aggregate (RCA) in structural applications may accelerate sustainable development programmes. As a result, a thorough knowledge of stress-strain relations of this substitute material is inevitable in order to assess its structural potential. Moreover, if the stress-strain relationship accurately depicts the behaviour under loading, it might serve as a foundation for structural applications of RAC. Numerous compressive behaviour indicators, such as peak-stress (referred as compressive strength), peak-strain corresponds to peak stress, ultimate stress where the failure is defined in terms of certain percentage of peak stress in the post-peak region, ultimate strain and secant modulus are derived from the stress-strain relationship of concrete, making it crucial for theoretical and numerical assessments of structures and engineering designs.

There are different theories of constitutive modelling are available in the literature [9]. However, it can be categorised into two major groups: Empirical models that derived from the regression analysis of measured data and models based on continuum mechanics theories. The continuum mechanics theories like elasticity, plasticity, continuum damage mechanics, plastic fracturing, endochronic theory, microplane models, etc. are too dependent of experimental data for their validation. The group of empirical models itself is huge and consists variety of constitutive models for uniaxial, biaxial, triaxial, impact and cyclic loading. Under the class of uniaxial stress-strain models, many models for NAC are available, however, very limited models are available on the RAC. Moreover, due to various influencing factors such as shape and size of test specimens, aspect ratios, loading rate, duration of loading, type of testing machine etc., these models give different results especially in post peak region. The form of mathematical formulation also affects the prediction of test results. Therefore, it is evident to carry out comparative theoretical analysis of these models in order to ascertain the level of accuracy.

In this study, the empirical stress-strain relationships for RAC proposed by Xiao et al. [10], Du et al. [11], Belén et al. [12], and Suryawanshi et al. [13] have been considered for comparison of predictive efficacy. Besides comparison of graphical representation of measured and predicted stress-strain relationships, Normalised toughness ($A$), Ductility index ($\mu$) have been evaluated. Further, the accuracy of the predictions of selected models in terms of $A$ and $\mu$ is verified by employing statistical tools such as Root Mean Square Error ($RMS$) and Coefficient of Variance ($V$). It has been observed that all the models yield reasonably similar results in pre-peak region but the predictions of post-peak region are deviating from their respective counterparts may be due to the formulation approach. However, the model of higher degree polynomial yields comparatively better results and its applicability in differential and integral calculus is also simple and easy.

## 2. SUMMARY OF STRESS-STRAIN MODELS

A small number of stress-strain models are available for RAC with the different replacement ratios of recycled coarse aggregates as a function. A brief and critical review of these models reported in different studies is as follows. The basic forms of these mathematical formulations for rising and falling branches of complete stress-strain curve (SSC) have also been reviewed.

Guo and Zhang [14] defined the stress-strain relationship for NAC and subsequently, it was modified by Xiao et al. [10] to fit it for RAC. The formulation consists of two equations to model ascending and descending portion of SSC and is the function of replacement level of natural aggregate.

$$\bar{\sigma} = \begin{cases} a\bar{\epsilon} + (3-2a)\bar{\epsilon}^2 + (a-2)\bar{\epsilon}^3, for\ \bar{\epsilon} < 1, \\ \dfrac{\bar{\epsilon}}{b(\bar{\epsilon}-1)^2+\bar{\epsilon}}, for\ \bar{\epsilon} \geq 1 \end{cases} \quad (1)$$

In Equation (1), $\bar{\sigma}$ is the normalised stress with respective to peak stress ($\sigma/f_c$) whereas $\bar{\epsilon}$ is the normalised strain with respective to strain corresponds to peak stress ($\epsilon/\epsilon_0$,). The coefficients, $a$ and $b$ are outcomes of regression analysis, dependent on replacement level of natural aggregate in percentage ($r$), and to be determined as follows:

$$a = 2.2(0.748r^2 - 1.231r + 0.975) \quad (2)$$

$$b = 0.8(7.6483r + 1.142) \quad (3)$$

This model gives reasonably more accurate predictions for the ascending portion of the SSC, however, the descending portion is not predicted as accurately.

Du et al. [11] tried to model the falling branch of SSC after peak load, relating it to the area falling under the experimentally measured SSC. The expression for rising branch of SSC is similar to that proposed by Xiao et al. [10].

$$y = ax + (3-2a)x^2 + (a-2)x^3, (0 \leq x < 1) \quad (4)$$

where, $y$ is the normalised stress with respective to peak stress ($\sigma/\sigma_{max}$) and $x$ is the normalised strain with respective to strain corresponds to peak stress ($\varepsilon/\varepsilon_0$).

$a$ is represented by the ratio of initial tangent modulus and secant modulus correspond to peak point and the origin.

The expression for falling branch of SSC is as follows:

$$y = \alpha e^{\frac{(x-1)^2}{2\beta_1^2}} + (1-\alpha)e^{\frac{(x-1)^2}{2\beta_2^2}}, (1 \leq x < +\infty) \quad (5)$$

where, $\alpha$, $\beta_1$, $\beta_2$ are the parameters may be referred to in the respective reference [11].

The recommended model by Du et al. [11] is not fit for routine applications due to associated relative complexity in the formulation, especially for descending branch of SSC. Moreover, the transformation of $\alpha$, $\beta_1$, $\beta_2$ parameters with the replacement level of natural aggregate and concrete grade involves comparatively more compound approach.

Linear regression analysis of test data was used by Belén et al. [12] to determine elastic modulus, ultimate strain and peak strain transformation coefficients and modified the stress-strain model recommended in Eurocode 2 [15], to outfit the RAC. An analytical expression of the SSC that considers the percentage of replacement was established by making use of the findings of the experiments. Moreover, the stress-strain expression recommended in Eurocode 2 [15], is also adhered by the Spanish code, EHE-08 [16]. The modified expression for RAC was generated for the ascending branch and subsequently, descending branch limited to the strain level of 0.0035.

$$\frac{\sigma_c}{f_{cm}} = \frac{k*n-n^2}{1+(k-2)n} \quad (6)$$

where,

$n = \frac{\varepsilon_c}{\varepsilon_{c1}}$ and $k = 1.05 * E_{cm} * |\varepsilon_{c1}|/f_{cm}$

The Eurocode 2 [15] recommends the following expressions to determine the secant modulus of elastic and peak strain, respectively as follows:

$$E_{cm} = 22 * (f_{cm}/10)^{0.3} \quad (7)$$

$$\varepsilon_{c1} = 0.7 * (f_{cm})^{0.31} \quad (8)$$

According to Belén et al. [12], the Eurocode 2 [15] expression for conventional concrete could be used for recycled concretes by employing transformation coefficients for secant modulus ($E_{cm}$), peak strain ($\varepsilon_{c1}$) and the ultimate strain ($\varepsilon_{cu1}$) and $\varepsilon_{cu2}(\beta_{cu}^{rec})$. The following modified coefficients are the products of regression analysis of the test data.

$$(\varphi_{cm}^{rec}) = -0.0020\, x\, \%\text{RCA} + 1 \quad (9)$$

$$(\propto_c^{rec}) = 0.0021\, x\, \%\text{RCA} + 1 \quad (10)$$

$$(\beta_{cu}^{rec}) = 0.0022\, \text{x}\, \%\text{RCA} + 1 \quad (11)$$

Although the model exhibits good efficacy for ascending branch, yet it is not that much effective in predictions for descending branch.

The theoretical relationship for RAC proposed by Bhikshma and Kishore [17], is the modified version of the model evolved by Saenz [18] for conventional concrete. This model has limited predictive efficacy for RAC; hence the results of the analysis are not reported here.

A fourth-degree polynomial expression was proposed by Suryawanshi et al. [13] to model the experimentally observed behaviour in normal-strength RAC. The model incorporated the influence of RCA replacement level respectively on elastic modulus, peak strain, peak stress and ultimate strain. This single equation works for both the pre-peak and post-peak parts of the SSC with the limiting value of normalised strain is equal to 2.

$$\overline{\sigma} = a(\overline{\varepsilon}) + b(\overline{\varepsilon})^2 + c(\overline{\varepsilon})^3 + d(\overline{\varepsilon})^4 \quad (12)$$

where $\overline{\sigma}$ is normalised stress $(\sigma/f'_c)$ and $\overline{\varepsilon}$ is the normalised strain.

Coefficients $a$, $b$, $c$ and $d$ are derived by doing regression analysis of the measured test data and function of replacement level of natural aggregate in percentage. The coefficient '$a$' implies the ratio of initial tangent modulus and the secant modulus ($E_{itm}/E_p$). The secant modulus is the slope of line joining the origin of the SSC and the point corresponding to peak stress

$$a = (1.8242 - 0.0076R) \quad (13)$$

$$b = (4.67 - 2.86a) \quad (14)$$

$$c = (2.51a - 5) \quad (15)$$

$$d = (1.33 - 0.65a) \quad (16)$$

The compressive stress ($f'_c$) and the peak strain ($\varepsilon_o$) of RAC are the inputs required to handle the model. In absence of values of these input parameters for RAC, following equations may be referred to generate them from the test results of NAC.

$$f'_{c,\text{RAC}} = (1 - 0.0012R) f'_{c,\text{NAC}} \quad (17)$$

$$\varepsilon_{0,\text{RAC}} = (0.6 + 0.002R)10^{-3}\left(f'_{c,\text{RAC}}\right)^{0.33} \quad (18)$$

## 3. ASSESSMENT OF STRESS-STRAIN MODELS

The relative performance of the analytical models in terms of their ability to reproduce the experimentally observed SSC on selected test specimens have been examined. Table 1 reveals the details of typical test specimens and measured values of compressive stress along with the corresponding values of peak and ultimate

**TABLE 1.** Summary of specimen details and experimentally obtained results

| Author | Specimen type and size | Specimen Id | Replacement ratio | Compressive strength of concrete (MPa) | Peak strain | Ultimate strain |
|---|---|---|---|---|---|---|
| Xiao et al. [10] | Prism (100x100x300) mm | NC | 0% | 26.90 | 0.0018 | 0.0028 |
| | | RC-50 | 50% | 23.60 | 0.0019 | 0.0026 |
| | | RC-100 | 100% | 23.80 | 0.0022 | 0.0028 |
| Belén et al. [12] | Cylinder (150x300) mm | H-0.65-0% | 0% | 31.92 | 0.0017 | 0.0037 |
| | | H-0.65-50% | 50% | 32.35 | 0.0019 | 0.0042 |
| | | H-0.65-100% | 100% | 30.13 | 0.0022 | 0.0045 |
| | | H-0.50-0% | 0% | 44.81 | 0.0019 | 0.0036 |
| | | H-0.50-50% | 50% | 37.45 | 0.0019 | 0.0040 |
| | | H-0.50-100% | 100% | 40.54 | 0.0022 | 0.0044 |
| Suryawanshi et al. [13] | Cylinder (150x300) mm | R00 | 0% | 38.00 | 0.0019 | 0.0036 |
| | | R100 | 100% | 34.50 | 0.0024 | 0.0037 |

strains. The stress and the strain values have been derived from the reported information and subsequently the SSC models except the model proposed by Du et al. [11] are compared with each measured stress-strain relationship. Du et al. [11] proposed the stress-strain model explicitly for concrete containing 100% recycled aggregates [19].

Besides the graphical comparison, the area under curves of the measured SSC and predicted SSC has been calculated and compared. Moreover, root have been reproduced. The predictions of all the selected mean square error (*RMS*) value and coefficients of variance (*V*) are calculated in order to decide the efficacy of models on statistical grounds. The *RMS* error is the standard deviation of the prediction errors (residuals). Residuals are the distances between the data points and the regression line. It refers to the propagation of these residuals. Thus, it is the indicative of the concentration of the cluster of the data points around the line of best fit. This is one of the effective techniques in regression analysis to verify experimental results. The effectiveness of prediction model may be evaluated in terms of variance of the predicted data. It is defined as extent of spread from the average value. Variance is the dependent quantity of the standard deviation of the data. The value of variance is directly correlated to scatter of data. Therefore, it is the indicator of a data spread with respect to mean. More the value of variance, the more the data scatter and vice a versa. The quality of fit of the predicted SSC to the experimental SSC is investigated in terms of "*RMS*" and "*V*" respectively in order to quantify the predictive evaluation of various analytical models, according to procedure reported by Khan et al. [20] and Ayub et al. [21]. The stress values from the experiments and the predicted stress values correspond to the same strain values were used to figure out these parameters. "*RMS*" and "*V*" have been estimated using Equations (19) and (20), respectively; which are reported in Tables 2-4:

$$RMS = \sqrt{\frac{\sum|t_i - o_i|^2}{n}} \tag{19}$$

$$V = 1 - \frac{\sum|t_i - o_i|^2}{\sum|o_i|^2} \tag{20}$$

where, "$t_i$", "$o_i$" and "$n$" indicate the measured outcomes (used as target), predicted outcomes (used as output) and the total amount of observations, respectively.

## 4. DISCUSSION

The relative efficacy of selected stress-strain models with their ability to predict the stress-strain relationships have been appraised. Figures 1, 2 and 3 reveal the comparison of measured stress-strain relationship by Xiao et al. and the predicted stress-strain relationships of Xiao's model along with the predictions of other selected models. It is quite obvious that the predictive efficacy of the model expected to be comparatively more accurate against own measured data as the respective model itself built on the regression analysis of that data. However, there are considerable amount of deviations in measured and predicted relations of descending portions especially for concrete containing 100% RCA. Figures 4-9 depict the measured stress-strain relationships of Belén et al. [12] against the predictions of selected models. There is reasonable match in the ascending branch except Figures 5 and 6. On the contrary, there is significant discrepancy in the measured and predicted relationships in the descending branches of SSCs. In Figures10 and 11, the comparison of measured stress-strain relationship of Suryawanshi et al. [13] and predictions of selected

**TABLE 2.** Summary of measured and estimated areas under stress-strain curves

| Specimen Id | Measured | | | | Xiao et al. [10] | | | | Belén et al. [12] | | | | Suryawanshi et al. [13] | | | |
|---|---|---|---|---|---|---|---|---|---|---|---|---|---|---|---|---|
| | $A_1$ | $A_2$ | A | μ | $A_1$ | $A_2$ | A | μ | $A_1$ | $A_2$ | A | μ | $A_1$ | $A_2$ | A | μ |
| NC | 0.70 | 0.86 | 1.56 | 0.55 | 0.68 | 0.85 | 1.53 | 0.56 | 0.70 | 0.81 | 1.51 | 0.54 | 0.65 | 0.77 | 1.42 | 0.540 |
| RC-50 | 0.61 | 0.64 | 1.24 | 0.51 | 0.60 | 0.64 | 1.24 | 0.51 | 0.66 | 0.60 | 1.26 | 0.48 | 0.63 | 0.64 | 1.27 | 0.507 |
| RC-100 | 0.61 | 0.65 | 1.26 | 0.52 | 0.59 | 0.53 | 1.12 | 0.47 | 0.67 | 0.71 | 1.38 | 0.51 | 0.62 | 0.62 | 1.24 | 0.500 |
| H-0.50-0% | 0.62 | 0.76 | 1.39 | 0.55 | 0.68 | 0.86 | 1.54 | 0.56 | 0.64 | 0.50 | 1.14 | 0.44 | 0.65 | 0.77 | 1.43 | 0.543 |
| H-0.50-50% | 0.61 | 0.81 | 1.42 | 0.57 | 0.60 | 0.64 | 1.23 | 0.51 | 0.66 | 0.64 | 1.30 | 0.49 | 0.62 | 0.78 | 1.41 | 0.557 |
| H-0.50-100% | 0.62 | 0.80 | 1.42 | 0.56 | 0.58 | 0.60 | 1.19 | 0.51 | 0.65 | 0.58 | 1.23 | 0.47 | 0.61 | 0.69 | 1.31 | 0.531 |
| H-0.65-0% | 0.67 | 0.89 | 1.56 | 0.57 | 0.68 | 0.89 | 1.57 | 0.57 | 0.68 | 0.76 | 1.44 | 0.53 | 0.65 | 0.79 | 1.44 | 0.548 |
| H-0.65-50% | 0.67 | 0.82 | 1.49 | 0.55 | 0.60 | 0.65 | 1.24 | 0.52 | 0.68 | 0.75 | 1.43 | 0.52 | 0.64 | 0.70 | 1.34 | 0.525 |
| H-0.65-100% | 0.68 | 0.85 | 1.52 | 0.56 | 0.59 | 0.87 | 1.46 | 0.60 | 0.69 | 0.78 | 1.47 | 0.53 | 0.62 | 0.62 | 1.24 | 0.500 |
| R00 | 0.69 | 0.81 | 1.51 | 0.54 | 0.68 | 0.53 | 1.21 | 0.44 | 0.66 | 0.63 | 1.29 | 0.49 | 0.65 | 0.77 | 1.42 | 0.542 |
| R100 | 0.59 | 0.66 | 1.25 | 0.53 | 0.59 | 0.53 | 1.12 | 0.47 | 0.67 | 0.71 | 1.38 | 0.51 | 0.62 | 0.60 | 1.22 | 0.493 |

**TABLE 3.** Comparison of Root Mean Square (RMS) of the all predictive models

| Specimen Id | Xiao et al. [10] | Du et al. [11] | Belén et al. [12] | Suryawanshi et al. [13] |
|---|---|---|---|---|
| NC | 0.023 | -- | 0.199 | 0.053 |
| RC-50 | 0.021 | -- | 0.077 | 0.030 |
| RC-100 | 0.098 | 0.136 | 0.085 | 0.030 |
| H-0.65-0% | 0.021 | -- | 0.135 | 0.096 |
| H-0.65-50% | 0.144 | -- | 0.102 | 0.113 |
| H-0.65-100% | 0.088 | 0.226 | 0.076 | 0.193 |
| H-0.50-0% | 0.076 | -- | 0.174 | 0.056 |
| H-0.50-50% | 0.105 | -- | 0.138 | 0.040 |
| H-0.50-100% | 0.122 | 0.196 | 0.149 | 0.074 |
| R00 | 0.208 | -- | 0.219 | 0.074 |
| R100 | 0.103 | 0.152 | 0.098 | 0.071 |

**TABLE 4.** Comparison of Coefficient of Variance **(**V) of the all predictive models

| Specimen Id | Xiao et al. [10] | Du et al. [11] | Belén et al. [12] | Suryawanshi et al. [13] |
|---|---|---|---|---|
| NC | 0.9989 | -- | 0.9941 | 0.9793 |
| RC-50 | 0.9989 | -- | 0.9874 | 0.9979 |
| RC-100 | 0.9702 | 0.9577 | 0.9853 | 0.9978 |
| H-0.65-0% | 0.9992 | -- | 0.9603 | 0.9800 |
| H-0.65-50% | 0.9415 | -- | 0.9779 | 0.9689 |
| H-0.65-100% | 0.9837 | 0.8745 | 0.9881 | 0.8985 |
| H-0.50-0% | 0.9878 | -- | 0.9165 | 0.9927 |
| H-0.50-50% | 0.9685 | -- | 0.9546 | 0.9963 |
| H-0.50-100% | 0.9551 | 0.8952 | 0.9446 | 0.9862 |
| R00 | 0.8847 | -- | 0.8893 | 0.9886 |
| R100 | 0.9680 | 0.9457 | 0.9798 | 0.9873 |

models have been presented. Perusal of all these figures clearly indicates that the predictions of the model in the form of polynomial expression proposed by Suryawanshi et al. [13] gives comparatively more accurate results irrespective of pre-peak or post-peak regions.

In order to verify the predictivity of selected models, the areas under the curves have been calculated by developing the program in Microsoft-Excel. The program employed the Trapezoidal rule to calculate the area. The area under the curve up to the peak is designated as $A_1$ and area after the peak is nomenclatured as $A_2$. The summation of $A_1$ and $A_2$ is treated as a normalised toughness ($A$), since the SSC is in non-dimensional form. The predictive efficacy of the selected models have been checked against the ductility index ($\mu$). The ductility index may be defined as the ratio of $A_2$ and $A$. The measured and estimated values of $A_1$, $A_2$, $A$ and $\mu$ are compiled together in Table 2. It has been observed that the values of normalised toughness predicted by Suryawanshi et al. [13] are in good agreement compared to the predictions of other models. As stated in section 3, the quality of fit of predictions of stress-strain relationships with that the experimentally obtained, is investigated in terms of the values of root mean square error, *RMS*, and the coefficient of variance, *V*, respectively. The comparison of values of *RMS* and *V* are depicted in Tables 3 and 4, respectively. The model that conceives the lowest value of *RMS* and the unit value of *V* is considered as the most effective model. On the parameters of *RMS* and *V*, it is seen that the predictions of Suryawanshi et al. [13] are reasonably acceptable compared to the outputs of counterpart models.

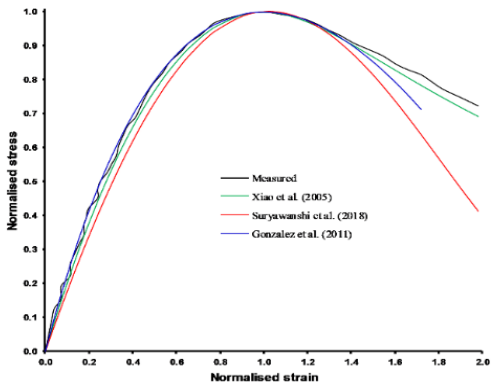


**Figure 1.** Comparison of measured (NC, Xiao et al. [10]) and predicted Stress-strain relationships

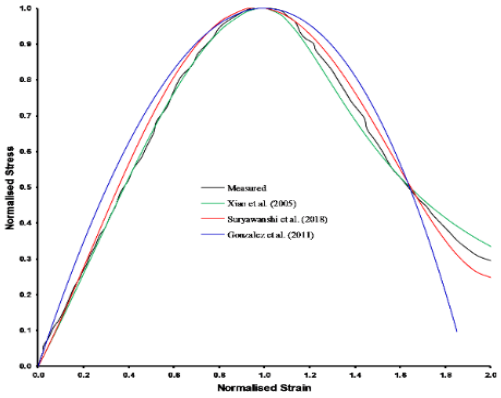


**Figure 2.** Comparison of measured (RC-50, Xiao et al. [10]) and predicted Stress-strain relationships

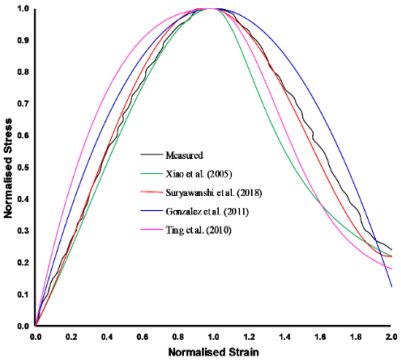


**Figure 3.** Comparison of measured (RC-100, Xiao et al. [10]) and predicted Stress-strain relationships

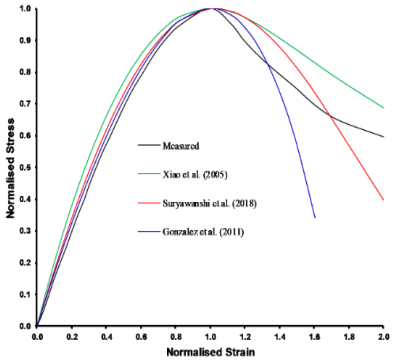


**Figure 4.** Comparison of measured (H-0.50-0%, Belén et al. [12]) and predicted Stress-strain relationships

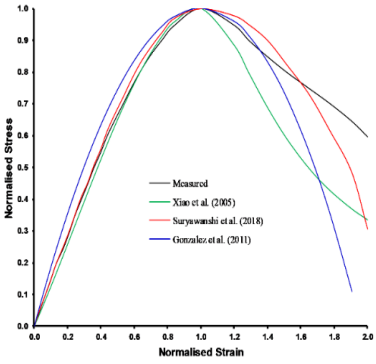


**Figure 5.** Comparison of measured (H-0.50-50%, Belén et al. [12]) and predicted Stress-strain relationships

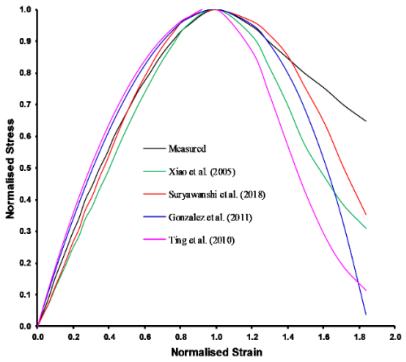


**Figure 6.** Comparison of measured (H-0.50-100%, Belén et al. [12]) and predicted Stress-strain relationships

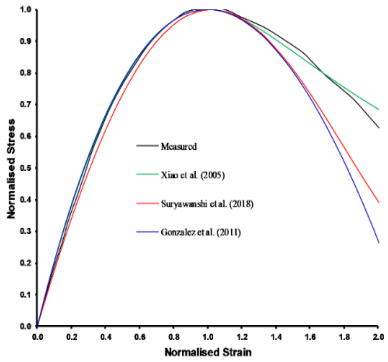


**Figure 7.** Comparison of measured (H-0.65-0%, Belén et al. [12]) and predicted Stress-strain relationships

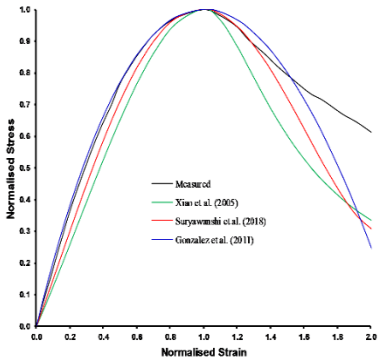


**Figure 8.** Comparison of measured (H-0.65-50%, Belén et al. [12]) and predicted Stress-strain relationships

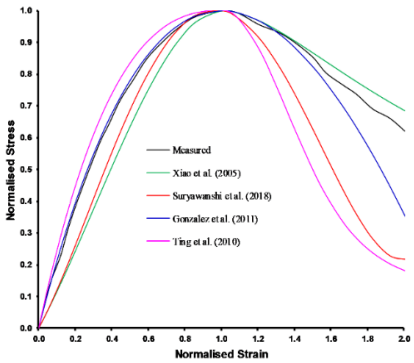


**Figure 9.** Comparison of measured (H-0.65-100%, Belén et al. [12]) and predicted Stress-strain relationships

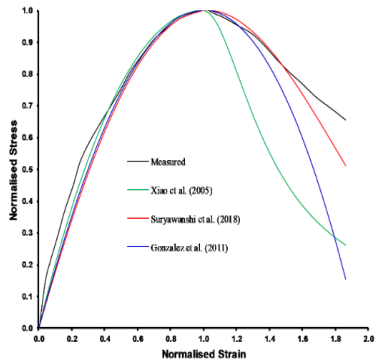


**Figure 10.** Comparison of measured (R00, Suryawanshi et al. [13]) and predicted Stress-strain relationships

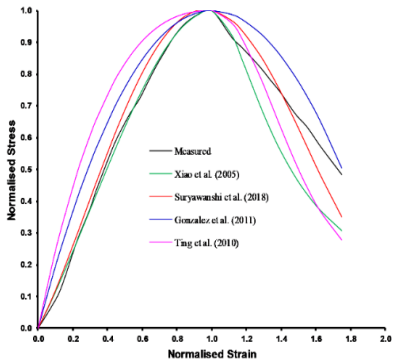


**Figure 11.** Comparison of measured (R100, Suryawanshi et al. [13]) and predicted Stress-strain relationships

## 5. CONCLUSION

In this work, the published models to define stress-strain relationships for RAC have been calibrated against the experimentally measured outcomes which are reported in the literature. The measured value of peak compressive stress and associated peak strain value were utilized as input parameters to operate prediction models in order to reproduce entire SSC. The findings of this study may be summarised as follows:

- The predictive efficacy of selected models is more or less similar for the ascending portion while it is found that the level of prediction accuracy is of varying degree for descending portion of the SSCs. This may be due to the approach adopted in the formulation of the model. Nevertheless, the stress-strain generated by polynomial expressions are more relatable.
- The predictive efficiency of the models has also been evaluated in terms of normalised toughness and ductility index. The predictions of models proposed and reported in literature are found closer to measured values.
- The accuracy of the outputs of the considered models in terms of normalised toughness and ductility index are further evaluated on statistical grounds. This was revisited by comparing the values of the *RMS* and *V*. The model that conceives the lowest value of *RMS* and the unit value of *V* is considered as the most effective model. On the parameters of *RMS* and *V*, it is seen that the predictions of polynomial expression are reasonably acceptable compared to the outputs of counterpart models.
- The use of commercial packages has become an integral part of the modern analysis of concrete structures. Some of the commercial computer programs offer freedom to the users to define the materials through the user-defined material models in the form of laboratory evaluated stress-strain relationships. The use of the stress-strain relationship in the form of polynomial expression may play crucial role in the simulation of the concrete structures and may yield near practical results.

## 6. REFERENCES


1. Poon, C.S., Shui, Z. and Lam, L., "Effect of microstructure of itz on compressive strength of concrete prepared with recycled aggregates", ***Construction and Building Materials***, Vol. 18, No. 6, (2004), 461-468. https://doi.org/https://doi.org/10.1016/j.conbuildmat.2004.03.005
2. Fathifazl, G., Razaqpur, A.G., Isgor, O.B., Abbas, A., Fournier, B. and Foo, S., "Creep and drying shrinkage characteristics of concrete produced with coarse recycled concrete aggregate", ***Cement and Concrete Composites***, Vol. 33, No. 10, (2011), 1026-1037. https://doi.org/https://doi.org/10.1016/j.cemconcomp.2011.08.004
3. Kaza, S., Yao, L., Bhada-Tata, P. and Van Woerden, F., "What a waste 2.0: A global snapshot of solid waste management to 2050, World Bank Publications, (2018).
4. Yasin Mousavi, S., Tavakkoli, A., Jahanshahi, M. and Dankoub, A., "Performance of high-strength concrete made with recycled ceramic aggregates (research note)", ***International Journal of Engineering, Transactions C: Aspects,*** Vol. 33, No. 6, (2020), 1085-1093. https://doi.org/10.5829/ije.2020.33.06c.05
5. Masne, N. and Suryawanshi, S., "Analytical and experimental investigation of recycled aggregate concrete beams subjected to pure torsion", ***International Journal of Engineering, Transactions A: Basics,*** Vol. 35, No. 10, (2022), 1959-1966. doi. https://doi.org/10.5829/ije.2022.35.10A.14
6. Kou, S.-C., Poon, C.-S. and Wan, H.-W., "Properties of concrete prepared with low-grade recycled aggregates", ***Construction and Building Materials***, Vol. 36, (2012), 881-889. https://doi.org/https://doi.org/10.1016/j.conbuildmat.2012.06.060
7. Kou, S. and Poon, C.S., "Enhancing the durability properties of concrete prepared with coarse recycled aggregate", ***Construction and Building Materials***, Vol. 35, (2012), 69-76. https://doi.org/https://doi.org/10.1016/j.conbuildmat.2012.02.032
8. McNeil, K. and Kang, T.H.-K., "Recycled concrete aggregates: A review", ***International Journal of Concrete Structures and Materials***, Vol. 7, No. 1, (2013), 61-69. https://doi.org/10.1007/s40069-013-0032-5
9. Raveendra, B.R., Benipal, G.S. and Singh, A.K., "Constitutive modelling of concrete: An overview", (2005).
10. Xiao, J., Li, J. and Zhang, C., "Mechanical properties of recycled aggregate concrete under uniaxial loading", ***Cement and Concrete Research***, Vol. 35, No. 6, (2005), 1187-1194. https://doi.org/https://doi.org/10.1016/j.cemconres.2004.09.020
11. Du, T., Wang, W., Liu, Z., Lin, H. and Guo, T., "The complete stress-strain curve of recycled aggregate concrete under uniaxial compression loading", ***Journal of Wuhan University of Technology-Mater. Sci. Ed.***, Vol. 25, No. 5, (2010), 862-865. https://doi.org/10.1007/s11595-010-0109-9
12. Belén, G.-F., Fernando, M.-A., Diego, C.L. and Sindy, S.-P., "Stress–strain relationship in axial compression for concrete using recycled saturated coarse aggregate", ***Construction and Building Materials***, Vol. 25, No. 5, (2011), 2335-2342. https://doi.org/https://doi.org/10.1016/j.conbuildmat.2010.11.031
13. Suryawanshi, S., Singh, B. and Bhargava, P., "Equation for stress–strain relationship of recycled aggregate concrete in axial compression", ***Magazine of Concrete Research***, Vol. 70, No. 4, (2018), 163-171. https://doi.org/10.1680/jmacr.16.00108
14. Dacheng, G.Z.Z.X.Z. and Ruqi, W., "Experimental investigation of the complete stress-strain curve of concrete", ***Journal of Building Structures***, Vol. 3, No. 01, (1982), 1.
15. Européen, C., "Eurocode 2: Design of concrete structures—part 1-1: General rules and rules for buildings", London: British Standard Institution, (2004).
16. Rosa, G., González, G., Sánchez, P. and Prieto, B., "Review of the quality control of concrete reinforced with steel fibers according to the spanish structural concrete code ehe 08", in 2nd Building and Management International Conference. Proceedings., (2019).
17. Bhikshma, V. and Kishore, R., "Development of stress-strain curvesfor recycled aggregate concrete", (2010). https://www.sid.ir/en/Journal/ViewPaper.aspx?ID=185482
18. Desayi, P., Sundara Raja Iyengar, K. and Sanjeeva Reddy, T., "Equation for stress-strain curve of concrete confined in circular steel spiral", ***Matériaux et Construction***, Vol. 11, No. 5, (1978), 339-345.
19. Peng, J.-L., Du, T., Zhao, T.-S., Song, X.-q. and Tang, J.-J., "Stress–strain relationship model of recycled concrete based on strength and replacement rate of recycled coarse aggregate", ***Journal of Materials in Civil Engineering***, Vol. 31, No. 9, (2019), 04019189. https://doi.org/10.1061/(ASCE)MT.1943-5533.0002847
20. Khan, S., Ayub, T. and Rafeeqi, S., "Prediction of compressive strength of plain concrete confined with ferrocement using artificial neural network (ANN) and comparison with existing mathematical models", ***American Journal of Civil Engineering and Architecture***, Vol. 1, No. 1, (2013), 7-14. https://doi.org/10.12691/ajcea-1-1-2
21. Ayub, T., Shafiq, N. and Nuruddin, M.F., "Stress-strain response of high strength concrete and application of the existing models", ***Research Journal of Applied Sciences, Engineering and Technology***, Vol. 8, No. 10, (2014), 1174-1190.

Persian Abstract

**چکیده**

تقاضای فزاینده ای برای مواد جایگزین مناسب از مواد تشکیل دهنده بتن به ویژه سنگدانه های ریز و درشت به منظور دستیابی به توسعه پایدار در عصر شهرنشینی سریع وجود دارد. بنابراین، فرآیند ساخت بتن با استفاده از سنگدانه های بازیافت شده از زباله های ساخت و ساز و تخریب به عنوان یک هدف اولیه برای بسیاری از سازمان های دولتی پدیدار شده است. در نتیجه، استفاده از بتن سنگدانه های بازیافتی (RAC) در کاربردهای سازه ای جنبه ضروری می شود. با این حال، RAC را می توان در کاربردهای ساختاری تنها در صورتی به کار برد که رابطه تنش-کرنش موثر موجود باشد. مدل‌های تنش-کرنش توسعه‌یافته برای بتن سنگدانه طبیعی (NAC) برای RAC کاملاً مناسب نیستند. از این رو، انتخاب مدل خوب که دارای ظرفیت پیش بینی دقیق است، نقش مهمی ایفا می کند. علاوه بر این، مدل‌های تنش-کرنش مبنایی را برای تحلیل و رویه‌های طراحی مدرن به ویژه در بسته‌های FEA فراهم می‌کنند. در مطالعه حاضر، مدل‌های تنش-کرنش برای RAC از ادبیات انتخاب شده و به منظور ارزیابی کارایی پیش‌بینی‌کننده آن‌ها مورد بررسی انتقادی قرار گرفته‌اند. نمونه های آزمایشی در قالب روابط تنش-کرنش اندازه گیری شده به دست آمده از ادبیات، با پیش بینی های هر مدل انتخاب شده مقایسه شده اند. علاوه بر مقایسه پروفیل‌های تنش-کرنش اندازه‌گیری شده و پیش‌بینی‌شده، خروجی مدل‌های انتخابی از نظر چقرمگی نرمال شده و شاخص شکل‌پذیری مورد ارزیابی قرار گرفت. سازگاری خروجی مدل ها با استفاده از ابزارهای آماری مانند ضریب واریانس و ریشه میانگین مربعات خطا ارزیابی می شود. نتایج مدل در قالب بیان چند جمله ای نسبتاً دقیق تر از سایر همتایان بود.

IJE TRANSACTIONS B: Applications Vol. 35, No. 11, (November 2022) 2111-2119

International Journal of Engineering

Journal Homepage: www. ije. ir

# Numerical Analysis to Study Lateral Behavior of Cement Fly Ash Gravel Piles under the Soft Soil

N. B. Umravia*, C. H. Solanki

*Civil Engineering Department, Sardar Vallabhbai National Institute of Technology Surat, Gujarat. India*

*PAPER INFO*

*Paper history:*
Received 06 April 2022
Received in revised form 13 July 2022
Accepted 27 July 2022

*Keywords*:
*Cement Fly Ash Gravel Pile*
*Plaxis 3D*
*Axial Load*
*Lateral Load*
*Lateral Behaviour*

*ABSTRACT*

Cement Fly ash and Gravel Piles are modern soil improvement techniques widely used in China for infrastructure development. It significantly impacts the fundamental characteristics of load-carrying capacities and deformation. The cement fly ash and gravel (CFG) piles are located on highways, railway embankments, essential projects, and problematic soil. These are often subjected to high risk of external load like flooding, seismic, etc. In such a case, foundation design can be governed by a required lateral resistance. The present study is based on the deformation behaviour of a CFG pile subjected to axial, lateral, and combined loading in soft clay. Numerical analysis using Plaxis 3D on a CFG pile with various influencing parameters soil condition, diameters, length, length to diameter ratio, and pile head loading condition to observe its effect. Overall, the pile study found variations in initial stress level, pile type, and pile head constraint. Still, these were minor compared to the impact of soil behaviour and mobility. The soil models varied stiffness and strength properties. The effects originating from the boundary conditions used were responsible for significantly decreasing lateral resistance for inner CFG piles under the active and passive loading.

***doi**: 10.5829/ije.2022.35.11b.06*

**NOMENCLATURE**

| | | | |
|---|---|---|---|
| *CFG* | Cement Fly Ash Gravel | *LE* | Linear Elastic Model |
| *S* | Spacing (Center to center distance of Piles) | *UD* | Undrained condition (B) |
| *NSF* | Negative Skin Friction | *DC* | Drained Condition |
| *D* | Diameter of CFG pile (mm) | *SS* | Soft Soil Model |
| *L/D* | Length / Diameter ration | $C'_{ref}$ | Cohesion |
| *FEM* | Finite Element Method | *E* | Young's modulus |
| *MC* | Mohr column model | $\mu$ | Position ratio |
| $k_x$; $k_{y;}$ $k_z$ | Permeability in x; y (horizontal) ; and Z (vertical) direction | OCR | Over consolidation ratio |
| φ' | Friction angle | φ' | Dilatancy angle |
| $\lambda$* | Modified compression index | $\kappa$* | Modified compression index |
| $E_{50}^{ref}$/ $E_{oed}^{ref}$ | Secant stiffness in standard drained triaxial test/ odometer loading | $E_{ur}^{ref}$ | Unloading / reloading stiffness |

## 1. INTRODUCTION

Population growth and rapid industrial expansion are land areas that have been highly required for road and railways embankments needed for the urban area for infrastructure development. As a result, lands once considered unsuitable for growth, such as low-lying areas, river bays, and coastal regions, are increasingly used for various infrastructural projects. India has a 7516-kilometre-long coastline, a 1596 km long coastal area in Gujarat state, and deposits of soft clayey soils can be found all along the coast and in nearby delta areas. The effect of the dispositional and weathering coastal area creates complex problems in geotechnical material across

*Corresponding Author Institutional Email: ds15am002@amd.svnit.ac.in (N. B. Umravia)

Please cite this article as: N. B. Umravia, C. H. Solanki, Numerical Analysis to Study Lateral Behavior of Cement Fly Ash Gravel Piles under the Soft Soil, ***International Journal of Engineering, Transactions B: Applications***, Vol. 35, No. 11, (2022) 2111-2119

the region. The embankments are constructed on soft and highly compressible silty clay or soft clays. Experience a large vertical and lateral settlement; therefore, ground improvement like column technology is an obvious choice in the embankment to provide the reinforcing and enhance foundation soil strength [1-8]. Cement-fly ash gravel (CFG) piles the most effectively under axial and lateral load reduced the settlement and deformation, respectively, among the various ground in improvement techniques [8-12]. The CFG is a composite foundation made of cement, fly ash, gravel, aggregate chips, sand, and moderate water. The soil between the piles is a soil solidification process using a technique. A dry or wet binder variable mix is mechanically combined with in situ natural soil to build columns for improved soil. This type of foundation, called a composite foundation crowned with a cushion layer, [11, 13-15] that indirectly carrying the foundation load and enhances the bearing capacity of soft ground. Hence the cushion's deformability depends on its characteristics. Piles' head pricks into the mattress layer, which leads to relative CFG pile settlement that creates based on negative side friction (NSF) characteristic of soil and pile [11]. On the upper side, 15–50 percents of the pile length has achieved a high bearing capacity and small differential settlement. The fly-ash is an industrial waste that reacts with the cement and makes a natural bonding gel that increases the concrete's strength Feng et al. [16] A combination of multiple piles with differing stiffness introduced by Cao and Liu [8], Lai et al. [10] and length [11, 12] has been used in practice to achieve further economic advantages of CFG pile reinforced ground. Performed numerical analyses, by unit cell approach by Yu et al., [5] the CFG piles using embankment numerical analysis done by Dresden and Approach [7]. Liu and Jia [17] developed a differential equation based on a typical unit calculation model to derive the depth of neutral plane and pile-soil stress ratio calculation formulas. Many areas are subjected to temperature variation. Therefore, the effect of temperature and heart exchange soil and CFG pile behaviour studied by Nguyen and Phan [18]. According to Wu et al. [19], the CFG pile ground improvement treatment is very effective on a field test on different ground improvement techniques. It is also uhelpful for an important highway project by Nguyen and Phan [18]; Wu et al. [19]; Hashemi et al. [20], and Hamidi and Lajevardi [21]. It has been a less vertical settlement and minimum lateral deformation than other ground improvement tests. The technical china code for ground improvement treatment for railway engineering (TB -10106-2010) explains the installation spacing and further specification of CFG piles.

Moreover, after installing CFG pile quality, bearing capacity under the soft soil, and efficiency check (less than 1-4% of total pile installation), it is required a loading test conducted by Anand and Sarkar [22], Abbas et al. [23], Zheng et al. [24]. The loading at field test suggested by with Chinese technical requirements for building foundation inspection (JGJ340-2015), Technical code for testing building foundation piles (JGJ106-2014), and Technical code for building ground treatment (JGJ106-2014) (JGJ 79-2012) [25]. Moreover, the basic concept of group CFG pile application with the geosynthetics materials that react like as a piled raft foundation behaviour [26-33]. The previous research focuses on various CFG pile composite foundation concepts and experiments to study the deformation behaviour under an axial (vertical) load. Moreover, there has been limited research on the design selection and parameter optimization of CFG pile (like length, diameters and grade of CFG) composite foundations, particularly in the deformable Indian soft soil condition.

Based on the literature review, the research gap was found there were fewer studies on the deformation behaviour of the single CFG pile subjected to active the passive lateral load. These techniques enhance the soft ground bearing capacity in the field, although lateral displacement was not deeply studied.

## 2. METHOD OF ANALYSIS

The numerical simulation approach is very significant in studying the behaviours of foundation, soil, and pile interaction. Moreover, CFG pile composite foundations have mechanical properties intermediate between shallow and deep foundations that depend on their stiffness nature. They are typically an unconnected form of foundation. The Finite Element Method (FEM); [16, 26-29] has risen in importance in geoengineering and design during the last two decades. In this study, the FEM constitutive models are used to simulate the structural characteristics of soils, and model parameters describe specific features of soil behaviour. These constitutive models can range in complexity from simple to complex. Simple models, in general, require only a small number of parameters to be chosen, but they may be missing some important aspects of soil behaviour. More complex models may encompass more aspects of soil behaviour, but they also necessitate the selection of more parameters based on soil investigation data. The main objective of present work is to understand the behaviour of a single CFG pile subjected to axial, lateral, and combined load in soft soil.

## 3. NUMERICAL MODEL DESCRIPTION

**3. 1. Model Description** The finite-element model was created using the commercial FE software PLAXIS 3D. The Mohr-coulomb (MC) consecutive models worked on the elastic and elastic-plastic

behaviours of soil and structure interaction due to the MC model considered for the clay and soft soil. The CFG piles behaviour is linear; therefore, the CFG pile is considered a Linear elastic (LE) model [35]. The usual mesh geometry used in the model is depicted in Figure 1.

In numerical analysis, the effect of stress at the boundary was minimized by providing a large length and width (10D). The homogeneously treated soil medium was produced at least five times as broad as the foundation ($b_r$) in the lateral extent and more than twice as deep as the long pile length vertically. A stiff sand layer has been provided below the soft soil (approximately 2 m after soft ground) that fixed base to avid the significant vertical displacement. Hence, considering computational expenses without compromising accuracy, the mesh density was finer in the neighbourhood of structural members with gradual change to coarser mesh sizes for farther locations. Each part was discretized using a fifteen-node linear brick element with reduced integration and hourglass control.

The surrounding vertical boundaries were modeled to restrain lateral displacements, while the bottom was set to constrain both horizontal and vertical displacements. The top surface boundary was set to be free in each direction. The analysis was initiated by generating $K_0$ geostatic stress field within the soil mass that produced minimal deformation yet was in equilibrium with pore water pressure. The initial condition was followed by introducing piles sequentially, considering the soil and CFG pile surface are rough. Construction vibration has not been accountable. The shear strength effect increases with depth, the variation of the lateral factor with depth, and the impact of strength anisotropy.

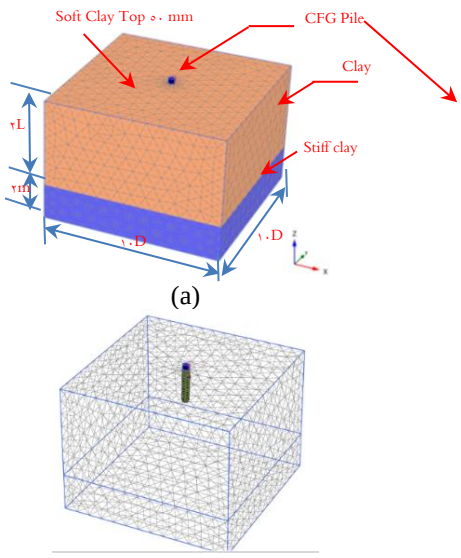


(a)

(b)

**Figure 1.** (a) Model Geometry (b) Finite Element Model (FEM) with model mesh

The selection of a constitutive model of soil mass when defining material properties is critical to the outcome. The Tresca yield criterion, von Mises yield criterion, Drucker–Prager yield criterion, Mohr-Coulomb yield criterion, and double-shear stress yield criterion are now used in geotechnical engineering. The present study considers the axial and lateral behaviour of a single CFG pile under the single layer soft soil model and an MC model. "Hard" contact in the normal direction and Coulomb friction in the tangent direction were used to represent the contact behaviour at the pile-soil surface. The Mohr-Coulomb model is based on graphing Mohr's circle in the main and minor axes for stress states at yield because a typical geotechnical test determines cohesiveness ($C$) and internal friction angle ($\varphi$). It plays an essential role in practical application and is extensively used. The present study is on the numerical analysis of axial behaviours of three different diameters (0.5, 0.7, and 0.9 m) with different L/D ratios (6, 12, and 18) of CFG piles. Its effect has been analyzed under the lateral load. To study behaviour under the combined load of axial and lateral. Moreover, the lateral behaviour of the CFG pile when its soil is subjected to passive lateral load. A settlement and deformation study was considered the prescribed 50 mm under the axial and 15 mm in lateral displacement, respectively.

**3. 2. Model Assessment Criteria** Four different metrics materials models, LE, MC, SS, and HS, were chosen to appraise and compare the behaviours of CFG pile under the horizontal and verticle loading. The CFG pile foundation selects the LE model [34]. In order to model the interaction between pile and soil, ensure that the pile's element node coincides with the soil's element node and that the soil's mesh size is the same as the pile's mesh size. Effect of pile size on lateral displacement, pile diameter is set to 0.5, 0.7, and 0.9 m: active loading and passive loading condition. The CFG pile head, approximately 0.3 m above the ground level, was subjected to the lateral load in the active state. Therefore circular plate is fixed and loads in one direction. In the case of lateral load subjected soil passive, the upper 0.3 m soil mass moved, creating the lateral thrust. When the MC model, the upper layer of 0.3 m collapsed in numerical analysis; therefore, it was modified with the soft clay SS soil model in passive condition soil. This approach gives comparative results on lateral in active and passive loading conditions. Solid elements used. The Poisson ratio, cohesive, deformation modulus, and specific parameters are listed in Table 1.

## 4. RESULT AND DISSCUSION

Discuss the effect of D - 0.5, 0.7, and 0.9 m diameter CFG pile subjected to relative axial load conditions on

**TABLE 1.** Details of Material properties of pile and soil

| Parameter | Unit | CFG pile | Clay | Soft Clay | Stiff Clay |
|---|---|---|---|---|---|
| Material Model | - | LE | MC | SS | HS |
| Drainage Types | | Nonporous | UD | UD | Drained |
| Unit Weight | $\gamma$ (kN/m$^2$) | 22 | 14 | 16 | 18 |
| Young's Modulus | $\grave{E}$ (kN/m$^2$) | 2.4x10$^6$ | 12.5 x10$^3$ | 9x10$^3$ | 15 x10$^3$ |
| Undrained shear strength | $C'_{ref}$ (kN/m$^2$) | 1.0 | 45 | 10 | 18 |
| Poisson ratio | $\mu$ | 0.15 | 0.25 | 0.4 | 0.3 |
| Friction angle | $\varphi'$ | -- | 0 | 23 | 25 |
| Dilatancy angle | $\psi$ | -- | 0 | 0 | 25 |
| Modified compression index | $\lambda^*$ | -- | -- | 0.18 | -- |
| Modified swelling index | $\kappa^*$ | -- | -- | 0.04 | -- |
| Secant stiffness in standard drained triaxial test | $E_{50}^{ref}/ E_{oed}^{ref}$ (kN/m$^2$) | -- | -- | -- | 50x 10$^3$ |
| Reloading Stiffness | $E_{ur}^{ref}$ (kN/m$^2$) | -- | -- | -- | 150x10$^3$ |
| Power of stress- stiffness | $m$ | -- | -- | -- | 0.5 |
| Permeability | $k_x$ ; $k_y$, $k_z$ (m/day) | -- | -- | -- | 0.25x 10$^3$ |
| Over consolidation Ratio | $OCR$ | 1.0 | 1.5 | 1.0 | 1.0 |
| Pre overburden pressure | $POP$ | 0.0 | 0.0 | 5.0 | 0.0 |

deformation based on lengths 6D, 12D, and 18D. Significant the Effect of length that enhanced the load-carrying capacity of CFG pile.

**4. 1. Study the Influence of Pile Length under Axial Load** The CFG pile was subjected to axial load analysis performed in two conditions. Frist condition is to analyze that have a direct axial load only. Then, it was analyzed under the combined axial and lateral load. The first condition analysis result of D -0.5 m with influences the variable pile length 6D, 12D, and 18D, respectively, as shown in Figure 2. The load settlement curve is nonlinear behaviour. Its plastic point of deformation is near an 8- 12 mm settlement. The CFG Pile length is categorized into short, medium, and long piles. The long pile has an extended NSF resistivity than the medium and short pile. Therefore 12D and 18D lengths of CFG pile's ultimate load-carrying capacity increased 1.93 and 9.25 times than the 6D length. The test results plot the load-displacement curve; the ultimate load is obtained by the tangent intersection method [35].

**4. 2. Study the Influence of Pile Length under Axial Load** In order to compare the load settlement curve of D-0.5, 0.7, and 0.9 with the 6D length of the short pile shown in Figure 3. Its nature is, as usual, nonlinear, but the deformation curve's plastic point increased with increased diameters because of the weak contained effect of the CFG pile and the low shearing strength of the soil. As a result, the axial load carrying remarkable increases with the increased diameter. For example, in D-0.9 m and 0.7 m dia. of CFG pile, ultimate axial load are 4.08 and 8.78 times higher than D-0.5 m.

Similar behaviour is shown in a higher length CFG pile, as shown in Figure 4. The CFG pile length 12D and D- 0.5 and 0.7m diameter plastic point of deformation was found in soil near 10- 15 mm settlement. While in higher length, it may increase with increased diameter. The plastic deformation point is important in finding the ultimate load using the double tangent method.

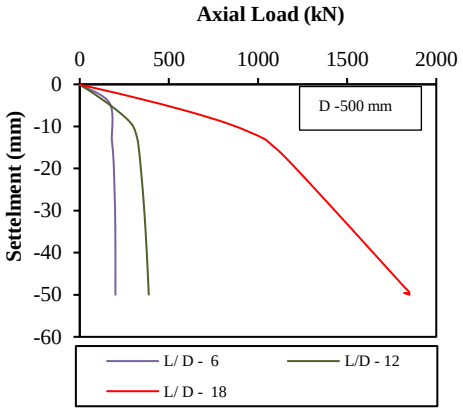


**Figure 2.** Relation between axial load and settlement of D – 0.5 m with variable length of CFG pile

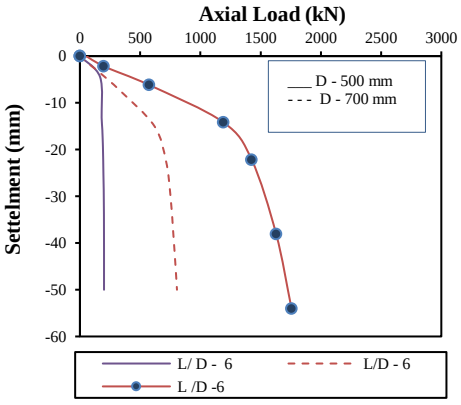


**Figure 3.** Relation between axial load and settlement with a variable diameter of CFG pile

Therefore, its ultimate load capacity is increased. However, to compare the stress concentration of 0.5 D value is significantly higher than the 0.7 and 0.9 D., The effective stress in the same diameter pile in a longer length of CFG, was found to be approximately 20 % higher than smaller length CFG pile in 0.5, 0.7 and 0.9 diameters.

**4. 3. Study the Impact of Verticle Deformation under the Combined Load** In the numerical analysis of piles, many researchers study axial or lateral load subjected to understand the behaviours of the pile under the settlement and its deformation nature. Still, it may be subjected to a combined effect in the field. For example, a combined load of axial and lateral pile D - 0.7 behaviours under the vertical settlements is shown in Figure 5. The axial load capacity has been decreased near 20- 30 % compared to only axial load subjected to CFG pile. In analysis, the CFG pile is a LE model subjected to only a one-dimensional effect in axial load. Still, in a combined load, the two-dimensional load effect of pile deformation has been distributed in both dimensional.

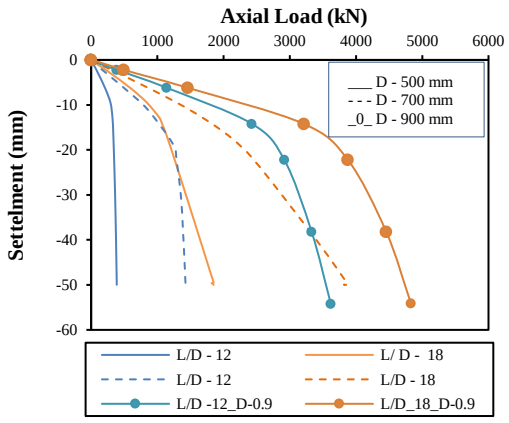


**Figure 4.** Relation between axial load and settlement with a variable diameter of CFG pile

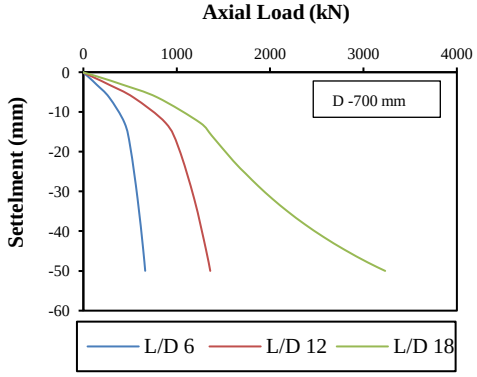


**Figure 5.** Load and settlement curve with variable length of CFG pile

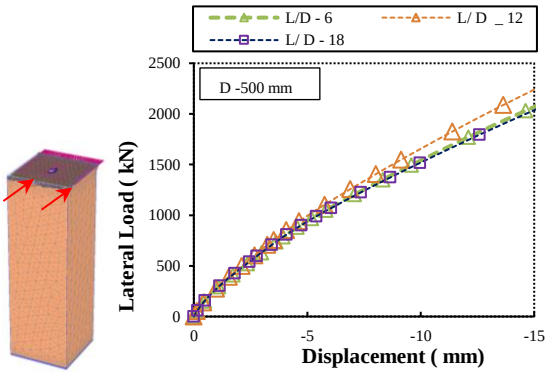


**Figure 6.** Lateral load and displacement curved of single CFG pile with passive load

**4. 4. Study the Influence of Pile under The Lateral Load** The CFG pile subjected to only the lateral load with variable length study has been considered. Normally, the lateral load is directly applied at the pile top and evaluated its deformation. However, our study has considered the three different conditions of lateral deformation.

Following loading conditions, (I) the lateral deformation of the CFG pile is subjected to only lateral load; (II) lateral deformation of CFG pile under the combined load of axial and lateral; (III) Lateral deformation of CFG pile under the passive. Figure 6 explains the relationship between the passive lateral load and variable-length CFG pile deformation. The upper 0.3, m. modelling soil layer moved horizontally; therefore, the condition of load on CFG pile top is defined as passive lateral load. The model of upper soil is defined as SS-type Soft soil considering. The results are very near in all diameter conditions. The pile bodies and top lateral displacements change slightly as the pile diameter grows from 0.6 m to 0.9 m. The CFG pile body and pile top lateral displacements were barely at 1500 KN and were reduced, rarely decreasing from 10.15 mm to 10.42 mm. However, when the pile diameter increased from 0.7 to 0.9 m, the maximum lateral displacement at the pile top reduced to 2.31 mm at increased diameter, indicating a nonlinear connection.

**4. 5. Study of the Influence of Pile with Variable Lateral Load** The soil mass in front of piles creates active earth pressure, whereas the soil mass behind piles generates passive earth pressure due to the lateral displacement of piles (axis direction). When the ground pressure exceeds the strength of the soil mass, plastic displacement occurs. Figure 7 explains the greatest primary plastic strain of soil mass under (I) and (II) under three loading conditions. The lateral displacements of the pile body are rather modest. Moreover, there are no plastic zones in the foundation soil. However, with increasing operating conditions (III),

the lateral displacement of the pile body grows, and the soil mass range in the accessory section around the piles creates a plastic zone.

In comparison to Figures 7(a), 7(b), and 7(c) detail the relationship of the lateral displacements of the CFG pile with variable length subjected lateral load under the active passpile. When the diameter was 0.5 to 0.7 and 0.7 to 0.9 m increased, the lateral load was 67.5 and reduced by 16.5 percents, respectively, Because providing lateral force at the pile top is comparable to imposing one constraint, this conclusion suggests that the load at the pile top can greatly minimize the lateral displacement of the pile body. As a result, the pile top's free displacement turned into restricted displacement, limiting pile top movement to some extent. However, one uninformative result was found that lateral capacity of CFG pile is increased nominal with increased length in case (I) and (II) loading, but it is remarkable increased lateral load (8- 24 % ) in equal length and equal diameter of CFG pile in case (I) to case (II) loading. Because in case II loading, the resistance of CFG pile is increased due to the axial load (overburden load)on it that prevention the lateral movement.

Figure 7(c) shows lateral load vs settlement of L/D-6 and L/D-12 behavious under the active lateral load is a non linear as which is explain that pile failed with

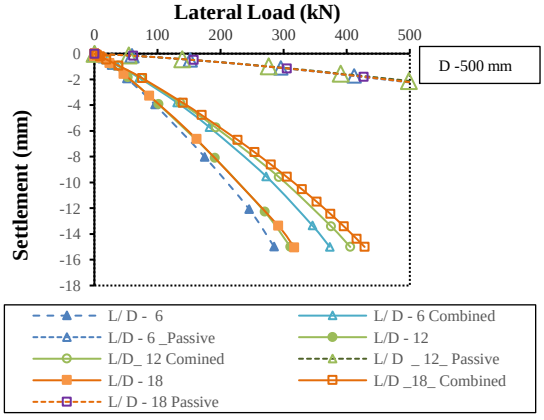


(a)

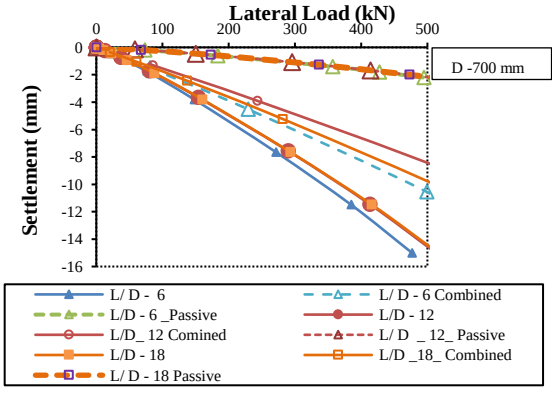


(b)

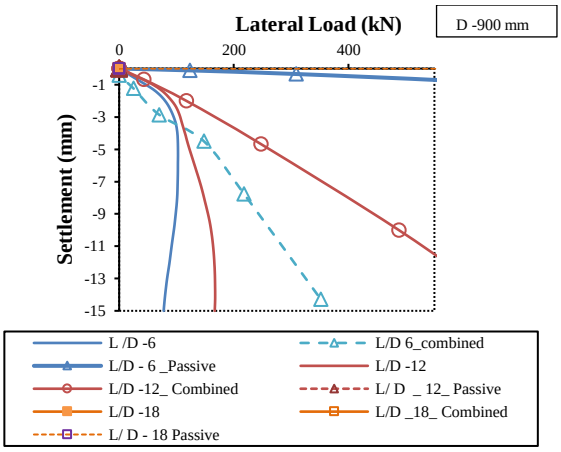


(C)

**Figure 7.** (a) 0.5 D (b) 0.7 D (c) 0.9 D ; Lateral load deflection curved Inflence with varable L/D ratio

subjected to a nominal load. Because both cases were considered floating pile conditions. The CFG pile subjected to only displacement it loadloadlementent relation linear it is like as a Figure 12(a) and if Pile is sudden fail as a Figure 12(b).

**4. 6. To study the Stiffness of CFG pile Under The Variable Diameter** It is termed long if the effective length is higher than 12 times its least diameter. The pile is deemed short if the effective length to the least lateral dimension ratio is less than or equal to 12. Figures 8, 9, and 10 show the lateral displacement distribution cloud diagram of the CFG pile body subjected to the case (III) passive loading conditions for various pile diameters and its constant L/D -6, 12, and 18 ratios. The computed indicates that as the pile diameter increases, the lateral displacements of the CFG pile body and pile top decrease gradually. When foundation soil mass reacts under the load, increased deformation depends on stiffness, the necessary foundation treatment to be identified, and the pile body's lateral resistance demands to be satisfied. For square and hexagonal piles, the primary interpreted failure loads correspond to settlements of 0.1d, where d is the equivalent pile diameter, which refers to an equivalent circle diameter. Such a formulation ignores the elastic shortening of the pile, which might be significant for long piles but insignificant for small piles. The settlement, in actuality, refers to the movement of the superstructure (pile with soil), not the capacity of the soil in reaction to the loads delivered to the pile in a static loading test. The lateral stress effect is with the increased diameter of the CFG pile. According to the studies, a substantial lateral displacement will be created under structural stress to measure its safety. The movement of the CFG pile process was implemented by incorporating the findings of the parameter analysis in case (III). Spinning pile processing can improve the strength of the

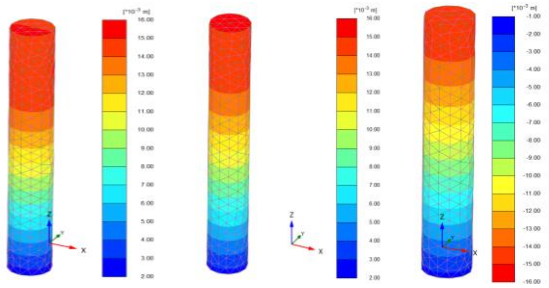

(a) D-0.5 m (b) D-0.7 m (c) D-0.9 m

**Figure 8.** Passive Lateral effect of Sigle CFG pile in Soft clay L/D -6

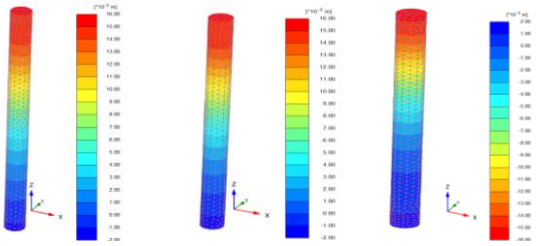

(a) D-0.5 m (b) D-0.7 m (c) D-0.9 m

**Figure 9.** Passive Lateral effect of Sigle CFG pile at L/D -12, in soft clay

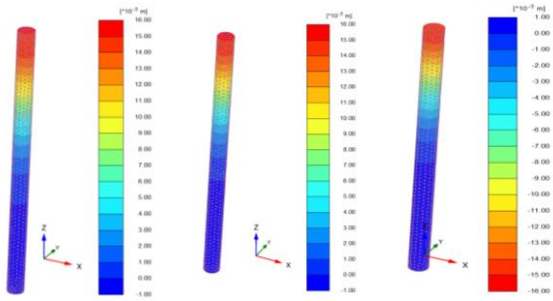

(a) D-0.5 m (b) D-0.7 m (c) D-0.9 m

**Figure 10.** Passive Lateral effect of Sigle CFG pile at L/D -18 in Soft clay

soil mass encircling the pile top, limiting the pile body's lateral movement. After processing, the Lateral displacement at the pile top is just 3.6 mm.

In the case of lateral loads, the CFG pile acts as a transversely loaded beam, transferring the lateral load to the surrounding soil via the earth's lateral resistance. When a weight is applied to a pile, it bends, rotates, or moves horizontally, resulting in bending, rotation, or translation.

Furthermore, the processing can enhance CFG pile stiffness depending upon its L/D ratio. A long pile load-carrying capacity is lower than a short column with the same cross-sectional area. Crushing is the cause of the short CFG pile failure shown in Figure 11 explains the effect of the length of the CFG pile under the lateral deformation. When the CFG pile length is short (L/D< 15), it behaves like a rigid, as shown in Figures 11(a) and 11(b) the failure pattern defined under the shear. While the long pile failed Due to buckling, all of the long CFG piles failed like Figure 11(c). because It has a larger radius gyration, and its stiffness compared to a shorter CFG pile is less.

### 4. 7. Model Validation Sivapriya and Gandhi [36]

Sivapriya and Gandhi [36] studied experiment and numerical analysis to determine lateral deformation subjected to lateral load on the horizontal and sloping ground using instrumented (aluminium pile) single pile having a diameter of 16 mm outer diameters with 450 mm length. The geotechnical properties of the soil used in the model are given in Table 2.

To validate the model, a numerical analysis is conducted using PLAXIS, and compared to the present study the results are very closer to each other as shown in Figure 13.

(a) L/D -6 (b) L/ D -12 (c) L/ D -18

**Figure 11.** CFG Pile model behaviours under variation length


(a)_ (b)

**Figure 12.** Failure Parton of CFG pile (a) Lateral displacement without fail (b) Failure under the horizontal trust

**TABLE 2.** Input parameters –a numerical study

| Parameter | Name | Clay | Pile |
|---|---|---|---|
| Material Model | Model | MC | LE |
| Drainage type | type | Undrained C | - |
| Young's Modulus | E (kPa) | 8025 | 70e6 |
| Unit weight | Γ (kN/ $m^3$ ) | 17.9 | 25 |
| Poisson's ratio | μ | 0.495 | 0.21 |
| Cohesion | C(kPa) | 30 | - |
| $K_o$ | - | Automatic | Automatic |

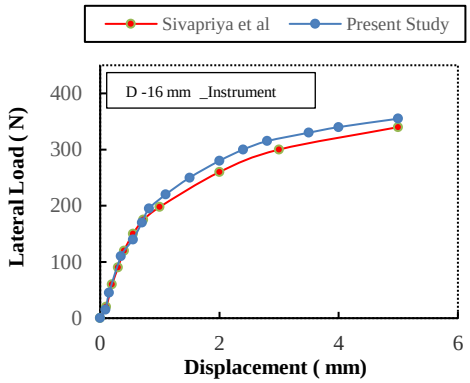


**Figure 13.** Model Validation

## 5. CONCLUSION

This study is based on a series of three-dimensional analyses to investigate the behaviour of a single CFG pile subjected to vertical, lateral, and combined vertical and lateral load. Separate numerical evaluations were performed on the single pile under combined loading with varying diameters and lengths to evaluate vertical load. In terms of lower diameter and thick sands situations, the effects of relevant factors such as pile/soil interface friction coefficient and shear strength (angle of internal friction and dilatation angle) of soil. For instance, in dense sand, the results reveal that pile behaviour under a combination of vertical and lateral loads has higher lateral load resistance than pile behaviour under single lateral stress. The cause may be traced back to the creation of extra lateral soil strains in front of the pile and increased frictional resistance throughout its length. In addition, the increase in enhancement depths until the CFG pile tips approach or are immersed in the strong strata significantly lowers both settlement and lateral movement while also increasing the overall bearing of soft soil.

## 6. REFERENCES

1. Jennings, K., "An investigation of geosynthetic reinforced piled embankments with particular reference to embankment extremities", Institute of Technology, Sligo, (2013),
2. Huang, J., Han, J. and Collin, J.G., "Geogrid-reinforced pile-supported railway embankments: A three-dimensional numerical analysis", ***Transportation Research Record***, Vol. 1936, No. 1, (2005), 221-229. doi: 10.3141/1936-25.
3. Zhang, C.-l., Jiang, G.-l., Liu, X.-f. and Wang, Z.-m., "Lateral displacement of silty clay under cement-fly ash-gravel pile-supported embankments: Analytical consideration and field evidence", ***Journal of Central South University***, Vol. 22, No. 4, (2015), 1477-1489. doi: 10.1007/s11771-015-2665-9.
4. Fonseca, E.C., Palmeira, E.M. and Barrantes, M.V., "Load and deformation mechanisms in geosynthetic-reinforced piled embankments", ***International Journal of Geosynthetics and Ground Engineering***, Vol. 4, No. 4, (2018), 1-12. doi: 10.1007/s40891-018-0150-x.
5. Yu, Y., Bathurst, R.J. and Damians, I.P., "Modified unit cell approach for modelling geosynthetic-reinforced column-supported embankments", ***Geotextiles and Geomembranes***, Vol. 44, No. 3, (2016), 332-343. doi: 10.1016/j.geotexmem.2016.01.003.
6. Chai, J., Lu, Y. and Uchikoshi, T., "Behavior of an embankment on column–slab improved clay deposit", ***International Journal of Geosynthetics and Ground Engineering***, Vol. 4, No. 4, (2018), 1-12. doi: 10.1007/s40891-018-0151-9.
7. Shahraki, M., Sadaghiani, M., Witt, K. and Meier, T., "3d modelling of train induced moving loads on an embankment", ***Plaxis Bulletin***, Vol. 36, No., (2014), 10-15.
8. Cao, H.Y. and Liu, Y.F., "Optimum design of cfg pile compound foundation based on numerical simulation method", in Applied Mechanics and Materials, Trans Tech Publ. Vol. 578, (2014), 346-350.
9. Umravia, N. and Solanki, C., "Experimental evaluation of bearing capacity of single cfg pile", in Proceedings of the Indian Geotechnical Conference 2019, Springer., (2021), 23-37.
10. Lai, J., Liu, H., Qiu, J. and Chen, J., "Settlement analysis of saturated tailings dam treated by cfg pile composite foundation", ***Advances in Materials Science and Engineering***, Vol. 2016, (2016). doi: 10.1155/2016/7383762.
11. Chen, J., Chen, W., Zhang, K. and Li, L., "The application of cfg pile composite foundation in the reconstruction of the dujiangyan", in IOP Conference Series: Earth and Environmental Science, IOP Publishing. Vol. 300, (2019), 022159.
12. Chen, Q.-n., Zhao, M.-h., Zhou, G.-h. and Zhang, Z.-h., "Bearing capacity and mechanical behavior of cfg pile composite foundation", ***Journal of Central South University of Technology***, Vol. 15, No. 2, (2008), 45-49. doi: 10.1007/s11771-008-0434-8.
13. Zhang, B. and Cui, S., "Field tests of cement fly-ash steel-slag pile composite foundation", ***Journal of Testing and Evaluation***, Vol. 45, No. 3, (2016), 860. doi: 10.1520/jte20140422.
14. Jiang, A.L. and Wang, M.X., "Composite foundation on bearing characteristics and simulation analysis cfg pile for the high speed railway", in Applied Mechanics and Materials, Trans Tech Publ. Vol. 71, (2011), 3827-3831.
15. Al-Tememy, M., Al-Neami, M. and Asswad, M., "Finite element analysis on behavior of single battered pile in sandy soil under pullout loading", ***International Journal of Engineering, Transactions C: Aspects***, Vol. 35, No. 6, (2022), 1127-1134. doi: 10.5829/ije.2022.35.06c.04.
16. Feng, J., Wu, X. and Zhang, J., "Settlement formula of stabilized layer in cfg composite foundation of high-speed railway", ***Electron. J. Geotech. Eng***, Vol. 19, (2014), 6867-6878.
17. Liu, J. and Jia, Y., "Temperature analysis of cfg pile composite foundation in high latitudes and low altitude island permafrost", ***International Journal of Structural Integrity***, (2019). doi: 10.1108/IJSI-07-2018-0045.
18. Nguyen, D. and Phan, V., "Engineering properties of soil stabilized with cement and fly ash for sustainable road construction", ***International Journal of Engineering, Transactions B: Applications***, Vol. 34, No. 12, (2021), 2665-2671. doi: 10.5829/IJE.2021.34.12C.12.
19. Wu, X.Z. and Xin, J.-X., "Probabilistic analysis of site-specific load-displacement behaviour of cement-fly ash-gravel piles", ***Soils and Foundations***, Vol. 59, No. 5, (2019), 1613-1630. doi: 10.1016/j.sandf.2019.07.003.
20. Hashemi, M., Marandi, S.M. and Vahidi, M., "The effect of heat on the settlement properties of cement-stabilized clay soil", ***International Journal of Engineering, Transactions B:***

***Applications,***, Vol. 35, No. 5, (2022), 1056-1063. doi: 10.5829/ije.2022.35.05b.20.

21. Hamidi, M. and Lajevardi, S., "Experimental study on the load-carrying capacity of single stone columns", ***International Journal of Geosynthetics and Ground Engineering***, Vol. 4, No. 3, (2018), 1-10. doi: 10.1007/s40891-018-0142-x.
22. Anand, A. and Sarkar, R., "Experimental and numerical investigation on load-settlement behaviour of stone column reinforced fly ash backfill", in Proceedings of Indian geotechnical conference (IGC 2017), IIT Guwahati, Guwahati, India., (2017).
23. Abbas, J.M., Chik, Z.H. and Taha, M.R., "Single pile simulation and analysis subjected to lateral load", ***Electronic Journal of Geotechnical Engineering***, Vol. 13, No. E, (2008), 1-15.
24. Zheng, G., Liu, S. and Chen, R., State of advancement of column-type reinforcement element and its application in china, in Advances in ground improvement: Research to practice in the united states and china. 2009.12-25.
25. Gunnvard, P., Evaluation of the efficiency of the standardized norrland method: Analyses with the finite element program plaxis on the case of road 685 vibbyn-skogså, boden municipality. 2016.
26. A. Edwin, D. Satish Pranav and M. Ganesh, "Experimental and finite element research of laterally loaded pile", ***International Journal of Innovative Technology and Exploring Engineering***, Vol. 8, No. 6, (2019), 858–863. doi: 10.35940/invitee.F1173.0486S419.
27. Teng, Q., Yao, X., Li, S. and Guan, J., "Finite element analysis of bearing capacity on the composite foundation of group pile", in IOP Conference Series: Earth and Environmental Science, IOP Publishing. Vol. 304, (2019), 032061.
28. Abusharar, S.W., Zheng, J.-J. and Chen, B.-G., "Finite element modeling of the consolidation behavior of multi-column supported road embankment", ***Computers and Geotechnics***, Vol. 36, No. 4, (2009), 676-685. doi: 10.1016/j.compgeo.2008.09.006.
29. Khanmohammadi, M. and Fakharian, K., "Evaluation of performance of piled-raft foundations on soft clay: A case study", ***Geomechanics and Engineering***, Vol. 14, No. 1, (2018), 43-50. doi. http://dx.doi.org/10.12989/gae.2018.14.1.043
30. Poulos, H., "Piled raft foundations: Design and applications", ***Geotechnique***, Vol. 51, No. 2, (2001), 95-113.
31. Khanmohammadi, M. and Fakharian, K., "Numerical simulation of soil stress state variations due to mini-pile penetration in clay", ***International Journal of Civil Engineering***, Vol. 16, No. 4, (2018), 409-419. https://doi.org/10.1007/s40999-016-0141-z
32. Leung, Y.F., Klar, A. and Soga, K., "Theoretical study on pile length optimization of pile groups and piled rafts", ***Journal of Geotechnical and Geoenvironmental Engineering***, Vol. 136, No. 2, (2010), 319-330.
33. Khanmohammadi, M. and Fakharian, K., "Numerical modelling of pile installation and set-up effects on pile shaft capacity", ***International Journal of Geotechnical Engineering***, (2017). https://doi.org/10.1080/19386362.2017.1368185
34. Ali, A., Abbas, H. and Abed-Awn, S., "Behavior of raft foundation built on layered soil under different earthquake excitation", ***International Journal of Engineering, Transactions B: Applications***, Vol. 35, No. 8, (2022), 1509-1515. doi: 10.5829/IJE.2022.35.08B.07.
35. Goudar, S. and Kamatagi, A., "An experimental evaluation of axial load bearing capacity of belled and straight piles embedded in sand", ***International Journal of Engineering, Transactions B: Applications***, Vol. 35, No. 8, (2022), 1599-1607. doi: 10.5829/IJE.2022.35.08B.16.
36. Sivapriya, S. and Gandhi, S., "Experimental and numerical study on pile behaviour under lateral load in clayey slope", ***Indian Geotechnical Journal***, Vol. 43, No. 1, (2013), 105-114.

## Persian Abstract

**چکیده**

خاکستر بادی سیمان و توده های شنی تکنیک های مدرن بهبود خاک هستند که به طور گسترده در چین برای توسعه زیرساخت استفاده می شود. این به طور قابل توجهی بر ویژگی های اساسی ظرفیت های باربری و تغییر شکل تأثیر می گذارد. شمع های فلاش و شن سیمان (CFG)ر بزرگراه ها، خاکریزهای راه آهن، پروژه های ضروری و خاک مشکل دار قرار دارند. اینها اغلب در معرض خطر بالای بار خارجی مانند سیل، لرزه، و غیره هستند. در چنین حالتی، طراحی فونداسیون را می توان با مقاومت جانبی مورد نیاز کنترل کرد. مطالعه حاضر بر اساس رفتار تغییر شکل یک شمع CFG تحت بارگذاری محوری، جانبی و ترکیبی در خاک رس نرم است. تجزیه و تحلیل عددی با استفاده از Plaxis 3D بر روی یک شمع CFG با پارامترهای موثر بر شرایط خاک، قطر، طول، نسبت طول به قطر و شرایط بارگذاری سر شمع برای مشاهده اثر آن. به طور کلی، مطالعه شمع تغییراتی را در سطح تنش اولیه، نوع شمع و محدودیت سر شمع پیدا کرد. با این حال، اینها در مقایسه با تأثیر رفتار و تحرک خاک جزئی بودند. مدل‌های خاک ویژگی‌های سختی و مقاومتی متفاوتی داشتند. اثرات ناشی از شرایط مرزی استفاده شده مسئول کاهش قابل توجه مقاومت جانبی برای شمع‌های CFG داخلی تحت بارگذاری فعال و غیرفعال بودند.

International Journal of Engineering

Journal Homepage: www.ije.ir

# Bending Strength Evaluation of Glulam Beams Made from Selected Nigerian Wood Species

O. O. Ekundayo*[a], C. Arum[b], J. M. Owoyemi[c]

[a] *Department of Building Technology, Federal University of Technology, Akure, Nigeria*
[b] *Department of Civil Engineering, Federal University of Technology, Akure, Nigeria*
[c] *Department of Forestry and Wood Technolog, Federal University of Technology, Akure, Nigeria*

*PAPER INFO*

*Paper history:*
Received13 April 2022
Received in revised form 06 July 2022
Accepted 28 July 2022

*Keywords*:
*Adhesives*
*Density*
*Glulam*
*Load Direction*
*Wood Species*

*ABSTRACT*

Bending strength, was assessed in glued laminated beams made from local wood species bonded with phenol resorcinol formaldehyde, polyurethane and urea-formaldehyde adhesives. The 3- point loading was used as the basis of bending strength assessment along the directions parallel and perpendicular to the glue line. The load orientation parallel to the glue line offered higher bending strength. Furthermore, the characteristic values of bending strength obtained were 35.16 N/mm$^2$, 40.79 N/mm$^2$, 47.34 N/mm$^2$, 60 N/mm$^2$, and 67 N/mm$^2$ for Afara, Akomu, Gmelina, Iroko, and Omocedar wood species. These values are similar to strength values given in EN 1194-1999 for glulam beams. Consequently, the findings of the study are beneficial to architects and structural engineers in exploring the dimensional, strength, and architectural flexibility glulam affords for both beam and column design and holds the potential for creating an industrial hub for enhancing the value chain around engineered wood and allied industries.

***doi**: 10.5829/ije.2022.35.11b.07*

## 1. INTRODUCTION

Support for sustainability in the built environment continues to grow as threats to the natural environment have been identified [1, 2]. A part of this support focuses on sustainable and renewable building and civil engineering materials [3, 4]. Construction materials that advance the course of sustainability are energy efficient, have low carbon emissions, and are eco-friendly [2]. Wood has been identified as a construction material with excellent environmental credentials to support sustainable development. According to Stokke et al. [5], wood is a porous and permeable cellular solid. It is a hard, fibrous tissue that makes up most of the trunks, branches, and roots of trees in the family of plants known as gymnosperms and dicotyledons.

Wood is a hard fibrous substance that essentially constitutes a tree's trunk and branches. It is defined as a naturaly occurring lignocellulosic polymer material that does not age significantly and is flexible for manufacturing high-quality innovative materials such as glued laminated timber (glulam) [6]. Glulam is an engineered wood product (EWP) composed of stress graded wood bonded horizontally with structural adhesives that can withstand torsion forces and applied service loads [7-9]. Glulam, therefore, has higher strength performance than sawn timber of equal dimension due to the permeability of the wood cellular structure to adhesives which creates a strong bond between selected defect-free laminates [9]. Glulam, a product of adhesive joining offers superior properties than sawn wood and wood joined by other mechanical methods. This is because adhesives ensure uniform stress distribution with lightness of the structure or a high strength - to -weight ratio within the structure and are as such a better and more prevalent jointing method with merits that outweigh other methods of joining wood composite structures [10, 11]. The world over, structural wood application is continuously being advanced as exemplified by low to medium-rise buildings built of

*Corresponding Author Institutional Email: ooekundayo@futa.edu.ng
(O. O. Ekundayo)

Please cite this article as: O. O. Ekundayo, C. Arum, J. M. Owoyemi, Bending Strength Evaluation of Glulam Beams Made from Selected Nigerian Wood Species, ***International Journal of Engineering, Transactions B: Applications***, Vol. 35, No. 11, (2022) 2120-2129

wood. One of such examples is the Stellar cultural center, Skelleftea in Sweden almost totally built with wood [12]. The availability of wood in Nigeria is vast and should be explored in producing eco-friendly engineering wood products for the building industry. Therefore, this study was conducted to investigate the performance of glulam constituted of native wood. Previous studies have proven that engineering innovations such as EWPs, particularly glulam, improve the mechanical properties of wood beyond its natural limits [9, 13]. Numerous studies spanning decades have constantly established the engineering capability of wood as structural material [14, 15]. Glulam have on these accounts emerged in developed societies as a structural material for a wide range of construction and civil engineering applications [9, 15].

However, Nigeria's academia and building industry have not considered sufficiently the forestry sector as a viable supplier of structural fabrics for extensive structural application beyond ordinary roof and formwork. Therefore, many of the researchers in structural materials have paid little attention to the use of timber for structural purposes. Most of the studies in wood as a construction material have focused on sawn timber [16-19]. Only a few research works have investigated the use of indigenous wood species for glued laminated timber [20, 21].

However, the mechanical and physical properties of timber species such as; Southern pine (Pinus taeda L.), Douglas fir (Pseudotsuga menziesii) and Larch (Larix) wood species have been examined both in the sawn and glulam form [22-24]. Likewise, mechanical behaviour of some Nigerian wood species such as Strombosia pustulata, Macrocarpa bequaerti, Nauclea diderrichii and Entandrophragma cylindrica have similarly been studied [16-17]. However, these studies have either considered glulam elements of foreign timber species or sawn indigenous wood species. Thus, there is a rarity of indigenous research focused on developing Nigerian wood species into glulam beams.

Furthermore, for the few indigenous studies on glulam only non-structural adhesives such as polyvinyl acetate (PVAc) has been considered [20, 22]. PVAc is not suitable for structural wood bonding. The suitability of structural synthetic glues like phenol resorcinol formaldehyde (PRF), Urea-formaldehyde (UF) and Polyurethane (PU) on many Nigerian grown woods have not been extensively studied within the environmental conditions in Nigeria in line with literature [25].

An Implication of the few research efforts in glue lamination of local wood species is the insufficient information on the mechanical capabilities of glulam from Nigeria grown timber species. Hence, this prevents the understanding necessary for setting domesticated performance requirements for glulam structural elements within the local environmental conditions which can influence the mechanical properties of glued structural elements. As the problem of property variance is common to all wood species, it will be inappropriate to directly apply to native wood species performance criteria for exotic species and wood commonly used for glulam most of which are not native to Nigeria. Therefore, it is only proper to study native wood species extensively for their behavior as adhesively bonded structural elements.

Consequently, this study, taking into cognisance the variability of wood (both within and between species as a result of differences in growth conditions due to variation in climatic conditions and silvicultural practices) aims to establish by standard procedures the undocumented characteristic bending strength values of glulam beams produced from Nigerian grown Afara (Terminalia superba) , Akomu (Pycnanthus angolensis), Gmelina (Gmelina aborea), Iroko (Milicia excelsa) and Omocedar (Stereospermum accuminatissimum) using phenol resourcinol , urea formaldehyde and polyurethane structural wood adhesives. Furthermore, this work reports for the first time the effectiveness of these structural adhesives on the Nigerian grown selected wood species. Hence, the glulam beams from these species can offer higher mechanical strength, higher dimension and design flexibility than wood in the traditional form. Therefore, the result of the study is useful for structural design of glulam beams produced from the wood species considered.

## 2. MATERIALS AND METHODS

The materials used in this research were five freshly cut wood samples of *Terminalia superba* (Afara), *Pycnanthus angolensis* (Akomu), *Gmelina arborea* (Gmelina), *Milicia excelsa* (Iroko) and *Steroespermum acuminatissimum* (Omocedar) with average age of 10 – 15 years obtained from one of the sawmills in Akure. Wood samples of 20mm x 20mm x 60mm and 20mm x 20mm x 300mm were prepared for determination of density and bending strength. Likewise, three (3) structural adhesives; Phenol resorcinol formaldehyde with the hardener component, Polyurethane and Urea Formaldehyde were used as binder. The moisture content of the wood samples was controlled in an electric oven regulated within a temperature range of 103±30 C to attain an average moisture content of 13%. Measurement for density was determined using an electronic weighing balance with precision to 0.1 decimal place. Bending strength test was conducted for determination of bending strength otherwise known as modulus of rupture (MOR) on a 20kN universal testing machine equipped with a computerized data acquisition system at the Department of Forestry and Wood Technology, Federal University of Technology Akure. Planks for the production of glulam

specimens made up of three laminates were sized to 6mm x 50mm x 650mm laminates as shown in plate 1 and glued up horizontally on a clamping device for pressure application for 24 hours as shown in plate 2. After setting, laminated samples were resized to a final dimension of 20mm x 20 mm x 300mm as shown in plate 3 for bending strength evaluation.

**2. 1. Moisture Content** Moisture content was determined by oven drying at a temperature of 105 0C for 24 hours and was then determined as extracted from literature [26] using Equation (1):

$$MC = \frac{W_g - W_d}{W_d} \times 100 \quad (1)$$

where $W_g$ is the green weight and $W_d$ is the oven dry weight.

**2. 2. Density Determination** Density (ρ) was determined according to ASTM [27] after oven-drying for 24 hours using Equation (2):

$$\rho = \frac{M}{V} \quad (2)$$

**Plate 1.** Wood laminates for glue lamination

**Plate 2.** Improvised clamping system for pressure application

**Plate 3.** Finished glued laminated beam ready for testing

**2. 3. Static Bending Test** Bending strength (σ) was determined on a total of 50 solid wood beam specimens (control sample) and 300 glulam wood beam specimens using 3-point loading applied at a distance of 130mm away from each support as shown in Figure 1.

The modulus of rupture was then calculated using Equation (3):

$$\sigma = \frac{3 \times P_{max} \times L}{2 \times b \times h^2} \quad (3)$$

where $P_{max}$ is the maximum load applied to point of failure (N), $L$ is span of the specimen (mm), $b$ is breadth of the specimen (mm) and $h$ is depth of specimen (mm).

**2. 4. Modulus of Elasticity (MOE)** This was determined using Equation (4):

$$MOE = \frac{PL^3}{4 \times \Delta \times b \times h^3} \quad (4)$$

where P is load at the limit of proportionality (N), L is the loading span of the test specimen (260 mm), b and h are breadth and depth of the test specimen (mm) and Δ is deflection at the limit of proportionality (mm).

## 3. RESULTS AND DISCUSSION

**3. 1. Density** The result of the density of control specimen and glued laminated beams for each wood species laminated with PR, PU, and UF adhesives respectively is illstrated in Figure 2. The effect of adhesive type on the density of the glulam beams was assessed using ANOVA. It is observed across all the species laminated with PR, PU and UF adhesives that no significant change in density was recorded as a result of the different adhesives when the species type is held constant. Similarly, the difference in density between the treatment and control group was marginal and as a result insufficient to adduce to the gluing process. This is due to the fact that the glue lines of the laminated beams are thin and that the pressure application of the gluing process did not densify the laminated beams to give rise to significant density increase in the laminated wood beams over that of the raw material. This finding is similar to the reported data by Komariah et al. [28].

**3. 2. Influence of Wood Species, Load direction and Adhesive on the Bending Strength of Glulam Beams** The mean bending strength of glued

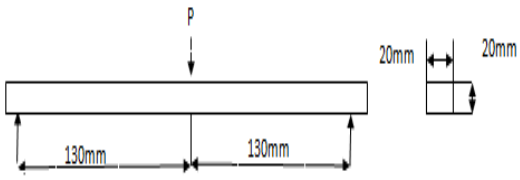


**Figure 1.** Static bending test setup

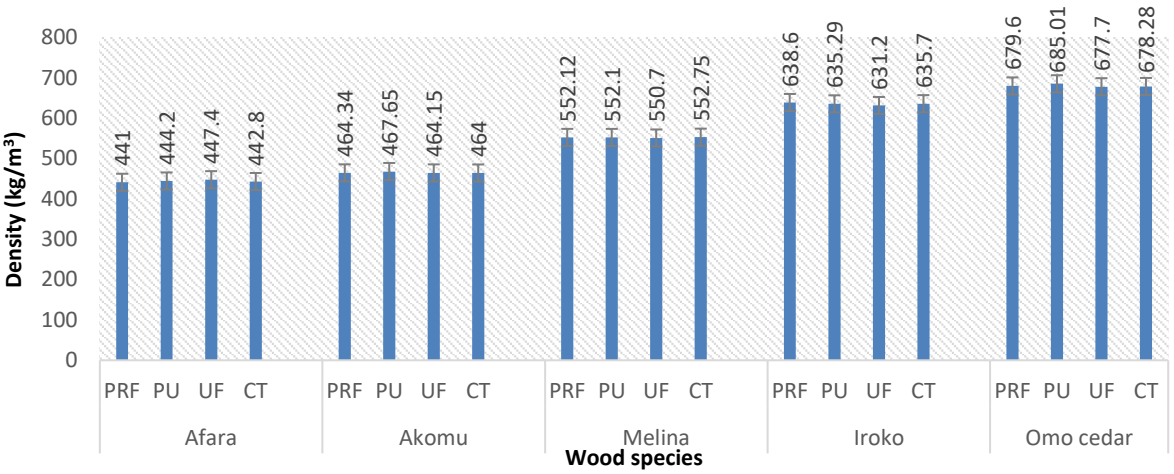


**Figure 2.** Density of glued laminated wood species at an average moisture content of 13%, CT is the Control specimen for each of the species

laminated beams of *Afara*, *Akomu*, *Gmelina*, *Iroko* and *Omocedar* species bonded with phenol resorcinol, polyurethane and urea-formaldehyde adhesive in Figure 3 showed that wood species and load direction had a significant effect ($p < 0.05$) on MOR values of the glued laminated beams. On the contrary, the effect of adhesive was not significant ($p > 0.05$) on the MOR values of glued laminated beams. Thus, the finding aligned with that reported in literature [29-31].

Similarly, the load direction had a statistically significant effect on the MOR values of the glued laminated beams. Load direction has a significant effect on the mean bending strength values of wood composites thus agreeing with some earlier studies [31-33]. Furthermore, the findings of this study also align with data reported by Burdurlu et al. [32] that mean bending strength values are higher in the edgewise direction than in the flatwise direction. The edgewise direction, which is the direction when the load application is parallel to the glue line is the stronger axis and the preferable axis for load application for non- bi-axially loaded beams [34].

The adhesive types in this study have no significant difference in the mean MOR values of the glulam beams. This is not because adhesive type do not affect mechanical properties in wood. However, for this study, the adhesive types considered are adhesives belonging to the same class type generally known as thermosetting adhesives; these are important adhesives in the class of wood adhesives used for structural gluing and standardized in EN 301 [35]. Therefore, the apparent lack of statistically significant difference in performance is due to class relationships and the consequent similarity in performance. This observation is similar to the findings reported by Bal and Bektaş [31].

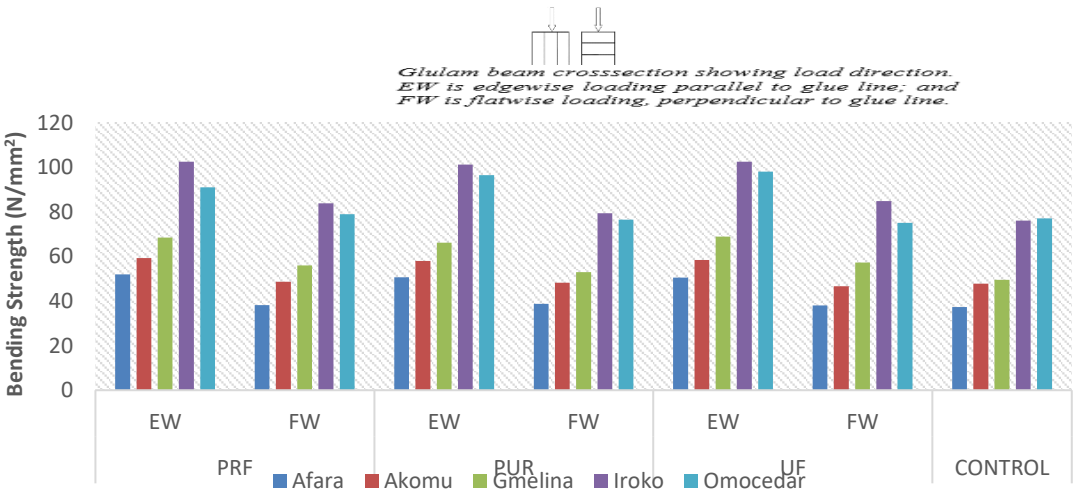


**Figure 3.** Effect of wood species, load direction, and adhesive on MOR of glulam beams

**3. 3. Relationship between Density and Bending strength of Glulam Beams** The influence of density on the mechanical property of structural elements is well established [36, 37]. This relationship in glued laminated beams was investigated. Bending strength - density plots were generated from the experiments conducted. The representative plot for the MOR – density relationship for the specimens is shown in Figures 4a and 4b. A good relationship was generally found between the density of glued laminated beams and the respective bending strength values. By a good relationship, it is meant that the positive correlation between MOR and wood density ranged from moderate to strong. Moderate positive correlation ranging from 0.3 to 0.7 while strong positive correlation ranges from 0.7 to 1.0 [38]. While control specimens showed similar relationship, the correlation values between bending strength and density were largely higher in glued laminated beams (0.54) in Figure 4a compared to the control specimen (0.47) in Figure 4b. This trend could be due to the fact that it is possible to select laminates of known density prior to gluing as against the natural constitution of solid wood beams which cannot be altered in the sawn state.

**3. 4. Characterization of Reference Properties of Glulam Beams from the Selected Species** The characteristic reference material properties such as density, MOE and MOR for the glulam beams were derived using Equation (5):

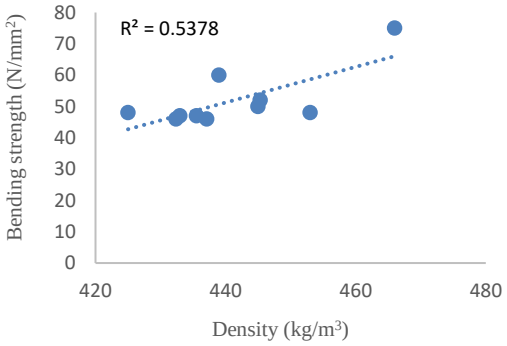


(a) Glulam beams

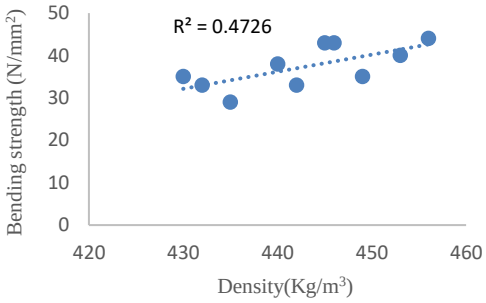


(b) Control beam

**Figure 4.** MOR - Density plot for *Afara* glulam beam and Control beam specimens

$$C_{bs} = \text{Xfb} - 2.33\text{S} \quad (5)$$

where $C_{bs}$ is the chatacteristic material property , Xfb is the mean of the property considered and S is the standard deviation of the population.

The characteristic values represents a lower limit value which 99% of the samples surpass [39, 40]. The characteristic values of bending strength which is the index property for glued laminated beam for strength classification were considered along the edgewise load direction as shown in Tables 1, 2 and 3. It is seen from this study that the values were 35.16N/mm2 for Afara beams, 40.79N/mm$^2$ for Akomu, a higher value of 47.34N/mm$^2$ was recorded for Gmelina beams, while 60N/mm$^2$ and 67N/mm$^2$ were obtained for Iroko and Omocedar beams respectively. The characteristic bending strength values obtained from this study compares with values of glued laminated timber beams used for structural application. BS EN 1194 [41] gives the characteristic bending strength class of glulam beams. This standard recognizes four strength classes; GL 24, GL 28, GL32 and GL 36. These strength classes mean glued laminated beams with characteristics bending strength of 24N/mm$^2$, 28 N/mm$^2$, 32N/mm$^2$, and 36N/mm$^2$. For example, GL 32 means glued laminated beam with characteristic bending strength of 32N/mm$^2$. Thus, the values obtained in this study for the selected species compares with the classification of BS EN 1194 [41] as shown in Table 3.

**TABLE 1.** Characteristic value of density of edgewise loaded glued laminated beams from the selected wood species

| Species | Mean Density (kg/m$^3$) | Standard deviation | Coefficient of Variation | Characteristic value of Density (kg/m$^3$) |
|---|---|---|---|---|
| Afara | 444.13 | 11.48 | 2.58 | 417 |
| Akomu | 462.50 | 20.62 | 4.46 | 414 |
| Gmelina | 552.73 | 9.76 | 1.76 | 530 |
| Iroko | 634.23 | 24.97 | 3.93 | 576 |
| Omo cedar | 681.53 | 33.18 | 4.86 | 604 |

**TABLE 2.** Characteristic MOE value of edgewise loaded glued laminated beams from the selected wood species

| Species | Mean MOE (N/mm$^2$) | Standard deviation | Coefficient of variation | Characteristic value of MOE (N/mm$^2$) |
|---|---|---|---|---|
| Afara | 5203 ± 344.4 | 922 | 17.72 | 3054 |
| Akomu | 6583 ± 314.27 | 841 | 12.78 | 4622 |
| Gmelina | 7316 ± 669.56 | 1793 | 24.51 | 3138 |
| Iroko | 10566 ± 1419.97 | 3802 | 35.99 | 1706 |
| Omo cedar | 10966 ± 863.18 | 2311 | 21.08 | 5580 |

**TABLE 3.** Characteristic MOR value of edgewise loaded glued laminated beams from the selected wood species

| Species | Mean MOR (N/mm$^2$) | Standard deviation | Coefficient of Variation | Characteristic value of MOR (N/mm$^2$) |
|---|---|---|---|---|
| Afara | 51 | 6.8 | 0.13 | 35.16 |
| Akomu | 58.5 | 7.6 | 0.13 | 40.79 |
| Gmelina | 67.8 | 8.78 | 0.13 | 47.34 |
| Iroko | 102.6 | 18.4 | 0.18 | 60 |
| Omo cedar | 97.08 | 12.92 | 0.13 | 67 |

**3. 4. Adjustment of Three Point Edgewise Bending Strength to Four Point Values** It is established in literature that the value of MOR is dependent on the method of strength evaluation. Destructive strength evaluation of MOR using 3-point loading yields higher values of MOR than evaluation by 4-point loading as a result of the location of the maximum moment and maximum axial fiber stress [42]. Hence, to make the results of this study comparable to EN 408 standard and EN384 based on the 4-point method of bending strength evaluation, the values of MOR from this study were corrected to values equivalent to 4-point evaluation. The conversion was done using the regression equation between 3-point and 4-point MOR as proposed by Hein and Brancheriau [42]. The properties of the regression equation used for this conversion are; $R^2$ of 0.74, Standard error of estimation (SEE) of 7.87. Figure 5 shows the MOR values from the laboratory test using the 3-point evaluation and the adjustment to the corresponding 4-point values according to Hein and Brancheriau [42] using Equation (6):

$$MOR4p = 0.889 \times MOR3p + 5.14 \quad (6)$$

The values of bending strength are presented in Figure 5 for all the glued laminated beams from the selected species evaluated by 3-point bending test and adjusted to 4-Point bending strength values using equation 6. It is shown from Figure 5 that there was strength reduction when the 3-point MOR values were adjusted to 4-point MOR values. The mean value of Afara which was 51N/mm$^2$ upon adjustment is seen to be 50.47N/mm$^2$. Similarly, Akomu glued laminated beams upon adjustment were reduced from a mean 3–point MOR of 58.53N/mm$^2$ to 4-point MOR of 57.16 N/mm$^2$. Likewise, Gmelina glulam beams with a mean bending strength of 67.76N/mm$^2$ from the 3-point evaluation are reduced to 65.38N/mm$^2$ equivalent 4-point MOR. Also, Iroko beams with 102.6N/mm$^2$ mean 3- point MOR were

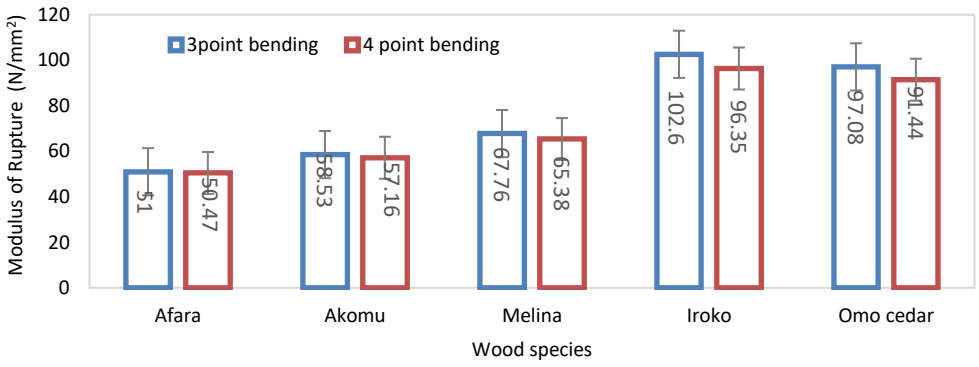


**Figure 5.** 3- point MOR adjusted to 4- Point MOR values

adjusted to a 4 –point MOR reduced mean value of 96.35N/mm$^2$. Lastly, Omo cedar glulam with mean 3-point MOR of 97.08 N/mm$^2$ were also adjusted to 91.44N/mm$^2$.

**3. 5. Adjustment of Four Point Edgewise Bending Strength to Reference Depth of 150mm** The values of the bending strength were adjusted to the reference depth of 150 mm using Equation (7). This equation is applied because the depth of the test piece deviates from the specimen specification of EN 408 [43]. This adjustment is permissible only for bending strength and tensile strength according to clause 5.3.4.3 of EN 384 [44]. The adjustment of bending strength to reference depth is achieved by multiply the bending strength of the test specimen by a factor obtained using Equation (7):

$$k_h = \left(\frac{150}{h}\right)^{0.2} \quad (7)$$

where $k_h$ is the depth adjustment factor as specified by EN 408 [43] and h is the depth of the specimen which is 20 mm The results of applying this value is shown in Figure 6. From Equation (7) the mean 4-point bending strength of the glued laminated beam in Figure 5 are scaled up to reference depth of 150 mm such that for any given glued laminated beam with bending strength β N/mm$^2$ at the depth h = 20 mm for the test specimen, the adjusted bending strength to reference depth would be $\beta \times k_h$:

where $k_h$ is $\left(\frac{150}{20}\right)^{0.2} = (7.5)^{0.2} = 1.149$

Therefore, the adjusted bending strength to reference depth of 150mm = β N/mm$^2$ × 1.149.

The result in Figure 6 termed 4p MOR adjusted to 150mm ref. depth was obtained by multiplying results of the corresponding 4p MOR by a factor of 1.149 so as to reflect MOR values to the reference depth of 150 mm. Shown in Figure 6 are values of glued laminated beams from the selected wood species. The results were converted to 4-point MOR values using Equation (6). These results were further scaled up to reference depth of 150mm in line with EN 408 [43]. It is shown in the same figure that the bending strength of *Afara* with mean 4-point MOR of 50.47 N/mm$^2$ was scaled up to a 75.5N/mm$^2$ .Similarly, *Akomu* glulam beams were scaled up to a mean MOR of 85.52 N/mm$^2$. Also, *Gmelina* show a mean MOR of 97.81 N/mm$^2$ at the reference depth of 150 mm. Likewise, the mean MOR of *Iroko* and *Omocedar* increased to 144.14 N/mm$^2$ and 136.8 N/mm$^2$ respectively. Furthermore, the values of stiffness (MOE) for the edgewise and flatwise tested glued laminated beams from the selected species are presented in Figure 7.

**3. 6. Fracture Mechanism in Glulam Beams** The fracture of the glulam beams investigated in this

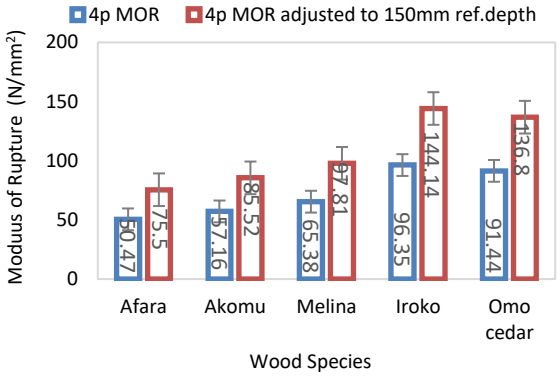


**Figure 6.** 4- point MOR values adjusted to reference depth of 150mm

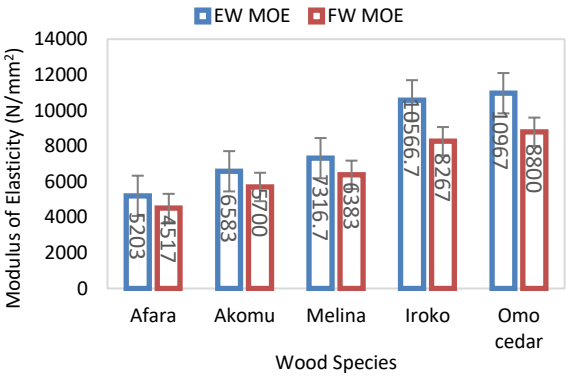


**Figure 7.** Stiffnes values in the edgewise (EW) and flatwise (FW) load direction

research was characterized by different forms of tension failure at the ultimate stress limit which developed at the bottom fiber of the beams under the applied load towards the compression region at the top as shown in plate 4. The fracture is seen as cracks which developed due to tension parallel to grain splitting the bottom laminates of the wood. Where wood grains are oriented parallel to the longitudinal axis, simple tension failure mechanism develops as the major fracture pattern [45].

From the topmost beam which is *Afara* to *Akomu* the second beam, splintering tension failure was observed with ragged breaks occurring in the wood fiber. The glue lines are shown to be avoided along the path of the crack progression. This indicates the integrity of the glue lines. Furthermore, from the middle third beam which is *Gmelina*, to *Iroko* and *Omo cedar*, the fracture is characterized by a combination of simple tension failure and some cross-grain tension failure occurring from the bottom fibers towards the compression region. Furthermore, plate 5 shows the case of severe cross- grain tension failure in *Afara*, *Gmelina* and *Omo cedar* glulam beams. Cross-grained tension is characterized by a diagonal crack from the bottom and splitting through to

**Plate 4.** Fracture form of glulam beams from up to down: Afara, Akomu, Gmelina, Iroko and Omo cedar wood species

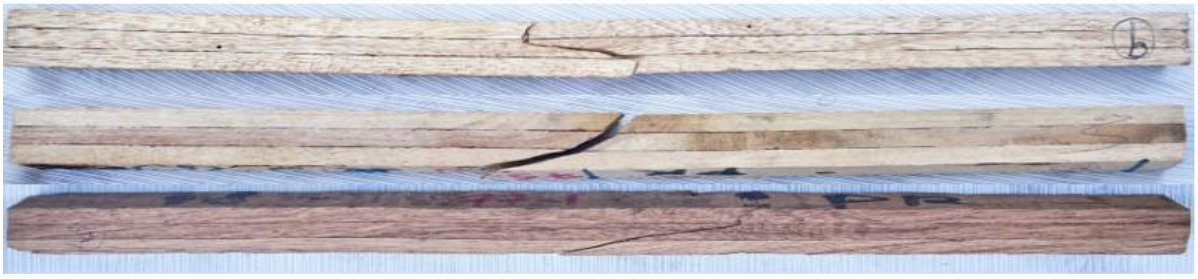

**Plate 5.** Cross grain tension failure in glulam beams

the top of the wood. Cross grain results when the grain of the wood deviates from being parallel to the longitudinal axis. Consequently, tensile stress resulting from flexural load acts in a manner sloping to the grains to produce oblique cracks as shown in plate 5. The tensile capacity of wood is severely low across the grain than parallel to the grain [45]. As a result, cross-grained wood resulting from wrong sawing method or natural defect is not suitable for glulam elements designed as flexural members as such members relying on tensile strength perpendicular to grain (which is reportedly 10% that parallel to the grain) suffer severe tension failure [45, 46]. For the topmost and bottom member in *Afara* and *Omo cedar*, the cross-grain failure was relatively ductile as the beam was not completely severed. However, for *Gmelina*, the cross-grain tension failure was brittle as seen by the complete severing of the beam into two from bottom to top. Thus, the study corroborates findings in literature that tension failure is severe in cross grain wood under flexural stress [45-46].

## 4. CONCLUSION

The selected Nigerian wood species are glueable using PR, PUR and UF hence the advantages of higher strength and dimension for extensive structural application can be derived from these wood species in the glulam form than wood in the traditional form. It is shown also that wood species with higher densities offer higher characteristic bending strength values as seen in Omo cedar with the highest values in density of 681.53 kg/m$^3$, MOE of 10966N/mm$^2$ and characteristic bending strength of 67N/mm$^2$ compared to Afara (with the lowest values in density of 444.13kg/m$^3$, MOE of 5203N/mm$^2$ and characteristic bending strength of 35.66N/mm$^2$. Hence, the choice of wood by the effect of the wood density must be considered in obtaining the desired engineeing properties. Furthermore, results of glulam beams in edgewise bending versus the control shown thus is: 51N/mm$^2$; 37.3N/mm$^2$, 58.5N/mm$^2$; 47.8N/mm$^2$, 67.8N/mm$^2$; 49.5N/mm$^2$, 102.1N/mm$^2$; 76.1N/mm$^2$ and 95.1N/mm2; 77.1N/mm$^2$ from Afara through Omocedar. The results thus shows that the glulam beams were significantly higher than the control (custom wood) especially in the edgewise direction. Hence these wood species can be engineered for higher bending strength. Similarly, the bending strength of glulam specimens in edgewise bending and flatwise bending were: 51N/mm$^2$; 38.3N/mm$^2$, 58.5N/mm$^2$; 47.8N/mm$^2$, 67.8N/mm$^2$; 55.3N/mm$^2$, 102.1N/mm$^2$; 82.6N/mm$^2$ and 95.1N/mm$^2$; 76.8N/mm$^2$ from Afara through Omocedar. It is seen from these values that glulam beams were significantly higher in bending strength along the edgewise direction than the flatwise direction and as such square sections should be loaded in the edgewise direction. Also, the axis of loading for higher bending strength in glulam beams should be parallel to the glue line as against perpendicular to glueline due to the combination of the anisotrophy of wood and higher shear capacity of the

glueline in contributing to the bending strenght. The results further show that low and high density wood species can be mixed for glulam production by using low density wood species in the core of glulam beams where tension and compression is neutral while high density species used as the outtermost member where these forces are extreme so as to derive structral elements of higher mechanical strength. Based on the failure patterns observed, glue lines in glulam beams resist failure effectively by transferring forces to wood fibre. The failure modes also show that cross grain wood is not suitable for glulam production.

## 5. REFERENCES


1. Ortiz, O., Castells, F. and Sonnemann, G., "Sustainability in the construction industry: A review of recent developments based on lca", ***Construction and Building Materials***, Vol. 23, No. 1, (2009), 28-39. doi: 10.1016/j.conbuildmat.2007.11.012.
2. Pacheco-Torgal, F. and Labrincha, J., "The future of construction materials research and the seventh un millennium development goal: A few insights", ***Construction and Building Materials***, Vol. 40, (2013), 729-737. doi: 10.1016/j.conbuildmat.2012.11.007.
3. Ametepey, S.O. and Ansah, S.K., "Impacts of construction activities on the environment: The case of ghana", ***Journal of Construction Project Management and Innovation***, Vol. 4, No. sup-1, (2014), 934-948. doi.
4. Mehta, M., Scarborough, W. and Armpriest, D., "Building construction: Principles, materials, and systems, Pearson Prentice Hall Ohio, (2008).
5. Stokke, D.D., Wu, Q. and Han, G., "Introduction to wood and natural fiber composites, John Wiley & Sons, (2013).
6. Duggal, S.K., "Building materials, Routledge, (2017).
7. D3737-18e1, A., "Standard practice for establishing allowable properties for structural glued laminated timber (GLULAM)", ASTM International West Conshohocken, (2018). doi: 10.1520/D3737-18E01.
8. Moody, R.C. and Hernandez, R., "Glued-laminated timber", Forest Product Laboratory. USDA Forest Service. Madison, Winconsin, (1997).
9. Nadir, Y. and Nagarajan, P., "The behavior of horizontally glued laminated beams using rubber wood", ***Construction and Building Materials***, Vol. 55, (2014), 398-405. https://doi.org/10.1016/j.conbuildmat.2014.01.032
10. Yousefsani, S.A., Tahani, M. and Selahi, E., "Analytical solution of stress field in adhesively bonded composite single-lap joints under mechanical loadings", ***International Journal of Engineering, Transactions C: Aspects***, Vol. 27, No. 3, (2014), 475-486. doi: 10.5829/idosi.ije.2014.27.03c.16.
11. Marchione, F., "Analytical stress analysis in single-lap adhesive joints under buckling", ***International Journal of Engineering, Transactions B: Applications***, Vol. 34, No. 2, (2021), 313-318. doi: 10.5829/ije.2021.34.02b.02.
12. Morales Sabogal, A.A., "Tall mass-timber building", Virginia Tech, (2017),
13. Milner, H. and Woodard, A., Sustainability of engineered wood products, in Sustainability of construction materials. 2016, Elsevier.159-180.
14. Smith, I., Snow, M. and Asiz, A., "Failure characteristics of engineered wood products connections", in World Conf. on Timber Engineering, Engineered Wood Products Association, Madison, WI., (2008).
15. Yang, T.-H., Wang, S.-Y., Tsai, M.-J. and Lin, C.-Y., "The charring depth and charring rate of glued laminated timber after a standard fire exposure test", ***Building and Environment***, Vol. 44, No. 2, (2009), 231-236. https://doi.org/10.1016/j.buildenv.2008.02.010
16. Abubakar, I. and Nabade, A., "Physical and mechanical properties of some common nigerian timber species based on limit state design approach", ***Study of Civil Engineering and Architecture (2),(2013a)***, (2013), 90-97.
17. Aguwa, J., "Structural reliability of the nigerian grown abura timber bridge beam subjected to bending and deflection forces", ***Nigerian Journal of Technology***, Vol. 32, No. 2, (2013), 241-252.
18. Kaura, J., Abubakar, I. and Aliyu, I., "En 338 strength grade and uncertainty models of material properties for nigerian grown terminalia superba (white afara) timber specie", ***Nigerian Journal of Technology***, Vol. 34, No. 1, (2015), 21-27.
19. Idris, A. and Muhammad, N.A., "Bending strength classification of some common nigerian timber species", ***Jordan Journal of Civil Engineering***, Vol. 159, (2014), 1-7.
20. Ezeagu, C., Eromosele, A., Okoro, H., Chukwujwkwu, U. and Emetomo, T., "Flexural strength of solid and glue-laminated timber beams", ***American Journal of Engineering Science and Technology Research***, Vol. 3, No. 1, (2015), 1-14.
21. Arum, C., Olofintuyi, I. and Ekundayo, O.O., "Glulam beams: Performance of pva and pur adhesives on bending strengths of locally selected nigerian timber species", ***Nigerian Journal of Technology***, Vol. 40, No. 3, (2021), 363-370. http://dx.doi.org/10.4314/njt.v40i3.2
22. Falk, R.H. and Hernandez, R., "Performance of glued-laminated timber beams of european manufacture", ***Forest Products Journal***, Vol. 45, No. 7/8, (1995), 27.
23. Bakar, S.A. and Mohamed, Z.B., "Factors affecting ultimate strength of solid and glulam timber beams", ***Malaysian Journal of Civil Engineering***, Vol. 16, No. 1, (2004). https://doi.org/10.11113/mjce.v16.15660
24. Mohamad, W.H.W., Razlan, M.A. and Ahmad, Z., "Bending strength properties of glued laminated timber from selected malaysian hardwood timber", ***International Journal of Civil & Environmental Engineering***, Vol. 11, No. 4, (2011), 7-12.
25. *Ncp 2., nigerian standard code of practice, ncp 2. Grade stresses for nigerian timbers*: Nigerian Standard Organisation, Federal Ministry of Industries, Lagos, Nigeria.
26. Owoyemi, J.M., Zakariya, H.O. and Elegbede, I.O., "Sustainable wood waste management in nigeria", ***Environmental & Socio-economic Studies***, Vol. 4, No. 3, (2016), 1-9. doi: 10.1515/environ-2016-0012.
27. *Astm d143-21. "Standard test methods for small clear specimens of timber"*, . 2009: ASTM International, West Conshohocken, PA,.
28. Komariah, R.N., Hadi, Y.S., Massijaya, M.Y. and Suryana, J., "Physical-mechanical properties of glued laminated timber made from tropical small-diameter logs grown in indonesia", ***Journal of the Korean Wood Science and Technology***, Vol. 43, No. 2, (2015), 156-167. https://doi.org/10.5658/WOOD.2015.43.2.156
29. Shukla, S. and Kamdem, D.P., "Properties of laminated veneer lumber (lvl) made with low density hardwood species: Effect of the pressure duration", ***Holz als Roh-und Werkstoff***, Vol. 66, No. 2, (2008), 119-127. doi: 10.1007/s00107-007-0209-1.
30. Nazerian, M., Ghalehno, M.D. and Gozali, E., "Effects of wood species, particle sizes and dimensions of residue obtained from trimming of wood–cement composites on physical and mechanical properties of cement-bonded particleboard", ***Wood***

***Material Science & Engineering***, Vol. 6, No. 4, (2011), 196-206. https://doi.org/10.1080/17480272.2011.601816

31. Bal, B.C. and Bektaş, İ., "The mechanical properties of heartwood and sapwood of flooded gum (eucalyptus grandis) grown in karabucak, turkey", ***Düzce Üniversitesi Ormancılık Der***, Vol. 9, No. 1, (2013), 71-76.
32. Burdurlu, E., Kilic, M., Ilce, A.C. and Uzunkavak, O., "The effects of ply organization and loading direction on bending strength and modulus of elasticity in laminated veneer lumber (lvl) obtained from beech (fagus orientalis l.) and lombardy poplar (populus nigra l.)", ***Construction and Building Materials***, Vol. 21, No. 8, (2007), 1720-1725. https://doi.org/10.1016/j.conbuildmat.2005.05.002
33. Kılıç, M., "The effects of the force loading direction on bending strength and modulus of elasticity in laminated veneer lumber (lvl)", ***BioResources***, Vol. 6, No. 3, (2011), 2805-2817.
34. Linville, J.D., "Timber construction manual, John Wiley & Sons, (2012).
35. EN, B., "301.(2013). Adhesives, phenolic and aminoplastic, for load-bearing timber structures-classification and performance requirements", ***British Standards Institution***.
36. Blomberg, J., Persson, B. and Blomberg, A., "Effects of semi-isostatic densification of wood on the variation in strength properties with density", ***Wood Science and Technology***, Vol. 39, No. 5, (2005), 339-350. https://doi.org/10.1007/s00226-005-0290-8
37. Gunduz, G., Korkut, S., Aydemir, D. and Bekar, Í., "The density, compression strength and surface hardness of heat treated hornbeam (carpinus betulus l.) wood", ***Maderas. Ciencia y Tecnología***, Vol. 11, No. 1, (2009), 61-70. http://dx.doi.org/10.4067/S0718-221X2009000100005
38. Ratner, B., "The correlation coefficient: Its values range between+ 1/− 1, or do they?", ***Journal of Targeting, Measurement and Analysis for Marketing***, Vol. 17, No. 2, (2009), 139-142. https://doi.org/10.1057/jt.2009.5
39. Desch, H. and Dinwoodie, J., Strength, elasticity and toughness of wood, in Timber structure, properties, conversion and use. 1996, Springer.102-128.
40. Jimoh, A. and Adefemi, J., "Re-evaluation of characterisation and classification of apa (afzelia bipindensis) timber for structural use", ***Nigerian Journal of Technology***, Vol. 36, No. 4, (2017), 1022-1029. https://doi.org/10.4314/njt.v36i4.5
41. "Bs en 1194:1999 timber structures - glued laminated timber - strength classes and determination of characteristic values (withdrawn), 389 Chiswick High Road, London, W4 4AL, UK, (1999).
42. Hein, P.R.G. and Brancheriau, L., "Comparison between three-point and four-point flexural tests to determine wood strength of eucalyptus specimens", ***Maderas. Ciencia y Tecnología***, Vol. 20, No. 3, (2018), 333-342. http://dx.doi.org/10.4067/S0718-221X2018005003401
43. EN, C., "408 timber structures: Structural timber and glued laminated timber-determination of some physical and mechanical properties", ***CEN/TC124***, (2003).
44. 384., E., "Structural timber- determination of characteristic values of mechanical properties and density", (2016).
45. Record, S.J., "The mechanical properties of wood: Including a discussion of the factors affecting the mechanical properties, and methods of timber testing, Good Press, (2020).
46. Ferreira, D., Fonseca, E., Pinto, C. and Borges, P., "Tensile strength of pine and ash woods–experimental and numerical study", in 6th International Conference on Mechanics and Materials in Design M2D2015, Edições FEUP-INEGI., (2015), 2341-2348.

## Persian Abstract

**چکیده**

ترکیب خاک با استفاده از جاذب‌ها باعث بهبود ساختار خاک شده و مقاومت برشی خاک را نیز تقویت می‌کند. از سویی دیگر می‌توان اینگونه تفسیر کرد که ترکیب خاک با جاذب، به شرط رعایت طرح اختلاط و نسبت بهینه، قدرت جذبِ آبِ خاک را افزایش داده و احتمال نفوذ و نشت آب‌های زیر زمینی حاوی مواد خطرساز را کاهش می‌دهد و از این طریق، مولفه‌های مقاومتی خاک را تقویت می‌کند. در این مقاله، تاثیر فلزات سنگین و جاذب‌ها بر روی رفتار ژئوتکنیکی خاک‌های ماسه-رسی حاوی نیترات سرب و روی به عنوان فلزات سنگین و زئولیت و خاکستر سبوس پوسته برنج (پسماند کشاورزی) به عنوان جاذب، مورد مطالعه قرار گرفته است. نتایج نشان می‌دهد که جایگزین کردن خاکستر پوسته برنج و زئولیت در ترکیب دانه‌بندی خاک با ۲۰ درصد رس کائولینیتی به شکل قابل توجهی منجر به کاهش نیترات روی و سرب می‌شود. همچنین، سطح متخلخل خاکستر پوسته برنج به عنوان یک مزیت تاثیرگذار در افزایش جذب و تعدیل نشت آلودگی، می‌تواند در صورت جایگزینی با کائولینیت، قدرت جذب خاک را ارتقا دهد. جایگزین کردن ۱۵ درصد خاکستر پوسته برنج با کائولینیت قدرت جذب نیترات‌های سرب و روی را به ترتیب ۲۲۸.۸ و ۲۹۱.٦ درصد افزایش می‌دهد. شایان ذکر است که افزودن فلزات سنگین نیتراتی به کائولینیت حدود روانی و پلاستیک خاک را افزایش می‌دهد همچنین باعث تغییر پارامترهای تحکیم خاک می‌گردد بر اساس نتایج به دست آمده، با افزاش حضور فلزات سنگنین به مقدار ۵۰۰۰ ppm مقدار حد روانی از ٤۹.۸ به ۵۹.۱ می‌رسد در حالی که، حد پلاستیک از ۳۱ (در حالت عدم حضور فلز سنگین) به ۳٦.٤ (در حضور ۵۰۰۰ ppm فلز سنگین) میل می‌کند.

IJE TRANSACTIONS B: Applications Vol. 35, No. 11, (November 2022) 2130-2138

International Journal of Engineering

Journal Homepage: www.ije.ir

# Identification of Factors Causing Risky Driving Behavior on High-speed Multi-lane Highways in India Through Principal Component Analysis

S. M. Damodariya*, C. R. Patel

*Department of Civil Engineering, Sardar Vallabhbhai National Institute of Technology, Surat, Gujarat, India*

*PAPER INFO*

*Paper history:*
Received 10 June 2022
Received in revised form 28 July 2022
Accepted 31 July 2022

*Keywords*:
*Road Safety*
*Risky Driving Behavior*
*Multi-lane High Speed Highways*
*Questionnaire*
*Principal Component Analysis*

*ABSTRACT*

In developing countries like India, Multilane high-speed National Highways (NHs) are victims of high accident rates. The Indian National Highway network comprises only 2% of the Indian road network, but transports 40% of traffic, resulting in traffic accidents on National Highways. As observed from past studies, drivers are the main responsible factors for accident causation due to their risky behavior. Hence, to determine significant factors causing the risky behavior of drivers on multi-lane high-speed highways, the personal interview survey through questionnaire was conducted for the road users of NH-47 comprising of the responses to the drivers' demographics, attitude towards vehicle condition and maintenance, traffic regulations/ enforcement following attitude characteristics, and roadway environment characteristics. Principal component analysis (PCA) was applied to the questionnaire variables, and significant category-wise variables for risky driving were identified. Fifteen important variables contributed to risky driving behavior from the questionnaire database by PCA. They are Roadway environment characteristics like improper signals, roadside accident prevention infrastructure, improper pavement, and no safe crossing points; Driver's age and experience; Using mirrors while overtaking, using lights and dipper during night-time, and using hand signals during daytime; Using helmets and seatbelts while driving and having a valid vehicle insurance policy; age of the vehicles, vehicle service frequency, and lane preference in their decreasing significance based on the questionnaire database. The authorities can take suitable measures to control the significant variables causing risky driving behavior on high speed multi-lane highways and reduce the accidents scenarios on the multilane highways.

***doi**: 10.5829/ije.2022.35.11b.08*

## 1. INTRODUCTION

In developing countries like India, Multilane National Highways (NHs) are victims of high accidents even after preventive measures. In India, driver error is the leading cause of accidents due to their risk-taking behavior [1]. For one such high-speed stretch, NH-47, the number of accidents has increased by 10.78% since the NH opened in 2014. Hence, to determine significant factors causing the dangerous behavior of drivers on such multi-lane highways, the personal interview survey was conducted for the road users of NH-47 comprising of the responses to the drivers' demographics, attitude towards vehicle condition and maintenance, traffic regulations/ enforcement following attitude characteristics, and roadway environment characteristics.

Questionnaire data are subjected to principal component analysis (PCA) to identify the significant factors that address the variability of risk-driven driving behavior.

In this paper, PCA has been conducted for the questionnaire survey responses, broadly categorized as 1. Driver's characteristics (10 variables) 2. Vehicle-related characteristics (8 variables) 3. Driver's regulation/enforcement following attitude characteristics (4 variables) and 4. Roadway environment review characteristics (5 variables).

Few studies have been undertaken to judge driver behavior by in-field questionnaire surveys and data

*Corresponding Author Institutional Email: smdamodariya@gmail.com (S. M. Damodariya)

Please cite this article as: S. M. Damodariya and C. R. Patel, Identification of factors causing Risky Driving Behavior on high-speed multi-lane highways in India through Principal Component Analysis, ***International Journal of Engineering, Transactions B: Applications***, Vol. 35, No. 11, (2022) 2130-2138

analysis using PCA for heterogeneous traffic circumstances and high-speed multi-lane highways in developing nations like India. Compared to previous questionnaire-based research, this questionnaire includes extra questions such as the driver's attitude toward vehicle maintenance. In earlier road safety questionnaire-based research, such parameters were rarely considered. As a result, it was necessary to investigate NH-47, a multi-lane high-speed highway stretch. The researchers could identify several key characteristics contributing to unsafe driving behavior through PCA. Authorities can act appropriately to regulate these significant elements and limit the number of accidents and fatalities on multi-lane highways.

## 2. LITERATURE REVIEW

Road traffic deaths and injuries are important global public health issues, attracting increasing attention [2].

Because one part of sustainable transportation is safety, the elasticity of road accident variables concerning demographic, economic, and transportation supply factors across time were constructed and analyzed. A composite road safety sustainability index was proposed based on the established elasticities. According to the assessment of road accidents for Asia Pacific countries, road accidents have constituted a looming public safety concern for the area. The study found that the severity of the road accident problem differed significantly among countries [3].

The Road Safety Development Index (RSDI) was proposed [4], which includes eight road safety dimensions related to the human-vehicle-road-environment-regulation system: traffic risk, personal risk, road user behavior, socio-economic background, vehicle safety, road situation, road safety organization, and enforcement. Each dimension contained one or more quantitative indicators, the utility of which was judged based on the data available. To combine the Safety Performance Indicators (SPIs) that correspond to the eight domains indicated above into a composite index, three primary methodologies (objective and subjective) were used: the simple average, the application of theoretical weights, and the PCA (RSDI).

A log-linear model utilized categorical analysis techniques on drivers involved in traffic accidents or regulation infractions to determine the association between reckless driving behavior and influencing elements such as age, marital status, and educational level. The normal reckless driving qualities of drivers were uncovered using PCA in factor analysis [5]. The variations in reactivity between risky driving behavior and driver attributes were compared using odds multipliers from logit models.

The SUNflower technique was used to develop an integrated and comprehensive set of indicators that collaborated with a composite index (the so-called SUNflower Index) to condense the vast amount of data on road safety [6, 7]. The authors classified the indicators into three categories: road safety performance indicators (outcome indicators), implementation performance indicators (process indicators), and policy performance indicators (the quality of national road safety plans). The three categories of indicators were also placed in a policy context in an attempt to add some background variables: a country's structure and culture. Using PCA and Common Factor Analysis (CFA), the fundamental indicators were combined into a composite index, weighting based on statistical models.

The relationship between road safety management and road safety performance was explored [8]. The 'SUNflower' pyramid is a five-level structure that describes road safety management systems: For that reason, (i) structure and culture, (ii) programs and measurements, (iii) 'intermediate' outcomes - safety performance indicators (SPIs), (iv) final outcomes - fatalities and injuries, and (v) social costs were selected. As for road safety performance indicators, they looked at mortality and fatality rates, the percentage reduction in fatalities over time, a composite indicator of road safety outcomes, and a composite indicator of 'intermediate' outcomes (SPIs). According to the findings, road safety management can be represented by three composite indicators: "vision and strategy," "budget, assessment, and reporting," and "measurement of road user attitudes and behaviors." When a statistical association between road safety management and 'intermediate' outcomes was found to affect 'final' outcomes, the SUNflower method to the sequential effect of each layer was confirmed.

Using the driver behaviour questionnaire [9], the authors attempted to identify the factors that influence driving behavior, develop a factor model, identify the role of age, gender, annual kilometers driven, and social status, and investigate the relationship between self-reported driver behavior and self-reported accident involvement and offenses among Czech drivers (DBQ). They used Varimax rotation to run the 50-item DBQ through PCA. They discovered that a three-factor approach to data evaluation is the most effective. The three-factor model could be responsible for 31.75 percent of the total variation.

The relationship between risk perceptions of drivers and potential predictive characteristics was looked into the incidence of texting and driving in Jordan [10]. Data were collected anonymously at several locations using a self-report questionnaire, with 423 drivers participated. The authors employed statistical analysis to demonstrate the relationship between risk levels and the drivers' demographics and exposure factors. Despite being aware of the risks and legal requirements, 93.1 percent of drivers, mostly young male college students, engaged in this dangerous behavior. According to the research, cell

phone was used while driving was associated with gender, employment status, age, education level, driving experience, and daily driving distance.

Factor analysis was conducted to identify the major components influencing road traffic crashes with high fatalities [11]. Twenty variables were collected: personnel, vehicles, roads, and the environment. Validity was checked on the significance of their correlations. The most important factors in accidents were fault behavior, driving experience, vehicle purpose, vehicle safety condition, driver, road surface condition, roadside protection facilities, road lighting, and road terrain.

Drivers face difficult road traffic circumstances [12]. Drivers may become aggressive and impatient due to the constant pressure of traffic congestion. As a result, dangerous driving conduct was commonplace in everyday life. They concluded that the mental burden of drivers was a key determinant in unsafe driving behavior.

An attitudinal questionnaire was developed [13] based on Ajzen's Theory of Planned Behavior (TPB) [14]. The findings validated the explanatory utility of the market segmentation approach in comprehensively relating the relationship between attitudes, behaviors, and the socio-demographic characteristics of drivers. The authors concluded that the technique effectively distinguishes between safe and risky drivers and may thus be utilized as the foundation for road safety initiatives.

The impact of socio-demographic and behavioral variables on perceived and aggressive driving behavior varies in size and direction depending on the driver group [15]. The discovery of a relationship between unobserved qualities revealed the complexities of the driving choice mechanism, especially when fundamental drivers of aggressive driving were present.

A study of young student drivers' and riders' views on road safety issues investigated driving practices in hypothetical settings, risk perception, and concerns [16]. The authors discovered that motorcyclists were likelier to break traffic laws than car drivers. The more common risk-taking behaviors among motorcycle riders appear to be a trait of riding a motorcycle rather than a feature of being a motorcycle rider. The study projected that, unlike cars, the structural features of motorcycles allow for dangerous driving behavior. Motorcycles that are smaller and lighter take up less road space. They are more agile and quicker than cars; therefore, they are more direct and responsive.

The relationship between bus driver safety culture and unsafe behavior was investigated [17]. Two questionnaires were used to analyze risky behavior and safety culture among 336 public transportation bus drivers in Tehran, Iran: The Driver Safety Culture Questionnaire (DSCQ) and the Public Transport Driver Behavior Questionnaire (PTDBQ). In addition, a questionnaire was devised to examine socio-demographic factors and the frequency of accidents. The DSCQ and PTDBQ had acceptable psychometric properties. The data shows a negative relationship between accidents, safety culture, and drivers' harmful activities. Accidents and unsafe behaviors were also found to have a positive association. On the other hand, Unsafe behavior significantly mediated the link between safety culture and accidents.

A self-report questionnaire was used to collect demographic information, psychological features, and driving practices from 245 cab drivers [18], while the DBQ was calibrated for the Iranian driver population and investigate their abnormal driving behavior and sample of 524 Iranian drivers [19].

In developing nations like India, few studies have been undertaken to judge driver behavior by in-field questionnaire surveys for heterogeneous traffic circumstances on high-speed multi-lane highways. Hence, a questionnaire was conducted to judge risky driving factors, which included categorized responses to driver characteristics, attitude towards vehicle status and maintenance, traffic rules/regulation compliance and road environment in NHs. In addition, for the questionnaire data, PCA was not used on exclusive multi-lane highways. This questionnaire also includes additional questions such as the driver's attitude toward vehicle upkeep and the regulations attitude being followed by road users. In earlier road safety questionnaire-based research, such parameters were rarely considered. As a result, it was required to conduct research for users of NH-47, a multi-lane high-speed highway segment.

## 3. METHODS AND DATA

**3. 1. Study Area Characteristics** The NH-47, one of the country's most important roads, connects Ahmedabad with Indore. It is an important link connecting the major cities of Indore and Ahmedabad with the fertile lands of Gujarat, Rajasthan, and Madhya Pradesh. This is a national road NH-47 from Ahmedabad to Indore. The Godhra bypass is the first of the selected section. On this national highway, the end is the border of Gujarat-MP, as shown in Figure 1. The route covers two regions: the first, PanchMahals, with 1210 villages and 14 percent of the urban population. Second, according to the 2011 Indian Census, Dohad has 696 villages with an urban population of 9%. Due to many communities crossing this national highway, many central access points and adjacent NH access points intersect with residential areas.

**3. 2. Accident Data** Table 1 shows the annual trend of accidents on the stretch for 2012-2020, compiled from the First Inspection Reports (FIRs) of police


(a) Location of the stretch on the Indian map

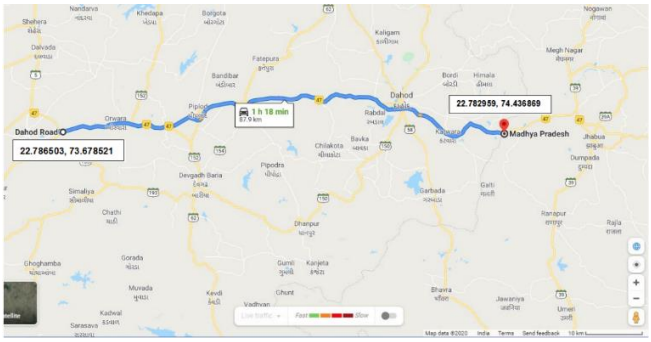


(b) The stretch location on Google map

(c) A photograph of the stretch

**Figure 1.** The selected stretch of NH-47

**TABLE 1.** Year-wise Accidents for the stretch

| Year | Classification of accident | | | | | |
|---|---|---|---|---|---|---|
| | Fatal | Grievous Injury | Minor Injury | Non-Injury | Total | Increase in total accidents % |
| 2012 | 11 | 22 | 25 | 0 | 58 | -- |
| 2013 | 18 | 6 | 27 | 0 | 51 | -- |
| 2014 | 9 | 32 | 11 | 2 | 54 | 5.88 |
| 2015 | 26 | 27 | 10 | 5 | 68 | 25.93 |
| 2016 | 16 | 34 | 11 | 0 | 61 | -10.29 |
| 2017 | 31 | 29 | 12 | 1 | 73 | 19.67 |
| 2018 | 35 | 32 | 13 | 1 | 81 | 10.96 |
| 2019 | 39 | 35 | 15 | 2 | 91 | 12.35 |
| 2020 | 45 | 40 | 14 | 2 | 101 | 10.99 |
| Total | 230 | 257 | 138 | 13 | 638 | |
| Avg. Increase | | | | | | 10.78 |

**3. 3. Access Density** On the stretch, access points and their chainage were also noted. However, it is a toll road with 31 middle access points, 41 left side access points, and 53 right side carriageway access points on the stretch; the stretch has an overall access density of 1.36/km, increasing conflicting sites on the stretch.

**3. 4. Monthly Annual Daily Traffic (ADT) Data** ADT data has continuously increased over the years since the opening of the toll road in 2014.

**3. 5. Questionnaire Survey** For around two weeks, these surveys were conducted on the side of the toll road near restaurants, gas stations, and bus lay-bys on weekdays from 9 a.m. to 1 p.m. and 3 p.m. to 7 p.m. The questionnaires were filled out on paper by trained persons who interviewed all major vehicle categories' drivers. 43 two-wheeler (2w) drivers, 67 four-wheeler (4w) drivers, 84 bus drivers, and 64 truck drivers were questioned for the questionnaire study.

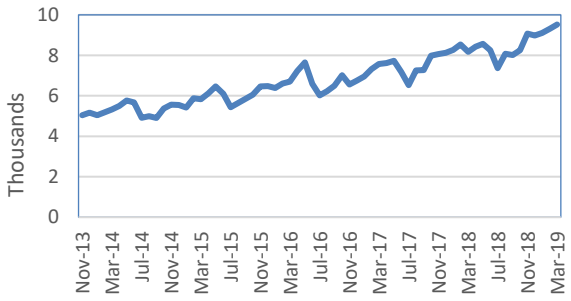


**Figure 2.** The trend of ADT data over the years
Source: Office of the Manager, Godhra Expressway Limited, Godhra

The responses of all the respondents noted in questionnaire forms were then converted into a tabular form in excel. Each question response was converted on a likert scale from 1-to 7, based on the questionnaire variable data. After this final data set was obtained in excel, PCA was applied through IBM SPSS version 25.

## 4. PRINCIPAL COMPONENT ANALYSIS (PCA)

Large datasets are becoming more frequent, yet they can be difficult to comprehend [20]. The basic goal of the PCA is to minimize a data set's dimensionality. Many connected variables try to preserve as much diversity as possible in the data collection. The uncorrelated principal components ordered are transformed into a new set of variables to achieve this dimension reduction. The first few keep most of the variation in the original variables while reducing information loss. The concept is straightforward: lower the dimensionality of a dataset while keeping as much 'variability' (i.e., statistical information) as possible. For a positive-semidefinite symmetric matrix, computing the primary components reduces the eigenvalue-eigenvector issue [21].

PCA can be based on either the covariance matrix or the correlation matrix.

Steps in SPSS for conducting PCA:

1. Importing data of questionnaire survey from Excel into SPSS.
2. Analyse > Dimension Reduction > Factor...> Selecting variables> Descriptives - Univariate descriptives - Initial solution - KMO and Bartlett's Test-. Checking whether it is coming more than 0.5, then only proceed for PCA.
3. Extraction > Method -Principal component > Analyse -Correlation matrix; Extract - Based on Eigen value>1>Display - Unrotated factor solution, Scree plot> Maximum iterations for convergence – 25
4. Rotation> Method> Display- Rotated solution
5. Score> Display- factor score coefficient matrix greater than 0.4. Lesser values will be ignored.
6. Options> Missing values> Coefficient Display format- Sorted by size- Suppressing small co-efficient (Absolute value below 0.4).
7. Repeat the steps from 1 to 6 until there are no components matrix values in Negative or no two variables repeated in any Principal component.

In the study methodology for extracting the final essential variables from the questionnaire, the data was first entered in Excel format and converted into a Likert scale from 1-to 7. PCA for the whole questionnaire was done after verifying obtained KMO 0.634>0.5 and extracted Eigenvalues more significant than 1. The steps in SPSS for PCA are repeated until no component's matrix values in negative or no two variables are repeated in any principal component.

**4. 1. Data Analysis** There were 27 questions in the questionnaire for which the response was obtained. There were ten questions about the driver's characteristics, eight about vehicle characteristics, four about regulation/enforcement characteristics, and five about roadway environment characteristics. Table 2 shows the questionnaire variable names and section categories of the variables.

**TABLE 1.** Questionnaire variables' names and categories

| Sr. | Variable name | Question | Category |
|---|---|---|---|
| 1 | Age | Age | Driver personal |
| 2 | Gender | Gender | |
| 3 | Quali | Educational Qualification | |
| 4 | Driving_exp | How much is the driver's driving experience on the highway? | |
| 5 | Val_DL | Whether the driver holds a valid driving license? | |
| 6 | Helmet_SB | Whether the driver wears the helmet/seat belt? | |
| 7 | Drunken_condn | Whether the driver in a drunken condition? | |
| 8 | Break_km_range | While driving for longer journeys, how many km do you take breaks if you are tired? | |
| 9 | Break_hrs_range | How many hours will you drive continuously for long journeys >80km? | |
| 10 | Accident_freq_range | How often have you met with an accident in your driving career until now? | |
| 11 | Veh_cat | Vehicle category | Vehicle |
| 12 | Age_vehicle | What is the age of the vehicle? | |
| 13 | Age_wheels_range | What is the age of the wheels of your vehicle? | |
| 14 | All_Mirror_ availability | Whether all Mirrors available on the vehicle? | |
| 15 | All_light_availability | Are sidelights, headlights, brake lights, and dipper working correctly? If not mentioned, what is not working? | |
| 16 | Veh_service_freq | At what frequency (km or Period of 3 months, six months, or Yearly) do you get your vehicle serviced? | |
| 17 | Valid_veh_insur_ policy | Whether you hold a valid insurance policy for the vehicle? | |
| 18 | Dents_ availability | Whether any dents (ghoba-damages) on the vehicle? If yes, then how many and their location? | |

| | | | |
|---|---|---|---|
| 19 | Using_ handsignals_ daytime | How often do you use hand signals (Driver)while driving the vehicle in DAY time? | |
| 20 | Using_lights_dipper_ nightime | How often do you use sidelights, headlights, and dipper while driving the vehicle during night-time? | Regulation/ enforcement |
| 21 | Using_mirrors_ overtaking | How often do you use Mirrors while overtaking maneuvers? | |
| 22 | Lane_preference | Which lane do you prefer for driving? | |
| 23 | Feeling_improper_ pavement | How often do you feel that pavement is not maintained correctly? | |
| 24 | Feeling_improper_ signals | How often do you feel the signals are not properly located and maintained at intersections? | |
| 25 | Feeling_ nosafetypoints | How often do you feel no safe crossing points are provided on highways? | Roadway environment |
| 26 | Feeling_roadsideinfra | How often do you feel the roadside accident prevention infrastructure is improper? | |
| 27 | Feeling_improper_ markings | How often do you feel the road markings are not proper? | |

**4. 2. PCA for Road Safety Questionnaire** After trial and error, 15 out of 27 items made 6 principal components. They satisfied the cumulative covariance and eigenvalues criteria. Rotation method use was Equamax with Kaiser Normalization.

For the questionnaire's data, the Kaiser-Meyer-Olkin measure of sampling adequacy was found as 0.634, which is more than 0.5, as shown in Table 3. Hence, PCA analysis can be carried out for the questionnaire database.

From PCA, significant variation, i.e., 66.85%, was obtained with the first six principal components. Also, Eigenvalues for these components were more than 1. Hence, the other principal components were ignored for the PCA. The details of cumulative %variance is mentioned in Table 4.

From the scree plot shown in Figure 3, scree was observed near 1.0 Eigenvalue for the first 6 principal components. Hence, only the first six principal components were extracted for PCA. The results of the rotated component matrix are enumerated in Table 5.

**TABLE 3.** KMO and Bartlett's Test - PCA for Road safety questionnaire

| | | |
|---|---|---|
| **Kaiser-Meyer-Olkin Measure of Sampling Adequacy.** | | 0.634 |
| **Bartlett's Test of Sphericity** | **Approx. Chi-Square** | 810.943 |
| | ***df*** | 105 |
| | ***Sig.*** | 0.000 |

**TABLE 4.** Total Variance Explained - PCA for Road safety questionnaire

| Component | Initial Eigenvalues | | | Extraction Sums of Squared Loadings | | | Rotation Sums of Squared Loadings | | |
|---|---|---|---|---|---|---|---|---|---|
| | **Total** | **% of Variance** | **Cumulative %** | **Total** | **% of Variance** | **Cumulative %** | **Total** | **% of Variance** | **Cumulative %** |
| 1 | 2.51 | 16.75 | 16.75 | 2.51 | 16.75 | 16.75 | 2.46 | 16.40 | 16.40 |
| 2 | 2.16 | 14.41 | 31.17 | 2.16 | 14.41 | 31.17 | 2.02 | 13.45 | 29.84 |
| 3 | 1.90 | 12.64 | 43.81 | 1.90 | 12.64 | 43.81 | 1.76 | 11.70 | 41.54 |
| 4 | 1.30 | 8.65 | 52.47 | 1.30 | 8.65 | 52.47 | 1.33 | 8.84 | 50.38 |
| 5 | 1.14 | 7.61 | 60.08 | 1.14 | 7.61 | 60.08 | 1.32 | 8.81 | 59.19 |
| 6 | 1.02 | 6.78 | 66.85 | 1.02 | 6.78 | 66.85 | 1.15 | 7.66 | 66.85 |
| 7 | 0.81 | 5.43 | 72.28 | | | | | | |
| 8 | 0.78 | 5.21 | 77.49 | | | | | | |
| 9 | 0.70 | 4.69 | 82.18 | | | | | | |
| 10 | 0.59 | 3.91 | 86.08 | | | | | | |
| 11 | 0.55 | 3.69 | 89.78 | | | | | | |
| 12 | 0.50 | 3.34 | 93.12 | | | | | | |
| 13 | 0.43 | 2.90 | 96.01 | | | | | | |
| 14 | 0.39 | 2.61 | 98.63 | | | | | | |
| 15 | 0.21 | 1.37 | 100.00 | | | | | | |

Extraction Method: Principal Component Analysis.

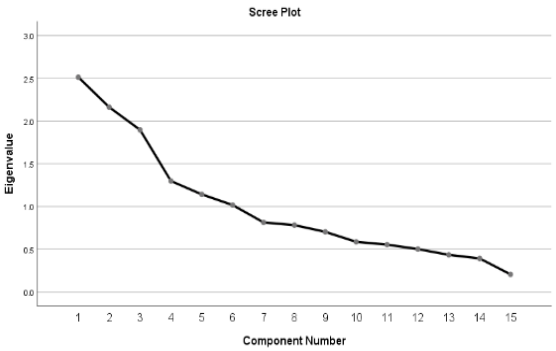


**Figure 3.** Scree plot - PCA for Road safety questionnaire

## 5. RESULTS

The final output results – significant contributing factors are given in Table 6:

From PCA, the following points can be deduced:

1 1st principal component factor is explained by roadway factors like 1. Signal location and maintenance, followed by 2. Roadside accident prevention infrastructure, 3. Pavement maintenance, and 4. No safety crossing points in decreasing order.

2 2nd principal component factor is explained by two driver personal characteristics factors 1. Driving experience, and 2. Driver's age.

**TABLE 5.** Rotated component matrix - PCA for Road safety questionnaire

| Sr. | Question | Component | | | | | |
|---|---|---|---|---|---|---|---|
| | | 1 | 2 | 3 | 4 | 5 | 6 |
| 1. | How often do you feel the signals are not properly located and maintained at intersections? | 0.799 | | | | | |
| 2. | How often do you feel the roadside accident prevention infrastructure is improper? | 0.797 | | | | | |
| 3. | How often do you feel that pavement is not maintained correctly? | 0.746 | | | | | |
| 4. | How often do you feel no safe crossing points are provided on highways? | 0.721 | | | | | |
| 5. | How much is the driver's driving experience on the highway in years? | | 0.907 | | | | |
| 6. | Driver's age in years | | 0.899 | | | | |
| 7. | How often do you use Mirrors while overtaking maneuvers? | | | 0.815 | | | |
| 8. | How often do you use sidelights, headlights, and dipper while driving the vehicle night-time? | | | 0.751 | | | |
| 9. | How often do you use hand signals (Driver) while driving the vehicle in day time? | | | 0.677 | | | |
| 10. | Whether the driver wears a helmet/seat belt? | | | | 0.731 | | |
| 11. | Whether you hold a valid insurance policy for the vehicle? | | | | 0.697 | | |
| 12. | What is the age of the wheels of your vehicle? | | | | | 0.707 | |
| 13. | At what frequency (km or Period of 3 months, six months, or Yearly) do you get your vehicle serviced | | | | | 0.665 | |
| 14. | Which lane do you prefer for driving? | | | | | 0.521 | |
| 15. | Whether the driver holds a valid driving license? | | | | | | 0.877 |

**TABLE 6.** Output interpretation of PCA for Questionnaire

| Significance Level | Variable | Factor section in the Questionnaire |
|---|---|---|
| 1 | Feeling_improper_signals<br>Feeling_roadsideinfra<br>Feeling_improper_pavement<br>Feeling_nosafetypoints | Roadway Environment |
| 2 | Driving_exp<br>Age | Driver personal |
| 3 | Using_mirrors_overtaking<br>Using_lights_dipper_nightime<br>Using_handsignals_daytime | Regulation/ enforcement |
| 4 | Helmet_SB<br>Valid_veh_insur_policy | Driver personal<br>Vehicle |
| 5 | Age_vehicle<br>Veh_service_freq<br>Lane_preference | Vehicle<br>Vehicle<br>Regulation/ enforcement |
| 6 | Val_DL | Driver personal |

3 3rd principal component factor is explained by three regulation/enforcement factors 1. Use of mirrors while overtaking maneuvers 2. Use of sidelights, headlight, and dipper while driving the vehicle during night-time 3. Use of hand signals (Driver)

while driving the vehicle in the daytime in decreasing order.

4 4th principal component is explained by one driver's factor, helmet/seatbelt wearing, and the second vehicle factor, namely holding a valid vehicle insurance policy in decreasing order.

5 5th principal component is explained by two-vehicle factors, namely the age of wheels, vehicle service frequency, and one regulation/enforcement factor named lane preference.

6 6th principal component is explained by the driver's factor, namely holding a valid driving license.

Overall, Roadway environment characteristics namely improper signals, roadside accident prevention infrastructure, improper pavement, and no safe crossing points together show 16.40% of the variance of the questionnaire database, which is the maximum of six significant principal components. Driver's age and experience contribute 13.45% variance in the questionnaire database. Using mirrors while overtaking, using lights and dipper during night-time, and using hand signals during daytime constitute an 11.70% variance of the questionnaire database. Using helmets and seatbelts while driving and having a valid vehicle insurance policy contributes to an 8.84% variance in the database. Age of the vehicles, vehicle service frequency, and lane preference combinedly constitute an 8.81% variance in the database. Holding of valid driving license contributes to a 7.66% variance in the questionnaire database.

## 6. CONCLUSION

Driver's fault is the main factor for accident causation due to their risky behavior (1). Questionnaire survey by personal interview is conducted on a high- speed multi-lane highway stretch NH-47 to determine significant factors responsible for drivers' risky behavior on multi-lane NHs. The interview questionnaire comprised of the questions related to the drivers' demographics, attitude towards vehicle condition and maintenance, traffic regulations/ enforcement following attitude characteristics, and roadway environment characteristics of the NH. Principal component analysis (PCA) is applied to the questionnaire database, and significant category-wise variables for risky driving are identified.

The most significant variables from the principal component analysis for the highway are Roadway environment characteristics namely improper signals, roadside accident prevention infrastructure, improper pavement, and no safe crossing points; Driver's age and experience; Using mirrors while overtaking, using lights and dipper during night-time, and using hand signals during daytime; Using helmets and seatbelts while driving and having a valid vehicle insurance policy; age of the vehicles, vehicle service frequency, and lane preference in their decreasing significance based on the questionnaire database.

The authorities can take suitable measures to control the significant variables causing risky driving behavior, mainly roadway environment for the highway under consideration, followed by driver's attitude towards enforcement/ regulation, driver's attitude toward proper upkeep of the vehicle on National highways and reduce the number of accidents and fatalities scenarios on the high-speed multi-lane highways.

Similar studies may be further conducted on other rural and urban high-speed multi-lane highway stretches with greater sample sizes. Comparisons can be made for significant factors responsible for risky driving behavior under different traffic, vehicle composition, vehicle condition and demographics of the road users of the multi-lane high-speed highways.

## 7. REFERENCES


1. Singh, S. K. "Road Traffic Accidents in India: Issues and Challenges." ***Transportation Research Procedia***, Vol. 25, (2017), 4708-4719. https://doi.org/10.1016/j.trpro.2017.05.484
2. Wei, Z. "Effects of deceleration on secondary collisions between adult occupants and vehicle in frontal crash accidents." ***International Journal of Engineering, Transactions B: Applications***, Vol. 34, No. 12, (2021), 2658-2664. https://doi.org/10.5829/IJE.2021.34.12C.11
3. Vaziri, M. "A comparative appraisal of roadway accident for Asia-Pacific countries." ***International Journal of Engineering, Transactions A: Basics***, Vol. 23, No. 2, (2010), 111-126.
4. Al Haji, G. *Towards a road safety development index (RSDI)*. ***Development of an international index to*** measure road safety performance." PhD diss., Linköping University Electronic Press, 2005.
5. Jang, T. Y. "Analysis on reckless driving behavior by log-linear model." ***KSCE Journal of Civil Engineering***, Vol. 10, No. 4, (2006), 297-303. https://doi.org/10.1007/bf02830784
6. Wegman, F., and Oppe, S. "Benchmarking road safety performances of countries." ***Safety Science***, Vol. 48, No. 9, (2010), 1203-1211. https://doi.org/10.1016/j.ssci.2010.02.003
7. Wegman, F., Aarts, L., and Bax, C. "Advancing sustainable safety. National road safety outlook for The Netherlands for 2005-2020." ***Safety Science***, Vol. 46, No. 2, (2008), 323-343. https://doi.org/10.1016/j.ssci.2007.06.013
8. Papadimitriou, E., and Yannis, G. "Is road safety management linked to road safety performance?" ***Accident Analysis & Prevention***, Vol. 59, (2013), 593-603. https://doi.org/10.1016/j.aap.2013.07.015
9. Sucha, M., Sramkova, L., and Risser, R. "The Manchester driver behaviour questionnaire: self-reports of aberrant behaviour among Czech drivers." ***European Transport Research Review***, Vol. 6, No. 4, (2014), 493-502. https://doi.org/10.1007/s12544-014-0147-z
10. Ismeik, M., Al-Kaisy, A., and Al-Ansari, K. "Perceived risk of phoning while driving: A case study from Jordan." ***Safety Science***, Vol. 78, (2015), 1-10. https://doi.org/10.1016/j.ssci.2015.02.011
11. Chen, T., Zhang, C., and Xu, L. "Factor analysis of fatal road traffic crashes with massive casualties in China." ***Advances in***

***Mechanical Engineering***, Vol. 8, No. 4, (2016), 1-11. https://doi.org/10.1177/1687814016642712

12. Qin, X., Shen, Z., and Wehbe, N. "Predicting collision risk between trucks and interstate overpasses." ***Journal of Transportation Engineering***, Vol. 142, No. 8, (2016), 04016026. https://doi.org/10.1061/(ASCE)TE.1943-5436.0000848
13. Batool, Z., and Carsten, O. "Attitudinal segmentaion of drivers in Pakistan: The potential for effective road safety campaigns." ***Accident Analysis and Prevention***, Vol. 114, No. February, (2018), 48-54. https://doi.org/10.1016/j.aap.2017.05.027
14. Ajzen, I. "The Theory of Planned Behavior." ***Organizational Behavior and Human Decision Process***, Vol. 50, (1991), 179-211.
15. Fountas, G., Pantangi, S. S., Hulme, K. F., and Anastasopoulos, P. C. "The effects of driver fatigue, gender, and distracted driving on perceived and observed aggressive driving behavior: A correlated grouped random parameters bivariate probit approach." ***Analytic Methods in Accident Research***, Vol. 22, (2019), 100091. https://doi.org/10.1016/j.amar.2019.100091
16. Cordellieri, P., Sdoia, S., Ferlazzo, F., Sgalla, R., and Giannini, A. M. "Driving attitudes, behaviours, risk perception and risk concern among young student car-drivers, motorcyclists and pedestrians in various EU countries." ***Transportation Research Part F: Traffic Psychology and Behaviour***, Vol. 65, (2019), 56-67. https://doi.org/10.1016/j.trf.2019.07.012
17. Mokarami, H., Alizadeh, S. S., Rahimi Pordanjani, T., and Varmazyar, S. "The relationship between organizational safety culture, unsafe behaviors, and accidents among public transport bus drivers using structural equation modeling." ***Transportation Research Part F: Traffic Psychology and Behaviour***, Vol. 65, (2019), 46-55. https://doi.org/10.1016/j.trf.2019.07.008
18. Parishad, N., Aghabayk, K., Rezaei, R., Samerei, A. an., and Mohammadi, A. "Validation of the Driver Behaviour Questionnaire in a representative sample of drivers in Australia." ***Civil Engineering Infrastructures Journal***, Vol. 53, No. 1, (2020), 161-171. https://doi.org/10.22059/ceij.2019.283780.1593
19. Aghabayk, K., Mashhadizade, L., and Moridpour, S. "Need safer taxi drivers? Use psychological characteristics to find or train!" ***Sustainability (Switzerland)***, Vol. 12, No. 10, (2020), 1-11. https://doi.org/10.3390/su12104206
20. Jollife, I. T., and Cadima, J. "Principal component analysis: A review and recent developments." ***Philosophical Transactions of the Royal Society A: Mathematical, Physical and Engineering Sciences***, Vol. 374, No. 2065, (2016). https://doi.org/10.1098/rsta.2015.0202
21. Syms, C. Principal components analysis. ***Encyclopedia of Ecology*** (2nd ed.). New York: Springer Berlin Heidelberg. https://doi.org/10.1016/B978-0-12-409548-9.11152-2

## Persian Abstract

**چکیده**

در کشورهای در حال توسعه مانند هند، بزرگراه های ملی پرسرعت Multilane (NHs) قربانی نرخ بالای تصادفات هستند. شبکه بزرگراه ملی هند تنها ۲ درصد از شبکه جاده های هند را شامل می شود، اما ٤٠ درصد از ترافیک را حمل می کند که منجر به تصادفات رانندگی در بزرگراه های ملی می شود. همانطور که در مطالعات گذشته مشاهده شد، رانندگان به دلیل رفتار پرخطر خود، عامل اصلی ایجاد تصادفات هستند. از این رو، برای تعیین عوامل مهم ایجاد کننده رفتار مخاطره آمیز رانندگان در بزرگراه های پرسرعت چند بانده، نظرسنجی مصاحبه شخصی از طریق پرسشنامه برای کاربران جاده NH-47 شامل پاسخ به اطلاعات جمعیت شناختی رانندگان، نگرش نسبت به وسیله نقلیه انجام گردید. شرایط و نگهداری، مقررات ترافیکی/اجرای ویژگی‌های نگرش، و ویژگی‌های محیط راه. تجزیه و تحلیل مؤلفه اصلی (PCA) برای متغیرهای پرسشنامه اعمال شد و متغیرهای دسته بندی قابل توجهی برای رانندگی پرخطر شناسایی شدند. پانزده متغیر مهم به رفتار رانندگی پرخطر از پایگاه داده پرسشنامه توسط PCA کمک کردند. آنها ویژگی های محیطی جاده مانند سیگنال های نامناسب، زیرساخت های پیشگیری از تصادفات کنار جاده ای، روسازی نامناسب و عدم وجود نقاط عبور ایمن هستند. سن و تجربه راننده؛ استفاده از آینه در هنگام سبقت گرفتن، استفاده از چراغ و چراغ در طول شب و استفاده از سیگنال های دستی در طول روز. استفاده از کلاه ایمنی و کمربند ایمنی هنگام رانندگی و داشتن بیمه نامه معتبر خودرو؛ عمر وسایل نقلیه، فرکانس سرویس وسیله نقلیه، و اولویت خط در کاهش اهمیت آنها بر اساس پایگاه داده پرسشنامه. مسئولان می توانند اقدامات مناسبی را برای کنترل متغیرهای مهم ایجاد کننده رفتار پرخطر رانندگی در بزرگراه های چند بانده با سرعت بالا و کاهش سناریوهای تصادفات در بزرگراه های چند بانده انجام دهند.

International Journal of Engineering

Journal Homepage: www.ije.ir

# Effect of Adsorbents on Resistance Parameters of Heavy Metal-contaminated Clayey Sand Soils

S. A. Nosrati[a], A. Negahdar*[b], H. Negahdar[a], M. Siavoshnia[a]

[a] *Department of Civil Engineering, Faculty of Civil and Earth Resources Engineering, Islamic Azad University, Central branchTehran, Iran*
[b] *Faculty of Engineering, Department of Civil Engineering, University of Mohaghegh Ardabili, Ardabil, Iran*

*PAPER INFO*

*Paper history:*
Received 13 June 2022
Received in revised form 23 July 2022
Accepted 31 July 2022

*Keywords*:
*Shear Strength*
*Heavy Metals*
*Rice Husk Ash*
*Zeolite*
*Soil Structure Modification*

*ABSTRACT*

Combining soil with some adsorbents improves soil structure and shear strength. Thus, an optimal ratio of some adsorbents in the soil composition enhances soil adsorption capacity, reduces the possibility of groundwater contamination with these hazardous compounds, and leads to increase soil resistance parameters. This paper investigates the effect of heavy metals and adsorbents on the geotechnical behavior of clayey sand soils contaminated with lead and zinc as heavy metals as well as zeolite and rice husk ash as adsorbents. Clayey sand (mixture of sand with 20% kaolinite or bentonite) was considered as a base composition and the behavior of it was studied in both contaminated and uncontaminated states. Then, for increasing the heavy metal adsorption capacity of clayey sand, two types of adsorbents (zeolite and rice husk ash ) were added to the base composition and their behavior were investigated in the case of Lead and Zinc contamination. The results revealed that replacing the rice husk ash and zeolite adsorbents in the sand combination with 20% kaolinite clay significantly reduced the concentration of lead and zinc nitrate in the solution. Replacing 15% of rice husk ash with kaolinite heightened the absorption of lead nitrate and zinc nitrate by 228.8% and 291.6% in kaolinite sand. It was also found that adding nitrate to kaolinite increased the liquid and plastic limits. According to the results, in kaolinite, the value of the liquid limit rose from 49.8 to 59.1 upon elevating the concentration of lead to 5000 ppm, while the plastic limit also increased from 31 in the non-contaminated state to 36.4 in 5000 ppm in the infected state. According to obtained results, the dispersed structure is formed by increasing the concentration of lead nitrate in composition of sandy clay with low plasticity adsorbent; thus, shear resistance decreased. Changing in type of clay minerals to high plasticity cause the different trend in shear resistance parameters. Increasing the concentration of lead nitrate in bentonite composition, lead to flocculated structure be formed and shear strength increased.

***doi**: 10.5829/ije.2022.35.11b.09*

## 1. INTRODUCTION

The expansion of industrial areas over the past few decades, followed by an increase in industrial effluents, has led to the spread of soil contaminations. The leakage of heavy and toxic metals is one of the most important causes of soil contamination. Heavy elements enter the environment through wastewater contaminated with these metals or through leakage from their storage tanks, which results in contamination of soil and groundwater with these toxic compounds [1]. Note that one of the components of crude oil is heavy metals. Thus, in addition to industrial areas, oil-rich areas are also exposed to this pollution from various aspects, from the stage of oil extraction to the transfer and refining of petroleum products [2]. Soil pollution, in addition to being one of the environmental crises, also leads to changes in its geotechnical parameters [3].

Soil type, initial concentration of heavy metals, and their extent in the soil cause changes in soil resistance parameters. As such, studying the behavior of soils contaminated with heavy metals and finding methods to deal with these contaminants is also of great interest in terms of geotechnical issues [4]. One of the most important processes affecting the cause of pollutants in the soil is their absorption by soil particles or adsorbents in the soil composition [5]. The absorption of heavy metals in fine-grained soils is higher than in granular soils

*Corresponding Author Institutional Email: Negahdar@uma.ac.ir
(A. Negahdar)

Please cite this article as: S. A. Nosrati, A. Negahdar, H. Negahdar, M. Siavoshnia, Effect of Adsorbents on Resistance Parameters of Heavy Metal-contaminated Clayey Sand Soils, ***International Journal of Engineering, Transactions B: Applications***, Vol. 35, No. 11, (2022) 2139-2154

[5]. Also, the presence of heavy metals in the soil alters the structure and fundamental behavior of the soil, causing variations in the mechanical, physical, and chemical parameters of the soil. These changes can improve or weaken the geotechnical parameters of the soil [6].

Combining soil with some adsorbents improves soil structure and enhances soil shear strength [7, 8]. Thus, soil composition with an optimal ratio of some adsorbents, in addition to reduce the mobility of heavy elements in the soil and boosting the soil adsorption capacity, reduces the possibility of groundwater contamination with these hazardous compounds and results in increased soil resistance parameters [9, 10]. Also pH of pore fluids has important effect on the physico-chemical and mechanical behavior of clays [11].

Given economic considerations as one of the basic principles in projects, the use of natural and inexpensive adsorbents with sufficient abundance in nature has been presented as one of the solutions to improve contaminated soils [12, 13]. By studying the effect of heavy metals on the properties of kaolinite, it was found that shear strength has been affected by heavy metal contamination [14]. The results showed that the heavy metal contaminants increased the intermolecular space and caused more movement of particles in soils containing kaolinite. Thus, shear strength decreased in contaminated kaolinite by divalent heavy metals [15]. According to reported data in literature [16], due to the number of tanks containing heavy metals as well as pressurized pipelines to transport these compounds to other industrial areas, a huge amount of pollutants always enter through leaks from pipes or tanks. Thus, a significant amount of heavy metals has been reported in the soils around refineries and industrial areas in Iran as well as in different countries [17]. In addition to the possibility of contamination under the beds of reservoirs and pipelines, there is also a chance of contamination by transportations, road communication and road construction sites in such locations. Notably, heavy metal leakage causes bedrock instability and leaves detrimental impacts on the environment. Heavy metals in soils not only induce considerable alterations in resistance parameters, but also yield changes in the soil structure (especially fine-grained soils). However, few studies have been performed on changes in resistance parameters in soils contaminated with heavy metals. The presence of heavy metals in soils containing clay fine grains causes the water thickness of its double layer to decline and due to the presence of heavy metals, a flocculent structure forms in clay soils [18]. One of the important issues in flocculated structures is the possibility of high-pressure subsidence. Thus, it is important to study the behavior of soils contaminated with heavy metals that contain clay (generally charged fine grains). The use of heavy metal adsorbents is one of the appropriate methods to prevent the spread of pollutants and to improve the behavioral performance of soils. Accordingly, the use of a combination of soil and adsorbent can be considered as one of the suitable methods for bedding reservoirs from which contaminants can leak. An important point in this regard is to study the structural changes and variations in soil resistance parameters [19].

Oni [20] studied the CFD Behavior of Transition Flow in Distinct Tubes of Miscellaneous Tape Insertions. They used three different tubes with with crossed-axes-circle-cut tape insert (C-C tube), plain tube with crossed-axes-triangle-cut tape insert (C-T tube), and plain tube with crossed-axes-ellipse-cut tape insert (C-E tube). Results showed that Reynolds number of C-T tubes is fewer than the other tubes [20]. In a study led by Nikhhah Nasab and Abdeh Keykha [21] on the geotechnical characteristics of clayey sand contaminated with lead(II), it was found that the presence of heavy metal cations in the mixture caused a reduction in the shear strength of sand and kaolinite samples. On the contrary, due to the shrinkage of diffuse double layer of bentonite in the presence of lead ion, shear strength of sand and bentonite mixtures increased. Also, the consolidation behavior of both the mixtures contained kaolinite and bentonite was decreased [21].

According to studies conducted by Shang [22] and given the lack of enough data to explore the effect of heavy metals and adsorbents on the geotechnical behavior of soils, the main question that arises is whether addition of adsorbents such as zeolite and rice husk ash (RHA) to soil contaminated with heavy metals such as lead and zinc can alter the resistance parameters of this soil. For this purpose, this paper will investigate the effect of the presence of heavy metals and adsorbents on the geotechnical behavior of clayey sandy soils. Thus, 20% kaolinite is used in combination with sand. A mineral adsorbent called zeolite and an organic adsorbent called rice husk ash (RHA) are also used. The reason for choosing zeolite is its high adsorption power [9]. Further, the impact of zeolite on soil resistance parameters is greater than that of other organic adsorbents (RHA, sawdust, and the like), since organic adsorbents decompose and lose their functionality within a short period. Additionally, lead and zinc pollutants are employed in this research as they have the largest impact on the environment and are present in most industrial effluents. Note that due to the presence of clay in the soil composition, the CU test is conducted in soils containing fine grains.

## 2. MATERIALS AND METHODS

**2. 1. Sand** In order to provide sand materials, Firoozkooh siliceous sand, called 161 sand, was used. This sand was exploited from mines located in

Firoozkooh, 130 km northeast of Tehran, and has a golden yellow color profile. The unified classification system categorizes it as poorly grained sand (SP). Due to non-plastic fine grains in this sand (about 2% of soil weight), the sand was washed using a 0.075 mm diameter sieve to remove all fine grains so that only sand grains would remain. The specifications of the sand and its granulation diagram are presented in Table 1 and Figure 1.

**2. 2. Clay Fines** There are two main factors such as the bond between the constituent of clay and double-layer water around particles that can affect clay behavior. As for the difference between the constituents and the arrangements of particles within both kaolinite and bentonite, considering the effects of clay mineral type on the characteristics of contaminated soil, in the present study two different clay minerals (with high and low plasticity) were used. For the low plasticity clay, kaolinite was used which gained from eastern Azerbaijan (Iran). The used kaolin is white powder. It is noteworthy that the main mineral of this type of soil is kaolinite. Also, for the providing the high plastic clay, Iran Barit Bentonite was purchased. In The properties and particle size distribution curves for kaolinite are shown in Table 2 and Figure 2, respectively.

**2. 3. Zeolite** With Iran's extensive resources of zeolite and by increasing exploitations of these resources in different regions, such as Semnan, this resource has considerable potential to remove heavy metals and even organic pollutants [3, 13]. Although zeolites (as adsorbents) can absorb a range of heavy metals, including lead, copper, zinc, cadmium, nickel, and silver, from contaminated water, their ability to absorb organic contaminants is limited [18]. In this study, to highlight the role of zeolite in the adsorption of heavy metals, zeolite under 1500 sieve has been used. This zeolite sample, which contains particles with diameters of less than 7 micrometers, is one of the newest products of Negin Powder Company of Semnan. Due to its tiny particles, it has greater absorption capacity as well as plasticity than the company's other products. The characteristics and granulation curve of consumable zeolite are outlined in Table 3 and Figure 3, respectively.

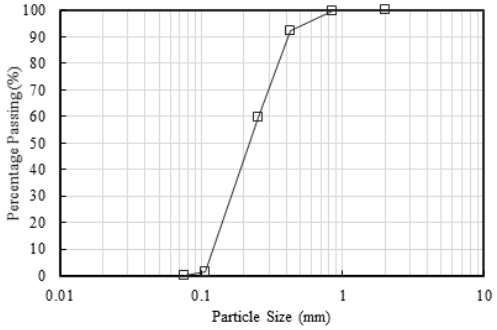


**Figure 1.** Grain size distribution curve for soil

**TABLE 1.** Physical and mechanical properties of sand

| Property | Value |
|---|---|
| $D_{50}$(mm) (ASTM D2487, 2017) ، Medium grain size | 0.23 |
| $C_u$ (ASTM D2487, 2017) ، Coefficient of uniformity | 1.9 |
| Cc (ASTM D2487, 2017) ، Coefficient of curvature | 0.89 |
| Gs (ASTM D854, 2014) ،Specific gravity | 2.65 |
| $e_{min}$ (ASTM D4253, 2016) ،Minimum void ratio | 0.59 |
| $e_{max}$ (ASTM D4254, 2016) ، Maximum void ratio | 0.91 |
| (ASTM D2487, 2017) USCS classification | SP |

**TABLE 2.** Physical and mechanical compositions of the clay sample (kaolinite, montmorillonite)

| Properties | Value (%) | |
|---|---|---|
| | Kaolinite | Montmorillonite |
| USCS | CL | CH |
| Plasticity index PI (%) | 18.8 | 86.1 |
| Plastic Limit PL (%) | 31 | 53.9 |
| Liquid Limit LL (%) | 49.8 | 140 |
| Specific Gravity | 2.58 | 2.62 |

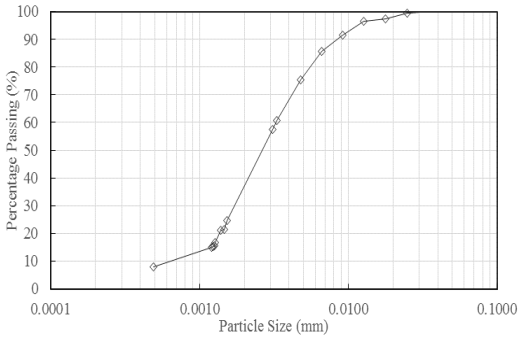


**Figure 2.** Particle size distribution curves for Kaolinite

**TABLE 3.** Chemical and mechanical composition of Zeolite

| Property | Value |
|---|---|
| Component | Zeolite |
| USCS classification | CL |
| Plasticity index-PI(%) | 15.1 |
| Plastic limit-PL(%) | 25 |
| Liquid limit-LL(%) | 40.1 |
| Specific gravity-Gs | 2.58 |

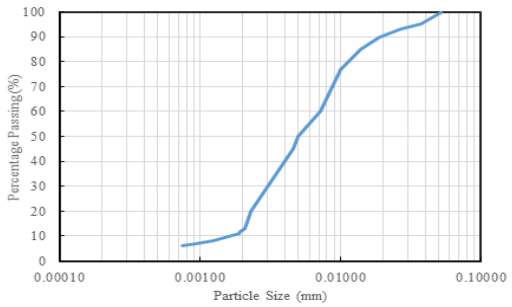


**Figure 3.** Particle size distribution curves for zeolite

The lattice structure in zeolite allows heavy metals in the solution to pass through infra-structural channels and adsorb reactive surfaces [11]. Figure 4 depicts an overview of the three dimensional structure of the natural zeolite [8].

**2. 4. Rice Husk Ash** Iran has vast resources of rice husks, with extensive lands, for instance, in Guilan, which are dedicated to cultivating this product. Thus, this resource can be widely used to remove environmental pollutants, including heavy metals and organic pollutants. The rice husk ash (RHA) utilized in this study is a Gilan Kesht product with more capabilities than the company's other products due to its fine particles. The chemical composition of RHA is shown in Table 4. For RHA to burn well and generate good results, the appropriate burning temperature is determined by X-ray diffraction and lime activity measurement tests, whose results are either crystalline or non-crystalline. It is also possible to identify the produced ash.

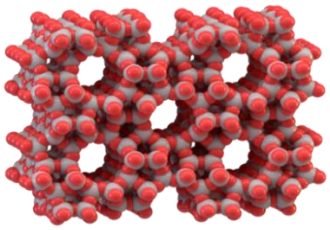

**Figure 4.** Three-dimensional view of zeolite particles

**TABLE 4.** Chemical characteristic of rice husk ash.

| Component | Value (%) |
|---|---|
| Calcium oxide (CaO) | 0.67 |
| Silicon dioxide ($SiO_2$) | 88.32 |
| Magnesium oxide (MgO) | 0.44 |
| Aluminium oxide ($Al_2O_3$) | 0.46 |
| Iron oxide ($Fe_2O_3$) | 0.67 |
| Sulfate ($SO_4$) | - |
| Potassium/Sodium oxide | 3.13 |

**2. 5. Heavy Metals Lead and Zinc** The chemical compounds of lead nitrate ($Pb(No_3)_2$) and zinc nitrate ($Zn(No_3)_2$) were used in this study to induce lead and zinc contamination. These chemical substances were imported from the German company Merck, with their specifications presented in Table 5. Lead nitrate and zinc nitrate both have purity levels exceeding 99.99%.

**2. 5. Specimen Preparation and Experiments** In this paper, sampling involved sand combined with different clay minerals. Some compounds also contained RHA and zeolite. The names of the required compounds are given below, and the reasons for choosing these compounds and the percentages of clay minerals are discussed in the subsequent sections.

- Sand with 20% kaolinite (K20)
- Sand with 10% kaolinite and 10% zeolite (K10-Z10)
- Sand with 10% kaolinite and 10% RHA (K10-R10)
- Sand with 20% montmorillonite (M20)
- Sand with 10% montmorillonite and 10% zeolite (M10-Z10)
- Sand with 10% montmorillonite and 10% RHA (M10-R10)

A standard projector test as per ASTM D-698 was used to obtain the maximum specific gravity. Further, soil ether boundaries were calculated according to the ASTM D4318 standard. The values obtained from this test for soil have been expressed in both contaminated and non-contaminated conditions. Also, a static triangle device was installed to evaluate the impact of clay particles with low and high plastic properties, as well as the effect of zeolite and RHA adsorbents, on the static behavior of soils polluted with heavy metals under saturated conditions. Microstructural experiments determined the structure of the micro-results. Atomic absorption spectroscopy is an analytical technique for measuring the concentration of elements. It is so precise and sensitive that it can measure even minute quantities of contaminants per gram of the sample. In order to determine the concentration of lead and zinc adsorbed in

**TABLE 5.** Chemical characteristic of Lead (II) and Zinc nitrate

| Properties | Value (%) | |
|---|---|---|
| | Lead (II) nitrate | Zinc nitrate |
| Assay (complexometric) | 99.5> | 99.3> |
| Insoluble matter | 0.005< | 0.03< |
| Cl (Chloride) | 0.0005< | 0.005< |
| Ca (Calcium) | 0.005< | 0.005< |
| Fe (Iron) | 0.0003< | 0.0002< |
| K (Potassium) | 0.005< | 0.0005< |
| Na (Sodium) | 0.02< | 0.001< |
| Pb (Lead) | - | 0.006< |

each of the desired compounds, the equilibrium test of soil saturation suspension was performed.

Since a material's microstructure is linked with its physical and mechanical properties, the study of structural changes is as important as resistance changes as it can reveal the origin of behavioral changes. The photography was done at Razi Metallurgical Research Center. In this research, the concentration of all elements in zeolite, montmorillonite, and kaolinite fine particles from sodium to uranium was determined using X-ray fluorescence (XRF) analysis based on the predominant cations used in cation exchange capacity specification. Further, the CEC of fine particles would serve as the basis of the overall technique in the study. Note that the concentration of various elements in the particulate matter was determined by Spectro XRF at Sharif University of Technology. A consolidation test was used to determine the speed and extent of soil compaction. Laboratory studies are often performed using reconstructed samples.

This research used wet compaction—one of the proposed methods in ASTM-D5311 standard—to make laboratory samples. This procedure is optimal for making compacted wet samples or soil samples in general. Because of the capillary effect and the formation of surface tension among soil grains, this sampling method is deemed beneficial for producing semi-dense and dense samples.

This study analyzed the behavior of two sets of samples: those contaminated with heavy metals and uncontaminated ones. As for non-contaminated samples, the dry weight of each compound's components (namely, sand, kaolinite, montmorillonite, zeolite, and RHA), with their percentages indicated, was first computed based on the dimensions of the mold and 95% of the maximum density of each compound. Different lead and zinc nitrate concentrations were added to each compound to contaminate the samples with heavy metals. First, lead nitrate or zinc nitrate was dissolved appropriately into water to prepare 1000, 2000, and 5000 ppm solutions. The concentrations were selected based on relevant studies reviewed. For contaminated samples, the optimal humidity in each composition comprised varying lead and zinc nitrate concentrations. After fabrication, the samples were processed for seven days at room temperature and inside a zipper bag. They were subsequently placed inside the unconfined or three-axial apparatus for testing once they had been made and processed.

## 3. ANALYSIS OF RESULTS

### 3. 1. Changes in the Concentration of Heavy Metals

In this paper, adsorbents of RHA and zeolite were used in the studied soil compositions. A batch analysis was undertaken to determine the optimal quantity of adsorbents to be utilized with the soils examined in this study. The analysis was conducted by passing a solution containing 5,000 ppm of lead nitrate and zinc nitrate from primary soil samples through an atomic absorption apparatus and combining it with 2, 5, 7, 10, 12, and 15% of RHA and zeolite. In the original composition, a portion of the adsorbent was replaced with clay mineral, where the results were variations in the concentrations of lead nitrate and zinc nitrate in the soil effluent solution (Cf), as depicted in Figures 6-9. As shown, replacing RHA and zeolite adsorbents with kaolinite in the sand composition with 20% kaolinite clay significantly reduced lead and zinc nitrate concentrations in the output solution. In other words, this replacement significantly enhanced the absorption of contaminants by the soil composition. For example, according to Figure 6, replacing 15% of zeolite with kaolinite has boosted the adsorption of lead nitrate and zinc nitrate in kaolinite sand by 241.8 and 325.4%, respectively. The increased absorption rate of heavy metal pollutants by replacing zeolite with kaolinite can be attributed to the higher specific surface area of zeolite, and thus the ability to absorb more zeolite rather than kaolinite. Also, the reason for the higher adsorption of lead nitrate than zinc nitrate in the composition of primary kaolinite sand and all amounts of zeolite substitution is the greater tendency of divalent cations ($Pb^{+2}$) to exchange with monovalent cations ($H^{+}$) than cations ($Zn^{+2}$).

RHA has a significant porous surface. Thus, it has a considerable capacity to absorb and retain contaminants. When applied to the soil, it boosts the absorption of heavy metal pollutants. Thus, replacing 15% of RHA with kaolinite increased the absorption of lead nitrate and zinc nitrate in kaolinite sand by 228.8% and 291.6% (Figure 6). In addition, Figures 5 and 6 show that zeolite performed better in the adsorption of lead and zinc heavy metals in kaolinite-adsorbent clayey sand mixture than RHA. This better performance could be attributed to the specific surface area and the higher cation exchange capacity of zeolite than RHA. Figures 6 and 7 reveal that the composition of sand with 20% montmorillonite, due to its specific surface area and higher cation exchange capacity of montmorillonite than kaolinite, had a far higher capacity to adsorb heavy metals than the composition of sand with 20% kaolinite. For example, 4077 ppm lead nitrate was adsorbed by sand containing 20% montmorillonite. On the other hand, in the sand with 20% kaolinite, the adsorbed concentration was 850 ppm, representing 81.5% and 17% absorption of lead nitrate, respectively. Also, Figures 6 and 7 indicate that, unlike kaolinite sand, the replacement of RHA and zeolite adsorbents with montmorillonite in combination of sand with 20% montmorillonite reduced the absorption of lead and zinc nitrate by the soil composition. This indicated increased contamination in the output solution. For

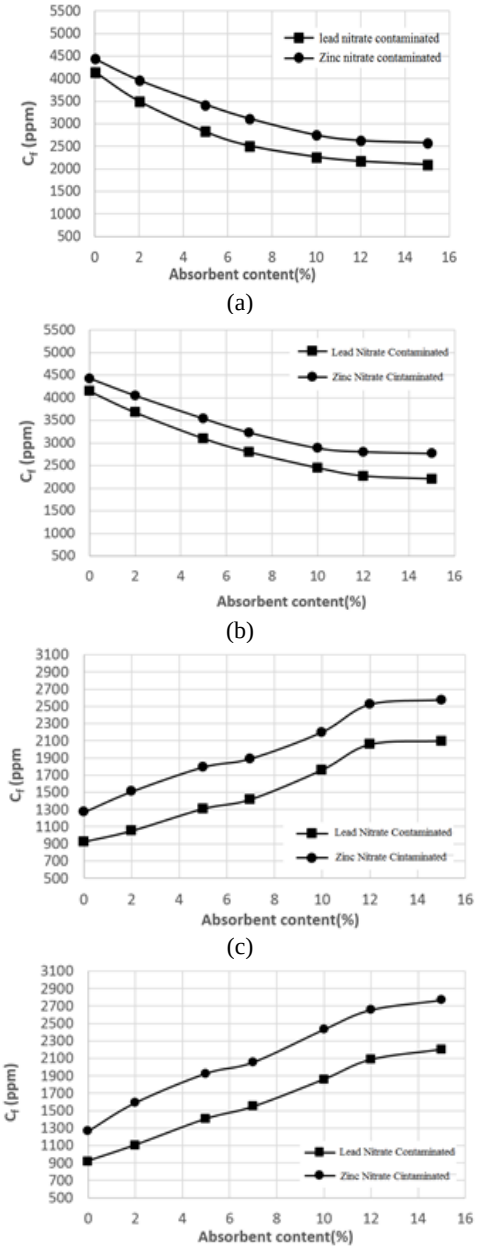


**Figure 5.** Heavy metal concentrations in extracted solution vs. absorbent content for: A) combination of kaolinite sand with different percentages of zeolite, B) combination of kaolinite sand with different percentages of rice bran ash, C) combination of montmorillonite sand with different percentages of zeolite, D) combination of montmorillonite sand with different percentages of rice bran ash

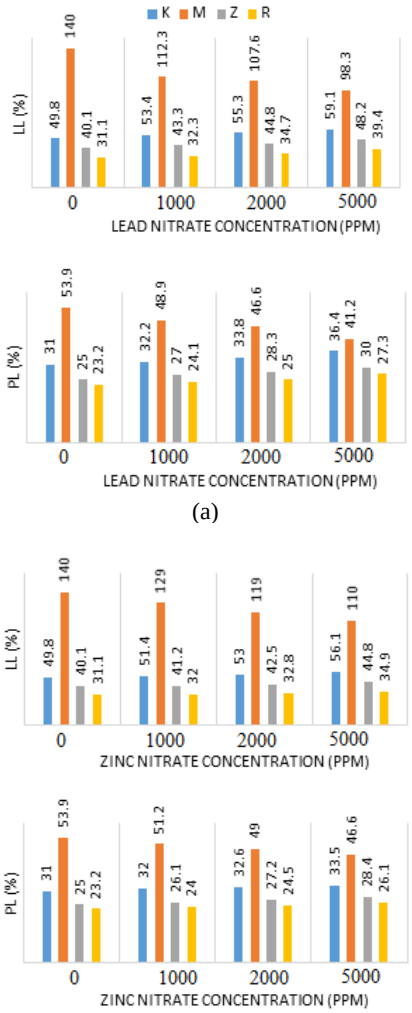


**Figure 6.** Liquid limit (LL) and plastic limit (PL), and plasticity index (PI) for a) contaminated by lead nitrate and b) contaminated by zinc-nitrate

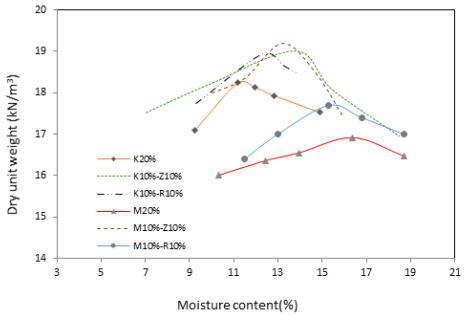


**Figure 7.** Dry density versus water content for various mixtures

example, replacing 15% of zeolite with montmorillonite reduced lead nitrate and zinc nitrate adsorption in montmorillonite sand by 29.7% and 35.1%, respectively (Figure 7). This diminished absorption could be related to the specific surface area and the lower cation exchange capacity of zeolite than montmorillonite. The replacement of 15% of RHA with montmorillonite lowered lead nitrate and zinc nitrate adsorption in montmorillonite sand by 31.4% and 40.2%, respectively

(Figure 8). Regarding RHA, it can be stated that despite its porous texture, which can absorb and retain contaminants, it reduces the absorption of heavy metal contaminants if replaced with montmorillonite due to its significantly lower cation exchange capacity than montmorillonite clay. Also, as with kaolinite sand, zeolite has a better performance in adsorption of lead and zinc in the sand-montmorillonite-adsorbent mixture than RHA due to its special surface area and higher cation exchange capacity.

**3. 2. Determining the Atterberg Limits for Contaminated with Lead and Zinc Nitrate** In this paper, fine grains of kaolinite, montmorillonite, zeolite, and RHA were used. Due to the different plasticity of clay minerals in the study compounds, Atterberg limits tests, including liquid limit (LL), plastic limit (PL), and plasticity index (PI), were performed on these fine particles (Figure 6). In the non-contaminated state, montmorillonite had the highest liquid and plastic contents due to its higher specific surface area; it thus displayed a higher water absorption capacity than kaolinite. The significant plasticity of montmorillonite could be attributed to the high thickness of the double water layer (DDL) among the minerals. Lead nitrate and zinc nitrate were used as contaminants at concentrations of 1000, 2000, and 5000 ppm and were added to the desired soil composition. In order to investigate the effect of these two contaminants on the plastic properties of different fine-grained ether sheets, tests were performed on soil contaminants contaminated with these heavy metals. Adding lead nitrate to kaolinite would enhance liquid and plastic limits. The results indicated that in kaolinite, upon raising the concentration of lead nitrate to 5000 ppm, the liquid limit value increased from 49.8 to 59.1. The plastic limit also rose from 31 in the non-contaminated state to 36.4 in the contaminated state (5000 ppm).

The increment in the plastic limit was less than the increase in the liquid limit in contaminated kaolinite. In kaolinite, elevation of the concentration of heavy metal pollutants weakened the hydrogen bond between kaolinite particles due to replacing divalent cations of lead and zinc metals with monovalent hydrogen, which causes a slight increase in soil fluidity. The results indicated that, similar to kaolinite, raising the concentration of lead nitrate increased the liquid limit of zeolite and RHA, which was attributed to their minerals' dissimilar behavior toward heavy metal contaminants. For instance, in zeolite, the yield point and the plastic limit in the non-contaminated state were 40 and 25, respectively, and with the entry of lead nitrate at a concentration of 5000 ppm, the liquid limit and the plastic limit increased to 48 and 30, respectively. Note that the changes of Atterberg limits in zeolite and RHA were far less than in kaolinites, to which the greater relative stability of these two fine grains than kaolinite could be attributed.

The paste properties of high plastic clay soils are primarily related to layer thickness (DDL). By increasing concentration of heavy metals and cation exchange would lower the soil pH, thus reducing the thickness of the double layer (DDL) in montmorillonite clay, as well as the liquid limit, plastic limit, and plasticity index of the montmorillonite. According to the results obtained in non-contaminated montmorillonite, the liquid limit and the plasticity limit were 140 and 53, respectively. Following the introduction of lead nitrate at its maximum concentration, the value of Atterberg limits decreased to 98 and 41, respectively. Also, lead nitrate was found to have a greater effect on increasing the liquid and plastic content of kaolinite, zeolite, and rice husk than zinc nitrate. This more significant effect could be attributed to the higher liquid limit of soils contaminated with lead nitrate than zinc nitrate contaminants can be considered stronger covalent bonds formed between lead cations ($Pb^{2+}$) than zinc cations ($Zn^{2+}$).

**3. 3. Soil Consolidation Behavior** The sand density curve and its parameters with different fine grains (different percentages of montmorillonite, kaolinite, RHA, and zeolite) are shown in Figure 7 and Table 6, respectively. In order to explore the effect of clay mineral types on settlement changes as well as $t_{50}$ and $c_v$ parameters at different solidification pressures, the values of these parameters for combining sand with 20% kaolinite and montmorillonite were obtained from logarithm-logarithm curves of time at each solidification pressure.

As can be seen in Figure 8, the sedimentation rate of clayey-coated sand samples has grown with increasing compaction pressure, but the rate of increment has been higher, especially at high compaction pressures for montmorillonite sand. As displayed in Figure 8, the settlement rate of kaolinite specimens has grown with increasing compression pressure. This rise is more prominent in the montmorillonite specimens, especially at high compression pressures.

**TABLE 6.** Parameters obtained from compaction tests for sand with fine grains

| Specimen | $\gamma_{d\ max}$ $(kN/m^3)$ | $\omega_{opt}$ (%) |
|---|---|---|
| K20 | 18.2 | 11.1 |
| K10-Z10 | 19.05 | 13.8 |
| K10-R10 | 17 | 16.5 |
| M20 | 18.5 | 11.7 |
| M10-Z10 | 18.88 | 12.6 |
| M10-R10 | 19.17 | 13.2 |

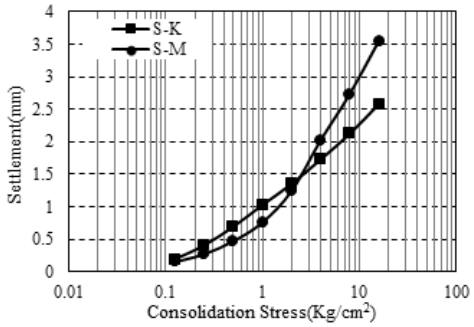


**Figure 8.** Sedimentation changes for different sand compositions with clay minerals at different stresses

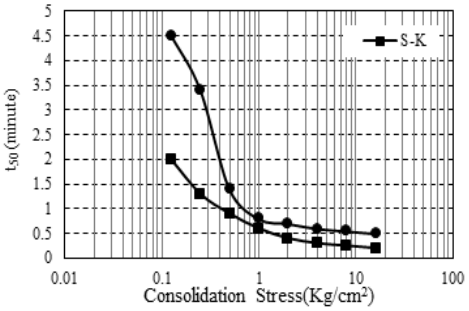


**Figure 9.** Changes of $t_{50}$ for Specimen of clayey sand minerals at different stresses

As presented in Figure 9, the changes of $t_{50}$ are different from the increment of stress for kaolinite and montmorillonite sands. In the combination of sand with 20% kaolinite, due to greater drainage and less water absorption as well as storage of kaolinite than montmorillonite, the time to reach 50% of the sample solidification is shorter at all solidification pressures and often within the first minutes of sample loading to reach 50%. In general, since 80% of the study compounds were sand, the values of $t_{50}$ for sand compounds with 20% kaolinite and montmorillonite were very low. The value of the consolidation coefficient depends on several parameters such as $t_{50}$ and the length of the drainage path, which is affected by the amount of sample subsidence at each consolidation stress. The values of the hardening exponent for kaolinite sand samples were higher than those of montmorillonite sand due to the lower settlement rate, which would increase the length of the drainage path and high drainage capacity, thus reducing the $t_{50}$ value of the sample. In addition, the results of these tests are presented in Figures 10 and 11. They display the changes in the porosity ratio of the sample during the loading and unloading stages for sand with 20% kaolinite and 20% montmorillonite. As shown, the decline in the porosity ratio of the sample with the increase of consolidation stress was greater in the montmorillonite sand than in the kaolinite sand due to the higher amount of consolidation settlements. The compaction coefficient ($C_c$) and the swelling coefficient ($C_s$) are the important parameters that can be extracted from the porosity-logarithm of the reinforcement stress diagram. These parameters are very useful in identifying the behavior of clay soils and are equal to the slope. The smooth part (fixed slope) of the porosity-logarithm curve is the reinforcement stress and the slope of the bearing part of the curve. According to Figure 10, the values of compaction coefficient and the swelling coefficient for kaolinite sand are 0.113 and 0.004, respectively. Also, these values are obtained have been 0.194 and 0.03 for montmorillonite sand respectively, according to Figure 12.

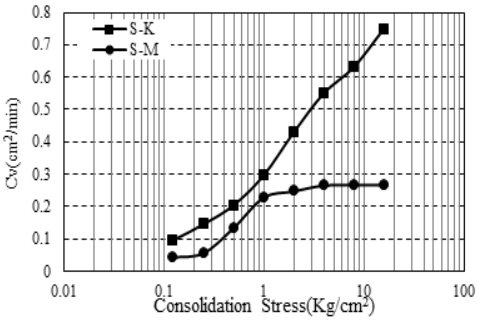


**Figure 10.** Variation coefficient for different combination of sand with clay mineraks in different stress

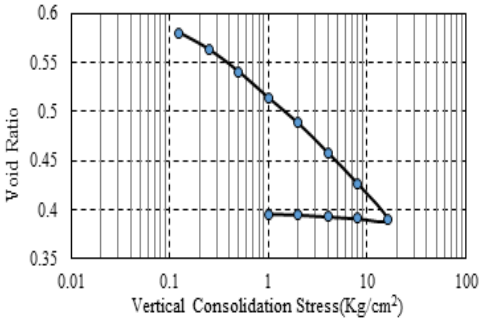


**Figure 11.** Changes in the porosity ratio of sand composition with 20% kaolinite in different stresses

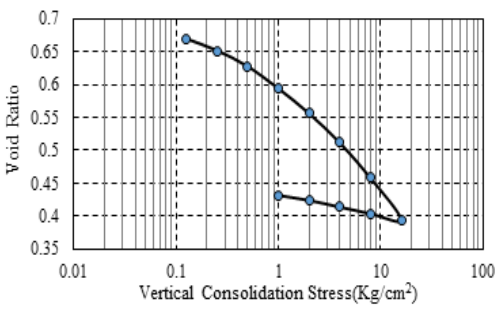


**Figure 12.** Changes in the porosity ratio of sand composition with 20% montmorillonite in different stresses

**3. 4. Sand-clay-adsorbent Composition in Non-contaminated State** In this section, in order to investigate the effect of the presence of zeolite adsorbents and RHA on changes in the consolidation parameters of sand composition with clay minerals, an odometer consolidation experiment was performed.

As revealed in Figure 13, replacing zeolite with kaolinite enhanced the settlement of the kaolinite sand sample, which could be attributed to the higher specific surface area of zeolite and more significant ability to absorb water than kaolinite and increased settlements due to drainage of excess water pressure. Unlike zeolite, the addition of RHA elevated the settlement rate of kaolinized sand at low setting pressures due to its high porosity and the lower specific gravity of RHA than kaolinite.

Regarding changes in the time to reach 50% of the setting ($t_{50}$) (Figure 14), replacing zeolite with kaolinite increased the $t_{50}$ of kaolinite sand. Also, replacing kaolinite with RHA reduced the $t_{50}$ of the sample. Replacing the zeolite and rice husk adsorbents with montmorillonite in the montmorillonite sand composition reduced $t_{50}$.

The solidification coefficient ($c_v$) by replacing RHA and zeolite with clay mineralization in samples is indicated in Figure 15.

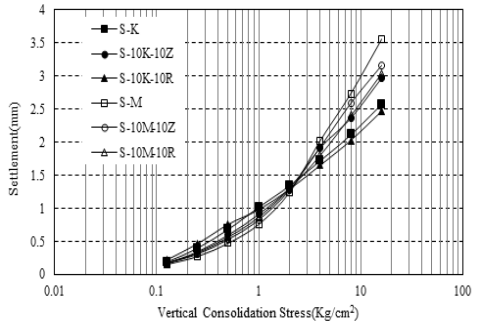


**Figure 13.** Sedimentation changes of different sand-clay-adsorbent specimens in non-contaminated state at different stresses

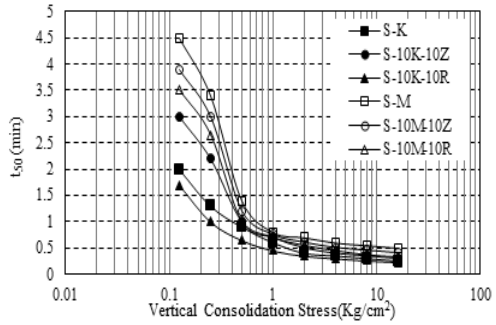


**Figure 14.** Changes of $t_{50}$ for different sand-clay-adsorbent specimens in uncontaminated state at different stresses

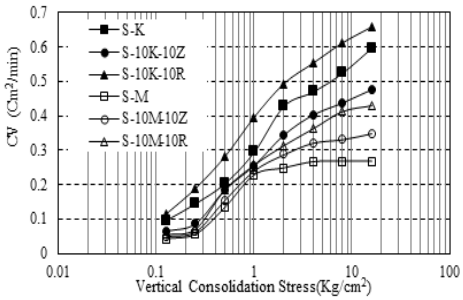


**Figure 15.** Consolidation coefficient ($c_v$) of different sand-clay-adsorbent specimens in non-contaminated state at different consolidation stresses

According to Figure 16, the replacement of RHA and zeolite lowered the swelling of the soil during the loading stage due to lower swelling properties of the adsorbents used than montmorillonite clay. It is believed that in the case of kaolinized sand, the use of adsorbents instead of kaolinite generally would have little effect on the swelling behavior of kaolinite sand.

**3. 5. Sand-clay-adsorbent Composition in Contaminated State** This section investigates the audiometric solidification test results for different sand-clay-adsorbent compounds in both clean and contaminated states with different concentrations of lead nitrate and zinc nitrate in terms of variations in leakage parameters, solidification coefficient (cv), compaction coefficient (Cc), and swelling coefficient (Cs).

As reported in Table 7, the contamination of all sand-kaolinite-adsorbent compounds with lead nitrate and zinc nitrate increased settlement and reduced the coefficient of consolidation at different reinforcement stresses, augmenting the compression coefficient and lowering the swelling coefficient. It was observed that the contamination of kaolinite sand with 5000 ppm zinc nitrate elevated the compaction coefficient by 13.5% and reduced the swelling coefficient by 15.9%. Elevation of the nitrate concentration of lead and zinc from 1000 to 5000 ppm increased the settlement increment rate at different reinforcement stresses and compaction

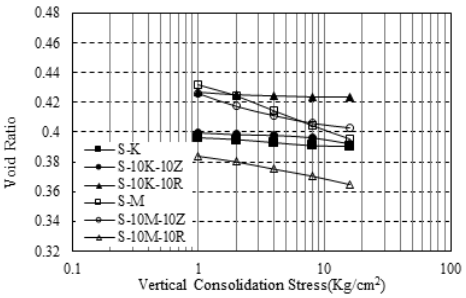


**Figure 16.** Changes in the porosity ratio of different sand-clay-adsorbent specimens in non-contaminated state

coefficients and accelerated the descending rate of swelling coefficient of sand-kaolinite-adsorbent compounds. The increased settlement in kaolinized sand with raising the concentration of heavy metals could be attributed to the breakdown of strong hydrogen bonds between kaolinite particles and creating a more porous and more structure settlement in the combination of sand and kaolinite. Despite increasing the time to 50% solidification ($t_{50}$) by replacing the divalent cations of $Pb^{2+}$ and $Zn^{2+}$ with monovalent cation $H^{+}$, increased settlement in kaolinite sand due to elevated nitrate concentration of lead and zinc contents augmented the consolidation coefficient at different consolidation stresses.

**TABLE 7.** Consolidation parameters of K20 Specimen in both clean and lead and zinc nitrate contaminated mixtures

| Contaminant concentratuion (ppm) | Consolidation stress (kg/cm$^2$) | Lead II Nitrate | | | | Zinc Nitrate | | | |
|---|---|---|---|---|---|---|---|---|---|
| | | Settlement (mm) | $C_v$ (cm$^2$/min) | $C_c \times 10^{-2}$ | $C_s \times 10^{-2}$ | Settlement (mm) | $C_v$ (cm$^2$/min) | $C_c \times 10^{-2}$ | $C_s \times 10^{-2}$ |
| 0 | 0.125 | 0.189 | 0.096 | 11.25 | 0.44 | 0.189 | 0.096 | 11.25 | 0.44 |
| | 0.25 | 0.401 | 0.146 | | | 0.401 | 0.146 | | |
| | 0.5 | 0.686 | 0.204 | | | 0.686 | 0.204 | | |
| | 1 | 1.022 | 0.296 | | | 1.022 | 0.296 | | |
| | 2 | 1.346 | 0.428 | | | 1.346 | 0.428 | | |
| | 4 | 1.725 | 0.470 | | | 1.725 | 0.470 | | |
| | 8 | 2.119 | 0.525 | | | 2.119 | 0.525 | | |
| | 16 | 2.578 | 0.598 | | | 2.578 | 0.598 | | |
| 1000 | 0.125 | 0.193 | 0.092 | 11.46 | 0.44 | 0.199 | 0.095 | 11.63 | 0.43 |
| | 0.25 | 0.410 | 0.145 | | | 0.418 | 0.150 | | |
| | 0.5 | 0.702 | 0.204 | | | 0.723 | 0.209 | | |
| | 1 | 0.046 | 0.285 | | | 1.088 | 0.293 | | |
| | 2 | 1.396 | 0.426 | | | 1.438 | 0.437 | | |
| | 4 | 1.801 | 0.466 | | | 1.855 | 0.477 | | |
| | 8 | 2.221 | 0.502 | | | 2.265 | 0.515 | | |
| | 16 | 2.659 | 0.570 | | | 2.739 | 0.581 | | |
| 2000 | 0.125 | 0.200 | 0.097 | 12.12 | 0.42 | 0.216 | 0.099 | 12.47 | 0.42 |
| | 0.25 | 0.425 | 0.135 | | | 0.423 | 0.139 | | |
| | 0.5 | 0.727 | 0.193 | | | 0.759 | 0.198 | | |
| | 1 | 1.083 | 0.271 | | | 1.116 | 0.278 | | |
| | 2 | 1.427 | 0.378 | | | 1.460 | 0.387 | | |
| | 4 | 1.869 | 0.405 | | | 1.925 | 0.414 | | |
| | 8 | 2.316 | 0.481 | | | 2.372 | 0.493 | | |
| | 16 | 2.793 | 0.540 | | | 2.857 | 0.552 | | |
| 5000 | 0.125 | 0.217 | 0.084 | 12.58 | 0.39 | 0.224 | 0.086 | 12.77 | 0.37 |
| | 0.25 | 0.461 | 0.125 | | | 0.470 | 0.129 | | |
| | 0.5 | 0.789 | 0.182 | | | 0.813 | 0.187 | | |
| | 1 | 1.175 | 0.249 | | | 1.222 | 0.256 | | |
| | 2 | 1.568 | 0.372 | | | 1.615 | 0.381 | | |
| | 4 | 2.024 | 0.398 | | | 2.085 | 0.407 | | |
| | 8 | 2.477 | 0.432 | | | 2.526 | 0.433 | | |
| | 16 | 2.967 | 0.476 | | | 3.033 | 0.487 | | |

The effect of zinc nitrate on the changes in the consolidation parameters of various sand-kaolinite-adsorbent compounds was found to be greater than that of lead nitrate: The contamination of sand composition with 10% kaolinite and 10% zeolite with 5000 ppm lead nitrate and nitrate on the compaction coefficient increased the sample by 7.3% and 10.6%, respectively.

**3. 6. Shear Strength Parameters of Contaminated Soil** According to the previous sections, about heavy metal absorption and also according to reported data in literature [1-12], it can be concluded that the effect of lead nitrate on shear strength parameters is much higher than that of zinc nitrate. Accordingly, shear strength parameters in lead nitrate contaminated soil were investigated. In order to determine the shear strength parameters, series of consolidated undrained (CU) triaxial test was used. The triaxial device is shown in Figure 17.

In Figure 18, the ultimate shear strength changes for sand with 20% kaolinite in two contaminated and uncontaminated states are shown. Generally, the results show that in the different confining stresses at 1000 ppm concentration of lead nitrate in clayey sand, the amount of the ultimate shear strength compared to the uncontaminated state decreased approximately about 13%. Higher concentration of lead nitrate to 2000 ppm and 5000 ppm caused the ultimate shear strength in the contaminated samples to decrease about 23% and 30% respectively. Changes in shear strength parameters (cohesion and effective internal friction angle) for uncontaminated and contaminated samples are shown in Figure 19. In uncontaminated soil, the internal friction angle and cohesion are 37 degrees and 17 kPa, respectively. Changing the behavior of kaolinite in heavy metal contaminated soil, caused the cohesion to increase and the internal friction angle decrease.

Similar to the previous part, the ultimate strength at different concentrations of lead nitrate in the combination of sand with 20% bentonite is shown in Figure 20. The trend of ultimate shear strength of sand with 20% bentonite showed the ultimate shear strength increased by changing of lead nitrate concentration from 0 to 1000 ppm about 11%. The further increase in the concentration to 5000 ppm caused the ultimate shear strength increase to 45. The changes of internal friction angle and cohesion for sand-bentonite samples in two contaminated and uncontaminated states are shown in Figure 21. Increasing the cations of heavy metal into the sand-bentonite mixtures, the structure of the mineral changed and the

**Figure 17.** Used triaxial device

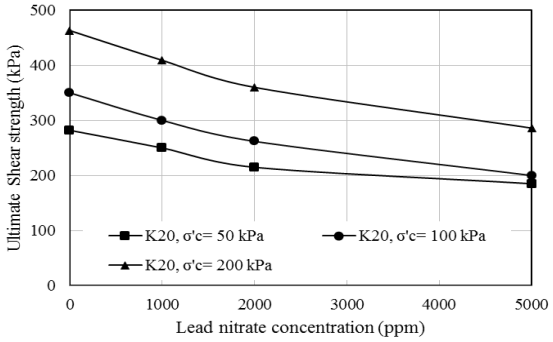


**Figure 18.** The changes of ultimate shear strength for composition of sand with 20% kaolinite

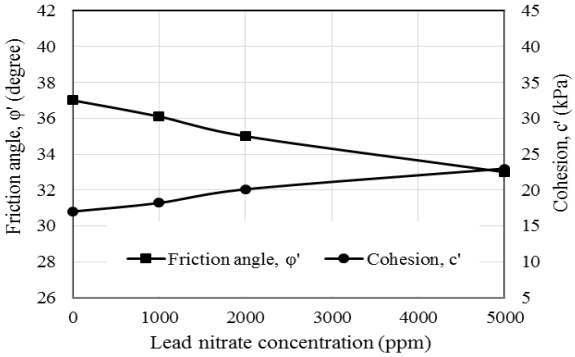


**Figure 19.** The changes in the internal friction angel and cohesion for composition of sand with 20% kaolinite

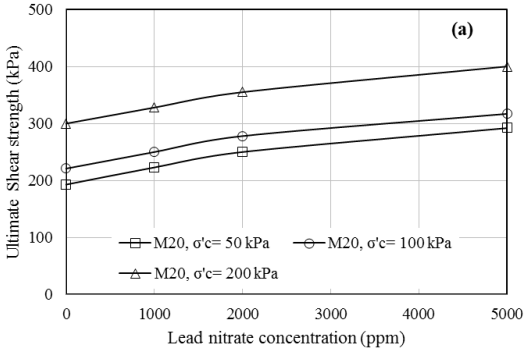


**Figure 20.** The changes of ultimate shear strength for composition of sand with 20% bentonite

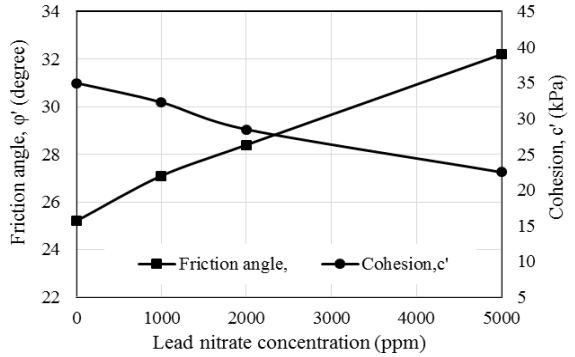


**Figure 21.** The changes in the internal friction angel and cohesion for composition of sand with 20% bentonite

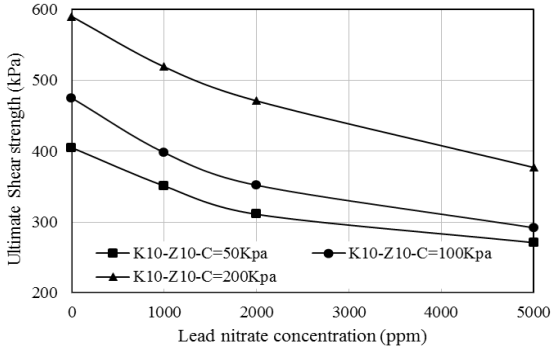


**Figure 22.** The changes of ultimate shear strength for composition of sand with 10% kaolinite and 10% zeolite

behavior of the soil changed to flocculated from. Increasing the concentration up to 5000 ppm caused decrease in cohesion to 22 kPa. Although increasing the concentration of heavy metals in sand-bentonite mixtures caused reduction of the cohesion, but it caused the internal friction angle increase. The angle of internal friction for the sample with 20% bentonite is about 25.2 degree, which by increasing in concentration to 5000 ppm, caused the friction angle to raise about 25% compared to the uncontaminated state. It should be noted that the shear strength parameters (in both contaminated and uncontaminated state) are obtained based on Mohr's criteria.

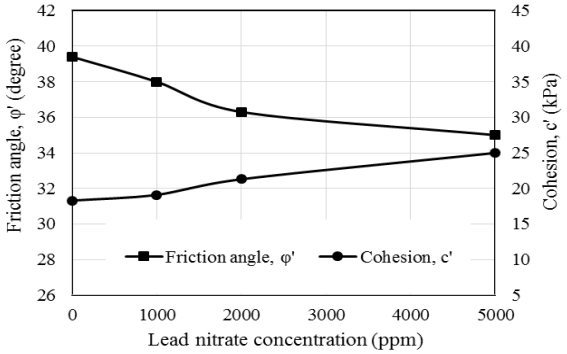


**Figure 23.** The changes in the internal friction angel and cohesion for composition of sand with 10% kaolinite and 10% zeolite

**3. 7. Shear Strength Parameters of Contaminated soil-adsorbent Mixture** According to the results provided in the field of absorption capacity of Zeolite is higher than rice husk ash, therefore, the shear strength parameters of the soil with zeolite in two contaminated and uncontaminated states are studied. It should be mentioned that the method in this research is replacing the absorbent to fine-grained part. Accordingly, the amount of kaolinite or bentonite in the mixtures is decreased as the adsorbent content increased. Figure 22 shows shear strength of the sand- kaolinite composition with 10% zeolite. Comparing the results of the mixtures including 10% kaolinite and 10% zeolite shows that the replacement of zeolite with kaolinite has increased the ultimate strength in both contaminated and uncontaminated soils compared to the soil without absorbent. Based on this, it can be concluded that the addition of zeolite, as well as increasing the absorption capacity in the soil, increase the ultimate shear strength. The strength value in the soils with kaolinite and zeolite has increased by about 50% compared to the soil without absorbent in both contaminated and uncontaminated states.

The cohesion changes are shown in Figure 23. According to the results, in the sand- kaolinite and adsorbent composition, internal friction angle decreased and cohesion increased, respectively. The amount of cohesion in the contaminated soil with concentrations of 1000, 2000, 5000 ppm, were 19.1, 22 and 25 kPa and the friction angles of soils were about 38, 36 and 34 degrees, respectively.

The ultimate shear strength ,which resulting from the triaxial test in different confining stresses, for the combination of bentonite sand with zeolite absorbent are shown in Figure 24. Similar to the previous part, the amount of bentonite decrease and zeolite is replaced. It can be seen that by reducing the amount of bentonite and adding zeolite, the trend of changes in the shear strength in contaminated soil is different from the trend that mentioned for the mixtures of sand with 20% bentonite. Accordingly to results , shear strength of samples with adsorbent increase about 50% to 60% in the uncontaminated state compared to sand-bentonite mixtures. Therefore, according to the appropriate absorption capacity of zeolite, the combination of zeolite and bentonite, in addition to provide a suitable environmental composition, is also an ideal mixture in terms of shear strength parameters. Thus this combination is suitable from both environmental and geotechnical aspects. In 1000 ppm concentration, the

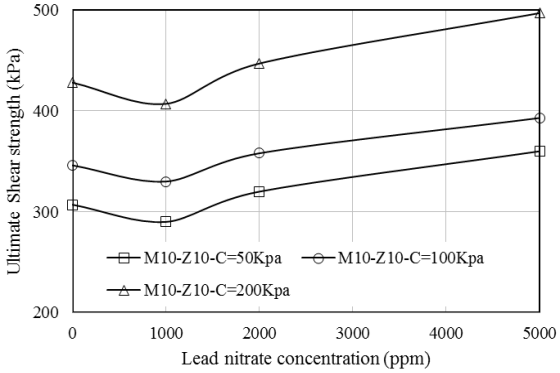


**Figure 24.** The changes of ultimate shear strength for composition of sand with 10% bentonite and 10% zeolite

ultimate shear strength in the sand-bentonite-absorbent mixtures decreases. One of the reasons is different reaction of two types of fine grains, bentonite and zeolite in contaminated case. Considering that the absorption capacity is high in both bentonite and zeolite minerals, therefore, at low concentrations, they almost neutralize each other, and it caused to shear strength decreas approximately 7 to 10%. By increasing the concentration of lead nitrate, the shear strength of sand-bentonite-zeolite composition increases. The results show that by increasing the concentration of lead nitrate to 5000 ppm, the ultimate shear strength has been increase by about 15-17% compared to the uncontaminated soil. The changes in cohesion and angle of friction are also shown in Figure 25. The cohesion has decreased and the internal friction angle has increased. With the increase of concentration from 1000 ppm to 2000 ppm, the amount of cohesion decreased by about 15%, while the internal friction angle also increased from 32 to 34.7 degree. By further increasing the concentration of lead nitrate to 5000 ppm in the sand with bentonite-zeolite, cohesion decreases to 17kPa, and internal friction angle increases to 19 degree.

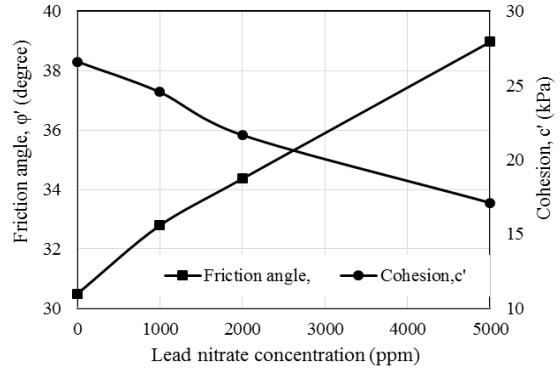


**Figure 25.** The changes in the internal friction angel and cohesion for composition of sand with 10% bentonite and 10% zeolite

**3. 8. Microstructure of Contaminated Soil** To examine the microscopic structure of contaminated and uncontaminated soil, photographic images by using scanning electron microscope (SEM) analyses was conducted. SEM test is a standard test to determine the dispersion and flocculation structure of soils. In flocculated structure, there is strong attractive force between the particles giving a stable structure. While in dispersed structure, the repulsive forces between the particles or between the fabrics units are more. Because of the attractive force at the particle contacts, soils with flocculated structure possess better resistance to external loads and thus have high shear strength. In dispersed structure, the repulsive forces are dominant over attractive forces, thus the shear strength of soils is low and the thickness of DDL around the particle is large [23]. The shear behavior of bentonite is controlled by the DDL, while for kaolinite and zeolite, as the DDL expansion is almost absent, the shearing is controlled by interparticle contacts [24]. The scanning electron microscope (SEM) results for uncontaminated and contaminated kaolin and bentonite are shown in Figure 26. The results show that kaolinite in the uncontaminated state have flocculated structure while the bentonite structure is dispersed in the uncontaminated state. The bond between the kaolinite minerals are hydrogen and ion binding, which led to the formation of flocculated structure in uncontaminated state, while the bond between the bentonite particles attributed to weak Van

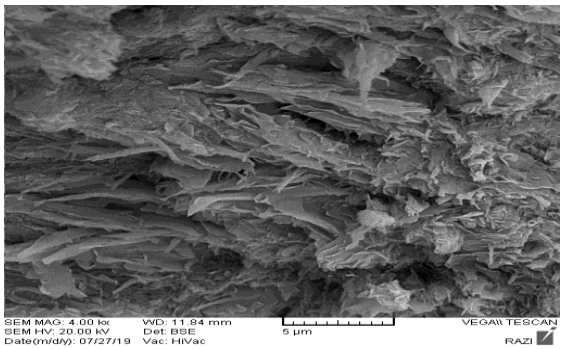


(a)

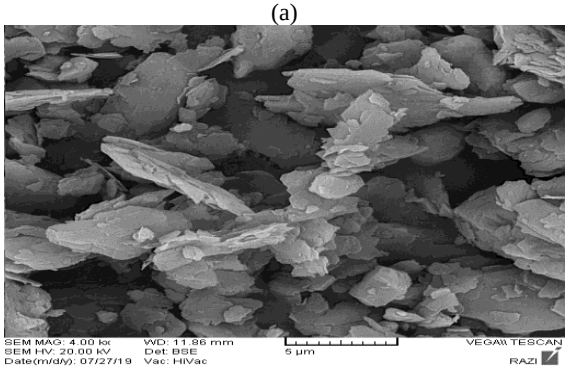


(b)

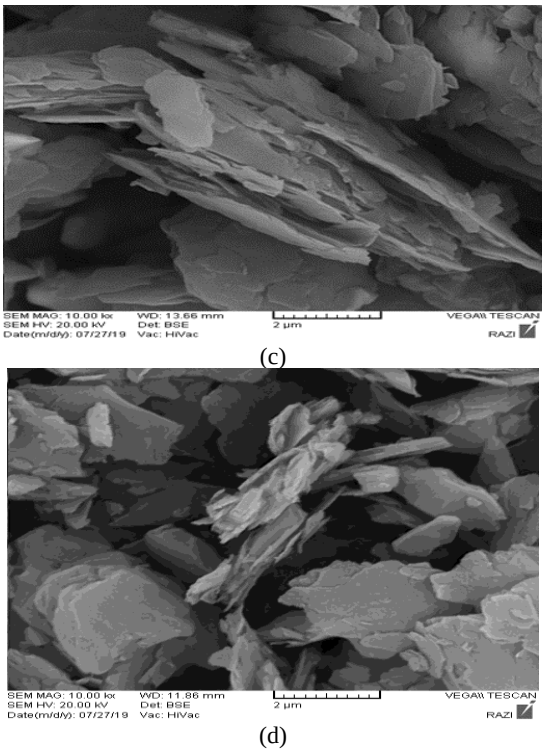


**Figure 26.** Structural changes for (a) uncontaminated and (b) contaminated bentonite, (c) uncontaminated and (d) contaminated kaolinite

Der Waals type and showed higher water absorption, which caused a dispersed structure in uncontaminated state. The results for kaolinite in the contaminated state show that an increase in the tendency of the soil to form a dispersed structure. The results for bentonite in both uncontaminated and contaminated states reveals that ,the flocculated structure is occurred in the case of contaminated state. In contaminated bentonite with lead or Zinc nitrate, cation exchange occurs between lead ($Zn^{+2}$ or $Pb^{+2}$) and sodium ($Na^{+}$) ions and leading to reduce the thickness of the DDL and flocculate the clay particles. Reducing the thickness of the water double-layer forms a flocculated structure in the bentonite, which increases the shear resistance of the soil.

## 4. CONCLUSION

By the expansion of the industrial zones, heavy metals entered the environment through industrial wastewater or leakage from storage tanks, which contaminated the soil and groundwater. Heavy metal contamination caused significant changes in shear strength and soil structure. This study aimed to achieve optimal amounts of zeolite adsorbents and RHA to replace clay in the initial composition of the study soil and continue the laboratory study process based on the determined percentages. The optimum amounts of zeolite and RHA to replace the kaolinite in combination with sand for lead nitrate contaminants were found to be 10%. With greater amounts, the process of reducing the concentration of contaminants in the output solution was almost constant. However, the amounts of zeolite and RHA for absorbing zinc nitrate contamination were 10%. Regarding montmorillonite sand, replacing the studied adsorbents with montmorillonite clay in all amounts lowered the adsorption of lead and zinc in the sand-clay montmorillonite-adsorbent composition. Identical optimal adsorbent amounts in the composition of kaolinite sand were used in the experiments on montmorillonite sand. The results also indicated that the rate of reduction of subsidence and the coefficient of consolidation in different consolidation stresses as well as the rate of reduction of the compression coefficient of the studied adsorbents were lower than those of montmorillonite sand. For instance, contamination of sand composition with 20% montmorillonite, sand composition with 10% montmorillonite and 10% zeolite, along with sand composition with 10% montmorillonite and 10% RHA with 5000 ppm zinc nitrate reduced the compression coefficient by 1.17, 0.16, and 2.15% respectively. This decline in the presence of adsorbents can be related to the lower cation exchange capacity and hence smaller double layer thickness (DDL) in the presence of adsorbents as well as lower sensitivity of RHA and zeolite to increasing cation concentrations.

Also, similar to kaolinite compounds, at all concentrations of lead and zinc heavy metals nitrate, the settlement values in reinforcement stresses were lower than 1 $kg/cm^2$ for montmorillonite-containing samples with RHA due to more porous and ductile ash texture. Also, the effect of zinc nitrate on reducing settlement, compaction coefficient, and swelling coefficient of different sand-montmorillonite-adsorbent compounds was more pronounced than lead nitrate. The contamination of the sand composition with 10% montmorillonite and 10% RHA with 5000 ppm lead nitrate and nitrate on the compaction coefficient reduced the sample by 13.1% and 15.2%, respectively. Due to the greater tendency of divalent cations ($Zn^{2+}$) to exchange with monovalent cations of montmorillonite than cations ($Pb^{2+}$) in soil structures, the adsorption of zinc nitrate was higher than that of lead nitrate in various montmorillonite-containing compounds.

In the composition of sand with 20% kaolinite, in the contaminated state with 1000 ppm and 2000 ppm of lead nitrate, the ultimate shear resistance value decreased on average by 13% and 23% compared to the uncontaminated state. Contrary to the behavior of sand with 20% kaolinite, in the composition of sand with 20% bentonite, the ultimate shear resistance increased by an average of 11% and 22% with the increasing of lead nitrate concentration from 0 to 1000 ppm and 2000 ppm. Also, the further increase of concentration to 5000 ppm

almost caused a 40-50% increase in the ultimate resistance. According to the results, replacing 10% of zeolite with kaolinite increasing the ultimate shear resistance in both contaminated and non-contaminated conditions up to 50% compared to the soil without absorbent. Thus, by adding zeolite, in addition to increasing the absorption capacity in the composition, shear resistance has increased. In uncontaminated state, by reducing the amount of bentonite and adding zeolite, the ultimate shear resistance increased about 50 to 60% compared to only bentonite composition. By considering the proper absorption capacity of zeolite, the combination of zeolite and bentonite, in addition to providing a combination with suitable environmental characteristics, is also an ideal combination in terms of resistance parameters, therefore, this combination is suitable from both environmental and geotechnical aspects.

## 5. REFERENCES


1. Arasan, S., "Effect of chemicals on geotechnical properties of clay liners: A review", ***Research Journal of Applied Sciences, Engineering and Technology***, Vol. 2, No. 8, (2010), 765-775. https://www.researchgate.net/publication/281080503_Effect_of_Chemicals_on_Geotechnical_Properties_of_Clay_Liners_A_Review
2. Arasan, S., "Effect of inorganic salt solutions on the consistency limits of two clays", ***Turkish Journal of Engineering and Environmental Sciences***, Vol. 32, No. 2, (2008), 107-115. https://www.researchgate.net/publication/285898519_Effect_of_inorganic_salt_solutions_on_the_consistency_limits_of_two_clays
3. Alpaslan, B. and Yukselen, M.A., "Remediation of lead contaminated soils by stabilization/solidification", ***Water, Air, and Soil Pollution***, Vol. 133, No. 1, (2002), 253-263. doi: 10.1023/A:1012977829536.
4. Kumar CL, M., KG, S., Sunagar, P. and Noroozinejad Farsangi, E., "Studies on contaminated mine soil and its remediation using soil washing technique-a case study on soil at kolar gold fields", ***International Journal of Engineering***, ***Transactions A: Basics***, Vol. 35, No. 1, (2022), 201-212. doi: 10.5829/IJE.2022.35.01A.19.
5. Chu, Y., Liu, S.-y., Cai, G.-j. and Bian, H.-l., "A study in the micro-characteristic and electricity properties of silt clay contaminated by heavy metal zinc", ***Japanese Geotechnical Society Special Publication***, Vol. 2, No. 14, (2016), 556-559. doi: 10.3208/jgssp.CHN-17.
6. Chu, Y., Liu, S., Wang, F., Cai, G. and Bian, H., "Estimation of heavy metal-contaminated soils' mechanical characteristics using electrical resistivity", ***Environmental Science and Pollution Research***, Vol. 24, No. 15, (2017), 13561-13575. doi: 10.1007/s11356-017-8718-x.
7. Hong, S.-S., Kim, Y.-S. and Lee, Y.-S., "Characteristics of waste lime and soil mixture for reusing of roadbed embanking material", ***Journal of the Korea Academia-Industrial Cooperation Society***, Vol. 11, No. 12, (2010), 5157-5164. doi: 10.5762/KAIS.2010.11.12.5157.
8. Karkush, M., Zaboon, A. and Hussien, H., "Studying the effects of contamination on the geotechnical properties of clayey soil", ***Coupled Phenomena in Environmental Geotechnics***, (2013), 599-607. doi: 10.1201/b15004.
9. Li, J.-s., Xue, Q., Wang, P. and Li, Z.-z., "Effect of lead (ii) on the mechanical behavior and microstructure development of a chinese clay", ***Applied Clay Science***, Vol. 105, (2015), 192-199. doi: 10.1016/j.clay.2014.12.030.
10. Joanna, F. and Kazimierz, G., "Evaluation of zeolite-sand mixtures as reactive materials protecting groundwater at waste disposal sites", ***Journal of Environmental Sciences***, Vol. 25, No. 9, (2013), 1764-1772. doi: 10.1016/S1001-0742(12)60270-8.
11. Mahabadi, A.A., Hajabbasi, M., Khademi, H. and Kazemian, H., "Soil cadmium stabilization using an iranian natural zeolite", ***Geoderma***, Vol. 137, No. 3-4, (2007), 388-393. doi: 10.1.1.715.775&rep=rep1&type=pdf.
12. Negahdar, A., Shabanian, M. and NikGhalbPour, M., "The effect of heavy metal contaminants on the strength parameters of sandy clay", ***Amirkabir Journal of Civil Engineering***, Vol. 50, No. 5, (2018), 835-844. doi: 10.22060/ceej.2017.12869.5287.
13. Ojuri, O.O. and Oluwatuyi, O.E., "Strength characteristics of lead and hydrocarbon contaminated lateritic soils stabilized with lime-rice husk ash", ***Electronic Journal of Geotechnical Engineering***, Vol. 19, (2014), 10027-10042. https://www.researchgate.net/publication/283288352
14. Ouhadi, V.R., Fakhimjoo, M.S. and Omid Naeini, S.T., "The comparison of plastic and permeability behavior of bentonite in the presence of organic and heavy metal contaminants", ***Journal of Civil and Environmental Engineering***, Vol. 46, No. 85, (2017), 25-36. https://ceej.tabrizu.ac.ir/article_5914.html?lang=en
15. Park, J., "Assessment of shear strength characteristics and zinc adsorption capacities of zeolite-amended soils for adsorptive fill materials", (2017),
16. Patel, A.V., "A study on geotechnical properties of heavy metal contaminated soil", ***Indian J Res***, Vol. 3, No. 6, (2014), 62-63. https://www.worldwidejournals.com/paripex/recent_issues_pdf/2014/June/June_2014_1403953078__20.pdf
17. Resmi, G., Thampi, S.G. and Chandrakaran, S., "Impact of lead contamination on the engineering properties of clayey soil", ***Journal of the Geological Society of India***, Vol. 77, No. 1, (2011), 42-46. doi: 10.1007/s12594-011-0007-6.
18. Schmitz, R.M., Schroeder, C. and Charlier, R., "Chemo–mechanical interactions in clay: A correlation between clay mineralogy and atterberg limits", ***Applied Clay Science***, Vol. 26, No. 1-4, (2004), 351-358. doi: 10.1016/j.clay.2003.12.015.
19. Sridharan, A. and Prakash, K., "Percussion and cone methods of determining the liquid limit of soils: Controlling mechanisms", ***Geotechnical Testing Journal***, Vol. 23, No. 2, (2000), 236-244. doi: 10.1520/GTJ11048J.
20. Oni, T.O., "Cfd study of behavior of transition flow in distinct tubes of miscellaneous tape insertions", ***HighTech and Innovation Journal***, Vol. 3, No. 2, (2022), 130-139. doi: 10.28991/HIJ-2022-03-02-02.
21. Nikkhah Nasab, S. and Abdeh Keykha, H., "Physicochemical changes of lead (ii) contaminated sand–clay mixture", ***SN Applied Sciences***, Vol. 2, No. 9, (2020), 1-15. doi: 10.1007/s42452-020-03299-5.
22. Shang, H., "Geotechnical laboratory characterization of sand-zeolite mixtures", (2015). doi: 10.18297/etd/2210.
23. Taheri, S., Ebadi, T., Maknoon, R. and Amiri, M., "Predicting variations in the permeability and strength parameters of a sand-bentonite mixture (sbm) contaminated simultaneously with lead (ii) and diesel", ***Applied Clay Science***, Vol. 157, (2018), 102-110. doi: 10.1016/j.clay.2018.01.007.
24. Zhang, Y., Zheng, Y., Han, S., Wan, D., Yang, H. and Duan, M., "Experimental study on deformation of heavy metal contaminated expansive soil under cyclic loading", in IOP Conference Series: Earth and Environmental Science, IOP Publishing. Vol. 237, (2019), 022026.

Persian Abstract

**چکیده**

ترکیب خاک با استفاده از جاذب‌ها باعث بهبود ساختار خاک شده و مقاومت برشی خاک را نیز تقویت می‌کند. از سویی دیگر می‌توان اینگونه تفسیر کرد که ترکیب خاک با جاذب، به شرط رعایت طرح اختلاط و نسبت بهینه، قدرت جذبِ آبِ خاک را افزایش داده و احتمال نفوذ و نشت آب‌های زیر زمینی حاوی مواد خطرساز را کاهش می‌دهد و از این طریق، مولفه‌های مقاومتی خاک را تقویت می‌کند. در این مقاله، تاثیر فلزات سنگین و جاذب‌ها بر روی رفتار ژئوتکنیکی خاک‌های ماسه–رسی حاوی نیترات سرب و روی به عنوان فلزات سنگین و زئولیت و خاکستر سبوس پوسته برنج (پسماند کشاورزی) به عنوان جاذب، مورد مطالعه قرار گرفته است. نتایج نشان می‌دهد که جایگزین کردن خاکستر پوسته برنج و زئولیت در ترکیب دانه‌بندی خاک با ۲۰ درصد رس کائولینیتی به شکل قابل توجهی منجر به کاهش نیترات روی و سرب می‌شود. همچنین، سطح متخلخل خاکستر پوسته برنج به عنوان یک مزیت تاثیرگذار در افزایش جذب و تعدیل نشت آلودگی، می‌تواند در صورت جایگزینی با کائولینیت، قدرت جذب خاک را ارتقا دهد. جایگزین کردن ۱۵ درصد خاکستر پوسته برنج با کائولینیت قدرت جذب نیترات‌های سرب و روی را به ترتیب ۲۲۸.۸ و ۲۹۱.٦ درصد افزایش می‌دهد. شایان ذکر است که افزودن فلزات سنگین نیتراتی به کائولینیت حدود روانی و پلاستیک خاک را افزایش می‌دهد همچنین باعث تغییر پارامترهای تحکیم خاک می‌گردد بر اساس نتایج به دست آمده، با افزاش حضور فلزات سنگنین به مقدار ۵۰۰۰ ppm مقدار حد روانی از ٤۹.۸ به ۵۹.۱ می‌رسد در حالی که، حد پلاستیک از ۳۱ (در حالت عدم حضور فلز سنگین) به ۳٦.٤ (در حضور ۵۰۰۰ ppm فلز سنگین) میل می‌کند.

International Journal of Engineering

Journal Homepage: www.ije.ir

# Evaluating and Ranking Digital Stores' Suppliers using TOPKOR Method

M. A. Beheshtinia*, P. Falsafi, A. Qorbani, H. Jalinouszade

*Industrial Engineering department, Semnan University, Semnan, Iran*

*PAPER INFO*

*Paper history:*
Received 10 March 2022
Received in revised form 14 May 2022
Accepted 25 July 2022

*Keywords*:
*Digital Supply Chain*
*Supplier Selection*
*Multiple-criteria Decision-making*
*Analysis Hierarchy Process*
*TOPKOR*

*ABSTRACT*

Due to the expansion of cyberspace in the context of internet use and public access to this platform, many stores try to use the online sales platform to eliminate geographical zones restrictions and the number of intermediaries. This approach has many other advantages such as reducing completed costs, lower shipping costs and faster speed of product delivery, etc. Proper evaluation and suppliers ranking plays an important role in increasing the productivity of these types of stores. This research provides an approach to evaluate and rank suppliers in digital stores using a combination of two multi-criteria decision-making (MCDM) techniques called Analysis Hierarchy Process (AHP) and TOPKOR. First, the effective criteria in evaluation and the ranking of suppliers in digital stores are identified and their weights are determined using AHP technique. Then, the score of each supplier in each criterion is determined. Finally, the suppliers are ranked based on TOPKOR technique. The results not only show the final rank of suppliers but also identified 8 criteria for evaluation and ranking the suppliers. Moreover, the results show the criteria of support, easy access and flexibility are the most important in evaluating and ranking digital stores' suppliers, respectively.

***doi***: *10.5829/ije.2022.35.11b.10*

**NOMENCLATURE**

| | | | |
|---|---|---|---|
| A | Pairwise comparison matrix (AHP) | $V_{ij}$ | Normalized weight matrix |
| $a_{ij}^{*}$ | Normalized in the verses of the matrix of pairwise comparisons | $PIS_j$ | The positive ideal solution in criterion j |
| $W_i$ | The final weight of each criterion | $NIS_j$ | The negative ideal solution in criterion j |
| X | Decision matrix | $Q_i$ | VIKOR index |
| $n_{ij}$ | Normalized in the verses of the decision matrix | $CC_i$ | Final proximity index |

## 1. INTRODUCTION

Online stores can be considered as one of the most important strategic points for business growth. There are several factors for the decision-maker to consider when evaluating and ranking online store suppliers. Nowadays, the need for online stores is increasing. Various factors in the evaluation and ranking of online store suppliers are effective and it can be considered as a multi-criteria decision problem. Multi-criteria decision making is considered as the most important branch of operational research; because, it involves complex decisions of people's lives. There are several multi-criteria decision models. Researchers by considering current problems and criteria, use decision-making techniques. Analytical Hierarchy Process with multi-criteria decision model which has been introduced by Saaty [1] is one of the most powerful methods for calculating the weight of criteria and sub-criteria. Weight criteria and sub-criteria are calculated by the pairwise comparison matrix. Uncertainty is not considered in the main model of the analytical hierarchy process, also several researchers have integrated the fuzzy model with an analytical hierarchy process to reduce inaccuracies in decision making.

The model is also widely used in a variety of fields including engineering, economics and operations management. Factors such as environmental and social factors to choose the source of supply for online businesses and economics and building a long-term

Corresponding Author Institutional Email: beheshtinia@semnan.ac.ir
(M. A. Beheshtinia)

Please cite this article as: M. A. Beheshtinia, P. Falsafi, A. Qorbani, H. Jalinouszade, Evaluating and Ranking Digital Stores' Suppliers using TOPKOR Method, ***International Journal of Engineering, Transactions B: Applications***, Vol. 35, No. 11, (2022) 2155-2163

relationship with it is crucial to maintain a competitive advantage. For example, the environmental criterion is one of the considered factors by societies and governments that has been highly emphasized and for this criterion, there are many programs for companies, such as the use of environmentally-friendly and degradable materials, the design of environmental products and pollution monitoring in production processes [2, 3].

However, an organization's environmental performance depends not only on its sustainable behaviors but also on its suppliers and how they work. Consequently, choosing a good supplier that meets these criteria in the supply chain is a top priority for companies. In the current study, this research provides a method for evaluating and ranking suppliers in digital stores. First, effective criteria in evaluating and ranking suppliers in digital stores are identified and the score of each supplier is determined in each criterion. Then a hybrid approach by combining of two multi-criteria decision-making (MCDM) techniques called Analysis Hierarchy Process (AHP) and TOPKOR are provided for ranking suppliers.

The main research question of this research is as follow:

How the digital stores' suppliers are ranked using a combination of AHP and TOPKOR techniques?

The research sub questions are as follows:

What criteria should be used to rank digital stores' suppliers?

What is the weight of each used criterion?

What is the score of each alternative in each criterion?

## 2. LITERATURE REVIEW

These days in digital age, the way we choose and understand the structures of online businesses has changed. Retail section in recent years has seen significant changes and continues to grow at an unprecedented rate [4]. Therefore, the nature of retail the tradition has shifted to online retail. As a result of the emergence of online retail from the early twentieth century by the emergence of international big brands such as, M&H, Mango and ZARA, which have started online retail, has become popular. More of the growth of this industry is in developed countries, but developing countries are also accepting this with respect to time. About two-thirds of EU countries buy their clothes online and the amount of revenue generated by this industry to is worth $17 billion [5]. Total sales related to the global garment industry are estimated to be approximately $680 billion. As a result, one can see how important the online retail industry can be. On the other hand, with the development of the internet in most countries of the world, the platform for using this industry is provided. For example, e-commerce in India has been known as the fastest and the most attractive method for trading in recent years, India's e-commerce market has increased to 60 billion US dollars by 2019 and by 2026, it will increase to 200 billion US dollars [6]. However, if the right suppliers are not selected in this industry, it will have a very negative impact on the amount of income. Therefore, choosing the right supplier in e-commerce and online retail is very important [7].

On the other hand, the safer and the more attractive the structure is, the more popular the online store becomes. Shopping in an online store makes the experience special because there are many choices without having to enter a physical space and go from place to place, there will be something for you that adds to the appeal of the purchase.

Because online stores function in choosing locations similar to chain stores and here are the famous stores compared to other malls because of the less tax and no other additional costs to pay, the more possibility of being able to offer more discounts and convenient packages to the customer. Also, most people associate the price of a product with its quality, and that makes them have negative comments about products in online stores. Because there are many shopping malls with similar products, choosing to buy one has become a new challenge [8]. Universal design for these cases is designed in a way which is available to all people [9]. Research is limited in this area because studies on these specific sections of the community have not been done [10, 11]. Previous important features such as parking capacity and area size are now under the influence of the environmental criteria, design aesthetics and ergonomics, with studies proving recent impact criteria have a stronger effect on customer satisfaction [12]. Ergonomic and aesthetic factors such as interior design provide more entertainment and comfort to customers [13]. Environmental criteria such as access to facilities, noise pollution, air pollution and traffic jams also plays a key role in the attractiveness of buying a market for its potential customers [14]. Of course, the choice of location is an important factor. It is necessary to identify, evaluate and select from the available options. This process is influenced by qualitative criteria, such as quantitative related and supporting industries, proximity to the raw material market, infrastructure conditions, market size and demand, capital costs, natural conditions and human resources [15, 16]. Hence, it seems that choosing a place for a mall is an important factor that determines the success of the business.

**2. 1. MCDM Technique** Liu, Quan, Li and Wang [17] also wrote a new decision model and alternative method of queuing 6 multi-criteria for selecting a sustainable supplier by combining the best and worst methods at a valuable time interval. Also, Kaushik, Khare, Boardman and Cano [18] examined the factors

that motivate consumers to buy online fashion retailers and these factors were evaluated using the analytical hierarchy process method. Sánchez-Lozano, Teruel-Solano, Soto-Elvira and García-Cascales [19] in their research which was based on a geographic information system (GIS) and they used multi-criteria decision-making methods the optimal choice of solar power plants. They calculate the weight of these criteria using the analysis process Hierarchical (AHP) and TOPSIS method to evaluate the criteria. Konstantinos, Georgios and Garyfalos [20] Used the combined AHP method and Geographic Information System (GIS) to determine the most appropriate sites used to install wind farms and then the TOPSIS method to rank the construction sites of wind farms. Sedady and Beheshtinia [21] described a new method for prioritizing the construction of renewable power plants which their evaluating factors are: technical factors, economic, social, political and environmental criteria, each of which includes five sub-criteria, and using Hierarchical analysis method and a new method called TOPKOR to prioritize places.

**2. 2. Sustainability Supply Chain** On the other hand, Liou, Chang, Lo and Hsu [22] In a study ranked and evaluated the criteria of green supply chain in the field of electronic services. They ranked and evaluated the criteria by combining the best and worst fuzzy methods with fuzzy TOPSIS. Hsu, Yu, Chang, Liu and Sun [23] in their study, they reduced the destructive effects on the sustainable supply chain in the electronics manufacturing industry. By evaluating the effective criteria using QFD and FMEA methods, they evaluated and ranked the criteria by combining AHP and DEMATEL methods with a gray approach. Zakeri, Yang and Konstantas [24] in their research, they evaluated and ranked suppliers in order to select them correctly in the sustainable supply chain. They used the ARPASS[2] method for ranking and final selection of suppliers.

Karami, Ghasemy Yaghin and Mousazadegan [25] enabled the logistics department to evaluate and systematically select suppliers using quantitative and qualitative decision criteria. They also built a three-step approach to tackle selection problem and evaluation in the industry. Abdel-Basset, Manogaran, Mohamed and Chilamkurti [26] presented a new evaluation function to calculate the weight of options for a better choice in his paper. As well as the selected criteria to increase the quality and service and reduce costs and control time to select the best suppliers. Fanita and Sinaga [27] in their paper provide a framework based on the integrated fuzzy-hierarchical analysis approach for selecting a global supplier that considers sustainability risks from sub-suppliers. Boran, Genç, Kurt and Akay [28] also presented an approach for the problem of selecting a model supplier based on fuzzy decision making with TOPSIS method. Mohammed, Yazdani, Oukil and Gonzalez [29] they examined the impact of environmental, social and economic disturbances on the selection of suppliers in the sustainable supply chain. Using the DEMATEL method, they measured the impact of these disorders on supplier selection and combined the MABAC-OCRA-TOPSIS-VIKOR (MOTV) methods to rank suppliers.

De Boer [30] has worked on procedural rationality issue in supplier selection, in which he provided three innovative methods for selecting supplier selection criteria. Laurentia and Septiani [31] have focused on choosing a place issue YPBM University of Tourism by combining the two methods of cutting point and hierarchical analytical process to investigate that their goal was analyzing the location for the construction of the new campus. Torkayesh, Iranizad, Torkayesh and Basit [32] also examined the methods of selecting suppliers in the online sustainable supply chain. They used a combination of BWM and WASPAS methods to rank suppliers by determining the criteria influencing supplier selection.

Ghorui, Ghosh, Algehyne, Mondal and Saha [33] have worked on hierarchical analysis issue and order prioritization analysis by similarity of the answer to the idea of TOPSIS to choose the place of purchase with fuzzy data. Accordingly, to select the place of purchase from the analysis process, Fuzzy hierarchy and fuzzy analysis were used to prioritize the order by similarity to the ideal answer. The dynasty hierarchy analysis was used to obtain the weight factors and also the fuzzy hierarchical analysis process were used to rank the criteria, and the sub-criteria were used to integrate fuzzy weights. Qu, Zhang, Qu and Xu [34] have worked on selecting a green supplier based on procedure issue with the help of TOPSIS fuzzy approaches. These researches were accompanied by a case study in a Chinese Internet company which was aimed to show the appropriate green chain suppliers based on a framework with the help of fuzzy TOPSIS and ELECTRE. This framework is presented based on green supply chain management. The TOPSIS and ELECTRE approaches were used to rank green chain suppliers and the results of the proposed framework with the obtained ratings, by higher grades and incompatibility was compared with the measurements of the fuzzy electro-method. Shaikh, Memon, Prokop and Kim [35] have worked on a hybrid approach issue based on the hierarchical analysis process and TOPSIS to select the optimal location using spatial data. Štirbanović, Stanujkić, Miljanović and Milanović [36] in their studies on multi-criteria decision-making methods, such as TOPSIS and VIKOR focused that they used these methods to select floating vehicles as a result,

[2] alternatives' stability scores multi-criteria

in this research The AHP and TOPKOR methods have been used to select the right supplier among the 11 available suppliers. Table 1 summarized the researches in the scope of sustainable supplier selection. The innovations of this research are as follows:

- Providing a comprehensive list of criteria in the scope of sustainable supplier selection.
- Employing these criteria to evaluate and rank the digital stores' suppliers
- Using a combination of AHP and TOPKOR methods in sustainable supplier selection scope

## 3. METHODOLOGY

**3. 1. Research Steps** To answer the research questions, the following steps are implemented:

Step 1: Determine the effective criteria in evaluating and ranking suppliers in digital stores.

Step 2: Determine the weight of the criteria using the AHP method. The steps of the AHP method are as follows:

Step 2.1: Form a matrix of pairwise comparisons: If $n$ criteria exist and the numerical equivalent of the two

**TABLE 1.** Summary of effective criteria in determining suppliers

| Criteria | Boran, Genç, Kurt and Akay [28] | De Boer [30] | Devi and Wardhana [37] | Abdel-Basset, Manogaran, Mohamed and Chilamkurti | Štirbanović, Stanujkić, Miljanović and Milanović | Qu, Zhang, Qu and Xu [34] | Shaikh, Memon, Prokop and Kim [35] | Ghorui, Ghosh, Algehyne, Mondal [33] | Torkayesh, Iranizad, Torkayesh and Basit [32] | Laurentia and Septiani [31] | Karami, Ghasemy Yaghin and Mousazadegan [25] | Liou, Chang, Lo and Hsu [22]. | Mohammed, Yazdani, Oukil and Gonzalez [29] | Hsu, Yu, Chang, Liu [23] | Zakeri, Yang and Konstantas [24] | The number of repetitions |
|---|---|---|---|---|---|---|---|---|---|---|---|---|---|---|---|---|
| Economical | ✓ | ✓ | ✓ | ✓ | | | | ✓ | ✓ | ✓ | ✓ | ✓ | ✓ | | ✓ | 11 |
| Environmental | | ✓ | ✓ | ✓ | | | ✓ | | ✓ | ✓ | ✓ | ✓ | ✓ | | | 9 |
| Social | | ✓ | ✓ | | | | | | ✓ | | ✓ | ✓ | ✓ | | ✓ | 7 |
| Quality | ✓ | | ✓ | ✓ | ✓ | | | | | | | ✓ | ✓ | | | 6 |
| Competitors | | | ✓ | | | ✓ | | | | | | | | ✓ | | 3 |
| Easy availability | | | | | ✓ | ✓ | | ✓ | ✓ | ✓ | | | ✓ | ✓ | ✓ | 8 |
| Supported | | ✓ | | ✓ | ✓ | ✓ | ✓ | | | | | | | | | 5 |
| Geographical location | ✓ | | | ✓ | | | | | ✓ | | | | | ✓ | ✓ | 5 |

| Criteria | Qu, Zhang, Qu and Xu [34] | Shaikh, Memon, Prokop and [illegible] | Ghorui, Ghosh, Algehyne, [illegible] | Laurentia and Septiani [31] | De Boer [30] | Boran, Genç, Kurt and Akay | Devi and Wardhana [37] | Abdel-Basset, Manogaran, Mohamed and Chilamkurti | Karami, Ghasemy Yaghin and Mousazadegan [25] | Štirbanović, Stanujkić, Miljanović and Milanović [36] | Liou, Chang, Lo and Hsu [22]. | Hsu, Yu, Chang, Liu [23] | Zakeri, Yang and Konstantas [24] | Mohammed, Yazdani, Oukil and Gonzalez [29] | Torkayesh, Iranizad, Torkayesh and Basit [32] | The number of repetitions |
|---|---|---|---|---|---|---|---|---|---|---|---|---|---|---|---|---|
| Economical | | | ✓ | ✓ | ✓ | ✓ | ✓ | ✓ | ✓ | | ✓ | | ✓ | ✓ | ✓ | 11 |
| Environmental | | ✓ | | ✓ | ✓ | | ✓ | ✓ | ✓ | | ✓ | | | ✓ | ✓ | 9 |
| Social | | | | | ✓ | | ✓ | | ✓ | | ✓ | | ✓ | ✓ | ✓ | 7 |
| Quality | | | | | | ✓ | ✓ | ✓ | | ✓ | ✓ | | | ✓ | | 6 |
| Competitors | ✓ | | | | | | ✓ | | | | | ✓ | | | | 3 |
| Easy availability | ✓ | | ✓ | ✓ | | | | | | ✓ | | ✓ | ✓ | ✓ | ✓ | 8 |
| Supported | ✓ | ✓ | | | ✓ | | | ✓ | | ✓ | | | | | | 5 |
| Geographical location | | | | | | ✓ | | ✓ | | | | ✓ | ✓ | | ✓ | 5 |

criteria comparison $i$ and $j$ are shown with $a_{ij}$, Then the pairwise comparison matrix of a matrix $\boldsymbol{n} \times \boldsymbol{n}$ in relation (1) is shown:

$$A = [a_{ij}] . a_{ij} = \frac{1}{a_{ij}} \quad . i.j = 1.2. \ldots . n \tag{1}$$

Step 2.2: Using Equation (2), the matrix comparison is normalized. $a_{ij}^{*}$ is the normalized value of the parameter $a_{ij}$.

$$a_{ij}^{*} = a_{ij} / \sum_{i=1}^{n} a_{ij} \tag{2}$$

Step 2.3: The final weight of each criterion is obtained from the following Equation (3). $W_i$ is the final weight of the criteria $i$.

$$W_i = \sum_{i=1}^{n} \frac{a_{ij}^{*}}{n} \qquad i.j = 1.2. \ldots . n \tag{3}$$

Step 3: Determine the candidate points (Alternatives).
Step 4: Determine the decision matrix
Step 5: Rank the alternatives using TOPKOR method

TOPKOR method is a combination of two different multi-criteria decision-making methods called TOPSIS and VIKOR. In TOPSIS method, a good alternative is one that its total distance from the positive ideal solution (PIS) is low and its total distance from the negative ideal solution (NIS) is high. But in VIKOR method, a good alternative is one that its total distance from PIS (utility index) and its maximum distance from PIS in each criterion (regret) are low. It means, TOPSIS neglects the distance of each alternative from PIS in each criterion while VIKOR neglects the total distance from NIS.

TOPKOR method tries to integrate both mentioned methods. In TOPKOR, a good alternative is one that its total distance from PIS and its maximum distance from PIS in each criterion are low and simultaneously its total distance from NIS is high.

The steps of this method are as follows:

Step 1: Consider the X as decision matrix in which $x_{ij}$ is the score of alternative $i$ in criterion $j$. Additionally, consider $W_i$ is the weight of criterion j. Also, $n$ is the number of criteria and $m$ is the number of alternatives.

$$X = [x_{ij}]_{m \times n} = \begin{matrix} \\ A_1 \\ \vdots \\ A_m \end{matrix} \begin{matrix} \begin{matrix} C_1 & \cdots & C_n \end{matrix} \\ \begin{bmatrix} x_{11} & \cdots & x_{1n} \\ \vdots & \ddots & \vdots \\ x_{n1} & \cdots & x_{mn} \end{bmatrix} \end{matrix} \tag{4}$$

Step 2: Obtain the normalized decision matrix using Equation (5), where $n_{ij}$ is the normalized value of $x_{ij}$ .

$$n_{ij} = x_{ij} / \sum_{i=1}^{m} x_{ij}^{2} \qquad \forall\, i.j \tag{5}$$

Step 3: Form the normalized weighted decision matrix using Equation (6).

$$V_{ij} = x_{ij} \times w_{ij} \qquad \forall\, i.j \tag{6}$$

Step 4: Using Equations (7) and (8), obtain PIS and NIS.

$$PIS_j = \underset{i}{\mathrm{Max}}\, v_{ij} \quad and \quad NIS_j = \underset{i}{\mathrm{Min}}\, v_{ij} \quad if\ j \in B \tag{7}$$

$$PIS_j = \underset{i}{Min}\, v_{ij} \ and \ NIS_j = \underset{i}{Max}\, v_{ij} \ if\ j \in C \tag{8}$$

B is the type of profit and C is the type of cost.

Step 5: Calculate the distance of each alternative from PIS and NIS.

$$d_i^{-} = \sqrt{\sum_{j=1}^{n} \left(v_{ij} - NIS_j\right)^2} \quad i = 1. \ldots . m \tag{9}$$

$$d_i^{+} = \sqrt{\sum_{j=1}^{n} \left(v_{ij} - PIS_j\right)^2} \quad i = 1. \ldots . m \tag{10}$$

$d_i^{+}$ and $d_i^{-}$ the sum of the distance from PIS and NIS, respectively.

Step 6: Find the maximum distance between each alternative from PIS in each criterion. This parameter in the VIKOR method is called the regret index and is denoted by R.

$$R_i = \underset{j}{\mathrm{Max}}\, d\left(v_{ij}.PIS_j\right). \ i = 1.2. \ldots . m \ \Big| \quad d\left(v_{ij}.PIS_j\right) = \left|PIS_j = v_{ij}\right| \tag{11}$$

Step 7: Obtain the VIKOR index ($Q_i$) from Equation (12).

$$Q_i = v \times \left[\frac{d_i^{+} - DMIN_i^{+}}{DMAX_i^{+} - DMIN_i^{+}}\right] + (1 - v) \times \left[\frac{R_i - RMIN_i}{RMAX_i - RMIN_i}\right] \tag{12}$$

In Equation (12), $DMIN_i^{+} = min_i d_i^{+} . DMAX_i^{+} = max_i d_i^{+} . RMIN_i = min_i R_i^{-} . RMAX = max_i R_i^{-}$. Also, $v$ is a parameter that its value is between 0 and 1 and represents the relative importance of total distance from PIS against regret index. In this research, the value of this parameter is considered 0.5.

Step 8: Calculate the closeness coefficient for each alternative $i$ ($CC_i$) using Equation (13). Any alternative with a higher $CC_i$ value is a better alternative.

$$CC_i = \frac{d_i^{-}}{d_i^{-} + Q_i} . \qquad i = 1.2. \ldots . m \tag{13}$$

**3. 2. The Used Questionaries** Two questionaries are used to perform the research steps. The first questionnaire is related to the pairwise comparisons in AHP technique. In this questionary, the answer of each question is determined by the shown choices in Table 2. The second questionnaire was also used to determine the score of each supplier (alternative) in each criterion (to form a matrix decision) based on the Likert scale has been used (Table 2). Both questionaries are answered by a sample of 10 expert including 5 academics staff and 5 managers with more than 8 years' experience in the digital stores industry. The used questionaries are standard questionaries and their validity is versified. Moreover, the reliability of the first questionary is justified.

**TABLE 2.** The used linguistic variables in each questioner and their values

| First questioner | | Second questioner | |
|---|---|---|---|
| 1 | Very low preference | 1 | Very little |
| 3 | Low preference | 2 | Low |
| 5 | Medium preference | 3 | Medium |
| 7 | High preference | 4 | High |
| 9 | Very high preference | 5 | Very high |

The hierarchical inconsistency ratio with value of 0.06 verifies the reliability of the first questionnaire. Moreover, Cronbach's alpha with the value of 0.88 verifies the reliability of the second questionnaire.

## 4. RESULTS

Results of the performance of research steps are presented in this section. First, we identify the effective criteria for evaluation and suppliers ranking using subject literature and expert opinions. A list of identified criteria is shown in Table 3. Then, using the first questionnaire and hierarchical analysis, the weight of each effective criteria was calculated and shown in Table 3.

Finally, after identifying 11 suppliers for one item of the products, each supplier's score on each of the criteria (The decision matrix) was determined using the experts' opinions and according to the Likert scale, the results of which are shown in Table 4.

The calculations based the research method according to the criteria and decision matrix (experts' opinion) with TOPKOR method final ranking are shown in Table 5.

**TABLE 3.** Effective criteria in evaluating and ranking suppliers

| Row | The final criterion is selected | Type of criteria | Weight criteria |
|---|---|---|---|
| 1 | Economical | Profit | 0.12043383 |
| 2 | Supported | Profit | 0.20690794 |
| 3 | Environmental | Cost | 0.09808552 |
| 4 | Work experience | Profit | 0.06197201 |
| 5 | Social | Profit | 0.09105958 |
| 6 | Quality | Profit | 0.10985684 |
| 7 | Easy availability | Profit | 0.17477045 |
| 8 | flexibility | Profit | 0.13691384 |

**TABLE 4.** Decision matrix

| The final matrix of alternative/criteria | Economical | Supported | Environmental | Work experience | Social | Quality | Easy availability | flexibility |
|---|---|---|---|---|---|---|---|---|
| Supplier 1 | 5 | 5 | 5 | 4 | 4 | 5 | 5 | 2 |
| Supplier 2 | 4 | 2 | 4 | 1 | 2 | 4 | 4 | 2 |
| Supplier 3 | 3 | 3 | 3 | 2 | 2 | 1 | 4 | 1 |
| Supplier 4 | 3 | 4 | 4 | 2 | 3 | 5 | 5 | 2 |
| Supplier 5 | 5 | 4 | 3 | 2 | 3 | 3 | 3 | 3 |
| Supplier 6 | 4 | 5 | 5 | 4 | 4 | 5 | 5 | 4 |
| Supplier 7 | 1 | 1 | 2 | 4 | 5 | 4 | 2 | 5 |
| Supplier 8 | 2 | 3 | 2 | 5 | 4 | 2 | 5 | 4 |
| Supplier 9 | 3 | 2 | 5 | 3 | 3 | 3 | 4 | 3 |
| Supplier 10 | 5 | 2 | 5 | 5 | 1 | 4 | 2 | 3 |
| Supplier 11 | 3 | 4 | 3 | 3 | 4 | 4 | 2 | 2 |

**TABLE 5.** Ranking of suppliers by TOPKOR method

| Suppliers | Distance from PIS | Distance from NIS | Index R | Index $CC_i$ | Rank |
|---|---|---|---|---|---|
| 1 | 0.004398 | 0.010882 | 0.003092 | 0.13968 | 3 |
| 2 | 0.010243 | 0.005125 | 0.0088485 | 0.007004 | 9 |
| 3 | 0.011217 | 0.003553 | 0.0088485 | 0.004521 | 11 |
| 4 | 0.007391 | 0.007783 | 0.005899 | 0.019238 | 6 |
| 5 | 0.007236 | 0.007403 | 0.005899 | 0.018727 | 7 |
| 6 | 0.003375 | 0.011096 | 0.0029495 | 0.966391 | 1 |
| 7 | 0.00366 | 0.013247 | 0.0029427 | 0.447672 | 2 |
| 8 | 0.005128 | 0.010249 | 0.0033441 | 0.076901 | 5 |
| 9 | 0.007146 | 0.007079 | 0.005899 | 0.01816 | 8 |
| 10 | 0.012111 | 0.006184 | 0.011798 | 0.006164 | 10 |
| 11 | 0.0051 | 0.009869 | 0.003092 | 0.084322 | 4 |

## 5. CONCLUSION

This research provided a way to evaluate and rank suppliers in digital stores. First, the effective criteria in identifying and ranking suppliers in digital stores were identified and the rating of each supplier in each criterion was determined. Then a hybrid approach with a combination of hierarchy analysis methods and TOPKOR for supplier ranking is presented. As it can be seen, the effectiveness of the criteria is, from big to small, as follows; support, accessibility, flexibility, economic, quality, environmental, social status and finally work experience, which is the result of TOPKOR method calculations, the order of suppliers is shown in Table 5. Suppliers No. 6, 7 and 1 have allocated ranking to themselves first to third, respectively. TOPKOR method is a combination of two different multi-criteria decision-making methods called TOPSIS and VIKOR. In TOPSIS method, a good alternative is one that its total distance from the positive ideal solution (PIS) is low and its total distance from the negative ideal solution (NIS) is high. But in VIKOR method, a good alternative is one that its total distance from PIS (utility index) and its maximum distance from PIS in each criterion (regret) are low. It means, TOPSIS neglects the distance of each alternative from PIS in each criterion while VIKOR neglects the total distance from NIS.

TOPKOR method tries to integrate both mentioned methods. In TOPKOR, a good alternative is one that its total distance from PIS and its maximum distance from PIS in each criterion are low and simultaneously its total distance from NIS is high. It means that TOPKOR have a more comprehensive view than TOPSIS and VIKOR and considered all the three parameters.

Providing other multi-criteria decision-making methods for evaluating and ranking digital store suppliers can be considered as a basis for future research. Also identifying newer criteria about supplier evaluation can be considered as another field for future research.

## 6. REFERENCES


1. Saaty, T.L., "The analytic hierarchy process mcgraw-hill", ***New York***, Vol. 324, (1980).
2. Tavana, M., Yazdani, M. and Di Caprio, D., "An application of an integrated anp–qfd framework for sustainable supplier selection", ***International Journal of Logistics Research and Applications***, Vol. 20, No. 3, (2017), 254-275. https://doi.org/10.1080/13675567.2016.1219702
3. Wang, K.-Q., Liu, H.-C., Liu, L. and Huang, J., "Green supplier evaluation and selection using cloud model theory and the qualiflex method", ***Sustainability***, Vol. 9, No. 5, (2017), 688. https://doi.org/10.3390/su9050688
4. Izogo, E.E. and Jayawardhena, C., "Online shopping experience in an emerging e-retailing market", ***Journal of Research in Interactive Marketing***, (2018). https://doi.org/10.1108/JRIM-02-2017-0015
5. Fernie, J. and Grant, D.B., "Fashion logistics: Insights into the fashion retail supply chain, Kogan Page Publishers, (2019).
6. Behl, A., Dutta, P., Lessmann, S., Dwivedi, Y.K. and Kar, S., "A conceptual framework for the adoption of big data analytics by e-commerce startups: A case-based approach", ***Information systems and E-business Management***, Vol. 17, No. 2, (2019), 285-318. https://doi.org/10.1007/s10257-019-00452-5
7. Kaushik, V., Kumar, A., Gupta, H. and Dixit, G., "A hybrid decision model for supplier selection in online fashion retail (OFR)", ***International Journal of Logistics Research and Applications***, Vol. 25, No. 1, (2022), 27-51. https://doi.org/10.1080/13675567.2020.1791810
8. Raajpoot, N.A., Sharma, A. and Chebat, J.-C., "The role of gender and work status in shopping center patronage", ***Journal of Business Research***, Vol. 61, No. 8, (2008), 825-833. https://doi.org/10.1016/j.jbusres.2007.09.009
9. Sanford, J.A., Story, M.F. and Ringholz, D., "Consumer participation to inform universal design", ***Technology and Disability***, Vol. 9, No. 3, (1998), 149-162. doi: 10.3233/TAD-1998-9306.
10. Stephanidis, C. and Savidis, A., "Universal access in the information society: Methods, tools, and interaction technologies", ***Universal Access in the Information Society***, Vol. 1, No. 1, (2001), 40-55. https://link.springer.com/article/10.1007/s102090100008
11. Zajicek, M. and Brewster, S., *Design principles to support older adults*. 2004, Springer.111-113.

12. Vink, P., "Comfort and design: Principles and good practice, CRC press, (2004).
13. Ahmed, Z.U., Ghingold, M. and Dahari, Z., "Malaysian shopping mall behavior: An exploratory study", ***Asia Pacific Journal of Marketing and Logistics***, (2007). https://doi.org/10.1108/13555850710827841
14. Özmen, M. and Aydoğan, E.K., "Robust multi-criteria decision making methodology for real life logistics center location problem", ***Artificial Intelligence Review***, Vol. 53, No. 1, (2020), 725-751. https://doi.org/10.1007/s10462-019-09763-y
15. Durmuş, A. and Turk, S.S., "Factors influencing location selection of warehouses at the intra-urban level: Istanbul case", ***European Planning Studies***, Vol. 22, No. 2, (2014), 268-292. doi. https://doi.org/10.1080/09654313.2012.731038
16. Yang, J. and Lee, H., "An ahp decision model for facility location selection", ***Facilities***, (1997). https://doi.org/10.1108/02632779710178785
17. Liu, H.-C., Quan, M.-Y., Li, Z. and Wang, Z.-L., "A new integrated mcdm model for sustainable supplier selection under interval-valued intuitionistic uncertain linguistic environment", ***Information Sciences***, Vol. 486, (2019), 254-270. https://doi.org/10.1016/j.ins.2019.02.056
18. Kaushik, V., Khare, A., Boardman, R. and Cano, M.B., "Why do online retailers succeed? The identification and prioritization of success factors for indian fashion retailers", ***Electronic Commerce Research and Applications***, Vol. 39, (2020), 100906. https://doi.org/10.1016/j.elerap.2019.100906
19. Sánchez-Lozano, J.M., Teruel-Solano, J., Soto-Elvira, P.L. and García-Cascales, M.S., "Geographical information systems (gis) and multi-criteria decision making (mcdm) methods for the evaluation of solar farms locations: Case study in south-eastern spain", ***Renewable and Sustainable Energy Reviews***, Vol. 24, (2013), 544-556. https://doi.org/10.1016/j.rser.2013.03.019
20. Konstantinos, I., Georgios, T. and Garyfalos, A., "A decision support system methodology for selecting wind farm installation locations using ahp and topsis: Case study in eastern macedonia and thrace region, greece", ***Energy Policy***, Vol. 132, (2019), 232-246. https://doi.org/10.1016/j.enpol.2019.05.020
21. Sedady, F. and Beheshtinia, M.A., "A novel mcdm model for prioritizing the renewable power plants' construction", ***Management of Environmental Quality: An International Journal***, (2019).
22. Liou, J.J., Chang, M.-H., Lo, H.-W. and Hsu, M.-H., "Application of an mcdm model with data mining techniques for green supplier evaluation and selection", ***Applied Soft Computing***, Vol. 109, (2021), 107534. https://doi.org/10.1016/j.asoc.2021.107534
23. Hsu, C.-H., Yu, R.-Y., Chang, A.-Y., Liu, W.-L. and Sun, A.-C., "Applying integrated qfd-mcdm approach to strengthen supply chain agility for mitigating sustainable risks", ***Mathematics***, Vol. 10, No. 4, (2022), 552. https://doi.org/10.3390/math10040552
24. Zakeri, S., Yang, Y. and Konstantas, D., "A supplier selection model using alternative ranking process by alternatives' stability scores and the grey equilibrium product", ***Processes***, Vol. 10, No. 5, (2022), 917. https://doi.org/10.3390/pr10050917
25. Karami, S., Ghasemy Yaghin, R. and Mousazadegan, F., "Supplier selection and evaluation in the garment supply chain: An integrated dea–pca–vikor approach", ***The Journal of the Textile Institute***, Vol. 112, No. 4, (2021), 578-595. https://doi.org/10.1080/00405000.2020.1768771
26. Abdel-Basset, M., Manogaran, G., Mohamed, M. and Chilamkurti, N.K., "Three-way decisions based on neutrosophic sets and ahp-qfd framework for supplier selection problem", ***Future Gener. Comput. Syst.***, Vol. 89, (2018), 19-30.
27. Fanita, D. and Sinaga, B., "Supplier selection decision support system drug wighted methods product (wp)", ***Journal of Computer Networks, Architecture and High Performance Computing***, Vol. 2, No. 1, (2020), 135-139. doi. 10.47709/cnapc.v2i1.377
28. Boran, F.E., Genç, S., Kurt, M. and Akay, D., "A multi-criteria intuitionistic fuzzy group decision making for supplier selection with topsis method", ***Expert systems with applications***, Vol. 36, No. 8, (2009), 11363-11368. https://doi.org/10.1016/j.eswa.2009.03.039
29. Mohammed, A., Yazdani, M., Oukil, A. and Gonzalez, E.D., "A hybrid mcdm approach towards resilient sourcing", ***Sustainability***, Vol. 13, No. 5, (2021), 2695.
30. De Boer, L., "Procedural rationality in supplier selection: Outlining three heuristics for choosing selection criteria", ***Management Decision***, (2017). https://doi.org/10.1108/MD-08-2015-0373
31. Laurentia, N.T. and Septiani, W., *Ypbm university tourism building location selection with a combination of cut off point and ahp topsis method*. 2021, EasyChair.
32. Torkayesh, S.E., Iranizad, A., Torkayesh, A.E. and Basit, M.N., "Application of bwm-waspas model for digital supplier selection problem: A case study in online retail shopping", ***Journal of Industrial Engineering and Decision Making***, Vol. 1, No. 1, (2020), 12-23. doi: 10.31181/jiedm200101012t.
33. Ghorui, N., Ghosh, A., Algehyne, E.A., Mondal, S.P. and Saha, A.K., "Ahp-topsis inspired shopping mall site selection problem with fuzzy data", ***Mathematics***, Vol. 8, No. 8, (2020), 1380. https://doi.org/10.3390/math8081380
34. Qu, G., Zhang, Z., Qu, W. and Xu, Z., "Green supplier selection based on green practices evaluated using fuzzy approaches of topsis and electre with a case study in a chinese internet company", ***International Journal of Environmental Research and Public Health***, Vol. 17, No. 9, (2020), 3268. https://doi.org/10.3390/ijerph17093268
35. Shaikh, S.A., Memon, M.A., Prokop, M. and Kim, K.-s., "An ahp/topsis-based approach for an optimal site selection of a commercial opening utilizing geospatial data", in 2020 IEEE International Conference on Big Data and Smart Computing (BigComp), IEEE., (2020), 295-302.
36. Štirbanović, Z., Stanujkić, D., Miljanović, I. and Milanović, D., "Application of mcdm methods for flotation machine selection", ***Minerals Engineering***, Vol. 137, (2019), 140-146. doi: 10.1109/BigComp48618.2020.00-58.
37. Devi, D.K. and Wardhana, A., "Analysis and design of the best suppliers selection case study: Department store kopetri with the ahp and topsis methods", ***International Journal of Computer Science and Mobile Computing***, Vol. 7, No. 6, (2018), 109-120.

## Persian Abstract

**چکیده**

با توجه به گسترش فضای مجازی در بستر استفاده از اینترنت و دسترسی همگانی به این بستر، کمتر از پیش تولید گنندگان و فروشگاه‌ها به صورت مستقیم بازاریابی را انجام می‌دهند، بلکه بیشتر سعی می‌کنند از بستر فروش اینترنتی برای خود استفاده می‌کنند تا حتی الامکان از واسطه ها که در همه‌ی سیستم‌های فروش وجود دارد کاسته شود. این رویکرد مزیت‌های زیاد دیگری نظیر کاهش بهای تمام شده، کاهش هزینه‌های حمل و نقل، سرعت ارسال محصول و غیره دارد. در نتیجه استفاده از فروشگاه‌های دیجیتالی به صورت فزاینده‌ای مورد اسقبال قرار گرفته اند. ارزیابی و رتبه بندی درست تامین کنندگان، نقش مهمی در افزایش بهره‌وری این نوع فروشگاه‌ها دارد. این پژوهش به ارائه روشی جهت ارزیابی و رتبه بندی تامین کنندگان در فروشگاه‌های دیجیتالی می‌پردازد. ابتدا معیارهای موثر در ارزیابی و رتبه بندی تامین کنندگان در فروشگاه‌های دیجیتالی شناسایی شده است و امتیاز هر تامین کننده در هر معیار تعیین می‌گردد. سپس یک رویکرد ترکیبی با تلفیق روش‌های تحلیل سلسله مراتبی و تاپکور جهت رتبه بندی تامین کنندگان ارائه می‌شود. نتایج علاوه بر نشان دادن اولویت تامین کنندگان نشان می‌دهد که معیارهای پشتیبانی، سهولت دسترسی و انعطاف پذیری به ترتیب بیشترین اهمیت را در ارزیابی و رتبه بندی تامین کنندگان فروشگاه‌های دیجیتالی دارند.

IJE TRANSACTIONS B: Applications Vol. 35, No. 11, (November 2022) 2164-2175

International Journal of Engineering

Journal Homepage: www.ije.ir

# Retrofitting of Reinforced Concrete Beams using Lightweight RC Jacket Containing Silica Nano Particles and Glass Fiber

M. Ghanbari[a], O. Kohnehpooshi*[b], M. Tohidi[c]

*Civil Engineering Department, Sanandaj Branch, Islamic Azad University, Sanandaj, Iran*

*PAPER INFO*

*Paper history:*
Received 23 June 2022
Received in revised form 10 August 2022
Accepted 13 August 2022

*Keywords*:
*Laboratory Study Beam*
*Lightweight Concrete Jacket*
*Silica Nano Particles*
*Glass Fiber*
*Retrofitting*

*ABSTRACT*

The concrete jacket method is a common method used in retrofitting buildings. Although this method has many advantages, engineers criticize it due to an increase in the structure's weight. In the present study, lightweight concretes containing silica nanoparticles (SNPs) and glass fibers (GF) have been used in concrete jackets to strengthen concrete beams. Several reinforced concrete (RC) beams were constructed and retrofitted using the proposed lightweight concrete jackets and their response to four-point loading was evaluated. The SNPs amount in the lightweight concrete jackets was 0, 2, 4, and 6% by weight of cement and the amount of GF was 1.5% by volume of concrete. Load-deflection curves were extracted and the response of the beams was examined by parameters such as crack load, yield load, maximum load, energy absorption capacity, and ductility. The proposed lightweight concrete jacket containing 1.5% of GFs in which 0, 2, 4, and 6% of SNPs were used, increased the energy absorption capacity by 33%, 54%, 61%, and 62%, respectively. The presence of SNPs in lightweight concrete reinforced by GFs leads to the filling of small cavities in the concrete. Also, the bearing capacity of the retrofitted RC beams increased with an increase in SNPs in the concrete jacket. A portion of this increase can be attributed to an increase in tensile and compressive strength of the proposed concrete, and the other part can be attributed to the effect of SNPs on the surrounding surfaces of the main beam and jacket.

***doi:*** *10.5829/ije.2022.35.11b.11*

## 1. INTRODUCTION

One of the major issues in the building's design is the materials' self-weight. Many engineers have always focused on reducing the building dead load using concretes with lower specific gravity and higher compressive strength. This issue is important since the seismic loads on the structure are proportional to the structural mass, and the mass structure reduction is the most important factor in reducing the earthquake impact [1-3].

The lightweight materials reduce the dead load and the weight, ultimately leading to economical design. The concrete's relatively high specific gravity (about 2400 kg/m$^3$ for unreinforced concrete) in RC buildings increases the concrete structure building weight and, as a result, increases the dead weight of the building, causing increases in the gravitational forces and seismic forces. This ultimately requires large elements that require a larger concrete volume with more reinforcement bars. Increasing the dimensions of the structural elements is one of the important disadvantages of RC buildings, which creates architectural problems and reduces useful infrastructure.

On the other hand, RC jackets and increasing cross-sections are more accessible and economical than other techniques in retrofitting of RC beams. This technique effectively improves bearing capacity and stiffness; however, adding concrete and steel to repair the beams increases the beam's weight, which is not desirable. For this purpose, lightweight concrete for retrofitting may be desired.

Numerous manuscripts have been published about retrofitting RC beams. Narayanan et al. [4] investigated the seismic retrofitting of beams using concrete jackets. A number of experiments were performed to investigate

* Corresponding Author Email: Omidkohnehpooshi@gmail.com
(O. Kohnehpooshi)

Please cite this article as: M. Ghanbari, O. Kohnehpooshi, M. Tohidi, Retrofitting of RC Beams using Lightweight RC Jacket Containing Silica Nano Particles and Glass Fiber, ***International Journal of Engineering, Transactions B: Applications,*** Vol. 35, No. 11, (2022) 2164-2175

the interaction between new and old concrete. Then several beams were retrofitted using the concrete jacket. In the next step, several beam-column connection specimens were retrofitted using concrete jackets. Finally, analytical studies were performed. The results showed that self-compacting concrete or shotcrete could be used to make the concrete jacket. Because the self-compacting concrete flowability causes the concrete to be completely in the space between the formwork and the old concrete, and no space remains. Rayal and Dave [5] investigated the different methods of retrofitting RC beams using RC jackets. For this purpose, ten RC beams were made. The four beam surfaces were perfectly smooth, and the other four roughened. Eight beams were retrofitted using RC jackets with a thickness of 60 mm, and two beams were examined as control samples. In beams with rough surfaces, concrete jackets had a more significant effect on improving the bending behavior of beams.

Pandian and Karthick [6] compared the shear strength of concrete beams retrofitted by polymer and concrete jackets. The retrofitted beams with RC jackets have excellent flexural strength, and the bending strength of the beams has increased using the proposed strengthening method. RC jackets can increase the RC beam's ductility, while the CFRP method cannot provide sufficient ductility. Shadmand et al. [7] evaluated the efficiency of a new retrofitting method in improving the bearing capacity of reinforced concrete beams. They investigated a type of composite steel-concrete jacket in RC beams and found that the proposed method can increase the bearing capacity of RC beams by about 2.25 times. Hassan et al. [8] retrofitted damaged beams using strain-hardening cementitious composites. They showed that the proposed method could increase the shear capacity of the damaged beam by about 27%. Mohsenzadeh et al. [9] evaluated the behavior of RC beams with RC jackets containing glass fibers and micro silica gel. The results of the tests indicated that the proposed jackets could increase the energy absorption capacity by about four times. Song and Eun [10] investigated the beams retrofitted with glass fiber-reinforced polyuria. The proposed method increased flexural ductility about 8.52 to 13.9 times.

Vulnerability and an increase in age of concrete buildings have caused new solutions for retrofitting. The lightweight of the proposed method is one of the factors that should be considered. The concrete jacket method is a common method used in retrofitting buildings. Although this method has many advantages, engineers criticize it due to an increase in the structure's weight. In the present study, lightweight concretes containing silica nanoparticles (SNPs) and glass fibers have been used in concrete jackets to strengthen concrete beams. According to the literature review, SNPs can replace a part of cement and improve concrete's mechanical characteristics and durability. Also, glass fibers can be considered a desirable reinforcing option and improve the tensile strength of concrete. In fact, in this research, an attempt has been made to introduce a lightweight concrete jacket that, in addition to increase in the load-bearing capacity of concrete beams, decreases the structure's weight compared to ordinary concrete jackets.

The study flowchart is presented in Figure 1. Rheological, durability, and mechanical properties were investigated in a study conducted by Ghanbari et al. [11], and the experiment results are summarized in Table 1. The samples in which 1.5% of GFs were used have higher tensile and flexural strengths than other samples; therefore, this amount of fibers was selected as the most optimal and was used to make the proposed concrete jackets. In general, five RC beams were made. One beam was not retrofitted, and the other four beams were retrofitted using lightweight concrete jackets containing GF, SNPs, and zeolite. The variable studied is the SNPs amount used in the jacket, which was considered 0, 2, 4, and 6% by weight of cement, respectively.

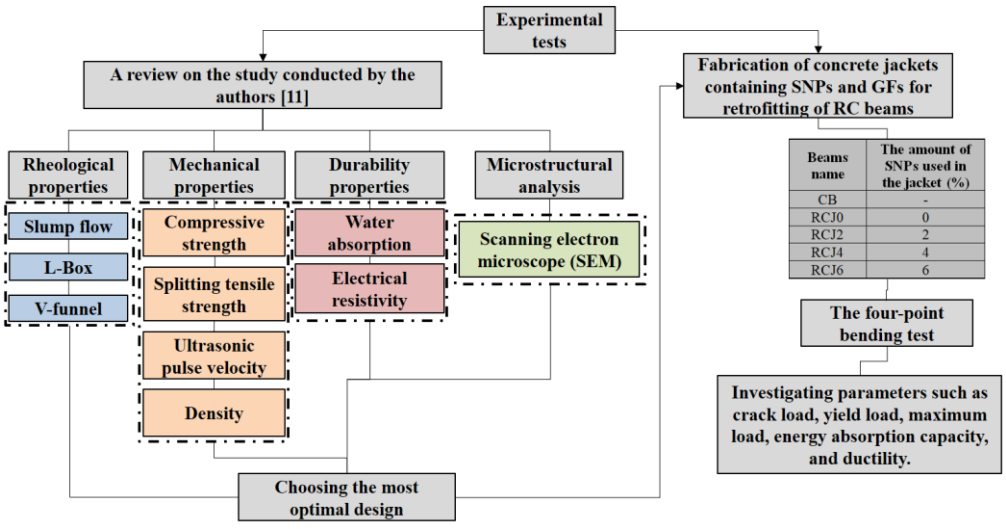


**Figure 1.** The study flowchart

**TABLE 1.** The properties of specimens containing SNPs and GF [11]

| Mix ID | Slump flow | | V-funnel time (s) | L-box ($H_2/H_1$) | Density (kg/m$^3$) | Compressive strength (MPa) | Ultrasonic pulse velocity (UPV) | Spilitingtensile strength (MPa) | Electrical resistivity | Water absorption percentage |
|---|---|---|---|---|---|---|---|---|---|---|
| | D (mm) | $T_{50}$ (s) | | | | | | | | |
| NS0F0 | 747 | 3 | 8.1 | 0.93 | 1886 | 27.2 | 3891 | 2.19 | 55 | 4.50 |
| NS0F0.25 | 733 | 3.2 | 8.7 | 0.92 | 1885 | 27.1 | 3887 | 2.25 | 53 | 4.89 |
| NS0F0.50 | 721 | 3.3 | 8.9 | 0.89 | 1887 | 26.9 | 3881 | 2.28 | 52 | 4.95 |
| NS0F0.75 | 716 | 3.3 | 9.3 | 0.88 | 1888 | 26.5 | 3878 | 2.38 | 51 | 4.99 |
| NS0F1 | 691 | 3.5 | 9.5 | 0.86 | 1888 | 26.4 | 3868 | 2.45 | 50 | 5.01 |
| NS0F1.5 | 683 | 3.5 | 9.9 | 0.84 | 1890 | 26.3 | 3858 | 2.49 | 45 | 5.03 |
| NS2F0 | 717 | 3.1 | 9.1 | 0.9 | 1888 | 35.1 | 3923 | 2.48 | 130 | 2.85 |
| NS2F0.25 | 713 | 3.3 | 9.6 | 0.89 | 1890 | 35.1 | 3921 | 2.58 | 128 | 2.87 |
| NS2F0.50 | 677 | 3.4 | 9.6 | 0.88 | 1890 | 34.9 | 3920 | 2.63 | 127 | 2.91 |
| NS2F0.75 | 656 | 3.4 | 9.9 | 0.87 | 1891 | 34.6 | 3911 | 2.76 | 126 | 2.95 |
| NS2F1 | 645 | 3.6 | 10.1 | 0.85 | 1892 | 34.5 | 3895 | 2.83 | 125 | 2.96 |
| NS2F1.5 | 635 | 3.7 | 10.6 | 0.84 | 1891 | 34.3 | 3893 | 2.91 | 124 | 2.98 |
| NS4F0 | 692 | 3.3 | 9.9 | 0.88 | 1890 | 40 | 4001 | 3.23 | 151 | 2.66 |
| NS4F0.25 | 684 | 3.5 | 10.2 | 0.87 | 1890 | 39.9 | 3995 | 3.27 | 150 | 2.69 |
| NS4F0.50 | 665 | 3.8 | 10.6 | 0.86 | 1892 | 39.8 | 3991 | 3.31 | 149 | 2.75 |
| NS4F0.75 | 642 | 3.9 | 10.6 | 0.85 | 1891 | 39.7 | 3990 | 3.35 | 149 | 2.81 |
| NS4F1 | 614 | 4 | 10.9 | 0.83 | 1893 | 39.5 | 3990 | 3.38 | 148 | 2.85 |
| NS4F1.5 | 609 | 4.2 | 11.3 | 0.82 | 1894 | 39.6 | 3989 | 3.41 | 148 | 2.87 |
| NS6F0 | 677 | 3.7 | 10.6 | 0.81 | 1893 | 39.7 | 3999 | 2.95 | 162 | 2.89 |
| NS6F0.25 | 667 | 3.9 | 10.9 | 0.79 | 1893 | 39.1 | 3992 | 2.98 | 161 | 2.91 |
| NS6F0.50 | 642 | 4 | 11.2 | 0.77 | 1894 | 38.9 | 3991 | 3.1 | 160 | 2.93 |
| NS6F0.75 | 619 | 4.3 | 11.5 | 0.76 | 1895 | 38.8 | 3990 | 3.15 | 159 | 2.95 |
| NS6F1 | 608 | 4.6 | 11.7 | 0.74 | 1896 | 38.7 | 3990 | 3.21 | 158 | 2.98 |
| NS6F1.5 | 601 | 4.8 | 11.9 | 0.72 | 1897 | 38.4 | 3988 | 3.25 | 157 | 2.99 |
| *EFNARC recommendatis [12]* | | | | | | | | | | |
| Min. | 550 | 2 | 6 | 0.8 | NS: Nani silica particles<br>F: Glass Fiber | | | | | |
| Max. | 850 | 5 | 12 | 1 | | | | | | |

## 2. LABORATORY PROGRAM

**2. 1. Geometric Characteristics of the Beams** The jacket thickness on each side (left, right, and bottom sides) was 40 mm. The total length of the beams is 1200 mm. The beam cross-section is a rectangle with dimensions of 150×200 mm (Figure 2). The examined beams were slender because the shear span to effective depth ratio was more than 2.5. Shear span means the distance from the support to the loading point. The characteristic of the investigated beams is presented in Table 2.

**2. 2. Material** The materials used in this work are shown in Figure 3. The coarse aggregates used in this research are lightweight Scoria prepared from Qorveh city (Kordestan Iran). The 24-hour water absorption

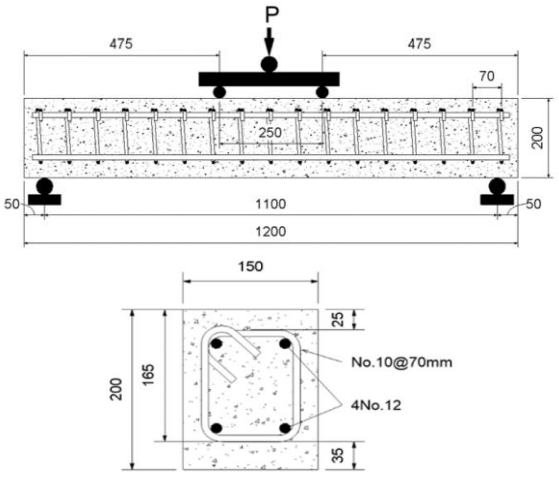


**Figure 2.** Geometric characteristics of the main beams and cross section (without retrofitting)

**TABLE 2.** The investigated beams

| Beams name | Diameter of jacket reinforcement bars (mm) | Jacket thickness (mm) | GF used in the jacket (%) | SNPs used in the jacket |
|---|---|---|---|---|
| CB | - | - | - | - |
| RCJ0 | 8 | 40 | 1.5 | 0 |
| RCJ2 | | | | 2 |
| RCJ4 | | | | 4 |
| RCJ6 | | | | 6 |

**CB:** Control beam (beam without retrofitting)
**RCJ:** Reinforcement concrete jacket

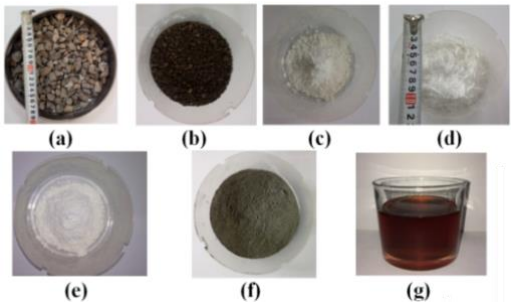


**Figure 3.** Materials a: Scoria aggregates b: Sand c: Zeolite d: GFs e: SNPs and f: Cement: g: Super-plasticizier

percentage, elastic modulus, and specific weight of scoria were 16%, 12.8 GPa, and 680 kg/m$^3$, respectively. The mineral chemical and physical characteristics of scoria aggregates are presented in Table 3. ASTM C136 [13] was used for grading coarse aggregates. The grading characteristics are presented in Table 4. The used cement is Portland type II with a specific weight of 3150 kg/m$^3$ (Table 3). The chemical analysis of SNPs and zeolite are presented in Table 3. GFs are very thin filaments of glass. The fibers used in this study type A with a size of 12 mm.

**2. 3. Mix Design** The mixed design specifications of the RC jacket are presented in Table 5. The desired mixing design was obtained using past experimental studies and according to ACI-211 [14]. The main purpose was to investigate the changes in SNPs. The water in all samples was considered constant. Also, the amount of water relative to the binder (cement and SNPs) was investigated. Variables includes SNPs (0, 2, 4 and 6% by weight of cement) and GF (0, 0.25, 0.50, 0.75 and 1 and 1.5% by weight of cement).

## 3. STEPS OF MAKING THE BEAMS AND CONCRETE JACKET

The materials included Portland cement type II, coarse aggregates, fine aggregates, deformed steel bars with 12 mm diameter for longitudinal reinforcement, deformed steel bars with 10 mm diameter for transverse reinforcement, wire, wooden boards for making molds, nails, superplasticizers, and burnt oil.

1. Squared timbers were used to make the molds. Vertical backs were used to create resistance to lateral pressure of concrete and to prevent mold distortion. These struts were made using four 50×50 mm lathes. The wooden molds picture is shown in Figure 4a.
2. Longitudinal and transverse reinforcement bars were cut to the desired dimensions using guillotine.
3. The mold's inner surfaces were impregnated with an oil to prevent the concrete from sticking to the mold. The reinforcement mesh bar was placed inside the mold by creating a cover (Figures 4b and 4c).
4. The main concrete beam compressive strength was considered to be 32 MPa. Coarse and fine aggregates, water, and cement were poured into the mixer according to the mix design and placed into the molds. The beams are shown in Figure 4d.

**TABLE 3.** Properties of Portland cement, Scoria, zeolite and SNPs

| Description | Scoria | Portland cement | Zeolite | SNPs |
|---|---|---|---|---|
| $SiO_2$ (%) | 58.8 | 21.54 | 67.79 | 99.98 ≥ |
| $Al_2O_3$ (%) | 32.16 | 4.95 | 13.66 | - |
| $Fe_2O_3$ (%) | 3.98 | 3.82 | 1.44 | - |
| CaO (%) | 3.28 | 63.24 | 1.68 | - |
| MgO (%) | 1.5 | 1.55 | 1.20 | - |
| $SO_3$ (%) | 0.75 | 2.43 | 0.5 | - |
| $K_2O$ (%) | - | 0.54 | 1.42 | - |
| $Na_2O$ (%) | - | 0.26 | 2.04 | - |
| Loss on ignition | 3.02 | - | 10.23 | 1.00 ≤ |
| Specific gravity (kg/m$^3$) | 680 | 3.15 | 1.1 | 0.5 |
| Specific surface area (m$^2$/g) | – | 326 | 1.1 | 200 |

**TABLE 4.** Granulation characteristics of coarse and fine aggregates

| Sieve size (mm) | ASTM-C33 for coarse aggregates | Percent passing (Scoria) | ASTM-C33 for fine aggregates | Percent passing (sand) |
|---|---|---|---|---|
| 12.5 | 90-100 | 91 | - | - |
| 9.5 | 40-80 | 63 | - | - |
| 4.75 | 0-20 | 10 | - | - |
| 2.36 | 0-10 | 6 | 95-100 | 95 |
| 1.18 | - | - | 40-80 | 60 |
| 0.30 | - | - | 10-35 | 25 |
| 0.15 | - | - | 5-25 | 17 |

5. The molds were opened twenty-four hours after concreting. The beams were cured inside the laboratory (18ºC) by spraying water every twenty-four hours until 28 days. The images of the main beams after opening the molds are shown in Figure 4e.
6. In order to make lightweight RC jackets containing SNPs and GF, wooden molds were made again according to the mold dimensions. The jacket's thickness on each side was considered to be 40 mm. In other words, the main beams' wooden molds dimensions were increased (Figure 5a).
7. In order to make lightweight self-compacting concrete jackets containing SNPs and GF, several holes were performed in the main beam surfaces using a drill. The hole depth was considered to be about 40 mm. Dust in the holes was cleaned with a brush. Then 8 mm L-shaped bars were placed inside the holes. The epoxy adhesive firmly connected these L-shaped reinforcement bars to the beam body. The epoxy adhesive brand is injection epoxy adhesive (IEA). This adhesive is a two-component paste or reinforcement bar implant adhesive with high mechanical strength (Table 6). This product has a high viscosity, and in addition to planting reinforcement bars and reinforcement, it is suitable for installing various strips and sheets such as FRP laminate on horizontal and vertical surfaces. This adhesive can also be used to plant steel rods and install steel sheets (Figures 5b and 5c).
8. The jacket's steel reinforcement bars' distances from each other were approximately 50 mm.
9. In order to make concrete jackets, the most optimal mixing design obtained from the technology study section (mentioned in the previous sections) was selected, and its manufacturing steps were performed. Scoria aggregates, sand, cement, zeolite, superplasticizer, GF, and SNPs (0, 2, 4, and 6%) were used to make the desired lightweight concrete in the jacket.

**TABLE 5.** Mix properties of RC jacket containing SNPs and GFs

| Mix ID | Water to binder ratio | Cement | SNPs | | Zeolite | | GF (%) | Water (kg) | Sand (kg) | Scoria (kg) | Superplasticizer | |
|---|---|---|---|---|---|---|---|---|---|---|---|---|
| | | | Percentage | Amount (kg) | Percentage | Amount (kg) | | | | | Percentage | Amount (kg) |
| NS0F0 | 0.4 | 405 | 0 | 0 | 10 | 45 | 0 | 180 | 950 | 393 | 1.62 | 7.45 |
| NS0F1.5 | 0.4 | 405 | 0 | 0 | 10 | 45 | 1.5 | 180 | 950 | 393 | 1.62 | 7.45 |
| NS2F1.5 | 0.4 | 396.9 | 2 | 9 | 10 | 44.1 | 1.5 | 180 | 950 | 393 | 1.62 | 7.45 |
| NS4F1.5 | 0.4 | 388.8 | 4 | 18 | 10 | 43.2 | 1.5 | 180 | 950 | 393 | 1.62 | 7.45 |
| NS6F1.5 | 0.4 | 380.7 | 6 | 27 | 10 | 42.3 | 1.5 | 180 | 950 | 393 | 1.62 | 7.45 |

(a)

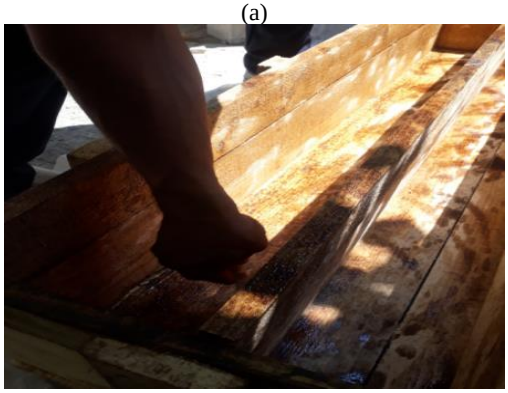

(b)

(c)

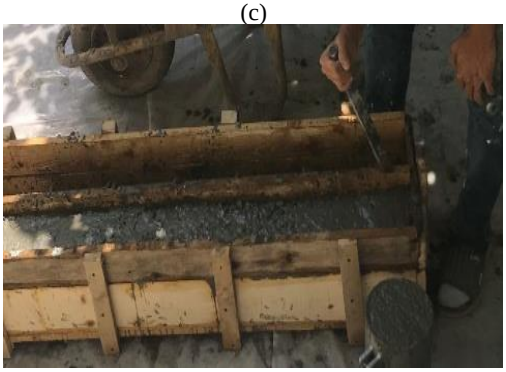

(d)

(e)

**Figure 4.** Steps of making main beams a: Wooden formwork used to make the main beams b: Dipping the mold using oil c: Place the reinforcement mesh bar inside the mold d: Concreting the main beams e: Main beams made after molding

**TABLE 6.** Mechanical parameters of IEA

| **Compressive strength (MPa)** | **9** |
|---|---|
| Density (kg/m$^3$) | 1400 |
| Bond strength (MPa) | 16 |
| Color | Gray |
| Substrate temperature (ºC) | 5-40 |
| Ambient temperature (ºC) | 5-40 |

(a)

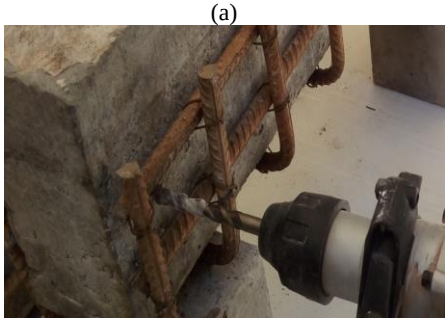

(b)

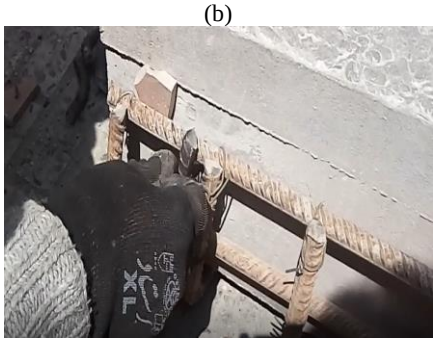

(c)

(d)

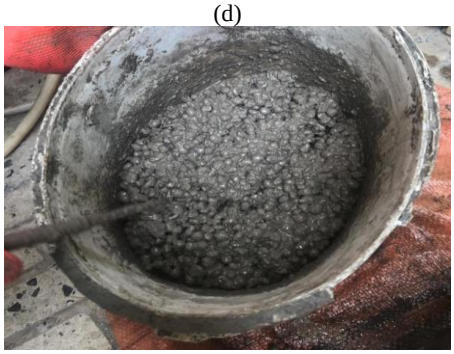

(e)

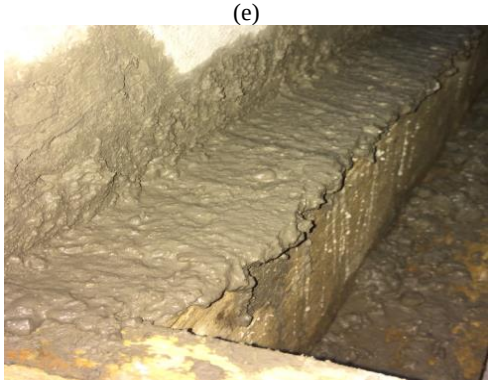

(f)

**Figure 5.** Steps of making concrete jackets a: Making wooden molds to install the jacket b: Making holes on the beam surfaces to install L-bars rebars c: Making holes on the beam surfaces to install L-bars reinforcement bars d: Placing the reinforcement mesh bars on the main beam body e: Making lightweight concrete samples used in the jacket and f: Concrete jacket after concreting

10. The main beams made were placed inside wooden molds, which were impregnated with oil, and light concrete was poured between the mold and the beams. Due to the self-compaction of lightweight concrete, the space between the reinforcement bars was completely filled, and the necessary compaction was created (Figure 5d).
11. Twenty-four hours after concreting, the wooden molds were carefully and gently opened, and the RCs were stored in the laboratory for 90 days.
12. As seen in Table 2, the variables in the beams laboratory reinforcement section are the amount of SNPs used in the jacket, which was considered 0, 2, 4, and 6%

by weight of cement, respectively. The half-span ratio to beam depth (a/h) was considered 1.5. According to this ratio, the value was considered to be 300 mm. A schematic picture of how the beam is loaded with an a/h ratio of 1.5 is shown in Figure 6.

13. The bending jack used in the bending load test has a capacity of 200 tons. This jack has the ability to record the deflection corresponding to the applied force in the span center. The LVDT device is located in the center of the opening and can record a deflection up to 50 mm. The Applying load method is in the force control form. Information about the force amount and the span center displacement was transmitted to the computer via a cable installed on the device and extracted from there (Figure 7).

## 4. LABORATORY RESULTS RELATED TO THE CONTROL AND RETROFITTED BEAMS RESPONSE

The loading was considered as four points and the corresponding load-deflection values were extracted in the form of load-deflection curves. According to research on four-point loading of concrete beams, parameters such as crack load, yield load, maximum load and ultimate load, ductility and energy absorption capacity are usually extracted and evaluated to measure the behavior of beams [14-17]. Therefore, each of the mentioned parameters is illustrated in Figure 8.

The crack distribution in the CB beam (control beam) and the load-deflection curv are shown in Figures 9 and 10, respectively. In this beam, no elements were used to strengthen the beam, and in fact, this beam was made with the aim of investigating the the effectiveness of the proposed retrofitting method. The crack load and deflection of CB are 88.5 kN and 0.902. The yield load and deflection of this beam is 97.2 kN and 1.38 mm, respectively. On the other hand, the maximum bearing capacity is 125 kN.

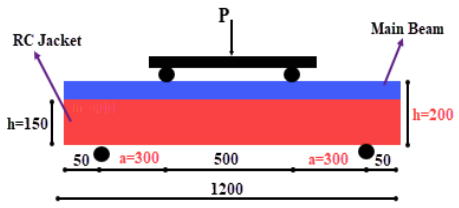


**Figure 6.** Schematic image of the load test set up


**Figure 7.** Bending jack used in the beams flexural load test

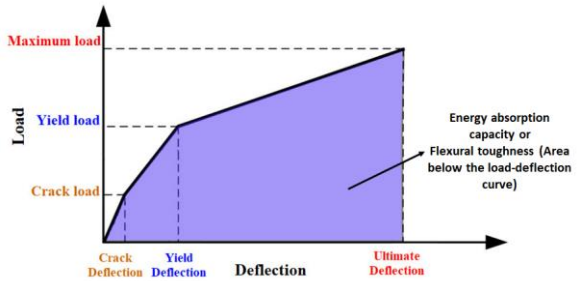


**Figure 8.** Introduction of the studied parameters in load-deflect curves

**Figure 9.** The failure mode of control beam

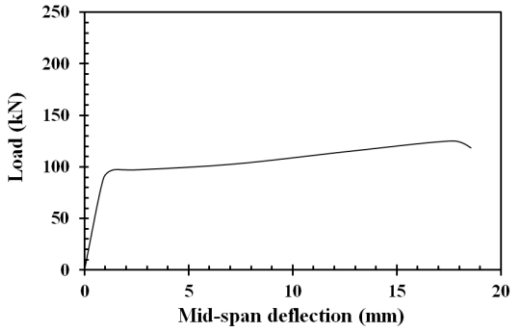


**Figure 10.** Load-deflection curve of control beam (without jacket)

The failure mode of the beam retrofitted with lightweight concrete jackets containing 1.5% GF and 0% SNPs (RCJ0) is shown in Figure 11. In this beam, the crack load are 126 kN and 0.826 mm, respectively. The proposed concrete jackets addition has caused the crack load to increase by approximately 42%. The RCJ2 beam yield and maximum loads are 168 and 180 kN, respectively (Figure 12). The RCJ2 beam energy absorption capacity is 2633 kJ, which is an increase in about 34% compared to the control beam.

The crack disterbution which retrofitted with lightweight concrete jackets containing 1.5% GF and 2% SNPs (RCJ2) is shown in Figure 13. The load and

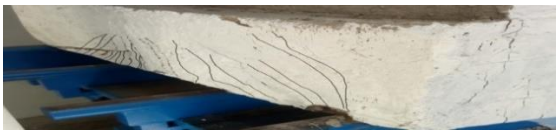

**Figure 11.** Beam failure and crack distribution of RCJ0 beam

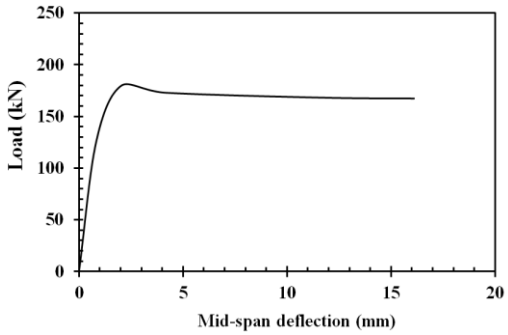


**Figure 12.** Load-deflection curve of RCJ0 beam

**Figure 13.** Beam failure and crack distribution of RCJ2 beam

deflection corresponding to the first crack are 142 kN and 0.69 mm, respectively. The proposed concrete jackets addition has increased the load corresponding to the first crack by about 60%. The yield and maximum loads of RCJ2 beam are 176 and 201 kN, respectively (Figure 14). The energy absorption capacity of the RCJ2 beam is 3044 kJ, which is an increase of about 54% compared to the control beam. Due to the high specific surface area and high reactivity, SNPs lead to calcium hydroxide, which is rapidly formed during hydration, especially at an early age, and the pores of the calcium silicate gel structure are filled, resulting in more and more dense hydrated products. It turns out that this process ultimately leads to improved bearing capacity.

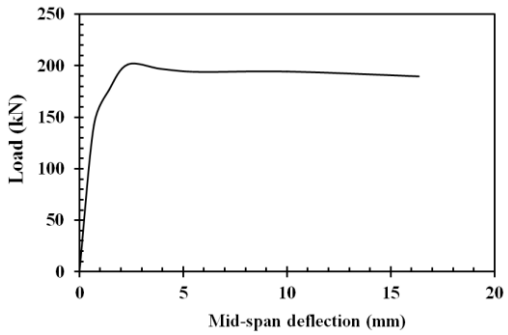


**Figure 14.** Load-deflection curve of RCJ2 beam

The retrofitted beams with lightweight concrete jackets containing 1.5% GF and 4% SNPs (RCJ4) and load-deflection curve are shown in Figures 15 and 16. In this beam, the first crack load and deflection are 146 kN and 0.72 mm, respectively. The proposed concrete jackets addition has caused the crack load to increase by about 65%. The yield and maximum loads of RCJ4 beam are 183 and 205 kN, respectively. The energy absorption capacity of the RCJ4 beam is 3175 kJ, which is an increase of about 61% compared to the control beam.

The retrofitted beams with lightweight concrete jackets containing 1.5% GF and 6% SNPs (RCJ6) and load-deflection curve are shown in Figures 17 and 18. In this beam, the load and deflection corresponding to the first crack are 145 kN and 0.71 mm, respectively. The proposed concrete jackets addition has increased the crack load by about 65%. The yield and maximum loads of RCJ6 beam are 500 and 600 kN, respectively. The RCJ6 beam energy absorption capacity is 3190 kJ, which is an increase of about 62% compared to the control beam.

## 5. RESULTS INTERPRETATION

The crack load, yield load, maximum load, deflection values, ductility, and energy absorption capacity are presented in Table 7. Also, the load-deflection curves of the beams are compared in Figure 19. The lightweight RC jackets containing SNPs and GF significantly increased energy absorption capacity. The energy absorption capacity of the retrofitted beams with jackets containing 1.5% GF in which 0, 2, 4, and 6% of SNPs were increased by 33%, 54%, 61%, and 62%, respectively (Figure 20). The presence of SNPs in

**Figure 15.** Beam failure and crack distribution of RCJ4 beam

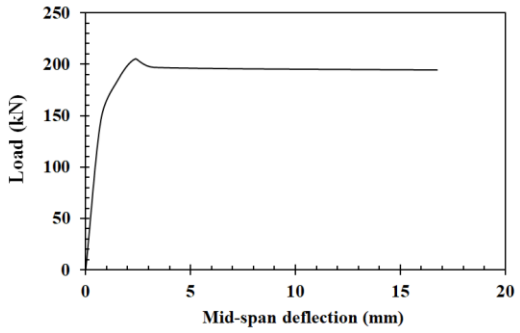


**Figure 16.** Load-deflection curve of RCJ4 beam

**Figure 17.** Beam failure and crack distribution of RCJ6 beam

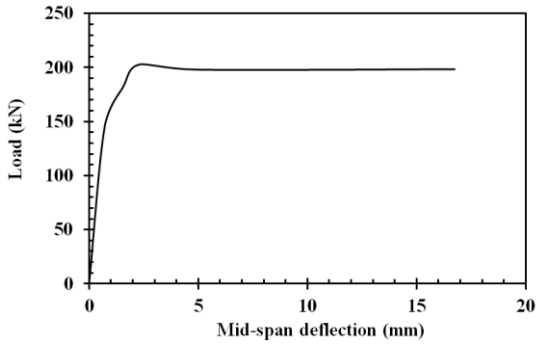


**Figure 18.** Load-deflection curve of RCJ6 beam

lightweight concrete reinforced by GF led to filling small holes in the concrete and significantly improved the retrofitted beams' behavior. The combined use of SNPs and zeolite effectively filled holes and reduced the concrete porosity.

**TABLE 6.** Results of the flexural test

| Beams name | Load (kN) | | | Deflection (mm) | | |
|---|---|---|---|---|---|---|
| | $P_c$ | $P_y$ | $P_{max}$ | $P_c$ | $P_y$ | $P_{max}$ |
| CB | 88.5 | 97.2 | 125 | 0.902 | 1.38 | 3.47 |
| RCJ0 | 126 | 168 | 180 | 0.826 | 2.03 | 1.87 |
| RCJ2 | 142 | 176 | 201 | 0.69 | 1.44 | 2.43 |
| RCJ4 | 146 | 183 | 205 | 0.72 | 1.48 | 2.19 |
| RCJ6 | 145 | 182 | 203 | 0.71 | 1.55 | 1.90 |

$P_c$: Crack load, $P_y$: Yield load, $P_{max}$: Maximum load,

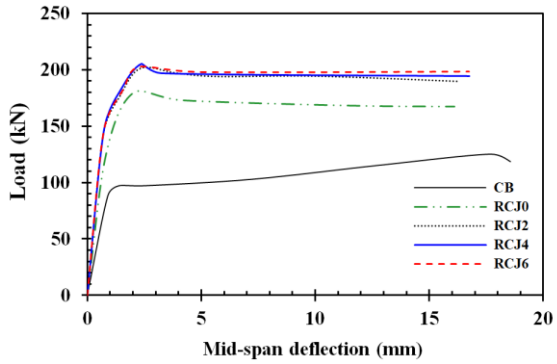


**Figure 19.** Comparison load-deflection curves

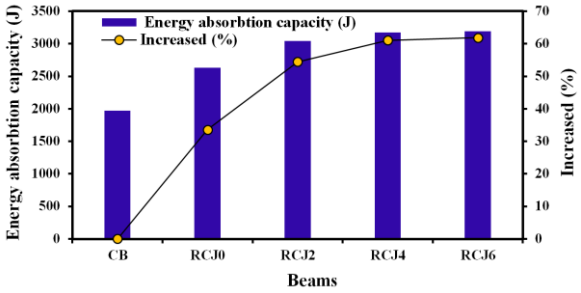


**Figure 20.** Energy absorption capacity

The crack, yield, and maximum loads are presented in Figure 21. The lightweight RC jackets containing GF and SNPs improved the response of the beam. The crack, yield, and maximum loads increased by 65, 88, and 64%. Among the jackets made, the jacket in which 1.5% of GF and 4% of SNPs (RCJ4) were used significantly increased beams crack, yield, and maximum loads. The use of concrete jackets containing 0, 2, 4, and 6% SNPs in which 1.5% of GF have increased the crack load by 42, 60, 65, and 63%, respectively. The yield load also increased by 72, 81, 88 and 87% and the maximum load increased (ultimate load capacity) by 44, 60, 64 and 62%, respectively.

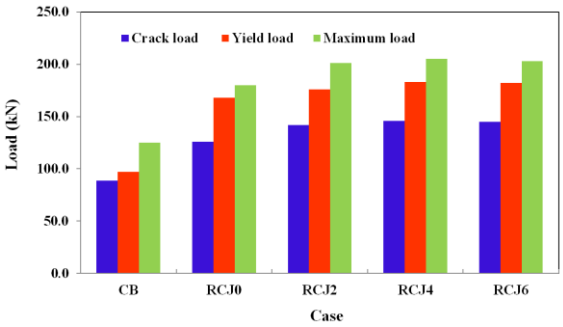


**Figure 21.** Comparison of the beams loads

In concrete structures retrofitting using different methods, sometimes it is possible that a decrease in ductility accompanies an increase in strength and stiffness, and the element can have a significant bearing capacity (maximum load bearing capacity); While its ductility has decreased. Ductility is one of the important features in reliable design for any structural element retrofitting [18]. In the previous sections, it was observed that the lightweight concrete jacket containing GF and SNPs could significantly increase the beam bearing capacity. In this section, the efficiency of the proposed method in ductility terms is considered. Ductility is obtained by using ultimate deformations and yielding in accordance with Equation (1):

$$\mu = \frac{\Delta_u}{\Delta_y} \quad (1)$$

In this equation, Δu and Δy are the ultimate deflection and yield deflection values, respectively. The beam's ductility and bearing capacity in different states compared simultaneously are shown in Figure 22. The deflection ductility coefficients of CB, RCJ0, RCJ2, RCJ4, and RCJ6 beams are 2.51, 0.92, 1.68, 1.47, and 1.22, respectively. Meanwhile, the maximum bearing capacity of CB, RCJ0, RCJ2, RCJ4 and RCJ6 beams is 125, 180, 201, 205, and 203 kN, respectively. As it is known, the proposed method has reduced the beam's ductility compared to the control beam but has increased the beam's ultimate bearing capacity. In strengthening concrete structures using different methods, sometimes a decrease in ductility may accompany an increase in strength and stiffness. An element can have a significant bearing capacity (maximum load); while its ductility has decreased [18]. This is true for RCJ0 and RCJ6 beams, and although these beams have a higher load-bearing capacity than the control beam, they have less ductility.

In order to compare the performance of the proposed method in this section, a comparative study of this method with similar studies has been done. Figure 23. mentions a number of studies that have been carried out in the field of retrofitting of RC beams. In the study conducted by Ying et al. [19], the method of steel plates was used to strengthen RC beams, and the highest rate of increase in bearing capacity was reported as 1.47. Jabr et al. [20] studied the jackets containing cement mortars reinforced with glass fibers and carbon fibers were used to strengthen the beams, and the bearing capacity of the beams increased by 1.33 times in the most cases. Abdullah et al. [21] investigated the strengthening of beams using the method of CFRP rebars. The maximum ratio of load capacity increase compared to the reference samples was reported as 1.59. Nanda and Behra [22] used the method of gluing GFRP sheets in strengthening beams. The results showed that this method can increase the carrying capacity by 1.34 times. Yu et al. [23] investigated the strengthening of severely damaged concrete beams using CFRP sheets. They showed that the use of CFRP sheet installation method can increase the maximum beam load by about 2.13 times. Zhang et al. [24] used concrete layers containing high-strength

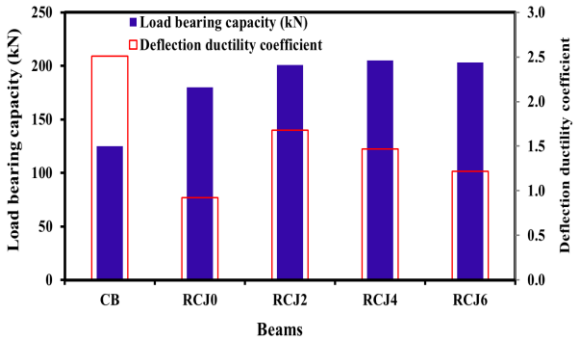


**Figure 22.** Comparison of deflection ductility coefficient

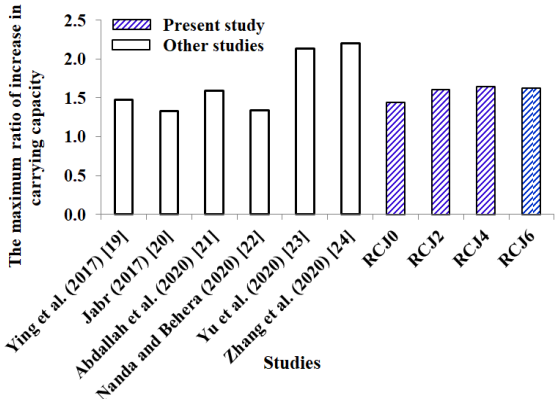


**Figure 23.** Comparison of the maximum ratio of increase in carrying capacity compared to reference samples

concretes to strengthen RC beams and showed that this method can increase the load-bearing capacity by about 2.2 times. The results of the present study also showed that the method of using lightweight RC Jacket containing SNPs and GFs can increase the load-bearing capacity of beams by about 1.64 times.

## 7. CONCLUSION

In this study, the retrofitting of RC beams was investigated using lightweight concrete jackets containing GFs and SNPs. A number of RC beams were made and retrofitted using the proposed concrete jacket and their response to four-point loading was evaluated. The variables were the amount of SNPs used in the concrete jacket, which were considered 0, 2, 4, and 6% by weight of cement, respectively. The most important results are presented in this section.

- The proposed self-compacting lightweight concrete jacket has a high capability. The RC beams bearing capacity and energy absorption capacity can increase and the beam cracking can be delayed .
- The use of the proposed self-compacting concrete jackets containing 1.5% of GF and different amounts of SNPs increased the energy absorption capacity by 33 to 64%. GFs lead to the filling of tiny cavities in concrete and have a significant effect on improving the retrofitted beams' behavior .
- The use of concrete jackets containing 0, 2, 4, and 6% SNPs in which 1.5% of GF was used, has increased the load corresponding to the first crack by 42, 60, 65, and 63%, respectively.
- SNPs can withstand higher stresses without the expansion of the unstable crack than conventional concrete, delaying the cracks spread in the beam and increasing the beam's resistance to cracking.
- The combined use of fibers and SNPs increases the beam yield capacity. The retrofitted beams yield load with the proposed self-compacting concrete jackets

containing 0, 2, 4 and 6% of SNPs increased 72, 81, 88, and 87%, respectively, compared to the control sample.
- The retrofitted beam bearing capacity increased by about 125 to 203% depending on the SNPs amount. With an increase in SNPs in the concrete jacket, the bearing capacity of the retrofitted concrete beams increased. Part of this increase can be attributed to an increase in the proposed concrete tensile and compressive strength, and the other part can be attributed to the SNPs and zeolite effect at the primary concrete and the jacket connection.

In order to develop the present study, the researcher can evaluate topics such as follows:
- Investigating the use of the proposed retrofitted method on deep RC beams
- Evaluating the use of FRP reinforcement bars in the proposed concrete jackets and comparing them with steel reinforcement bars
- Investigating the combined use of the proposed concrete jackets and FRP sheets in the retrofitting of RC beams
- Investigating the main beams' longitudinal and transverse reinforcement percentage changing effect on the present study results
- Investigating the jackets containing SNPs and GF movement effect on the old concrete surface
- Retrofitting of RC beams using lightweight RC jacket containing SNPs and GF against impact loading

## REFERENCES


1. Niu, J., Bian, Y. and Zuo, F. "Study on the Seismic Performance of High-Performance Polypropylene Fiber-Reinforced Lightweight Aggregate Concrete Columns", ***European Journal of Environmental and Civil Engineering***, Vol. 26, No. 9, (2020), 1-19, doi: 10.1080/19648189.2020.1830306
2. Assaad, J. J. and El Mir, A. "Durability of polymer-modified lightweight flowable concrete made using expanded polystyrene", ***Construction and Building Materials***, Vol. 249, 118764, doi: 10.1016/j.conbuildmat.2020.118764.
3. Singh, V. and Sangle, K. "Analysis of Vertically Oriented Coupled Shear Wall Interconnected with Coupling Beams", ***HighTech and Innovation Journal***, Vol. 3, No. 2, (2022), 230-242, doi: 10.28991/HIJ-2022-03-02-010.
4. Narayanan, V. T. and Badari, A. K. S. "Seismic retrofit of beams in buildings for flexure using concrete jacket", ***ISET Journal of Earthquake Technology 46***, Vol. 49, No. 1-2, (2012), 1-22.
5. Raval, S. and Dave, U., "Effectiveness of Various Methods of Jacketing for RC Beams", ***Procedia Engineering***, Vol. 51, (2013), 230-239, doi.org/10.1016/j.proeng.2013.01.032.
6. Arun pandian, V. and Karthick, S., "Comparative Study on RC Jacketed and FRP Strengthened RC Beams", ***International Journal of Engineering Science and Computing***, Vol. 6, No. 5, (2016), 4918-4922, doi: 10.4010/2016.1118.
7. Shadmand, M., Hedayatnasab, A. and Kohnehpooshi, O. "Retrofitting of Reinforced Concrete Beams with Steel Fiber Reinforced Composite Jackets", ***International Journal of Engineering, Transactions A: Basics***, Vol. 33, No. 5, (2020), 770-783, doi: 10.5829/ije.2020.33.05b.08.
8. Hassan, A., Baraghith, A. T., Atta, A. M. and El-Shafiey, T. F., "Retrofitting of shear-damaged RC T-beams using U-shaped SHCC jacket", ***Engineering Structures***, Vol. 245, (2021), 112892, doi: 10.1016/j.engstruct.2021.112892.
9. Mohsenzadeh, S., Maleki, A. and Lotfollahi-Yaghin, M. "Strengthening of RC Beams Using SCC Jacket Consisting of Glass Fiber and Fiber-Silica Fume Composite Gel", ***International Journal of Engineering, Transactions B: Applications***, Vol. 34, No. 8, (2021), 1923-1939, doi: 10.5829/ije.2021.34.08b.14.
10. Song, J. H. and Eun, H. C. "Improvement of flexural and shear strength of RC beam reinforced by glass fiber-reinforced polyurea (GFRPU)", ***Civil Engineering Journal***, Vol. 7, No. 3, (2021), 407-418, doi: 10.28991/cej-2021-03091662.
11. Ghanbari, M., Kohnehpooshi, O. and Tohidi, M. "Experimental Study of the Combined Use of Fiber and Nano Silica Particles on the Properties of Lightweight Self Compacting Concrete", ***International Journal of Engineering, Transactions B: Applications***, Vol. 33, No. 8, (2020), 1499-1511. doi: 10.5829/ije.2020.33.08b.08.
12. "Self-Compacting Concrete European Project Group". The European guidelines for self-compacting concrete: Specification, production and use, International Bureau for Precast Concrete, (2005).
13. ASTM C136/C136M-19, Standard Test Method for Sieve Analysis of Fine and Coarse Aggregates, ASTM International, West Conshohocken, PA, (2019).
14. ACI Committee 211, American Concrete Institute, Farmington Hills, Michigan, (1991).
15. Hosen, M. A., Jumaat, M. Z., Alengaram, U. J. and Sulong, N. R. "CFRP strips for enhancing flexural performance of RC beams by SNSM strengthening technique", ***Construction and Building Materials***, Vol. 165, (2018), 28-44, doi: 10.1016/j.conbuildmat.2017.12.052
16. Rahmani, I., Maleki, A. and Lotfollahi-Yaghin, M. A. A., "Laboratory Study on the Flexural and Shear Behavior of RC Beams Retrofitted with Steel Fiber-Reinforced Self-compacting Concrete Jacket", ***Iranian Journal of Science and Technology, Transactions of Civil Engineering,*** Vol. 45, (2021), 2359-2375, doi: 10.1007/s40996-020-00547-x.
17. Shadmand, M., Hedayatnasab, A. and Kohnehpooshi, O. "Strengthening of RC Beams using Steel Plate-Fiber Concrete Composite Jackets (Finite Element Simulation and Experimental Investigation)", ***International Journal of Engineering, Transactions A: Basics***, Vol. 35, No. 1, (2022), 73-92, doi: 10.5829/ije.2022.35.01A.07.
18. Hussein, M., Kunieda, M. and Nakamura, H. " Strength and ductility of RC beams strengthened with steel-reinforced strain hardening cementitious composites", ***Cement and Concrete Composites***, Vol. 34, No. 9, (2012), 1061-1066, doi: 10.1016/j.cemconcomp.2012.06.004
19. Ying, H., Huawei, P., Xueyou, Q., Jun, P., Xiancun, L., Qiyun, P. and Bao, L. "Performance of Reinforced Concrete Beams Retrofitted by a Direct-Shear Anchorage Retrofitting System", ***Procedia Engineering***, Vol. 210, (2017), 132-140, doi: 10.1016/j.proeng.2017.11.058
20. Jabr, A. "Flexural Strengthening of RC beams using Fiber Reinforced Cementitious Matrix, FRCM", ***Electronic Theses and Dissertations,*** (2017), 5942, https://scholar.uwindsor.ca/etd/5942
21. Abdallah, M., Al Mahmoud, F., Boissiere, R., Khelil, A. and Mercier, J. "Experimental study on strengthening of RC beams with Side Near Surface Mounted technique-CFRP bars", ***Composite Structures***, Vol. 234, (2020), 111716, doi: 10.1016/j.compstruct.2019.111716.
22. Nanda, R. P. and Behera, B. "Experimental Study of Shear-Deficient RC Beam Wrapped with GFRP", ***International***

***Journal of Civil Engineering***, Vol. 18, (2020), 655-664, doi: 10.1007/s40999-020-00498-4.

23. Yu, F., Zhou, H., Jiang, N., Fang, Y., Song, J., Feng, C. and Guan, Y. "Flexural experiment and capacity investigation of CFRP repaired RC beams under heavy pre-damaged level", ***Construction and Building Materials***, Vol. 230, (2020), 117030, doi: 10.1016/j.conbuildmat.2019.117030.

24. Zhang, Y., Li, X., Zhu, Y. and Shao, X. "Experimental study on flexural behavior of damaged reinforced concrete (RC) beam strengthened by toughness-improved ultra-high performance concrete (UHPC) layer", ***Composites Part B: Engineering***, Vol. 186, (2020), 107834, doi: 10.1016/j.compositesb.2020.107834.

## Persian Abstract

**چکیده**

روش ژاکت بتنی روشی رایج است که در مقاوم سازی ساختمان ها استفاده می شود. اگرچه این روش مزایای زیادی دارد اما مهندسان به دلیل افزایش وزن سازه از آن انتقاد می کنند. در تحقیق حاضر از بتن های سبک حاوی نانوذرات سیلیس و الیاف شیشه در ژاکت های بتنی برای تقویت تیرهای بتنی استفاده شده است. چندین تیر بتن مسلح با استفاده از ژاکت‌های بتنی سبک پیشنهادی ساخته و مقاوم‌سازی شدند و پاسخ آنها به بارگذاری چهار نقطه‌ای ارزیابی شد. مقدار نانوذرات سیلیس در ژاکت های بتن سبک ۰، ۲، ٤ و ٦ درصد وزنی سیمان و مقدار الیاف شیشه درصد حجمی بتن بود. منحنی‌های بار-انحراف استخراج شد و پاسخ تیرها با پارامترهایی مانند بار ترک، بار تسلیم، حداکثر بار، ظرفیت جذب انرژی و شکل‌پذیری مورد بررسی قرار گرفت. ژاکت بتنی سبک پیشنهادی حاوی ۱.۵ درصد الیاف شیشه که در آن ۰، ۲، ٤ و ٦ درصد نانوذرات سیلیس استفاده شده است، ظرفیت جذب انرژی را به ترتیب ۳۳، ٥٤، ٦١ و ٦٢ درصد افزایش داد. وجود نانوذرات سیلیس در بتن سبک تقویت شده توسط الیاف شیشه منجر به پر شدن حفره های کوچک در بتن می شود. همچنین ظرفیت باربری تیرهای بتن مسلح مقاوم سازی شده با افزایش نانوذرات سیلیس در ژاکت بتنی افزایش یافت. بخشی از این افزایش را می توان به افزایش مقاومت کششی و فشاری بتن پیشنهادی نسبت داد و بخشی دیگر را می توان به اثر نانوذرات سیلیس بر روی سطوح اطراف تیر اصلی و ژاکت نسبت داد.

IJE TRANSACTIONS B: Applications Vol. 35, No. 11, (November 2022) 2176-2185

International Journal of Engineering

Journal Homepage: www.ije.ir

# Optimization Study of Isolated Building using Shape Memory Alloy with Friction Pendulum System under Near-fault Excitations

D. Sreeman, B. Kumar Roy*

*Department of Civil engineering, National Institute of Technology Silchar, India*

*PAPER INFO*

*Paper history:*
Received 01 July 2022
Received in revised form 04 August 2022
Accepted 08 August 2022

*Keywords*:
*Near-fault Earthquake*
*Friction Pendulum System*
*Base Isolation*
*Shape Memory Alloy*

*ABSTRACT*

Structures close to causative earthquake faults may exhibit substantially different seismic responses than those recorded away from the excitation source. In the near-fault zone, long duration intense velocity pulses can induce unexpected seismic demands on isolated buildings. This study investigates the performance of a five-storey building frame isolated with a shape memory alloy based friction pendulum system (SMA-FPS) under near-fault excitations. The effectiveness of SMA-FPS is quantified by comparing the same isolated structure subjected to a friction pendulum system (FPS). Parametric studies, optimal analysis and numerical simulations are carried out on the structural parameters of the isolation systems. For this, the particle swarm optimization (PSO) method is used to acquire optimal characteristic strengths of SMA-FPS. The transformation strength of SMA and frictional coefficient are selected as two design variables to minimize the top storey acceleration, which is used as the objective function to optimize the seismic reduction efficiency of SMA-FPS system. The optimal seismic response of the structure isolated by SMA-FPS achieves superior performance over FPS under near-fault excitations. Moreover, the study reveals that the optimal SMA-FPS system significantly reduces the bearing displacement as compared to the FPS system. Finally, the computational results are validated with numerical simulation performed in SAP2000 which provides the consistent result.

***doi***: *10.5829/ije.2022.35.11b.12*

## 1. INTRODUCTION

Passive vibration control systems of civil engineering structures such as tuned mass dampers [1-2] energy dissipation systems [3] and base isolation [4] systems are the most widely used structural vibration control techniques implemented in seismic prone areas to mitigate the detrimental effects of seismic excitations. The uses of passive, active, semi-active dampers and their effectiveness in vibration control systems for wind turbines, bridges and buildings were studied [5]. Among them, the base isolation (BI) system is one of the most effective vibration control methods which decouple the structure from earthquake ground motions. BI system by virtue of lower lateral stiffness shifts the fundamental time period of structure much higher and provides additional structural damping. Many investigations [6,7] proved that the BI could mitigate the seismic response of the structural systems, and minimum energy is transferred to the superstructure [8]. Among the most common isolators, FPS has become a popular approach for retrofitting structures, industrial buildings and bridges due to its remarkable features. The FPS bearings consist of an articulated slider rested on concave surface [9]. The unique characteristic of the FPS is that in the presence of friction, the system acts like pendulum motion, and it can mitigate a large amount of energy through sliding and recenter by itself. In case of seismic activity, the spherical surface also provides a dynamic friction force that acts as a damping mechanism [10]. The horizontal displacement considerably minimizes the forces transmitted to the building even during large magnitude ground motions.

*Corresponding Author Institutional Email: bijan@civil.nits.ac.in (B. Kumar Roy)

Please cite this article as: D. Sreeman, B. Kumar Roy, Optimization Study of Isolated Building using Shape Memory Alloy with Friction Pendulum System under Near-fault Excitations, ***International Journal of Engineering, Transactions B: Applications***, Vol. 35, No. 11, (2022) 2176-2185

However, optimization technologies have been employed to design isolators with the optimal seismic behaviour [11]. Bucher [12] proposed a Pareto-type optimization technique to maximize the behaviour of FPS considering competing objectives related to the radius of curvature and frictional coefficient. To reduce the dynamic response of superstructure in aspects of displacement, the optimal ranges of coefficient of friction have been derived as a function of system parameters with different soil conditions [13]. Ozturk [14] proposed seismic drift assessment of structures in near-fault (NF) region. Numerous investigations have been conducted to examine an optimum design of FPS bearings under NF excitations [15]. NF ground motion records differ significantly from far fault (FF) earthquake records, where the engineering site distance is not more than 20 kilometres away from the fault rupture. NF seismic excitations contain long period velocity pulse in the normal fault direction, which stems from a permanent static offset of the ground [16]. NF ground motions might produce considerable ductility demands on FPS based structures, particularly at lower levels and it has also been shown that the pulse duration of seismic excitations substantially impacts the building's behaviour [17].

The study on NF excitations has become a research interest because of its sudden large impulse type of ground motion experienced by the structures. However, as seismic isolation technology advanced, the effectiveness of conventional isolators has been questioned in certain scenarios. Significantly, the behaviour of classical isolators under NF excitations has aroused severe concerns. Even though installing an isolation system reduces the building's response significantly, the velocity pulse found in NF excitations may induce amplification in the structural response of such long period buildings [18]. According to earlier investigations, a significant impact occurs when the slider of the FPS bearings is obstructed by the restrainer rims, resulting in severe damages such as the uplift of the isolator and detachment of isolator elements [19]. When structures using FPS systems are subjected to NF seismic excitations, the isolation level exhibits substantial deformations [20]. To address this issue, shape memory alloys (SMA) have been proposed as supplemental smart materials to reduce significant isolator displacement by mitigating the input earthquake forces [21]. SMA are alloys with significant damping properties, considerable dissipation of energy and has the ability to restore its original shape after large deformations [22]. SMAs significantly decrease the response of a structure since they are very effective energy absorbers and do not transmit energy from fundamental to higher vibration modes [23]. An overview of SMA with an isolation system and its prospective advantages in vibration techniques is studied [24]. Several efforts have been made to develop an SMA restrainer coupled with a sliding type BI system to mitigate the bearing displacement [25]. Gur et al. [26] developed and designed a stochastic optimization method with two competing objectives and concluded that the combination of transformation strength of SMA and coefficient of friction mitigates the acceleration at floors and improves its isolation efficiency. The significant improvement of the SMA based rubber isolator over the elastomeric isolator for the isolated structure under NF motions was investigated [27]. An adaptive isolation system developed using an SMA based gap damper and low friction sliding surfaces is intended to mitigate significant deformations in the isolation system by introducing supplementary energy dissipation unless the deformations reaches a threshold value [28].

Although there have been several studies on the dynamic behaviour of FPS isolated buildings, limited studies have been done with SMA based LRB isolated buildings under NF seismic excitations. However, the influence of the building's response to NF excitations is not explored to the best of authors' knowledge using SMA-FPS system. A comparative study of the SMA-FPS isolation system with the FPS isolation system is performed to validate the efficiency of the SMA-FPS system on the seismic response of the building. In the parametric study, top storey acceleration and displacement in the isolator are used to measure the response quantities for this work. It is observed that there are some specific values of Fso and frictional coefficient that minimize the superstructure's acceleration and improve its isolation efficiency. Therefore, the parameters in SMA-FPS such as Fso and frictional coefficient are taken as design variables for performing particle swarm optimization of top storey acceleration as an objective function. The optimum values and corresponding design variables of SMA-FPS system are compared with the FPS system under the considered ground motions. Further, the results obtained from MATLAB 2D model are compared with the ones obtained in SAP2000 software package 3D model under NF earthquake ground motions.

## 2. RESPONSE EVALUATION OF SMA-FPS ISOLATED BUILDING USING NF GROUND MOTION

Figures 1(a) and 1(b) depict an N-storey shear-type building incorporated on the SMA-FPS and FPS isolator and their mechanical models, respectively. As the base isolation system significantly reduces the building's response, the superstructure behaviour may be considered linear. The lateral displacement is considered as degree of freedom for isolator mass and at each storey of a building. In matrix form, the dynamic equation of motion of an N-storey superstructure subjected to seismic input $\ddot{z}_g$ is given as follows:

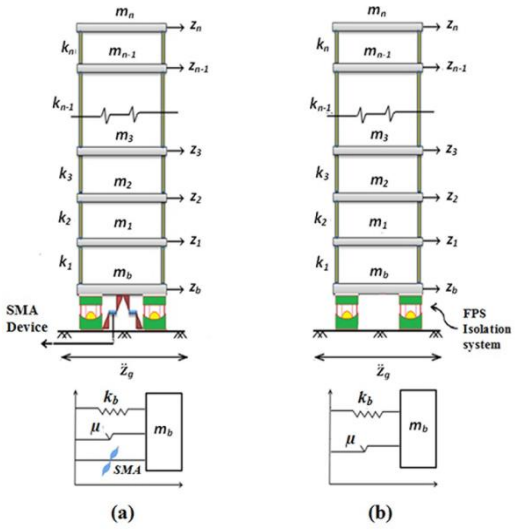


**Figure 1.** a) Flexible building and mechanical model with SMA-FPS b) Flexible building and mechanical model with FPS

$$[M]\{\ddot{z}\}+[C]\{\dot{z}\}+[K]\{z\}=-[M]\{r\}\left(\ddot{z}_g+\ddot{z}_b\right) \quad (1)$$

where $[M],[C]$ and $[K]$ are the matrices of size $N\ X\ N$ indicating the superstructure's mass, damping and stiffness, respectively. Here $\{z\}=\{z_1,z_2,z_3.....z_n\}^T$ represents the displacement vector that containing each storey's lateral displacement with respect to isolator. $\ddot{z}_g$ is the acceleration of earthquake excitation. $\ddot{z}_b$ is the isolator mass acceleration corresponding to its ground mass.

The generalized equation of motion of isolator mass is given as follows:

$$m_b\ddot{z}_b+F_b-c_1\dot{z}_1-k_1z_1=-m_b\ddot{z}_g \quad (2)$$

where $m_b$ is the isolator mass, $c_1$ and $k_1$ represent the damping and stiffness of the first storey building, respectively; $F_b$ is the isolator's restoring force. The term $F_b$ in two different isolation systems is expressed as follows:

$$F_b\left(z_b,\dot{z}_b\right)=\begin{Bmatrix} k_bz_b+F_x & for\ FPS\ Isolator \\ k_bz_b+F_x+F_{SMA} & for\ SMA-FPS\ Isolator \end{Bmatrix} \quad (3)$$

The element $k_bz_b$ in Equation (3) represents restoring force of the bearings, where $k_b=\frac{W}{R}$ and $W=Mg$ represents weight supported by the bearings, g represents acceleration due to gravity and $M=\left(m_b+\sum_{i=1}^{n}m_i\right)$ indicates system's total mass. The element $F_x$ in Equation (3) denotes the friction force $(F_x)$ generated at the sliding interface, which is calculated using the viscoplasticity model and expressed as $F_x=\mu WZ$. Where $\mu$ indicates FPS's frictional sliding coefficient and $Z$ is a non-dimensional parameter considering $Z=\text{sgn}(\dot{z}_b)$, where sgn (˙) is the signum function [29]. The signum function is equivalent to +1 or -1 based on whether $\dot{z}_b$ is positive or negative, respectively. $F_{SMA}$ is the SMA's restoring force. However, the functioning of the bearing system is nonlinear because a reversible phase transition of SMA induced by cycle loading-unloading, which dissipates the energy, as shown in Figure 2. A SMA alloy comes in variety of forms, including Nickel-Titanium (Ni-Ti) alloys, Cu alloys, Fe-Mn-Si alloys etc. Among them Ni-Ti alloys are frequently used in for seismic applications [30], which is considered in this study. For analysing the dynamic behaviour of SMA based structures, the Graesser-Cozarelli model [31] has been widely used. The system depends on the generic Bouc-wen model [32], with an additional component to account for super-elasticity effects and expressed as follows:

$$\dot{F}_{SMA}=k_s\left[\dot{z}_s-\left|\dot{z}_s\right|\left|\frac{\dot{F}_{SMA}-\beta}{F_{TS}}\right|^{\eta-1}\left(\frac{\dot{F}_{SMA}-\beta}{F_{TS}}\right)\right] \quad (4)$$

$$\beta=k_s\alpha_s\left[z_s-\frac{F_{SMA}}{k_s}+f_t\left|z\right|^{c'}erf\left(a'z_s\right)\right] \quad (5)$$

in which $\beta$ is the one-dimensional back stress expressed in Equation (5). The term $k_s$ and $z_s$ are the initial stiffness and displacement of the SMA, $u_y$ is the yield displacement of SMA, $\alpha_s$ is a constant that defines the ratio of pre (OA) to post yield (AB) stiffness. $F_{TS}$ is the force that initiates the phase transition from austenite to martensite. The yield transformation strength of SMA is easily normalized to the total weight of the structure

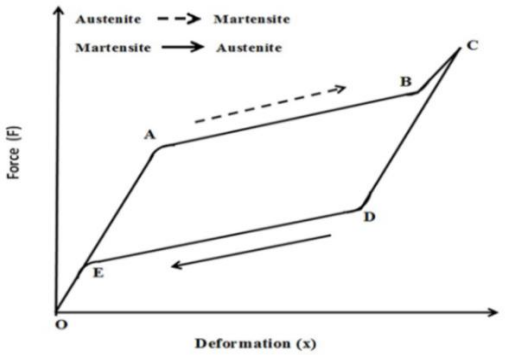


**Figure 2.** Hysteresis behaviour of shape memory alloy

$(F_{so})$. The term $f_t$ is a constant, which controls the deformation loops. $c'$ represents the slope of the unloading path (DE). $\eta$ governs the sharpness of forward and backward transformation. The amount of recovery from unloading is governed by the constant $a'$. $|z_s|$ is the absolute value of $z_s$ and dot over a variable indicates its time derivative. $erf(z_s)$ is the error function with an argument $z_s$, given as:

$$erf(z_s) = \frac{2}{\sqrt{\pi}} \int_0^{z_s} e^{-t^2} dt \tag{6}$$

By combining Equations (2) and (3), the resultant isolator equation given as follows:

$$\begin{aligned} m_b \ddot{z}_b + k_b z_b + F_x - c_1 \dot{z}_1 - k_1 z_1 &= -m_b \ddot{z}_g \\ m_b \ddot{z}_b + k_b z_b + F_x + F_{SMA} - c_1 \dot{z}_1 - k_1 z_1 &= -m_b \ddot{z}_g \end{aligned} \tag{7}$$

The fundamental time period of SMA-FPS isolated system is expressed as $T_b = 2\pi \sqrt{\frac{M}{k_b + \alpha_s k_s}}$. The governing equations for the behaviour of the superstructure-isolator system involve nonlinearity; therefore, the classical superposition technique cannot be applied. Furthermore, the isolation-superstructure system includes damping discrepancies, making the structure non-classically damped. Consequently, the governing Equations (1) and (7) are computed to determine the response of isolator and building by using Newmark's beta approach with a linear variation of acceleration and analyzed in MATLAB computer program.

## 3. NUMERICAL STUDY

A linear five storey shear building is considered in this study. Nonlinear dynamic analysis is used to evaluate the response of the SMA-FPS isolated building subjected to several NF real earthquake pulses. The parameters considered for this study are structural damping ratio $(\xi_s)$, superstructure's time period $(T_s)$ and taken as 2 %, 0.5 seconds, respectively. For simplicity, the stiffness $(k_i)$, mass $(m_i)$ and the damping ratio of all the storeys are kept constant. The isolator mass to superstructure storey mass ratio $\left(\frac{m_b}{m}\right)$ is taken as 1. For this analysis, the numerical values taken for the components to characterise the hysteretic behaviour of SMA-FPS and the FPS isolation system are provided in Table 1. The response parameters considered for evaluating the seismic behaviour of an isolated building are isolator displacement and top storey acceleration. For this analysis, seven numbers of actual NF earthquake records are taken from PEER strong motion database with a wide range of broad spectrum and displacement amplitudes with relevant Peak ground acceleration (PGA), as shown in Table 2. The records selected are from earthquakes with magnitude ($M_w$) > 6.5.

**TABLE 1.** Parameter values for SMA-FPS and FPS

| Superstructure parameters | SMA-FPS/ FPS parameters | SMA parameters (Ni–Ti) |
|---|---|---|
| $\xi_s$ = 2% | $T_b$ =2.5 seconds<br>$u_y$ = 0.025m | $\alpha_s$ =0.10, $f_T$ =0.07,<br>$F_{so}$ =0.10 |
| $T_s$ = 0.5 seconds | $\mu$ = 0.05 | $\eta$ = 3, $a'$ = 2500,<br>$c'$ = 0.001 |

The storey accelerations are considered as one of the essential seismic characteristics that are proportional to the external forces caused by the induced seismic activities. Figure 3(a) and (b) shows top storey acceleration and bearing displacement response of isolated building with SMA-FPS and FPS for NF ground motion (GM-1), respectively. Furthermore, NF records possess higher induced top storey acceleration and bearing displacement values. It has been observed that there is a superior performance of SMA-FPS over the FPS in mitigating the top storey acceleration and displacement in the isolator, especially under earthquakes with long period pulses encountered in the NF ground motions. Figure 4(a) and (b) depicts the hysteretic behaviour of an FPS and SMA-FPS bearings for NF ground motion, respectively. Hysteresis loops are

**TABLE 2.** Near-fault earthquake data

| Sl. No. | Year | Earthquake | Station | $M_w$ | PGA (g) |
|---|---|---|---|---|---|
| 1. | 1979 | Imperial Valley (GM - 1) | El Centro array #5 | 6.53 | 0.38 |
| 2. | 1979 | Imperial Valley (GM - 2) | El Centro array #7 | 6.53 | 0.46 |
| 3. | 1999 | Chi-Chi (GM - 3) | TCU068 | 7.6 | 0.51 |
| 4. | 1994 | Northridge (GM – 4) | Rinaldi | 6.7 | 0.87 |
| 5. | 1994 | Northridge (GM – 5) | Sylmar Converter | 6.7 | 0.85 |
| 6. | 1999 | Kocaeli (GM – 6) | Duzce | 7.5 | 0.40 |
| 7. | 1999 | Chi-Chi (GM - 7) | TCU067 | 7.6 | 0.49 |

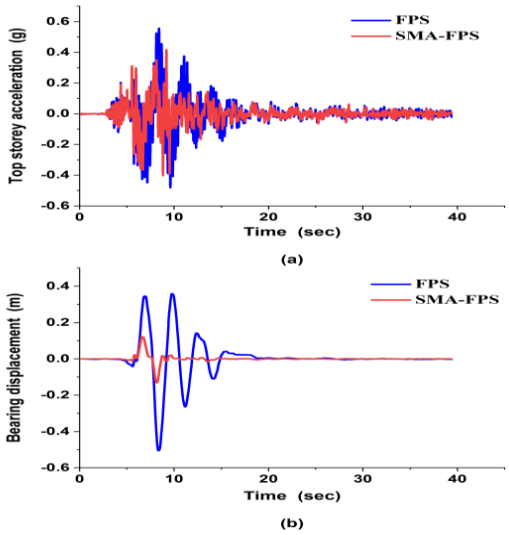


**Figure 3.** (a) Top storey acceleration (b) Bearing displacement of FPS and SMA-FPS isolated building against Imperial Valley ground motion (GM -1)

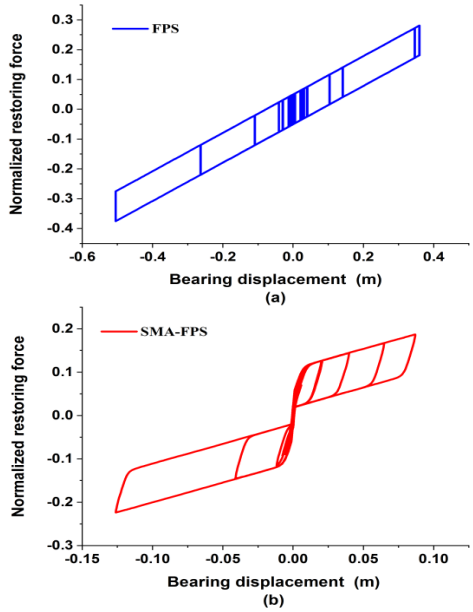


**Figure 4.** Hysteresis behaviour of FPS and SMAFPS isolated building under Imperial Valley ground motion (GM -1)

important for assessing the structural behaviour equipped with SMA-FPS and FPS isolators during seismic excitations. These hysteresis loops can extract and quantify seismic performance characteristics such as yield displacement, equivalent viscous damping, ductility, elastic and secant stiffness, ultimate displacement, ultimate load and yield load. It is observed that the hysteretic behaviour of SMA-FPS is fatter than FPS, hence SMA-FPS has better dissipation of energy than FPS system. However, additional dissipation of energy in the SMA wires gives superior control efficiency in the SMA-FPS isolation system, especially in view of minimal displacement in the isolator.

The coefficient of friction and Fso are two important elements that affect the force deformation mechanism of SMA-FPS, and the response parameters (i.e. maximum top storey acceleration and isolator displacement) are evaluated by varying these two parameters. The average responses are then evaluated by combining these individual responses are shown in the respective figures by the thick line.

The effect of frictional coefficient and Fso on the response of isolated building is shown in Figure 5 as a whole. It is observed that with the increase in Fso values, the top storey acceleration decreases initially and reaches a minimum (optimal) value of response with respect to Fso in the SMA-FPS system (Figure 5a), and the same phenomenon is observed with an increase in frictional coefficient values (Figure 5c). As the Fso and frictional coefficient values increases, the isolator displacement decreases (Figure 5b) and SMA device in FPS system mitigates the isolator displacement significantly (Figure 5d), increasing its isolation efficiency under different NF seismic excitations. The base isolation system gets away from its ideal behaviour by increasing the frictional coefficient and restricting the free mobility of the isolation at the base level. As a result, increasing the frictional coefficient increases the maximum seismic energy penetrating the superstructure. However, the action of the SMA restrainer in FPS also prohibits excessive sliding from enhancing the acceleration.

Therefore, SMA-FPS gives a feasible alternative to the FPS system under NF seismic excitations.

## 4. PARTICLE SWARM OPTIMIZATION

In 1995, Eberhart and Kennedy [33] initially developed PSO. This algorithm is widely utilised in engineering applications. This optimization technique is based on evolutionary computational intelligence and can obtain a convergent solution utilising fish schooling and bird flocking models. PSO is a collective local and global search algorithm that can identify the optimal solution with limited memory and processing power. One of the major benefits of PSO is its capacity to save prior solutions for comparison with new ones. It is also simple to use because just a few parameters must be specified or modified. Each swarm member is distinguished by two characteristics, namely position and velocity. These two parameters are then utilised to update their particles. For estimating the next particle velocity and position are given in Equations (8) and (9).

$$u_i^{j+1} = \omega u_i^j + c_1 rand_1(pbest_i - y_i^j) + c_2 rand_2(gbest - y_i^j) \quad (8)$$

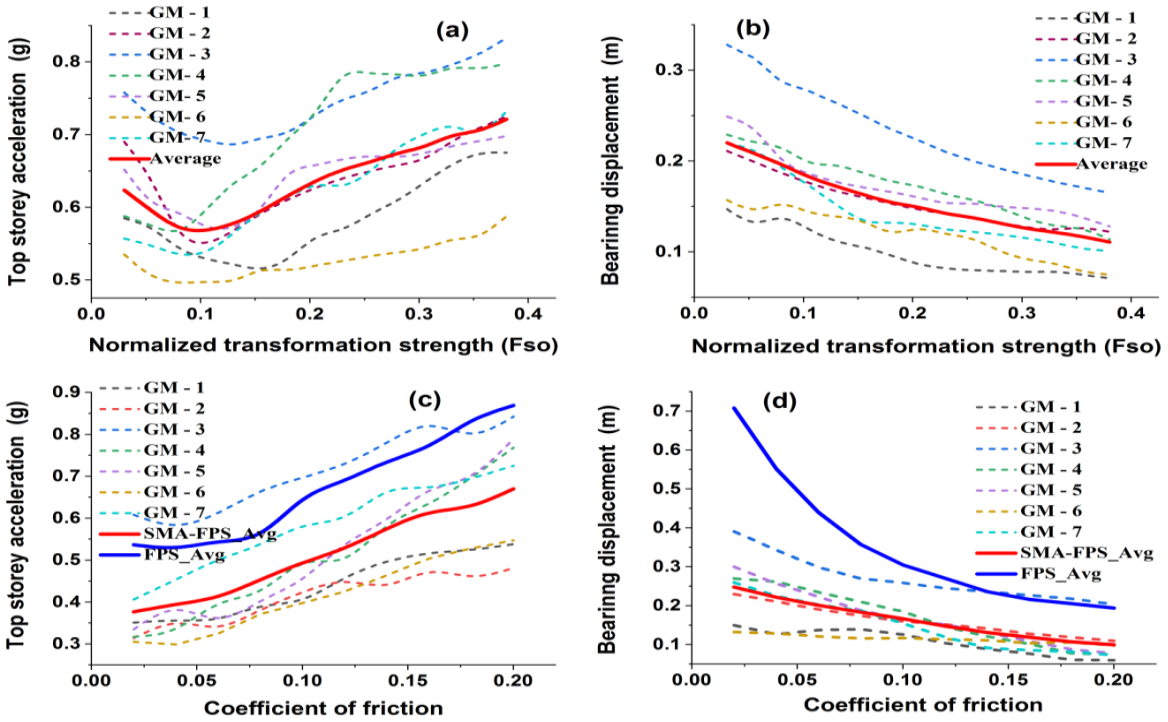


**Figure 5.** Variation of a) Top storey acceleration, (b) Isolator displacement against Fso of SMA-FPS and (c) Top storey acceleration, (d) Isolator displacement against coefficient of friction of FPS and SMA-FPS for all NF earthquake data

$$y_i^{j+1} = y_i^j + u_i^{j+1} \tag{9}$$

where *pbest* is the particle's best previous position and *gbest* represents the position of the best particle up to that iteration in the entire swarm. $c_1$ and $c_2$ are the acceleration coefficients, $rand_1$ and $rand_2$ are two random numbers with a uniform distribution within the domain of [0,1]. $\omega$ denotes inertia weight factor that influences the impact of velocity memory on local and global search. The flow chart of PSO is shown in Figure 6.

## 5. PARAMETERS OPTIMIZATION OF SMA-FPS ISOLATION SYSTEM USING PSO

The building must remain operational even after a strong excitation to assist restoration efforts, thus optimal seismic design is required. Under these excitations, the SMA-FPS isolated building has some specific values of Fso and frictional coefficient that mitigate the structural accelerations and increases its isolation efficiency. For this, the PSO method is used to acquire optimal parameters (i.e., Fso and friction coefficient) of the SMA-FPS system. The relevant range for the design variables must be specified in the optimization formulation. It is important to note that for both isolation systems, the objective function corresponds to the minimization of top storey superstructure accelerations.

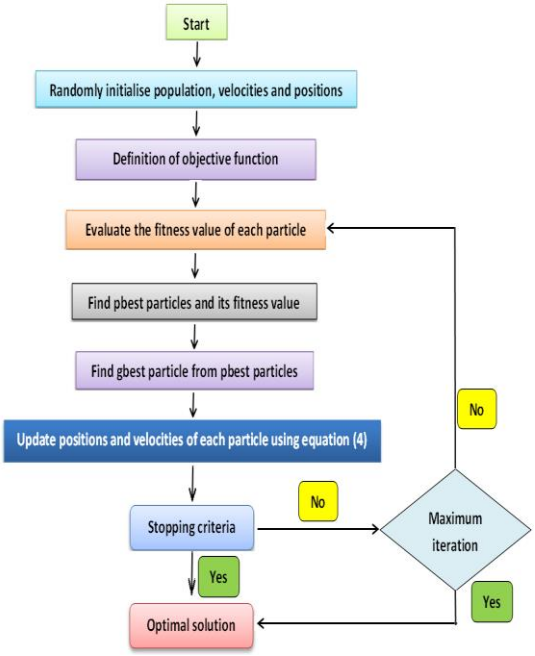


**Figure 6.** Flow chart of PSO algorithm for parameter identification

The optimized top storey acceleration value and corresponding design variables such as Fso and frictional coefficients are obtained for different levels of the isolator time period, as depicted in Figure 7(a, b and c) as well as the associated bearing displacement of SMA-FPS and FPS isolation systems are depicted in Figure 7d for different NF seismic excitations. It can be found that the optimal parameter of Fso decreases with the increasing isolation time period, whereas the frictional resistance value increases. As the displacement related to SMA's phase transition remains constant for different levels of the time period of isolator. Consequently, lower stiffness values require increasing the isolation period, resulting in lower Fso values. Moreover, the frictional coefficient needs to be enhanced to avoid additional bearing displacement. Therefore, with an increase in time period of the isolator, the bearing dis placement increases and the top storey acceleration reduces. Figures 8(a), 8(b) and 8(c) show the optimal top storey acceleration value and respective design variables, such as Fso and frictional coefficients, are obtained by varying superstructure flexibilities. Figure 8 (d) shows the corresponding bearing displacement of SMA-FPS and FPS isolation systems. The results found that, with an increase in superstructure flexibility, the optimal Fso and frictional resistance for the SMA-FPS system decreases because the coefficient of friction values should be lower to keep the isolation system efficient. The superiority of SMA-FPS over FPS in aspects of mitigating acceleration at top storey and large isolator displacements is further emphasized in Figures 8c and 8d. Although the top storey acceleration in the SMA-FPS system is typically lower than that in the FPS system, the differences between them are not significant for various isolator and superstructure time periods (Figures 7c and 8c). However, SMA-FPS is more effective in minimizing the effects of significant bearing displacement.

## 6. NUMERICAL SIMULATION OF FPS ISOLATED BUILDING WITH SMA

In this section, the numerical analysis of isolated building with SMA-FPS is carried out and compared with the computational model for better reliability. The reinforced concrete building frame of five storeys has similar floor height of 3m each with three bays along shorter direction and four bays along longer direction of 3m width. To achieve the fundamental time period of building as 0.5 seconds, the elements and in both models (computational and numerical simulation) are adjusted accordingly. Two separate isolators namely FPS and SMA-FPS are modelled in SAP2000 software. In this work, SMA is modelled with the combination of two non-linear elements such as multi linear element elastic (MLE) and multi linear plastic (MLP) elements to simulate the superelastic and the force deformation behaviour of SMA wires. To model the SMA-FPS isolation system in software, the MLE, MLP link elements and friction isolator elements are arranged in parallel. Table 3 shows property of the multi linear elements that are employed in the softwares to portray FPS and SMA-FPS systems. A typical three dimensional RC building used for the purpose of numerical study is depicted in Figure 9.

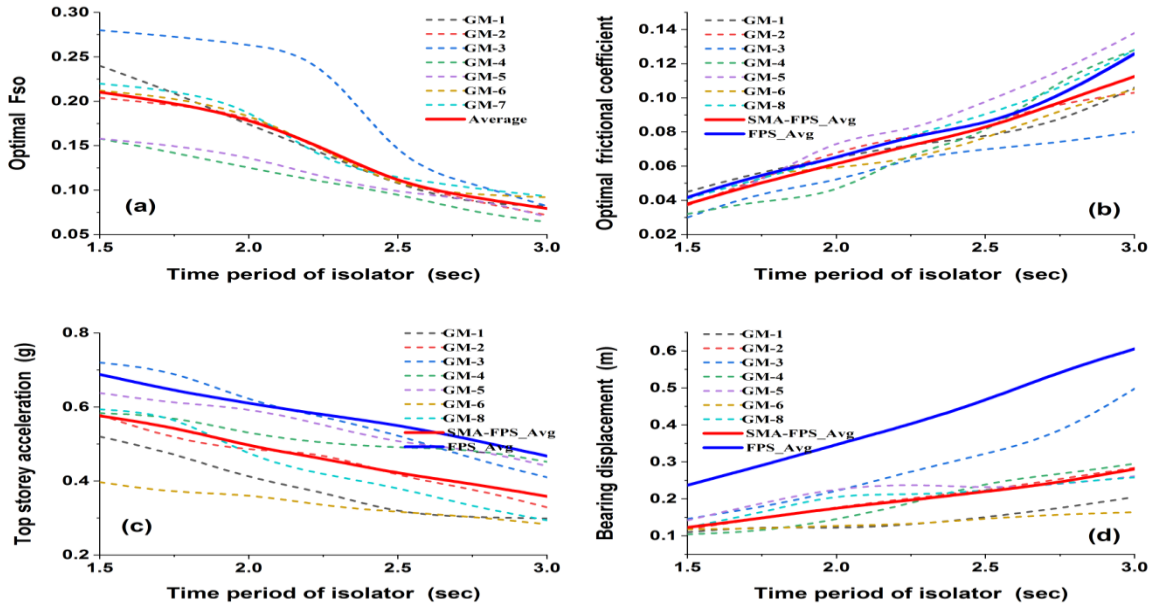


**Figure 7.** Optimum (a) Fso (b) coefficient of friction (c) top storey acceleration (d) bearing displacement against isolator time period for all NF earthquake data

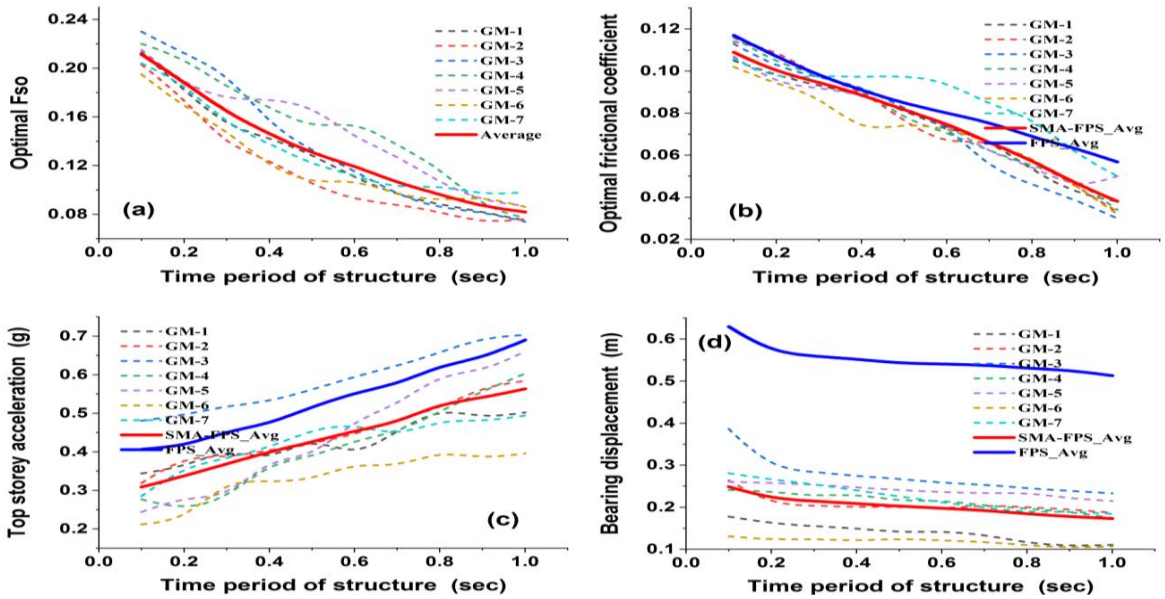


**Figure 8.** Optimum (a) Fso (b) coefficient of friction (c) top storey acceleration (d) bearing displacement against structural time period for all NF earthquake data

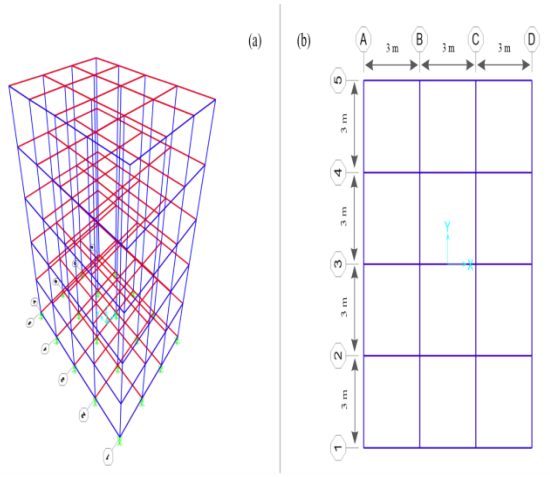


**Figure 9.** Building frame isolated with SMA-FPS (a) 3D view (b) Plan view

**TABLE 3.** Parameter values used in SAP2000

| FPS parameters | Multi linear elastic | Multi linear plastic |
|---|---|---|
| **$K_v$(vertical stiffness) = 170595 KN/m** | Post yield stiffness ratio = 0.105 | Yield exponent = 1 $\alpha = \infty$ , $\beta = 0$ |
| **$K_{eff}$ = 720KN/m R = 1.75m** | Yield displacement = 20mm | Yield displacement = 20mm |

From the study, the comparison of computational and numerical results of top storey acceleration and bearing displacement response of isolated building with SMA-FPS and FPS isolation systems are shown in Figure 10 (a) and (b) respectively for GM-1 ground motion. The results obtained from the 3D model using SAP2000 are validated with those achieved from the computational results obtained in section 3. It can be mentioned here that in both the study similar trend of results are obtained for FPS and SMA-FPS isolation system. However, particular minor discrepancies are observed (from Table 4) among results which are approximately around 5% for top storey acceleration and 8% in case of bearing displacement for FPS and SMA-FPS base isolation systems respectively for computational and numerical model.

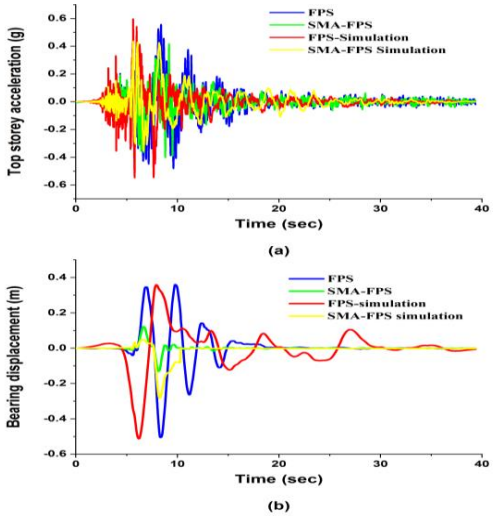


**Figure 10.** Comparison of a) Top storey acceleration b) Bearing displacement of computational and numerical simulation results

**TABLE 4**. Comparison of response parameters for computational and numerical model

| Response parameters | Base isolators | Computational model | Numerical simulation | Error |
|---|---|---|---|---|
| Top storey acceleration (g) | FPS | 0.552 | 0.581 | 4.99 % |
| | SMA-FPS | 0.391 | 0.415 | 5.77% |
| Bearing displacement (m) | FPS | 0.51 | 0.53 | 4.7% |
| | SMA-FPS | 0.189 | 0.207 | 8.8 % |

## 7. CONCLUSIONS

This study focuses on the effectiveness of SMA-FPS in mitigating the seismic response of isolated building under NF earthquakes. A parametric study and optimal analysis are carried out to determine the effect of SMA-FPS parameters on the responses of building and to investigate optimal parameters of the SMA-FPS isolation system using the PSO optimization technique. Comparative evaluation of SMA-FPS and FPS isolated building is conducted to emphasize its relative importance under the set of seven real earthquake ground motions. A parametric study reveals that the top storey acceleration and isolator displacement amplify significantly for the FPS isolation system subjected to NF pulses. However, the SMA-FPS isolation system mitigates the top storey acceleration and isolator displacement substantially compared to FPS isolation system. For structures subjected to NF seismic excitation, the SMA-FPS system can provide more effective energy dissipation than the FPS system. It is observed that there are some specific values of Fso and frictional coefficient that minimize the superstructure's top storey acceleration and improve its isolation efficiency. The Fso values decrease with increasing isolation time period as well as superstructure flexibilities, but the differences in optimal frictional coefficient remain relatively consistent for both isolation systems. Although the top storey acceleration in SMA-FPS system consistently lower than FPS system, but the differences between them are not significant for various isolator and superstructure time periods. However, the reductions in bearing displacement with increasing superstructure and isolator time periods are substantially reduced in SMA-FPS isolation system than FPS isolation system. Overall, by using SMA-FPS isolation system the response of the building can be improved over FPS system under the NF seismic ground motions. By comparing the response of the isolated structures modelled in numerical and computational methods, the results show a similar tendency in both the methods. However, there is a slight minor discrepancy in results obtained in numerical and computational methods, which proposed that the computational model can be used as a reliable study. However, the same study can be performed by conducting hybrid experimental setup in future to validate the computational method.

## 8. REFERENCES


1. Pal, S., Roy, B, and Choudhury, S, "Comparative performance study of tuned liquid column ball damper for excessive liquid displacement on response reduction of structure", ***International Journal of Engineering, Transactions B: Applications***, Vol. 33, No. 5, (2020), 753-759, doi: 10.5829/ije.2020.33.05b.06.
2. Ozturk, B., Cetin, H, and Aydin, E, "Optimum vertical location and design of multiple tuned mass dampers under seismic excitations", ***Engineering Structures***, (2022), 1141-1163, doi: 10.1016/j.engstruct.2020.110536.
3. Barkhordari, M, and Tehranizadeh, M, "Ranking passive seismic control systems by their effectiveness in reducing responses of high-Rise buildings with concrete shear walls using multiple-Criteria decision making", ***International Journal of Engineering, Transactions B: Applications***, Vol. 33, No. 8, (2020), 1479-1490, doi: 10.5829/ije.2020.33.08b.06.
4. Naeim, F, and Kelly, J. M, "Design of seismic isolated structures: from theory to practice", ***John Wiley & Sons***, (1999), doi: 10.1002/9780470172742.
5. Basu, B., Bursi, O. S., Casciati, F., Casciati, S., Del Grosso, A. E., Domaneschi, M., Faravelli, L., Holnicki-Szulc, J.,Irschik, H, and Krommer, M, "A European Association for the Control of Structures joint perspective. Recent studies in civil structural control across Europe", ***Structural Control and Health Monitoring***, Vol. 21, No. 12, (2014), 1414-1436, doi: 10.1002/stc.1652.
6. Buckle, I. G, and Mayes, R. L, "Seismic isolation: history, application, and performance—a world view", ***Earthquake Spectra***, Vol. 6, No. 2, (1990), 161-201, doi: 10.1193/1.1585564.
7. Jangid, R, and Kelly, J, "Base isolation for near-fault motions", ***Earthquake Engineering & Structural Dynamics***, Vol. 30, No. 5, (2001), 691-707, doi: 10.1002/eqe.31.
8. Hessabi, R. M., Mercan, O, and Ozturk, B, "Exploring the effects of tuned mass dampers on the seismic performance of structures with nonlinear base isolation systems", ***Earthquakes and Structures***, Vol. 12, No. 3, (2017), 285-296, doi: 10.12989/eas.2017.12.3.285.
9. Zayas, V. A., Low, S. S, and Mahin, S. A, "A simple pendulum technique for achieving seismic isolation", ***Earthquake Spectra***, Vol. 6, No. 2, (1990), 317-333, doi: 10.1193/1.1585573.
10. Mokha, A., Constantinou, M, and Reinhorn, A, "Teflon bearings in base isolation I: Testing", ***Journal of Structural Engineering***, Vol. 116, No. 2, (1990), 438-454, doi: 10.1061/(ASCE)0733-9445(1990)116:2(438).
11. Farzam, M. F., Jalali, H. H., Gavgani, S. A. M., Kayabekir, A. E, and Bekdaş, G, "Current trends in the optimization approaches for optimal structural control", ***Advances in Structural Engineering-Optimization***, Vol. 326, (2021), 133-179, doi: 10.1007/978-3-030-61848-3-5.
12. Bucher, C, "Probability-based optimal design of friction-based seismic isolation devices", ***Structural Safety***, Vol. 31, No. 6, (2009), 500-507, doi: 10.1016/j.strusafe.2009.06.009.
13. Castaldo, P, and Ripani, M. "Optimal design of friction pendulum system properties for isolated structures considering different soil conditions", ***Soil Dynamics and Earthquake Engineering***, Vol. 90, (2016), 74-87, doi: 10.1016/j.solidyn.2016.08.025
14. Ozturk, B. M, "Seismic drift response of building structures in seismically active and near-fault regions", Purdue University, 2003.

15. Jangid, R, "Optimum friction pendulum system for near-fault motions", ***Engineering Structures***, Vol. 27, No. 3, (2005), 349-359, doi: 10.1016/j.engstruct.2004.09.013.
16. Iwan, W. D, "Near-field considerations in specification of seismic design motions for structures" Proceedings of the Tenth European Conference on Earthquake Engineering, Vienna, Austria, August, (1994), 257-267.
17. Mazza, F, and Vulcano, A, "Effects of near-fault ground motions on the nonlinear dynamic response of base-isolated rc framed buildings", ***Earthquake Engineering & Structural Dynamics***, Vol. 41, No. 2, (2012), 211-232, doi: 10.1002/eqe.1126.
18. Mazza, F., Vulcano, A, and Mazza, M, "Nonlinear dynamic response of RC buildings with different base isolation systems subjected to horizontal and vertical components of near-fault ground motions", ***The Open Construction & Building Technology Journal***, Vol. 6, No. 1, (2012), doi: 10.2174/1874836801206010373.
19. Becker, T. C., Bao, Y, and Mahin, S. A, "Extreme behavior in a triple friction pendulum isolated frame", ***Earthquake Engineering & Structural Dynamics***, Vol. 46, No. 15, (2017), 2683-2698, doi: 10.1002/eqe.2924.
20. Mazza, F, "Lateral-torsional response of base-isolated buildings with curved surface sliding system subjected to near-fault earthquakes", ***Mechanical Systems and Signal Processing***, Vol. 92, (2017), 64-85, doi: 10.1016/j.ymssp.2017.01.025.
21. Ozbulut, O. E, and Hurlebaus, S, "Seismic assessment of bridge structures isolated by a shape memory alloy/rubber-based isolation system", ***Smart Materials and Structures***, Vol. 20, No. 1, (2010), 015003, doi: 10.1008/0964-1726/20/1/015003.
22. Rouhbakhsh, D. A, and Sadrnezhad, S, "A 3d micro-plane model for shape memory alloys", ***International Journal of Engineering, Transactions A: Basics***, Vol. 21, No. 1, (2008).
23. Casciati, F, and Faravelli, L, "A passive control device with SMA components: from the prototype to the model", ***Structural Control and Health Monitoring***, Vol. 16, No. 7-8, (2009), 751-765, doi: 10.1002/stc.328.
24. Ozbulut, O. E., Hurlebaus, S, and DesRoches, R, "Seismic response control using shape memory alloys: a review", ***Journal of Intelligent Material Systems and Structures***, Vol. 22, No. 14, (2011), 1531-1549, doi: 10.1177/1045389X11411220.
25. Ozbulut, O. E, and Hurlebaus, S, "A comparative study on the seismic performance of superelastic-friction base isolators against near-field earthquakes", ***Earthquake Spectra***, Vol. 28, No. 3, (2012), 1147-1163, doi: 10.1193/1.4000070.
26. Gur, S, and Mishra, S. K, "Multi-objective stochastic-structural-optimization of shape-memory-alloy assisted pure-friction bearing for isolating building against random earthquakes", ***Soil Dynamics and Earthquake Engineering***, Vol. 54, (2013), 1-16, doi: 10.1016/j.solidyn.2013.07.013.
27. Gur, S., Mishra, S. K, and Chakraborty, S, "Performance assessment of buildings isolated by shape-memory-alloy rubber bearing: comparison with elastomeric bearing under near-fault earthquakes", ***Structural Control and Health Monitoring***, Vol. 21, No. 4, (2014), 449-465, doi: 10.1002/stc.1576.
28. De Domenico, D., Gandelli, E, and Quaglini, V, "Adaptive isolation system combining low-friction sliding pendulum bearings and SMA-based gap dampers", ***Engineering Structures***, Vol. 212, (2020), 110536, doi: 10.1016/j.engstruct.2020.110536.
29. Castaldo, P., Palazzo, B, and Della Vecchia, P, "Seismic reliability of base-isolated structures with friction pendulum bearings", ***Engineering Structures***, Vol. 95, (2015), 80-93, doi: 10.1016/j.engstruct.2015.03.53.
30. Dolce, M., Cardone, D, and Marnetto, R, "Implementation and testing of passive control devices based on shape memory alloys", ***Earthquake Engineering & Structural Dynamics***, Vol. 29, No. 7, (2000), 945-968, doi: 10.1002/1096-9845(200007)29:7<945::AID-EQE958>3.0.
31. Graesser, E, and Cozzarelli, F, "Shape-memory alloys as new materials for aseismic isolation", ***Journal of Engineering Mechanics***, Vol. 117, No. 11, (1991), 2590-2608, doi: 10.1061/(ASCE)0733-9399(1991)117:11(2590).
32. Wen, Y. K, "Equivalent linearization for hysteretic systems under random excitation", ***Journal of Applied Mechanics,*** Vol. 47, No. 1, (1980), 150-154, doi: 10.1115/1.3153594.
33. Eberhart, R, and Kennedy, J, "A new optimizer using particle swarm theory", MHS'95. Proceedings of the Sixth International Symposium on Micro Machine and Human Science, (1995), 39-43.


## Persian Abstract


**چکیده**

سازه‌های نزدیک به گسل‌های زلزله‌ای ممکن است واکنش‌های لرزه‌ای متفاوتی نسبت به سازه‌هایی که دور از منبع تحریک ثبت شده‌اند نشان دهند. در ناحیه نزدیک به گسل، پالس‌های سرعت شدید طولانی مدت می‌توانند تقاضاهای لرزه‌ای غیرمنتظره‌ای را در ساختمان‌های جدا شده ایجاد کنند. این مطالعه عملکرد یک قاب ساختمان پنج طبقه ایزوله شده با سیستم آونگ اصطکاکی مبتنی بر آلیاژ حافظه شکل (SMA-FPS) را تحت تحریکات نزدیک به گسل بررسی می کند. اثربخشی SMA-FPS با مقایسه همان ساختار جدا شده تحت یک سیستم آونگ اصطکاکی (FPS) اندازه‌گیری می‌شود. مطالعات پارامتریک، تحلیل بهینه و شبیه‌سازی عددی بر روی پارامترهای ساختاری سیستم‌های جداسازی انجام می‌شود. برای این کار، از روش بهینه سازی ازدحام ذرات (PSO) برای به دست آوردن نقاط قوت مشخصه بهینه SMA-FPS استفاده می شود. قدرت تبدیل SMA و ضریب اصطکاک به عنوان دو متغیر طراحی برای به حداقل رساندن شتاب طبقه بالایی انتخاب شده‌اند که به عنوان تابع هدف برای بهینه‌سازی راندمان کاهش لرزه‌ای سیستم SMA-FPS استفاده می‌شود. پاسخ لرزه ای بهینه سازه ایزوله شده توسط SMA-FPS به عملکرد برتر نسبت به FPS تحت تحریکات نزدیک به گسل دست می یابد. علاوه بر این، این مطالعه نشان می‌دهد که سیستم بهینه SMA-FPS به طور قابل توجهی جابجایی بلبرینگ را در مقایسه با سیستم FPS کاهش می‌دهد. در نهایت، نتایج محاسباتی با شبیه‌سازی عددی انجام‌شده در SAP2000 اعتبارسنجی می‌شوند که نتیجه سازگار را فراهم می‌کند.

International Journal of Engineering

Journal Homepage: www.ije.ir

# Cost-based Risk Approach for Spinning Reserve Assessment in Bulk Power Systems

F. Rashidi*, A. Harifi

*Faculty of Engineering, University of Hormozgan, Bandar-Abbas, Iran*

*PAPER INFO*

*Paper history:*
Received 02 August 2021
Received in revised 14 June 2022
Accepted 13 August 2022

*Keywords*:
*Spinning Reserve*
*Power System Security*
*Risk Assessment*
*Bulk Power Systems*

*ABSTRACT*

Spinning reserve (SR) is one of the most prevalent methods for balancing grid uncertainties, such as generator faults, to maintain grid reliability. Literature review shows that several deterministic as well as probabilistic methos have been proposed for determining SR. It is always a challenge for a system operator to decide which approach better from security and reliability point of view. This is important because the allocated SR may provide in some cases a misleading sense of confidence with respect to safe, secure, reliable and economic operation of power systems. This paper presents a cost-based risk index approach for assessing the spinning reserve requirements in a power system. To that end, the performance of spinning reserve is classified in three types, namely, not-effective, partially-effective, and not-meeting-load. Then probability of each type and its consequences are subsequently computed and finally that the risk associated with any spinning reserve value is determined. It is shown that one might consider various spinning reserve values for an operating condition (randomly or using approaches proposed in literature), then calculate risks associated with each value, and finally use the calculated risk indices to determining the optimal level of spinning reserve. As an example, we have shown that in the studied network with 6600MW load, maintaining 240MW SR will increase cost of 1MW hour energy by \$0.154 while the optimal value of 200MW SR will increase cost of 1MWhour energy by just \$0.126. This paper initially focuses on providing a measure of the quality of an ex-ante specified spinning reserve, latter on the flowchart of using the proposed approach for determining optimal level of spinning reserve is presented. The proposed risk index can also be used for comparing different deterministic as well as probabilistic approaches presented in literature for spinning reserve requirements.

***doi***: *10.5829/ije.2022.35.11b.13*

## 1. INTRODUCTION

For frequency stabilization, meeting varying load demand, and backing up in case of any unexpected loss of generation as well as solar power variation, power systems are operated with significant SR. Although there is no widely used agreement on the amount of active power which should be kept as SR, traditionally, SR requirement has been based on deterministic criteria such as loss of the largest online generator or a given percentage of the load [1-3]. Deterministic criteria normally provide suboptimal SR because they consider only basic factors including unit size, unit availability and etc., without taking in to account the stochastic nature of power system components such as probability of generation and transmission outage, uncertainties in load forecast, variation of solar power especially in cloudy sky days, and security criteria [4-5].

Asgari et al. [5] reported that the network constraints in the SR interval were neglected because transmission lines are generally allowed to be overloaded and operated at emergency capacity for a short time. Anstine et al. [6] were the first who proposed the consideration of probabilistic nature of load forecast in SR determination. Thereafter, various researches focused on determining SR using probabilistic methods considering a tradeoff between system reliability and economy. In literature, one or joint combination of loss of load probability (LOLP), expected energy not supplied (EENS) and unit commitment were used as probabilistic reliability indices for reserve assessment [7]. Ansari and Malekshah [8] have used the combination of LOLP and EENS for reserve allocation. Amirahmadi and Akbari Foroud [9] have used hybrid probabilistic and deterministic based approaches for security assessments and optimal spinning reserve allocation. Although in hybrid

*Corresponding Author Institutional Email: rashidi@hormozgan.ac.ir (F. Rashidi)

Please cite this article as: F. Rashidi, A. Harifi, Cost-based Risk Approach for Spinning Reserve Assessment in Bulk Power Systems, ***International Journal of Engineering, Transactions B: Applications***, Vol. 35, No. 11, (2022) 2186-2195

approaches reliability indices are directly included in the model, due to the heavy computation and complexity of these indices, it is difficult to obtain the optimal solution [10-11].

Zhang et al. [12] presented a linearized technique for determining a risk based index for dynamic security assessment. The risk based static security indices were also presented by Emarati et al. [13], Datta and Vittal [14]. Wang et al. [15] presented a method suitable to examine impacts of a high penetration of renewable energy on the total transfer capability considering uncertainties associated with the renewable energy. Jabari et al. [16] have proposed a probabilistic security evaluation algorithm for bulk power system based on analytical approach to consider the single or double failure of line or transformer as well as the multiple failures caused by protection relays. De Caro [17] presented an approach to evaluate the composite system indices under a security constrained framework. Wang [18] has investigated the impact of transmission system failures on spinning reserve allocation and he has proposed a technique to determine the locations of spinning reserve based on the minimum unit commitment risk. A probabilistic based approach was proposed by Rajabdorri et al. [19] to calculate the appropriate reserve margin value based on loss of load expectation index. Bento and Ramos [20] suggested a model for estimating spinning reserves in power systems containtnig renewable-energy sources. Rather than quantifying spinning reserve conditions, the model focuses on factors of stability. The proposed approach's numerical efficiency is accomplished by the use of the cross entropy (CE) concept.

Bento [21] has provided a cost-benefit analysis-based approach for calculating the reserves needs of integrated grid networks. To minimize the total number of buses in the power grid, the suggested model employs the radial-equivalent-independent approach. The optimization of reserve requirements is performed using either security constrained unit commitment (SCUC) or security constrained economic dispatch.

The stochastic nature of load demand, generation and transmission outages along with other uncertainties have made the effectiveness of SR an uncertain parameter such that its effectiveness is very dependent on operating condition, probability of contingencies and randomness of other parameters. In other words, it is always a challenge to decide which approach or what SR value, works best for a power system from economic as well as security and reliability point of view.

Literature review showed that several deterministic as well as probabilistic methods have been proposed for determining SR. However, as emerging technology and business mechanisms arise, this paper proposes a cost-based risk evaluation framework which can be used to determine the optimal level of SR requirement. To that end, the performance of SR is classified in to three possible types, namely, not-effective, partially-effective, and not-meeting-load. The probability of occurrence of each performance type is subsequently computed and associated risk is determined. Thereafter, the flowchart and procedure of using the proposed index for determining the optimal level of SR to economically respond to generation outages, error in load forecasts, and other uncertainties related to renewable resource generation is presented.

## 2. COST-BASED RISK INDEX FOR SR ASSESSMENT

Performance of SR can be classified in three possible types, namely, not-effective, partially-effective, and not-meeting-load demand.

In a system operating with a predefined level of SR, under some conditions (conditions like over forecasting of system load, no generation failure, etc.) the allocated SR will not be utilized to supply the load demand, and system continues to serve the load without utilizing any part of allocated SR. This condition is named as not necessary or not effective (NEFF) SR. On the other hand, there will be conditions that only a portion of allocated SR (from zero plus to 100 percent of the allocated SR) is needed and will be used to serve the load demand. This condition is termed as partially- effective (PEFF) SR. The third scenario is conditions in which allocated SR is not sufficient to supply the load demand. This is termed as not sufficient or notmeeting (NMEET) SR. Therefore, the general expression for a comprehensive risk index shall include all type of SR as below:

$$\begin{aligned} R(X_0) = {} & p(NEFF \mid X_0) \times \\ & Expected\,[Impact(NEFF)] + p(PEFF \mid X_0) \times \\ & Expected\,[Impact(PEFF)] + p(NMEET \mid X_0) \times \\ & Expected\,[Impact(NMEET)] \end{aligned} \quad (1)$$

where, $R(X_0)$ is the risk associated with operating condition $X_0$. Moreover, $p(NEFF \mid X_0)$ is probability that SR being not-effective $p(PEFF \mid X_0)$ is probability that SR being partially-effective, probability of SR and $p(NMEET|X_0)$ is probability that SR is not sufficient to meet demand $Expected\,[Impact(NEFF)]$ is the expected consequence when SR is not-effective, . $Expected\,[Impact(PEFF)]$ is the expected consequence when SR is partially-effective, and $Expected\,[Impact(NMEET)]$ is the expected consequence when SR is not sufficient to meet demand.

## 3. BENEFIT, IMPACT AND PROBABILITY OF SR PERFORMANCE

As stated before, Regardless of the method used for determining the level of SR requirement, performance of

SR is a random and uncertain parameter which is affected by several factors such as stochastic nature of power systems, accuracy of load forecast, generation failure, variability of renewable resources, transmission contingencies, etc. Randomness of SR may let us classify its performance in three possible types named as not-effective, partially-effective, and not-meeting-load.

**3. 1. Probability, Benefit and Impact of Not Effective SR** If allocated SR is not used for supplying the load demand, the allocated SR is not-effective (NEFF). This condition may happen in case of over forecasting of load demand, under-forecasting of renewable resource generations, load tripping, etc. for example, if actual load demand is lower than forecasted load demand, the SR will not be utilized for supplying load demand and will not be effective. Accordingly, probability of SR being not-effective if contingency $Event_i$ happens can be calculated using Equation (2):

$$p(NEFF|Event_i) = \begin{cases} p(\Delta L_i < 0|E_i) & if\ Event_i = E_i \\ p(\Delta L_i < -Capacity(G_i)|G_i) & if\ Event_i = G_i \end{cases} \quad (2)$$

where, $E_i$ is equipment failure (except generation tripping), $G_i$ is generation tripping contingency and $\Delta L_i$ is load variation. From Equation (2) it is observed that if equipment failure $E_i$ causes load reduction, the SR will not be utilized and will be not-effective. The same is applicable if capacity of generation tripping is lower than load reduction, for example, if load reduces by 200MW when only 100MW generation trips. Considering all events, total probability of not-effective SR is as below [20]:

$$p(NEFF|Event_i) = \sum_{E_i} p(\Delta L_i < 0|E_i) \times p(E_i) + \sum_{G_i} p(\Delta L_i < -Capacity(G_i)|G_i) \times p(G_i) \quad (3)$$

No benefit is derived from a not effective SR, however, cost of its provision can be considered as negative impact of not-effective SR.

**3. 1. Probability, Benefit and Impact of Partially Effective SR** If only limited portion of allocated SR is used for supplying the load demand, the allocated SR is partially-effective (PEFF). This condition may happen if actual load exceeds the forecasted load by less than load margin, or actual output of renewable resource generations is less than the forecasted ones, or capacity of generation tripping is less than load variation, etc. Accordingly, probability of SR being partially-effective if contingency $Event_i$ happens can be calculated using Equation (4):

$$p(PEFF|Event_i) = \begin{cases} p(0 < \Delta L_i < \Delta M_i|E_i) & if\ Event_i = E_i \\ p\left(\begin{matrix} -Capacity(G_i) < \Delta L_i \\ < M_i - Capacity(G_i) \end{matrix}\middle| G_i\right) & if\ Event_i = G_i \end{cases} \quad (4)$$

where, $E_i$ is equipment contingency (except for generation tripping), $G_i$ is generation tripping contingency, $\Delta L_i$ is load variation and $M_i$ is load margin (load margin is the amount of additional load which can be supplied without any security and reliability criteria violation such as voltage violation, equipment overloading, etc.). From equation (4) it is observed that if equipment failure $E_i$ causes load to increase and amount of this increase is lower than the SR, only small part of SR will be utilized to supply the load and remaining portion of SR will not be utilized. The same is applicable if capacity of generation tripping is higher than load increase, for example, if load increases by 200MW when 300MW generation trips but load margin is 250MW. Considering all events, total probability of partially-effective SR is as follows [13]:

$$p(PEFF|Event_i) = \sum_{E_i} p(0 < \Delta L_i < M_i|E_i) \times p(E_i) + \sum_{G_i} p\left(\begin{matrix} -capacity(G_i) < \Delta L_i \\ < M_i - capacity(G_i) \end{matrix}\middle| G_i\right) \times p(G_i) \quad (5)$$

Negative impact of partially-effective SR is cost of provision for not utilized portion of SR. The benefit derived from partially-effective SR is additional energy served through partially-effective SR.

**3. 2. Probability, Benefit and Impact of Not Meeting SR** If allocated SR is not sufficient to supply the load demand, it is called not-meeting (NMEET) SR. This condition may happen if actual load significantly exceeds the forecasted load, or actual output of renewable resource generations is significantly lower than the forecasted ones, or capacity of generation tripping is more than load variation, etc. Accordingly, probability of not-meeting SR if contingency $Event_i$ happens can be calculated using the following equation [21]:

$$pp(NMEET|Event_i) = \begin{cases} p(\Delta L_i > M_i|E_i) & if\ Event_i = E_i \\ p\left(\begin{matrix} \Delta L_i > \\ M_i - Capacity(G_i) \end{matrix}\middle| G_i\right) & if\ Event_i = G_i \end{cases} \quad (6)$$

where, $E_i$ is equipment contingency (except for generation tripping), $G_i$ is generation tripping contingency, $\Delta L_i$ is load variation and $M_i$ is load margin. Considering all events, total probability of not meeting SR is as below [21]:

$$p(NMEET|Event_i) = \sum_{E_i} p(\Delta L_i > M_i|E_i) \times p(E_i) + \sum_{G_i} p(\Delta L_i > M_i - capacity(G_i)|G_i) \times p(G_i) \quad (7)$$

when SR is not sufficient to supply the load demand, load curtailment will be necessary. Therefore, negative impact of not meeting SR is cost of non-served energy and the benefit derived from not meeting SR is the additional energy served through allocated SR.

## 4. CASE STUDY

As an illustration, the proposed cost- based risk approach for spinning reserve assessment is applied to a power system with 6600MW system load and 235MW as the largest capacity of online units. Assume that SR under current operating condition is 240MW (one might consider that 240MW SR has been derived based on either of deterministic or probabilistic methods proposed literature methods. However, this value is only a figure for us here to explain the proposed approach). The power system under study includes 45 online generators and consists of, in addition to the generator buses, 400kV (10 buses), 230kV (5 buses), 132kV (101 buses), 63kV (68 buses) and 20kV (149 buses) voltage level. Number of 400kV, 230kV, 132kV and 63kV circuits is 29, 9, 160 and 87 circuits, respectively. The quality of the allocated 240MW SR using the proposed cost-based risk evaluation approach is measured. The time frame is considered to be one hour and during this one hour, it is assumed that the forecasted expectation of system is the same as the current operating condition. Standard deviation for system load is assumed to be 2%. Therefore, expected system load is 6600MW and its standard deviation is 132MW. Figure 1 shows probability density function (PDF) for the system load and Table 1 summarizes list of online generation units along with their capacity and output.

There are several uncertainties associated with SR such as transmission and generation outages, forecasted load, forecasted wind power in wind power generation, forecasted solar power of photovoltaic generation and other parametric deviations, e.g. failure of a generation unit to synchronize, etc.

However, for the simplicity, we consider only 5 different contingencies in the next one hour as shown in Table 2 (the occurrence probability is just for illustrative purpose).

Further simulations using power flow and contingency analysis showed that load margin (i.e. additional load which can be supplied without any security and reliability criteria violation such as voltage violation, equipment overloading, etc.) for contingency 1, 4 and 5 is 240MW and for contingency 2 and 3 is only 93MW and 96MW respectively. In other words, when system load is more than 6693MW and contingency 2 occurs, cascaded circuit overloading will take place which can result in brownout or entire system black out. The same was observed in contingency 3 for load greater than 6696MW. Therefore, in case of requirement, only 93MW of allocated 240MW SR for contingency 2 and 96MW for contingency 3 can be utilized for supplying the load demand.

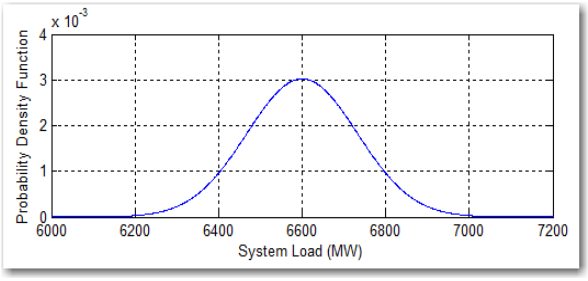


**Figure 1.** PDF of system load

**TABLE 1.** List of online generation units and their respective capacity and MW outputs

| Station | Units and Capacities (MW) | Units and Outputs (MW) | SR (MW) |
|---|---|---|---|
| APOW | $420 = 3 \times 140$ | 408=3×136 | 12 |
| BPOW | $3 \times 216 + 2 \times 135$ | 3×210+2×131 | 26 |
| CPOW | 3×135 | 3×131 | 12 |
| DPOW | 7×68 | 420=7×60 | 56 |
| EPOW | 5×91+1×105 | 5×85+1×100 | 35 |
| FPOW | 4×135+1×70 | 4×130+1×65 | 25 |
| GPOW | 3×216+2×155+ 2×235+2×226 | 3×214+2×150+ 2×230+2×220 | 38 |
| HPOW | 4×235+1×221 | 4×230+1×215 | 26 |
| IPOW | 2×205 | 400=2×200 | 10 |

**TABLE 2.** Probability of contingencies

| Contingency Number | Contingency | Occurrence Probability | Load margin (MW) |
|---|---|---|---|
| 1 | No Outage | 0.999 | 240 |
| 2 | Outage of L1321-1322 circuit | $2.5 \times 10^{-4}$ | 93 |
| 3 | Outage of L1321-1323 circuit | $2.5 \times 10^{-4}$ | 96 |
| 4 | Tripping of FPOW-5 generator with 70MW capacity | $2.5 \times 10^{-4}$ | 240 |
| 5 | Tripping of HPOW-5 generator with 221MW capacity | $2.5 \times 10^{-4}$ | 240 |

**4. 1. Probability and Impact When SR does not Meet Load Variation** We would like to calculate the probability and associated impacts when SR is not sufficient to supply the load demand and therefore, it does not meet load variation during the one-hour study horizon. As stated before and depicted in Figure 1, the system load has normal distribution with 6600MW expected value and 132MW standard deviation. Randomness of the system load and uncertainties in contingencies will lead to randomness and uncertainties

of SR. For contingency 1 to 5, the probability that SR does not meet load variation is as below:

$$p(NMEET|E_1) = p(Load > 6840|E_1) = 0.0345 \quad (8)$$

$$p(NMEET|E_2) = p(Load > 6693|E_2) = 0.2405 \quad (9)$$

$$p(NMEET|E_3) = p(Load > 6696|E_3) = 0.2335 \quad (10)$$

$$p(NMEET|G_4) = p(Load > 6770|G_4) = 0.0989 \quad (11)$$

$$p(NMEET|G_5) = p(Load > 6619|G_5) = 0.4428 \quad (12)$$

Therefore, the probability that SR is not sufficient to supply load demand over the next hour is as below:

$$p(NMEET|Load = 6600MW) = 0.999 \times 0.0345 + 2.5 \times 10^{-4} \times 0.2405 + 2.5 \times 10^{-4} \times 0.2335 + 2.5 \times 10^{-4} \times 0.0989 + 2.5 \times 10^{-4} \times 0.4428 = 0.0347 \quad (13)$$

The associated impact when SR is not sufficient to supply load variation is load interruption which can be interpreted in two different ways. The first option is to assume that if the system load is greater than generation capacity, the outcome is the entire system blackout, i.e. there is no manual or automatic load shedding protection to prevent system against frequency instability. The second option which may be more realistic is assuming that manual or automatic load shedding will be activated to reestablish the balance between load and generation. Here the second option was considered in which, if for example in contingency 1, the system load becomes 6900MW, only 6840MW of the load demand will be supplied and the remaining 60MW load will be shed manually or automatically to reestablish generation and load balance. Figures 2 to 6 show the amount of load which will be shed when SR does not meet load demand in contingency 1 to 5, respectively.

Considering 4 hours load interruption with expected cost of \$20 per MW hour, the expected load interruption when SR is not sufficient to meet load variation is:

$$Expected\big(Impact(NMEET|Load = 6600MW)\big) = 4 \times 20 \times (0.999 \times 0.0345 \times 50.97 + 2.5 \times 10^{-4} \times 0.2405 \times 77.18 + 2.5 \times 10^{-4} \times 0.2335 \times 76.45 + 2.5 \times 10^{-4} \times 0.0989 \times 61.91 + 2.5 \times 10^{-4} \times 0.4428 \times 98.23) = \$142.27 \quad (14)$$

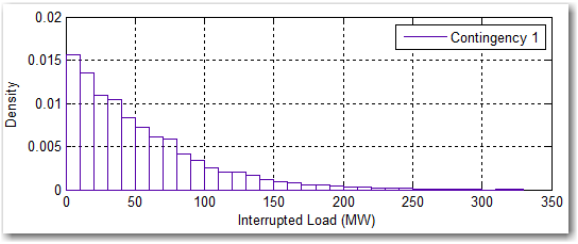


**Figure 2.** Load interruption in contingency 1

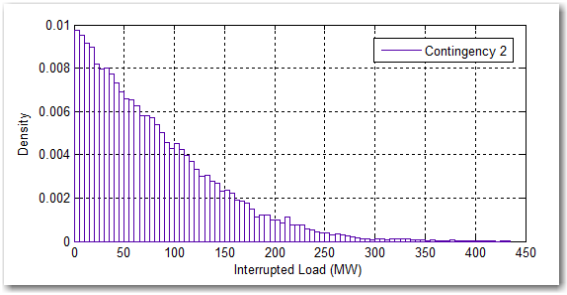


**Figure 3.** Load interruption in contingency 2

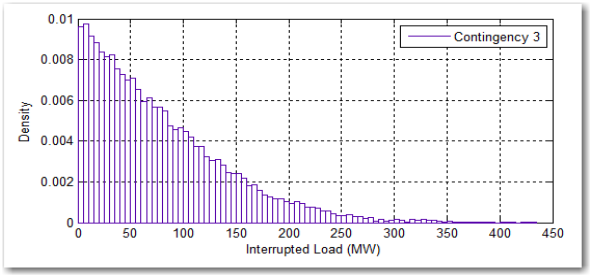


**Figure 4.** Load interruption in contingency 3

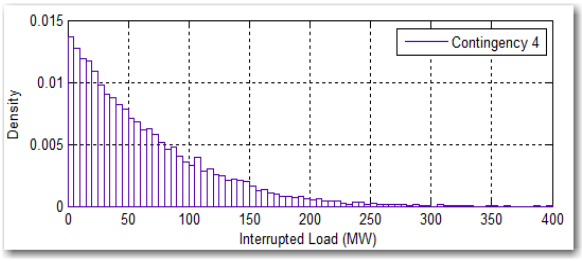


**Figure 5.** Load interruption in contingency 4

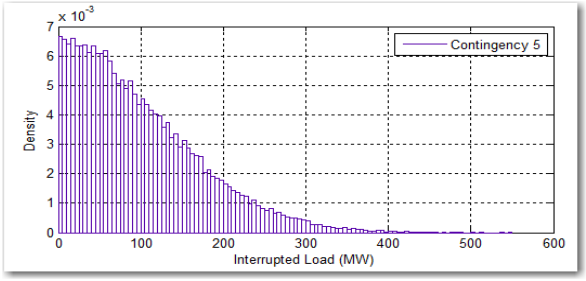


**Figure 6.** Load interruption in contingency 5

The expected benefit from SR when SR is not sufficient to meet load variation is as below:

$$Expected\big(Benefit(NMEET|Load = 6600MW)\big) = 1 \times 20 \times (0.999 \times 0.0345 \times 240 + 2.5 \times 10^{-4} \times 0.2405 \times 93 + 2.5 \times 10^{-4} \times 0.2335 \times 96 + 2.5 \times 10^{-4} \times 0.0989 \times 240 + 2.5 \times 10^{-4} \times 0.4428 \times 240) = \$166.31 \quad (15)$$

Table 3 summarizes probability of not-effective SR and its associated impact and benefit for each contingency.

**4. 2. Probability and Impact When SR is Not Effective** For contingency 1 to 5 the probability that SR is not necessary to meet load demand is as below:

$$p(NEFF|E_1) = p(Load < 6600|E_1) = 0.5 \quad (16)$$

$$p(NEFF|E_2) = p(Load < 6600|E_2) = 0.5 \quad (17)$$

$$p(NEFF|E_3) = p(Load < 6600|E_3) = 0.5 \quad (18)$$

$$p(NEFF|G_4) = p(Load < (6600 - 70)|G_4) = 0.298 \quad (19)$$

$$p(NEFF|G_5) = p(Load < (6600 - 221)|G_5) = 0.047 \quad (20)$$

Therefore, the probability that SR is not required to supply load demand over the next hour is as below:

$$p(NEFF|Load = 6600MW) = 0.999 \times 0.5 + 2.5 \times 10^{-4} \times 0.5 + 2.5 \times 10^{-4} \times 0.5 + 2.5 \times 10^{-4} \times 0.298 + 2.5 \times 10^{-4} \times 0.047 = 0.4998 \quad (21)$$

Considering \$10 per MW hour as expected cost of maintaining SR, the expected impact of not effective SR is as below:

$$Expected\big(Impact(NEFF|Load = 6600MW)\big) = 1 \times 10 \times (0.999 \times 0.5 \times 240 + 2.5 \times 10^{-4} \times 0.5 \times 240 + 2.5 \times 10^{-4} \times 0.5 \times 240 + 2.5 \times 10^{-4} \times 0.298 \times 240 + 2.5 \times 10^{-4} \times 0.047 \times 240) = \$1199.6 \quad (22)$$

The expected benefit which is derived from SR when SR is not necessary to meet load variation is as below:

$$Expected\big(Benefit(NEFF|Load = 6600MW)\big) = \$0.0 \quad (23)$$

Table 4 summarizes probability of not effective SR and its associated impact and benefit for each contingency.

**4. 3. Probability and Impact When SR is Partially-Effective** For contingency 1 to 5 the probability that SR is partially effective is as below:

$$p(PEFF|E_1) = p(6600 < Load < 6840|E_1) = 0.4655 \quad (24)$$

$$p(PEFF|E_2) = p(6600 < Load < 6693|E_2) = 0.2595 \quad (25)$$

$$p(PEFF|E_3) = p(6600 < Load < 6696|E_3) = 0.2665 \quad (26)$$

$$p(PEFF|G_4) = p(6530 < Load < 6770|G_4) = 0.6032 \quad (27)$$

$$p(PEFF|G_5) = p(6379 < Load < 6619|G_5) = 0.5102 \quad (28)$$

Therefore, the probability that SR is partially effective (i.e. only limited portion of allocated SR will be utilized to supply the load demand) over the next hour is as below:

**TABLE 3.** Probability and impact when SR does not meet load variation

| Contingency# | Contingency | Occurrence Probability | Probability of not meeting load | Impact: Load interruption (MW) | Benefit: Load supplied through SR (MW) |
|---|---|---|---|---|---|
| 1 | No Outage | 0.999 | 0.0345 | 51.0 | 240 |
| 2 | Outage of L1321-1322 circuit | $2.5 \times 10^{-4}$ | 0.2405 | 77.2 | 93 |
| 3 | Outage of L1321-1323 circuit | $2.5 \times 10^{-4}$ | 0.2335 | 76.5 | 96 |
| 4 | Tripping of FPOW-5 generator with 70MW capacity | $2.5 \times 10^{-4}$ | 0.0989 | 61.9 | 240 |
| 5 | Tripping of HPOW-5 generator with 221MW capacity | $2.5 \times 10^{-4}$ | 0.4428 | 98.2 | 240 |

**TABLE 4.** Probability and impact when SR is not effective

| Contingency# | Contingency | Occurrence Probability of Contingency | Probability of NEFF SR | Impact: Not utilized SR (MW) | Benefit: Load supplied through SR (MW) |
|---|---|---|---|---|---|
| 1 | No Outage | 0.999 | 0.5 | 240 | 0.0 |
| 2 | Outage of L1321-1322 circuit | $2.5 \times 10^{-4}$ | 0.5 | 240 | 0.0 |
| 3 | Outage of L1321-1323 circuit | $2.5 \times 10^{-4}$ | 0.5 | 240 | 0.0 |
| 4 | Tripping of FPOW-5 generator with 70MW capacity | $2.5 \times 10^{-4}$ | 0.298 | 240 | 0.0 |
| 5 | Tripping of HPOW-5 generator with 221MW capacity | $2.5 \times 10^{-4}$ | 0.047 | 240 | 0.0 |

**TABLE 5.** Probability and impact when SR is partially effective

| Contingency# | Contingency | Occurrence Probability of Contingency | Probability of PEFF SR | Impact: Not-utilized SR (MW) | Benefit: Load supplied through SR (MW) |
|---|---|---|---|---|---|
| 1 | No Outage | 0.999 | 0.4655 | 149.8 | 91.2 |
| 2 | Outage of L1321-1322 circuit | $2.5 \times 10^{-4}$ | 0.2595 | 195.5 | 44.5 |
| 3 | Outage of L1321-1323 circuit | $2.5 \times 10^{-4}$ | 0.2665 | 194.1 | 45.9 |
| 4 | Tripping of FPOW-5 generator with 70MW capacity | $2.5 \times 10^{-4}$ | 0.6032 | 132.5 | 107.5 |
| 5 | Tripping of HPOW-5 generator with 221MW capacity | $2.5 \times 10^{-4}$ | 0.5102 | 95.5 | 144.5 |

$$p(PEFF|Load = 6600MW) = 0.999 \times 0.4652 + 2.5 \times 10^{-4} \times 0.2595 + 2.5 \times 10^{-4} \times 0.2665 + 2.5 \times 10^{-4} \times 0.6032 + 2.5 \times 10^{-4} \times 0.5102 = 0.4651 \quad (29)$$

Figures 7 to 11 shows the amount of SR which is not utilized in contingency 1 to 5, respectively. Considering \$10 per MW hour as expected cost of maintaining SR, the expected impact of partially effective SR is as below:

$$Expected\big(Impact(PEFF|Load = 6600MW)\big) = 1 \times 10 \times (0.999 \times 0.4652 \times 148.8 + 2.5 \times 10^{-4} \times 0.2595 \times 195.5 + 2.5 \times 10^{-4} \times 0.2665 \times 194.1 + 2.5 \times 10^{-4} \times 0.6032 \times 132.5 + 2.5 \times 10^{-4} \times 0.5102 \times 95.5) = \$692.1 \quad (30)$$

The expected benefit which is derived from SR when SR is partially effective is as below:

$$Expected\big(Benefit(NEFF|Load = 6600MW)\big) = 1 \times 20 \times (0.999 \times 0.4652 \times 91.2 + 2.5 \times 10^{-4} \times 0.2595 \times 44.5 + 2.5 \times 10^{-4} \times 0.2665 \times 45.9 + 2.5 \times 10^{-4} \times 0.6032 \times 107.5 + 2.5 \times 10^{-4} \times 0.5102 \times 144.5) = \$848.49 \quad (31)$$

Table 5 summarizes probability of partially effective SR and its associated impact and benefit for each contingency.

**4. 4. Total Risk** Quality of SR can be assessed using a cost-based risk index. Considering three possible types of SR performance (i.e. not-effective, partially-effective, and not-meeting load), expected impact of maintaining 240MW SR under current operating

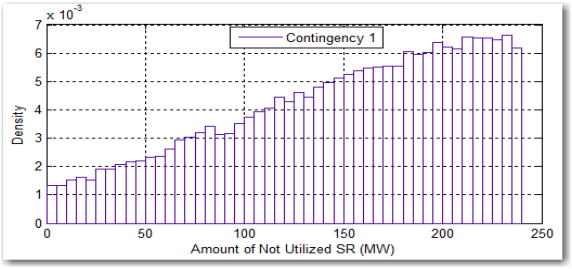


**Figure 7.** Amount of non-effective SR in contingency 1

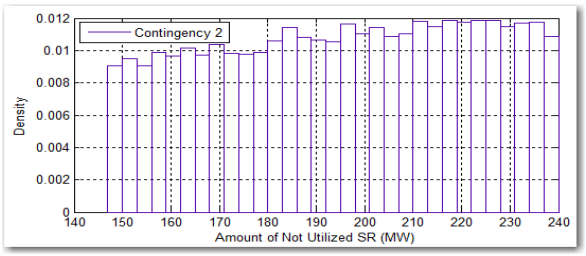


**Figure 8.** Amount of non-effective SR in contingency 2

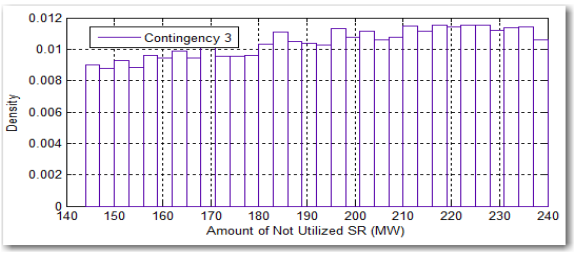


**Figure 9.** Amount of non-effective SR in contingency 3

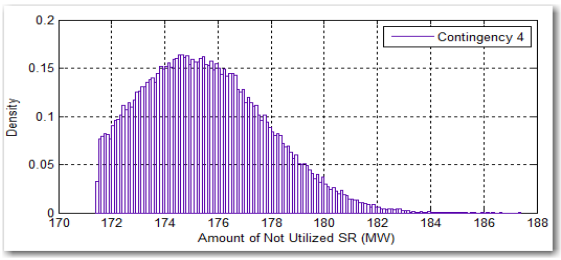


**Figure 10.** Amount of non-effective SR in contingency 4

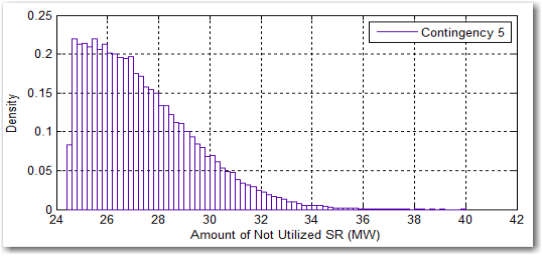


**Figure 11.** Amount of non-effective SR in contingency 5

condition is \$2034 over the next hour which is sum of three parts; i.e. impact of not-effective, impact of partially-effective and impact of not-meeting-load. The expected benefit derived from maintaining 240MW SR is \$1016 over the next hour which is sum of three parts, i.e., benefit derived from not-effective, benefit derived from partially-effective and benefit derived from not-meeting-load.

This implies that total risk associated with maintaining 240MW SR under current operating condition is \$1018 (=\$2034-\$1016). Therefore, maintaining 240MW SR imposes additional cost of \$1018 to the system, hence, \$0.154 additional implicit cost will be added to the cost of 1MW hour of delivered energy. As it is shown in next section, using the proposed procedure, one might consider various level of SR for an operating condition, calculate risks associated with each level of the considered SR, and finally use the calculated risks as indicators for determining the optimal level of SR.

## 5. OPTIMAL LEVEL OF SR

In previous sections it was shown that performance of SR can be calculated through a cost-based risk index. Using this index, the optimal level of SR can be determined such that the calculated risk is either minimum or less than a chosen risk level. Figure 12 shows the flowchart of determining the amount of required SR according to a given desired level of risk. Using this flowchart, a plot of risk associated with different level of SR for the studied system with 6600MW has been depicted in Figure 13.

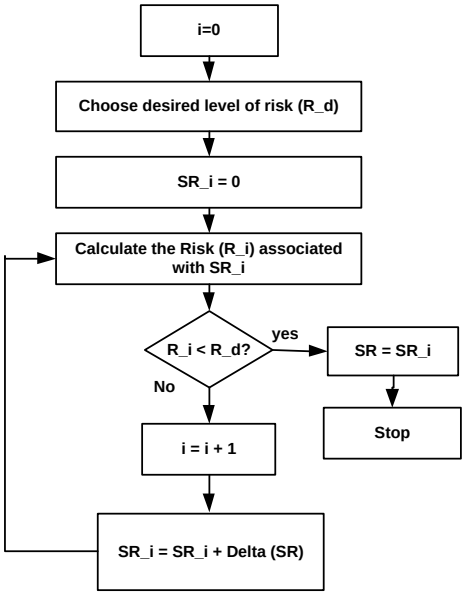


**Figure 12.** Determining the optimal level of SR according to a desired level of risk

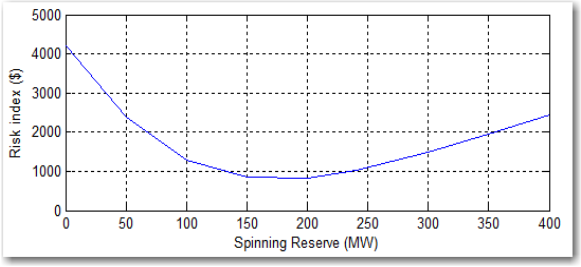


**Figure 13.** Calculated Risk associated with different level of SR

This figure provides a quantitative measurement of efficacy of different level of SR for current operating condition which can be used as a decision-making tool in determining the optimal level of SR. For example, it suggests optimal value of 200MW spinning reserve for the system with an expected total risk of \$831 which adds \$0.126 as additional implicit cost to the cost of 1MW hour of delivered energy. It is worth mentioning that the proposed risk index provides an expectation of future cost associated with the allocated SR; however, it does not guarantee that the future cost of allocating SR is exactly the same as this expectation (one might consider the variance of calculated risk also to make better operational decision about the optimal level of SR requirement).

## 6. CONCLUSION

A cost-based risk index approach for assessing the spinning reserve requirement in a power system is presented in this paper. In order to evaluate the efficacy of the allocated SR for a power system, the performance of SR was classified in three possible types, namely, not-effective, partially-effective, and not-meeting-load. The probability of occurrence of each performance type and its consequences were subsequently computed so that the associated risk could be determined. The flowchart of using the proposed cost-based risk approach for determining the optimal level of spinning reserve was presented. It is shown that the proposed index can be used as an indicator for determining the optimal level of SR in a power system.

## 7. REFERENCES

1. Ye, L., Yao, J., Ouyang, X., Zhu, X. and Yang, S., "Risk analysis and utility function-based decision-making model for spinning reserve allocations." ***IEEE Access***, Vol. 9, (2021), 18752-18761, doi: 10.1109/ACCESS.2021.3054404.
2. Nikolaidis, P. and Poullikkas, A., "A novel cluster-based spinning reserve dynamic model for wind and PV power reinforcement." ***Energy***, Vol. 234, (2021), 121270, doi: 10.1016/j.energy.2021.121270.

3. Basiri, M.H., Sharifi, M.R. and Ostadi, B., "Reliability and risk assessment of electric cable shovel at chadormalu iron ore mine in iran", ***International Journal of Engineering, Transactions A: Basics***, Vol. 33, No. 1, (2020), 170-177, doi: 10.5829/ije.2020.33.01a.20.
4. Malekshah, S., Alhelou, H.H. and Siano, P., "An optimal probabilistic spinning reserve quantification scheme considering frequency dynamic response in smart power environment." ***International Transactions on Electrical Energy Systems***, Vol 31, No. 11, (2021), e13052,doi: 10.1002/2050-7038.13052.
5. Asgari, S., Menhaj, M., Suratgar, A.A. and Kazemi, M., "A disturbance observer based fuzzy feedforward proportional integral load frequency control of microgrids", ***International Journal of Engineering, Transactions A: Basics***, Vol. 34, No. 7, (2021), 1694-1702, doi: 10.5829/ije.2021.34.07a.13.
6. Anstine, L., Burke, R., Casey, J., Holgate, R., John, R. and Stewart, H., "Application of probability methods to the determination of spinning reserve requirements for the pennsylvania-new jersey-maryland interconnection", ***IEEE Transactions on Power Apparatus and Systems***, Vol. 82, No. 68, (1963), 726-735, doi: 10.1109/TPAS.1963.291390.
7. Khoshjahan, M., Dehghanian, P., Moeini-Aghtaie, M. and Fotuhi-Firuzabad, M., "Harnessing ramp capability of spinning reserve services for enhanced power grid flexibility." ***IEEE Transactions on Industry Applications***, Vol. 55, No. 6, (2019), 7103-7112, doi: 10.1109/TIA.2019.2921946.
8. Ansari, J. and Malekshah, S., "A joint energy and reserve scheduling framework based on network reliability using smart grids applications", ***International Transactions on Electrical Energy Systems***, Vol. 29, No. 11, (2019), e12096, doi: 10.1002/2050-7038.12096.
9. Amirahmadi, M. and Akbari Foroud, A., "A new approach to locational pricing and settlement of day-ahead spinning reserve market", ***International Transactions on Electrical Energy Systems***, Vol. 26, No. 1, (2016), 155-174, doi: 10.1002/etep.2078.
10. Bhattacharya, B., Chakraborty, N. and Mandal, K.K., "A cost-optimized power management strategy for combined wind thermal–pumped hydro generation considering wind power uncertainty", ***International Transactions on Electrical Energy Systems***, Vol. 29, No. 7, (2019), e12104, doi: 10.1002/2050-7038.12104.
11. Gupta, A., Verma, Y.P. and Chauhan, A., "Financial analysis of reactive power procurement in pool-based deregulated power market integrated with dfig-based wind farms", ***International Transactions on Electrical Energy Systems***, Vol. 29, No. 3, (2019), e2739, doi: 10.1002/etep.2739.
12. Zhang, L., Yuan, Y., Yuan, X., Chen, B., Su, D. and Li, Q., "Spinning reserve requirements optimization based on an improved multiscenario risk analysis method", ***Mathematical Problems in Engineering***, Vol. 2017, (2017),doi: 10.1155/2017/6510213.
13. Emarati, M., Keynia, F. and Rashidinejad, M., "A two-stage stochastic programming framework for risk-based day-ahead operation of a virtual power plant", ***International Transactions on Electrical Energy Systems***, Vol. 30, No. 3, (2020), e12255, doi: 10.1002/2050-7038.12255.
14. Datta, S. and Vittal, V., "Operational risk metric for dynamic security assessment of renewable generation", ***IEEE Transactions on Power Systems***, Vol. 32, No. 2, (2016), 1389-1399, doi: 10.1109/TPWRS.2016.2577500.
15. Wang, Y., Vittal, V., Abdi-Khorsand, M. and Singh, C., "Probabilistic reliability evaluation including adequacy and dynamic security assessment", ***IEEE Transactions on Power Systems***, Vol. 35, No. 1, (2019), 551-559, doi: 10.1109/TPWRS.2019.2923844.
16. Jabari, F., Shamizadeh, M. and Mohammadi-Ivatloo, B., "Risk-constrained day-ahead economic and environmental dispatch of thermal units using information gap decision theory", ***International Transactions on Electrical Energy Systems***, Vol. 29, No. 2, (2019), e2704, doi: 10.1002/etep.2704.
17. De Caro, F., Vaccaro, A. and Villacci, D., "A markov chain-based model for wind power prediction in congested electrical grids", ***The Journal of Engineering***, Vol. 2019, No. 18, (2019), 4961-4964, doi: 10.1049/joe.2018.9247.
18. Wang, Y., "Probabilistic spinning reserve adequacy evaluation for generating systems using an markov chain monte carlo-integrated cross-entropy method", ***IET Generation, Transmission & Distribution***, Vol. 9, No. 8, (2015), 719-726, doi: 10.1049/iet-gtd.2014.0763.
19. Rajabdorri, M., Sigrist, L., Lobato, E., Prats, M.D.C. and Echavarren, F.M., "Viability of providing spinning reserves by RES in Spanish island power systems." ***IET Renewable Power Generation***, Vol. 15, No. 13 (2021), 2878-2890,doi: 10.1049/rpg2.12216.
20. Bento, M.E. and Ramos, R.A., "An approach for monitoring and updating the load margin of power systems in dynamic security assessment", ***Electric Power Systems Research***, Vol. 198,, (2021), 107365, doi: 10.1016/j.epsr.2021.107365.
21. Bento, M.E., "Monitoring of the power system load margin based on a machine learning technique", ***Electrical Engineering***, Vol. 104, No. 1, (2022), 249-258, doi: 10.1007/978-0-387-32935-2

Persian Abstract

**چکیده**

یکی از مرسوم ترین روشها برای ایجاد تعادل بین تولید و مصرف به هنگام عدم قطعیت در شبکه استفاده از رزرو چرخان است. روشهای قطعی و احتمالی مختلفی برای تعیین مقدار رزرو چرخان در مقالات مختلف ارایه شده است. انتخاب روش مناسب از بین روشهای موجود برای تعیین مقدار رزرو چرخان همواره یک چالش برای اپراتور شبکه است چرا که ممکن است رزرو چرخان انتخاب شده باعث اطمینان کاذب برای اپراتور شبکه از نقطه نظر عملکرد پایدار و مطمین شبکه گردد. در این مقاله یک روش مبتنی بر ریسک–هزینه برای ارزیابی رزرو چرخان ارایه شده است. برای این کار کارایی رزرو چرخان به سه دسته غیر موثر، نسبتا موثر و ناکافی تقسیم شده است. سپس احتمال و پیامد هر کدام از این سه دسته محاسبه شده و در نهایت ریسک مرتبط با رزرو چرخان های مختلف مشخص شده است. همچنین نشان داده شده است که با استفاده از روش ارایه شده در این مقاله می‌توان مقادیر مختلفی رزرو چرخان در نظر گرفته و ریسک مرتبط با هر رزرو را محاسبه کرده و از آن برای تعیین مقدار بهینه رزرو چرخان استفاده کرد. بعنوان مثال برای شبکه مورد مطالعه با ٦٦٠٠ مگاوات بار نشان داده شده است که ٢٤٠ مگاوات رزرو چرخان باعث افزایش قیمت انرژی به اندازه ٠.١٥٤ $/MWh خواهد شد در حالیکه مقدار بهینه ٢٠٠ مگاوات رزرو چرخان تنها ٠.١٢٦ $/MWh قیمت انرژی را افرایش می‌دهد. روش ارایه شده در این مقاله را می‌توان برای مقایسه روشهای مختلف تعیین رزرو چرخان نیز استفاده کرد.

International Journal of Engineering

Journal Homepage: www.ije.ir

# Data Consumption Analysis by Two Ordinal Multivariate Control Charts

A. Hakimi[a], H. Farughi*[a], A. Amiri[b], J. Arkat[a]

[a] *Department of Industrial Engineering, Faculty of Engineering, University of Kurdistan, Sanandaj, Iran*
[b] *Department of Industrial Engineering, Faculty of Engineering, Shahed University, Tehran, Iran*

*PAPER INFO*

*Paper history:*
Received 01 Febraury 2022
Received in revised form 01 August 2022
Accepted 28 August 2022

*Keywords*:
*Statistical Process Monitoring*
*Ordinal Multivariate Processes*
*Data Consumption*
*Customer Behavior*

*ABSTRACT*

The process quality is described by one or more important factors called multivariate processes. Contingency tables used to demonstrate the relevance between these factors and modeled by log-linear model. There are also two types of statistical variables that are nominal and ordinal. In this paper, the variables are ordinal and two new control charts have been used to monitor the process of analyzing subscribers' consumption. These two multivariate ordinal chart are the MR chart and the multivariate ordinal categorical (MOC) used to monitor processes based on the ordinal log-linear model in Phase II. In addition, with a real numerical example, about analyzing the internet usage of mobile subscribers, two control charts are drawn and compared with each other in terms of average run length. In this case, we focus on customer behavior and in real action, by marketing department, changing in data consumption has been seen and analyzed. The study of the two proposed charts was performed using simulation based on real example in different situation, and the MOC performed relatively better.

***doi**: 10.5829/ije.2022.35.11b.14*

## 1. INTRODUCTION

Multivariate processes have many applications in today's world, both in manufacturing organizations and in services. By increasing such processes, the importance of monitoring them also increased and different methods were suggested to them [1]. There are generally two forms of log-linear models, which are the nominal log-linear model (NMLLM) and ordinal log-linear model (OLLM), associates the expected frequency of multivariate categorical characteristic with two or more variables. The multivariate ordinal processes include more than one ordered factor, for which multivariate categorical control charts based on the OLLM are used. Statistical Process Monitoring (SPM) uses contingency tables to monitor multivariate category processes simultaneously [2]. As well as, OLLM used to demonstrate the relevance between ordinal variables and correlative observations in an ordinal contingency table (OCT) cell. Thus, Yamamoto and Morakami [3] proposed the square OCT model, this study also considered the assumption of an unbalanced normal distribution applied to dental caries.

Many researches have also been done on multivariate monitoring processes, for example: Maleki et al. [4] proposed chart to monitor multivariate process mean and variation simultaneous in the existence of measurement error with linearly increasing variance under additive covariate model. Rasay et al. [5] explained and extended multivariate control charts applications for condition-based maintenance. Khedmati et al. [6] proposed auto-regressive integrated moving average and machine learning approaches for forecasting Bitcoin price. A generalized likelihood ratio test (GLRT) proposed by Li et al. [7] for monitoring multivariate categorical processes, in phase II. They proposed the EWMA-GLRT to improve the GLRT chart performance for detecting small shifts. In another related research, an integrated multivariate spatial-sign test with EWMA procedure proposed to monitor the model parameters of the multivariate nonparametric processes in phase II [8]. Li et al. [9] proposed a new multivariate categorical statistic based on binomial/multinomial by considering the

*Corresponding Author Institutional Email: h.farughi@uok.ac.ir
(H. Farughi)

Please cite this article as: A. Hakimi, H. Farughi, A. Amiri, J. Arkat, Data Consumption Analysis by Two Ordinal Multivariate Control Charts, ***International Journal of Engineering, Transactions B: Applications***, Vol. 35, No. 11, (2022) 2196-2204

correlation between categorical variables. In phase II, they showed that the proposed control chart was robust to detect different shifts. Afterwards, the GLT statistic proposed to monitor multivariate processes in phase-II by Kamranrad et al. [2]. As well as, GLT is mixed with an EWMA statistic to enhance performance in small and medium shifts.

For monitoring categorical ordinal processes, Li et al. [10] proposed a new ordinal categorical control chart to determine changes in univariate ordinal processes in phase-II. Furthermore, they comparison that method with two charts and they showed this new method had good performances. Wang et al. [11] proposed two control chart for monitoring multivariate ordinal process (MOP) in phase II, which one of them is MOC chart, based OLLM. On that research, it was shown the MOC chart performed better than the LMBM chart. New multivariate ordinal based method known as multivariate ordinal-normal statistic (MONS) became brought by Hakimi et al. [12]. Additionally, the performance of the MONS approach became in comparison with the MG-p technique and outcomes showed the superiority of the MONS method under the small and slight shifts in OLLM parameters. Furthermore, Hakimi et al. [13] proposed MR statistic which is develop R statistic by Li et al, [10] and they showed have good performance to detect shifts. In addition, in phase I, one research has been done by Hakimi et al. [14], which used MR and LRT methods for estimating OLLM parameters. In this article, they monitor drug dissolution process as case study.

According to reviews by the authors, there are few studies in the field of monitoring the MOP. This paper aims to use two statistics for monitoring ordinal process. Ramakrishnan and Pecht [15] proposed a methodology life consumption monitoring for electronic systems. Our chosen process is about data consumption and subscriber consumption analysis is one of the most important indicators [16]. On the other hand, some research have been done on behavior's customer in mobile network field. Mehrotra et al. [17] analyze power consumption via mobile applications by using fuzzy clustering approach. Sarker [18] a machine learning based robust prediction model proposed for real-life mobile phone data. Jiang et al. [19] did the analysis by big data based network behavior insight of cellular networks applications of industry 4.0. Zhao et al. [20] proposed a method for monitoring data based by bottom-up modeling and its application for energy consumption prediction of campus building.

According to the studies summarized in Table 1, some of which are mentioned above, few articles have been done in the field of MOP. On the other hand, examining a real process in an up-to-date field such as internet use by subscriber can arouse the desire among researchers to conduct more research in this field. Moreover, the following bullet points can be identified

**TABLE 1.** Related works in multivariate process

| Reference No. | Phase | Univariate/ Multivariate | Ordinal/ Nominal |
|---|---|---|---|
| [2] | II | Multivariate | Nominal |
| [7], [8], [9] | I , II | Multivariate | Nominal |
| [10] | II | Univariate | Ordinal |
| [11], [12], [13] | II | Multivariate | Ordinal |
| [14] | I | Multivariate | Ordinal |

for the innovation of this paper:

- Comparing two charts for an ordinal multivariate process (It should be noted that these two charts were not compared with each other until now and both have recently been generalized)
- Using a real and up-to-date case study to compare charts and analyze them

The rest of the article is organized as follows. In next section the MOP is described, then in section 3, control charts for that process described one by one. In section 4, we describe the case study and analyze those charts for that. And at the end, we have mentioned conclusions and suggestions for future research.

## 2. MULTIVARIATE ORDINAL PROCESS

The MOP has at least two factors with more than one ordered level known as OCT. The OLLM is used to analyze the OCT. The OLLM demonstrates the main and interaction effects between ordinal factors; hence, it is applied to propose multivariate ordinal control charts. In fact, the OCT displaying a simultaneous relationship between two or more ordinal variables. $p$ variables such as $y_1, y_2, \ldots, y_p$ consider each with $h_i, i = 1, 2, \ldots, p$ conceivable levels. Hence, the table cells demonstrate $h_1 \times h_2 \times \ldots \times h_p$ the value of possible frequencies (for more information refered to cited literature [2]). OLLM has been introduced in the literature to model the relationship between the level of an ordinal factor and its corresponding number in each cell. Assume the contingency table with two ordinal variables $(y_1, y_2)$ with $h_1$ and $h_2$ levels. Thus, the OLLM is defined as the Equation (1):

$$\log \mu_{ij} = \mu + \alpha_i + \beta_j + \varphi(u_i - \bar{u})(v_j - \bar{v}), \quad (1)$$

where $\mu_{ij}$ is the mean value of observations for cell (*i*,*j*) and calculated by $\mu_{ij} = N\pi_{ij}$ , which N is count cells in contingency table and $\boldsymbol{\pi}_{ij}$ is probably of occurs cells (for more information refered to cited literature [12]). Therefore, $\mu$ is the constant effect, $\alpha_i$ and $\beta_j$ are the main effect of the *i*th row and *j*th column, respectively.

In addition, $\varphi$ is defined as linear by linear interaction parameter in OLLM, which can be estimated by the Equation (2):

$$\log\left(\frac{\mu_{ij}\ \mu_{i+1,j+1}}{\mu_{i,j+1}\mu_{i+1,j}}\right)=\varphi(u_i-u_{i+1})(v_j-v_{j+1}), \quad (2)$$

where, $(u_i-u_{i+1})=1$ and $(v_j-v_{j+1})=1$. Notice that, parameters at OLLM in phase I can be estimated by iterative Newton's single-dimensional algorithm (for more information refered to cited literature [18, 19]).

For more than two variables, the OLLM with $p$ factors is defined as Equation (3):

$$\begin{aligned} Log\ \boldsymbol{\mu} = \beta_0+\beta_1 y_1+\cdots+\beta_p y_p+\beta_{12}(y_1-\overline{y_1})(y_2-\overline{y_2})+\cdots+\beta_{1p}(y_1-\overline{y_1})(y_p-\overline{y_p})+\beta_{2p}(y_2-\overline{y_2})(y_p-\overline{y_p})+\cdots+\beta_{p-1,p}(y_{p-1}-\bar{y}_{p-1})(y_p-\overline{y_p})+\\ \cdots+\varphi(y_1-\overline{y_1})\dots(y_{p-1}-\bar{y}_{p-1})(y_p-\overline{y_p}) \end{aligned} \quad (3)$$

where $\overline{y}_i$; $(i=1,2,..,p)$ is the average of the $i$th ordinal variable.

## 3. MULTIVARIATE ORDINAL CONTROL CHARTS

Wang et al. [11] proposed two control charts for monitoring multivariate ordinal processes, one of which was the chart presented by Li et al. [10]. This control chart has been used and compared under the Log-linear Multivariate Binomial/Multinomial (LMBM) in their paper. In addition, they presented another multivariate control chart called the Multivariate Ordinal Categorical (MOC), which showed that the MOC chart performed better in all shifts. Hakimi et al. [12, 13] also generalized three multivariate control chart statistics to monitor this type of process. These three statistics proposed by Li et al. [10] for univariate processes. One of them was the generalized multivariate generalized-p, which was integrated with EWMA statistics. Another statistic called multivariate ordinal-normal statistic (MONS) was presented by Hakimi et al. [12] showed that this statistic performs better than the generalized-p chart in small and medium shifts. Furthermore, Hakimi et al. [13] proposed a new control chart and they called MR statistic, which has better performance in these three charts. In this article, we intend to compare the best methods from these two articles that means bt Wang et al. [11] and Hakimi et al. [13], namely MOC and MR chart. Therefore, we should first explain how to calculate each statistic in below and the flowchart of monitoring multivariate control chart with categorical ordinal data is illustrated in Figure 1.

**3. 1. MR Control Chart** Hakimi et al. [13] proposed this statistic and showed that it has better performance rather than others. $p$-way OCT consider ($p$-ordinal variables) each with $h_1$, $h_2$,…, $h_p$ levels. Hence,

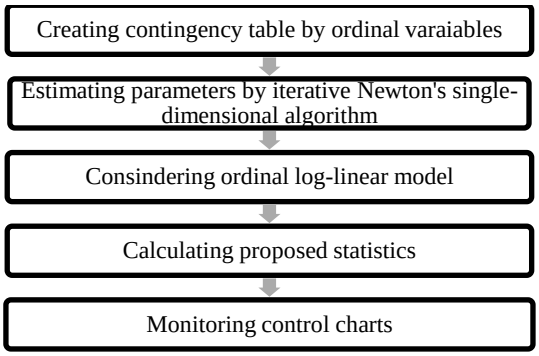


**Figure 1.** The flowchart of monitoring ordinal multivariate control chart

the known in-control (IC) probabilities for the ordinal cell is calculate by following equation:

$$\pi^{(0)}_{ijk\dots p}=\frac{f(i,j,k,...,p)}{\sum_{i=1}^{h_1}\sum_{j=1}^{h_2}\sum_{k=1}^{h_3}\dots\sum_{p=1}^{h_p}f(i,j,k,...,p)} \quad (4)$$

where, $f(i,j,k,...,p)$ is the abundance in the cell $(i,j,k,\dots,p)$. Thus, the MR statistic for each time is defined by Equation (5):

$$MR_t=\left|\sum_{i=1}^{h_1}\sum_{j=1}^{h_2}\sum_{k=1}^{h_3}\dots\sum_{p=1}^{h_p}(F^{(0)}_{ijk\dots p-1}+F^{(0)}_{ijk\dots p}-1)z_{ijk\dots p}\right|, \quad (5)$$

where, $F^{(0)}_{ijk\dots p}=\sum_{i=1}^{h_1}\sum_{j=1}^{h_2}\sum_{k=1}^{h_3}\dots\sum_{p=1}^{h_p}\pi^{(0)}_{ijk\dots p}$. In addition, $\mathbf{z}_t$ is:

$$\mathbf{z}_t=a^{-1}_{0,t,\lambda}\sum_{s=1}^{t}(1-\lambda)^{t-s}\mathbf{n}_t, \quad (6)$$

where, $a^{-1}_{t_1,t_2,\lambda}=\sum_{t=t_1+1}^{t_2}(1-\lambda)^{t_2-t_1}$ and

$\boldsymbol{n}_t=[n_{111\dots1t},n_{112\dots1t},\dots,n_{11h_3\dots h_pt},n_{121\dots1t},\dots,n_{12h_3\dots h_pt},\dots,n_{h_1h_21\dots1t},\dots,n_{h_1h_2h_3\dots h_pt}]$

Pseudo-code for $MR_t$ calculated:

*Step1:* Consider a $p$ way matrix which each cell has a number called f(i,j,..,p).
*Step2:* Calculate $\pi^{(0)}$ for each cell by Equation (4), then calculate $F^{(0)}$.
*Step3:* Consider $\mathbf{n_t}$ and calculate $a^{-1}$ by specified λ, then calculate $\mathbf{z_t}$ by Equation (6).
*Step4:* Finally, compute $MR_t$ by Equation (5).

Also, if $UCL_1$ indicates the upper limit of MR chart, we set $MR_t>UCL_1$ and this is done by simulation.

**3. 2. MOC Control Chart** As mentioned, Wang et al. [11] presented this control chart for monitoring multivariate ordinal processes, which we want to describe here. Assuming a ordinal contingency table that has p ordinal variables and each levels $h_1$, $h_2$,…,$h_p$, the statistics they use are calculated according to the following equation:

$$R_t = \frac{1}{N}\left(z_t - Np^{(0)}\right)^T Y\left(Y^T \Lambda^{(0)} Y\right)^{-1} Y^T \left(z_t - Np^{(0)}\right) \quad (7)$$

In equation (7), N represents the total number of samples and $z_t$ is actually a vector based on EWMA, which is calculated as follows:

$$\boldsymbol{z}_t = (1-\lambda) z_{t-1} + \lambda n_t \quad (8)$$

We also know that $0 < \lambda \leq 1$. In Equation (8) the vector $n_t$ represents the sample vector, same as MR statistic.

In Equation (7), $p^{(0)}$ the probability vector is in the controlled state which has dimensions of $1 \times h$. Y is also a vector for contingency table elements (refer to literature[11] for more information). The variance matrix $\Lambda^{(0)}$ is also calculated using the reference [21] IC state in Equation (9) as follows:

$$\Lambda^{(0)} = diag\left(p^{(0)}\right) - p^{(0)} p^{T(0)} \quad (9)$$

In the above equation, daig(x) means a square matrix with x values on its original diameter, and finally it is necessary to calculate the value of the upper limit of control of this chart.

Pseudo-code for $R_t$ calculated:

*Step1:* Consider a *p* way matrix and N is the total number of samples.
*Step2:* Consider $\mathbf{n_t}$ and calculate $\mathbf{z_t}$ by specified λ in equation (8), as well as, $z_0$ is a vector with values of one.
*Step3:* Consider $p^{(0)}$ the probability vector and calculate Y and $\Lambda^{(0)}$ by equation (9).
*Step4:* At the end, calculate $R_t$ by equation (7).

If $UCL_2$ indicates the upper limit of this chart, we set $R_t > UCL_2$ and this is done by simulation.

## 4. DATA CONSUMPTION ANALYSIS

In this section, we have presented a real example which is based on given examples by Agresti [21]. In companies offering data SIM cards, an important characteristic is the amount of data consumption (that mean the volume of Internet consumption) because the amount of repurchase of data packages is directly related to it. Some research focus on usage in mobile networks and analyze that by new methods like machine learning and big data (For additionl information see literature [17, 18]). On the other hand, marketing department in that companies try to increase their customers and offer plans to retain subscribers. As a case study, we set up a mobile virtual network operator (MVNO) company to monitor data usage and we will analyze the effects of marketing department offers on customer behavior. The company, which has more than half a million subscribers, wants to analyze the behavior of its subscribers. To do this, in the next section, a sample of subscribers is taken and analyzed. In this analysis, we want to discover the changes made and measure the changes using the control charts proposed in the previous section.

**4. 1. Select and Categorize Data** Here we are dealing with a large number of subscribers and we have to choose a good example of them. The number of samples with stratified sampling method and calculated by Equation (10) (based on Zhao et al. [23]):

$$n = \frac{\left(\sum_{l=1}^{L} N_l.\sigma_l\right)^2}{\sigma^2 + \sum_{l=1}^{L} N_l.\sigma_l^2} \quad (10)$$

where $N_l$ and $\sigma_l$ are the number and standard deviation of each stratum, respectively and $\sigma^2$ is the variance of the total data set. After that calculation and with roundup numbers received to 2,000 subscribers to monitor the data consumption behavior who have entered the network within a period of one month. Here are three variables: Ages, education level, and data usage over a period for all of these subscribers. For the subscribers' age, three levels are considered young (less than 24 years), middle-aged (between 24 and 35 years), and old (more than 35 years). Also, for the education level, two levels of diploma (which includes diploma and lower) and higher education (which includes students and university graduates) and for data consumption in a period of time, three levels of low consumption (less than 1 GB), Medium consumption (between 1 to 3 GB) and high consumption (more than 3 GB) are considered. The following table shows the number of subscribers for each level:

**TABLE 2.** OCT for data consumption behavior of 2,000 subscribers

| | **Ages** | | | | | | | |
|---|---|---|---|---|---|---|---|---|
| | Young | | Middle-Aged | | Older | | | |
| | **Education Level** | | | | | | | |
| **Data Usage (GB)** | Diploma | Higher education | Diploma | Higher education | Diploma | Higher education | Total | Percentage |
| Low consumption | 106 | 127 | 101 | 99 | 90 | 102 | 625 | 31.3% |
| Medium consumption | 121 | 133 | 131 | 125 | 66 | 121 | 697 | 34.9% |
| High consumption | 139 | 155 | 125 | 112 | 57 | 90 | 678 | 33.9% |
| Total | 366 | 415 | 357 | 336 | 213 | 313 | 2000 | 100% |

Also, the covariance matrix used for the ordinal log-linear model estimates is as follows:

$$\text{cov}(\boldsymbol{\beta}) = \{\mathbf{X}'[\mathbf{diag}(\boldsymbol{\mu}) - \boldsymbol{\mu}\boldsymbol{\mu}'/N]\mathbf{X}\}^{-1}, \quad (11)$$

where $\boldsymbol{\mu}$ and $\mathbf{X}$ are the mean counts' vector and matrix values of the contingency table cells, respectively. As well as, $\mathbf{diag}(\boldsymbol{\mu})$ is a matrix that diagonal and show mean of the contingency table cells [21]. Moreover, the IC parameter vector of the OLLM is assumed (based on Zafar [22]):

$$\boldsymbol{\beta} = [1, -0.5, -0.5, -0.5, 0.15, 0.15, 0.15, -0.025]$$

Besides, the IC standard deviations for this example are as follows:

$$\hat{\boldsymbol{\sigma}}_{0\boldsymbol{\beta}} = [2.09, 1.34, 1.31, 1.33, 0.79, 0.75, 0.77, 0.28]$$

The OLLM for OCT with three ordinal factors, including ages ($A$), education level ($E$), and data usage (D) under the IC condition is defined as Equation (12):

$$\text{Log}\,\boldsymbol{\mu} = 1 - 0.5A - 0.5E - 0.5D + 0.15(A - \bar{A})(E - \bar{E}) + 0.15(A - \bar{A})(D - \bar{D}) + 0.15(D - \bar{D})(E - \bar{E}) - 0.025(A - \bar{A})(E - \bar{E})(D - \bar{D});\ A = 1,2,3\ , E = 1,2\ , D = 1,2,3. \quad (12)$$

The UCLs of the MR and MOC charts in this contingency table are calculated equal to 37.2095 and 36.7201, respectively, that set through 10,000 simulation when $ARL_0$=370. All the simulations in this article and figures have been done and drawn by MATLAB software. Next, we want to be able to examine these control charts for this issue. This review is displayed in two modes: by changing the parameters and based on reality.

**4. 2. The Charts Performance When Parameters Change** In this subsection, we want to compare the two control charts presented in the previous section under the same conditions by simulating them. This comparison is made in phase II, so the measure of the average run length ($ARL_1$) in OC conditions.

Some comparisons, by change in some parameters, of these two charts is shown in the following tables:

In Tables 3 to 6 you can see, the $ARL_1$ values of the MOC chart are slightly smaller than MR's chart under small shifts. However, in medium and large shifts the performance is similar and sometimes the MR chart is better. Hence, the MOC chart works a little better compared to the MR in these mentioned shifts. Also, the value of λ has a relatively better performance in finding larger changes with a value of 0.2 compared to 0.1, but for small shifts, the average value of 0.1 has a shorter run length and can be detected sooner. Also, the parameter $\beta_1$ is more sensitive to shifts than other parameters and the width parameter from the origin is relatively less sensitive. Note that, the $\boldsymbol{\delta}$ value has been changed by parameter in the tables to better identify the evaluation rate in each one. Accordingly, the rest of the simulations have been by various simultaneous shifts of OLLM parameters based on λ = 0.15, some of which are shown in Figures 2 to 5.

**TABLE 3.** $ARL_1$ values and standard deviations in parentheses under the different shifts in the intercept ($\beta_0 + \delta.\sigma_{\beta_0}$)

| λ | $\delta$ | -1 | -0.75 | -0.5 | -0.25 | -0.1 | +0.1 | +0.25 | +0.5 | +0.75 | +1 |
|---|---|---|---|---|---|---|---|---|---|---|---|
| 0.1 | MR | 1.08 (0.04) | 24.03 (1.22) | 75.90 (1.61) | 188.72 (2.78) | 242.81 (3.01) | 240.04 (3.02) | 189.23 (2.71) | 79.24 (1.61) | 22.67 (1.21) | 1.05 (0.04) |
| | MOC | 1.03 (0.02) | 26.11 (1.18) | 76.82 (1.56) | 187.79 (2.68) | 224.06 (2.99) | 223.95 (2.99) | 185.56 (2.53) | 77.31 (1.62) | 23.10 (1.24) | 1.00 (0.02) |
| 0.2 | MR | 1.00 (0.01) | 25.39 (1.19) | 76.65 (1.63) | 193.11 (2.57) | 249.75 (3.01) | 249.01 (3.03) | 192.09 (2.82) | 78.33 (1.59) | 20.22 (1.21) | 1.00 (0.01) |
| | MOC | 1.00 (0.01) | 23.27 (1.09) | 75.44 (1.53) | 191.65 (2.48) | 232.79 (3.01) | 231.22 (3.00) | 190.17 (2.69) | 77.02 (1.57) | 20.53 (1.32) | 1.00 (0.00) |

**TABLE 4.** $ARL_1$ values and standard deviations in parentheses under the different shifts in A coefficient ($\beta_1 + \delta.\sigma_{\beta_1}$)

| λ | $\delta$ | -0.75 | -0.5 | -0.25 | -0.1 | -0.05 | +0.05 | +0.1 | +0.25 | +0.5 | +0.75 |
|---|---|---|---|---|---|---|---|---|---|---|---|
| 0.1 | MR | 1.00 (0.00) | 9.72 (1.00) | 37.12 (1.32) | 125.07 (2.21) | 202.61 (3.05) | 201.47 (3.00) | 122.45 (2.33) | 35.32 (1.29) | 7.09 (0.97) | 1.00 (0.00) |
| | MOC | 1.00 (0.00) | 9.91 (0.89) | 36.27 (1.27) | 121.45 (2.35) | 205.05 (3.03) | 203.23 (3.00) | 118.29 (2.15) | 33.92 (1.29) | 7.02 (0.89) | 1.00 (0.00) |
| 0.2 | MR | 1.00 (0.00) | 8.04 (0.68) | 35.81 (1.19) | 120.77 (2.26) | 204.79 (3.06) | 203.29 (3.04) | 122.99 (2.61) | 37.82 (1.26) | 8.00 (0.77) | 1.00 (0.00) |
| | MOC | 1.00 (0.00) | 8.05 (0.66) | 35.92 (1.25) | 119.93 (2.22) | 206.09 (3.03) | 204.97 (3.02) | 119.87 (2.56) | 35.73 (1.31) | 8.03 (0.69) | 1.00 (0.00) |

**TABLE 5.** $ARL_1$ values and standard deviations in parentheses under the different shifts in E,D coefficient $(\beta_{23} + \delta.\sigma_{\beta_{23}})$

| λ | δ | -0.75 | -0.5 | -0.25 | -0.1 | -0.05 | +0.05 | +0.1 | +0.25 | +0.5 | +0.75 |
|---|---|---|---|---|---|---|---|---|---|---|---|
| 0.1 | MR | 1.00 (0.00) | 9.04 (0.99) | 41.02 (1.40) | 129.34 (2.31) | 211.79 (3.03) | 209.54 (3.01) | 128.09 (2.24) | 40.35 (1.31) | 8.81 (0.83) | 1.00 (0.00) |
| | MOC | 1.00 (0.01) | 9.31 (0.87) | 39.95 (1.36) | 129.56 (2.36) | 208.00 (3.01) | 207.89 (3.01) | 124.99 (2.27) | 39.91 (1.30) | 8.37 (0.81) | 1.00 (0.00) |
| 0.2 | MR | 1.00 (0.00) | 8.95 (0.99) | 39.25 (1.39) | 130.27 (2.41) | 209.23 (3.03) | 210.08 (3.02) | 129.37 (2.31) | 38.39 (1.38) | 8.91 (0.79) | 1.00 (0.00) |
| | MOC | 1.00 (0.00) | 8.91 (0.93) | 39.07 (1.36) | 131.51 (2.38) | 211.79 (3.00) | 210.46 (3.01) | 128.88 (2.30) | 37.06 (1.32) | 8.73 (0.68) | 1.00 (0.00) |

**TABLE 6.** $ARL_1$ values and standard deviations in parentheses under the different shifts in A,E,D coefficient $(\varphi + \delta.\sigma_{\varphi})$

| λ | δ | -0.5 | -0.25 | -0.1 | -0.05 | -0.02 | +0.02 | +0.05 | +0.1 | +0.25 | +0.5 |
|---|---|---|---|---|---|---|---|---|---|---|---|
| 0.1 | MR | 1.00 (0.02) | 11.00 (1.01) | 42.26 (1.41) | 131.15 (2.39) | 211.06 (3.04) | 212.92 (3.03) | 130.67 (2.32) | 41.90 (1.32) | 10.03 (0.88) | 1.00 (0.00) |
| | MOC | 1.00 (0.02) | 11.02 (0.99) | 40.93 (1.35) | 130.87 (2.33) | 211.77 (3.03) | 209.80 (3.01) | 129.92 (2.25) | 40.07 (1.31) | 10.11 (0.89) | 1.00 (0.00) |
| 0.2 | MR | 1.00 (0.00) | 10.13 (0.98) | 38.21 (1.28) | 129.03 (2.32) | 212.65 (3.05) | 215.71 (3.03) | 128.64 (2.20) | 39.79 (1.30) | 9.12 (0.71) | 1.00 (0.00) |
| | MOC | 1.00 (0.00) | 10.21 (0.91) | 39.24 (1.31) | 129.05 (2.30) | 212.09 (3.04) | 211.68 (3.03) | 128.05 (2.24) | 39.44 (1.30) | 9.09 (0.70) | 1.00 (0.00) |

Figures 2 to 5 show the MR and MOC control charts efficiency under shifts in $\beta_2$ and $\varphi$. The OC alarms by the MR and MOC control charts happen at the 36th and 34th observation under $-0.25\sigma_{\beta_2}$ shift in $\beta_2$ and 51st and 47th observation under $0.1\sigma_{\varphi}$ shift in $\varphi$, respectively. Note that we chose different values for two separate parameters to show a fair comparison for these two charts. Nevertheless, the results demonstrate that the MOC control chart find the OC situation sooner.

**4. 3. The Charts Performance Based on Actual Change** Following this review, the company decided to design and send promotions to subscribers who belong to the low-consumption category. After two

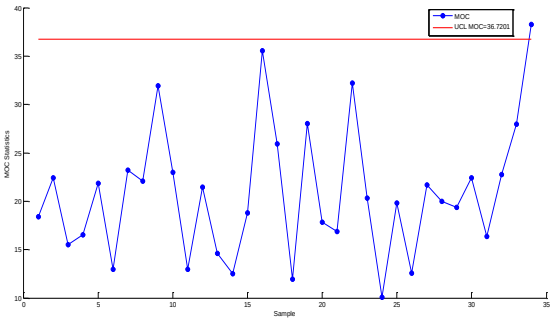


**Figure 3.** Performance of MOC control chart under $-0.1\sigma_{\beta_2}$ shift in $\beta_2$

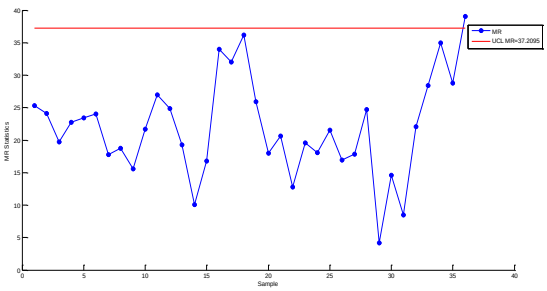


**Figure 2.** Performance of MR control chart under $-0.1\sigma_{\beta_2}$ shift in $\beta_2$

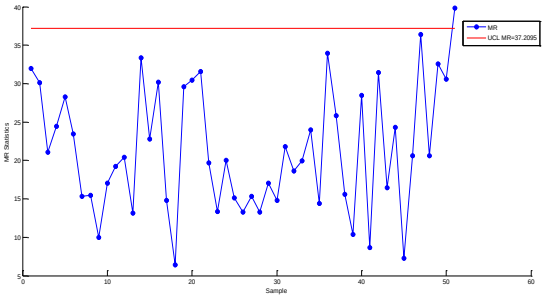


**Figure 4.** Performance of MR control chart under $0.1\sigma_{\varphi}$ shift in $\varphi$

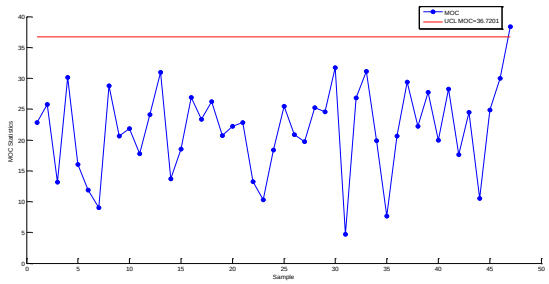


**Figure 5.** Performance of MOC control chart under $0.1\sigma_\varphi$ shift in $\varphi$

months, the above survey was conducted again for those 2000 subscribers, during which 1973 subscribers remained in the network, and the number and classification of these subscribers were as Table 7:

The above table shows that the company's promotions have responded, and the percentage of low-consumption subscribers has decreased compared to two months ago. However, the important thing for us is how the proposed control charts show the state of being out of control in a few samples, because in the second table, the average of the cells in the contingency table has changed and process is OC. Therefore, we want to examine the $ARL_1$ between the two proposed charts. The $ARL_1$ of these two charts shows the OC signals happen at the $7^{th}$ and $6^{th}$ sample in the MR and MOC control charts. Since the information in Table 1 is updated every week, a point in the chart is drawn for each week, which can be seen in Figures 6 and 7. The results again demonstrate the MOC chart finds the OC situation faster than the MR chart. It is noteworthy that both charts reveal the changes before the $8^{th}$ week (two month), which is related to Table 7. In other words, the marketing department can detect changes in customer usage sooner. Also, as mentioned, these changes (campaign) are real and the results clearly show that this campaign has had a relatively good effect on subscriber consumption.

**TABLE 7.** OCT for data consumption behavior after promotions

| | **Ages** | | | | | | | |
|---|---|---|---|---|---|---|---|---|
| | Young | | Middle-Aged | | Older | | | |
| | **Education Level** | | | | | | | |
| **Data Usage (GB)** | Diploma | Higher education | Diploma | Higher education | Diploma | Higher education | Total | Percentage |
| Low consumption | 93 | 94 | 89 | 80 | 84 | 89 | 529 | 26.8% |
| Medium consumption | 124 | 151 | 137 | 140 | 70 | 122 | 744 | 37.7% |
| High consumption | 141 | 164 | 129 | 113 | 56 | 97 | 700 | 35.5% |
| Total | 358 | 409 | 355 | 333 | 210 | 308 | 1973 | 100% |

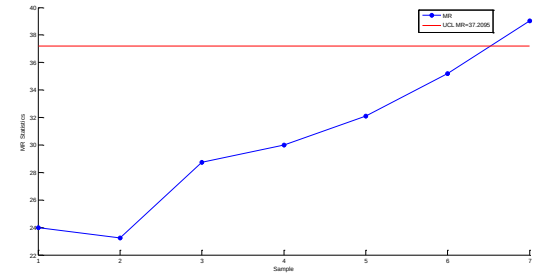


**Figure 6.** MR control chart performance in actual change

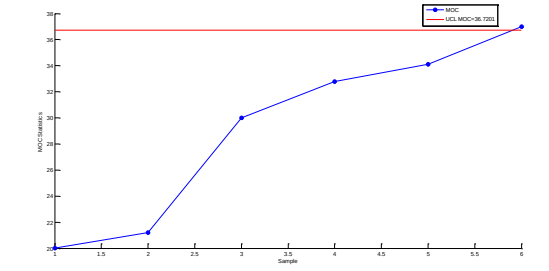


**Figure 7.** MOC control chart performance in actual change

## 5. CONCLUSION REMARKS

In this paper, the intention was to introduce statistics and charts for monitoring multivariate ordinal processes. This was done by using two charts from literature [11, 13], each of which was mentioned as the best control chart in their articles. For a better understanding, brief explanations of how the two statistics were calculated and explained; then, by simulation operations, both of them were set to 370 points with the ARL in IC state. In addition, a real example of customer behavior analysis was provided and with shifts in some parameters, these two control charts were compared. That case study, analyze the effects of marketing department offers on customer's usage data internet behavior. After that analysis and shifts in the values and coefficients of the log-linear relationship, the $ARL_1$ was compared for both charts. The results showed that the MOC chart performs better in finding changes, especially in smaller shifts. Moreover, using the actual changes that occurred within 8 weeks on the selected subscribers, we performed an analysis on these two charts. As future research, other

ordinal multivariate statistics can be used as further research, and new statistics can also be presented. Another research that could be interesting is to use charts to examine nominal and ordinal variables simultaneously.

## 6. ACKNOWLEDGMENT

Special thanks to the staff of Shatel Mobile for their cooperation with the authors. We are also grateful for Ms. Vafaie's efforts in collecting data.

## 7. REFERENCES

1. MacGregor, J. F. and Kourti, T. "Statistical process control of multivariate processes" ***Control Engineering Practice***, Vol. 3, No. 3, (1995), 403-414. doi: 10.1016/0967-0661(95)00014-L
2. Kamranrad, R., Amiri, A. and Niaki, S.T.A. "New Approaches in Monitoring Multivariate Categorical Processes based on Contingency Tables in Phase II" ***Quality and Reliability Engineering International***, Vol. 33, No. 5, (2017), 1105-1129. doi: 10.1002/qre.2103
3. Yamamoto, K., Murakami, H. "Model based on skew normal distribution for square contingency tables with ordinal categories" ***Computational Statistics & Data Analysis***, Vol. 78 (2014), 135-140. doi: 10.1016/j.csda.2014.04.007
4. Maleki, M. R., Ghashghaei, R. and Amiri, A. "Simultaneous monitoring of multivariate process mean and variability in the presence of measurement error with linearly increasing variance under additive covariate model" ***International Journal of Engineering, Transactions A: Basics***, Vol. 29, No. 4, (2016), 514-523. doi: 10.5829/idosi.ije.2016.29.04a.10
5. Rasay, H., Fallahnezhad, M. S. and ZareMehrjardi, Y. "Application of multivariate control charts for condition-based maintenance" ***International Journal of Engineering, Transactions A: Basics***, Vol. 31, No. 4, (2018), 597-604. doi: 10.5829/ije.2018.31.04a.11
6. Khedmati, M., Seifi, F. and Azizi, M. "Time Series Forecasting of Bitcoin Price Based on Autoregressive Integrated Moving Average and Machine Learning Approaches." ***International Journal of Engineering, Transactions A: Basics***, Vol. 33, No. 7, (2020), 1293-1303. doi: 10.5829/ije.2020.33.07a.16
7. Li, J., Tsung, F. and Zou, C. "Directional control schemes for multivariate categorical processes" ***Journal of Quality Technology***, Vol. 44, No. 2, (2012), 136-154, doi: 10.1080/00224065.2012.11917889
8. Li, Z., Zou, C., Wang, Z. and Huwang, L. "A multivariate sign chart for monitoring process shape parameters" ***Journal of Quality Technology***, Vol. 45, No. 2, (2013), 149-165, doi: 10.1080/00224065.2013.11917923
9. Li, J., Tsung, F. and Zou, C. "Multivariate binomial/multinomial control char" ***IIE Transactions***, Vol. 46, No. 5, (2014), 526-542, doi: 10.1080/0740817X.2013.849830
10. Li, J., Tsung, F. and Zou, C. "A simple categorical chart for detecting location shifts with ordinal information" ***International Journal of Production Research***, Vol. 52, No. 2, (2014), 550-562. doi: 10.1080/00207543.2013.838329
11. Wang, J., Li, J. and Su, Q. "Multivariate ordinal categorical process control based on log-linear modeling" ***Journal of Quality Technology***, Vol. 49, No. 2, (2017), 108-122. DOI: 10.1080/00224065.2017.11917983
12. Hakimi, A., Farughi, H., Amiri, A. and Arkat, J. "New phase II control chart for monitoring ordinal contingency table-based processes" ***Journal of Industrial and Systems Engineering***, Vol. 12, (2019), 15-34.
13. Hakimi, A., Farughi, H., Amiri, A. and Arkat, J. "Phase II Monitoring of the Ordinal Multivariate Categorical Processes" ***Advances in Industrial Engineering***, Vol. 55, No. 3, (2021), 249-267. doi: 10.22059/aie.2021.329719.1802
14. Hakimi, A., Farughi, H., Amiri, A. and Arkat, J. "Phase I Monitoring of Multivariate Ordinal based Processes: The MR and LRT Approaches (A real case study in drug dissolution process)" ***International Journal of Industrial Engineering & Production Research***, Vol. 33, No. 1, (2022), 1-18. doi: 10.22068/ijiepr.33.1.7
15. Ramakrishnan, A. and Pecht, M. G. "A life consumption monitoring methodology for electronic systems". ***IEEE Transactions on Components and Packaging Technologies***, Vol. 26, No. 3, (2003), 625-634. doi: 10.1109/TCAPT.2003.817654
16. Cooper, J. O., Heron, T. E. and Heward, W. L. "Applied behavior analysis" (2020). Pearson UK.
17. Mehrotra, D., Nagpal, D., Srivastava, R. and Nagpal, R. "Analyse Power Consumption by Mobile Applications Using Fuzzy Clustering Approach" ***International Journal of Engineering, Transactions C: Aspects***, Vol. 31, No. 12, (2018), 2037-2043. doi: 10.5829/ije.2018.31.12c.07
18. Sarker, I. H. "A machine learning based robust prediction model for real-life mobile phone data." ***Internet of Things***, Vol. 5, (2019), 180-193. doi: 10.1016/j.iot.2019.01.007
19. Jiang, D., Wang, Y., Lv, Z., Qi, S. and Singh, S. "Big data analysis-based network behavior insight of cellular networks for industry 4.0 applications" ***IEEE Transactions on Industrial Informatics***, Vol. 16, No. 2, (2019). 1310-1320. doi: 10.1109/TII.2019.2930226
20. Zhao, T., Xu, J., Zhang, C. and Wang, P. "A monitoring data-based bottom-up modeling method and its application for energy consumption prediction of campus building" ***Journal of Building Engineering***, Vol. 35, (2021), 101962. https://doi.org/10.1016/j.jobe.2020.101962
21. Agresti, A. "Analysis of ordinal categorical data" Department of Statistics University of Florida Gainesville, Florida: John Wiley & Sons, Inc., Hoboken, New Jersey. (2010).
22. Zafar, S. "Non-iterative Estimation Methods for Ordinal Log-linear Models" (2017), Doctoral dissertation, The University of Newcastle.
23. Zhao, X., Liang, J. and Dang, C. "A stratified sampling based clustering algorithm for large-scale data." ***Knowledge-Based Systems***, Vol. 163, (2019), 416-428. doi: 10.1016/j.knosys.2018.09.007

## Persian Abstract

**چکیده**

در برخی از کاربردهای پایش فرآیند آماری، کیفیت یک فرآیند یا محصول توسط یک یا بیش از یک عامل مهم به نام فرآیند چند متغیره توصیف می‌شود. برای نشان دادن رابطه‌ی بین این عوامل، از جداول توافقی استفاده می‌شود و با مدل لُگ‌خطی مدل‌سازی می‌شوند. همچنین دو نوع متغیر آماری وجود دارد که اسمی و ترتیبی می باشند. در این مقاله متغیرها از جنس ترتیبی بوده و از دو نمودار کنترل جدید برای پایش فرآیند بررسی مصرف مشترکین استفاده شده است. این دو نمودار ترتیبی چندمتغیره عبارتند از: نمودار MR و نمودار طبقه‌بندی شده چند متغیره (MOC) که برای نظارت بر فرآیندهای مبتنی بر مدل لُگ‌خطی ترتیبی در فاز ۲ استفاده شده است. همچنین با یک مثال عددی واقعی این دو نمودار کنترل رسم شده و با یکدیگر از لحاظ متوسط طول دنباله مقایسه می‌شوند. این مثال واقعی در مورد تحلیل مصرف اینترنت مشترکین در شبکه همراه می باشد. بررسی دو نمودار پیشنهادی با استفاده از شبیه سازی و مثال واقعی انجام شده و نمودار MOC عملکرد نسبتاً بهتری داشته است.

IJE TRANSACTIONS B: Applications Vol. 35, No. 11, (November 2022) 2205-2212

International Journal of Engineering

Journal Homepage: www.ije.ir

# Investigation on Physical and Mechanical Properties of High Density Polyethylene (PE100) Using Novel Catalyst

M. A. Nikoohemmat[a], H. Mazaheri[a], A. H. Joshaghani*[a], E. Joudaki[b]

[a] *Department of Chemical Engineering, Arak Branch, Islamic Azad University, Arak, Iran*
[b] *Department of Chemical Engineering, Faculty of Engineering, Arak University, Arak, Iran*

*PAPER INFO*

*Paper history:*
Received 29 Narch 2022
Received in revised form 10 August 2022
Accepted 18 August 2022

*Keywords*:
*Ziegler-Natta*
*High Density Poly Ethylene*
*Mechanical Strength*
*Hydrogen Responsibility*

*ABSTRACT*

Novel catalyst called super active catalyst for the production of high density polyethylene (HDPE) pipes grade 100 was prepared and localized for the first time in Iran. The purpose of this paper is to evaluate the performance of the new catalyst and compare it with Finix-112 catalyst which is a commercial catalyst for the production of HEPE grade 100. Extensive experiments were performed on the physical and mechanical properties of the product using both catalysts including melt flow index, particle size distribution, volatility, density, bulk density, scanning electron microscope-energy dispersive x-ray analysis, charpy impact strength. Comparison of the results showed that the hydrogen responsibility performance of the product with super active catalyst is 19%, charpy impact is 16.7% and pressure condition in first reactor about 28% was better than product with Finix-112 catalyst. Home-made super active catalyst can be a good alternative to imported finix-112 catalyst and save a considerable amount of foreign currency.

***doi**: 10.5829/ije.2022.35.11b.15*

**NOMENCLATURE**

| | | | |
|---|---|---|---|
| SAC-510 | Super activa catalyst | PE100 | Polyethylene pipe grade of 100 |
| PSD | Particle size distribution | g | Gravity ($m/s^2$) |
| MFI | Melt flow index | d | Diameter |
| GPC | Gel permeation chromatography | µ | Micron |
| HDPE | High density polyethylene | | |

## 1. INTRODUCTION

High density polyethylene (HDPE), because of its high tensile strength, is the most widely used plastic for the production of water pipes, packaging, butter tubs, garbage containers and oil and gas distribution network in the form of homopolymer and composite [1, 2]. Balanceing between mechanical properties and processablility of polyethylene is one of the key issues for better performance of the polymer [3]. However, HDPE production using Ziegler-Natta catalyst did not have the desired quality and longevity [4]. Many efforts have been done to modify this heterogeneous catalyst which plays an important role in the polymer morphology [5-10]. Upgrading the structure of the catalyst and changing some of its manufacturing instructions will increase the quality of the final products [11]. The effectiveness of quality improvement is achieved by measuring the physical and mechanical properties of pipe raw materials. Measurements of mechanical and physical properties can be obtained by performing some tests such as MFI, GPC, charpy impact and density. HDPE-PE100 is the best choice for replacement with concrete and steel pipes in terms of performance; it has unique properties that can withstand more pressure with more density and less weight and thickness [12]. The impact of the usage of new and advanced catalysts can be examined in two main factors: 1. Hydrogen responsibility, 2. Butylene

*Corresponding Author Institutional Email: a-hasani@iau-arak.ac.ir
(A. Hassani Joshaghani)

Please cite this article as: M. A. Nikoohemmat, H. Mazaheri, A. H. Joshaghani, E. Joudaki, Investigation on Physical and Mechanical Properties of High Density Polyethylene (PE100) Using Novel Catalyst, ***International Journal of Engineering, Transactions B: Applications***, Vol. 35, No. 11, (2022) 2205-2212

responsibility [13, 14]. The effect of the mentioned factors prevents the loss of consumption of valuable materials of hydrogen and butylene, reduces the by-product of wax and the costs of the production process [15].

Production of PE100 pipe grade raw materials in Iran's petrochemical industry is based on slurry, bimodal and under Hostalen technology. Finix-112 catalyst is classified as Ziegler-Natta catalysts and is used in these industries to produce PE100, which is imported and it is too expensive. Some problems using finix-112 includes difficult process control; high hydrogen injection and high operating pressure in reactors, which leads to high hydrogen emissions and costly production. To overcome this problem, super active catalyst with a unique formulation and nature was made to produce PE100 pipe grade for the first time in Iran. Then the results of product at laboratory scale and pilot plant were compared with both catalysts. The purpose of this paper is to investigate the physical and mechanical parameters of PE100 pipe grade using SAC-510 catalyst with improved structure, as well as removing barriers to production, including hydrogen responsibility, ease of production process and economic saving while maintaining product quality.

## 2. MATERIALS AND METHODS

**2. 1. Sieve Analysis in HDPE** The determination of the particle size distribution by sieve analysis is a more accurate and informative method compared to the bulk density method. The particle size distribution is determined by sieve analysis under an air jet. Equipments include balance, precision (500 g, 0.01 g), air jet sieve (0.063 – 0.500 mm), and ultra sonic cleaning device. About 25 g of powder is weighed on each sieve and the remaining powder is determined, after machining and suction [16].

**2. 2. Melt Flow Index (MFI) of HDPE** The melt flow rate depends on the polymer molecular weight and hence specifies individual product types. The melt flow rate can be used as a criterion for a first evaluation of their flow properties. Alternatively, the volume flow rate may be indicated. Determinations according to ISO 1133 are obligatory, in particular, for the final inspection of product batches destined for sale, and render binding results for delivery specifications, works certificates, etc. Equipment includes 50XC9001A-D (Melt viscosity test instrument), 50XC9002 (Balance, analytical (200 g, 0.1 mg), 50XC9024 (Muffle furane). The pressure container with the reactor sample delivered from the polymerization plant is carefully depressurized in a hood by respecting the safety regulations. The total content of the container will be emptied into the plastic beaker. The small crucible is filled half with the hot suspension while stirring continuously. After applying a vacuum the filter cake on the crucible is sucked dry for 5 minutes. Two Petri dishes are filled with the pre-dried powder to a height of 1 cm and dried for 15 minutes at 80 °C and 100 mbar in the vacuum dryer. When the melting time is over, the piston with a weight will be loaded. Then, pre-run time and the actual automatic measurement of piston travel starts until the lower ring mark has reached the upper edge of the cylinder. During the test period, at least 3 intermediate values for the piston travel at regular intervals is recorded. The test is finished when the upper ring mark has reached the upper edge of the cylinder or at least 25 minutes after the beginning of the melting time [16].

**2. 3. Volatiles in HDPE** This test is for the volatile concentration calculation (e.g. residual hexane or low boiling wax fractions) in HDPE powder or pellets by weighing. Equipment includes infrared or Halogen moisture analyzer with accessories and analytical balance (with accuracy of 0.1 mg). The analysis is performed on a representative sample at 105 °C until constant weight for 60 minutes. Sample amount should be 10.0 ± 0.1 g. For further information refer to the instruction manual of the instrument [16].

**2. 4. Mechanical Tests** Charpy Impact Strength was done at 23°C according to DIN EN ISO 179/1eA. Test specimen is made from a molded sheet of 4 mm and a diameter of 120 mm. The specimen is sawed to size and the notch is planned on it. The test is carried out on a pole of 80 mm x 10 mm x 4 mm, which is notched in the center and is tested in a lying position by a pendulum hammer impact on the narrow side opposite to the notch. The Charpy impact strength is the impact energy attained at the breaking of the test specimen.
Note the measured values for impact energy at break of test specimen and break type [16].

**2. 5. Bulk Density of HDPE** The bulk density is determined according to DIN EN ISO 60 by weighing out special calibrated beakers. Equipment's includes Bulk density measurement, laboratory balance (1,000 g, 0.1 g). Testing powder the empty beaker is weighed. The bulk density measurement consists of a 200 ml funnel and a 100 ml beaker. The funnel bottom is equipped with a flap from where the powder flows into the beaker. 110 – 120 ml of powder are gently transferred into the funnel and then the flap is opened. The accumulated heap of powder exceeding the beaker rim is levelled off with a cardboard at an angle of 45°. The filled beaker is weighed [16].

**2. 6. Density of HDPE** According to ISO 1183 the density is one of the two characteristic properties of

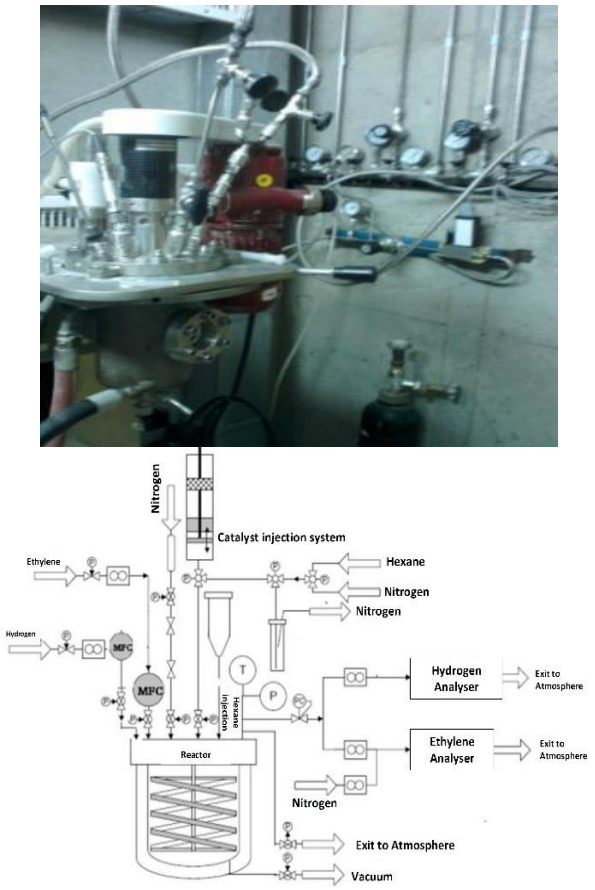


**Figure 1.** The experimental set up for copolymerization of ethylene/1-butylene and its scheme

polyethylene. The density results from the different buoyancies of the specimen in air and in butyl acetate.

**2. 7. Polymerization** Figure 1 shows the experimental equipment of ethylene slurry polymerization. The jacketed stainless steel reactor with a volume of 1 liter and Buchi model is used. The volume of the reactor jacket is 300 ml, the maximum pressure allowed on the reactor is 60 bar, for the jacket this amount is 20 bar and the reactor test pressure is 10 bar. The temperature range of the reactor and its jacket is from -10°C to 250°C. The setup has the ability to inject catalyst under nitrogen atmosphere by operator, and co-catalyst injection is also done from the same route. The catalyst injection system consists of a pipe with valves at both ends, one end of the pipe is connected to the reactor and the other end is connected to nitrogen. Injection is done by pressurizing the catalyst with nitrogen into the reactor. The reactor temperature is determined using a sensor (Keller druck messtechnik). Ethylene and hydrogen enter the reactor through the mass flow controller. 400 ml of dry hexane stored in a molecular sieve and a sodium strip are injected into the reactor at room temperature. Pressure and temperature are controlled throughout the polymerization. The reactor is equipped with a temperature jacket that keeps the polymerization temperature constant at the desired point. To keep the pressure constant during polymerization, a control system is used which enters the monomer into the reactor at the same rate of consumption. Prior to polymerization, the reactor is degassed by a stream of nitrogen gas. Degassing is repeated for 30 minutes and about 20 times. Finally, the reactor is saturated with ethylene gas. The mixing speed of the reactor was set at 2800 rpm. The flow of nitrogen, hydrogen and ethylene gas is free of any impurities by passing through a column consisting of molecular sieve. Antifouling, co-catalyst and catalyst injections are performed in the presence of ethylene pressure. In the copolymerization test, 4g of 1-butene co-monomer is injected into the container as a density controller after injecting other components. In all experiments, the amount of hydrogen is introduced into the polymerization container with a partial pressure of 4 bar as a chain transfer agent. The polymerization is kept constant at 80°C and ethylene is continuously fed into the reactor vessel. The ethylene pressure is kept constant by the continuous entry of ethylene monomer in the amount of 6.4 bar for one hour of the test. At the end of the reaction, the monomer flow is stopped and the polymerization temperature is brought to ambient temperature and the reaction is stopped [16].

## 3. RESULTS AND DISCUSSION

**3. 1. Particle Size Distribution (PSD)** Figures 2 and 3 show the particle size distribution for Finix-112 and SAC-150 catalysts, respectively. Table 1 summarized the comparison between particle size information for both catalysts. The average particle diameter is the same for both catalysts. However, the SAC-150 catalyst showed 10% of particles were smaller than 128 µm, which is smaller than commercial one. Coarse particles with a very small amount of fine particles showed a lower

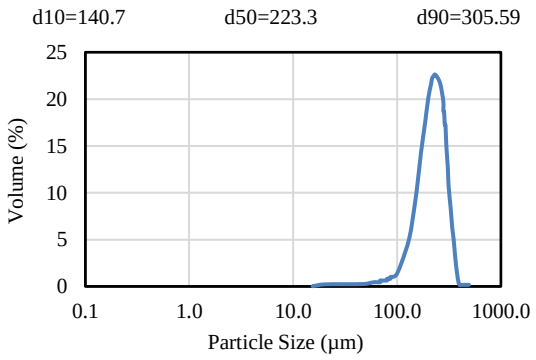


**Figure 2.** PSD for HDPE powder using Finix-112 catalyst

viscosity compared to the suspension containing course particles and suspension with fine particles containing some course particles. They did not show much changes compared to the suspension containing fine particles.

The presence of fine particles between large particles reduces the collision of large particles and fine particles act as a lubricant and facilitate the rotation of the particles and reduce the relative viscosity.

**3. 2. Sieve Analysis for HDPE Powder by Super Active and Finix-112 Catalysts** Table 2 shows the molecular sieving results of the HDPE powder product from the two catalysts. Also, bulk density and HDPE powder density are presented in this table. The results show that due to the higher bulk density condition, the product powder of SAC-510 catalyst is better than the product powder of Finix-112 catalyst. The low density of powder super active catalyst indicates its higher strength than the product powder with Finix-112 catalyst.

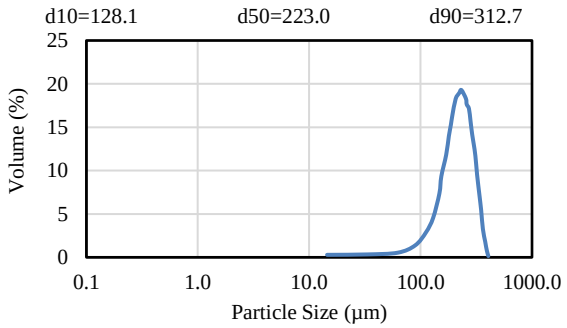


**Figure 3.** PSD for HDPE powder using SAC-150 catalyst

**TABLE 1.** Comparison of PSD

| Catalyst | SAC-510 | FINIX-112 |
|---|---|---|
| Sample Date | 25 October 2021 | 25 October 2021 |
| d(0.1) | 128.1 | 140.7 |
| d(0.5) | 223 | 223.3 |
| d(0.9) | 312.7 | 305.59 |
| Fine<63µm | 2.57 | 1.61 |
| Fine<125µm | 9.33 | 6.46 |

**TABLE 2.** Sieve Analysis results for HDPE powder

| | SAC-510 | | Finix-112 | |
|---|---|---|---|---|
| Sample | NO.1 | NO.2 | NO.1 | NO.2 |
| Bulk Density (g/cm$^3$) | 0.43 | 0.43 | 0.4 | 0.4 |
| Sieve (%<500) | 99 | 98 | 96 | 95 |
| Sieve (%<400) | 96 | 96 | 92 | 94 |
| Sieve (%<315) | 93 | 92 | 87 | 90 |
| Sieve (%<250) | 79 | 78 | 73 | 72 |
| Sieve (%<200) | 57 | 57 | 51 | 49 |
| Sieve (%<160) | 32 | 27 | 19 | 22 |
| Sieve (%<125) | 16 | 15 | 6 | 18 |
| Sieve (%<63) | 2 | 2 | 0 | 0 |
| Sieve(µd50) | 181 | 184.7 | 201 | 194 |
| Density (g/cm$^3$) | 0.947 | 0.948 | 0.949 | 0.95 |

**3. 3. Gel Permeation Chromatography (GPC)** Figure 4 shows the GPS diagram for both catalysts. The aim of the GPC test is to measure the molecular mass of the chains and to distribute the mean molecular weight of PE100. The nature of Ziegler-Natta catalyst slurry systems for the production of PE100 is such that the length of polymer chains is not the same [17].

When a GPC is taken from a product, its distribution graph is wide. This width is due to the nature of the catalyst as well as the bimodal property and the polymerization reaction in the two reactors. The purpose of GPC test was to evaluate the compatibility of PE100 product with SAC-510 catalyst with Finix-112 product, which shows good compatibility.

As can be seen in Table 3, the Mw/Mn parameter of the product with both catalysts is higher than 20, which indicates the wide molecular distribution and the parameter $M_{z+1}$ and $M_{z+2}$ of the product powder with catalyst SAC-510 is more than the product powder with catalyst Finix-112. This parameter indicates the number of long molecular chains and causes more polymer entanglement. However, the amount of co-monomer bulk in the parameter product powder with catalyst SAC-510 is less than Finix-112.

**3. 4. MFI Changes in SAC-510 and Finix-112** The melt flow rate is mainly controlled by the amount of hydrogen in the reactor. To be more precisely, it is the ratio of the partial pressures of hydrogen and ethylene in the gaseous phase which - at a given partial pressure of ethylene-exactly determines the average molecular weight. The partial pressures of hydrogen and ethylene are measured by analyzing the concentrations in the gaseous phase of the reactor. The concentrations of $H_2$

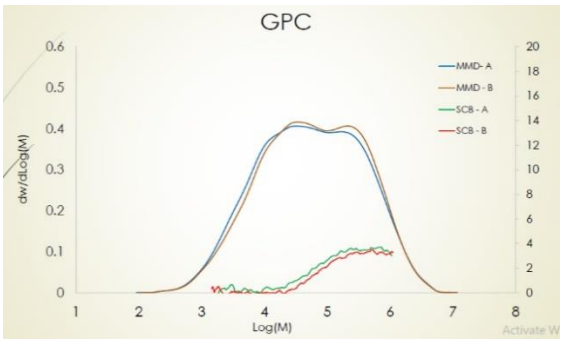


**Figure 4.** Comparison of GPC diagrams of PE100 product with both catalysts

**TABLE 3.** GPC results for HDPE-PE100 using SAC-510 and Finix-112 catalyst

| HDPE Powder | | |
|---|---|---|
| | **A (Finix)** | **B (SAC 150)** |
| Mw (g/mol) | 233372 | 241203 |
| Mn (g/mol) | 10546 | 11430 |
| Mw/Mn | 22.13 | 21.1 |
| Mz (g/mol) | 1185062 | 1178261 |
| Mz+1 (g/mol) | 2245649 | 2363459 |
| Mz+2 (g/mol) | 3035200 | 3501861 |
| Mv (g/mol) | 168265 | 176333 |
| Bulk $CH_3$/1000 C | 4.317 | 3.764 |
| Corrected Bulk $CH_3$/1000 C | 1.7 | 1.3 |
| Bulk comonomer wt% | 0.66 | 0.53 |
| Calculation method version | 2 | 2 |

and $C_2H_4$ in the hexane diluent are proportional to the composition of the gaseous phase.

Keep in mind that MFI control via hydrogen feed will not work properly if other process data like temperature, gas feed, and activator concentration are fluctuating.

It is clear that by increasing the melting flow index (MFI) in the first reactor, the length of the monomer chain is short and, in other words, the optimal crystalline is formed in the first reactor and by decreasing MFI in the second reactor; the fabrication of product strength and desirable product is achieved. As seen in the Figures 5 and 6, in a 24 hour period in the first reactor for every two hours, the MFI test was taken with a weight of 1.2 kg and in the second reactor every two hours of MFI test was taken with 5kg weight. As can be seen in Figure 5 the amount of MFI in both reactors is logical match using SAC-510 catalyst than the Finix-112 and showed the quality, strength and density of new catalyst did not drop, and even in some cases, there was a relative superiority to Finix-112 catalyst.

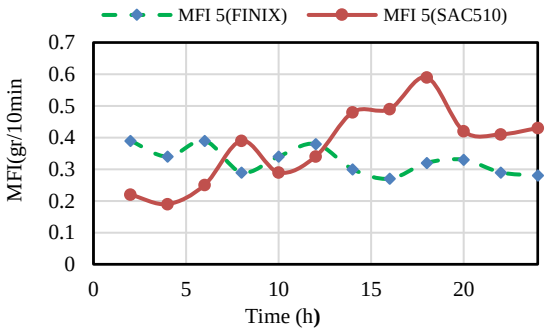


**Figure 5.** MFI of PE-100 in second reactor at 190°C and 5kg

According to Figure 6, it is observed that in the second reactor MFI with SAC-510 catalyst had a better performance than Finix-112 catalyst. This is indicating the optimal state of amorphous product using SAC-510 catalyst than Finix-112 catalyst.

**3. 5. Comparison of the Effect of Catalyst on Process Hydrogen Responsibility** Hydrogen is injected into the first reactor to shorten the polymer chain to control the density and crystallinity of the product. Hydrogen as a valuable substance the less it is consumed, the better it is economically. The injection of excess hydrogen into the first reactor increases the pressure of the reactor and subsequently pours larger amounts of the gas mixture, which also contains hydrogen. Therefore, it is desirable that the $H_2/C_2$ ratio, i.e. the ratio of hydrogen to ethylene, be a minimum value while maintaining the desired density and properties of the product. According to Figure 7, it is clear that the product hydrogen responsibility with SAC-510 had a better performance and was able to produce the desired product with less hydrogen.

**3. 6. Charpy Impact** Figure 8 shows the changes in charpy impact of pipe produced with SAC-510 catalyst and comparison with pipes produced with Finix-112 catalysts. The x- axis shows the time in terms of day and

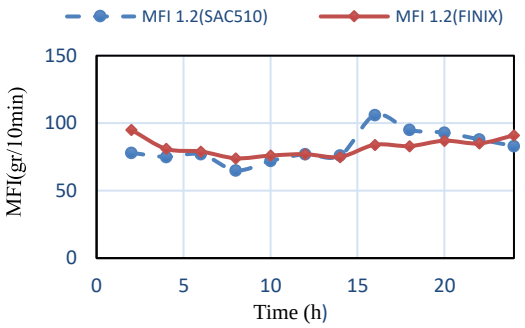


**Figure 6.** MFI of PE-100 in first reactor at 190C° and 1.2kg

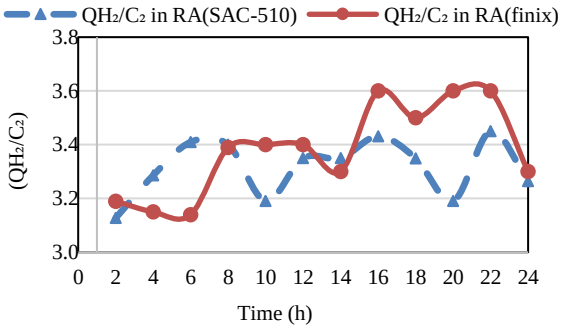


**Figure 7.** Comparison of product hydrogen responsibility SAC-510 catalyst with product with Finix-112 catalyst

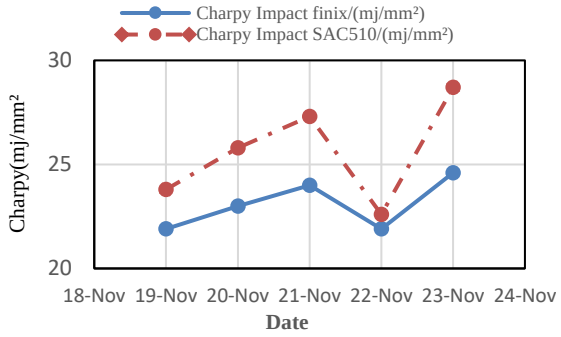


**Figure 8.** PE100 Charpy Impact using SAC-510 and Finix-112 catalysts

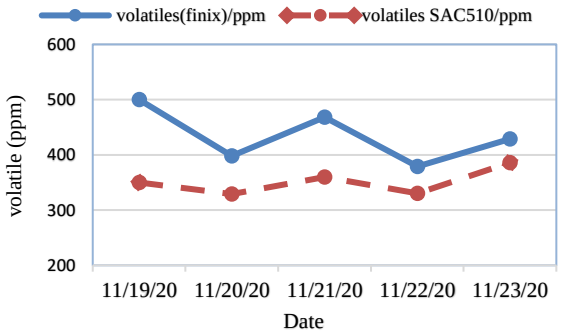


**Figure 9.** Comparison of volatile changes of PE-100 pipe grade using SAC-510 and Finix-112 catalyst

the y-axis charpy impact. The higher the, the stronger the pipe.

As shown in Figure 8, the average charpy impact in the diagram of a PE pipe grade100 made with a SAC-510 catalyst is greater than that of a pipe made with a Finix-112 catalyst. As a result, a pipe made with a SAC-510 catalyst has more strength and durability than a pipe made with a Finix-112 catalyst.

Charpy impact value obtained from the production of PE-100 with SAC-510 catalyst were also compared with the values of PE-100 produced in the most up-to-date articles [3].

Table 4 shows that the strength and durability of PE-100 with SAC-510 catalyst are greater than the strength of PE-100 mentioned in thisarticle.

**3. 7. Comparison of Volatile of Produced using SAC-510 and Finix-112 Catalysts** Figure 9 shows the volatile changes over time for the PE-100 product using the SAC-510 and Finix-112 catalysts. As it is proved in the previous section, the lower the volatile in the product, the better the quality of the catalyst used in the product. Therefore, according to Figure 9, the product using SAC-510 catalyst showed less volatile and this indicates better than SAC-510 catalyst.

Some effective mechanical parameters in PE-100 such as carbon black content, MFI and density for the product using SAC-510 and Finix-112 and all 3 catalysts are listed in Table 5.

**TABLE 4.** Charpy Impact for PE100 using SAC-510 and Finix-112 catalyst

| Sample Code | Charpy (KJ/m²) |
|---|---|
| N-100J2[a*] | 28.12±0.8 |
| B1-100J2[a*] | 26.17±1.3 |
| B2-100J2[a*] | 27.03±0.6 |
| $PE100ARMCRP_{finix}$ | 24.6±0.6 |
| $PE100ARMCRP_{SAC510}$ | 28.7±0.8 |

a*: Refer to literature [3]

**TABLE 5.** Quantitative analysis of contaminants and residual fillers for various HDPE samples

| Sample code | Density (g/cm³) | MFI1 (g/10min) 5kg, 190°C | Measured according MFI | MFI2 (g/10min) 2.16kg, 190°C |
|---|---|---|---|---|
| $PE100_{N\text{-}100j1}$[a*] | 0.952 | 0.22 | ISO 1133:1997 | 6.9 |
| $PE100_{N\text{-}100j2}$[a*] | 0.95 | 0.18 | ISO 1133:1997 | 6.2 |
| $PE100_{N\text{-}100jM}$[a*] | 0.951 | 0.21 | ISO 1133:1997 | 5.8 |
| $PE100ARMCRP_{finix}$ | 0.949 | 0.24 | ASTM D1238-ISO 1133 | 6.3 |
| $PE100ARMCRP_{SAC510}$ | 0.947 | 0.17 | ASTM D1238-ISO 1133 | 6.1 |

***a*:*** Refer to literature [3]

The amount of carbon in the product with SAC-510 catalyst is less than the product used with Finix-112 catalyst, which is due to the better quality of SAC-510 catalyst compared to Finix-112 catalyst. But this amount is slightly higher than the other three products in the article.

## 4. CONCLUSIONS

The Ziegler-Natta spherical super active catalyst was prepared for the polymerization of the ethylene slurry phase in the presence of titanium chloride using magnesium ethoxide substrate and internal coal catalysts and halocarbon. Appropriate particle size distribution and specific surface area and spherical catalyst morphology observed in scanning electron microscopy have resulted in high catalyst activity. These results can be achieved by comparing the product of PE100 polyethylene pipe using two catalysts SAC-510 and Finix-112: Hydrogen responsibility has improved

compared to catalyst Finix-112 Charpy impact PE100 with catalyst SAC is better than PE100 with catalyst Finix-112. Melt flow index values indicate that the powder and pellet conversion gap decreased in the product with SAC-510 catalyst and so we will have an easier process in production. Finally, due to the production of this valuable super active catalyst in Iran, we may not need to import expensive catalyst like Finix-112 and at a much lower cost than importing catalyst Finix-112. In fact, with the synthesized and experimented catalyst in this work, we have successfully achieved the production of HDPE PE100 pipe.

## 5. REFERENCES


1. Bachir-Bey, T. and Belhaneche-Bensemra, N. "Investigation of Polyethylene Pipeline Behavior after 30 Years of Use in Gas Distribution Network" ***Journal of Materials Engineering and Performance***, Vol. 29, No. 10, (2020), 6652-6660. doi: 10.1007/s11665-020-05118-9.
2. Ebrahimi, G., Falk, R. H., Tajvidi, M. and Behzad, M. "Dynamic mechanical analysis of compatibilizer effect on the mechanical properties of wood flour-High-density polyethylene composites" ***International Journal of Engineering, Transactions B: Applications,*** Vol. 17, No. 1, (2004), 95-104.
3. Li, W., Hui, L., Xue, B., Dong, C., Chen, Y., Hou, L., Jiang, B., Wang, J. and Yang, Y., "Facile high-temperature synthesis of weakly entangled polyethylene using a highly activated Ziegler-Natta catalyst" ***Journal of Catalysis***, Vol. 360, (2018), 145-151. doi: 10.1016/j.jcat.2018.01.024
4. Shamiri, A., Chakrabarti, M. H., Jahan, S., Hussain, M. A., Kaminsky, W., Aravind, P. V. and Yehye, W. A. "The influence of Ziegler-Natta and metallocene catalysts on polyolefin structure, properties, and processing ability" ***Materials***, Vol. 7, No. 7, (2014), 5069-5108. doi: 10.3390/ma7075069.
5. Aigner, P., Averina, E., Garoff, T. and Paulik, C. "Effects of Alterations to Ziegler–Natta Catalysts on Kinetics and Comonomer (1-Butene) Incorporation." ***Macromolecular Reaction Engineering***, Vol. 11, No. 6, (2017), 1700009. doi: 10.1002/mren.201700009.
6. Chammingkwan, P., Bando, Y., Terano, M. and Taniike, T. "Nano-dispersed Ziegler-Natta catalysts for 1 μm-sized ultra-high molecular weight polyethylene particles" ***Frontiers in Chemistry***, Vol. 6, (2018), 524 (1-11). doi: 10.3389/fchem.2018.00524.
7. Chen, M., Chen, Y., Li, W., Dong, C., Liang, P., Wang, N., Jiang, B., Wang, J. and Yang, Y., "Selective distribution and contribution of nickel based pre-catalyst in the multisite catalyst for the synthesis of desirable bimodal polyethylene" ***European Polymer Journal***, Vol. 135, (2020), 109878. doi: 10.1016/j.eurpolymj.2020.109878.
8. Chammingkwan, P., Bando, Y., Mai, L.T.T., Wada, T., Thakur, A., Terano, M., Sinthusai, L. and Taniike, T. "Less Entangled Ultrahigh-Molecular-Weight Polyethylene Produced by Nano-Dispersed Ziegler–Natta Catalyst" ***Industrial & Engineering Chemistry Research***, Vol. 60, No. 7, (2021), 2818-2827. doi: 10.1021/acs.iecr.0c05432.
9. Jafariyeh-Yazdi, E., Tavakoli, A., Abbasi, F., Parnian, M. J. and Heidari, A. "Bi-supported Ziegler–Natta TiCl4/MCM-41/MgCl2 (ethoxide type) catalyst preparation and comprehensive investigations of produced polyethylene characteristics" ***Journal of Applied Polymer Science,*** Vol. 137, No. 15, (2020), 48553. doi: 10.1002/app.48553.
10. Jandaghian, M. H., Maddah, Y., Nikzinat, E., Masoori, M., Sepahi, A. and Rashedi, R. "Investigation of the effects of heat treatment parameters during synthesis of titanium-magnesium-based Ziegler-Natta catalysts" ***Journal of Macromolecular Science, Part A***, Vol. 58, No. 5, (2021), 287-297. doi: 10.1080/10601325.2020.1845097.
11. Trivedi, P. M. and Gupta, V. K. "Progress in $MgCl_2$ supported Ziegler-Natta catalyzed polyolefin products and applications" ***Journal of Polymer Research,*** Vol. 28, No. 2, (2021), 1-20. doi: 10.1007/s10965-021-02412-5.
12. Moini Jazani, O., Khalafi, R., Khosravi, M., Hassanpour, M. R., Dadkhah, D., Mostafaeian, M. et al. "A Review of Manufacturing Process of Polyethylene Pipe and Connectors for Applying in High-Pressure Natural Gas Pipelines" ***Journal of Particle Science & Technology***, Vol. 1, No. 3 (2015), 129-140. doi: 10.22104/jpst.2015.136
13. Zifang, G., Wei, C., Junling, Z. and Hongxu, Y. A. N. G. "Novel high performance Ziegler-Natta catalyst for ethylene slurry polymerization" ***Chinese Journal of Chemical Engineering***, Vol. 17, No. 3 (2009), 530-534. doi: 10.1016/S1004-9541(08)60241-4.
14. Bazgir, H., Abbas-Abadi, M. S., Haghighi, M. N., Darounkola, M. R. R., Issaabadi, Z. and Rashedi, R., "Synthesis of novel Ziegler Natta catalyst in the presence of internal promoter and electron donors for ethylene and ethylene/1-hexene polymerization" ***Journal of Polymer Research***, Vol. 28, No. 8 (2021), 1-14.
15. Seifali Abbas-Abadi, M. "The production of high efficiency Ziegler–Natta catalyst with dual active sites nature using cyclohexyl chloride as promoter with super activity and produced superior polyethylene with controllable molecular weight distribution" ***Designed Monomers and Polymers***, Vol. 20, No. 1 (2017), 524-531. doi: 10.1080/15685551.2017.1394782.
16. Operating Manual. "Basel documents in Arak HDPE Plant". Chap (1, 2, and 3), (2000).
17. Kang, J., Chen, X. and Shao, Z. "Optimization of High-Density Polyethylene Process Based on Molecular Weight Distribution and Chemical Composition Distribution under Uncertainty" ***In Computer Aided Chemical Engineering***, Vol. 37, (2015), 881-886. doi: 10.1016/B978-0-444-63578-5.50142-0.

Persian Abstract

**چکیده**

کاتالیست جدید بنام کاتالیست فوق فعال برای تولید لوله پلی اتیلن با دانسیته بالا گرید ۱۰۰ برای اولین بار در ایران ساخته و بومی سازی شد. هدف از ارائه این مقاله ارزشیابی عملکرد کاتالیست جدید در مقایسه با کاتالیست Finix-112 که کاتالیستی متداول در تولید گرید لوله فوق الذکر است. با استفاده از آزمایشات متعدد بر روی خواص فیزیکی و شیمیایی محصول، عملکرد هر دو کاتالیست شامل توزیع اندازه ذرات، آنالیز پراکندگی اشعه ایکس، میکروسکوب اسکن الکترونی، فراریت، دانسیته، دانسیته بالک و ضربه چارپی ارزیابی گردید. نتایج نشان می‌دهد که عملکرد پاسخ‌پذیری هیدروژن محصول با کاتالیست جدید ۱۹، ضربه چارپی ۱۶.۷ و فشار عملیاتی در راکتور اول با کاتالیست جدید ۲۸ درصد بهبود یافته است. کاتالیست ساخت داخل می تواند جایگزین خوبی برای کاتالیست وارداتی finix-112 باشد و صرفه جویی ارزی قابل ملاحظه‌ای به ارمغان آورده است.

International Journal of Engineering

Journal Homepage: www.ije.ir

# Presenting an Adaptive Restraint Method to Improve Performance of Ground Differential Protection of Power Transformer

A. H. Z. Bkhaitawi, A. A. Abdoos*, A. Ebadi

*Department of Electrical and Computer Engineering, Babol Noshirvani, University of Technology, Babol, Iran*

*PAPER INFO*

*Paper history:*
Received 06 July 2022
Received in revised form 15 August 2022
Accepted 24 August 2022

*Keywords*:
*Power Transformer Protection*
*Ground Differential Protection*
*Jiles-Atherton Model*
*Current Transformer Saturation*

*ABSTRACT*

The ground differential (GD) relay is used to detect internal ground faults on the power transformer windings and terminals. In fact, this relay is employed as a complement to the phase differential (PD) relay. However, its stability is affected by magnetic saturation in current transformers (CTs) cores so that the spurious differential current caused by CT saturation may lead to the relay malfunction. In this paper, by modifying the restraining current definition in a conventional method, an adaptive restrain method is proposed. To evaluate the proposed method performance compared with conventional method, a real 230/63 kV power transformer under a large number of internal fault, external fault and in rush current cases are simulated in PSCAD/EMTDC environment. It is worth noting that Jiles-Atherton (JA) model is utilized to simulate CTs. MATLAB software is used to implement and analyze these methods using obtained simulation. Obtained results show that the proposed method is quite superior to the conventional method, despite its simplicity.

***doi***: *10.5829/ije.2022.35.11b.16*

**NOMENCLATURE**

| | | | |
|---|---|---|---|
| $I\_D$ | Differential current | $I\_R$ | Restraining current |
| $I\_n$ | Neutral current | $I\_TH$ | Threshold value of neutral current |
| $I\_a, I\_b, I\_c$ | Phase currents | $f$ | Fundamental frequency |

## 1. INTRODUCTION

Power transformers are expensive and extremely vital components of power system. Therefore, equipping them with secure, reliable, and fast protective relays to detect internal faults is very essential.

Among the protection schemes of transformers, the phase differential (PD) protection, being the most applied for transformers having ratings of 5 MVA and above [1]. However, when magnetizing inrush current passes through the power transformer windings and/or current transformer (CT) saturation occurs, a phase differential relay is prone to incorrectly operate. Hence, harmonic blocking and harmonic restraint logics have been used to improve its performance [2]. On the other hand, if the fault location is close to the neutral point of power transformer Y winding, or if the ground-fault current is restricted, this protection scheme may not be sufficiently sensitive for detection [3]. In order to overcome this issue, the ground differential (GD) protection is used as a supplementary protection method [4]. However, taking into account current transformer (CT) saturation is necessary when the adjustment of a ground differential protection and its performance are considered [5].

It is known that CT saturation is usually caused by the fault and magnetizing inrush currents, due to the high amplitude of current, the slowly decaying direct current (DC) component, and the CT core remanent flux [6]. It must be noted that the presence of the slowly decaying DC component in the primary CT current may lead to CT saturation, even if the primary current value is not high [7].

*Corresponding Author Institutional Email: a.abdoos@nit.ac.ir
(A.A. Abdoos)

Please cite this article as: A. H. Z. Bkhaitawi, A. A. Abdoos, A. Ebadi, Presenting an Adaptive Restraint Method to Improve Performance of Ground Differential Protection of Power Transformer, ***International Journal of Engineering, Transactions B: Applications***, Vol. 35, No. 11, (2022) 2213-2219

CT saturation effects can be decreased by the proper dimensioning but are not totally eliminated [8]. High-impedance GD relays are, to some degree, resistant to CT saturation. To use these relays, some prerequisites must be met, such as the same turn ratios and the closely similar saturation characteristics with high knee-point voltage of the CTs [9]. Nowadays, numerical low-impedance GD relays are widely used. A significant advantage of low-impedance GD relays is the fact that the use of these relays does not have the same prerequisites mentioned for the high-impedance GD relays. However, if CT saturation occurs, a false differential current appears and a low-impedance GD relay may malfunction. Adaptive restraint current [10] and directional supervision [11] methods can improve this relay operation, but the malfunction is still probable in some operating conditions [12]. Recently, artificial intelligence [13] and time frequency analysis [6] have been used to develop new methods for overcoming malfunction of low-impedance GD relays, however, these methods are complex and their computational burden are high.

At present paper, a simple effective algorithm is proposed for GD relay that is sensitive to detect internal ground faults and optimally safe against malfunction. The idea behind this new algorithm is to use a new definition for the restraint current so that its value depends on the second harmonics of the phase currents and the angle between the neutral and residual currents. The rest of this paper is organized as follows: In section 2, the proposed method is introduced. Simulation results are presented in section 3. Finally, the conclusion is made at the end of the paper in section 4.

## 2. PROPOSED METHOD

A Y winding of power transformer is shown in Figure 1. A low-impedance GD relay uses phase and neutral currents measured by CTs, as seen in this figure, to detect internal ground faults on the winding or transformer terminal. Figure 2 shows operating characteristic of a conventional GD relay. This characteristic is based on two parameters including $I\_D$ (differential current) and $I\_R$ (restraining current). Equations (1) and (2) show how to calculate these parameters [13]:

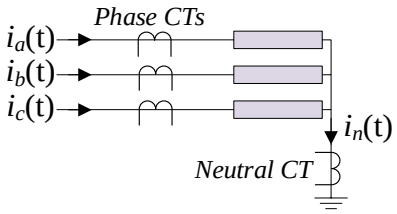


**Figure 1.** A sample Y winding of power transformer

$$I\_D = |I\_a + I\_b + I\_c - I\_n| \quad (1)$$

$$I\_R = 0.5 \times (max\{|I\_a|, |I\_b|, |I\_c|\} + |I\_n|) \quad (2)$$

Here, $I_a$, $I_b$ and $I_c$ are phase currents and $I_n$ is neutral current. Although a relay with such a characteristic often has good performance, its malfunction is possible due to the deep saturation of current transformers [5]. As before mentioned, transformer inrush current and severe external faults may make CT saturate and relay malfunction. To detect the inrush current in power transformer protection, the value of the second harmonic component of the currents is compared with a predetermined value [7]. On the other hand, in some conventional GD relays, the angle between residual and neutral currents is used to avoid malfunction during external ground faults (and some inrush current cases) [14, 15]. But these methods do not guarantee malfunction prevention. In this paper, it is proposed to modify the formula for calculating the restraining current ($I_R$) so that this parameter increases by increasing the maximum value of second harmonic components in phase currents or decreasing the angle between the residual and neutral currents. It is notable that the mentioned angle is 0 during external fault and inrush current conditions. Equation (3) shows the modified restraining current ($MI_R$). As can be seen, $MI_R$ is obtained by multiplying the restraining current by the proposed factors $F_1$ and $F_1$ which are calculated using Equations (4) and (5).

$$MI_R = I_R \times F_1 \times F_2 \quad (3)$$

$$F_1 = 1 + \alpha \times max\left\{\frac{I_a(2f)}{I_a(f)}, \frac{I_b(2f)}{I_b(f)}, \frac{I_c(2f)}{I_c(f)}\right\} \quad (4)$$

$$F_2 = 1 + \beta \times (\pi - \theta) \quad (5)$$

Here, $f$ is the fundamental frequency and $\theta$ is the angle between residual current (summation of phase currents) and neutral current that varies 0 to $\pi$ radians. Also, $\alpha$ and $\beta$ are constants that are described in the following how to calculate them in four steps.

**Step 1:** it is need to simulate a large number of inrush current, internal and external fault cases of a power transformer so that the most severe conditions from CT saturation point of view are considered.

**Step 2:** set F2=1, for each internal ground fault case, a sliding time window with a length of one cycle must move from the moment in which $I_D = 0.1\,pu$ to one cycle later and $max\left\{\frac{I_a(2f)}{I_a(f)}, \frac{I_b(2f)}{I_b(f)}, \frac{I_c(2f)}{I_c(f)}\right\}$ at each time step must be computed. Then, the minimum of these values is saved. After we do this for all internal fault cases, the maximum of these minimum values ($HR_{Mm}$) is considered to find suitable value for $\alpha$.

**Step 3:** set F1=1, for each internal ground fault case, a sliding time window with a length of one cycle must move from the moment in which $I_D = 0.1\,pu$ to one

cycle later and the angle between neutral and residual currents at each time step must be computed. Then, the maximum of these values is saved. After we do this for all internal fault cases, the minimum of these maximum values ($\theta_{mM}$) is considered to find suitable value for $\beta$.

**Step 4:** With assumptions $max\left\{\frac{I_a(2f)}{I_a(f)}, \frac{I_b(2f)}{I_b(f)}, \frac{I_c(2f)}{I_c(f)}\right\} = HR_{Mm}$ and $\theta = \theta_{mM}$ in Equation (3), the suitable values for $\alpha$ and $\beta$ are found based on trial and error method so that all of internal ground faults be detected in first fault cycle.

**Step 5:** Using $\alpha$ and $\beta$ found in before step, $MI_R$, and GD relay operating characteristic shown in Figure 2. The proposed algorithm shown in Figure 3 is implemented and analyzed for inrush current and external fault cases. It is seen that the new relay only activates the and operates when the neutral current ($I_n$) exceeds a threshold value ($I_{TH}$), because this current always increases during a ground fault. It is obvious that if phase currents are zero and the neutral current is higher than its threshold value, this situation can be only an internal ground fault. If malfunction number of the modified GD algorithm is significantly lower than conventional method, its efficiency will be validated.

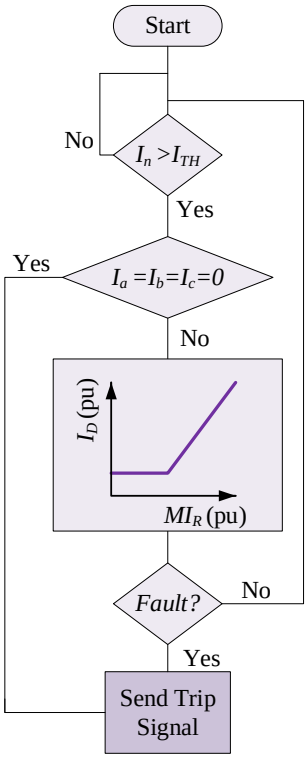


**Figure 3.** The modified GD algorithm

## 3. SIMULATION AND RESULTS

In this section, a power transformer operation is simulated under a large number of fault and inrush current condition, then the obtained results are used to implement and analyze proposed methos.

### 3. 1. Power Transformer Operation Simulation

As depicted in Figure 4, a part of a high-voltage (HV) substation located in Iran is chosen to study [13]. It includes 230/63 kV power transformer, a grounding transformer and CTs. Tables 1 and 2 presents detailed information about the transformers. It should be noted, Jiles-Atherton (J-A) model is used to simulate CTs. All simulations are done by PSCAD/EMTDC software package and obtained results are saved to use for implementing and analyzing the proposed method in MATLAB environment.

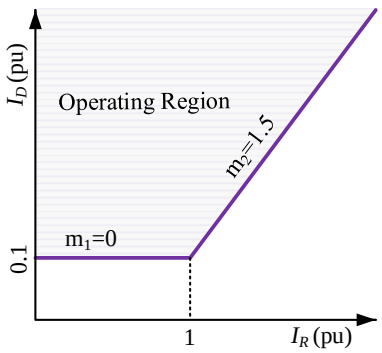


**Figure 2.** Operating characteristic of a conventional GD relay with a recommended setting [13]

For more explanation, to have a wide range of internal ground faults, voltage source is connected to the HV terminal of power transformer while it is fully loaded. 10 points with distances of 0%, 10%, …, 90% of winding length from a Y side terminal and 11 points distributed uniformly on the one phase winding of Δ connection between its middle and the terminal, are considered as fault locations. For each location, fault resistance has three different values. The lowest is 0 Ω and the highest is adjusted to obtain the lowest detectable fault current ($I_D$=10 %) and the third value is between them. Also, 11 points in a time cycle are chosen as fault occurrence time. On the other hand, -85%, 0% and +85% of rated flux are used for the remnant flux of CTs. In total, 1053 internal ground faults are simulated.

For external faults, 880 cases are simulated which includes line-to-ground (L-G) faults, line-to-line (L-L) faults, line-to-line-to-ground (L-L-G) faults and three-phase (L-L-L) faults. These faults have very low resistance to saturate CTs. On the other hand, two scenarios are considered for fault locations. In the first scenario, they locate on the Y side (F3) while the voltage source is connected to Δ side terminal and the power transformer is fully loaded. In the second scenario, the faults locate on the Δ side (F4) while and the voltage supply is connected to Y side terminal and the power

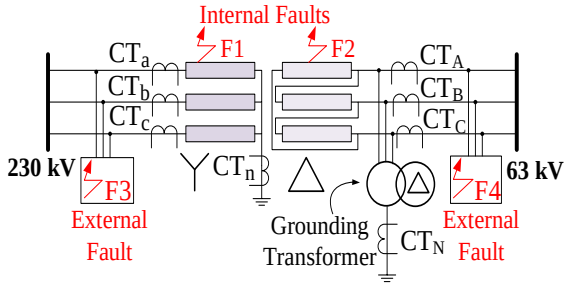


**Figure 4.** The power system under study

**TABLE 1.** Parameters of CTs

| Technical Data | HV side CTs | LV side CTs |
|---|---|---|
| Rated primary current | 600 A | 2000 A |
| Rated secondary current | 1 A | 1 A |
| Magnetic path length | 84.8 cm | 54.8 cm |
| Core cross section area | 32.9 $cm^2$ | 10.36 $cm^2$ |
| CT winding resistance | 4.3 ohm | 7.77 ohm |
| Total burden | 30 VA | 30 VA |

**TABLE 2.** Power transformer specifications

| Technical Data | Rated Value |
|---|---|
| Rated power | 160 MVA |
| HV rated voltage | 230 kV |
| LV rated voltage | 63 kV |
| Short-circuit impedance | 14 % |
| No-load losses | 0.06 % |
| Copper losses | 0.2% |

transformer is fully loaded. Residual flux of CTs and fault inception time are considered similar to internal fault simulations.

To study inrush current conditions, the unloaded power transformer is energizied from both sides, separately. It should be noted that the switching angle varies with step size of 7.2o between 0o and 360o. The remnant flux is set -85% or +85% of nominal value for power transformer and CTs. All in all, 510 simulation cases of inrush current are provided.

**3. 2. Finding α and β** As explained in section 2, $HR_{Mm}$ and $\theta_{mM}$ have been computed 0.1128 and 2.09 rad, respectively. Using these values, $\alpha$ and $\beta$ have been found 2.4823 and 0.2669, respectively. It is worth remembering that trial and error method has been used to find the suitable values for them. As before mentioned, if the use of these values for implementing the proposed method leads to a significant improvement in the relay safety, the validity of the proposed method will be confirmed.

**3. 3. The Proposed Method Accuracy Evaluation** Now, the modified GD algorithm shown in Figure 3 can be implemented. All that remains is to set $I_{TH}$. This parameter must be determined according to the power system condition in which the power transformer is installed. In this research, it is set to 0.01 pu as a very small value to evaluate the proposed method performance very rigorously.

Initially, three scenarios are considered to show the modified GD algorithm proper performance compared with conventional algorithm. It should be noted that the recommended setting [13] is used for both of them. The first scenario is a severe line to ground internal fault with zero resistance occurs at t=100 ms on Y side terminal when the full-load is supplied from Δ side.

The second is a severe line-to-line-to-ground external fault with zero resistance on the Δ side of the fully loaded transformer which occurs at t= 100 ms.

The last scenario is to energize unloaded transformer from Y side at t=100 ms which leads to appearing a significant inrush current. Instantaneous differential current computed for these three scenarios have been shown in Figures 5, 6 and 7, respectively. It is seen during internal fault that the differential current starts to increase just as the internal fault occurs and its wave form shape is affected by CT saturation phenomenon. As can be seen in Figures 6 and 7, differential currents appear only with the saturation of CTs during external fault and inrush current scenarios so that if the CTs was assumed to be unsaturated, differential currents would be remained zero.

Differential current trajectories of these scenarios based on both conventional and modified GD algorithms have been computed and shown in Figures 8, 9 and 10. As shown in Figure 8, differential current trajectories of both algorithms insert to operating region during internal fault with no issue so this fault is detected by them.

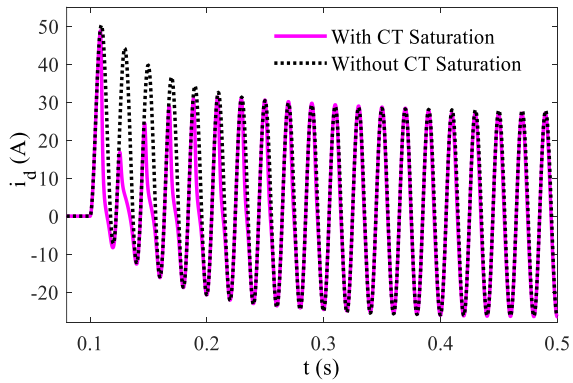


**Figure 5.** Differential current during internal fault

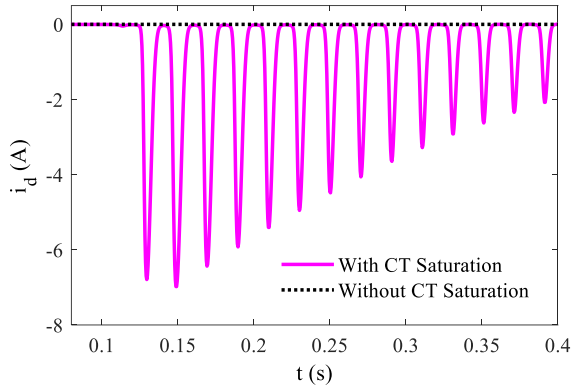


**Figure 6.** Differential current during external fault

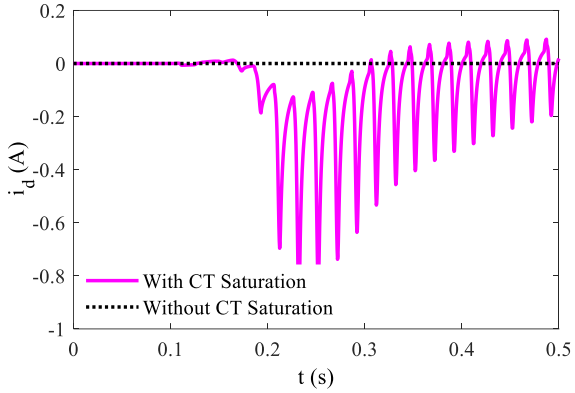


**Figure 7.** Differential current during inrush current

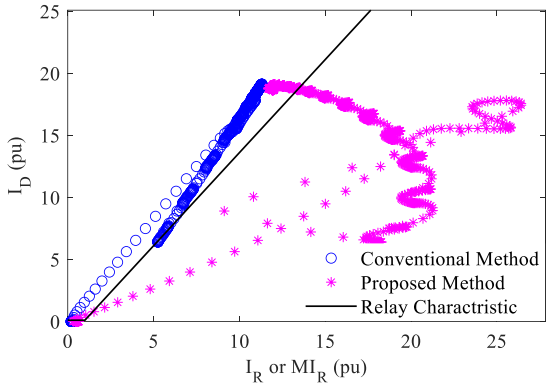


**Figure 8.** Differential current trajectory during internal faults

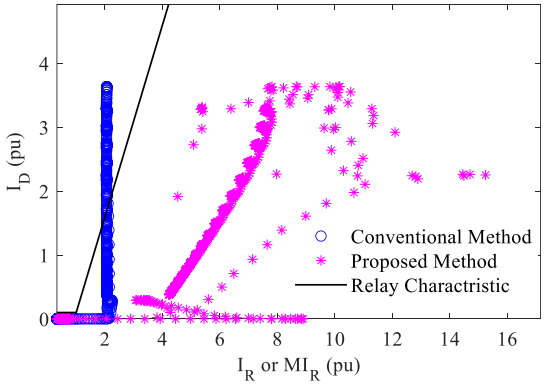


**Figure 9.** Differential current trajectory during external fault

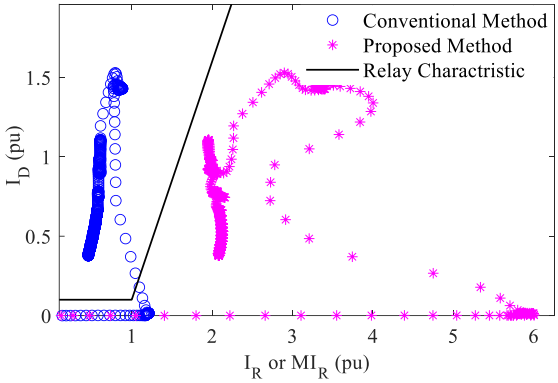


**Figure 10.** Differential current trajectory during inrush current

According to Figures 9 and 10, differential current trajectories computed based on conventional algorithm insert to operating region that means malfunction during external fault and inrush current scenarios while these figures show that the modified algorithm is stable for both critical scenarios.

To have a comprehensive assessment, both conventional and proposed methods performances have been evaluated for all simulation cases illustrated in section 3.1 and Table 3 presents the obtained results. According to this table, both methods detected all 1053 internal ground faults with no issue. However, the conventional method was not stable during 203 external faults but this number is 0 for the proposed method. On the other hand, the malfunction numbers of conventional and proposed methods for inrush current cases are 47 and 5, respectively. Based on these results, the overall accuracy of the conventional method is 89.76%; however, it is 99.79% for the proposed method. This means that the accuracy and stability of the proposed method is quite superior to the conventional method, despite its simplicity.

**TABLE 3.** Comparison results of two methods

| Method | # of misoperation for 1053 cases of internal fault | # of malfunc. for 880 cases of external fault | # of malfunct. for 510 cases of inrush current | Total Accuracy (%) |
|---|---|---|---|---|
| Conv. Method | 0 | 203 | 47 | 89.76 |
| Proposed Method | 0 | 0 | 5 | 99.79 |

## 5. CONCLUSION

Ground differential relay may not be stable during external fault and inrush current conditions if CTs are saturated, deeply. Hence, it is important to develop methods to improve the stability of this relay. In this relay, the restraining current definition in a conventional method has been modified so that an adaptive restrain method has been obtained. The new method performance has been analyzed compared with the conventional method based on a heavy simulation study. The obtained results show that:

- The accuracy and stability of the proposed method is quite superior to the conventional method, despite its simplicity.
- There are no assumptions about the power transformer of CTs nominal values in designing the proposed method so it is a general method similar to conventional method.
- The authors would propose to design GD relay algorithms based on operating characteristic curve with adaptive slopes, in next research works.

## 6. AKNOWLEDGEMENT

The authors gratefully acknowledge the funding support of Babol Noshirvani University of Technology with grant program number BNUT/370199/00.

## 7. REFERENCES

1. Ebadi, A., Hosseini, S.M. and Abdoos, "A New Simple Method to Avoid Maloperation of Transformer Restricted Earth Fault Relay during External Fault Events", ***International Journal of Engineering, Transactions C: Aspects***, Vol. 34, No. 9, (2021), 2070-2076. doi: 10.5829/IJE.2021.34.09C.04
2. Banaei Roudi, F. and Abdoos, A.A., "Detection of Internal Fault from External Fault and Inrush Current in Power Transformers Based on Combination of VMD And ELM", ***Computational Intelligence in Electrical Engineering***, Vol. 9, No. 1, (2018), 65-77. doi: 10.22108/ISEE.2018.110376.1115
3. Ebadi, A., Hosseini, S.M. and Abdoos, A.A., "Designing of a New Transformer Ground Differential Relay Based on Probabilistic Neural Network", ***Energy Engineering & Management***, Vol. 9, No. 4, (2020), 2-13.
4. Apostolopoulos, C. And Tsakiris, D., "Design and Performance Evaluation of a High-Impedance REF Scheme for MV/LV Transformers", ***IEEE Transactions on Industry Applications***, Vol. 51, No. 6, (2015), 5398-5409. doi: 10.1109/TIA.2015.2435003
5. Ebadi, A., Hosseini, S.M. and Abdoos, "Immunity Improvement of a Low-Impedance Restricted Earth Fault Relay by Making its Mechanism Intelligent based on Support Vector Machine", ***Computational Intelligence in Electrical Engineering***, Vol. 9, No. 2, (2018), 29-40. doi: 10.22108/ISEE.2018.111464.1132
6. Ebadi, A., Hosseini, S.M. and Abdoos, A.A., "A New Time-Frequency Analysis Based Supervision Method for the Transformer Restricted Ground Fault Relay", ***International Journal of Electrical Power and Energy Systems***, Vol. 129, (2021), 106858. doi: 10.1016/j.ijepes.2021.106858
7. Ebadi, A., Hosseini, S.M. and Abdoos, A.A., "A New Artificial Intelligence based Supervision Method for Low-Impedance REF Relays", ***Electric Power Systems Research***, Vol. 195, (2021), 107177. doi: 10.1016/j.epsr.2021.107177
8. Taghipour Gorji, R., Hosseini, S.M., Abdoos, A.A. and Ebadi, A., "A Hybrid Intelligent Method for Compensation of Current Transformers Saturation Based on PSO-SVR", ***Periodica Polytechnica Electrical Engineering and Computer Science***, Vol. 65, No. 1, (2021), 53-61. doi: 10.3311/PPee.16248
9. Subramanian, P.V. and Ajitha, L., "Practical Considerations for High Impedance Restricted Earth Fault Relay Settings", ***Journal of The Institution of Engineers (India): Series B***, Vol. 96, No. 1, 107-110, (2015), doi: 10.1007/s40031-014-0124-x
10. GE Co., Technical Documents of T60. Transformer Management Relay, UR Series Instruction Manual. Revision 4.8X; 2005.
11. Siemens Co., Technical Documents of 7UT6. Numerical differential protection relay for transformers, generators, motors, and branch points. 2003.
12. Davarpanah, M., M. Sanaye-Pasand, M. Iravani, R., "Performance Enhancement of the Transformer Restricted Earth Fault Relay", ***IEEE Transactions on Power Delivery***, Vol. 18, No. 1, (2012), 467-474. doi: 10.1109/TPWRD.2012.2208204
13. Ebadi, A., Hosseini, S.M. and Abdoos, A.A., "A New Restricted Earth Fault Relay Based on Artificial Intelligence", ***International Journal of Engineering, Transactions A: Basics***, Vol. 32, No. 1, (2019), 69-70. doi: 10.5829/ije.2019.32.01a.08
14. Krstivojevic, J.P. and Djurić, M.B., "A New Algorithm for Avoiding Maloperation of Transformer Restricted Earth Fault Protection Caused by The Transformer Magnetizing Inrush Current and Current Transformer Saturation", ***Turkish Journal of Electrical Engineering and Computer Sciences***, Vol. 24, No. 6, (2016), 5025-5042. doi: 10.3906/elk-1409-92
15. Krstivojevic, J.P. and Djurić, M.B., "A New Method of Improving Transformer Restricted Earth Fault Protection", ***Advances in Electrical and Computer Engineering***, Vol. 14, No. 3, (2014), 41-48. doi: 10.4316/AECE.2014.03005

## Persian Abstract

**چکیده**

رله دیفرانسیل زمین برای آشکارسازی خطاهای داخلی زمین روی سیم پیچ و ترمینال های ترانسفورماتورهای قدرت استفاده می شود. در واقع، این رله به عنوان مکمل رله دیفرانسیل فاز بکار می رود. با این حال، پایداری آن متاثر از اشباع مغناطیسی در هسته های ترانسفورماتورهای زمین است بطوریکه جریان دیفرانسیلی کاذب ناشی از اشباع ترانسفورماتورهای جریان ممکن است باعث عملکرد اشتباه این رله گردد. در مقاله پیش رو، با اصلاح تعریف جریان مقاوم کننده در یک روش متداول، یک روش مقاوم کننده تطبیق پذیر ارائه می شود. برای ارزیابی کارایی روش پیشنهادی در قیاس با روش متداول، یک ترانسفورماتور قدرت واقعی با نسبت تبدیل 230/63 kV تحت تعداد بزرگی از موارد خطای داخلی و خارجی و همینطور جریان هجومی، در نرم افزار PSCAD/EMTDC شبیه سازی می شود. قابل بیان است که مدل جیلز اثرتون برای شبیه سازی ترانسفورماتورهای جریان استفاده می شود. پیاده سازی و تحلیل روش های مذکور با ستفاده از نتایج حاصله، در محیط نرم افزار MATLAB انجام می پذیرد. نتایج حاصله، علی رغم سادگی روش پیشنهادی برتری کامل آن را در مقایسه با روش متداول نشان می دهد.

IJE TRANSACTIONS B: Applications Vol. 35, No. 11, (November 2022) 2220-2228

International Journal of Engineering

Journal Homepage: www.ije.ir

# An Advanced Modulation Technique Featuring Common Mode Voltage Suppression for Three-Phase Neutral Point Clamped Back to Back Converters

F. Tavassoli[a], H. Ghoreishy*[a], J. Adabi[a], M. Rezanejad[b]

[a] *Faculty of Electrical and Computer Engineering, Babol Noshirvani University of Technology, Mazandaran, Iran*
[b] *Faculty of Electrical Engineering, University of Mazandaran, Babolsar, Mazandaran, Iran*

*PAPER INFO*

*Paper history:*
Received 20 June 2022
Received in revised form 16 July 2022
Accepted 27 August 2022

*Keywords*:
*Electrical Drives*
*Inverter*
*Neutral Point Clamped*
*Common Mode Voltage*
*Amplitude Modulation*
*Space Vector Pulse Width and Amplitude Modulation*

*ABSTRACT*

Three-phase back-to-back converters are widely applied in various industrial, commercial, and domestic applications, such as AC motor drives. Due to the non-sinusoidal voltages they generate, a common mode voltage (CMV) appears, leading to problems in electrical drive systems and high-frequency applications. The CMV and rapid voltage changes can cause serious problems, including leakage currents flowing through the parasitic capacitors inside the motor, electromagnetic interference, shaft voltage, and bearing currents that reduce the motor's lifespan. In general, research to reduce these effects is divided into two methods: modifying the drive system's physical structure or improving the inverter's control algorithm. Pulse Width Modulation (PWM) methods are commonly used in control algorithms of converters to reduce the CMV. However, adding pulse amplitude modulation to the PWM helps reduce the CMV. The technique of simultaneous pulse width and amplitude modulation of space vectors is proposed in this paper to reduce the CMV and its destructive effects in drive systems. The proposed technique is based on the elimination of zero vectors and the inherent reduction of DC link voltage by amplitude modulation leading to a further reduction of the CMV; The obtained results of applying the proposed strategy to a three-phase back-to-back NPC converter with 738-watt steady-state operating point power showed the system's sufficient behavior with the efficiency of 98.62 percent. Finally, the transient performance of the converter from no-load to full-load condition ensures its sufficient behavior for industrial applications.

***doi***: *10.5829/ije.2022.35.11b.17*

## 1. INTRODUCTION

Electric drives are used in a wide range of power (from a few watts to several thousand kilowatts) in many applications such as pumps, textile and paper mills, elevators, cement and steel mills, and robotics. In Adjustable Speed Drive (ASD) systems, pulse width modulation (PWM) inverters are widely used to control the speed and position between the input and motor. PWM inverters convert DC input voltage to a three-phase AC voltage with adjustable frequency and amplitude for controlling the motor speed. ASD systems use power electronic switching devices to produce pulsed voltages to achieve the objective. With the development of semiconductor power devices such as IGBTs and MOSFETs, the high-frequency operation of PWM converters resulted in improvement of their performance [1]. However, these advances have also increased the adverse effects of these inverters. Due to the non-sinusoidal output waveforms of three-phase PWM inverters, a voltage appears between the neutral point of the load and ground, known as the Common Mode Voltage (CMV), which is the source of many problems in ASD systems. This voltage generates leakage currents that go to the ground through parasitic capacitors inside the motor [2]. These currents may adversely affect motor current control and cause electromagnetic interference, resulting in the malfunction of electronic devices nearby [3]. During the operation of the ASD system, various parasitic capacitors appeared in the motor structure, whereas they

*Corresponding Author Institutional Email: ghoreishy@nit.ac.ir (H. Ghoreishy)

Please cite this article as: F. Tavassoli, H. Ghoreishy, J. Adabi, M. Rezanejad, An Advanced Modulation Technique Featuring Common Mode Voltage Suppression for Three-Phase NPC Back to Back Converters, ***International Journal of Engineering, Transactions B: Applications***, Vol. 35, No. 11, (2022) 2220-2228

are negligible in low frequencies. Thanks to the development of switching devices and the possibility of applying higher switching frequencies, the impedance of these parasitic capacitors have become more significant, where they provide an easy path for leakage current at high frequencies.

Furthermore, the CMV contributes to the generation of shaft voltage and bearing currents, resulting in premature failure of the motor bearings [4]. These destructive effects reduce the motor's lifespan and adversely affect the surrounding electronic systems [5]. Therefore, CMV is an essential factor in designing and developing AC electrical drives, and its reduction techniques play a crucial role in reducing the high-frequency problems of these systems. Therefore, numerous techniques for reducing CMV have been discussed in the literature, where optimization is based on pulse width. However, this paper presents simultaneous amplitude and pulse width modulation (PWAM) modulation of space vectors as a new strategy, namely Space Vector Pulse Width and Amplitude Modulation (SVPWAM). This scheme is suitable for medium voltage and high-power AC electrical drive applications. In the proposed method, the ability to change the pulse amplitude is added to the control algorithm of the converter along with the pulse width. In this way, it will further improve the quality of the conventional PWM methods.

Nevertheless, the realization of the PAM part requires changing the DC sources with ones having appropriate transient behavior. Due to the variability of intermediate DC sources in the system, the design of converter parameters is associated with various challenges. The CMV is significantly reduced by regulating the DC link voltage, reducing the harmonic amplitude using PAM, and realizing the SVM method in it (leading to eliminating zero vectors). Moreover, the motor torque ripple is reduced, and a significant improvement in the THD of output voltage and current is achieved [6]. Therefore, the control circuit of the back-to-back converter must be designed to respond to the dynamic speed and produce the DC link voltage with mentioned specifications. In other words, the mentioned parameters have different values in the whole range of the amplitude modulation index.

For this purpose, a solution to select the optimal values is proposed. Despite proposing several reduction methods, it is an evolving field of research required a vast range of theoretical and laboratory analysis. Therefore, less costly and more flexible methods are worth promoting and using in modern industrial applications. Hence, this paper proposed a novel strategy to reduce the CMV, ergo its associated adverse effects in inverters. Implementation of the new SVPWAM modulation strategy is recommended to reduce these effects. Applying the proposed method results in a CMV reduction and low-order harmonics. Therefore, it significantly improves the THD of output voltage and current and decreases the torque ripple of the motor. The proposed strategy is applied to a three-phase three-level back-to-back NPC converter as a more suitable converter for industrial and residential applications. In this regard, the rest of the paper represents the proposed strategy. The second section presents the structure of a three-level back-to-back converter, describing the operation of both the rectifier and inverter. Furthermore, discussing the traditional methods, the CMV generated by them, and conventional methods to reduce the CMV in three-level three-phase inverters are surveyed in section three. Also, these methods' implementation and expansion problems are examined, and the PWAM modulation method is briefly reviewed. Section 4 verifies the proposed control structure's mathematical analyses via MATLAB software simulation results. Then, the harmonic content of the new strategy's output voltage, current, and switching losses are investigated. Afterward, a laboratory prototype is implemented to confirm the simulation results. Finally, the conclusion of the article is presented in the last section.

## 2. MULTILEVEL INVERTER

Multilevel inverters (MLIs) have attracted many researchers in high power applications such as Flexible AC Transmission (FACT) systems, Static Synchronous Compensators (STATCOM), High Voltage DC (HVDC) transmission, motor drives, active filters, as well as in distributed generation systems such as wind farms, due to the need for high output power and frequency [7]. Compared to two-level inverters, these inverters have advantages in high power applications, such as lower voltage stress on switching devices, reduction of harmonic content, and reduction of (dv/dt) stresses [8, 9]. Cascaded H-bridge, flying capacitor, neutral point (diode) clamped (NPC), and switched capacitors are the most popular topologies of MLIs [10, 11]. NPC MLIs can be configured as three, four, and five-level topologies, but only the three-level ones have been widely utilized in high-power drives [12].

Due to generating non-sinusoidal (asymmetric) pulses in these inverters, a CMV is produced, causing many unwanted problems in motors and drive systems, intensified in high-frequency applications [13]. One inexpensive way to reduce the CMV is to modify the modulation techniques used to control three-phase inverters. The main idea of these methods in MLIs is to select vectors that produce zero or the minimum possible amount of CMV [4, 14]. Zhang et al. [15] provided modulation methods for eliminating CMV based on space vector modulation and sinusoidal PWM

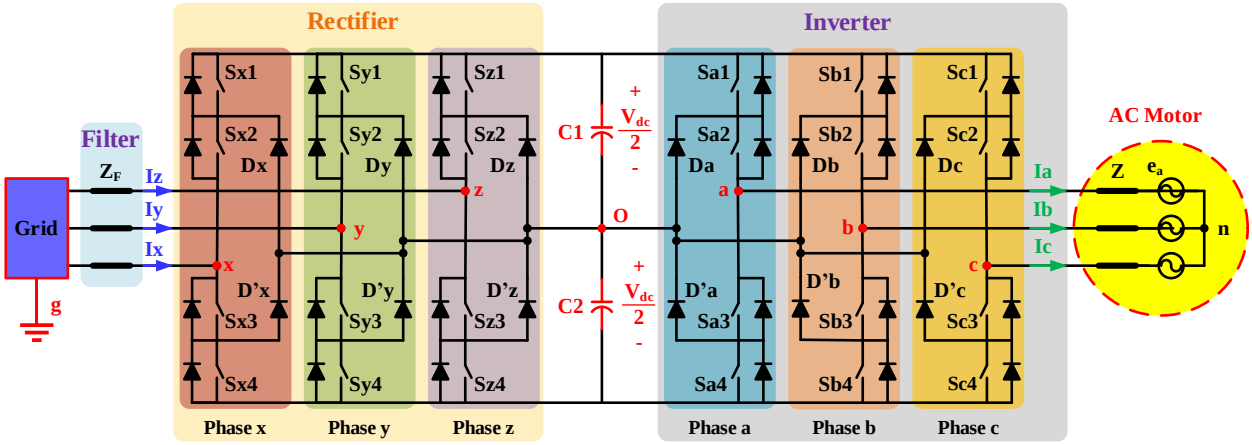


**Figure 1.** Circuit diagram of a three-level NPC back-to-back converter

in NPC MLI. A carrier-based CMV elimination method, along with neutral-balancing, is bybZheng et al. [16]. This method somewhat decreases the CMV; however, the output voltage's THD is considerably high. Furthermore, Xu et al. [17] proposed a zero voltage sequence (ZVS) injection method based on the phase-disposition pulse width modulation (PDPWM).

This method reduced the CMV up to Vdc/6. However, the output voltage THD significantly increases. Adabi et al. [4] proposed a PWM technique to reduce the CMV. These methods reduce the quality of the inverter's output currents because they are based on voltage control and eliminate some voltage vectors to achieve the desired CMV. In this regard, Figure 1 shows the circuit diagram of a three-level NPC-based back-to-back converter used in medium voltage AC drives. The operating conditions of the NPC MLI can be defined by the switching modes shown in Table 1. For example, for leg a of the inverter, the switching state P indicates that the upper two switches on this leg are ON, and the voltage between terminal a and the neutral point O (*Vao*) is $+V_{dc}/2$. Likewise, the N switching state indicates that the two lower switches on this leg are turned on and *Vao* $=-V_{dc}/2$. The state O indicates that the two internal switches are ON; in this case, *Vao* will be zero.

Hence, considering the total of three phases, there would be 27 combinations of switching states for the NPC inverter, which are listed in Table 2, along with the CMV and the resulting voltage vectors. These 27 switching states produce 19 different voltage vectors, of which the space vector diagrams are shown in Figure 2. This means that depending on the switching modes, some voltage vectors represent more than one switching mode and have different CMV. From Table 2, seven switching states result in a zero CMV, whereas twelve modes have a CMV with Vdc/6 amplitude. Also, 6 have a CMV of Vdc/3, and the two remaining modes produce a CMV of Vdc/2. As shown in Figure 2, the space vector diagram can be divided into six triangular sectors (1 to 6), and each of these sectors can again be divided into four triangular areas (regions or subsectors) (1 to 4) [12]. When the reference voltage ($V_{ref}$) rests in an area of a sector, it can be made by the three nearest vectors based on the voltage-sec balance rule. For instance, when the reference voltage is located in region 3 of Sector 1, the voltage-sec balance rule can be written as Equation (1). For a sample time (Ts), the terms T1, T7, and T13 are the times corresponding to the vectors V1, V7, and V13, respectively. Notably, other voltage vectors can also be used to form a reference voltage, yet they adversely distort the harmonic content of the output waveforms.

$$V_{ref}T_S = V_1T_1 + V_7T_7 + V_{13}T_{13}$$
$$T_S = T_1 + T_7 + T_{13} \quad (1)$$

## 3. OPERATION AND MODULATION STRATEGY

### 3. 1. sinusoidal pulse width Modulation (SPWM)

SPWM, widely used in converters, is based on comparing sinusoidal reference and triangular carrier signals [18] due to its simplicity. This scheme can be applied to achieve zero CMV, where a triangular signal with three balanced sinusoidal modulation signals ($V_{m1}$,

**TABLE 1.** Possible states of the NPC inverter per each phase

| State | Phase a switches | | | | Terminal Voltage |
|---|---|---|---|---|---|
| | S1 | S2 | S3 | S4 | |
| P | ON | ON | OFF | OFF | +Vdc/2 |
| O | OFF | ON | ON | OFF | 0 |
| N | OFF | OFF | ON | ON | -Vdc/2 |

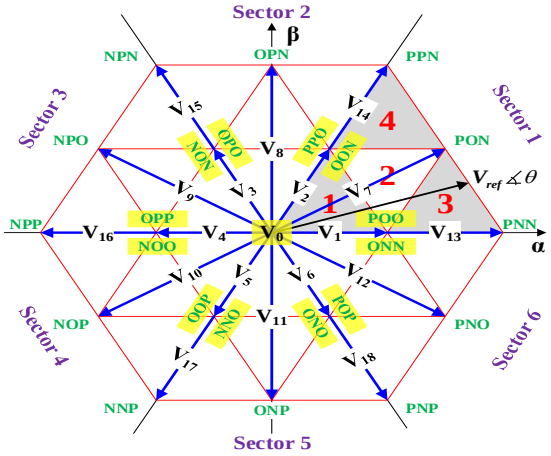


**Figure 2.** Space vector diagram for three-phase NPC inverter

**TABLE 2.** Overall switching states of the three-level NPC

| State | Vector | Amplitude | CMV |
|---|---|---|---|
| [OOO] | V0 | 0 | 0 |
| [NNN] | V0 | 0 | -Vdc/2 |
| [PPP] | V0 | 0 | +Vdc/2 |
| [POO] | V1 | Vdc/3 | +Vdc/6 |
| [ONN] | V1 | Vdc/3 | -Vdc/3 |
| [PPO] | V2 | Vdc/3 | +Vdc/3 |
| [OON] | V2 | Vdc/3 | -Vdc/6 |
| [OPO] | V3 | Vdc/3 | +Vdc/6 |
| [NON] | V3 | Vdc/3 | -Vdc/3 |
| [OPP] | V4 | Vdc/3 | +Vdc/3 |
| [NOO] | V4 | Vdc/3 | -Vdc/6 |
| [OOP] | V5 | Vdc/3 | +Vdc/6 |
| [NNO] | V5 | Vdc/3 | -Vdc/3 |
| [POP] | V6 | Vdc/3 | +Vdc/3 |
| [ONO] | V6 | Vdc/3 | -Vdc/6 |
| [PON] | V7 | √3Vdc/3 | 0 |
| [OPN] | V8 | √3Vdc/3 | 0 |
| [NPO] | V9 | √3Vdc/3 | 0 |
| [NOP] | V10 | √3Vdc/3 | 0 |
| [ONP] | V11 | √3Vdc/3 | 0 |
| [PNO] | V12 | √3Vdc/3 | 0 |
| [PNN] | V13 | 2Vdc/3 | -Vdc/6 |
| [PPN] | V14 | 2Vdc/3 | +Vdc/6 |
| [NPN] | V15 | 2Vdc/3 | -Vdc/6 |
| [NPP] | V16 | 2Vdc/3 | +Vdc/6 |
| [NNP] | V17 | 2Vdc/3 | -Vdc/6 |
| [PNP] | V18 | 2Vdc/3 | +Vdc/6 |

$V_{m2}$, and $V_{m3}$) is used [15]. The following formulas describe this modulation method:

$$\begin{cases} V_a = m_a.\sin(\omega t) \\ V_b = m_a.\sin(\omega t - 2\pi/3) \\ V_c = m_a.\sin(\omega t + 2\pi/3) \end{cases}, \quad \begin{cases} V_{pulse,a} = (V_1 - V_2)/2 \\ V_{pulse,b} = (V_2 - V_3)/2 \\ V_{pulse,c} = (V_3 - V_1)/2 \end{cases} \tag{2}$$

where $m_a$ is the index modulation, $V_a$, $V_b$, and $V_c$ are the phase a, b, and c reference waveforms. Moreover, $V_{pulse,a\text{-}c}$ are the pulses of the NPC inverter, in which $V_1$-$V_3$ are the generated signals obtained from comparing reference waveforms and carriers. Then, considering Figure 1, the CMV ($V_{no}$) can be calculated as follows:

$$V_{no} = \frac{V_{ao}+V_{bo}+V_{co}}{3} = \frac{(V_1-V_2)+(V_2-V_3)+(V_3-V_1)}{3} = 0 \tag{3}$$

Note that the switching modes are selected only from the ones that produce a zero CMV. The voltage vectors mentioned above are used to generate the reference voltage in a way to eliminate the CMV. For example, when the reference voltage is in sector 1, the switching modes are selected sequentially from the ones according to the vectors $V_0$, $V_7$, and $V_{14}$. So, the voltage-second balance rule can be used to determine the time of each switching state as follows:

$$\begin{cases} V_{ref}.T_s = V_0.T_0 + V_7.T_7 + V_{12}.T_{12} \\ T_s = T_0 + T_7 + T_{12} \end{cases} \tag{4}$$

In practical applications, implementation of the modulation method depends on the system structure, applications, customer demand, etc. Therefore, other methods have been proposed in addition to the mentioned ones. A SHEPWM method with a passive typical mode filter is proposed to reduce the CMV and shaft voltage [19]. Yulin et al. [20] proposed two strategies to reduce the switching losses and increase the quality of the output waveform in their CMV reduction method, which is based on the injection of zero vectors by calculating the optimal time of ($\Delta T^s$). Current predictive control has been increasingly used in power inverters due to precise current control, nonlinearity and system limitations, and low current ripple [21]. Hoseini et al. [22] proposed the AZSPWM-based predictive current control method is to reduce electromagnetic interference. Also, Vargas et al. [23] proposed a method based on sine wave pulse width modulation to reduce the CMV in a three-level NPC MLI.

**3. 2. Simultaneous Modulation of Pulse width and Amplitude** The pulse amplitude modulation (PAM) is applied simultaneously to PWM MLI. Suppose that the ability to change the pulse amplitude could be added to the power inverter, like changing the pulse width. In that case, the quality of conventional PWM control methods will be further improved [6]. The

PAM technique stabilizes the amplitude modulation index at specific values and instead changes the DC link voltage in the middle. Thus, a decrease in THD and improving the size of the output filter without increasing the switching frequency are resulted [24, 25]. According to the common methods of SHE-PWM and SHM-PWM, if the value of $V_i$ (i = 1,2,…, n) is fixed as a coefficient of the DC link voltage, i.e., $V_i = V_{dc}$, the odd coefficients of $b_n$ are represented as follows:

$$b_n = \frac{4v_{dc}}{n\pi}(cos(n\alpha_1)+cos(n\alpha_2)+...+cos(n\alpha_n)) \quad (5)$$

Accordingly, unknown angles ($n$) of α are considered degrees of freedom in solving equations resulting from this equation. Furthermore, by the equations obtained, the amplitude of the first harmonic can be controlled at $m_a \times nV_{dc}$, and the amplitude of the first (n-1) odd harmonics that are not a multiple of 3 can be decreased. In the SHM-PWM method, the problem-simplifying assumption of keeping the $V_i$ constant is removed So that all $V_i$ amplitudes can vary between 0 and Vdc. In this case, the degrees of freedom increase from n to 2n, and consequently, the variables of Equation (5) also increase. So, the optimal amplitude or amplitudes are found by solving the obtained equations and the optimal angles. Then, they can be used to control the amplitude of the first harmonic and lower harmonics to a higher order than before (6n-1) and reduce them even to zero [6, 26]. Considering $m_a$ as the modulation index (defined by Equation (6)), the phase voltage for a two-level CB-PWM with a triangular carrier signal has a harmonic spectrum as Equation (7), where $\omega_F$ and $\omega_c$ represent the reference and the carrier frequencies, respectively. Also, i is the group index, j is the side band harmonic index of each group, φ is the carrier wave phase shift, θ is the phase shift of the reference wave, and $J_0$ and $J_1$ are the first-type Bessel functions.

$$m_a = \frac{\sqrt{3}\ V_{ref}}{V_{dc}}, \quad 0 \le m_a \le 1 \quad (6)$$

By generalizing Equation (7) for multilevel inverters, the phase voltage of an N-level inverter is as Equation (8). V is the voltage amplitude of the inverter's output, $h=h_0$ (N-1)/2, and $h_0$ is the phase voltage group index. This relation consists of three expressions: The first denotes the fundamental harmonic amplitude and directly relates to the amplitude modulation index. The second expression represents the amplitude of the output voltage harmonics at frequencies equal to the natural coefficients of the carrier frequency (the central harmonics of each group). It shows that if h is a natural number, there will be no harmonics at these frequencies. The third expression defines the amplitude of the sideband harmonics on both sides of the central harmonic. Regarding $\sin((2h+j)\frac{\pi}{2})$, odd-order sideband harmonics for even-order harmonics and even-order sideband harmonics for odd-order center harmonics exist. Figure 3 shows the calculated per unit (based on V) values of the phase voltage harmonics in terms of modulation index for three-level converters. Equation (8) states that each harmonic solely depends on the amplitude modulation index and is independent of the frequency modulation index ($m_f$) and the reference's angles and carrier waves.

It can be deduced that each modulation index's critical harmonic is the first group's central harmonic. If this harmonic equals zero, the sideband harmonics will be the most important and harmful. Otherwise, they lead to more losses. The dominant harmonic amplitude of the phase voltage reaches zero or its minimum value at one or more points on the horizontal axis. Therefore, if the amplitude modulation index is adjusted at these points, the effect of the dominant harmonic is minimized. This is the main advantage of the proposed CB-PWAM technique. According to Equation (8), the harmonic amplitude depends only on the size of the modulation index. It is independent of the frequency modulation index and angles of the reference and carrier waves. Accordingly, $m_a$ and $V_{dc}$ are the main factors determining the value of the fundamental component of the output waveform. The CB-PWAM technique eliminates or reduces the central or sideband harmonics of the first group without increasing the frequency. For this purpose, instead of using different modulation indices, $m_a$ can always be considered equal to $m_{opt}$. In this case, to keep the amplitude of the fundamental harmonic constant, $V_{dc}$ must vary by $V_{dc} \times m_a/m_{opt}$. An alternative method is to use the hybrid solution (9), in which $V_{dc\text{-}new}$ is the new value of the bus voltage [6].

## 4. PERFORMANCE EVALUATION

To evaluate the proposed method, the three-phase back-to-back NPC converter was simulated in MATLAB Simulink based on the parameters of Table 3. Accordingly, the simulation results for the input and

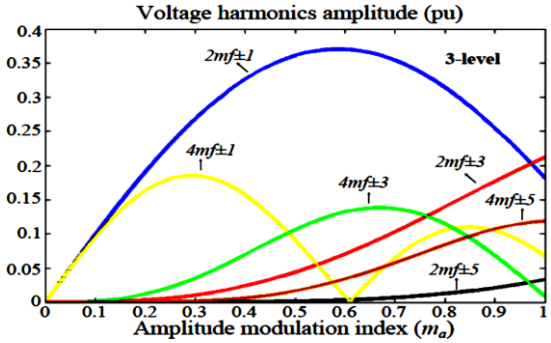


**Figure 3.** Phase voltage harmonics for different $m_a$

$$V_p(t)=m_a\frac{V_{dc}}{2}\cos(\omega_F t+\theta)+\frac{2V_{dc}}{\pi}\sum_{i=1}^{\infty}\frac{J_0(im_a\frac{\pi}{2})}{i}\sin(\frac{i\pi}{2})\cos(i(\omega_c t+\varphi)) + \frac{2V_{dc}}{\pi}\sum_{i=1}^{\infty}\sum_{j=\pm1}^{\infty}[\frac{Jj(im_a\frac{\pi}{2})}{i}\sin((i+j)\frac{\pi}{2})\times\cos(i(\omega_c t+\varphi)+j(\omega_F t+\theta))] \quad (7)$$

$$V_p(t)=m_aV_{dc}\cos(\omega_F t+\theta)+\frac{V_{dc}}{\pi}\sum_{h=1}^{\infty}\frac{J_0(hm_a\pi)}{h}\sin(h\pi)\cos(2h(\omega_c t+\varphi)) + \frac{V_{dc}}{\pi}\sum_{h=1}^{\infty}\sum_{j=\pm1}^{\infty}[\frac{Jj(hm_a\pi)}{h}\sin(2h+j)\frac{\pi}{2})\times\cos(2h(\omega_c t+\varphi)+j(\omega_F t+\theta))] \quad (8)$$

$$\begin{cases} m_a\le 0.61\rightarrow m_a=m_{opt}, & V_{dc,new}=V_{dc}\times\dfrac{m_a}{m_{opt}} \\ m_a>0.61\rightarrow m_a=1, & V_{dc,new}=V_{dc}\times m_a \end{cases} \quad (9)$$

output phase waveforms of the whole converter in steady-state mode are presented in Figure 4. The output power is 738 W leading to a 98.62 percent efficiency. Figure 4(c) shows that the DC link voltage overshoots initially and quickly settle on 200 V afterward. Yet, choosing larger capacitors dampens the overshoot and slows reaching the reference value. Applying the proposed method leads to a smooth input current with a unity power factor. In this condition, the harmonic content of the input current, output current, and voltage (without applying any filters) lead to a 2.73, 0.52, and 30.16 percent THD, respectively. Furthermore, the input and output line waveforms are included in Figure 5, where the output line voltage reaches 200 V. After all, the waveforms of resultant common mode voltages are shown in Figure 5(c), for the rectifier, inverter, and overall back-to-back converter. Notably, the amplitude of each CMV is less than 60 V, which is almost a quarter of the DC link voltage. To better evaluate the proposed method, the converter was also examined for various modulation indexes of the inverter ranging from 0.8 to 1.15 (Figure 6). The output power ranges from 500 to 900 W, while the efficiency slightly changes above 98 percent.

Obviously, the output power curve, as well as the efficiency one, varies according to the application, resulting in a different intersection point as a reference to choose the optimal modulation index. Moreover, the selection of $M_a$ depends on the desired input current THD, as well. Since the utility grid supplies the converter, it is essential that the input current THD remains below 5 percent (IEEE std.519-2014). Meanwhile, increasing $M_a$ leads to a decline in input current THD and a significant drop in the load voltage THD. A 700 W prototype of the three-level back-to-back converter was implemented to verify the simulation results (Figure 7). The proposed controller is applied by the DSP TMS320F28335. Figure 7.a depicts the rectifier side waveforms where the phase 'a' input current is in phase with the corresponding input voltage signifying the unity power factor. Moreover, the DC link voltage is regulated at 200 V with the help of the proposed method.

**TABLE 3.** Switching states of the three-level NPC inverter

| Parameter | Value |
|---|---|
| Grid phase voltage (RMS) | 50 V |
| Grid frequency | 50 Hz |
| Switching Frequency | 10 kHz |
| DC link voltage | 200 V |
| DC link capacitors | C1=C2=3300 µF |
| Modulation index | 0.95 |
| Input filter | 0.014 Ω+2 mH |
| Load | 20 Ω+30 mH |

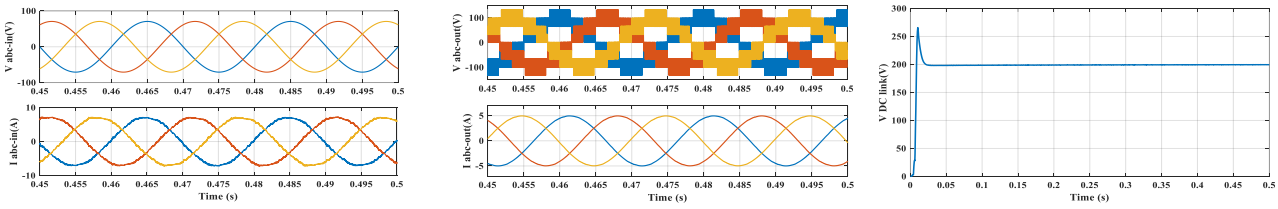


(a) (b) (c)

**Figure 4.** Phase waveforms: (a) rectifier's input and (b) inverter's output, (c) DC-Link voltage

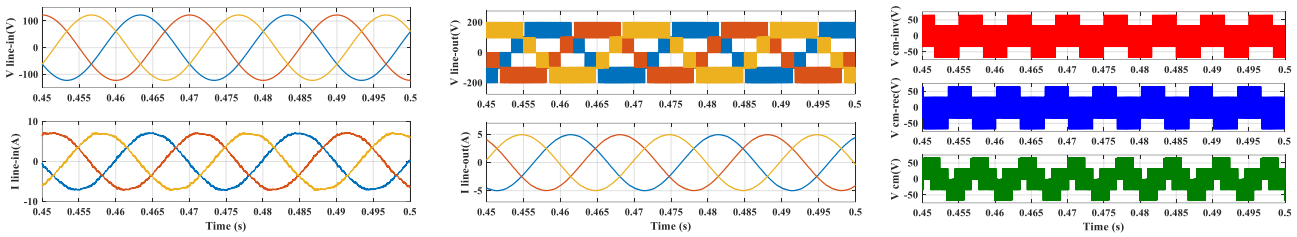


(a) (b) (c)

**Figure 5.** Line waveforms: (a) rectifier's input and (b) inverter's output, and (c) CMV

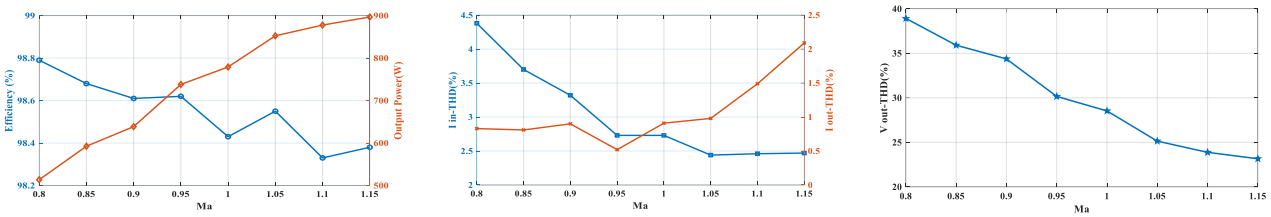


(a) (b) (c)

**Figure 6.** Simulation results for the converter: (a) efficiency, (b) current THD, and (c) load voltage THD for various values of Ma

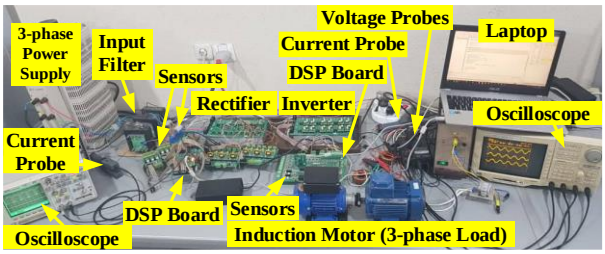


**Figure 7.** Test setup

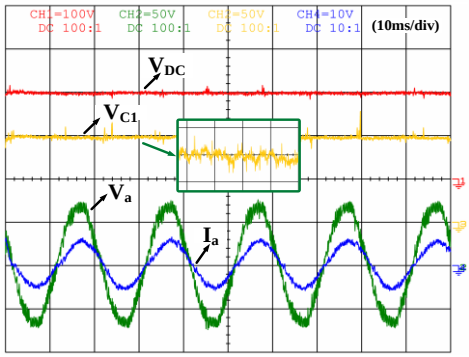


(a)

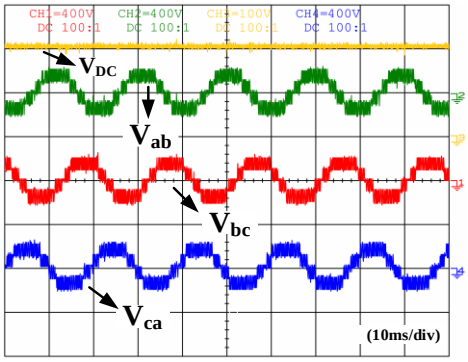


(b)

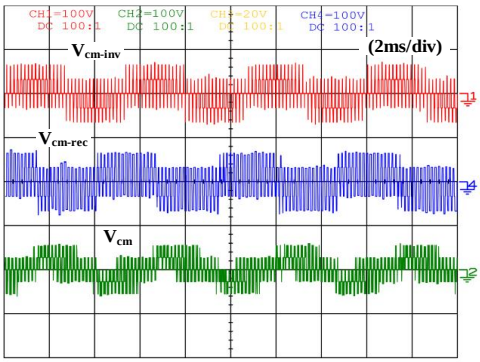


(c)

**Figure 8.** Experimental results for the waveforms of (a) rectifier, (b) inverter, and (c) CMV

In addition, as it is noticeable from the DC link and $C_1$ voltages, the capacitors' voltages are balanced. Figure 8.b describes the inverter's three-phase voltages. As can be perceived, all three voltages are symmetrical, and the proposed method can properly generate the reference voltage. Figure 8.c shows the common mode voltage of the inverter, rectifier, and the total back-to-back system. Notably, the total CMV's amplitude is also considerably low and symmetrical. In such conditions, the harmonic spectrum of the inverter's phase 'a' voltage is displayed in Figure 9.a, where its THD is 10.4 percent. Also, the harmonic spectrum of the rectifier's phase 'a' current is demonstrated in Figure 9.b, having a THD of 1.4 percent, satisfying the IEEE-519-STD.

Figure 10 illustrates the transient response of the converter when the output load alters from full-load to no-load and then from no-load to full-load condition. As can be seen, the controller reacts rapidly to this change

and the DC-link and C1 voltages. Moreover, the rectifier responds smoothly to this variation. It is noticed that the inverter output voltage performance is acceptable and follows the reference value during the test. Consequently, the system's stability is ensured despite sudden changes in the converter's operating point.

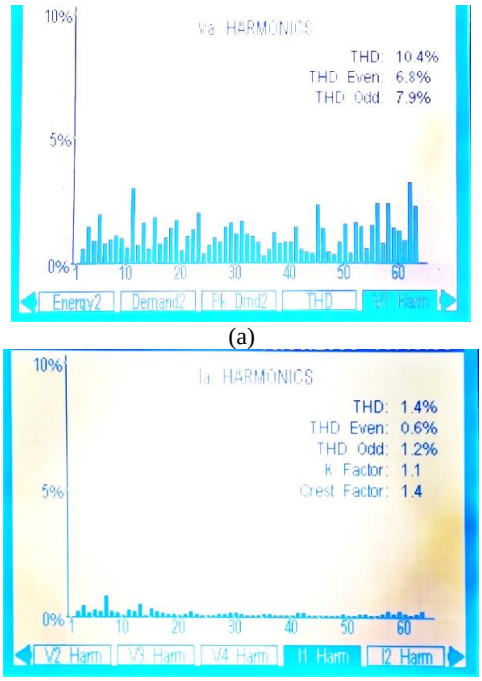


(a)

(b)

**Figure 9.** The experimental harmonic content of the output waveforms for phase A of (a) inverter's voltage and (b) rectifier's current

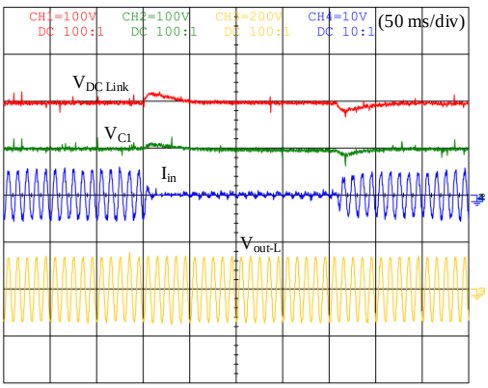


**Figure 10.** Transient response of the proposed technique

## 5. CONCLUSION

This paper proposed a novel modulation strategy to reduce the common mode voltage of non-sinusoidal voltages generated by multilevel inverters. Considering the significance of the back-to-back converters in industries on the one hand and the possible adverse impacts of CMV along with rapid voltage changes in high-frequency switching, on the other hand, requires further attention. Accordingly, a combination of simultaneous pulse width and amplitude modulation with space vector modulation technique is addressed to tackle this issue. In this regard, eliminating the zero vectors of the voltage waveform and regulation of the DC link voltage by amplitude modulation are applied. Applying the proposed strategy to a three-phase three-level NPC back-to-back converter resulted in an efficiency of 96.62 percent. Also, the input current THD of 2.73 percent was achieved with a unity power factor, whereas the THD for the output current was 0.52. These results are for a 738-watt prototype at the operating point with a 0.95 modulation index. Consequently, the proposed technique is suitable for various ASD, transmission lines, industrial, and residential applications.

## 6. REFERENCES

1. M. Rasouli Khatir, H. Ghoreishy, and S. A. Gholamian, "Virtual flux based direct power control on vienna rectifier," ***International Journal of Engineering, Transactions B: Applications***, Vol. 31, No. 2, (2018), 284-291, doi: 10.5829/ije.2018.31.02b.12.
2. J. Adabi, A. A. Boora, F. Zare, A. Nami, A. Ghosh, and F. Blaabjerg, "Common-mode voltage reduction in a motor drive system with a power factor correction," ***IET Power Electronics***, Vol. 5, No. 3, (2012), 366-375. doi: 10.1049/iet-pel.2011.0189.
3. F. Zare, "Practical approach to model electric motors for electromagnetic interference and shaft voltage analysis," ***IET Electric Power Applications***, Vol. 4, No. 9, (2010), 727-738. doi: 10.1049/iet-epa.2009.0305.
4. J. Adabi, F. Zare, G. Ledwich, and A. Ghosh, "Leakage current and common mode voltage issues in modern AC drive systems," Australasian Universities Power Engineering Conference, Perth, Australia, (2007), 1-6, doi: 10.1109/AUPEC.2007.4548097.
5. A. Willwerth and M. Roman, "Electrical bearing damage—a lurking problem in inverter-driven traction motors," IEEE Transportation Electrification Conference and Expo (ITEC), (2013), 1-4, doi: 10.1109/ITEC.2013.6573484.
6. H. Ghoreishy, A. Y. Varjani, S. Farhangi, and M. Mohamadian, "A novel pulse-width and amplitude modulation (PWAM) control strategy for power converters," ***Journal of Power Electronics***, Vol. 10, No. 4, (2010), 374-381, doi:10.6113/JPE.2010.10.4.374.
7. A. Khodaparast, M. J. Hassani, E. Azimi, M. E. Adabi, J. Adabi, and E. Pouresmaeil, "Circuit Configuration and Modulation of a Seven-Level Switched-Capacitor Inverter," ***IEEE Transactions on Power Electronics***, Vol. 36, No. 6, (2021), 7087-7096, doi: 10.1109/TPEL.2020.3036351.
8. M. Hassani, E. Azimi, A. Khodaparast, J. Adabi, and E. Pouresmaeil, "Fault-Tolerant Operation Strategy for Reliability Improvement of a Switched-Capacitor Multi-Level Inverter," ***IEEE Transactions on Industrial Electronics***, (2021), doi: 10.1109/TIE.2021.3135623.
9. A. Azimi, A. Khodaparast, M. Rasouli, and J. Adabi, "A Novel Sensorless Voltage Multiplier Inverter for Electric Vehicle

Application" 13th Power Electronics, Drive Systems, and Technologies Conference (PEDSTC), (2022), 609-614, doi: 10.1109/PEDSTC53976.2022.9767479.

10. E. Azimi, A. Tavasoli, H. Hafezi, and A. Nateghi, "A Dumbbell Type (D-Type) multilevel inverter based on switched capacitor concept," ***International Journal of Electronics***, (2021), doi: 10.1080/00207217.2021.1908621.
11. E. Azimi *et al.*, "X-type step-up multilevel inverter with reduced component count based on switched-capacitor concept," Electronics, MDPI (Switzerland), Vol. 9, No. 12, (2020), 1-18, doi: 10.3390/electronics9121987.
12. B. Wu and M. Narimani, *High-power converters and AC drives*. John Wiley & Sons, (2017).
13. [13] T. D. Nguyen and H.-H. Lee, "A new SVM method for an indirect matrix converter with common-mode voltage reduction," ***IEEE Transactions on Industrial Informatics***, Vol. 10, No. 1, (2013), 61-72, doi: 10.1109/TII.2013.2255032.
14. H.-N. Nguyen and H.-H. Lee, "An enhanced SVM method to drive matrix converters for zero common-mode voltage," ***IEEE Transactions on Power Electronics***, Vol. 30, No. 4, (2014), 1788-1792, doi: 10.1109/TPEL.2014.2348019.
15. H. Zhang, A. Von Jouanne, S. Dai, A. K. Wallace, and F. Wang, "Multilevel inverter modulation schemes to eliminate common-mode voltages," ***IEEE Transactions on Industry Applications***, Vol. 36, No. 6, (2000), 1645-1653, doi: 10.1109/28.887217.
16. X. Xu, Z. Zheng, K. Wang, B. Yang, and Y. Li, "A Carrier-Based Common-Mode Voltage Elimination Method for Back-to-Back Three-Level NPC Converters," ***IEEE Transactions on Power Electronics***, Vol. 37, No. 3, (2021), 3040-3052, doi: 10.1109/28.887217.
17. X. Xu, Z. Zheng, K. Wang, B. Yang, and Y. Li, "A comprehensive study of common mode voltage reduction and neutral point potential balance for a back-to-back three-level NPC converter," ***IEEE Transactions on Power Electronics***, Vol. 35, No. 8, (2019), 7910-7920, doi: 10.1109/TPEL.2019.2961385.
18. P. W. Hammond, "A new approach to enhance power quality for medium voltage AC drives," ***IEEE Transactions on Industry Applications***, Vol. 33, No. 1, (1997), 202-208, doi: 10.1109/28.567113.
19. G. Carrara, S. Gardella, M. Marchesoni, R. Salutari, and G. Sciutto, "A new multilevel PWM method: A theoretical analysis," ***IEEE Transactions on Power Electronics***, Vol. 7, No. 3, (1992), 497-505, doi: 10.1109/63.145137.
20. Z. Yulin, Z. Zhengming, and Y. Liqiang, "Suppression of common-mode and shaft voltages in inverter-driven induction motor," ***Journal of Tsinghua University (Science and Technology)***, Vol. 49, No. 1, (2009), 25-28.
21. X. Wu, G. Tan, Z. Ye, Y. Liu, and S. Xu, "Optimized common-mode voltage reduction PWM for three-phase voltage-source inverters," ***IEEE Transactions on Power Electronics***, Vol. 31, No. 4, (2015), 2959-2969, doi: 10.1109/TPEL.2015.2451673.
22. S. K. Hoseini, J. Adabi, and A. Sheikholeslami, "Predictive modulation schemes to reduce common-mode voltage in three-phase inverters-fed AC drive systems," ***IET Power Electronics***, Vol. 7, No. 4, (2014), 840-849, https://doi.org/10.1049/iet-pel.2013.0182.
23. R. Vargas, P. Cortés, U. Ammann, J. Rodríguez, and J. Pontt, "Predictive control of a three-phase neutral-point-clamped inverter," ***IEEE Transactions on Industrial Electronics***, Vol. 54, No. 5, (2007), 2697-2705, doi: 10.1109/TIE.2007.899854.
24. S. M. Mousavian, H. Ghoreishy, and M. R. Zahabi, "A Generalized Carrier-Based PWM Technique for Multilevel Back-to-Back Converters," ***Tabriz Journal of Electrical Engineering***, Vol. 48, No. 2, (2018), 919-930.
25. H. Ghoreishy, A. Y. Varjani, S. Farhangi, and M. Mohamadian, "Hybrid cascaded H-bridge inverter with even power distribution and improved total harmonic distortion: analysis and experimental validation," ***IET Power Electronics***, Vol. 5, No. 8, (2012), 1245-1253, doi: 10.1049/iet-pel.2012.0111.
26. H. Ghoreishy, Z. Zhang, O. C. Thomsen, and M. A. E. Andersen, "A fast-processing modulation strategy for three-phase four-leg neutral-point-clamped inverter based on the circuit-level decoupling concept," in Proceedings of the 7th International Power Electronics and Motion Control Conference, Vol. 1, (2012), 274-280, doi: 10.1109/IPEMC.2012.6258848.

## Persian Abstract

**چکیده**

مبدل‌های پشت‌به‌پشت سه‌فاز به‌طور گسترده در کاربردهای مختلف صنعتی، تجاری و خانگی مانند درایوهای موتور AC کاربرد دارند. با توجه به ولتاژهای غیرسینوسی که تولید می‌کنند، یک ولتاژ حالت مشترک ظاهر می‌شود که منجر به مشکلاتی در سیستم‌های محرک الکتریکی و کاربردهای فرکانس بالا می‌شود. CMV، همراه با تغییرات سریع ولتاژ، می‌تواند باعث مشکلات جدی از جمله جریان‌های نشتی که از خازن‌های انگلی داخل موتور عبور می‌کنند، تداخلات الکترومغناطیسی، ولتاژ شفت و جریان‌های بلبرینگ که طول عمر موتور را کاهش می‌دهند، شود. بنابراین، طراحان سیستم محرکه می‌بایست CMV و تداخل الکترومغناطیسی و همچنین، روش‌های کاهش آن‌ها را به‌عنوان عوامل مهم در طراحی خود در نظر بگیرند تا از اثرات نامطلوب آنها جلوگیری شود. به طور کلی، تحقیقات برای کاهش این اثرات به دو روش اصلاح ساختار فیزیکی سیستم محرک یا بهبود الگوریتم کنترل اینورتر تقسیم می‌شود. روش‌های مدولاسیون عرض پالس معمولاً در الگوریتم‌های کنترل مبدل‌ها برای کاهش CMV استفاده می‌شوند. با این حال، روش مدولاسیون همزمان پهنای پالس و دامنه بردارهای فضایی در این مقاله برای کاهش CMV و اثرات مخرب آن در سیستم های محرک پیشنهاد شده‌است. روش پیشنهادی، بر اساس حذف بردارهای صفر و کاهش ولتاژ لینک DC ناشی از مدولاسیون دامنه، منجر به کاهش بیشتر CMV می‌شود. سپس، استراتژی پیشنهادی روی یک مبدل NPC پشت‌به‌پشت سه‌فاز در نقطه کار ۷۳۸ وات اعمال می‌شود. نتایج به‌دست‌آمده، رفتار مناسب سیستم را با بازده ۹۸.۶۲ درصد را نشان می‌دهد. در نهایت، عملکرد گذرا مبدل از حالت بی‌باری به بار کامل، رفتار مناسب آن را برای کاربردهای صنعتی تضمین می‌کند.

International Journal of Engineering

Journal Homepage: www.ije.ir

# In Silico Analysis of Stem Cells Mechanical Stimulations for Mechnoregulation Toward Cardiomyocytes

M. Ebad, B. Vahidi*

*Faculty of New Sciences and Technologies, University of Tehran, Tehran, Iran*

*PAPER INFO*

*Paper history:*
Received 10 January 2022
Received in revised form 03 August 2022
Accepted 01 September 2022

*Keywords*:
*Cardiac Tissue Engineering*
*Pulsatile Flow*
*Cyclic Strain*
*Stress Phase Angle*
*Shear Stress*

*ABSTRACT*

Because of the ability of stem cells to self-renew and differentiate into cardiomyocytes, they are optimal cell sources for cardiac tissue engineering. Since heart cells experience cyclic strain and pulsatile flow in vivo, these mechanical stimuli are essential factors for stem cell differentiation. This study aimed to investigate the effect of a combination of pulsatile flow and cyclic strain on the shear stress created on the embryonic stem cell layer with a elastic property in a perfusion bioreactor by using the fluid-solid interaction (FSI) method. In this study, the frequency and stress phase angle had been assumed as a variable. The results show that the maximum shear stress at frequencies of 0.33, and 1 Hz and with frequency differences in cyclic strain (0.33 Hz) and pulsatile flow (1 Hz) are 0.00562, 0.02, and 0.01 dyn/cm², respectively. Moreover, in the stress phase angles 0, $\pi/4$, and $\pi/2$, the maximum shear stress are equal to 0.00562, 0.009, and 0.014 dyn/cm², respectively. The results of this study can be an effective step in developing cardiac tissue engineering and a better understanding of the effects of mechanical stimuli on stem cell differentiation.

***doi**: 10.5829/ije.2022.35.11b.18*

## 1. INTRODUCTION

Heart failure is the leading cause of mortality globally, and the methods of diagnosing this disease still have many shortcomings [1]. When blood flow to the heart muscle is abruptly interrupted, a heart attack occurs that leads to causes immutable myocardial ischemia, formation of a non-contractile scar, and loss of cardiac muscle cells (cardiomyocytes). Currently, surgical interventions for the treatment of heart disease have limitations such as heart donor shortage, the need to take immunosuppressant drugs after transplantation, and limited strength of transplanted organs [2]. Also, since adult mammalian heart muscle cell proliferation rapidly ceases after birth, this tissue has a limited ability to regenerate itself [3]. Therefore, cardiac tissue engineering offers new solutions to overcome these limitations using combinations of cells with regenerative capacity, scaffolds, growth factors, and mechanical and/or electrical stimuli [4]. In general, different types of stem cells are used in regenerative medicine for cardiovascular diseases including Bone marrow-derived mononuclear cells (MNCs), Mesenchymal stromal/stem cells (MSCs), Cardiac Stem Cells (CSCs), Embryonic stem cells (ESCs), and Induced pluripotent stem cells (iPSCs) [5]. Scaffolds or membranes used in cardiac tissue engineering are suitable substrates for controlled secretion of growth factors and replacement for some damaged extracellular matrices after myocardial infarction. [6]. To have successful cardiac tissue engineering, the use of bioreactors to mimic the native microenvironment of cardiomyocytes, accompanied by electrical and mechanical stimuli such as strain, pressure, and fluid flow, can be beneficial [7]. Cells sense a mechanical environment primarily through the integrin-mediated focal adhesion and actin cytoskeleton tension, which interact with external biophysical stimuli to evoke downstream signaling (mechanotransductive signaling) [8]. It has been demonstrated that fluid shear stress plays an essential role in embryonic development and organogenesis [9]. Cardiomyocytes or contractile cells are under cyclic strain and pulsatile flow due to the heart

*Corresponding Author Institutional Email: bahman.vahidi@ut.ac.ir (B. Vahidi)

Please cite this article as: M. Ebad, B. Vahidi, In Silico Analysis of Stem Cells Mechanical Stimulations for Mechnoregulation Toward Cardiomyocytes, ***International Journal of Engineering, Transactions B: Applications***, Vol. 35, No. 11, (2022) 2229-2237

being full and empty in-vivo [10]. These mechanical stimuli play a key role in differentiating stem cells, regulating cardiac tissue function, increasing gene expression, and homeostasis [2]. Therefore, it would be of great value to evaluate the effects of different mechanical stimuli on the differentiation of stem cells into cardiomyocytes. In the study by Mihic et al., by applying a single-axis cyclic stretch at a frequency of 1.25 Hz for 72h to embryonic stem cells, the length of cell and gap junction expression was increased [11]. In 2011, Tulloch et al. [12] stated that cells that are exposed to uniform cyclic stretching at 1 Hz for four days experienced an increase in cardiomyocyte elongation with sarcomere alignment. In another study, when the neonatal cardiac cellular constructs were exposed to pulsatile flow in a perfusion bioreactor for 24h, it significantly synthesized high levels of contractile protein and cell-cell adhesion [13]. In the study of Shen et al. [14] embryonic stem cells underwent a 1.48 mL/minute pulsatile flow rate and a 5% cyclic strain at the frequency of 0.33 Hz differentiated into cardiac cells at a shear stress of $5.6\times10^{-3}$ dyn/cm². Since most of the investigations performed on this subject have been studied experimentally [10, 15], we decided to study the effect of the frequency and stress phase angle (the phase difference between stress and strain) of mechanical stimuli (cyclic strain and pulsatile flow) on the maximum shear stress created on embryonic stem cell layer using finite element method.

## 2. MATERIALS AND METHODS

Finite element method was used in this study to simulate the problem. This method has various applications in different fields [16-18], as it can help us evaluate the effects of different parameters simultaneously and reduce the cost and time of our engineering investigations. In this computational analysis, the geometry of the problem is a 3D model of a cell-bioreactor complex that consists of a cell layer, membrane, silicon layer, and bioreactor (Figure 1). Using the two-way FSI analysis in COMSOL software, the combination of mechanical parameters of 1.48 mL/minute pulsatile flow and 5% cyclic strain was considered [14]. The inlet boundary conditions on the left and bottom of the bioreactor are 1.48 mL/minute pulsatile flow rate (water) and 5% cyclic strain (air), respectively. The fluid (water) was considered Newtonian, viscous, and incompressible with a viscosity of 8.1e-4 (Pa.s), and a density of 1000 kg/m$^3$. Also, Air pressure, Dynamic viscosity, and density of air were 1.35 atm, 2e-5 (Pa.s), and 1.225 kg/m$^3$, respectively [14, 19]. Moreover, the pressure of 0 Pa was considered as the outlet boundary condition [20]. The non-slip condition was applied to all the walls. It is assumed that all boundaries were fixed. The mechanical properties considered for the solid models are summarized in Table 1 [14].

The frequency and stress phase angle had been assumed as a variable. The amount of frequency in this study was

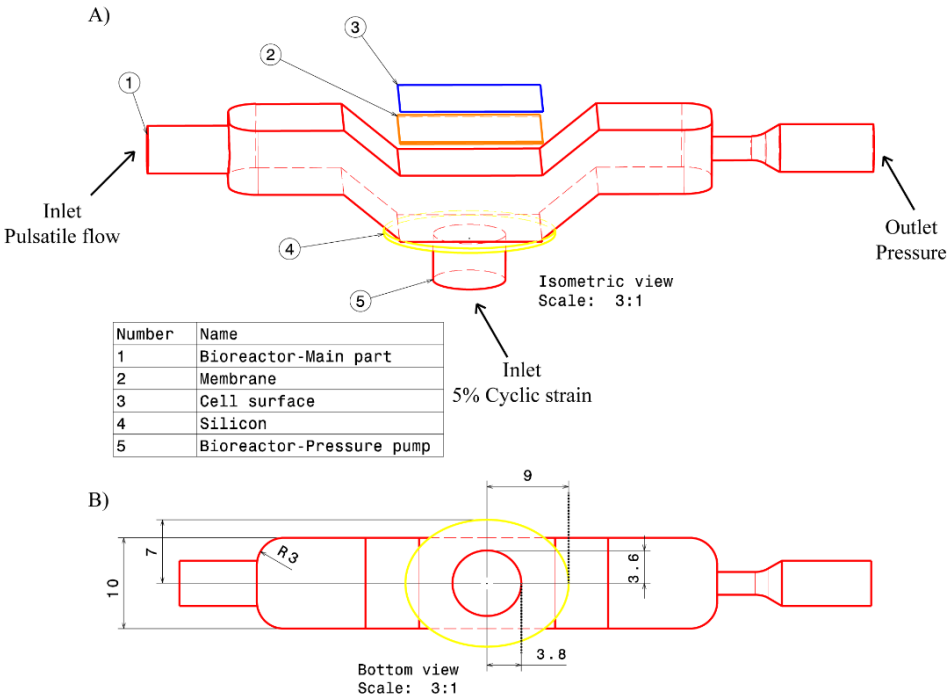


**Figure 1.** Geometry of bioreactor- stem cell layer complex A) isometric and B) bottom view [14]

**TABLE 1.** Mechanical properties of solid domain

| Solid domain | Elastic modulus (MPa) | Poisson's ratio | Density (kg/m³) |
|---|---|---|---|
| Embryonic stem cell | 0.01 [21] | 0.45 [21] | 1060 [22] |
| Cell-seeded membrane | 0.6 [23] | 0.44 [24] | 1400 [24] |
| Silicon membrane | 150 [25] | 0.49 [25] | 1030 [26] |

considered 0.33 Hz and 1Hz which are in the physiological range of the body [14, 27]. Besides, To analyze the effect of the stress phase angle, three phases 0, $\pi/4$ and $\pi/2$ were considered (Figure 2a) [28]. Navier–Stokes, pulsatile flow, and cyclic strain equations were used as the governing equations in the problem was noted in equations 1-3, respectively [29-32]:

$$\frac{\partial \rho \boldsymbol{V}}{\partial t} + \nabla \cdot (\rho \boldsymbol{V}\boldsymbol{V} - \tau) = \boldsymbol{f}^{B} \quad (1)$$

$$Q_{(t)} = Q_0 + Q_0 \sin(\omega t + \varphi) \quad \omega = 2 \times \pi \times f \quad (2)$$

$$\varepsilon_{(t)} = \varepsilon_0 \sin(\omega t) \quad (3)$$

wherein Equation (1), $\rho$ is the density, $\boldsymbol{V}$ is the velocity vector, $\tau$ is the stress tensor, and $\boldsymbol{f}^{B}$ is the body force vector of the fluid medium. In Equation (3), Q is the flow rate, $t$ is the time, $\omega$ is the angular velocity, $Q_0$ is the flow rate at $t$ =0 which is equal to 1.48 mL/minute, $\varphi$ is the phase angle, and f is the frequency. In Equation (4), $\varepsilon_0$ is the maximum amplitude of the strain is equal to 5%. Besides, kinematic equilibrium equation and traction equilibrium along the fluid–structure interfaces can be written as follows (Equations (4)-(5)) [33]:

$$\mathbf{u}_{fluid} = \mathbf{u}_w \cdot \mathbf{u}_w = \frac{\partial \boldsymbol{d}_{solid}}{\partial t} \quad (4)$$

$$\sigma.\mathbf{n} = \Gamma.\mathbf{n}\,, \quad \Gamma = [-\mathbf{P}\mathbf{I} + \mu\left(\nabla \mathbf{u}_{fluid} + \left(\nabla \mathbf{u}_{fluid}\right)^{T}\right) - {}^{2}/_{3}\,\mu(\nabla.\mathbf{u}_{fluid})\mathbf{I}] \quad (5)$$

According to Equation (4), this part is related to the coupling of fluid and solid velocities (which is the result of its deformation due to the flow) at the interface between these two domains, and equation 5 is related to the transfer of stress from fluid flow to the solid domain. In applying no-slip boundary conditions at the wall, the coupling conditions at the fluid-solid interface, $\boldsymbol{d}_{solid}$ is the solid displacement, μ is the dynamic viscosity, and $\nabla\ \mathbf{u}_w$ and $\mathbf{u}_{fluid}$ are the wall and fluid velocity, respectively. For this (FSI) physics, to create a computational mesh in the desired model tetrahedral elements were used (Figure 2(b)). To ensure the mesh independence of the solution, the geometry was discretized in five models with different element numbers (116157, 277892, 399663, 532159, and 678932), and the changes in shear stress magnitude were analyzed. However, there was no sensible change in the magnitude of the maximum shear stress with the number of elements beyond 399663. Therefore, this number of elements was used for the five models of this study (Figure 2(c)).

## 3. RESULTS

In this study, for the first time, using computational simulation, the effect of different mechanical parameters on the shear stress created on the embryonic stem cell layer was investigated. As a result, two parameters of frequency, and stress phase angle were analyzed.

**3. 1. Frequency** In the first study, the effect of frequency was investigated for three different models. In the first and second models, both pulsatile flow and cyclic strain had an equal frequency of 0.33 Hz, and 1Hz, respectively. Also, for the third model, the pulsatile flow and cyclic strain had a frequency equal to 0.33 Hz and 1 Hz, respectively. The air-fluid pressure fields for the model with different frequencies can be seen in Figure 3a. The maximum shear stress for the first group is 0.00562 (Figure 3(b)), which is very close to the shear stress obtained in the Shen et al. [14] study (0.0056 dyn/cm²). This shear stress is also evenly distributed on the surface of the cell layer during the period [0.65, 0.75, and 0.85 s] (Figure 4(a)) that the center of the cell layer experiences the maximum value of shear stress. When both mechanical stimuli, pulsatile flow, and cyclic strain, are performed at a frequency of 1 Hz, the amount of shear stress on the cell layer roses remarkably to 0.02 dyn/cm² Within the specified time (1.15, 1.25, and 1.35 s), but this magnitude shear stress is not uniformly spread on the surface of the stem cell layer (Figure 4b). In the third model, the difference between the frequencies of the mechanical parameters led to an increase in the maximum shear stress from 0.0056 dyn/cm² to 0.01 dyn/cm² at the specified time (1.15, 1.25, and 1.35 s). However, the maximum shear stress occurs on the left side of the embryonic stem cell layer, where the pulsatile flow was applied (Figure 4(c)).

**3. 2. Stress Phase Angle** For the second model, Since the effect of the stress phase angle parameter on cardiomyocytes has not been studied to date, in this study, the effect of this parameter on shear stress created on the cell layer was investigated. In the model where there was no phase difference between the mechanical parameters ($\varphi = 0$), the shear stress is equal to 0.00562 dyn/cm², and the whole cell surface was subjected to

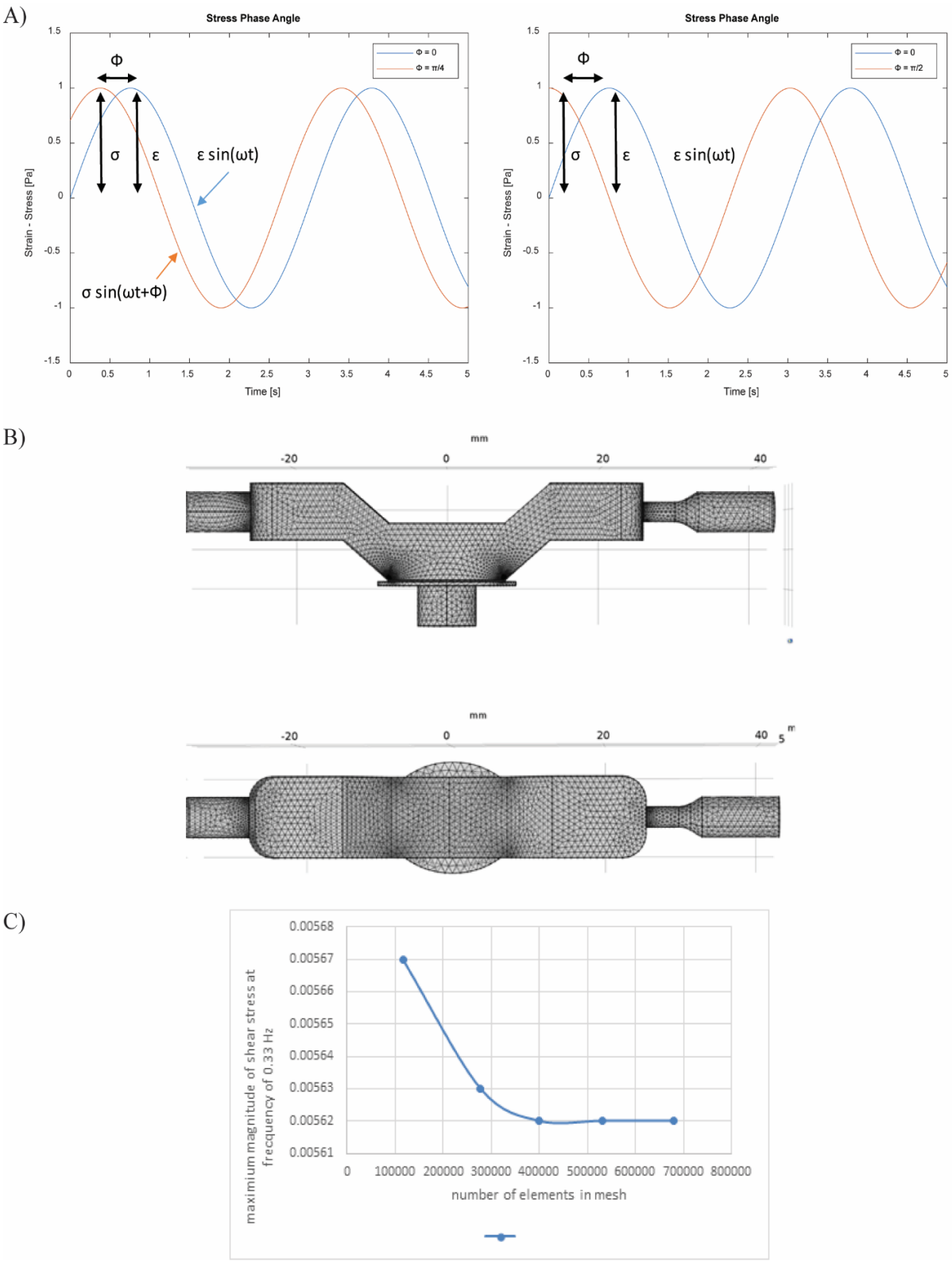


**Figure 2.** A) Schematic of stress phase angle (left) $\pi/4$ and (right$\pi/2$, B) Tetrahedral mesh of the geometry, C) Plot of mesh independency of the solution

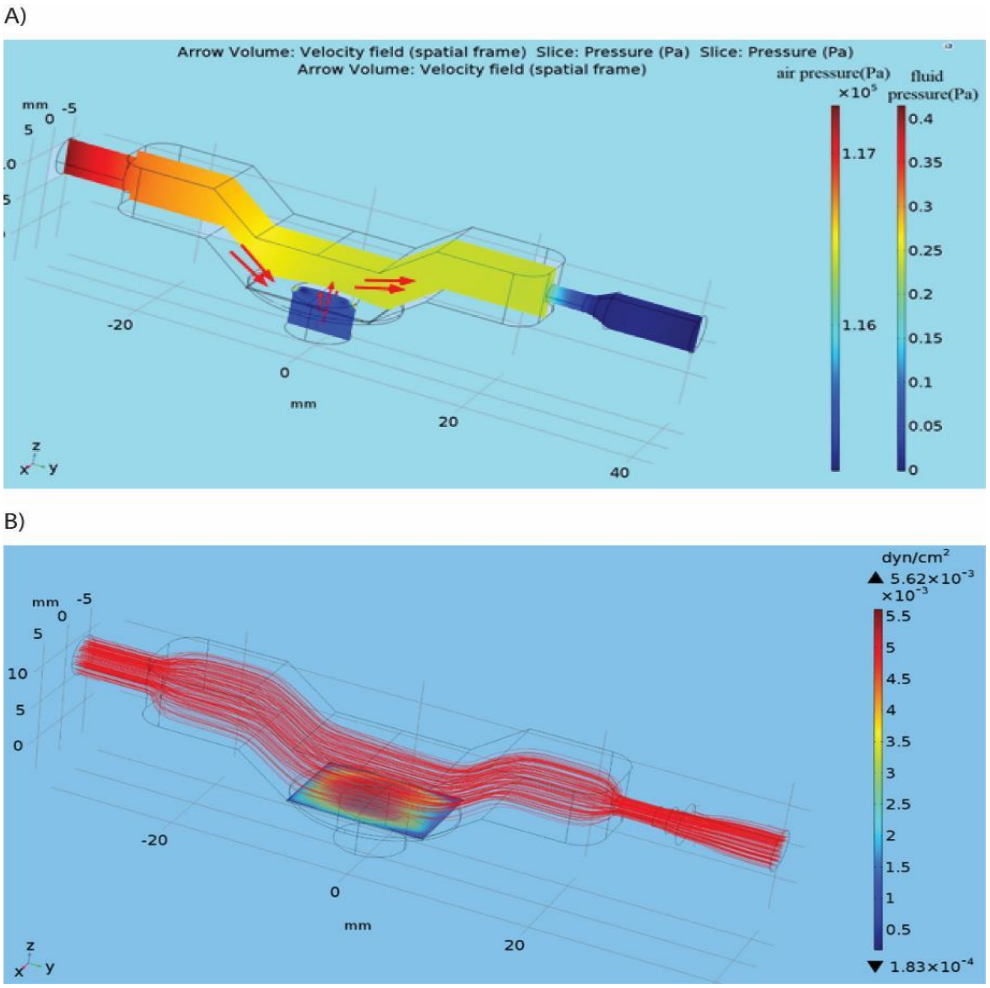


**Figure 3.** Pressure and shear stress contours in the model; A) Air- fluid pressure fields for the model with different frequencies (third model). (Red arrows indicate the direction of air-fluid movement.), B) The maximum magnitude of shear stress created on the stem cell layer with frequency of 0.33 Hz (Red stream lines indicate laminar flow)

uniform shear stress (Figure 4a). In the fourth model, where the stress phase angle between the mechanical parameters is $\pi/4$, the surface of the cell layer was unevenly subjected to 0.009 dyn/cm² during the period (3.3, 3.4, and 3.5 s) (Figure 4d). In the last model, where the phase angle is $\pi/2$, the maximum stress created on the cell layer is 0.014 dyn/cm² at the specified time (2.9, 3, and 3.1 s) (Figure 4e). As can be seen, this stress has the highest value in the position where the pulsatile flow is applied, and the right side of the cell layer experiences the least amount of stress. As shown in Figure 4(d-e), the phase $\pi/2$ has more value for the maximum magnitude of shear stress than the phase $\pi/4$, but both phases have a more non-uniform distribution than phase 0. In the following, a comparison of the effect of frequency and stress phase angle on the maximum magnitude of shear stress created on the surface of embryonic stem cells can be seen in Table 2.

## 4. DISCUSSION

As a result, it can be mentioned that both frequency and phase angle stress parameters have considerable effects on the distribution and amount of shear stress. By Increasing the frequency from 0.33 Hz to 1 Hz, the maximum shear stress increased. Besides, the frequency difference between the cyclic strain and the pulsatile flow also increases the maximum shear stress. At frequencies of 0.33, 1 Hz, and in the condition of different frequencies for each of the stimulations, shear stresses are equal to 0.00562, 0.02, and 0.01 dyn/cm², respectively. At frequencies of 0.33 Hz, 1 Hz, and the frequency difference between the mechanical parameters, the best shear stress distribution on the embryonic stem cell layer occurs at times 0.75s, 1.25s, and 1.25s, respectively (Figures 4(a2), 4(b2), and 4(c2)). However, in the third group, part of the surface of the cell layer experiences less shear stress, which poses

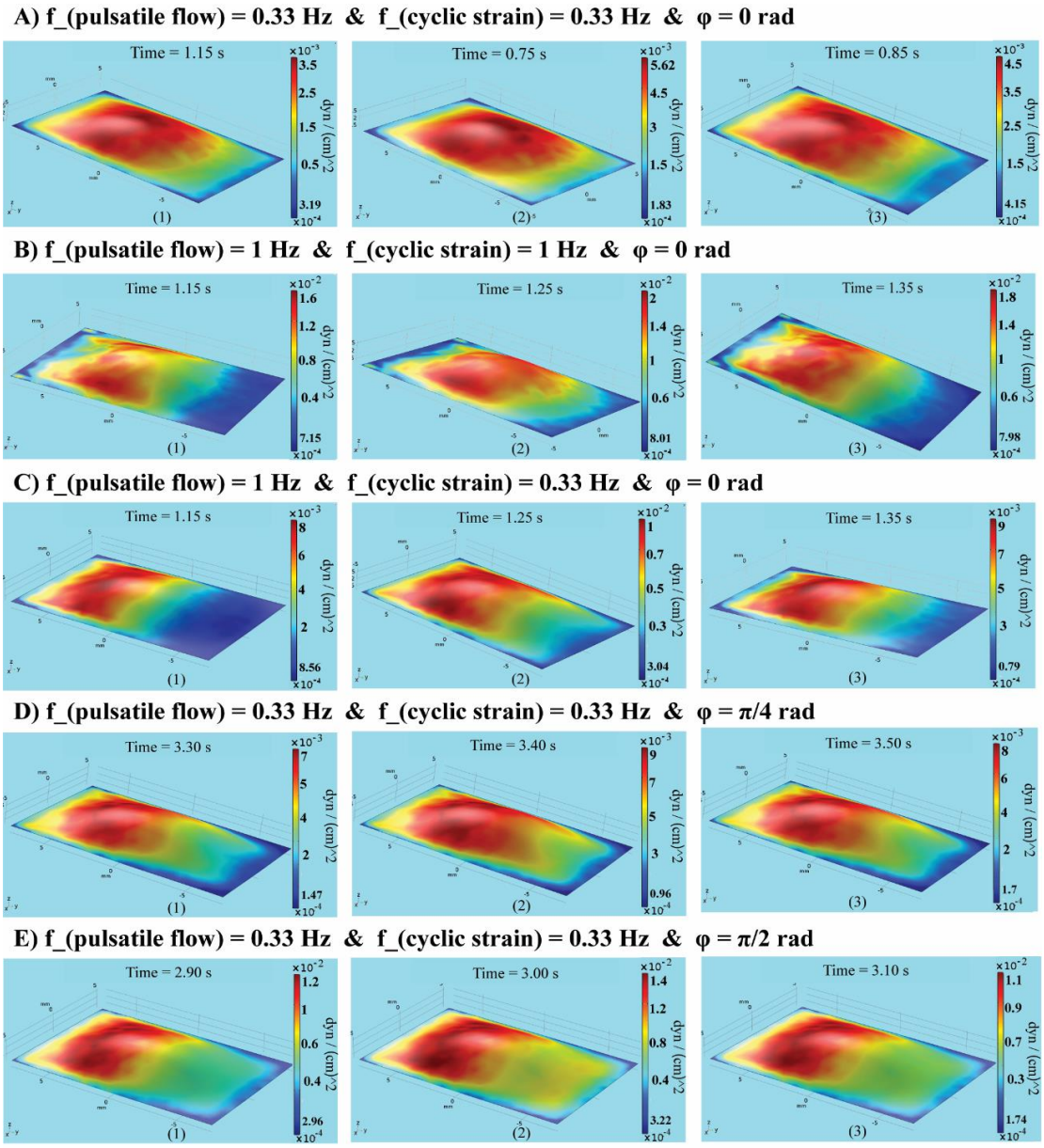


**Figure 4.** The maximum magnitude of shear stress created on the embryonic stem cell layer with frequency A) 0.33 Hz, B) 1 Hz C) different frequency between pulsatile flow and cyclic strain, and stress phase angle D) $^{\pi}/_{4}$, E) $^{\pi}/_{2}$

**TABLE 2.** Comparison of shear stress in the fifth models

| Models | Frequency at cyclic strain (Hz) | Frequency at Pulsatile flow (Hz) | Stress phase angle | Maximum nagnitude of shea stress (dyn/cm²) |
|---|---|---|---|---|
| 1 | 0.33 | 0.33 | 0 | 0.00562 |
| 2 | 1 | 1 | 0 | 0.02 |
| 3 | 0.33 | 1 | 0 | 0.01 |
| 4 | 0.33 | 0.33 | $^{\pi}/_{4}$ | 0.009 |
| 5 | 0.33 | 0.33 | $^{\pi}/_{2}$ | 0.014 |

challenges to ensure cell differentiation. Also, the existence of a phase difference between the pulsatile flow and cyclic strain leads to an increase in shear stress heterogeneously. The maximum shear stress in the stress phase angle $^{\pi}/_{4}$, and $^{\pi}/_{2}$ is equal to 0.009 dyn/cm² and 0.014 dyn/cm², which occurs in time 3s and 3.4s, respectively (Figure. 4(d2) and 4(e2)). The stress phase angle has also a significant effect on the distribution of shear stress created on the embryonic stem cell layer. Moreover, it was showed in a previous study [34] that at shear stress greater than 2.4 dyn/cm² cardiomyocytes

undergo apoptosis, whereas in our five models, the shear stress was below this critical point, from 0.00562 to 0.014 dyn/cm², which indicated that cell death did not occur. Another important point is that at low shear stress and low average velocity, beneficial effects occur in many tissue engineering systems [34]. Therefore, it can be stated that all the presented shear stress is in the appropriate range that cardiac cell differentiation occurs by activating cardiac proteins and genes [13, 14, 35]. According to the proposed models, we can conclude that the best condition for differentiating stem cells into heart cells occurs in the first model in which the frequency of mechanical parameters and stress phase angle are 0.33 Hz and 0, respectively. In this condition, the cells are exposed to a suitable and uniform range of shear stress, so that more cells are distinguished into cardiomyocytes.

## 5. LIMITATION AND FUTUR WORKS

In this study, a cell layer was considered to simplify and achieve a reliable computational model of cells cultured on the membrane. Also, the inability to simulate biochemical phenomena in computational software and the high computational costs of FSI analysis is the limitation of this study. For future studies, the effect of substrate surface nanotopography, as well as oscillatory flow, may be valuable to be analyzed. Besides, for investigating responses of the subcellular elements to mechanical stimuli, considering several cells with subcellular components instead of the cell layer can be worthwhile [10, 36, 37]. The assumption of viscoelastic and hyperelastic properties for embryonic stem seems to be closer to reality and is recommended for future studies.

## 6. CONCLUSION

Because of the physiological function of the heart, this tissue is subject to pulsatile flow and cyclic strain in vivo. Therefore, these mechanical parameters play an important role in differentiating stem cells to cardiomyocytes. In the present study, using fluid-solid interaction modeling and the combination of cyclic strain and pulsatile flow, the effect of frequency and stress phase angle parameters on the maximum shear stress applied to the embryonic stem cell layer in a perfusion bioreactor for mechanical modulation of the cells toward differentiating into cardiac cells, was investigated. For the first study, the three frequencies of 0.33 Hz, 1 Hz, and the frequency difference between the mechanical parameters were considered. Besides, the effect of stress phase angle $\pi/4$ , and $\pi/2$ on shear stress was considered in the second study. It can be stated that the stress phase angle, the increase, and the existence of frequency differences between the two distinct mechanical stimuli (pulsatile flow and cyclic strain) led to an increase in the maximum magnitude of shear stress on the embryonic stem cell layer. In the first model, the distribution of maximum shear stress created on the surface of the stem cell layer at a given time was more homogeneous than in other models. In general, according to the simulations, the optimal state of the bioreactor is at the frequency of 0.33 Hz, and the stress phase angle is 0 because the shear stress distribution is more uniform, which brings better differentiation.

## 7. REFERENCES


1. Zammaretti, P. and Jaconi, M., "Cardiac tissue engineering: Regeneration of the wounded heart", ***Current Opinion in Biotechnology***, Vol. 15, No. 5, (2004), 430-434. doi: 10.1016/j.copbio.2004.08.007.
2. Ye, F., Yuan, F., Li, X., Cooper, N., Tinney, J.P. and Keller, B.B., "Gene expression profiles in engineered cardiac tissues respond to mechanical loading and inhibition of tyrosine kinases", ***Physiological Reports***, Vol. 1, No. 5, (2013). doi: 10.1002/phy2.78.
3. Breckwoldt, K., Weinberger, F. and Eschenhagen, T., "Heart regeneration", ***Biochimica et Biophysica Acta (BBA)-Molecular Cell Research***, Vol. 1863, No. 7, (2016), 1749-1759. https://doi.org/10.1016/j.bbamcr.2015.11.010.
4. Grayson, W.L., Martens, T.P., Eng, G.M., Radisic, M. and Vunjak-Novakovic, G., "Biomimetic approach to tissue engineering", in Seminars in cell & developmental biology, Elsevier. Vol. 20, No. 6, (2009), 665-673. doi: 10.1016/j.semcdb.2008.12.008.
5. Mueller, P., Lemcke, H. and David, R., "Stem cell therapy in heart diseases–cell types, mechanisms and improvement strategies", ***Cellular Physiology and Biochemistry***, Vol. 48, No. 6, (2018), 2607-2655. doi: 10.1159/000492704.
6. Gandhimathi, C., Muthukumaran, P. and Srinivasan, D., Nanofiber composites in cardiac tissue engineering, in Nanofiber composites for biomedical applications. 2017, Elsevier.411-453. https://doi.org/10.1016/B978-0-08-100173-8.00017-X.
7. Vining, K.H. and Mooney, D.J., "Mechanical forces direct stem cell behaviour in development and regeneration", ***Nature Reviews Molecular Cell Biology***, Vol. 18, No. 12, (2017), 728-742. https://doi.org/10.1038/nrm.2017.108.
8. Kaitsuka, T. and Hakim, F., "Response of pluripotent stem cells to environmental stress and its application for directed differentiation", ***Biology***, Vol. 10, No. 2, (2021), 84. https://doi.org/10.3390/biology10020084.
9. Huang, Y., Jia, X., Bai, K., Gong, X. and Fan, Y., "Effect of fluid shear stress on cardiomyogenic differentiation of rat bone marrow mesenchymal stem cells", ***Archives of Medical Research***, Vol. 41, No. 7, (2010), 497-505. doi: 10.1016/j.arcmed.2010.10.002.
10. Saucerman, J.J., Tan, P.M., Buchholz, K.S., McCulloch, A.D. and Omens, J.H., "Mechanical regulation of gene expression in cardiac myocytes and fibroblasts", ***Nature Reviews Cardiology***, Vol. 16, No. 6, (2019), 361-378. doi: 10.1038/s41569-019-0155-8.
11. Mihic, A., Li, J., Miyagi, Y., Gagliardi, M., Li, S.H., Zu, J., Weisel, R.D., Keller, G. and Li, R.K., "The effect of cyclic stretch on maturation and 3d tissue formation of human embryonic stem cell-derived cardiomyocytes", ***Biomaterials***, Vol. 35, No. 9, (2014), 2798-2808. doi: 10.1016/j.biomaterials.2013.12.052.

12. Tulloch, N.L., Muskheli, V., Razumova, M.V., Korte, F.S., Regnier, M., Hauch, K.D., Pabon, L., Reinecke, H. and Murry, C.E., "Growth of engineered human myocardium with mechanical loading and vascular coculture", ***Circulation Research,*** Vol. 109, No. 1, (2011), 47-59. doi: 10.1161/circresaha.110.237206.
13. Dvir, T., Levy, O., Shachar, M., Granot, Y. and Cohen, S., "Activation of the erk1/2 cascade via pulsatile interstitial fluid flow promotes cardiac tissue assembly", ***Tissue Engineering***, Vol. 13, No. 9, (2007), 2185-2193. https://doi.org/10.1089/ten.2006.0364.
14. Shen, N., Knopf, A., Westendorf, C., Kraushaar, U., Riedl, J., Bauer, H., Pöschel, S., Layland, S.L., Holeiter, M. and Knolle, S., "Steps toward maturation of embryonic stem cell-derived cardiomyocytes by defined physical signals", ***Stem Cell Reports***, Vol. 9, No. 1, (2017), 122-135. doi: 10.1016/j.stemcr.2017.04.021.
15. Henderson, K., Sligar, A.D., Le, V.P., Lee, J. and Baker, A.B., "Biomechanical regulation of mesenchymal stem cells for cardiovascular tissue engineering", ***Advanced Healthcare Materials***, Vol. 6, No. 22, (2017), 1700556. doi: 10.1155/2019/1847098.
16. Band Band, H., Arbabtafti, M., Nahvi, A. and Zarei-Ghanavati, M., "Finite element simulation and experimental test of ovine corneal tissue cutting process in cataract surgery operation", ***International Journal of Engineering, Transactions B: Applications***, Vol. 34, No. 5, (2021), 1321-1328. doi: 10.5829/IJE.2021.34.05B.27.
17. Sarparast, Z., Abdoli, R., Rahbari, A., Varmazyar, M. and Reza Kashyzadeh, K., "Experimental and numerical analysis of permeability in porous media", ***International Journal of Engineering*, *, Transactions B: Applications***, Vol. 33, No. 11, (2020), 2408-2415. doi: 10.5829/IJE.2020.33.11B.31.
18. Hezarjaribi, Y., Yari Esbouei, M. and Azizollah Ganji, B., "Simulation and modeling of a high sensitivity micro-electro-mechanical systems capacitive pressure sensor with small size and clamped square diaphragm", ***International Journal of Engineering, Transactions C: Aspects***,, Vol. 30, No. 6, (2017), 846-850. doi: 10.5829/ije.2017.30.06c.04.
19. Visone, R., Talò, G., Lopa, S., Rasponi, M. and Moretti, M., "Enhancing all-in-one bioreactors by combining interstitial perfusion, electrical stimulation, on-line monitoring and testing within a single chamber for cardiac constructs", ***Scientific Reports***, Vol. 8, No. 1, (2018), 1-13. doi: 10.1038/s41598-018-35019-w.
20. Shen, N., Riedl, J.A., Berrio, D.A.C., Davis, Z., Monaghan, M.G., Layland, S.L., Hinderer, S. and Schenke-Layland, K., "A flow bioreactor system compatible with real-time two-photon fluorescence lifetime imaging microscopy", ***Biomedical Materials***, Vol. 13, No. 2, (2018), 024101. doi: 10.1088/1748-605X/aa9b3c.
21. Ma, G., Petersen, E., Leong, K.W. and Liao, K., "Mechanical behavior of human embryonic stem cell pellet under unconfined compression", ***Biomechanics and Modeling in Mechanobiology***, Vol. 11, No. 5, (2012), 703-714. doi: 10.1007/s10237-011-0344-9.
22. Consolo, F., Bariani, C., Mantalaris, A., Montevecchi, F., Redaelli, A. and Morbiducci, U., "Computational modeling for the optimization of a cardiogenic 3d bioprocess of encapsulated embryonic stem cells", ***Biomechanics and Modeling in Mechanobiology***, Vol. 11, No. 1-2, (2012), 261-277. https://doi.org/10.1007/s10237-011-0308-0.
23. Tremblay, D., Zigras, T., Cartier, R., Leduc, L., Butany, J., Mongrain, R. and Leask, R.L., "A comparison of mechanical properties of materials used in aortic arch reconstruction", ***The Annals of Thoracic Surgery***, Vol. 88, No. 5, (2009), 1484-1491. doi: 10.1016/j.athoracsur.2009.07.023.
24. Shahidan, S., "Concrete incorporated with optimum percentages of recycled polyethylene terephthalate (PET) bottle fiber", ***International Journal of Integrated Engineering***, Vol. 10, No. 1, (2018).
25. Kaplan, L., Høye, E., Balling, P., Muren, L., Petersen, J., Poulsen, P., Yates, E. and Skyt, P., "Determining the mechanical properties of a radiochromic silicone-based 3d dosimeter", ***Physics in Medicine & Biology***, Vol. 62, No. 14, (2017), 5612. doi: 10.1088/1361-6560/aa70cd.
26. Udupa, G., Sreedharan, P., Sai Dinesh, P. and Kim, D., "Asymmetric bellow flexible pneumatic actuator for miniature robotic soft gripper", ***Journal of Robotics***, Vol. 2014, (2014). https://doi.org/10.1155/2014/902625.
27. Chun, Y.W., Voyles, D.E., Rath, R., Hofmeister, L.H., Boire, T.C., Wilcox, H., Lee, J.H., Bellan, L.M., Hong, C.C. and Sung, H.-J., "Differential responses of induced pluripotent stem cell-derived cardiomyocytes to anisotropic strain depends on disease status", ***Journal of Biomechanics***, Vol. 48, No. 14, (2015), 3890-3896. doi: 10.1016/j.jbiomech.2015.09.028.
28. Shojaei, S., Tafazzoli-Shadpour, M., Shokrgozar, M.A., Haghighipour, N. and Jahromi, F.H., "Stress phase angle regulates differentiation of human adipose-derived stem cells toward endothelial phenotype", ***Progress in Biomaterials***, Vol. 7, No. 2, (2018), 121-131. doi: 10.1007/s40204-018-0090-5.
29. Qamar, A., Seda, R. and Bull, J.L., "Pulsatile flow past an oscillating cylinder", ***Physics of Fluids***, Vol. 23, No. 4, (2011), 041903. https://doi.org/10.1063/1.3576186.
30. Altenbach, J., "Book review: Martin h. Sadd, elasticity–theory, applications, and numerics", ***ZAMM-Journal of Applied Mathematics and Mechanics/Zeitschrift für Angewandte Mathematik und Mechanik: Applied Mathematics and Mechanics***, Vol. 85, No. 12, (2005), 907-908. https://doi.org/10.1002/zamm.200590048.
31. Bathe, K.-J. and Zhang, H., "A mesh adaptivity procedure for cfd and fluid-structure interactions", ***Computers & Structures***, Vol. 87, No. 11-12, (2009), 604-617. https://doi.org/10.1016/j.compstruc.2009.01.017.
32. Irfan, M., Waraich, A.S., Ahmed, S. and Ali, Y., "Characterization of various plant-produced asphalt concrete mixtures using dynamic modulus test", ***Advances in Materials Science and Engineering***, Vol. 2016, (2016). https://doi.org/10.1155/2016/5618427.
33. Donea, J., Huerta, A., Ponthot, J.P. and Rodríguez-Ferran, A., "Arbitrary l agrangian–e ulerian methods", ***Encyclopedia of Computational Mechanics Second Edition***, (2017), 1-23. https://doi.org/10.1002/9781119176817.ecm2009.
34. Mannhardt, I., Marsano, A. and Teuschl, A. "Perfusion bioreactors for prevascularization strategies in cardiac tissue engineering", ***Vascularization for Tissue Engineering and Regenerative Medicine***, (2021), 475-488 doi: 10.1007/978-3-319-54586-8_14.
35. Black, L.D., 3rd, Meyers, J.D., Weinbaum, J.S., Shvelidze, Y.A. and Tranquillo, R.T., "Cell-induced alignment augments twitch force in fibrin gel-based engineered myocardium via gap junction modification", ***Tissue Engineering Part A***, Vol. 15, No. 10, (2009), 3099-3108. doi: 10.1089/ten.TEA.2008.0502.
36. Lemoine, M.D., Mannhardt, I., Breckwoldt, K., Prondzynski, M., Flenner, F., Ulmer, B., Hirt, M.N., Neuber, C., Horváth, A. and Kloth, B., "Human ipsc-derived cardiomyocytes cultured in 3d engineered heart tissue show physiological upstroke velocity and sodium current density", ***Scientific Reports***, Vol. 7, No. 1, (2017), 1-11. https://doi.org/10.1038/s41598-017-05600-w.
37. Kharaziha, M., Memic, A., Akbari, M., Brafman, D.A. and Nikkhah, M., "Nano-enabled approaches for stem cell-based cardiac tissue engineering", ***Advanced Healthcare Materials***, Vol. 5, No. 13, (2016), 1533-1553.DOI: 10.1002/adhm.201600088.

Persian Abstract

**چکیده**

به دلیل توانایی سلول های بنیادی برای خود تجدید و تمایز به قلب، آنها منابع سلولی بهینه برای مهندسی بافت قلب هستند. از آنجایی که سلول های قلب کرنش سیکلی و جریان پالسی را در داخل بدن تجربه می کنند، این محرک های مکانیکی عوامل ضروری برای تمایز سلول های بنیادی هستند. این مطالعه با هدف بررسی اثر ترکیبی از جریان پالسی و کرنش سیکلی بر تنش برشی ایجاد شده بر روی لایه سلول‌های بنیادی جنینی با خاصیت ارتجاعی در یک بیورآکتور پرفیوژن با استفاده از روش برهمکنش سیال–جامد (FSI) اتجام شد. در این تحقیق، فرکانس و زاویه فاز تنش به عنوان یک متغیر در نظر گرفته شده است. نتایج نشان می دهند که حداکثر تنش برشی در فرکانس های ۰.۳۳ و ۱ هرتز و با اختلاف فرکانس در کرنش سیکلی(۰.۳۳ هرتز) و جریان پالسی (۱ هرتز) به ترتیب $dyn/cm^2$ ۰.۰۰۵۶۲، ۰.۰۲ و ۰.۰۱ می باشد. همچنین زاویه فاز تنش ۰، $\pi/4$ و $\pi/2$، حداکثر تنش برشی به ترتیب برابر با $dyn/cm^2$ ۰.۰۰۵۶۲، ۰.۰۰۹ و ۰.۰۱٤ است. نتایج این مطالعه می تواند گامی موثر در توسعه مهندسی بافت قلب و درک بهتر اثرات محرک های مکانیکی بر تمایز سلول های بنیادی می باشد.

International Journal of Engineering

Journal Homepage: www.ije.ir

# Rheological Properties of the In-house Prepared Magneto-rheological Fluid in the Pre-yield Region

S. Nagiredla*, S. Joladarashi, H. Kumar

*Department of Mechanical Engineering, National Institute of Technology Karnataka, Surathkal, Mangaluru, Karnataka, India*

*PAPER INFO*

*Paper history:*
Received 22 June 2022
Received in revised form 22 August 2022
Accepted 27 August 2022

*Keywords*:
*Magnetorheological Fluid*
*Viscoelastic Properties*
*Rheological Properties*
*Driving Frequency*
*Strain Amplitude*

*ABSTRACT*

The essence of the present work is to study the rheological properties of the in-house prepared magneto-rheological (MR) fluids in the pre-yield region since the rheological properties play a vital role in better understanding of vibration damping capabilities of MR fluids. In the present work, two different compositions of MR fluid samples were prepared with 24 and 30 volume percentages of carbonyl iron (CI) particles. Prepared MR fluid samples contain CI particles as a dispersive medium, silicone oil as a carrier fluid and white lithium grease as an anti-settling agent. The oscillating driving frequency and amplitude strain sweep tests are performed to investigate the rheological properties within the pre-yield region. The influences of driving frequency, strain amplitude, magnetic field and CI particles volume percentage on the rheological properties of the prepared MR fluids were assessed. The linear viscoelastic region of the prepared MR fluid sample was identified and the yield strain obtained was around 0.371%. It is observed that the volume percentage of CI particles in the MR fluid strongly influenced the rheological properties.

***doi***: *10.5829/ije.2022.35.11b.19*

## 1. INTRODUCTION

Magneto-rheological materials change their properties in a significant way when they are exposed to externally applied magnetic fields. Rabinow [1] reported the rheological effect of MR fluids for the first time in 1948. MR fluid typically contains CI particles, carrier fluid and an anti-settling agent (additive). CI particle size used in MR fluids typically vary in the range of 1-10 µm which are spherical for a better MR effect. Additives avoid settling high-density iron particles in the carrier fluid due to gravity in the MR fluid [2-4]. When an external magnetic field is applied, magnetic dipole makes the particles form strong interactions. This causes the iron particles to form a chain-like structure in the magnetic field direction. MR fluids response is in the range of a few milliseconds in the presence of external stimuli. MR fluids can produce higher yield stress values based on the iron particles volume percentage concentration and external field applied [5-10]. Response time of MR fluids has great importance in most applications. Because of the quick, controllable rheological properties and reversible quality of the MR fluids, they found many potential applications in the field of vibration control devices, dampers, brakes and clutch applications [11-15]. Dynamic characterization studies are conducted on the MR/ER fluids to meet the appropriate application design specifications [16-22]. The rheological properties like storage modulus, loss modulus and loss factor value of MR/ER fluids are found using a sinusoidally oscillating shear strain of frequency. The storage and loss modulus increased with the externally applied magnetic field [23-25]. The extensive usage of MR fluid for the last two decades in medical applications is reviewed and discussed the future perspective [26]. The strain-controlled rheometer was used to analyze the viscoelastic parameters of the MR fluids. The influence of particle size distribution, volume fraction percentage and applied field on the rheological parameters are reported [27-36]. Though few studies exist on commercially available MR

*Corresponding Author Institutional Email: surya_jrf@nitk.edu.in
(S. Nagiredla)

Please cite this article as: S. Nagiredla, S. Joladarashi, H. Kumar, Rheological Properties of the In-house Prepared Magneto-rheological Fluid in the Pre-yield Region, ***International Journal of Engineering, Transactions B: Applications***, Vol. 35, No. 11, (2022) 2238-2246

fluids, the rheological tests on the in-house prepared MR fluids are important because they are cost-effective. The present study aims to prepare the MR fluid samples with 24 and 30% volume fractions of iron particles to study the rheological properties in the pre-yield region. One of the main challenges of the present study is to identify the linear viscoelastic region of the prepared MR fluids and to study the rheological properties in the pre-yield region. The variation in rheological properties of MR fluids in the pre-yield region found potential structural-related damping applications. It is necessary to evaluate the influence of the different parameters on the properties of MR fluid in the pre-yield region. The parameters considered for the present study are driving frequency, shear strain, magnetic field and volume percentage of CI particles. Further, MR fluid samples are tested using an oscillatory strain-based rheometer with a flat plate type configuration. Oscillatory driving frequency and strain amplitude-based tests are performed to analyze the frequency and strain-dependent storage modulus and loss factor for the prepared samples. All the results reported in this work are within the region of yield and also reported the effect of iron particles volume percentage and an externally applied magnetic field on the rheological properties of the in-house prepared MR fluid samples.

## 2. MATERIALS AND METHODS

**2. 1. Materials and Equipment Used for The Preparation of MR Fluid Samples** MR fluid contains iron powder particles suspended in a carrier fluid medium. In this work, Iron particles are carbonyl iron particles (CPIs) and silicone oil is the carrier fluid. The CI particles powder, low in magnesium and manganese compounds with a purity of 99.5% is purchased from Sigma Aldrich with a density of 7.86 g/cm$^3$. Merck Life Science Private Limited supplied the silicone oil. The viscosity of the Silicone oil is 340 Cst (at 25$^0$C) and the density is of 0.970 g/cm$^3$ (at 25$^0$C). Scanning Electron Microscopy (SEM) analysis is conducted using the ZEISS FESEM instrument to study the surface morphology and size of the CI particles. Additionally, a small amount of white lithium grease is used as the surfactant (surface modifier or additive for the iron particles) to avoid the sedimentation of the iron particles [37, 38]. Permatex is supplied the white lithium grease, it looks as a paste-like substance. This surfactant will accumulate around the iron particles to make them suspend in the carrier fluid. Two types of MR fluid samples are prepared with the different compositions (different volume percentage). Table 1 shows the details of the sample composition.

**2. 2. MR Fluid Preparation Procedure** For the present study, MR fluid samples are prepared at a room temperature. Two types of fluids are prepared with different compositions to analyze the rheological properties in the region of pre-yield. Volume fraction calculations have been used to prepare MR fluid samples. The MRF-I sample is prepared with the 30% volume fraction of carbonyl group-based iron particles, 70% volume fraction of silicone oil and 2 grams of white lithium grease. The MRF-II sample is prepared with the 24% volume fraction of iron particles, 76% volume fraction of silicone oil and 2 grams of white lithium grease. The desired volume fraction calculations are converted into weight fractions using the density property of the iron particles and silicone oil. Weight fractions of the materials are easy to measure using the weighing machine. The required weight fraction proportions of the constituents for both the samples are measured using high precision weighing machine tool.

For MRF-I fluid sample, 44.8 grams of silicone oil is taken in the container. The container which contains the carrier fluid is kept under a Mechanical stirrer for the stirring. REMI RQ-5 Plus mechanical type stirrer is used to stir MR fluid. The stirrer shaft or rotator of the mechanical stirrer is arranged in such a way that it should not touch the base of the container. The 2 grams of white lithium grease is initially added to the carrier fluid while stirring. The speed maintained for this stirring process is 600 rpm. This process is continued for 2 hours for the uniform mixing of surface modifier in the carrier fluid. Then, to the stirred fluid, 155.2 grams of CI particles are added in small amounts while the fluid is stirring at 800 rpm. The stirring process is continued for at least 12 hours without interruption for uniform mixing of CI particles in the carrier fluid. For the MRF-II sample, 56.24 grams of silicone oil, 2 grams of white lithium grease, and 143.76 grams of CI particles are taken. The same procedure is followed for the preparation of the MRF-II sample. The quantity of additive added in the two types of fluid compositions is not changed. The small

**TABLE 1.** MR fluid samples composition

| SI.No. | Volume percentage (Vol%) | | Weight percentage (Wt%) | | Additive |
|---|---|---|---|---|---|
| | CI Particles | Silicone Oil | CI Particles | Silicone Oil | White Lithium Grease |
| MRF-I | 30 | 70 | 77.6 | 22.4 | 2 grams |
| MRF-II | 24 | 76 | 71.88 | 28.12 | 2 grams |

amounts of additive added will not have much influence on the rheological properties [38]. The additive will provide additional suspension action to MR particles. The mixing process of silicone oil and white lithium grease without adding CI particles is shown in Figure 1(a). The whitish color indicates the uniform mixing of white lithium grease in the carrier fluid. The mixing process of iron particles into the already prepared solution is shown in Figure 1(b). After this mixing process, the fluid is turned into black color because of the added CI particles.

### 2. 3. The Microstructure of Carbonyl Iron Particles

Scanning Electron Microscopy (SEM) test is performed on CI particles to confirm the surface morphology and particle size. It is observed that iron particles are spherical in shape. Figures 2(a) and 2(b) illustrate the shape of iron particles viewed at 4000x and at 25000x, respectively. The size of the few particles is marked in the SEM image to ensure the iron particles size. It is observed that the average iron particles size is around 4 to 9 µm.

### 2. 4. Experimental Setup

Rheological characterization of prepared MR fluid samples is done using Modular Compact Rheometer (MCR 702 Anton Paar make). Figure 3 shows the Rheometer setup with the magnetorheological device (MRD) cell used for the rheological study. The measuring system includes mainly MRD cell, a Chiller for the cooling, data processing sensors and a computer with the rheocompass software to take data from the sensors of the rheometer. The Rheometer is connected to RheoCompass software through which the user can specify the test conditions and store the acquired data. A MRD cell is a DC power supply device that provides the required magnetic field to the MRF sample poured on the stationary plate of the rheometer. During the tests, a small amount of MR fluid samples is poured in the bottom stationary parallel plate. A measuring gap of 0.5 mm is maintained for all the tests. For every test, approximately 0.4 ml of MR fluid sample is filled in the gap of two parallel plates configuration for rheological properties measurement.

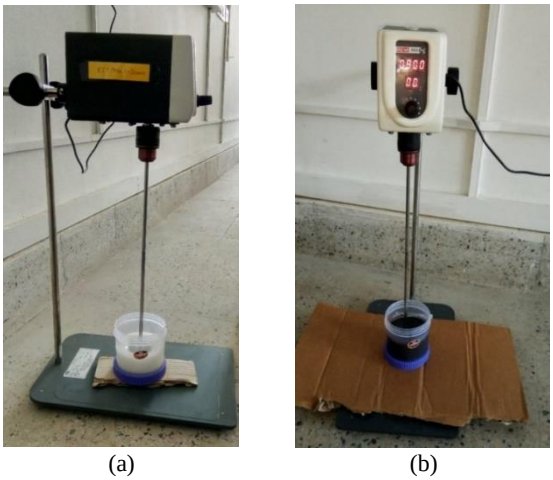

(a) (b)

**Figure 1.** (a) Silicone oil and white lithium grease solution (b) Mixing of CI particles in the prepared solution

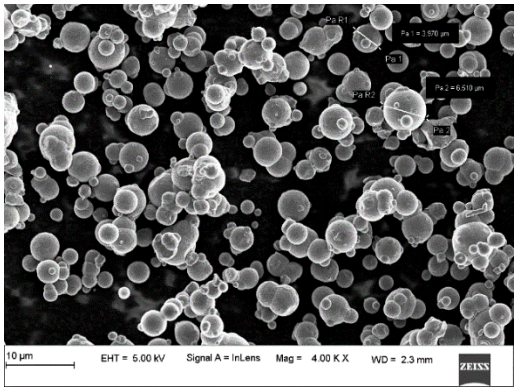


(a)

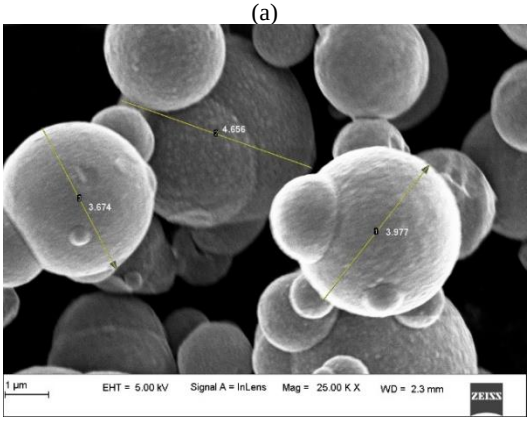


(b)

**Figure 2.** CI particles microstructure magnified view (a) at 4000x and (b) at 25000x

## 3. RESULTS AND DISCUSSION

Initial tests are conducted at a constant shear rate (1/s) to check the relation between the applied current (A) and the magnetic field. For this, the current is increased from 0 to 5A at a constant shear rate of 1/s. There will be a particular relationship between the applied current and the magnetic field produced for every MR fluid. MRF-132LD has a linear relation between the coil current and magnetic field developed [27]. Based on the results obtained, Figure 4(a) shows the linear relationship between applied coil current and the magnetic flux (T) developed for the prepared MR fluid. All the experimental results presented in this article are against the current. The current dependency of viscosity in the measuring gap is shown in Figure 4(b). From 0 to 2A, there is a rapid increment in the viscosity of the prepared

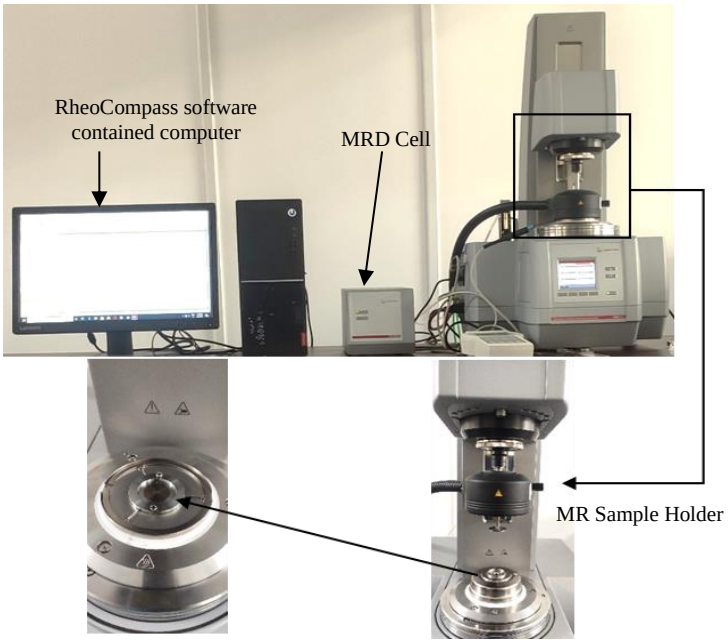


**Figure 3.** Rheometer experimental setup with MR cell

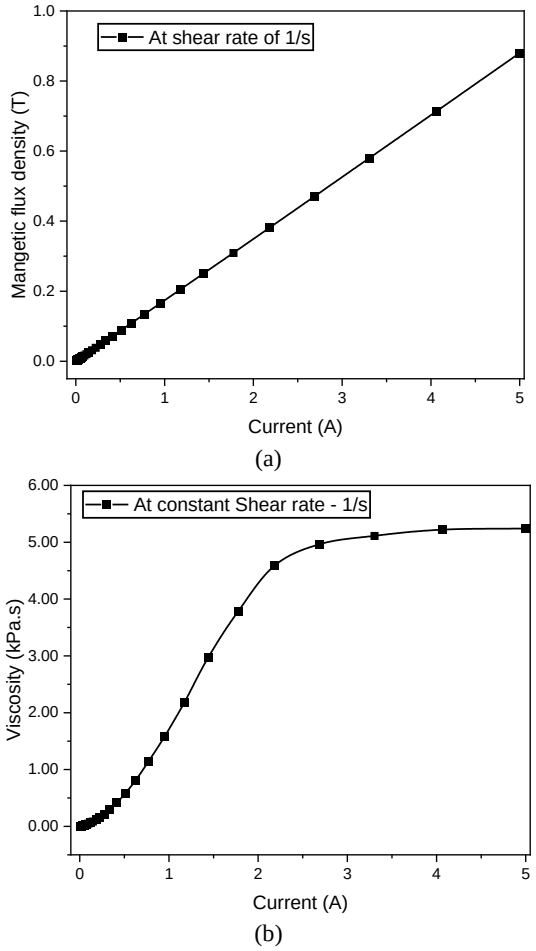


**Figure 4.** Variation in (a) Magnetic flux density and (b) Viscosity of the MRF-II sample with the applied current

sample. After 2A of current, change is not much in the viscosity curve. This means that the fluid's viscosity will not improve further even if the current value is increased. This implies that the change in the rheological properties beyond 2A current is not much appreciable for the prepared MR fluid sample.

Magnetorheological fluids exhibit linear rheological properties within the region of pre-yield [27]. MR fluid exhibits linear viscoelasticity when the developed shear strain is within the region of yield strain amplitude. So, MR fluid's yield strain amplitude is determined before conducting the other rheological measurement tests. The oscillatory shear strain amplitude method is used to determine yield strain [39-42]. The current of 2A is applied to determine the yield strain for the prepared MRF sample. Before applying the amplitude sweep, the magnetic field is set up by applying the suitable current for the tested fluid placed in the MR cell's parallel plate configuration. Amplitude sweep is taken logarithmically up to 1% shear strain amplitude. Strain amplitude is applied up to 1% because the experimentally obtained yield strain for most of the MR fluids is well below this range [8, 27]. From the stress-strain curve, the experimental yield strain of 0.371% is obtained as shown in Figure 5. The obtained yield strain for the prepared MR sample is in good agreement with the reported data in literature [27]. According to literature [27], the yield strain obtained is in the range of 0.2-0.6%. Once, the yield strain is determined from the strain amplitude test, remaining tests needed to be conducted with in the region of yield strain. For all the further experiments, maximum shear strain amplitude ($\gamma_0$ = 0.04%) is applied to ensure the obtained results are within the pre-yield region.

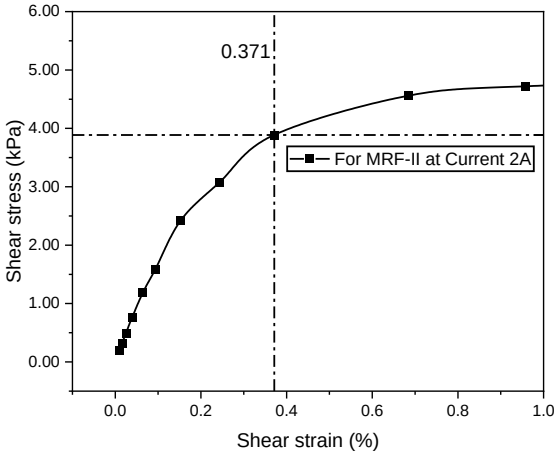


**Figure 5.** Yield strain from the shear stress-strain curve

**3. 1. Frequency-dependent Rheological Properties** A frequency sweep test is conducted for the prepared MR fluid samples at a constant shear strain amplitude ($\gamma_0$ = 0.04%). Frequency sweep is applied logarithmically from 1 to 100 Hz to evaluate the influence of driving frequency on rheological properties. Figures 6(a) and 6(b) illustrate the storage modulus and loss factor value plots with respect to the driving frequency at four different applied magnetic field values. From the results obtained, the storage modulus increases with the increment in the externally applied field. This is due to the alignment of CI particles in the MR fluid as the magnetic field is applied. This alignment of CI particles transforms liquid state of MR fluid into a semi-solid. This chain-like formation increases the storage modulus of the MR fluid. At any particular applied current, the value of the storage modulus is increasing with the oscillatory driving frequency, as we can observe from the Figure 6(a). The loss factor value at any particular magnetic field initially decreases and then increases as the driving frequency increasing [37]. At certain frequencies, the fluid becomes more viscous due to internal structure of the iron particles in the MR fluid. This attributed to the higher loss factor values [27]. In this case, the increase in loss factor values is observed after the frequency of 60 Hz. A similar trend is followed for the storage modulus and loss factor for all the applied magnetic fields.

At the current of 2A, the storage modulus attained a maximum value of 2.01 MPa as the frequency reaches 100 Hz. Storage modulus at current 2A is considerably very high compared to the value of storage modulus at current 0.5A for an oscillating driving frequency of 10Hz. The loss factor at current 0.5A is two times more than the value of the loss factor at 2A for an oscillating driving frequency of 10Hz.

**3. 2. Amplitude Strain Dependent Rheological Properties** An amplitude strain sweep is conducted for the MR fluid samples at a constant angular

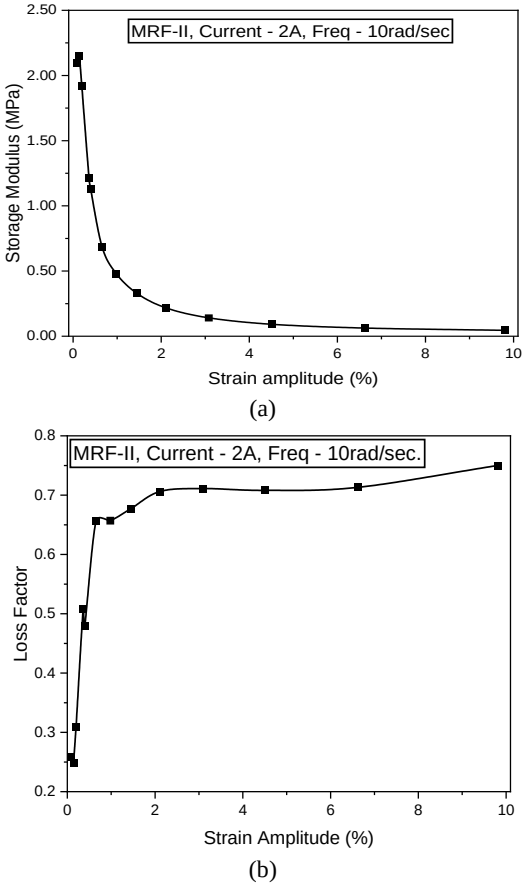


**Figure 6.** Frequency dependency of (a) Storage Modulus and (b) loss factor at different currents for MRF-II sample

frequency of 10 rad/s. Amplitude sweep is applied logarithmically from 1 to 10% of strain amplitude. Figures 7(a) and 7(b) illustrate the strain amplitude dependent storage modulus and loss factor values, respectively.

Experimental results concluded that the storage modulus decreases as the strain amplitude is increasing. For higher amplitude of shear strain, the chain formed between the iron particles will shear off due to higher displacements. This leads to the lower values of storage modulus at higher strain amplitudes. However, as the strain amplitude increases, there is an increment in the loss factor. Amplitude strain-dependent properties like storage modulus and loss factor values trend obtained in this research work are good agreement with the reported data in literature [27].

**3. 3. Magnetic Field Dependent Rheological Properties** In this section, magnetic field dependent storage modulus and loss factor at different driving frequencies 10, 20, 40,70, and 100 Hz at a constant strain amplitude of 0.04% are determined. Figure 8(a) shows that the storage modulus at any driving frequency increases with the applied magnetic field

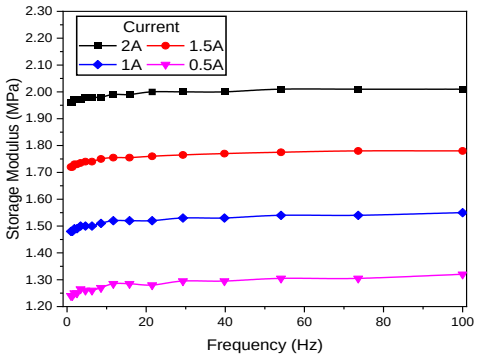


(a)

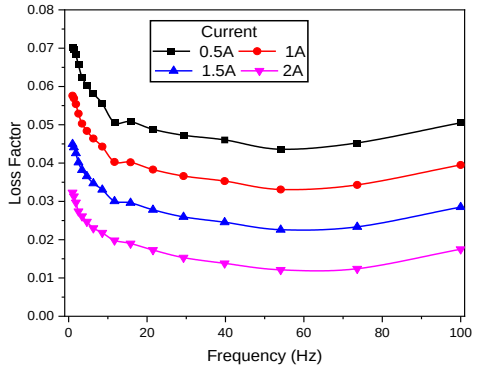


(b)

**Figure 7.** Strain amplitude dependency (a) storage modulus (b) loss factor at Current 2A for MRF-II sample

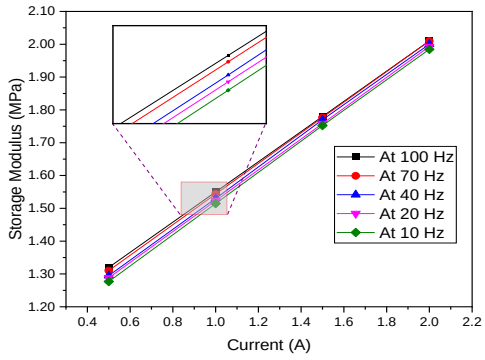


(a)

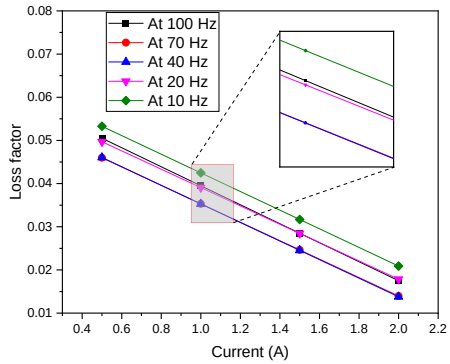


(b)

**Figure 8.** Magnetic field dependency of (a) Storage modulus (b) loss factor for the MRF-II sample at different driving frequencies

value. Iron particles in the MR fluid start to arrange in a chain-like structure with the applied magnetic field value. Because of this, fluid started to behave semi-solid. The semi-solid nature of the MR fluid increases the value of the storage modulus.

Storage modulus value increases with the driving frequency at any particular magnetic field value. However, the Loss factor value decreases with the applied field value at any driving frequency [27, 37].

**3. 4. Volume Fraction Dependent Rheological Properties** The rheological properties depend on the percentage of CI particles in the MR fluid [27, 32, 37]. The storage modulus and loss factor for two MR fluid samples with respect to frequency are shown in Figures 9(a) and 9(b).

The results show that the storage modulus value is higher for the MRF-II sample compared to the MRF-I sample. The magnetic field effect will be greater for the higher vol% of the CI particles MR fluid sample for any applied magnetic field value. However, the loss factor value for higher vol% of CI particles is less compared to the low vol% of CI particles MR fluid sample. This may

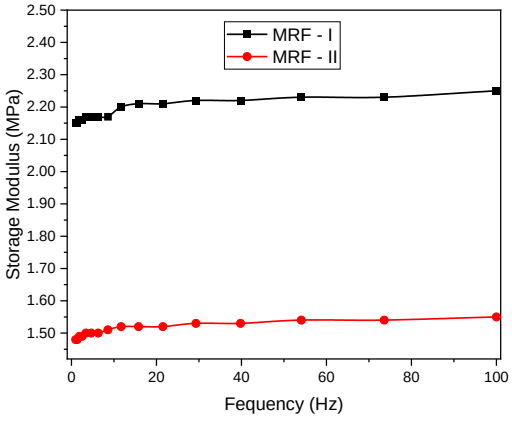


(a)

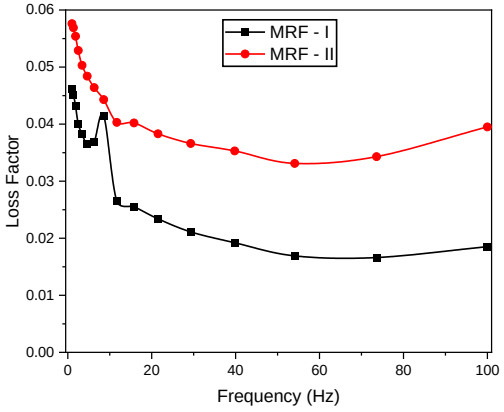


(b)

**Figure 9.** Volume fraction dependency of (a) Storage modulus (b) loss factor at Current 1A for MRF-I and MRF-II with respect to frequency

be due to more carrier fluid in the low vol% of CI particles sample. The results analyzed in this work confirmed that iron particle concentration in the MR fluid strongly influences the rheological properties.

The present study identified the linear viscoelastic shear strain region and the obtained yield strain is around 0.371% for the MRF samples under the amplitude strain sweep test. The driving frequency and strain amplitude have a considerable influence on the rheological properties. This study suggests that the volume percentage of CI particles in the MR fluid strongly influences the rheological properties. Though the present study explored the influence of different parameters on the rheological properties, the current study is limited to only two different compositions of MR fluid samples. Availability of the rheometer with MRD cell and testing cost of the prepared samples are one of the main limitations when it comes to MR fluids study.

## 4. CONCLUSIONS

The current research work presents rheological properties within pre-yield for the in-house prepared MRF samples. The variation in rheological properties like storage modulus and loss factor are determined for the applied driving frequency, amplitude strain, current, and volume percentage of CI particles to check the dependency of these factors on the prepared MR fluid samples. The results obtained in this research work can be summarised as follows:

• The linear viscoelastic shear strain region (pre-yield) is identified and the obtained yield strain is around 0.371% for the in-house prepared MRF samples under the amplitude strain sweep test.

• For all the magnetic fields applied, there is an increment in the storage modulus value with the driving frequency. This confirms that the driving frequency has a considerable influence on the rheological properties.

• For both the samples, the storage modulus value is increasing and the loss factor is decreasing with the strain amplitude.

• The storage modulus is increasing and the loss factor value is decreasing with the magnetic field and for any applied magnetic field, the loss factor is greater at low frequencies than at higher frequencies.

• The Storage modulus obtained for the MRF-II sample is relatively high compared to the MRF-I sample. This concludes that the volume percentage of CI particles in the MR fluid strongly influences the rheological properties.

The present study helps in identifying the linear viscoelastic region for the in-house prepared MR fluid samples and understanding the influence of different parameters on the rheological properties in the pre-yield region. The results obtained further can be utilized for the numerical/experimental studies of the sandwich beam or plate problems, where there is necessity of isolate the natural frequency from the resonance or reducing the amplitude of vibration.

## 5. ACKNOWLEDGMENTS

The authors acknowledge the support from the Department of Science and Technology (DST) file no. ECR/2016/001448 titled “Experimental Investigation of Passive, Semi-active and Active vibration control of Composite Sandwich Structure” funded by Science and Engineering Research Board, Government of India. Authors also acknowledge the support and experimental facility provided by smart structure laboratory, National Institute of Technology Karnataka, India.

## 6. REFERENCES

1. Rabinow, J. “The Magnetic Fluid Clutch.” ***Transactions of the American Institute of Electrical Engineers***, Vol. 67, (1948), 1308-1315. https://doi.org/10.1109/T-AIEE.1948.5059821
2. Ashtiani, M., Hashemabadi, S. H. and Ghaffari, A. “A review on the magnetorheological fluid preparation and stabilization.” ***Journal of Magnetism and Magnetic Materials***, Vol. 374, (2015), 711-715. https://doi.org/10.1016/j.jmmm.2014.09.020
3. Kciuk, M. and Turczyn, R. “Properties and applications of magnetorheological fluids” ***Frattura ed Integrita Strutturale***, Vol. 23, (2012), 57-61. https://doi.org/10.3221/IGF-ESIS.23.06
4. Elizabeth Premalatha, S., Chokkalingam, R. and Mahendran, M. “Magneto Mechanical Properties of Iron Based MR Fluids” ***American Journal of Polymer Science***, Vol. 2, No. 4, (2012), 50-55. https://doi.org/10.5923/j.ajps.20120204.01
5. Genç, S. and Phulé, P.P. “Rheological properties of magnetorheological fluids.” ***International Journal of Modern Physics B***, Vol. 21, No. 28-29, (2007), 4849-4857. https://doi.org/10.1142/s021797920704575x
6. López-López, M. T., Kuzhir, P., Lacis, S., Bossis, G., González-Caballero, F. and Durán, J. D. G. “Magnetorheology for suspensions of solid particles dispersed in ferrofluids.” ***Journal of Physics Condensed Matter***, Vol. 18, No. 38, (2006). https://doi.org/10.1088/0953-8984/18/38/S18
7. Iglesias, G. R., López-López, M. T., Durán, J. D. G., González-Caballero, F. and Delgado, A. V. “Dynamic characterization of extremely bidisperse magnetorheological fluids.” ***Journal of Colloid and Interface Science***, Vol. 377, No. 1, (2012), 153-159. https://doi.org/10.1016/j.jcis.2012.03.077
8. Genc, S. “Experimental Studies on Magnetorheological Fluids” ***Journal: Encyclopedia of Smart Materials,*** 248-259, https://doi.org/10.1016/B978-0-12-803581-8.12095-8
9. Muddebihal, A. B. and Patil, S. F. “Preparation and Study of Characteristics of Iron Based MR Fluids” ***Materials Today: Proceedings***, Vol. 24, (2020), 1132-1137. https://doi.org/10.1016/j.matpr.2020.04.426
10. Zhu, W., Dong, X., Huang, H. and Qi, M. “Iron nanoparticles-based magnetorheological fluids: A balance between MR effect and sedimentation stability” ***Journal of Magnetism and Magnetic Materials***, Vol. 491, (2019), 165556. https://doi.org/10.1016/j.jmmm.2019.165556
11. Olabi, A. G. and Grunwald, A. “Design and application of magneto-rheological fluid” ***Materials and Design***, Vol. 28, No.

10, (2007), 2658-2664. https://doi.org/10.1016/j.matdes.2006.10.009

12. HE, J. M. and HUANG, J. "Magnetorheological Fluids and Their Properties" ***International Journal of Modern Physics B***, Vol. 19, (2005), 593-596. https://doi.org/10.1142/S0217979205029110
13. Vishwakarma, P. N., Mishra, P. and Sharma, S. K. "Characterization of a magnetorheological fluid damper a review" ***Materials Today: Proceedings***, Vol. 56, (2022), 2988-2994. https://doi.org/10.1016/j.matpr.2021.11.143
14. Daniel, C., Hemalatha, G., Sarala, L., Tensing, D. and Sundar Manoharan, S. "Seismic Mitigation of Building Frames using Magnetorheological Damper" ***International Journal of Engineering, Transactions B: Applications***, Vol. 32, No. 11, (2019), 1543-1547. https://doi.org/10.5829/ije.2019.32.11b.05
15. Seid, S., Chandramohan, S. and Sujatha, S. "Design and evaluation of a magnetorheological damper based prosthetic knee" ***International Journal of Engineering, Transactions A: Basics***, Vol. 32, No. 1, (2019), 146-152. https://doi.org/10.5829/ije.2019.32.01a.19
16. Djavareshkian, M. H., Esmaeili, A. and Safarzadeh, H. "Optimal Design of Magnetorheological Fluid Damper Based on Response Surface Method" ***International Journal of Engineering, Transactions C: Aspects***, Vol. 28, No. 9, (2015), 1359-1367. https://doi.org/10.5829/idosi.ije.2015.28.09c.14
17. TharehalliMata, G., Krishna, H. and Keshav, M. "Characterization of magneto-rheological fluid having elongated ferrous particles and its implementation in MR damper for three-wheeler passenger vehicle" ***Proceedings of the Institution of Mechanical Engineers, Part D: Journal of Automobile Engineering***, (2022), 095440702210784. https://doi.org/10.1177/09544070221078451
18. Muhammad, A., Yao, X. and Deng, Z. "Review of magnetorheological (MR) fluids and its applications in vibration control" ***Journal of Marine Science and Application***, Vol. 5, No. 3, (2006), 17-29. https://doi.org/10.1007/s11804-006-0010-2
19. Kumbhar, B. K., Patil, S. R. and Sawant, S. M. "Synthesis and characterization of magneto-rheological (MR) fluids for MR brake application" ***Engineering Science and Technology, an International Journal***, Vol. 18, No. 3, (2015), 432-438. https://doi.org/10.1016/j.jestch.2015.03.002
20. Abdel-Wahab, A. A., Murmu, T. and Olabi, A.-G. "Applications of Magnetorheological (MR) Fluids in the Biomedical Field" ***Reference Module in Materials Science and Materials Engineering. UK: Elsevier,*** (2018), 284-307, https://doi.org/10.1016/B978-0-12-803581-8.11318-9
21. Kamble, V. G., Kolekar, S., Panda, H. S., Ammourah, S. and Jagadeesha, T. "Magneto rheological fluid: Fabrication and characterization of its temperature-dependent properties" ***Materials Today: Proceedings***, Vol. 45, (2021), 4813-4818. https://doi.org/10.1016/j.matpr.2021.01.292
22. Allahverdizadeh, A., Mahjoob, M. J., Nasrollahzadeh, N. and Eshraghi, I. "Optimal parameters estimation and vibration control of a viscoelastic adaptive sandwich beam incorporating an electrorheological fluid layer" ***JVC/Journal of Vibration and Control***, Vol. 20, No. 12, (2014), 1855-1868. https://doi.org/10.1177/1077546313483159
23. Khot, S. M. and Pramod Marathe, A. "Development and testing of low cost Magneto Rheological (MR) fluid using flake shaped magnetizable particles" ***Materials Today: Proceedings***, Vol. 62, (2022), 2700-2708. https://doi.org/10.1016/j.matpr.2021.11.519
24. Gamota, D. R. and Filisko, F. E. "High frequency dynamic mechanical study of an aluminosilicate electrorheological material" ***Journal of Rheology***, Vol. 35, No. 7, (1991), 1411-1425. https://doi.org/10.1122/1.550239
25. Weiss, K. D., Carlson, J. D. and Nixon, D. A. "Viscoelastic properties of magneto- and electro-rheological fluids" ***Journal of Intelligent Material Systems and Structures***, Vol. 5, No. 6, (1994), 772-775. https://doi.org/10.1177/1045389X9400500607
26. Liu, G., Gao, F., Wang, D. and Liao, W.-H. "Medical applications of magnetorheological fluid: a systematic review" ***Smart Materials and Structures***, Vol. 31, No. 4, (2022), 043002. https://doi.org/10.1088/1361-665X/ac54e7
27. Li, W. H., Chen, G. and Yeo, S. H. "Viscoelastic properties of MR fluids" ***Smart Materials and Structures***, Vol. 8, No. 4, (1999), 460-468. https://doi.org/10.1088/0964-1726/8/4/303
28. Chiriac, H. and Stoian, G. "Influence of particle size distributions on magnetorheological fluid performances" ***Journal of Physics: Conference Series***, Vol. 200, (2010). https://doi.org/10.1088/1742-6596/200/7/072095
29. Guo, Y. Q., Sun, C. L., Xu, Z. D. and Jing, X. "Preparation and tests of MR fluids with CI particles coated with MWNTS." ***Frontiers in Materials***, Vol. 5, (2018), 1-8. https://doi.org/10.3389/fmats.2018.00050
30. Jolly, M. R., Bender, J. W. and Carlson, J. D. "Properties and Applications of Commercial Magnetorheological Fluids" ***Journal of Intelligent Material Systems and Structures***, Vol. 10, No. 1, (1999), 5-13. https://doi.org/10.1177/1045389X9901000102
31. Allien, J. V., Kumar, H. and Desai, V. "Semi-active vibration control of MRF core PMC cantilever sandwich beams: Experimental study" ***Proceedings of the Institution of Mechanical Engineers, Part L: Journal of Materials: Design and Applications***, Vol. 234, No. 4, (2020), 574-585. https://doi.org/10.1177/1464420720903078
32. Acharya, S., Allien, V. J., N P, P. and Kumar, H. "Dynamic behavior of sandwich beams with different compositions of magnetorheological fluid core." ***International Journal of Smart and Nano Materials***, Vol. 12, No. 1, (2021), 88-106. https://doi.org/10.1080/19475411.2020.1871104
33. Kumar Kariganaur, A., Kumar, H. and Arun, M. "Effect of Temperature on Sedimentation Stability and Flow characteristics of Magnetorheological Fluids with Damper as the Performance Analyser" ***Journal of Magnetism and Magnetic Materials***, Vol. 555, (2022), 169342. https://doi.org/10.1016/j.jmmm.2022.169342
34. Kumar Kariganaur, A., Kumar, H. and Arun, M. "Influence of temperature on magnetorheological fluid properties and damping performance" ***Smart Materials and Structures***, Vol. 31, No. 5, (2022), 055018. https://doi.org/10.1088/1361-665X/ac6346
35. Ramkumar, G., Jesu Gnanaprakasam, A., Thirumarimurugan, M., Nandhakumar, M., Nithishmohan, M., Abinash, K. and Kishore, S. "Synthesis characterization and functional analysis of magneto rheological fluid- A critical review" ***Materials Today: Proceedings***, (2022). https://doi.org/10.1016/j.matpr.2022.04.104
36. Kumar, S., Sehgal, R., Wani, M. F. and Sharma, M. D. "Stabilization and tribological properties of magnetorheological (MR) fluids: A review" ***Journal of Magnetism and Magnetic Materials***, Vol. 538, (2021), 168295. https://doi.org/10.1016/j.jmmm.2021.168295
37. Allien, J. V., Kumar, H. and Desai, V. "Semi-active vibration control of SiC-reinforced Al6082 metal matrix composite sandwich beam with magnetorheological fluid core" ***Proceedings of the Institution of Mechanical Engineers, Part L: Journal of Materials: Design and Applications***, Vol. 234, No. 3, (2020), 408-424. https://doi.org/10.1177/1464420719890374
38. Zhang, X., Liu, X., Ruan, X., Zhao, J. and Gong, X. "The Influence of Additives on the Rheological and Sedimentary Properties of Magnetorheological Fluid" ***Frontiers in Materials***, Vol. 7, (2021), 1-9. https://doi.org/10.3389/fmats.2020.631069
39. Khecho, A., Ghaffari, S. A., Behzadnasab, M. and Rahmat, M. "Role of Mixing Method and Solid Content on Printability of

Alumina Inks for Stereolithography 3D Printing Process" ***International Journal of Engineering Transactions C: Aspects***, Vol. 35, No. 3, (2022), 580-586. https://doi.org/10.5829/IJE.2022.35.03C.11

40. Lijuan, P., Xiaoping, L., Wu, L., Fuhao, Z., Tongliang, W., Huang, W. and Fuwei, W. "Study on rheological property control method of 'Three high' water based drilling fluid" ***International Journal of Engineering, Transactions B: Applications***, Vol. 33, No. 8, (2020), 1687-1695. https://doi.org/10.5829/ije.2020.33.08b.28
41. Kenai, S., Hammat, S., Menadi, B., Khatib, J. and Kadri, E.-H. "Properties of Self-Compacting Mortar Containing Slag with Different Finenesses" ***Civil Engineering Journal***, Vol. 7, No. 5, (2021), 840-856. https://doi.org/10.28991/cej-2021-03091694
42. Soleimani, S., Pennati, G. and Dubini, G. "A study on ratio of loss to storage modulus for the blood clot" ***International Journal of Engineering, Transactions B: Applications***, Vol. 27, No. 8, (2014), 1167-1172. https://doi.org/10.5829/idosi.ije.2014.27.08b.01

## Persian Abstract

**چکیده**

ماهیت کار حاضر بررسی خواص رئولوژیکی سیالات مغناطیسی رئولوژیکی (MR) آماده شده داخلی در منطقه پیش تسلیم است زیرا خواص رئولوژیکی نقش حیاتی در درک بهتر قابلیت‌های میرایی ارتعاش سیالات MR ایفا می‌کند. در کار حاضر، دو ترکیب مختلف از نمونه‌های سیال MR با ۲۴ و ۳۰ درصد حجمی ذرات کربونیل آهن (CI) تهیه شد. نمونه های مایع MR آماده شده حاوی ذرات CI به عنوان یک محیط پخش کننده، روغن سیلیکون به عنوان مایع حامل و گریس لیتیوم سفید به عنوان یک عامل ضد ته نشینی هستند. فرکانس حرکت نوسانی و آزمون‌های جابجایی کرنش دامنه برای بررسی ویژگی‌های رئولوژیکی در ناحیه پیش تسلیم انجام می‌شوند. تأثیر فرکانس مورد ارزیابی قرار گرفت ، دامنه کرنش، میدان مغناطیسی و درصد حجم ذرات CI بر روی خواص رئولوژیکی سیالات MR تهیه شده مورد ارزیابی قرار گرفت. ناحیه ویسکوالاستیک خطی نمونه سیال MR تهیه شده شناسایی شد و کرنش بازده بدست آمده حدود ۰٫۳۷۱ درصد بود. مشاهده شده است که درصد حجمی ذرات CI در سیال MR به شدت بر خواص رئولوژیکی تأثیر می گذارد.

IJE TRANSACTIONS B: Applications Vol. 35, No. 11, (November 2022) 2247-2255

International Journal of Engineering

Journal Homepage: www.ije.ir

# Optimization of Material Removal Rate, Surface Roughness and Kerf Width in Wire-ED Machining of Ti-6Al-4V Using RSM and Grey Relation

D. Doreswamy[a], D. S. Shreyas[a], S. K. Bhat*[b]

[a] *Department of Mechatronics, Manipal Institute of Technology, Manipal Academy of Higher Education, Manipal, Karnataka, India*
[b] *Department of Mechanical and Manufacturing Engineering, Manipal Institute of Technology, Manipal Academy of Higher Education, Manipal, Karnataka, India*

*PAPER INFO*

*Paper history:*
Received 12July 2022
Received in revised form 08 August 2022
Accepted 14 August 2022

*Keywords*:
*Wire Electric Discharge Machining*
*Grey Relational Analysis*
*Ti-6Al-4V*
*Peak Current*
*Surface Roughness*
*Response Surface Methodology*

*ABSTRACT*

Wire-Electric Discharge (WED) Machining is one of the most suitable machining techniques for machining hard-to-cut materials such as Titanium, with precision. It is of utmost importance to optimize the control parameters to achieve the desired levels of machining performance characteristics. Considering this goal, this research investigates the effects of current, pulse on time ($T_{on}$) and pulse off time ($T_{off}$) on the material removal rate, surface roughness and kerf width of WED machined Ti-6Al-4V. The results of optimization showed that, current – 5.19 A, $T_{on}$ – 20 µs, $T_{off}$ – 30 µs, is the optimized settings for machining of Ti-6Al-4V alloy using molybdenum electrode for the best machining performance. Based on the analysis of grey relational grades, the order of influence of the control parameter is ranked as: $T_{on}$ – I, $T_{off}$ – II and Current – III. The efficacy of GRA based approach was evaluated through confirmation experiments wherein the theoretical predictions showed errors < 3%.

***doi**: 10.5829/ije.2022.35.11b.20*

## 1. INTRODUCTION

Ti-6Al-4V is one of the Titanium alloys which holds immense potential in diverse engineering domains including aerospace, automotive, marine and biomedical engineering because of its superior mechanical, thermal and chemical properties, as well as sustenance of these properties at high temperatures [1]. However, these very advantageous properties cause excessive machining forces, tool wear-rate, thermal as well as vibration related problems in case of the traditional machining of these alloys [2,3]. Therefore, non-traditional machining processes are preferred for their machining such as, Laser Beam Machining, Electro Chemical Machining, Abrasive Water Jet Machining, etc. But these techniques pose their own unique hurdles for obtaining the required machining characteristics due to their negative impact on the environment and their cost-effectiveness to achieve desirable properties on machined component [1,4]. Among the non-conventional machining techniques, Wire Electro Discharge Machining (WEDM) has risen as a technique of appropriate choice over other competing techniques for the task of machining of Titanium alloys [5-8].

The principle of operation of WEDM is basically a utilization of concentrated thermal energy through the application of repetitive and controlled amounts of sparks to achieve the erosion or evaporation of the work material, the thermal energy being from conversion of the electrical source energy to operate the machine [9]. The electrical sparks are applied on the work material by the means of an electrode in the shape of a wire, hence the name "wire"-electric discharge machining. These concentrated sparks of current generate extremely high temperatures around 10 000°C, which are more than sufficient to evaporate or erode the target material around the region of application of the sparks. The eroded material is flushed away by dielectric fluid medium,

*Corresponding Author Institutional Email: sk.bhat@manipal.edu
(S. K. Bhat)

Please cite this article as: D. Doreswamy, D. S. Shreyas, S. K. Bhat, Optimization of Material Removal Rate, Surface Roughness and Kerf Width in Wire-ED Machining of Ti-6Al-4V Using RSM and Grey Relation, ***International Journal of Engineering, Transactions B: Applications***, Vol. 35, No. 11, (2022) 2247-2255

which is constantly supplied during machining [9]. Numerous control parameters such as, pulse on time ($T_{on}$), pulse off time ($T_{off}$), discharge current, voltage, speed, feed and tension of wire, and flow rate of the dielectric fluid influence the obtained output characteristics of WEDM up to different extents [10]. $T_{on}$ is the time duration of discharge during which current is supplied and $T_{off}$ is the duration without discharge in between periods of successive $T_{on}$. Discharge current and voltage are measures of the total power supply required for machining. Wire speed, feed rate, and tension pertain to the mechanical arrangements of the electrode wire.

To achieve the required wire-ED machining performance, various optimization techniques [11-18] such as, Grey Relational Analysis (GRA), Principal Component Analysis, Taguchi method, Response Surface Methodology (RSM), etc., have been employed. Design of experiments approach has also been utilized to analyze the effects of process parameters on the machining characteristics of Titanium alloys [19,20]. Among these techniques, GRA is a normalization based statistical analysis technique, and is one of the most popular and effective techniques for multi-objective or multi-performance optimization of the process parameters, which can carry out minimization of certain parameters while simultaneously maximizing the others [11,17-18]. GRA is especially suitable when the system under consideration consists of a complex interplay of various factors and their overall effect in combination needs to be quantitatively analyzed.

In terms of the control parameters, current, pulse-on time and pulse-off time pivotal for controlling the machining performance of WEDM [11-20]. Therefore, these parameters were chosen for investigation in the present study. Among the response characteristics of Wire EDM, slot width or kerf width (KW), material removal rate (MRR), and surface roughness (SR) have been studied prominently [11-20], which are chosen in the present study. For the wire electrode in the WEDM of titanium alloys, various material combinations have been investigated [21,22]. However, molybdenum electrode wires have garnered comparatively lesser attention [23,24]. For the dielectric fluid media, oil and water are the key candidates, and water has been observed to be superior to oil in terms of its chemical stability and electrode wear rate [25]. In the present study, the electrode is made up of molybdenum and deionized water is used as the dielectric fluid.

GRA based multi-objective optimization of WED machining of Ti-6Al-4V has been conducted by other researchers by reviewing the effects of different process parameters on machining performance characteristics. However, most of the studies have utilized copper or brass as the electrode materials [11,26-30]. Using copper electrodes, the effects of current, $T_{on}$ and $T_{off}$ on MRR, SR and tool wear rate have been investigated [26,27,30]. Brass electrodes have been extensively used in the investigation of effects of current, $T_{on}$ and $T_{off}$ on MRR, SR and KW [11,28,29]. Further, using molybdenum wire electrodes, the effects of current, $T_{on}$ and $T_{off}$ on MRR and power consumption were studied [30]. However, as per the best knowledge of the authors, the simultaneous optimization of MRR, SR and KW has not been attempted for WEDM of Ti-6Al-4V in the literature. In the same vein, an important contribution of this paper is the investigation of the operating control settings, i.e., current, $T_{on}$ and $T_{off}$ with a wider range of values than that employed in literature [30]. Particularly, use of low current settings (2 A – 6 A) is a uniqueness of the present study. These are the lacunae in the research which is being bridged by the present study. The multi-response optimization of the WEDM can also improve the resistance of the finished product under impact and cyclic loadings due to the optimal surface roughness and microstructure of the processed titanium Ti-6Al-4V [31].

Among WED machining studies of Ti-6Al-4V in the literature, there still exists research gaps which need to be filled for improving the understanding of the effects of various control parameters on the machining performance characteristics. Therefore, the present study analyzes the optimum settings of peak current, $T_{on}$ and $T_{off}$ for obtaining the best possible machining performance characteristics, viz., MRR, SR and KW, using the Grey Relational Analysis, in conjunction with ANOVA and Response Surface Methodology during the use of molybdenum wire as the electrodes and deionized water as the dielectric fluid medium. In this paper, the multi-responses of Wire-ED machined Titanium alloy Ti-6Al-4V are optimized with respect to the process parameters. Moreover, the optimized machining responses obtained from GRA is compared with that obtained using the conventional RSM approach through confirmation experiments to verify the efficacy of the technique implemented in the present paper.

## 2. MATERIALS AND METHODS

**2. 1. Experimental Setup and Design of Experiments** The CNC Wire-EDM machine – Versa Cut 01 DK7732 (Make: Concord United Products Pvt. Ltd., Bengaluru, India) was used in this study having table dimensions of 320 mm × 400 mm (Figure 1). The work samples for the present study, the Ti-6Al-4V plate, is cut into a slab of 150 mm × 50 mm × 2 mm. Subsequently, machining experiments are performed on the samples by varying the control parameters as per the design of experiments for a length of 10 mm for each trial. Fifteen pieces are then removed and marked from the test sample for measuring the MRR, SR and KW along each side. Molybdenum wires of 0.18 mm diameter are used as the electrodes for machining and the dielectric

**Figure 1.** Experimental setup

fluid medium consists of demineralized/deionized water with cleanser gel during the Wire-EDM of the samples. The compositional information of test samples was obtained from tests conducted at Varsha Bullion Elemental Analab, Mumbai, India (Table 1). Based on previous studies on different materials using the current experimental setup [32-34], three imperative control factors $T_{on}$, $T_{off}$ and peak current are chosen for the present work. Remaining control parameters were kept constant throughout the experiments (Table 2). The experimental levels (Table 3) are designed using the central composite design of RSM.

## 2. 2. Measurement of Machining Responses

The machining responses chosen for optimization are MRR, SR and KW. MRR is principally a measure of the material volume removed in a unit time interval of machining (expressed in $mm^3$/min). The machining time for individual slot is obtained from the WED machine. The quantity of removed material is determined by computing the weight reduction of the test sample after machining. SR ($R_a$) of machined cut surfaces were measured utilizing the Surtronic® Surface Roughness Tester (Made by Taylor Hobson). The stylus probe of the tester was made to move along the surface for a sampling length of 2.5 mm for each measurement. For each sample, the readings were recorded at four different locations and its average $R_a$ is obtained. The slot/kerf width is measured using the IM7000 Series Mitutoyo Inverted Metallurgical Optical Microscope (Made by Meiji Techno). KW was measured at three different locations along the length and the average of the measurements is considered during the analysis. Table 4 presents the experimental plan and the measured response data.

**TABLE 1.** The composition of Ti-6Al-4V test samples used in the present study [31]

| Material composition | Ti | Al | V | Fe | C | Cr | Cu |
|---|---|---|---|---|---|---|---|
| % | 89.54 | 5.60 | 4.50 | 0.23 | 0.01 | 0.03 | 0.09 |

**TABLE 2.** Control parameters kept constant during the present work

| Parameters | Values with units |
|---|---|
| Wire speed | 4.4 m/s |
| Wire tension | 8 kg-f |
| Dielectric fluid | Deionized water + cleanser gel |
| Fluid pressure | 40 $dm^3$/minute |
| Servo Voltage | 90 V |

**TABLE 3.** The range of wire-EDM variable control parameters chosen in the present study

| Control parameters | Level 1 | Level 2 | Level 3 |
|---|---|---|---|
| Current (A) | 2 | 4 | 6 |
| $T_{on}$ (µs) | 20 | 35 | 50 |
| $T_{off}$ (µs) | 10 | 20 | 30 |

## 2. 3. Grey Relational Analysis

Taguchi technique is useful for optimizing the control parameters for a single response characteristic. However, the present work comprises of optimization of three machining responses namely, MRR, $R_a$ and KW. MRR is demands the "higher-the-better" characteristics, whereas $R_a$ and KW demand the "lower-the-better" response characteristics. Such scenarios can be tackled using the Grey Relational Analysis (GRA) wherein "Grey" indicates the situation wherein the available information is between black-and-

**TABLE 4.** Experimental design with correspondingly obtained machining response data

| Sl. No. | Current (A) | $T_{on}$ (µs) | $T_{off}$ (µs) | MRR ($mm^3$/min) | $R_a$ (µm) | KW (mm) |
|---|---|---|---|---|---|---|
| 1 | 2 | 20 | 20 | 0.931 | 6.32 | 0.100 |
| 2 | 4 | 35 | 20 | 1.675 | 7.35 | 0.112 |
| 3 | 2 | 50 | 20 | 1.071 | 8.36 | 0.115 |
| 4 | 6 | 35 | 10 | 3.027 | 8.34 | 0.123 |
| 5 | 4 | 20 | 30 | 1.118 | 5.59 | 0.098 |
| 6 | 6 | 20 | 20 | 2.040 | 8.37 | 0.113 |
| 7 | 4 | 50 | 30 | 1.115 | 7.04 | 0.117 |
| 8 | 2 | 35 | 30 | 0.722 | 6.93 | 0.105 |
| 9 | 4 | 50 | 20 | 1.704 | 9.63 | 0.118 |
| 10 | 6 | 50 | 20 | 1.930 | 9.88 | 0.123 |
| 11 | 4 | 35 | 20 | 1.680 | 7.54 | 0.117 |
| 12 | 2 | 35 | 10 | 1.600 | 7.50 | 0.107 |
| 13 | 6 | 35 | 30 | 1.360 | 6.56 | 0.108 |
| 14 | 4 | 50 | 10 | 2.388 | 7.75 | 0.108 |
| 15 | 4 | 20 | 10 | 2.124 | 7.98 | 0.098 |

white [35]. Here, black signifies no information condition, whereas white indicates the availability of complete information regarding the responses. The methodology of analysis involved in GRA is schematically presented in Figure 2.

## 3. RESULTS AND DISCUSSION

**3. 1. Computation of Grey Relation** Grey relation is computed by the linear normalization of the measured experimental results, viz., the machining performances (MRR, $R_a$ and KW), between zero to one. During this computation, the input data is dispersed uniformly and scaled to a proportionate range for subsequent analysis. For $R_a$ and KW, the normalization is carried out using "smaller-the-better" performance characteristics using Equation (1), whereas for MRR is normalized using the "higher-the-better" characteristic using Equation (2). Table 5 shows the original and linearly normalized responses.

$$X_{ijk} *= \frac{Max(X_{ijk}) - X_{ijk}}{Max(X_{ijk}) - Min(X_{ijk})} \text{ for j} = 1,2\ldots,15 \quad (1)$$

$$X_{ijk} *= \frac{X_{ijk} - Min(X_{ijk})}{Max(X_{ijk}) - Min(X_{ijk})} \text{ for j} = 1,2,\ldots,15 \quad (2)$$

**3. 2. Computation of Grey Relational Coefficient** Grey relational coefficient (ξ) establishes the association between the theoretical and normalized experimental results, which are computed using Equations (3) to (5). Since the machining performance characteristic responses chosen in this study are considered to be of identical importance, the characteristic coefficient which distinguishes between the response, $\xi \in (0,1)$ is taken as 1/3. Table 5 summarized the grey relational coefficients (GRC) computed with respect to the normalized responses.

$$R = Max(X *_{ijk}) = 1 \quad (3)$$

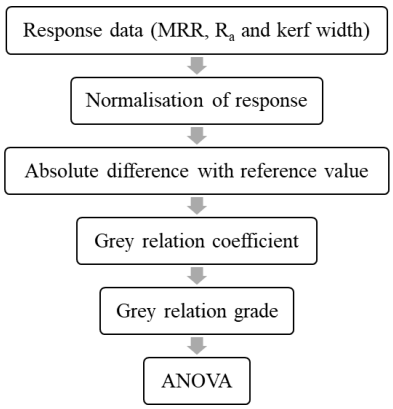


**Figure 2.** Steps involved in grey relational analysis

$$\Delta_{ijk} = |X *_{ijk} - R| \quad (4)$$

$$\xi_{ijk} = \frac{Min(\Delta_{ijk}) + \xi Max(\Delta_{ijk})}{\left(\Delta_{ijk} + \xi Max(\Delta_{ijk})\right)} \quad (5)$$

**3. 3. Computation of Grey Relational Grade** The grey relational grade (GRG) represents (Table 5) the degree of composite relationship among the output responses [36]. The grades for each experimental setting are computed by obtaining the mean value of the respective grey relational coefficients using Equation (6), where $m$ is the number of response or performance characteristics being analysed ($m = 3$).

**TABLE 5.** Grey relational computated values

| Trial No. | Normalized Response | | | GRC | | | GRG |
|---|---|---|---|---|---|---|---|
| | MRR | $R_a$ | KW | MRR | $R_a$ | KW | |
| 1 | 0.091 | 0.830 | 0.920 | 0.266 | 0.660 | 0.805 | 0.577 |
| 2 | 0.413 | 0.590 | 0.440 | 0.360 | 0.446 | 0.371 | 0.392 |
| 3 | 0.151 | 0.354 | 0.320 | 0.280 | 0.338 | 0.327 | 0.315 |
| 4 | 1.000 | 0.359 | 0.000 | 1.000 | 0.340 | 0.248 | 0.529 |
| 5 | 0.172 | 1.000 | 1.000 | 0.285 | 1.000 | 1.000 | 0.762 |
| 6 | 0.572 | 0.352 | 0.400 | 0.435 | 0.337 | 0.355 | 0.376 |
| 7 | 0.170 | 0.662 | 0.240 | 0.285 | 0.494 | 0.303 | 0.360 |
| 8 | 0.000 | 0.688 | 0.720 | 0.248 | 0.514 | 0.541 | 0.434 |
| 9 | 0.426 | 0.058 | 0.200 | 0.365 | 0.259 | 0.292 | 0.306 |
| 10 | 0.524 | 0.000 | 0.000 | 0.409 | 0.248 | 0.248 | 0.302 |
| 11 | 0.416 | 0.545 | 0.240 | 0.361 | 0.421 | 0.303 | 0.361 |
| 12 | 0.381 | 0.555 | 0.640 | 0.348 | 0.426 | 0.478 | 0.417 |
| 13 | 0.277 | 0.774 | 0.600 | 0.313 | 0.593 | 0.452 | 0.453 |
| 14 | 0.723 | 0.497 | 0.600 | 0.543 | 0.396 | 0.452 | 0.464 |
| 15 | 0.608 | 0.443 | 1.000 | 0.457 | 0.372 | 1.000 | 0.610 |

$$GRG = \gamma_i = \frac{1}{m}\sum_{i=1}^{m} \xi_{ik} \quad (6)$$

**3. 4. Analysis of Grey Relational Grade** Figure 3 presents the main effects plot with respect to GRG. The corresponding output response, i.e., GRG is observed to increase with rise of peak current until 4 A starting from 2 A, but further increase reduces the mean response of GRG. This is due to the fact that small current settings cause lesser amounts of MRR and higher surface unevenness, whereas the maximum current setting can lead to larger kerf widths because of excessive generation of the spark discharge energy. Therefore, current settings close to 4 A gives the best response for an overall

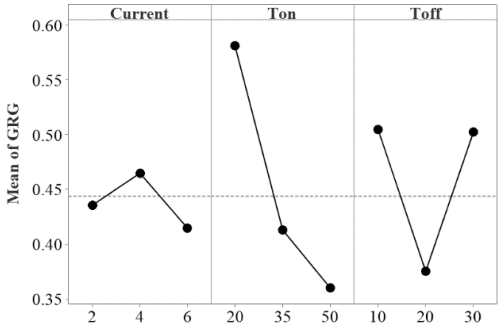


**Figure 3.** Main effects plot of grey relational grade

optimized response. Further, it is observed that the smallest duration of $T_{on}$ (20 µs) generates the best GRG, whereas maximum $T_{on}$ (50 µs) gives the least response. This is because, as $T_{on}$ increases, because of the continuous material removal, both MRR and KW tends to increase, and it also leads to excessive surface unevenness because of inadequate time intervals for the dielectric fluid medium to flush away the molten or evaporated work material. Therefore, $T_{on}$ duration of 20 µs gives the best GRG response. In case of $T_{off}$, both extremes of the range of values gives the best response of grey relational grade, but $T_{off}$ duration of 20 µs gives the least response.

The GRG is them examined through the analysis of variance (ANOVA) to evaluate the simultaneous effects of the individual control parameters on MRR, $R_a$ and KW at 95% confidence interval. From the standard Fisher's table, critical *F*-statistic is found to be 2.90 (error degree of freedom (DF) – 5). Input parameters having *F*-statistic greater than the critical *F*-statistic implies that the respective parameter possesses a statistically significant influence on the output response. Table 6 demonstrates that the individual effect of $T_{on}$ has a significant influence on the response, while other two parameters are observed to be statistically insignificant. The second-order terms of individual parameters $T_{on}$ and $T_{off}$, and interaction effect between $T_{on}$ and $T_{off}$ are found to be statistically significant. Lack-of-fit is observed to be statistically insignificant, indicating the effectiveness of the prediction of GRG in terms of the statistically significant terms.

Figure 4 shows the response surfaces of the interaction effects between the control parameters chosen in the present work. From Figure 4(a), it is observed that both current and $T_{on}$ have significant effect on each other's individual effects on the responses. At the minimum value of $T_{on}$ (10 µs), the current tends to reduce the output response, whereas at its maximum value (30 µs) current tends to increase the response GRG. The interaction between Current and $T_{off}$ (Figure 4(b)) shows a similar conclusion as shown in the main effect plots with respect to the nature of influence of $T_{off}$ and Current. The interaction between $T_{on}$ and $T_{off}$ (Figure 4(c)) shows that at minimum $T_{on}$ (10 µs) the effect of $T_{off}$ is much larger and as $T_{on}$ increases its impact on output response reduces.

**TABLE 6.** ANOVA of GRG for MRR, $R_a$ and KW

| Source | DF | Adj SS | Adj MS | F-Value | P-Value |
|---|---|---|---|---|---|
| Current | 1 | 0.000871 | 0.000871 | 0.17 | 0.698 |
| $T_{on}$ | 1 | 0.097469 | 0.097469 | 18.91 | 0.007 |
| $T_{off}$ | 1 | 0.000015 | 0.000015 | 0.00 | 0.960 |
| Current*Current | 1 | 0.002411 | 0.002411 | 0.47 | 0.524 |
| $T_{on}$*$T_{on}$ | 1 | 0.015563 | 0.015563 | 3.02 | 0.143 |
| $T_{off}$*$T_{off}$ | 1 | 0.063301 | 0.063301 | 12.28 | 0.017 |
| Current*$T_{on}$ | 1 | 0.008842 | 0.008842 | 1.72 | 0.247 |
| Current*$T_{off}$ | 1 | 0.002183 | 0.002183 | 0.42 | 0.544 |
| $T_{on}$*$T_{off}$ | 1 | 0.016289 | 0.016289 | 3.16 | 0.136 |
| Lack-of-Fit | 3 | 0.021906 | 0.007302 | 3.78 | 0.216 |

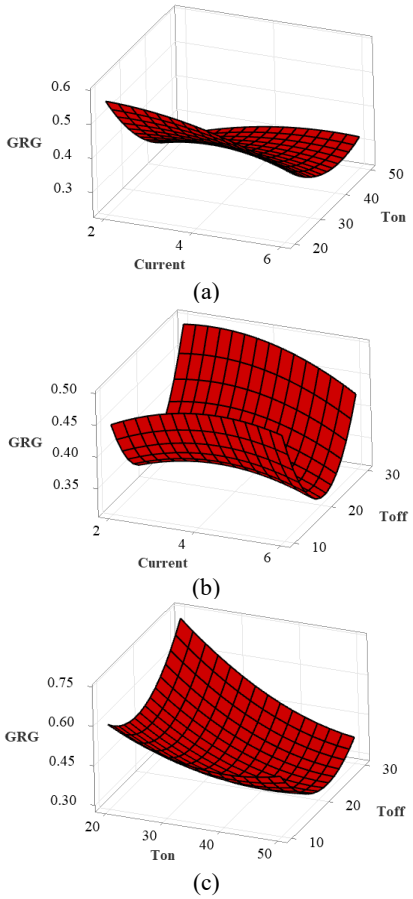


**Figure 4.** Interaction effects of (a) Current and $T_{on}$ at constant $T_{off}$ = 20 µs, (b) Current and $T_{off}$ at constant $T_{on}$ = 35 µs, and (c) $T_{on}$ and $T_{off}$ at constant Current = 4 A

### 3. 5. Simultaneous Multi-response Optimization

The mean GRG computed for process parameters at each control parameter settings is presented in Table 7. The maximum mean GRG (highlighted in bold text in Table 7) is observed at the settings, Current – 4 A, $T_{on}$ – 20 µs, $T_{off}$ – 10 µs.

Hence A2B1C1 is the optimum combination of settings for the best performance of MRR, $R_a$ and KW. Using Equation (7) the projected GRG is obtained as 0.6081 at the optimized set of control parameter settings. Confirmation experiments were carried out at the corresponding control parameter combination of A2B1C1, and the MRR, $R_a$ and KW obtained ranged 2.186 ± 0.131 $mm^3$/min, 7.60 ± 0.74 µm and 0.102 ± 0.018 mm. Further, based on the maximum GRG values in Table 7 for each process parameters, the order of significance of their influence on the response is ranked as, $T_{on}$ – I, $T_{off}$ – II and Current – III.

$$GRG_{optimum} = f(A_2 + B_1 + C_1) - 2\sum_{i=1}^{15} GRG_i/15 \quad (7)$$

Figure 5 shows the optimized Current, $T_{on}$ and $T_{off}$ settings and the corresponding output responses of MRR, $R_a$ and KW. Composite desirability is a statistical measure which indicates an overall optimal performance. In this study, a composite desirability of 0.664 is obtained, which is close to the mean value reported in a GRA based study on WEDM of Ti-6Al-4V [36]. It is observed from the optimization of individual parameters that maximum desirability and maximum GRG is attempted to be obtained such that the individual parameter's optimization goals are being satisfied to the best possible extent within the allowable parameter space.

The Pareto chart (Figure 6) lists the control parameters in the order of their influence from the highest to the smallest, along with a reference line which represents a statistical threshold. Parameters which cross the reference line representing this statistical threshold are considered to have statistically significant influence on the simultaneous response, i.e., GRG. The Pareto distribution shows that individual effect on $T_{on}$ and second-order effect of $T_{off}$ have the significant influence on the overall response, followed by other combinations.

### 3. 6. Comparison of GRA Based Multi-response Optimization with RSM

To validate the results obtained using GRA, it is compared with that from conventional single-response optimization using RSM. The optimal parameters and the corresponding machining responses from RSM based single-response

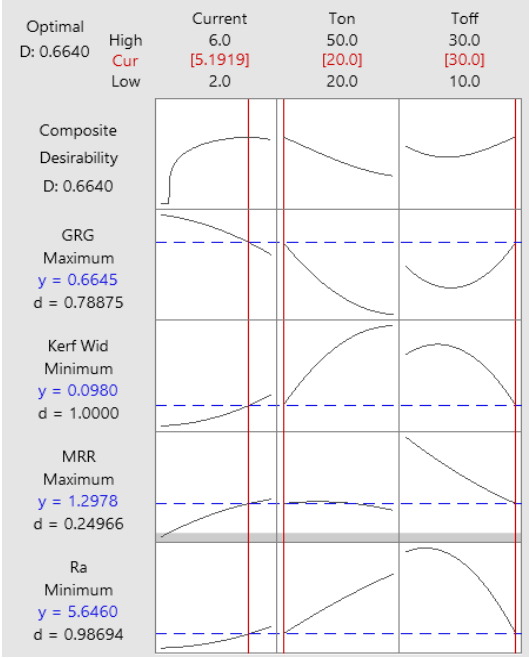


**Figure 5.** Response surface plots of composite desirability, GRG, MRR, $R_a$, KW as a function of control parameters

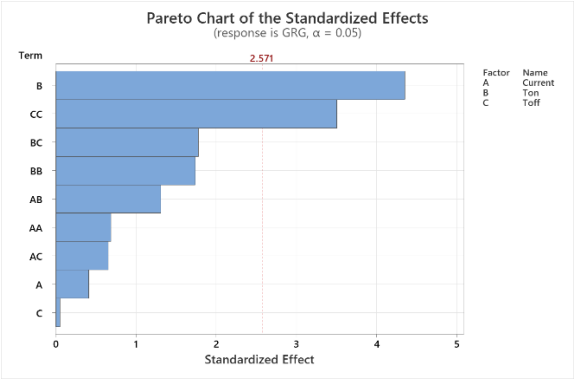


**Figure 6.** Pareto chart of the standardized effects of control parameters on GRG

**TABLE 7.** Mean grey relational grades at each levels of the control parametric

| Level | Current (A) | $T_{on}$ (µs) | $T_{off}$ (µs) |
|---|---|---|---|
| 1 | 0.4359 | **0.5259** | **0.5050** |
| 2 | **0.4650** | 0.4312 | 0.3756 |
| 3 | 0.4150 | 0.3603 | 0.5023 |

**TABLE 8.** Errors of GRA and RSM response predictions along with experimental responses

| Trial No. | GRA – Error (%) | | | RSM – Error (%) | | |
|---|---|---|---|---|---|---|
| | MRR | $R_a$ | KW | MRR | $R_a$ | KW |
| 1 | 1.6 | 4.3 | 1.0 | 2.7 | 3.2 | 7.0 |
| 2 | 3.0 | 1.4 | 3.9 | 3.8 | 4.0 | 5.9 |
| 3 | 2.4 | 0.9 | 3.0 | 3.9 | 7.0 | 8.0 |
| 4 | 2.4 | 0.7 | 1.0 | 9.9 | 9.5 | 13.4 |
| 5 | 3.7 | 0.9 | 1.0 | 7.2 | 4.0 | 1.6 |

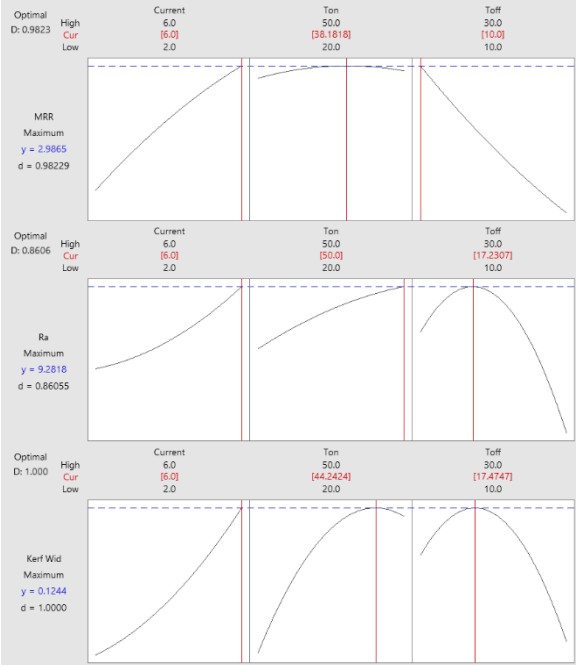


**Figure 7.** The effects of Current, $T_{on}$ and $T_{off}$ on individual responses – MRR, Ra and KW

optimization are presented in Figure 7. Five confirmation experiments were conducted using the optimal parameters obtained from the two methods and the experimental responses are compared with theoretical predictions, expressed as absolute % errors (Table 8). The mean error for GRA is < 3% and for RSM it is > 5%.

## 4. CONCLUSIONS

The following conclusions were drawn from the present study of GRA based multi-response optimization for the WED machining of Ti-6Al-4V using molybdenum wire electrode, through a comprehensive analysis of the effects of peak current, $T_{on}$, and $T_{off}$ on the machining responses, i.e., MRR, $R_a$ and KW:

- Main effects analysis of the individual control parameters revealed that intermediate level of current (4 A), minimum $T_{on}$ (20 µs) and either minimum or maximum $T_{off}$ (10 µs), gives the best output response.
- ANOVA of GRG indicated that the linear and quadratic term of $T_{on}$ and the quadratic term of $T_{off}$ have significant impact on the machining responses, whereas current was statistically insignificant. Further, the interaction effect of $T_{off}$ on $T_{off}$ is found to be significant whereas other interaction effects are statistically insignificant.
- Analysis of the Grey Relational Grades showed that within the experimental range, Current – 4 A, $T_{on}$ – 20 µs, $T_{off}$ – 10 µs, provided the best machining performance. The order of influence of the control parameter was ranked as: $T_{on}$ – I, $T_{off}$ – II and Current – III.
- The multi-response optimization considering the composite desirability showed that, current – 5.19 A, Ton – 20 µs, Toff – 30 µs, gave the optimal response of MRR, $R_a$ and KW.
- The comparison of GRA and RSM results with those from confirmation experiments showed that GRA had errors < 3%, demonstrating the efficacy of the optimization method.

## 5. REFERENCES


1. Qosim, N., Supriadi, S., Puspitasari, P., Kreshanti, P. "Mechanical Surface Treatments of Ti-6Al-4V Miniplate Implant Manufactured by Electrical Discharge Machining", ***International Journal of Engineering, Transactions A: Basics***, Vol. 31, No. 7, (2018), 1103-1108, doi: 10.5829/ije.2018.31.07a.14
2. Gupta, K., Laubscher, R. "Sustainable machining of titanium alloys: A critical review", ***Proceedings of the Institution of Mechanical Engineers, Part B: Journal of Engineering Manufacture***, Vol. 231, No. 14, (2016), 2543-2560, doi: 10.1177/0954405416634278
3. Pramanik, A. "Problems and solutions in machining of titanium alloys", ***The International Journal of Advanced Manufacturing Technology***, Vol. 70, (2014), 919-928, doi: 10.1007/s00170-013-5326-x
4. Oke, S.R., Ogunwande, G.S., Onifade, M., Aikulola, E., Adewale, E.D., Olawale, O.E. "An overview of conventional and non-conventional techniques for machining of titanium alloys", ***Manufacturing Review***, Vol. 7, No. 34, (2020). 24, doi: 10.1051/mfreview/2020029
5. Nishanth, B.S., Kulkarni, V.N., Gaitonde V.N. "A review on conventional and nonconventional machining of titanium and nickel-based alloys", ***AIP Conference Proceedings***, Vol. 2200, No. 020091, (2019), doi: 10.1063/1.5141261
6. Davim, J.P., Machining: Fundamentals and Recent Advances. London: Springer, 2008. ISBN: 978-1-84800-213-5
7. Davim, J.P., Nontraditional Machining Processes. London: Springer, 2013. ISBN: 978-1-4471-5179-1
8. Davim, J.P., Machining of Titanium alloys. Heidelberg: Springer Berlin, 2014. ISBN: 978-3-662-43902-9
9. Qudeiri, J.A.E., Mourad, A.H.I., Ziout, A. "Electric discharge machining of titanium and its alloys: review", ***The International Journal of Advanced Manufacturing Technology***, Vol. 96, (2018), 1319-1339, doi: 10.1007/s00170-018-1574-0
10. Patel, S.S., Prajapati, J.M. "Experimental Investigation of Surface Roughness and Kerf Width During Machining of Blanking Die Material on Wire Electric Discharge Machine", ***International Journal of Engineering, Transactions A: Basics***, Vol. 31, No. 10, (2018), 1760-1766, doi: 10.5829/ije.2018.31.10a.19
11. Saedon, J.B., Jaafar, N., Yahaya, M.A., Saad, N., Kasim, M.S. "Multi-objective Optimization of Titanium Alloy through Orthogonal Array and Grey Relational Analysis in WEDM", ***Procedia Technology***, Vol. 15, (2014), 832-840, doi: 10.1016/j.protcy.2014.09.057
12. Raj, S.O.N., Prabhu, S. "Modeling and analysis of titanium alloy in wire cut EDM using Grey relation coupled with principle component analysis", ***Australian Journal of Mechanical***

***Engineering***, Vol. 15, No. 3, (2017), 198-209, doi: 10.1080/14484846.2016.1251077

13. Mohamed, M.F., Lenin, K. "Optimization of Wire EDM process parameters using Taguchi technique", ***Materials Today: Proceedings***, Vol. 21, (2020), 527-530, doi: 10.1016/j.matpr.2019.06.662
14. Nourbakhsh, F., Rajurkar, K.P., Malshe, A.P., Cao, J. "Wire Electro-Discharge Machining of Titanium Alloy", ***Procedia CIRP,*** Vol. 5, (2013), 13-18, doi: 10.1016/j.procir.2013.01.003
15. Golshan, A., Ghodsiyeh, D, Izman, S. "Multi-objective optimization of wire electrical discharge machining process using evolutionary computation method: Effect of cutting variation", ***Proceedings of the Institution of Mechanical Engineers, Part B: Journal of Engineering Manufacture***, Vol. 229, No. 1, (2015), 75-85, doi: 10.1177/0954405414523593
16. Arikatla, S.P., Mannan, K.T., Krishnaiah, A. "Parametric Optimization in Wire Electrical Discharge Machining of Titanium Alloy Using Response Surface Methodology", ***Materials Today: Proceedings***, Vol. 4, (2017), 1434-1441, doi: 10.1016/j.matpr.2017.01.165
17. Chaudhari, R., Vora, J., Parikh, D.M., Wankhede, V., Khanna, S. "Multi-response Optimization of WEDM Parameters Using an Integrated Approach of RSM–GRA Analysis for Pure Titanium", ***Journal of The Institution of Engineers (India): Series D***, Vol. 101, No. 1, (2020, 117-126, doi: 10.1007/s40033-020-00204-7
18. Saindane, U.V., Soni, S., Menghani, J.V. "Friction and Wear Performance of Brake Pad and Optimization of Manufacturing Parameters using Grey Relational Analysis", ***International Journal of Engineering, Transactions C: Aspects***, Vol. 35, No. 03, (2022), 552-559, doi: 10.5829/ije.2022.35.03c.07
19. Khanna, N., Davim, J.P. "Design-of-experiments application in machining titanium alloys for aerospace structural components", ***Measurement***, Vol. 61, (2015), 280-290, doi: 10.1016/j.measurement.2014.10.059
20. Lauro, C.H., Filho, S.L.M.R., Brandao, L.C., Davim, J.P. "Analysis of behaviour biocompatible titanium alloy (Ti-6Al-7Nb) in the micro-cutting", ***Measurement***, Vol. 93, (2016), 529-540, doi: 10.1016/j.measurement.2016.07.059
21. Hascalik, A., Caydas, U. "Electrical discharge machining of titanium alloy (Ti–6Al–4V)", ***Applied Surface Science***, Vol. 253, No. 22, (2007), 9007-9016, doi: 10.1016/j.apsusc.2007.05.031
22. Phan, N.H., Dong, P.V., Muthuramalingam, T., Thien, N.V., Dung, H.T., Hung, T.Q., Duc, N.V., Ly, N.T. "Experimental Investigation of Uncoated Electrode and PVD AlCrNi Coating on Surface Roughness in Electrical Discharge Machining of Ti-6Al-4V", ***International Journal of Engineering, Transactions A: Basics***, Vol. 34, No. 04, (2021), 928-934, doi: 10.5829/ije.2021.34.04a.19
23. Chaudhari, R., Vora, J.J., Patel, V., Lacalle, L.N.Ld., Parikh, D.M. "Effect of WEDM Process Parameters on Surface Morphology of Nitinol Shape Memory Alloy", ***Materials***, Vol. 13, No. 21, (2020), 4943, doi: 10.3390/ma13214943
24. Devarasiddappa, D., Chandrasekaran, M., Arunachalam, R. "Experimental investigation and parametric optimization for minimizing surface roughness during WEDM of Ti6Al4V alloy using modified TLBO algorithm", ***Journal of the Brazilian Society of Mechanical Sciences and Engineering***, Vol. 42, (2020), 128. doi: 10.1007/s40430-020-2224-7
25. Chakraborty, S., Mitra, S., Bose, D. "Performance Analysis on Eco-friendly Machining of Ti6Al4V using Powder Mixed with Different Dielectrics in WEDM", ***International Journal of Automotive and Mechanical Engineering***, Vol. 17, No. 2, (2020), 8128-8139, doi: 10.15282/ijame.17.3.2020.06.0610
26. Kao, J.Y., Tsao, C.C., Wang, S.S., Hsu. C.Y. "Optimization of the EDM parameters on machining Ti–6Al–4V with multiple quality characteristics", ***The International Journal of Advanced Manufacturing Technology***, Vol. 47, (2010), 395-402, doi: 10.1007/s00170-009-2208-3
27. Kumar, S., Dhanabalan, S., Narayanan, C.S. "Application of ANFIS and GRA for multi-objective optimization of optimal wire-EDM parameters while machining Ti–6Al–4V alloy", ***SN Applied Sciences***, Vol. 1, (2019), 298, doi: 10.1007/s42452-019-0195-z
28. Sharma, N., Khanna, R., Sharma, Y.K., Gupta, R.D. "Multi-quality characteristics optimisation on WEDM for Ti-6Al-4V using Taguchi-grey relational theory", ***International Journal of Machining and Machinability of Materials***, Vol. 21, No. 1/2, (2019), 66-81, doi: 10.1504/IJMMM.2019.098067
29. Sonawane, S.A., Ronge, B.P., Pawar, P.M. "Multi-characteristic optimization of WEDM for Ti-6Al-4V by applying grey relational investigation during profile machining", ***Journal of Mechanical Engineering and Sciences***, Vol. 13, No. 4, (2019), 6059-6087, doi: 10.15282/jmes.13.4.2019.22.0478
30. Gugulothu, B., Rao, G.K.M., Bezabih, M. "Grey relational analysis for multi-response optimization of process parameters in green electrical discharge machining of Ti-6Al-4V alloy", ***Materials Today: Proceedings***, Vol. 46, No. 1, (2021), 89-98, doi: 10.1016/j.matpr.2020.06.135
31. Maruschak, P.O., Chausov, M.G., Konovalenko, I.V, Yasnii, O.P., Panin, S.V., Vlasov, I.V. "Effect of Shock and Vibration Loading on the Fracture Mechanisms of a VT23 Titanium Alloy", ***Strength of Materials***, Vol. 52 (2020), 252-261, doi: 10.1007/s11223-020-00172-z
32. Deepak, D., Shreyas, D.S., Bhat, S.K., Rao, R.N. "Optimization of material removal rate and surface characterization of wire electric discharge machined Ti-6Al-4V alloy by response surface method", ***Manufacturing Review***, Vol. 9, No. 15, (2022), 11, doi: 10.1051/mfreview/2022016
33. Doreswamy, D., Javeri, J. "Effect of Process Parameters in EDM of D2 Steel and Estimation of coefficient for Predicting Surface Roughness", ***International Journal of Machining and Machinability of Materials***, Vol. 20, (2018), 101-117, doi: 10.1504/IJMMM.2018.090542
34. Deepak, D., Shrinivas, P., Hemant, G., Iasy, R. "Optimisation of Current and Pulse Duration in Electric Discharge Drilling of D2 Steel Using Graphite Electrode", ***International Journal of Automotive and Mechanical Engineering***, Vol. 15, (2018), 5914-5926, doi: 10.15282/ijame.15.4.2018.14.0451
35. Devarajaiah, D., Muthumari, C. "Evaluation of power consumption and MRR in WEDM of Ti–6Al–4V alloy and its simultaneous optimization for sustainable production", ***Journal of the Brazilian Society of Mechanical Sciences and Engineering***, Vol. 40, (2018), 400, doi: 10.1007/s40430-018-1318-y
36. Deepak, D., Davim, J.P. "Multi-Response Optimization of Process Parameters in AWJ Machining of Hybrid GFRP Composite by Grey Relational Method", ***Procedia Manufacturing***, Vol. 35, (2019), 1211-1221, doi: 10.1016/j.promfg.2019.07.021

Persian Abstract

**چکیده**

ماشین کاری با تخلیه الکتریکی سیمی (WED) یکی از مناسب ترین تکنیک های ماشین کاری برای ماشین کاری مواد برش سخت مانند تیتانیوم با دقت بالا است. بهینه سازی پارامترهای کنترل برای دستیابی به سطوح مطلوب از ویژگی های عملکرد ماشین کاری بسیار مهم است. با در نظر گرفتن این هدف، این تحقیق به بررسی تاثیر جریان، زمان پالس در زمان (Ton) و زمان خاموش شدن پالس (Toff) بر میزان حذف مواد، زبری سطح و عرض کرف Ti-6Al-4V ماشین‌کاری WED می‌پردازد. نتایج بهینه‌سازی نشان داد که جریان – ۵.۱۹ A، تن – ۲۰ µs، Toff - 30 µs، تنظیمات بهینه برای ماشین‌کاری آلیاژ Ti-6Al-4V با استفاده از الکترود مولیبدن برای بهترین عملکرد ماشین‌کاری است. بر اساس تجزیه و تحلیل گریدهای رابطه خاکستری، ترتیب تأثیر پارامتر کنترل به صورت تن – I، تاف – II و جریان – III رتبه‌بندی می‌شود. اثربخشی رویکرد مبتنی بر GRA از طریق آزمایش‌های تاییدی مورد ارزیابی قرار گرفت که در آن پیش‌بینی‌های نظری خطاهای کمتر از ۳٪ را نشان دادند.

IJE TRANSACTIONS B: Applications Vol. 35, No. 11, (November 2022) 2256-2264

International Journal of Engineering

Journal Homepage: www.ije.ir

# Effect of Serpentine Aggregates on the Shielding, Mechanical, and Durability Properties of Heavyweight Concrete

A. Sayyadi[a], Y. Mohammadi*[b], M. R. Adlparvar[c]

[a] *Department of Civil Engineering, Qeshm Branch, Islamic Azad University, Qeshm, Iran*
[b] *Department of Civil Engineering, University of Mohaghegh Ardabili, Ardabil, Iran*
[c] *Department of Civil Engineering, University of Qom, Qom, Iran*

*ARTICLE*

*Paper history:*
Received: 30 August 2022
Received in revised form 19 September 2022
Accepted 21 September 2022

*Keywords*:
*Heavyweight Concrete*
*Serpentine Aggregates*
*Radiation Shielding Concrete*
*Gamma Rays*
*Mechanical Properties*
*Durability*

*ABSTRACT*

Concrete is a material that can easily absorb nuclear radiation, and in this process, the density of concrete is an essential factor in absorbing the rays. Therefore, due to performance limitations and thickness, heavyweight concrete is used. In this study, serpentine coarse aggregates (SCAg) and serpentine fine aggregates (SFAg) were used as a substitute for sand and gravel in heavyweight concrete containing lead slag to protect against gamma rays. Determination of mechanical properties (compressive strength, tensile strength, and ultrasonic pulse velocity), physical properties (water absorption and electrical resistivity), and shielding properties (shielding against gamma rays) were among the main objectives. The results indicated the positive effect of SFAg and SCAg on the shielding properties of concretes against gamma rays. The replacement of SFAg and SCAg with natural aggregates increased the density of the samples, which resulted in an increase in 3.8 to 42.9% in the linear attenuation coefficient against gamma rays. SFAg has a significant effect on gamma-ray attenuation, especially when these materials are made of high-density minerals, due to their property of reducing the pores in concrete.

***doi***: *10.5829/ije.2022.35.11b.21*

## 1. INTRODUCTION

Concrete is a primary consumable materials in civil engineering structures due to its technical advantages and better performance in terms of environmental and energy issues [1, 2]. On the other hand, today, with an increasing progress in science and technology, an increase in the use of radioactive radiation in various fields is observed. Despite radioactivity's many applications and benefits, protection against this harmful radiation to cells and living tissues is essential and unavoidable [3-5]. Heavyweight concrete has higher specific gravity than concretes made with conventional aggregates and is usually made using heavy aggregates and is specifically used as a shield against radiation. Today, a long period of time has passed since the production of heavyweight concrete. At first, heavyweight concrete was used to increase the safety of special buildings against earthquake. Heavyweight concrete has been used as a nuclear shield with the development of atomic energy and mainly to prevent the emission of deadly rays such as neutrons and gamma that can penetrate objects [6-9]. It is very important to repel or absorb radiation from radiation because it can be harmful to the environment. Concrete absorbs these rays, and in this process, concrete density is an essential factor in absorbing the rays. Therefore, heavyweight concrete is used due to performance limitations and thickness [10, 11]. Many studies have been done in the field of radiation-resistant concretes. Tekin et al. [13] examined the shielding attributes of hematite-serpentine concrete comprising tungsten ($WO_3$) and photocatalytic nanoparticles ($Bi_2O_3$). The results showed that adding nanoparticles to heavyweight concrete improved protective properties, with potential applications in civil engineering constructions and potential use as building materials for

*Corresponding Author Institutional Email: Yaghoubm@uma.ac.ir
(Y. Mohammadi)

Please cite this article as: A. Sayyadi, Y. Mohammadi, M. R. Adlparvar, Effect of Serpentine Aggregates on the Shielding, Mechanical, and Durability Properties of Heavyweight Concrete, ***International Journal of Engineering, Transactions B: Applications***, Vol. 35, No. 11, (2022) 2256-2264

nuclear facilities [13]. Çullu and Bakirhan [14] investigated lead-zinc mine waste rock and heavyweight concrete in the energy range of 662–1460 keV. The results showed that concrete strength affects radiation absorption [14]. Baalamurugan et al. [15] studied the utilization of steel slag from smelting furnaces in concrete as aggregates for protection against gamma rays. The results showed that using 50% slag is effective in gamma protection [15]. Zayed et al. [16] investigated the effect of heavy aggregates of hematite, barite, and serpentine on the shielding attributes of heavyweight concrete. Barite and hematite aggregates of 25 and 50% of the aggregate were used. Serpentine aggregates of 50% by weight were also used. The behavior of the samples was investigated using gamma ray, compressive strength, and fracture tensile tests. Unlike barite, hematite increases the porosity of concrete. Barite and hematite reduce the mechanical strength of concrete. The use of 50% barite showed the highest radiation resistance. It was found that in addition to barite and hematite, serpentine aggregates increase bulk density and decrease mechanical strength. In addition, unlike barite, hematite increases water absorption [16]. Masoud et al. [17] investigated barite and hematite's effects on concrete's shielding. For this purpose, a gamma radiation test was performed on the samples. The combination of barite and hematite has a negative effect on the physical properties of serpentine concretes and improves compaction. On the other hand, this combination improved the damping properties of serpentine base concretes. This improvement was more effective in the use of barite than hematite [17]. Mymrin et al. [18] investigated the use of waste materials from serpentine aggregates and recycled shards of glass to produce ceramics. XRD, XRF, flexural strength and water absorption tests were performed. The flexural strength of ceramics ranged from 2.85 to 56.97 MPa. The water absorption of the samples was 0.28 to 17.61. At the end, it was concluded that the use of serpentine waste and recycled glass fragments, in addition to being useful in the production of building materials can also be environmentally beneficial [18].

Constructing shielding structures against harmful radiation using concrete made with ordinary aggregates costs much more than making concrete with heavyweight aggregates. Structural elements with normal thickness cannot have a proper response against the radiation of the surrounding environment. Structural elements with normal thickness cannot have a proper response against the radiation of the surrounding environment. The design of structural elements with larger thicknesses, along with the addition of lead sheets, multiplies the project's cost. Also, the project's construction time is another important point in reducing construction costs. In the present study, the combination of serpentine aggregates and lead slag was used to construct heavyweight concretes so that all the above-mentioned cases could be solved. With this concrete, an environment-friendly structure can be provided with the possibility of designing structural and non-structural elements for further use.

The aggregates that can improve the density of concrete can play a role in affecting its shielding properties against radiation. Limited research has been conducted on heavyweight concrete containing serpentine aggregates. Access to waste from serpentine aggregates is easy in Iran, and studies have shown that they can be used in heavyweight concrete. In the present study, the use of serpentine aggregates in heavyweight concrete was investigated with the aim of protection against gamma rays. The purpose of making this concrete is to prevent gamma radiation, and its use is intended for structures related to nuclear facilities or wherever possible radioactive radiation. A combination of serpentine coarse aggregates (SCAg) and serpentine fine aggregates (SFAg) were used as a substitute for natural fine and coarse aggregates (sand and gravel).

## 2. EXPERIMENTAL PROCEDURES

The present study was conducted in a laboratory manner. The materials used include cement, natural aggregates, serpentine aggregates, water, and superplasticizer. The aggregates were graded according to ASTM C127 [19] and ASTM C128 [20] (Figure 1). Heavyweight aggregates (serpentine aggregates) were obtained from Zakaria mine in Mashhad city in Iran. A stone crusher crushed heavyweight aggregates. XRF analysis of serpentine aggregates is presented in Table 1. The physical and chemical characteristics of cement are shown in Table 1. The water used to make concrete meets the standards recommended by ASTMD-1129 [21]. The lead slag was prepared from the waste battery recycling center .The density of lead slag is equal to 4.08 g/cm$^3$. The chemical analysis of lead slag is presented in Table 1. The fresh properties were evaluated by slump test according to ASTM C143-78 [22].

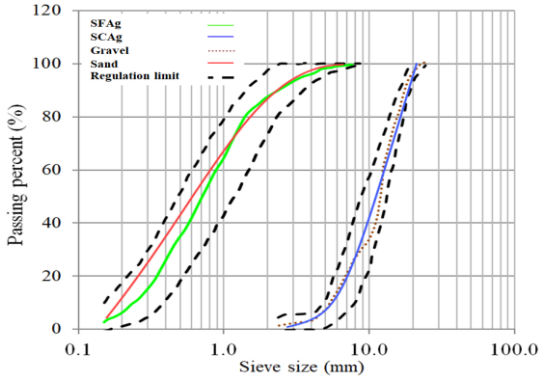


**Figure 1.** The size of the aggregates used in the investigated heavyweight concrete

**TABLE 1.** The chemical attributes of the materials used in the investigated heavyweight concrete

| Components (wt. %) | Cement | Serpentine aggregate | Lead slag |
|---|---|---|---|
| $Al_2O_3$ | 4.95 | 0.79 | 2.1 |
| CaO | 62.95 | 0.27 | 5.1 |
| $SiO_2$ | 21.27 | 41.98 | 11.8 |
| $Fe_2O_3$ | 4.03 | 7.02 | 12.9 |
| MgO | 1.55 | 38.55 | 0 |
| $SO_3$ | 2.26 | 0.03 | 0.05 |
| $K_2O$ | 0.65 | 0.03 | 0.18 |
| $Na_2O$ | 0.49 | 0 | 0.42 |
| $Mn_2O_3$ | - | 0.05 | - |
| $TiO_2$ | - | 0.04 | - |
| $P_2O_5$ | - | 0.03 | - |
| Cl | - | 0.02 | - |
| $Cr_2O_3$ | - | 0.32 | - |
| NiO | - | 0.38 | - |
| $CO_3O_4$ | - | 0.04 | - |
| PbO | - | - | 48.8 |
| LOI | - | 10.45 | 18.65 |
| Specific gravity | 3.15 | 2.79 | 4.08 |

The mechanical attributes of concrete samples were investigated by performing compressive strength, tensile strength, and ultrasonic pulse velocity (UPV) tests (Figure 2). The compressive strength test was performed according to ASTM C39 [23]. This test is one of the most important factors of quality control of concrete and it expresses the tolerance value of the sample in terms of compressive strength. Cube molds with dimensions of 150×150×150 mm were used to make the samples. After concreting, the molds were kept in open air for 24 hours. After this period, the molds were opened and the samples were placed in the water environment and tested. Splitting tensile strength test was performed according to ASTM C496 [24] in order to investigate the tensile strength of the samples. In this experiment, standard cylinders of 150×300 mm were used. The ultrasonic pulse velocity (UPV) was performed according to ASTM C597 [25].

The Durability of concretes was also checked by conducting water absorption [26], and electrical resistivity [27] tests (Figure 3).

A device for measuring the electrical resistivity with a variable frequency of 10 to 10,000 Hz was used. Copper plates were used to attach the two heads of specimen to the device. In order to prevent the copper plates from attaching to the floor and the worktable, 150×150 mm plastic molds were used, and the copper plates were

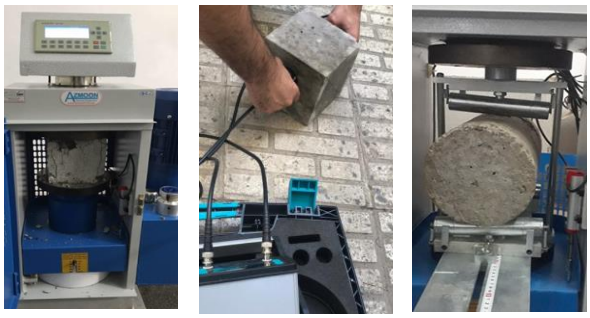

(a) (c) (b)

**Figure 2.** The mechanical attributes tests (a) Compressive strength (b) Splitting tensile strength (c) UPV

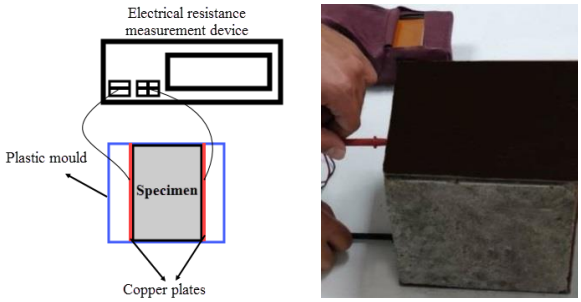


**Figure 3.** Electrical resistivity test

positioned 100 mm apart. Each of the wires of the device was connected to one of the copper plates, the frequency of the device was set at 10 Hz, and the electrical resistivity number was recorded [1, 27]. Estimation of corrosion probability of buried rebars in concrete based on electrical resistivity is presented in Table 2.

The shielding attributes were investigated using gamma-ray attenuation test (Figure 4). Concrete samples with dimensions of 10 cm were exposed to gamma rays for 10 minutes. In this experiment, radiation source, cs137 was used. A cylindrical lead collimator with an external diameter of 12.5 cm and an inner cavity in the form of an incomplete cone with a diameter of the lower base of 3 cm and a diameter of the upper base of 2 cm, and a height of 2 cm was used around the fountain. The concrete sample was placed at a distance of 4 cm from the spring.

**TABLE 2.** Estimation of corrosion probability of buried rebars in concrete based on electrical resistivity [28, 29]

| Electrical resistivity (kΩ-cm) | Estimation of corrosion probability |
|---|---|
| Less than 50 | Very high |
| Between 50 and 100 | High |
| Between 100 and 200 | Low |
| More than 200 | Very low |

**Figure 4.** Gamma-Ray Attenuation

## 3. MIXED DESIGN

Table 3 summarized the mixed design. Serpentine aggregates were placed in water for 24 hours before mixing to saturate. Then, their surface was dried with a cloth, and hot air flow to become saturated with the saturated surface dry (SSD). This action was done due to the water absorption of serpentine aggregates. The pores of the grains do not absorb the mixing water required for water and cement hydration activities, and the concrete does not suffer from dehydration and drying. The amount of river sand water absorption was considered 1.5% by weight. In the mixing stage, aggregates and cement were mixed in a mixer for several minutes. Then the mixing water, which was already mixed with the superplasticizer, was gradually added to the dry materials and mixed for 7 to 10 minutes. The concrete was taken out of the mixer, and after the slump test, they were poured into the desired molds.

## 4. RESULTS AND DISCUSSION

**4. 1. Workability** Figure 5 demonstrates slump of heavyweight concrete samples. The slump recommended range according to ACI 211.1-91 [30] for reinforced foundation walls, footings, plain footings, caissons, substructure walls, pavements, slabs, and mass concrete are in the range of 20 to 80 mm. In addition, the slump recommended range for beams, reinforced walls, and building columns are between 20 to 100 mm. The slump of all specimens is in the range of 59 to 74 mm.

Addition of 25% of SCAg and SFAg increased the slump to a negligible amount. However, adding more than 25% of SCAg and SFAg reduced the slump of heavyweight concrete samples. This decrease in slump can be attributed to the water absorption of serpentine aggregates and their rough surface, which has caused the workability of concrete to decrease.

**TABLE 3.** Mixture design

| Mix code | Cement (kg/m$^3$) | SFAg[a] | SCAg[b] | W/C | Sand | Geavel | LS | SP[d] |
|---|---|---|---|---|---|---|---|---|
| F0C0 | 400 | 0 | 0 | 0.4 | 430 | 275 | 1350 | 3 |
| F0C25 | 400 | 0 | 68.75 | 0.4 | 430 | 230 | 1350 | 3 |
| F0C50 | 400 | 0 | 137.5 | 0.4 | 430 | 185 | 1350 | 3 |
| F0C100 | 400 | 0 | 275 | 0.4 | 430 | 90 | 1350 | 3 |
| F25C0 | 400 | 107.5 | 0 | 0.4 | 360 | 275 | 1350 | 3 |
| F25C25 | 400 | 107.5 | 68.75 | 0.4 | 360 | 230 | 1350 | 3 |
| F25C50 | 400 | 107.5 | 137.5 | 0.4 | 360 | 185 | 1350 | 3 |
| F25C100 | 400 | 107.5 | 275 | 0.4 | 360 | 95 | 1350 | 3 |
| F50C0 | 400 | 215 | 0 | 0.4 | 300 | 275 | 1350 | 3 |
| F50C25 | 400 | 215 | 68.75 | 0.4 | 300 | 220 | 1350 | 3 |
| F50C50 | 400 | 215 | 137.5 | 0.4 | 300 | 180 | 1350 | 3 |
| F50C100 | 400 | 215 | 275 | 0.4 | 300 | 85 | 1350 | 3 |
| F100C0 | 400 | 430 | 0 | 0.4 | 160 | 275 | 1350 | 3 |
| F100C25 | 400 | 430 | 68.75 | 0.4 | 120 | 275 | 1350 | 3 |
| F100C50 | 400 | 430 | 137.5 | 0.4 | 70 | 275 | 1350 | 3 |
| F100C100 | 400 | 684.87 | 402.064 | 0.4 | 0 | 0 | 1350 | 3 |

SFA: Serpentine fine aggregates (SFAg)
SCA: Serpentine coarse aggregates (SCAg)
SP: Superplasticizer
W: Water
C: Cement
LS: Lead slag

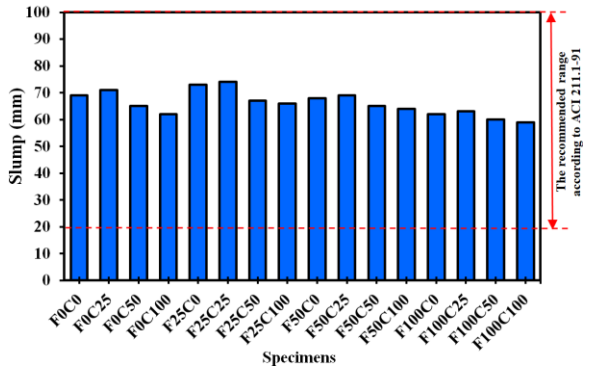


**Figure 5.** Slump results

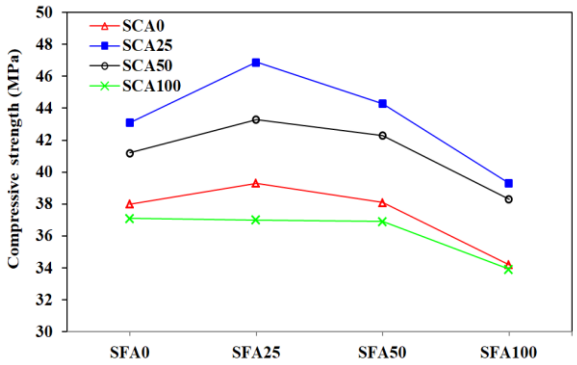


**Figure 7.** Compressive strength

**4. 2. Density** The concrete density depends on mixed design (material ratio, granularity distribution), compaction, porosity, humidity and curing method [31]. In Figure 6, the density of heavyweight concrete samples is presented. By increasing the replacement percentage of SCAg with normal aggregates, the density increases. The density of concrete containing 100% SFAg and 100% SCAg is about 15% higher than the control sample. According to EN 206-1 [32] heavyweight concrete has a density of higher than 2600 kg/m$^3$. The exact amount of this number depends on the weight and type of aggregates, the method of compaction and the aggregates discharge. All the manufactured samples have a density of more than 2600 kg/m$^3$. The use of 25, 50 and 100% SFAg has increased the density of samples by 1, 3 and 6%. In addition, the density of the samples containing 25, 50 and 100% SCAg increased by 1, 2 and 3%, respectively. The combined use of SFAg and SCAg increased the density of the samples by 1-15%.

**4. 3. Compressive Strength** The obtained compressive strengths are the average values of three samples (Figure 7). The compressive strength of samples contained 25% SFAg and 25% SCAg has increased by 23.4%. In fact, the lowest compressive strength corresponds to the sample in which 100% SFAg and 100% SCAg are used. With an increase in serpentine aggregates to more than 25%, the compressive strength of concrete has decreased. According to the observations made, maybe the reason for this decrease in compressive strength is weak hydration of cement paste and insufficient adhesion of cement paste with serpentine aggregates in concrete. The images of samples containing 100% SFAg and 100% SCAg are shown in Figure 8. As can be seen, after breaking the sample, the aggregates were not broken and the crack occurred between the boundaries of the aggregates. Due to the lack of cement around them, the aggregates did not show their performance and showed lower compressive strength.

According to the chemical analysis, about 42% of the chemical structure of serpentine consists of silica. By increasing the amount of serpentine aggregates to more than 25%, the amount of silica in the concrete mixture increases and is more than the released calcium hydroxide. This issue leads to excessive washing of silica and the formation of a weak zone, and a decrease in compressive strength.

**4. 4. Splitting Tensile Strength** Figure 9 shows the tensile strength of the samples. Each of the presented values is an average of the tensile strength of two 30 x 15 cm cylindrical samples. Similar to the compressive strength results, 25% substitution of SFAg and SCAg has

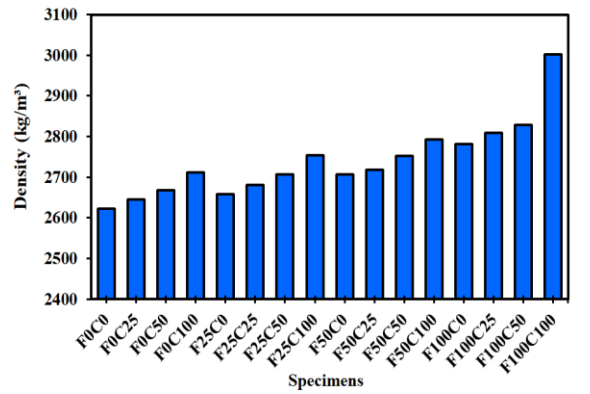


**Figure 6.** Density test results

**Figure 8.** Failure of the F100C100 sample

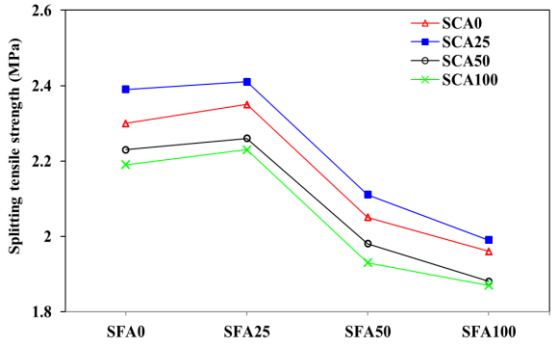


**Figure 9.** Splitting tensile strength

led to a slight increase in the tensile strength of the samples. The tensile strength of F25C0 and F25C25 samples has increased by 2.2% and 4.8%, respectively. In addition, the tensile strength of the F0C25 sample has increased up to 3.9%. In the other samples, addition of serpentine aggregates has reduced the splitting tensile strength. Among the factors that led to a decrease in the strength of heavy concrete samples containing serpentine aggregates, we can mention holes, concrete porosity and lack of hydration of cement, which were observed during the failure of cylindrical concrete samples.

**4. 5. UPV** Figure 10 shows the UPV in different designs. It can be seen that by replacing 25% of SFAg with natural fine aggregates, the UPV increased by 1.5%. In addition, the UPV of F25C0 and F25C25 samples increased by 1.26 and 2%, respectively. The UPV of other samples has decreased, but they are not significantly different from the control sample and have decreased by about 2% compared to the control sample.

Whitehurst [33] has made a proposal for the classification of concrete in terms of quality, and according to that, concrete is divided into 5 categories: excellent, good, questionable, poor and very poor. The UPV of the manufactured samples is in the range of 3500 to 4500 m/s. As long as the UPV values are in "good" and "excellent" categories; it means that the concrete in question does not have cracks or large holes that affect the integrity of the sample structure. Almost all the samples are in the range of good category.

**4. 6. Water Absorption** In Figure 11, the Water absorption percentages of the samples are compared with each other. According to CEB [26], concrete quality is divided into three categories. All samples are in the medium range. The water absorptions of F0C0, F0C25, F0C50 and F0C100 samples were 3.81, 3.95, 4.20 and 4.29%, respectively. Also, the water absorption of F25C0, F25C25, F25C50 and F25C100 samples were 3.61, 3.81, 4 and 4.02% respectively. The water absorptions of F50C0, F50C25, F50C50 and F50C100 samples were 4.1, 4.2 and 4.3% respectively. The water absorptions of F100C0, F100C25, F100C50 and F100C100 samples were 4.6, 4.7, 4.7 and 4.8%, respectively. The lowest water absorption was obtained in the samples in which 25% of SFAg was used. Also, SCAg increased the water absorption.

Adding SFAg up to 25% reduces water absorption. SFAg interrupt the flow channels inside the cement paste matrix and affect the micro cracks in the transition zone between the coarse aggregates and the cement paste, leading to a decrease in water absorption. The use of SCAg increased water absorption in all cases. By increasing the percentage of SCAg in the concrete mix due to an increase in slump and over time with the evaporation of the water in the concrete, holes are created in it, which increases the water absorption in the samples. The highest water absorption is related to the sample with 100% SCAg and 100% SCAg, and the lowest value is related to the concrete sample containing 25% SFAg. SFAg reduces water absorption due to an increase in cement adhesion to the aggregate and the filling of the pores of the aggregate.

**4. 7. Electrical Resistivity** The electrical resistivity is mainly affected by two basic factors of concrete pore structure and can be a suitable index to appraise the resistance of concrete against chloride

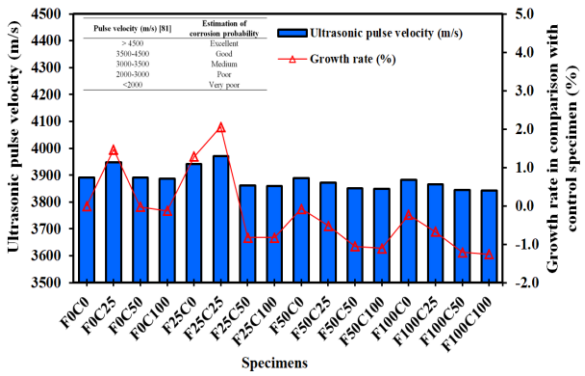


**Figure 10.** UPV

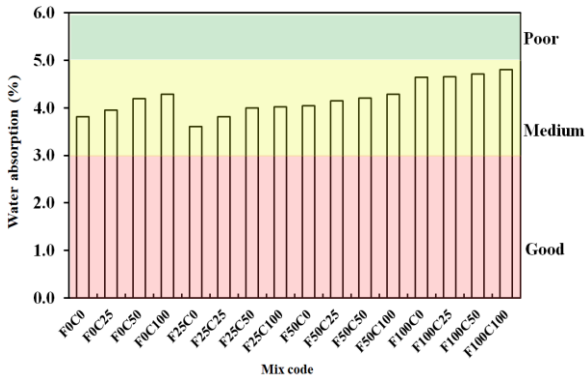


**Figure 11.** Water absorption

penetration. The samples electrical resistivity are presented in Figure 12. By increasing the amount of SFAs up to 25%, the electrical resistivity samples increased; The electrical resistivity of F25C0, F25C25, and F25C50 mixtures compared to the control sample increased by 11.5, 10.3, and 2.6%, respectively.

RILEM RECOMENDAION TC154-EMC [27] divided concrete samples into 4 categories based on electrical resistance and corrosion probability (Table 2). Based on this, all samples have a low probability of corrosion. An increase in electrical resistivity of samples containing 25% SFAs is due to pozzolanic reactions and reduction of pore liquid conductivity of concretes. The use of 25% SFAs increases electrical resistance and reduces corrosion as a result of increasing the durability. This effect can be justified due to the effect of SFAs on the adhesion of SFAs, which causes the creation of denser and fuller concrete, and as the density increases in concrete, the porosity decreases, which means increasing the durability of concrete.

**4. 8. Shielding Properties** The linear attenuation coefficient values of the samples in different states are presented in Figure 13. As it is known, the use of SFAg and SCAg has led to an increase in the linear attenuation coefficient. A higher linear attenuation coefficient means that the concrete is in a more ideal condition and shows a reduction in the output flux of gamma rays, which means more protection against radiation. In the samples where natural coarse aggregates were used, by addition of 25, 50 and 100% SFAg increased the linear attenuation coefficient by 3.8, 4.8 and 7.2%, respectively. In the samples containing 25% of SCAg, by addition of 0, 25, 50 and 100% of SFAg increased the linear attenuation coefficient by 24.9, 25.3, 26.3 and 28.7%, respectively. In the samples containing 50% of SCAg, by addition of 0, 25, 50 and 100% of SFAg increased the linear attenuation coefficient by 35.3, 35.6, 36.6 and 39.1%, respectively. In the samples containing 100% SCAg, by addition of 0, 25, 50 and 100% SFAg increased the linear attenuation coefficient by 39.1, 39.5, 40.5 and 42.9%, respectively. The replacement of SCAg, as seen before,

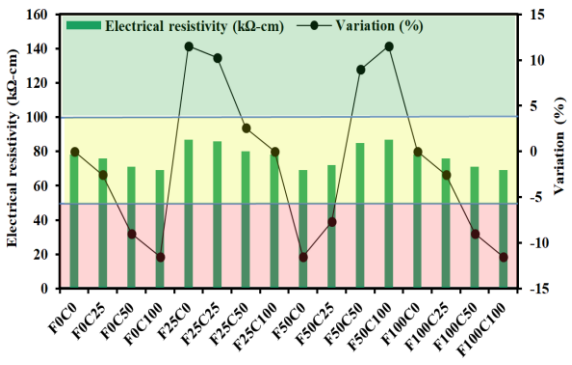


**Figure 12.** Electrical resistivity

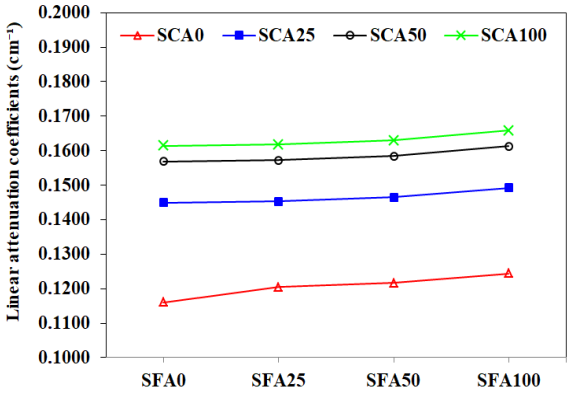


**Figure 13.** Linear attenuation coefficients

has increased the density of the obtained sample, which results in an increase in 3.8 to 42.9 percent of the linear attenuation coefficient against gamma rays. Just as the need for density of heavy concrete used as protection against radiation was mentioned earlier, the results obtained for concrete samples that were made from serpentine aggregates also confirm this. SFAg have a significant effect on gamma ray attenuation, especially when these materials are made from high-density minerals, due to their property of reducing the pores in concrete.

The two factors of reducing the pores and replacing low density materials with heavier materials are responsible for this improvement in the protective properties of concrete. In general, outcomes of the gamma ray test demonstrate, the great impact of pores on the shielding attributes of concrete; because, when these pores are empty, the radiation passes through it without any interaction or disturbance. It can also be concluded from the above that the effect of filling the pores to increase the radiation attenuation coefficient is greater than the presence of heavy elements. Based on the results, 25% SFAg and 25% SCAg can be considered as the optimal amount to improve the protective features against gamma rays. Because the mentioned values, in addition to improve the protective characteristics of heavy concrete, also lead to the improvement of the mechanical characteristics of concrete.

## 4. CONCLUSIONS

Workability, mechanical and shielding properties of heavy concrete containing serpentine aggregates were evaluated. For this purpose, SFAg was used as a partial replacement for sand (0, 25, 50 and 100%) and SCAg was used as a partial substitute for gravel (0, 25, 50 and 100%). Workability of heavy concrete samples was evaluated using slump test. The mechanical properties of the samples were investigated. The shielding properties

of heavy concrete samples were evaluated through gamma ray testing.

- Addition of 25% of SFAg and SCAg increased the slump values of the samples to a negligible amount. But adding more than 25% of SFAg and SCAg reduced the slump of heavy concrete samples. This decrease in slump can be attributed to the water absorption of SFAg and SCAg and their rough surface, which has caused the workability of concrete to decrease.
- The use of 25, 50 and 100% serpentine sand increased the density of the samples by 1, 3 and 6%, respectively. Also, the density of the samples contained 1, 2 and 3% SCAg increased by 8, 12 and 14%, respectively. In addtion, the combined use of SCAg and SFAg has improved the density of the samples by 1-15%.
- The lowest water absorption was obtained in the samples in which 25% of serpentine grains were used. Also, the use of serpentine aggregates in all samples has increased the water absorption.
- The use of large SCAg increased water absorption in all cases. By increasing the percentage of SCAg in the concrete mix due to an increase in slump and with respect to time with the evaporation of the water in the concrete, holes are created in the samples, which increases the water absorption in the samples. The highest water absorption is related to the sample with 100% SCAg and 100% SFAg, and the lowest value is related to the concrete sample containing 25% SFAg. SFAg reduces water absorption due to an increase in cement adhesion to the aggregate and the filling of the pores of the aggregate.
- The use of 25% of SFAs increased the electrical resistivity and reduced corrosion as a result of increasing the durability. This effect can be justified due to the effect of SFAs on the adhesion of slag paste, which caused the creation of denser and fuller concrete, and as the density increased in the concrete, the porosity decreased, which means the durability of concrete increased.
- Serpentine aggregates increased the density of the obtained sample, which results in an increase of 3.8 to 42.9% in the linear attenuation coefficient against gamma rays. SFAg have a significant effect on gamma ray attenuation, especially when these materials are made from high-density minerals, due to their property of reducing the pores in concrete.
- The two factors of reducing pores and replacing low density materials with heavier materials are the reasons for improving the protective properties of concrete. In general, gamma ray test shows the great impact of pores on the protective properties of concrete; because, when these pores are empty, the radiation passes through it without any interaction or disturbance.

## 5. REFERENCES


1. Ghanbari, M., Kohnehpooshi, O., Tohidi, M., "Experimental study of the combined use of fiber and nano silica particles on the properties of lightweight self compacting concrete. ***International Journal of Engineering, Transactions B: Applications***, Vol. 33, No. 8, (2020), 1499-1511. doi: 10.5829/ije.2020.33.08b.08
2. Heidarzad Moghaddam, H., Lotfollahi-Yaghin, M., Maleki, A, "Durability and Mechanical Properties of Self-compacting Concretes with Combined Use of Aluminium Oxide Nanoparticles and Glass Fiber". ***International Journal of Engineering, Transactions A: Basics,*** Vol. 34, No. 1, (2021), 26-38. doi: 10.5829/ije.2021.34.01a.04
3. Papachristoforou, M., & Papayianni, I. "Radiation shielding and mechanical properties of steel fiber reinforced concrete (SFRC) produced with EAF slag aggregates", ***Radiation Physics and Chemistry***, Vol.149, (2018), 26-32. doi: org/10.1016/j.radphyschem.2018.03.010
4. Gökçe, H. S., & Andiç-Çakır, Ö, "Bleeding characteristics of high consistency heavyweight concrete mixtures", ***Construction and Building Materials***, Vol. 194, (2019), 153-160. doi: org/10.1016/j.conbuildmat.2018.11.029
5. Tyagi, G., Singhal, A., Routroy, S., Bhunia, D., & Lahoti, M, "Radiation Shielding Concrete with alternate constituents: An approach to address multiple hazards", ***Journal of Hazardous Materials***, Vol. 404, (2021), 124201. doi: org/10.1016/j.jhazmat.2020.124201
6. Aslani, F., Hamidi, F., Valizadeh, A., & Dang, A. T. N, "High-performance fibre-reinforced heavyweight self-compacting concrete: Analysis of fresh and mechanical properties", ***Construction and Building Materials***, Vol. 232, (2020), 117230. doi: org/10.1016/j.conbuildmat.2019.117230
7. Topcu, İ. B, "Properties of Heavyweight Concrete Produced with Barite" ***Cement & Concrete Research,*** Vol. 33, No. 6, (2003), 815–822. doi: org/10.1016/S0008-8846(02)01063-3
8. Akkurt I, Basyigit C, Akkas A, Kilincarslan S, Gunoglu K, "Photon attenuation coefficients of concrete includes barite in different rate," ***Annals of Nuclear Energy***, Vol. 37, No. 7, (2010), 910-914, doi: org/10.1016/j.anucene.2010.04.001
9. Akkurt I, Basyigit C, Akkas A, Kilincarslan S, Mavi B, Gunoglu K, "Determination of Some Heavyweight Aggregate Half Value Layer Thickness Used for Radiation Shielding,"***Acta Physica Polonica-Series A General Physics"***, Vol. 121, No. 1, 138-140, doi: 10.12693/APhysPolA.121.138.
10. Kharita MH, Yousef S, Al Nassar, M, "The effect of the initial water to cement ratio on shielding properties of ordinary concrete", ***Progress in Nuclear Energy***, Vol. 52, No. 5, (2010), 491-493. doi: org/10.1016/j.pnucene.2009.11.005
11. Jaeger, R. G., Blizard, E. P., Chilton, A. B., Grotenhuis, M., Höning, A., Jaeger, Th. A., Eisenlohr, H. H, "Engineering Compendium on Radiation Shielding", Vol. II. ***Shielding Materials***, Springer, Berlin-Heidelberg, 1975, doi: org/10.1007/978-3-662-25858-3
12. Bashter I.I, "Calculation of radiation attenuation coefficients for shielding concretes," ***Annals of Nuclear Energy***, Vol. 24, No. 17, (1977), 1389-1401. doi: org/10.1016/S0306-4549(97)00003-0
13. Tekin, H. O., Sayyed, M. I. And Issa, S. A., "Gamma radiation shielding properties of the hematite-serpentine concrete blended with $WO_3$ and $Bi_2O_3$ micro and nano particles using MCNPX code", ***Radiation Physics and Chemistry***, Vol. 150, (2018), 95-100. doi: org/10.1016/j.radphyschem.2018.05.002
14. Çullu, M. and Bakırhan, E., "Investigation of radiation absorption coefficients of lead-zinc mine waste rock mixed heavy concrete at 662–1460 keV energy range", ***Construction and Building***

***Materials***, Vol. 173, (2018), 17-27. doi: org/10.1016/j.conbuildmat.2018.03.175

15. Baalamurugan, J., Kumar, V. G., Chandrasekaran, S., Balasundar, S., Venkatraman, B., Padmapriya, R. and Raja, V. B., "Utilization of induction furnace steel slag in concrete as coarse aggregate for gamma radiation shielding", ***Journal of Hazardous Materials***, Vol. 369, (2019), 561-568. doi:org/10.1016/j.jhazmat.2019.02.064
16. Zayed, A. M., Masoud, M. A., Rashad, A. M., El-Khayatt, A. M., Sakr, K., Kansouh, W. A. and Shahien, M. G., "Influence of heavyweight aggregates on the physico-mechanical and radiation attenuation properties of serpentine-based concrete", ***Construction and Building Materials***, Vol. 260, (2020), 120473. doi: org/10.1016/j.conbuildmat.2020.120473
17. Masoud, M. A., Kansouh, W. A., Shahien, M. G., Sakr, K., Rashad, A. M. and Zayed, A. M., "An experimental investigation on the effects of barite/hematite on the radiation shielding properties of serpentine concretes," ***Progress in Nuclear Energy***, Vol. 120, (2020), 103220. doi: org/10.1016/j.pnucene.2019.103220
18. Mymrin, V., Presotto, P., Alekseev, K., Avanci, M.A., Rolim, P.H., Petukhov, V., Taskin, A., Gidarakos, E., Valouma, A. and Yu, G., "Application of hazardous serpentine rocks' extraction wastes in composites with glass waste and clay-sand mix to produce environmentally clean construction materials", ***Construction and Building Materials***, Vol. 234, (2020), 117319. doi: org/10.1016/j.conbuildmat.2019.117319
19. International, ASTM C127-15 Standard Test Method for Relative Density (Specific Gravity) and Absorption of Coarse Aggregate, American Society for Testing and Materials, West Conshohocken, PA, 2016.
20. International, ASTM C128-15, Standard Test Method for Relative Density (Specific Gravity) and Absorption of Fine Aggregate, American Society for Testing and Materials, West Conshohocken, PA, 2016.
21. International, ASTM D1129 Testing and Materials International, American Society for Testing and Materials, West Conshohocken, PA, 2020.
22. International, ASTM C143-78 Standard test method for slump of hydraulic-cement concrete, American Society for Testing and Materials, West Conshohocken, PA, 2017.
23. International, ASTM C39 Standard Test Method for Compressive Strength of Cylindrical Concrete Specimens, American Society for Testing and Materials, West Conshohocken, PA, 2021.
24. International, ASTM C496-96 Standard test method for splitting tensile strength of cylindrical concrete specimens, American Society for Testing and Materials, West Conshohocken, PA, 2017.
25. International, ASTM C597-09 Standard Test Method for Pulse Velocity Through Concrete, American Society for Testing and Materials, West Conshohocken, PA, 2016.
26. CEB-FIP. "Diagnosis and assessment of concrete" structures-state of art report, CEB Bulletin 83. (1989).
27. Elsener, B., Andrade, C., Gulikers, J., Polder, R. and Raupach, M., "Half-cell potential measurements—Potential mapping on reinforced concrete structures", ***Materials and Structures,*** Vol. 36, No. 7, (2003), 461-471. doi: org/10.1007/BF02481526
28. Song, H.W. and Saraswathy, V., "Corrosion monitoring of reinforced concrete structures-a review," ***International Journal of Electrochemical Science***, Vol. 2, (2007), 1-28.
29. Elkey, W., and Sellevold, E.J, "Electrical Resistivity of Concrete", supplement 80, Norwegian Road Research Laboratory, Oslo, Norway, (1995).
30. ACI 211.1-91 (2002). "Standard practice for selecting properties for normal, heavy weight, and mass concrete." American Concrete Institute.
31. Faez, A., Sayari, A. and Manie, S. "Mechanical and rheological properties of self-compacting concrete containing $Al_2O_3$ nanoparticles and silica fume," ***Iranian Journal of Science and Technology, Transactions of Civil Engineering***, Vol. 44, No. 1, (2020), 217-227.
32. TS EN 206−1. Concrete-Part 1: Specification, Performance, Production and Conformity TSE. Ankara: Turkey; 2002.
33. Whitehurst, EA. "Soniscope tests concrete structures", ***In Journal Proceedings***, Vol. 47, No. 2, (1951), 443-444.

## Persian Abstract

**چکیده**

بتن ماده‌ای است که به راحتی می‌تواند تشعشعات هسته‌ای را جذب کند و در این فرآیند، چگالی بتن عاملی ضروری در جذب پرتوها است. بنابراین به دلیل محدودیت عملکرد و ضخامت، از بتن سنگین استفاده می شود. در این مطالعه، سنگدانه های درشت سرپانتین و سنگدانه های ریز سرپانتین به عنوان جایگزینی برای شن و ماسه در بتن سنگین وزن حاوی سرباره سرب برای محافظت در برابر اشعه گاما استفاده شدند. تعیین خواص مکانیکی (مقاومت فشاری، مقاومت کششی و سرعت پالس اولتراسونیک)، خواص فیزیکی (جذب آب و مقاومت الکتریکی) و خواص محافظ (محافظت در برابر پرتوهای گاما) از جمله اهداف اصلی بودند. نتایج حاکی از تأثیر مثبت ریزدانه‌ها و درشت دانه‌های سرپانتینی بر خواص محافظ بتن در برابر اشعه گاما بود. جایگزینی ریزدانه‌ها و درشت دانه‌های سرپانتینی با سنگدانه های طبیعی باعث افزایش چگالی نمونه ها شد که منجر به افزایش ۳.۸ تا ۴۲.۹ درصدی ضریب تضعیف خطی در برابر پرتوهای گاما شد. ریزدانه‌های سرپانتینی به دلیل خاصیت کاهش منافذ در بتن، اثر قابل توجهی بر تضعیف اشعه گاما دارد، به ویژه زمانی که این مواد از مواد معدنی با چگالی بالا ساخته شده باشند.

International Journal of Engineering

Journal Homepage: www.ije.ir

# Bionic Perception Method of Navel Orange Plucking Position Based on Fmincon and PD Angle Control

C. Yu[a,b], K. Liu*[a], L. Lai[b]

[a] *School of Information and Communication, Guilin University of Electronic Technology, Guilin, China*
[b] *School of Information and Communication Engineering, Hezhou University, Hezhou, China*

*PAPER INFO*

*Paper history:*
Received 21 July 2022
Received in revised form 11 August 2022
Accepted 21 August 2022

*Keywords*:
*Dynamic Unstructured Environment*
*Fmincon*
*Proportional Differential Angle Control*
*Bionic Perception*
*Picking Robot*

*ABSTRACT*

In this paper, a bionic perception method of navel orange plucking position based on Fmincon and Proportional Differential (PD) angle control is proposed to solve the problems of wind disturbance and green branches in dynamic unstructured environment. Different from these algorithms that limited to two-dimensional images, this method realizes picking position perception in three-dimensional. Meanwhile, the perception method and the picking robot control algorithm are achieved simultaneously. Firstly, an optimal solution model of the global target rotation angle of the control system based on Fmincon is established to solve the angle optimization problem of robot target approach motion. Secondly, a bionic perception system of plucking position based on PD angle control is constructed to solve specific perception problems. Finally, a joint simulation platform for picking robots based on Solidworks, Adams, and Simulink is given; the validity and accuracy of the algorithm were verified. The experimental results show that the picking accuracy rate is 95%, the angle error of each mechanism and the displacement error are less than 0.5 degrees and 10mm, respectively. The total time from the optimized angle calculation to the system's stability is only about 0.33s. This method is suitable for the rapid perception of plucking position and active angle control of picking robots under dynamic unstructured environment.

***doi**: 10.5829/ije.2021.35.11b.22*

## 1. INTRODUCTION

The rapid developement regarding the automation and artificial intelligence have been strongly pushing the robots to develop technology on agricultural sectors [1-3]. Agricultural robots, as the potential technology to develop intelligent agriculture, take great attention by governments and agricultural sectors [4-6].

The vision system of traditional fruit picking robots are generally based on color space Retinex, Harris and improved Chan-Vese [7-9]. Yu et al. [10] proposed a new strawberry picking robot based on rotating YOLO fruit attitude estimator. Furthermore, for the plucking position of a fruit picking robot, a visual positioning method was proposed by Lei and Lu [11]. Besides, attention model [12], Artificial Neural Network [13,14], Kalman Filter [14],Genetic Algorithm [15], Ant Colony Algorithm [16,17], R-CNN [18], GAN model [19], Greedy Algorithm [20], Synovium Control [21], Deep Learning [22, 23] and Lightweight deep learning methods [24,25] are also used in object perception and control.

However, higher hardware configuration requirements caused by the deep learning are unfriendly to processors with limited performance. Moreover, most algorithms have incomplete detection for low-pixel images under occlusion and different lighting conditions, make it unsuitable for plucking position perception with smaller targets and more precise requirements.

Simultaneously, limited by the computation-intensive, the traditional matching algorithm is not suitable for the plucking position's real-time perception. The shortage of the research on intersection of visual perception and control methods makes it clearly demarcated. The bottleneck problems (for example, the

*Corresponding Author Institutional Email: liukaidiligent@gmail.com (Kai liu)

Please cite this article as: C. Yu, K. Liu, L. Lai, Bionic Perception Method of Navel Orange Plucking Position Based on Fmincon and PD Angle Control, ***International Journal of Engineering, Transactions B: Applications***, Vol. 35, No. 11, (2022) 2265-2274

inaccuracy and instability of visual space perception and autonomous picking control of the target) still exist in the low-cost fruit picking robot under the dynamic unstructured environment [26], especially the automatic control and planning in dynamic environments [27].

In this paper, to solve the problems of precise perception of plucking position, a bionic perception method of navel orange plucking position based on Fmincon and PD angle control is proposed. Based on mathematical analysis, combined with the inherent characteristics of crops and rotation angle signal control, the automatic picking operation simulating human picking behavior and the bionic perception method of fruit picking position are established. Meanwhile, a cross-research of the control and perception is also tested in this study. Compared with the perception method based on the target's visual features. This approach can effectively enhance the perception initiative of the picking robot.

The rest of this paper is organized as follows: In section 2, a three-dimensional simulation model and its mathematical model of picking robot are built. In section 3, Fmincon is used to optimize the robot mathematical model's rotation angle. A picking position's bionic perception method based on PD angle control is designed. And in section 4, the experimental results are analyzed. Finally, some concluding remarks are shown in section 5.

## 2. RELATED WORKS

**2. 1. Picking Robot Model** Solidworks/Adams 3D Simulation Model. According to the requirements of navel orange fruit picking, a 3D simulation model based on Solidworks/Adams picking arm is designed, as shown in Figure 1.

The model is composed of six parts, which includes the Base, the Rotating Shaft (RS), marked as mechanism 1, the Big Arm (BA), marked as mechanism 2, the Small Arm (SA), marked as mechanism 3, the Wrist Arm (WA) and the Picking Effector (PE). The Wrist Arm and Picking Effector are called End-Effector (EE), marked as mechanism 4, to simplify the analysis. The Picking Effector is composed of Clamped Rod (CR) and two hemispheres of Picking Ball (PB) with a Gap for the mutual bite. The Internal Diameter is represented as IND, while the External Diameter is represented as END.

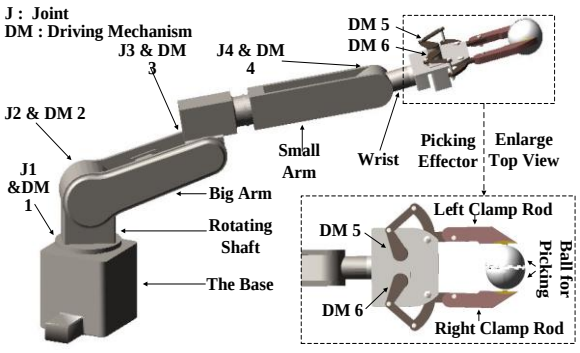


**Figure 1.** Deposition efficiency on a single square in channel

The corresponding drive is added to each joint ( $J_i$ ) as the robot's input variable, which is used to control the rotation of each mechanism around the joint in the system model.

The spatial position information of robot's ADAMS model is obtained and provided for the motion solution. Constraints and drivers are added to the imported virtual simulation model to realize the picking robot's kinematics and dynamics simulation.

**2. 2. Mathematical Model** Developing a "mathematical model" is an important step in robot design and analysis [28]. To further analyze and solve the relative motion and angle relation of each mechanism component, a mathematical analysis model is established based on the three-dimensional simulation $Robot = f\left(x_i, y_i, z_i\right), i = 1,2,3,4$ . The target measurement point's initial coordinates are expressed as $m_{ini}\left(x_{ini}, y_{ini}, z_{ini}\right)$ , and the target coordinate is $m_{obj}\left(x_{obj}, y_{obj}, z_{obj}\right)$ . In this paper's experiment, the spatial coordinate information of the measuring points at the end is output by the three-dimensional simulation software ADAMS.

In order to reduce the complexity and computation, a three-dimensional model is transformed into the two-dimensional mathematical model. There are two different states of the robot as a whole: the thin solid line(—) is used to express the initial state, and the short horizontal line(— • — • ) is used to express the target state. Two state curves in *xyz* coordinate are projected onto the *xz* plane to obtain two projected coordinate systems *x'y* and *x''y*. A three-dimensional mathematical model of the picking robot is shown in Figure 2.

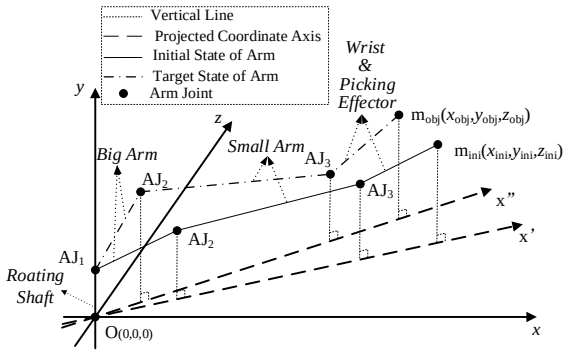


**Figure 2.** Three Dimensional Mathematical Model of Picking Robot

In the robot's mathematical analysis, the included angle between the two mechanisms is taken as the input variable of the control system. The control system's input is related only to the angle, not to the *xyz* axis coordinates in the original spatial position information. A two-dimensional simplified mathematical model $Robot = g(w_i, y_i)$ is proposed based on the robot's three-dimensional mathematical model and its projection model to simplify the analysis. The simplified model's coordinate axes are *w* and *y*, respectively, where the *w*-axis is the picking robot's projection axis in any state in space, as shown in Figure 3. Where, $l_i$ is the length value of mechanism *i*, $m_{ini}(w_{ini}, y_{ini})$ is the initial coordinate of the end measuring point, $m_{obj}(w_{obj}, y_{obj})$ is the target coordinate, $\theta_{i(i-1)\_ini}$ is the initially included angle between mechanism *i* and the connection mechanism, that is, the included angle between each mechanism of the robot in the case of unloaded drive, $\theta_{i(i-1)\_obj}$ is the target included angle between mechanism *i* and the connection mechanism. The included angle between the rotating shaft axis and the ground is a constant 90, that is, $\theta_{10\_obj}=\theta_{10\_ini}=90^{\circ}$.

A mathematical model is built according to Figure 1 to solve the picking robot's end-effector's operation control problem, as shown in Figure 4. The coordinate information of the left and right endpoints is used as the control system's input state variable. $L_{CR}$ is assumed as the length of the left and right clamp rods of the end-effector, and the left and right clamp rods are driven by Drive five and Drive six to carry out picking movement, respectively. $L_{DM}$ and $l_{CR}$ are assumed as the distance between Drive five and Drive six and the clamp rod's length projected on the line of endpoints, respectively. Furthermore, $\theta_{PA}$ is assumed as the included angle between the clamp rod and its perpendicular. $\theta_{PA}$ is assumed as the input of the real-time state variable of the control system, which initial included value is 1.11472°. It is varied when the picking task is operating.

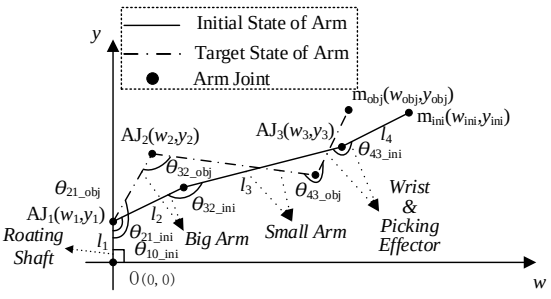


**Figure 3.** A Two-Dimensional Simplified Mathematical Model of a Picking Robot

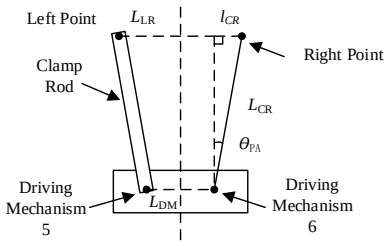


**Figure 4.** Two Dimensional Mathematical Model of Robot End-Effector

Equation (1) shows the included angle $\theta_{PA}$ between the robot end-effector's clamp rod and its perpendicular.

$$\theta_{PA}=arcsin\frac{l_{CR}}{L_{CR}} \tag{1}$$

The length value projected by the clamp rod on the endpoint line is shown in Equation (2).

$$l_{CR}=(L_{LR}-L_{DM})/2 \tag{2}$$

where, $L_{LR}$ is the distance between the left and right endpoints $L(x_L, y_L, z_L)$ and $R(x_R, y_R, z_R)$ of the clamp rod, as shown in Equation (3).

$$\begin{cases} L_{LR}=\left(\sum_{h=x}^{z}(h_L-h_R)^2\right)^{1/2} \\ h=(x,y,z) \end{cases} \tag{3}$$

## 3. PROPOSED METHOD

**3. 1. The Optimal Solution Method of Robot Mechanism's Rotation Angle Based on Fmincon Method** In this section, the nonlinear optimization equation of the robot's angle control is established according to the picking robot's established mathematical model. The robot's nonlinear equation inclued absolute values, sines and coines, inequalities, and equality constraints. A global optimal rotation angle $\Delta\theta_{i(i-1)}$ solution method based on Fmincon is designed to solve nonlinear constrained equations. The Fmincon is provided by the MATLAB optimization system toolbox.

$\Delta\theta_{i(i-1)}$ is assumed as the difference between the initial included angle $\theta_{i(i-1)\_ini}$ and the target included angle $\theta_{i(i-1)\_obj}$ of each mechanism, which can be solved by Equation (4).

$$\begin{cases} \Delta\theta_{i(i-1)}=\theta_{i(i-1)\_obj}-\theta_{i(i-1)\_ini} \\ i=1,2,3,4 \end{cases} \tag{4}$$

Set $\rho_{ij}(l_i, \theta_{ij\_obj})$ and $\theta_{ij\_obj}$ as the polar coordinates of mechanism *i* relative to mechanism *j* and the included

angle between mechanism $i$ and mechanism $j$, where $j$=0,1,2,3 and $j<i$, and mechanism $j$=0 represents the $w$-axis of the ground, in other words, $\theta_{i0\_obj}$ represents the polar coordinate included angle of mechanism $i$ relative to ground $w$-axis, formulated as Equation (5).

$$\begin{cases} \theta_{ij\_obj}=\left(\theta_{i(i-1)\_ini}+\Delta\theta_{i(i-1)}\right)-\sum_{k=j}^{i-j-1}\left(180^{\circ}-\left(\theta_{(k+1)k\_ini}+\Delta\theta_{(k+1)k}\right)\right) \\ 0\le j\le i-2 \end{cases} \tag{5}$$

$$\begin{aligned} min\quad & \left|\Delta\theta_{21}\right|+\left|\Delta\theta_{32}\right|+\left|\Delta\theta_{43}\right| \\ s.t.\quad & \begin{cases} \sum_{i=1}^{4}\left(\theta_{i(i-1)\_ini}+\Delta\theta_{i(i-1)}\right)+\theta_{end}+90^{\circ}=(6-2)*180^{\circ} \\ \sum_{i=1}^{4}l_i\,sin\left(\theta_{i0\_obj}\right)=y_{obj} \\ \sum_{i=1}^{4}l_i\,cos\left(\theta_{i0\_obj}\right)=w_{obj} \\ \Delta\theta_{10}=0^{\circ} \\ 45^{\circ}\le\theta_{end}\le 90^{\circ} \\ max\left\{-120^{\circ},-\left(\theta_{i(i-1)\_ini}+\Delta\theta_{i(i-1)}\right)\right\}\le\Delta\theta_{i(i-1)}\le min\left\{120^{\circ},360^{\circ}-\left(\theta_{i(i-1)\_ini}+\Delta\theta_{i(i-1)}\right)\right\} \\ i=1,2,3,4 \end{cases} \end{aligned} \tag{6}$$

The intention of objective function is to ensure each drive's minimum power consumption, namely the minimum sum of rotation angles. The constraint function is determined in polar coordinates to solve the projection distance between the $w$-axis and $y$-axis. The included angle $\theta_{end}$ between the end-effector and the $y$-axis is designed to ensure that the end-effector position conforms to the bionics and picking requirements during the picking.

Three parts are included in the optimization equation's constraint conditions: the global angle constraint, the coordinate axis projection distance constraint, and the permissible range constraint of the rotation angle of each mechanism. Among them, the purpose of the angle constraint in the global range and the distance projected by the coordinate axis is to ensure that the robot picking actuator accurately reaches the target position. In contrast, the range of rotation angle variation is designed to prevent the collision of various mechanisms in the process of moving. According to the robot's movement characteristics, the maximum bidirectional reference angle of rotation of the joint mechanism is taken to be 120 degrees to prevent the system from being out of balance due to too large angle change. The rotation angle is positive counterclockwise.

$\Delta\theta_{Roating\_x}$ is assumed as the rotating shaft's rotation angle concerning the $x$-axis in the three-dimensional model $Robot=f\left(x_i,y_i,z_i\right)$, formulated as Equation (7), where the target coordinate of the end measurement point is named as $m_{obj}\left(x_{obj},y_{obj},z_{obj}\right)$.

The optimization equation of rotation angle $\Delta\theta_{i(i-1)}$ of the robot mechanism based on the mathematical model is designed, formulated as Equation (6).

$$\Delta\theta_{Roating\_x}=arctan\frac{z_{obj}}{x_{obj}}-arctan\frac{z_{ini}}{x_{ini}} \tag{7}$$

With the nonlinear optimal angle objective Equation (5) to (7), the ideal rotation angle $\Delta\theta_{i(i-1)}$ is output to the Simulink control system, and the running time $t$ is recorded.

**3. 2. Bionic Perception Method Based on PD Angle Control** In this section, a real-time feedback control system of PD based on MATLAB/Simulink is designed to control a picking robot's picking operation in a dynamic unstructured environment. The two parts of the system form a closed loop based on Simulink and Adams, in which the 3D module outputs the displacement and included angle values of each mechanism and measurement points as the variable input of the control module. The rotation angle modulated by each picking robot mechanism is used as the output of PD angle control system. The closed-loop control method of picking system of picking robot is shown in Figure 5. The rotation angle $\Delta\theta_{i(i-1)}$ of the robot mechanism is used as the control system's initial input and continues the whole control process. The control algorithm of the intelligent picking system based on PD angle control is shown in ALGORITHM 1. where $k$ is the sequence number of complete closed-loop output formed by the control system.

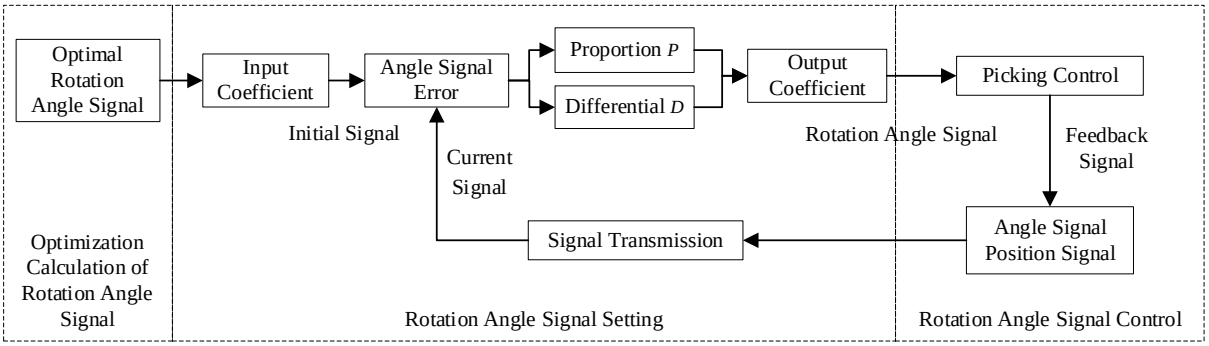


**Figure 5.** Deposition efficiency on a single square in channel

**ALGORITHM 1.** PD Control of Angle

1: Algorithm Start

2: Calculate the rotation angle value $\Delta\theta_{i(i-1)}$ of each mechanism.

3: The input coefficient $K_{in}=\frac{1}{0.2857}$ is introduced, the rotation angle is going to be $\Delta\theta_{i(i-1)}{}' = K_{in}\times\Delta\theta_{i(i-1)}$;

4: Calculate the difference $e(k)$ between $\Delta\theta_{i(i-1)}{}'$ and the rotation angle $\Delta\theta_{i(i-1)now}$ in the current state of the system, $e(k)=\Delta\theta_{i(i-1)}{}'-\Delta\theta_{i(i-1)now}$;

5: Calculate the rate of change of per unit sampling time $ec(k)=\frac{de}{dt}$ ;

6: PD Parameters: The empirical method is used to set the coefficient of proportion $K_p=2$ and differential $K_d=-0.01$ ;

7: PD Output : $u(k)=K_p e(k)+K_d ec(k)$ ;

8: The output coefficient $K_{out}$=0.2 is introduced, the rotation angle is going to be $\Delta\theta_{i(i-1)}{}''=K_{out}\times u(k)$;

9: Enter $\Delta\theta_{i(i-1)}{}''$ into the robot model, and get the current position $m_{now}(x_{now},y_{now},z_{now})$ and the current angle $\theta_{i(i-1)now}$.

10: According to $m_{now}(x_{now},y_{now},z_{now})$ and current angle $\theta_{i(i-1)now}$ of each mechanism, the rotation angle $\Delta\theta_{i(i-1)now}=\theta_{i(i-1)now}-\theta_{i(i-1)\_ini}$ is calculated.

11: Clamping Rod Operation: When time t=0.1s, the end-effector's clamp rods rotation makes the picking ball close, where, the rotation angle is $\theta_{PA}$=9.2° .

12: Bionic Perception: When time t=0.15s, the rotation angle $\Delta\theta'_{43}=\Delta\theta_{43}-5$ of the system's end-effector will automatically change, that is, rotate clockwise 5° to realize the bionic perception operation.

13: Feedback Control: Go back to Step 4 and calculate the angle error e and angle value until stable;

14: Algorithm End

The control system in a dynamic unstructured environment eliminates the robot mechanism rotation angle's motion error to ensure the accuracy and robustness in picking control. In this paper, an optimized PD angle control method is proposed based on the input and output auxiliary coefficients $K_{in}$ and $K_{out}$. Set $K_p$ and $K_d$ as the proportional and differential coefficients of the PD angle control system, respectively. Wherein, the coefficient $K_p$ and $K_d$ of proportion and differentiation in the PD angle control method are determined by the empirical method. In the picking experiment of the picking robot, the picking control system is in the most stable state when $K_p$ and $K_d$ take the above values, which is the basis for the fruit picking experiment's successful realisation. Moreover, set $m_{now}(x_{now},y_{now},z_{now})$ , $\theta_{i(i-1)now}$ and $\Delta\theta_{i(i-1)now}$ as the current coordinate of the end measuring point, the included angle, and each mechanism's rotation angle under the current system state, respectively. $\Delta\theta_{i(i-1)now}$, as shown in Equation (8).

$$\Delta\theta_{i(i-1)now}=\theta_{i(i-1)now}-\theta_{i(i-1)\_ini} \tag{8}$$

**3. 3. Bion Bionic Perception Method of Plucking Position Based on Control** Precise perception of the plucking position is essential for the success or failure of fruit picking without damage. The current algorithm has a relatively mature visual perception of navel orange and other fruits. However, few spatial perception methods for fruit plucking position in the dynamic unstructured environment, and these methods are less effective.

A bionic perception method of plucking position based on PD angle control to solve the above problems. The left and right clamp rods of the end-effector are opened, and the navel orange is included in the picking ball when the robot end-effector reaches the navel orange. Moreover, the navel orange leaves and branches

can protrude through the gaps between the picking balls. And then, the end-effector rotates clockwise for $\theta_w$ with the navel orange. Normal-growths navel oranges will cling to the picking ball's inner surface due to the bionics and plant branches' inherent properties. Moreover, we set the contact point as the picking point, as shown in Figure 6.

Navel oranges, for example, the Fuchuan navel orange we collected at the agricultural base of Guangxi Zhengfeng Group, are about 70-85*mm* in diameter, 250-300*g* in mass, and 3-5*mm* in diameter of terminal branches. Based on the design principles of the navel orange plant's tensile strength and the quality range of navel orange fruit, the rotation angle $\theta_w = -5^\circ$ is designed to prevent excessive angle or operation amplitude. Set $d_w$ as the displacement of navel orange in the end-effector, formulated as Equation (9). The elastic modulus, bending strength, breaking modulus and ultimate stress of navel orange branches are 8.5 *GPa*, 193.2 *MPa*, 67.3 *MPa* and 45.3 *MPa*, respectively.

$$d_w = 2 \times l_4 \times sin\left(\frac{|\theta_w|}{2}\right) \tag{9}$$

According to Equation (9), the displacement $d_w$ at the end measuring point is 6.2*mm*, which conforms to the picking process's bionics practice.

Compared with the perception method based on visual features, our method has more robust initiative, which can reduce the multiple losses of time and economy caused by the inaccurate perception of plucking position.

## 4. EXPERIMENTS AND RESULTS

**4. 1. Experimental Platform** The experimental platform is a 64-bit Windows 10 system equipped with Intel Core I7-6700 processor. MATLAB 2018B and Adams 2018 are used to construct the simulation system, and Solidworks 2012 is used to build the corresponding 3D model. A joint simulations is created with MATLAB/ Simulink and Adams Control, Communication Interval of MATLAB/Simulink control system is set to 5*ms*.

**4. 2. Results** In this section, the end-effector (marked as mechanism 4) of picking robot is taken as a concrete object for quantitative analysis to verify the proposed perception and control algorithm. We randomly select the target coordinates (377.862, 703.386, -1541.232), and the target rotation angle $\Delta\theta_{43}$ based on Fmincon method is 13.87760°. And the angle change and response speed for the algorithm are tracked. The analysis diagram of rotation angle $\Delta\theta_{43now}$, current angle $\theta_{43now}$, the coordinate of the end measuring point and the angle error *e* of the end-effector are shown in Figures 7, 8, 9 and 10, respectively.

Figures 7 and 8 show that the angle control system based on the algorithm can achieve system stability within 0.06*s* during the prophase perception and the bionic perception. The end measuring point on the end-effector reaches the target position quickly at the same time. The analysis of Figure 9 shows that the end-effector finally tends to set the target point and remains stable. At the beginning of the bionic perception operation, the end-effector change's angle and coordinates correspondingly, but there is only a small disturbance for the overall operation, which has little influence. According to the analysis of Figure 10, the difference in angle and displacement between the initial state of the robot and the target state is large, resulting in a large error from the initial state to the first working moment of the system. The error's variation value is relatively drastic, but eventually, all tend to zero and maintain a stable state.

A global analysis result for the robot is presented here. When the system randomly selects any coordinate

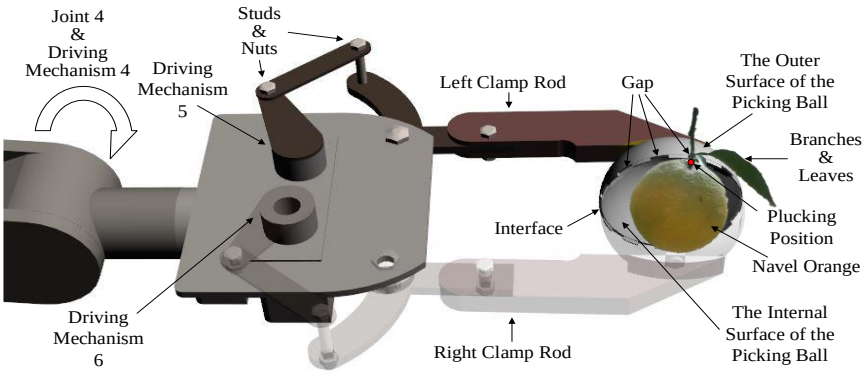


**Figure 6.** Bionic Perception Diagram of Plucking Position Based on System Control

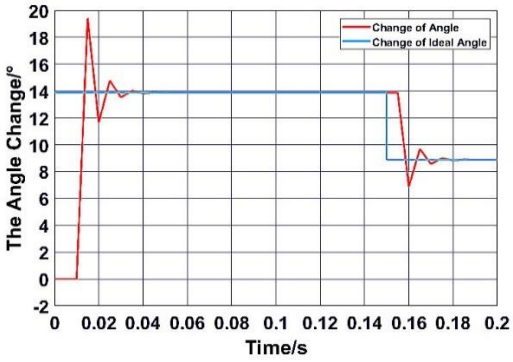


**Figure 7.** Rotation Angle $\Delta\theta_{43now}$ Tracking Diagram of End-Effector

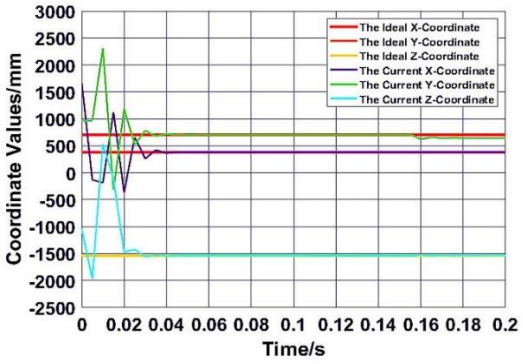


**Figure 9.** Coordinate Displacement Tracking Diagram of End Measuring Point


**Figure 8.** Current Angle $\theta_{43now}$ Tracking Diagram of End-Effector

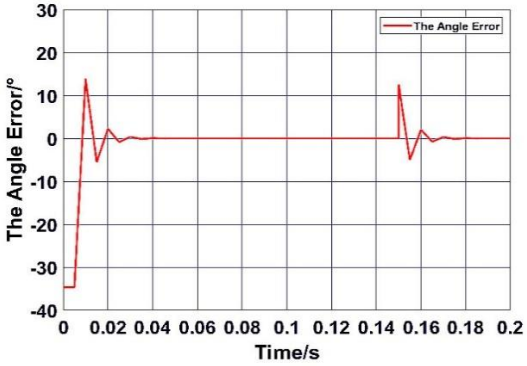


**Figure 10.** Analysis Diagram of Rotation Angle Error *e* of End-Effector

point, the average consumption time of calculating the rotation angle based on Fmincon method is 0.21021*s*. And when the system is stabilization, the rotation angle error *e* and its standard deviation SD of each mechanism are shown in Table 1. Where, PP and BP represent End-Effector in the prophase perception stage and the bionic perception stage, respectively.

As shown in Table 1, each mechanism of the picking robot's rotation angle error is $10^{-3}$ level. Since the picking robot base bears most of the mass of the mechanism, the rotation angle error of the shaft is large, which is about 0.2°. And the standard deviation of each picking robot mechanism's rotation angle is generally 0.0004-0.0013, and the maximum standard deviation appears at the

**TABLE 1.** Rotation angle error of picking robot

| No. | Error *e*/° | | | | | SD | | | | |
|---|---|---|---|---|---|---|---|---|---|---|
| | RS | BA | SA | End-Effector | | RS | BA | SA | EE | |
| | | | | PP | BP | | | | PP | BP |
| 1 | -0.21754 | 0.00220 | -0.00330 | 0.00000 | -0.00025 | | | | | |
| 2 | -0.21220 | 0.00310 | -0.00470 | 0.00070 | 0.00040 | | | | | |
| 3 | -0.16180 | 0.00080 | -0.00150 | 0.00000 | -0.00025 | 0.0932204 | 0.0007121 | 0.0013467 | 0.0006198 | 0.0004836 |
| 4 | -0.12807 | 0.00110 | -0.00310 | 0.00120 | 0.00090 | | | | | |
| 5 | -0.15860 | 0.00170 | -0.00340 | 0.00100 | 0.00060 | | | | | |
| Average | 0.17579 | 0.00144 | 0.00238 | 0.00077 | 0.00069 | | | - | | |

rotation axis RS and does not exceed 0.1. And the displacement error *ed* of the end measuring point and its standard deviation SD is shown in Table 2.

As shown in Table 2, the absolute value of displacement error *ed* of each mechanism relative to the target point of the picking robot is within the range of 0.1*mm*-5*mm*, and the mean displacement error values in *x*, *y* and *z*-axis directions are 1.52819*mm*, 4.50943*mm* and 3.15513*mm* respectively. Moreover, the standard deviations are 1.2165539, 0.681218 and 1.6084507, respectively. The mean displacement error of the straight-line distance between the measuring point at the end of the end-effector and the target point is 6.00608*mm*, and the standard deviation is 1.0408286. The system still has good accuracy in controlling the whole robot.

The accuracy evaluation index of robot picking is proposed to verify the performance of PD angle control and bionic perception method in dynamic unstructured environment: Set $d_e$ as the spatial distance between the coordinates $m_{now}(x_{now}, y_{now}, z_{now})$ of the end measuring point end-effector and the target coordinates $m_{obj}(x_{obj}, y_{obj}, z_{obj})$ in the prophase perception. And $d_{emax}$ is the maximum error. It is the successful picking when $d_e$ is less than the maximum error $d_{emax}$. We designed $d_{emax}$ to be 10 *mm* because of the dynamic unstructured environment's interference and the biophysical and inclusive nature of the picking ball.

$T_X$ is the number of experiments when $d_e$ is less than $d_{emax}$;while $T_D$ is the number of experiments when $d_e$ is greater than $d_{emax}$. In this paper, the picking perception accuracy (*P*) of the robot under different rotation angles is calculated, as shown in Equation (10).

$$P = \frac{T_X}{T_X + T_D} \times 100\% \tag{10}$$

The algorithm proposed in this paper has been tested many times under the condition of setting coordinates at will. According to Equation (9), the picking perception accuracy rate is 95%, which has a good picking effect. Comparison tests are conducted on the algorithms, and the results of different algorithms are shown in Table 3. Given the impact of the implementation methods and evaluation indexes of different algorithms on the experiment, this paper adopts the final picking accuracy *P* as the basic principle of comparison. Other methods compared to the Zhuang's method, the percentage of picking accuracy improved is marked by γ, and the percentage of time reduced is marked by λ other method's.

It can be seen from Table 3 that the plucking position perception method of the picking robot in this paper has better picking accuracy and faster perception time compared with other methods with similar functions. Different from these algorithms that limited to two-dimensional images, this method realizes picking

**TABLE 2.** Displacement error of picking robot

| No. | Error *ed*/mm | | | | SD | | | |
|---|---|---|---|---|---|---|---|---|
| | x | y | z | Sum | x | y | z | Sum |
| 1 | 1.66000 | 4.30000 | 4.10700 | 6.17358 | | | | |
| 2 | 0.83300 | 3.94700 | 2.63800 | 4.81993 | | | | |
| 3 | 0.70010 | 4.93020 | 3.64820 | 6.17304 | 1.2165539 | 0.681218 | 1.6084507 | 1.0408286 |
| 4 | -0.46900 | 4.80480 | 2.48600 | 5.43013 | | | | |
| 5 | 0.09200 | 4.63700 | 2.97900 | 5.51223 | | | | |
| Average | 1.52819 | 4.50943 | 3.15513 | 6.00608 | | | - | |

**TABLE 3.** Picking perception accuracy under different methods

| Algorithm | Method | Picking Point Dimension | *P*/% | γ/% | Time/*s* | λ/% |
|---|---|---|---|---|---|---|
| Zhuang et al. [8] | Computer Vision-based Localisation | 2D Image | 83.0 | - | 1.06 | - |
| Xiong et al. [7] | Morphological+Min-Circumscribed Rectangle+ Hough | 2D Image | 86.3 | 3.98 | 0.46 | 37.5 |
| Lei et al. [11] | Color Modol+Corner Detection+K-means | 2D Image | 89.2 | 7.47 | 0.65 | 38.68 |
| Yu et al. [10] | R-YOLO | 2D Image | 84.35 | 1.63 | 0.056 | 94.71 |
| Algorithm in this paper | Fmincon+PD Angle Control | 3D Dimensions | 95.0 | 14.46 | 0.33 | 68.88 |

position perception in three-dimensional. Meanwhile, the perception method and the picking robot control algorithm are achieved simultaneously. In addition, the bionic perception algorithm based on PD angle control in this paper realizes the plucking position perception and the picking behavior at the same time, which further saves time for the operation of the picking robot.

## 5. CONCLUSION

In this paper, a bionic perception method based on Fmincon and PD angle control is proposed to solve the problem of poor perception accuracy of navel orange and its plucking position in the agricultural dynamic unstructured environment.

Firstly, Fmincon method is used to optimize the value of target rotation angle based on three-dimensional simulation model in dynamic unstructured environment. Then, the picking control based on the optimized PD algorithm is carried out according to the target rotation angle. Finally, a bionic perception method based on system control is designed for the spatial perception of plucking position, and the validity and accuracy of the algorithm are verified by experiments.

The experimental results show that the picking accuracy of the bionic perception algorithm based on Fmincon method and optimized PD angle control is 95% and the time is 0.33*s*, which can effectively solve the environmental interference of low-cost picking robot in a dynamic unstructured environment and the problem of low navel orange perception accuracy. Different from other algorithms, perception method and picking robot control are achieved simultaneously. The method is simple, does not need expensive equipment, and is easier to use in developing countries and regions.

However, compared with the faster processing speed, this paper's real-time processing needs to be further improved. Higher real-time performance and its testing in the entity will focus on this paper in the future. With the increasing concern of food security and the rapid development of artificial intelligence, it is hoped that the research in this paper can contribute to the development of fast, efficient, accurate and low-cost picking robots.

## 6. ACKNOWLEDGMENT

This work is financially supported by the Dean Project of Guangxi Key Laboratory of Wireless Wideband Communication and Signal Processing (20171016), the Key Cultivation Project of Hezhou University (2019ZDPY02), the Natural Science Funding Project of Hezhou University (2019ZZZK01), the National Natural Science Foundation of China (6154055, 61863011), and the Science Research and Technology Development Program of Hezhou (No. 1707041).

## 7. REFERENCES

1. Klerkx, L., Jakku, E., and Labarthe, P. "A review of social science on digital agriculture, smart farming and agriculture 4.0: New contributions and a future research agenda", ***NJAS-Wageningen Journal of Life Sciences***, Vol. 2019, No. 90, (2019), 100315. doi: 10.1016/j.njas.2019.100315.
2. Vasconez, J. P., Kantor, G. A., and Cheein, F. A., A. "Human–robot interaction in agriculture: A survey and current challenges." ***Biosystems Engineering***, Vol. 2019, No. 179, (2019), 35-48. doi: 10.1016/j.biosystemseng.2018.12.005.
3. Fountas, S., Espejo-García, B., Kasimati, A., Mylonas, N., and Darra N. "The Future of Digital Agriculture: Technologies and Opportunities." ***IT Professional***, Vol. 22, No. 1, (2020), 24-28. doi: 10.1109/MITP.2019.2963412.
4. Bhimanpallewar, R. N., and Narasingarao, M. R. "AgriRobot: implementation and evaluation of an automatic robot for seeding and fertiliser microdosing in precision agriculture." ***International Journal of Agricultural Resources, Governance and Ecology***, Vol. 16, No. 1, (2020), 33-50.
5. Moundekar, D., Nakhate, P., Ghosh, S., and Kasetwar, A. R. "Agricultural Robot (Agribot): A Future of Agriculture." ***Agriculture International***, Vol. 6, No. 04, (2020), 06-10.
6. Leitner, J. "Picking the right robotics challenge." ***Nature Machine Intelligence***, Vol. 1, No. 3, (2019), 162-162. doi: 10.1038/s42256-019-0031-6.
7. Xiong J., Liu, Z., Lin, R., Bu, R., He, Z., Yang, Z., and Liang, C. "Green Grape Detection and Picking-Point Calculation in a Night-Time Natural Environment Using a Charge-Coupled Device (CCD) Vision Sensor with Artificial Illumination." ***Sensors***, Vol. 18, No. 4, (2018), 969-985. doi:10.3390/s18030969.
8. Zhuang, J., Hou, C., Tang, Y., He, Y., Guo, Q., Zhong, Z., and Luo, S. "Computer vision-based localisation of picking points for automatic litchi harvesting applications towards natural scenarios." ***Biosystems Engineering***, Vol. 187, (2019), 1-20. doi: 10.1016/j.biosystemseng.2019.08.016.
9. Ma, Y., Zhang, W., and Qureshi, W. S. "Autonomous Navigation for a Wolfberry picking robot Using Visual Cues and Fuzzy control." ***Information Processing in Agriculture***, (2020), doi: 10.1016/j.inpa.2020.04.005.
10. Yu, Y., Zhang, K., Liu, H., Yang, L., and Zhang, D. "Real-Time Visual Localization of the Picking Points for a Ridge-Planting Strawberry Harvesting Robot." ***IEEE Access***, Vol. 2020, No. 8, (2020), 116556-116568. doi: 10.1109/ACCESS.2020.3003034.
11. Lei, W., and Lu, J. "Visual positioning method for picking point of grape picking robot (in Chinese)." ***Jiangsu Journal of Agricultural Sciences***, Vol. 36, No. 4, (2020), 1015-1021. doi: 10.3969/j. issn.1000-4440.2020.04.029.
12. Wu, B., Akinola, I., Gupta, A., Xu, F., Varley, J., Watkins-Valls, D., and Allen, P. K. "Generative Attention Learning: a GenerAL framework for high-performance multi-fingered grasping in clutter." ***Autonomous Robots***, Vol. 2020, No. 44, (2020), 971-990. doi: 10.1007/s10514-020-09907-y.
13. Esfandian, N., and Hosseinpour, K. "A clustering-based approach for features extraction in spectro-temporal domain using artificial neural network." ***International Journal of Engineering, Transactions B: Applications***, Vol. 34, No. 2, (2021), 452-457. doi: 10.5829/IJE.2021.34.02B.17

14. Siddharth, D., Saini, D. K. J., and Singh, P. "An Efficient Approach for Edge Detection Technique Using Kalman Filter with Artificial Neural Network." ***International Journal of Engineering, Transactions C: Aspects***, Vol. 34, No. 12, (2021), 2604-2610. doi: 10.5829/ije.2021.34.12c.04
15. Lin, C. Y., Gussu, T. W., and Tsai, Y. N. "A multi objective genetic algorithm approach to a design parameter generation for a robot platform on three omnidirectional wheels." ***Journal of the Chinese Institute of Engineers***, Vol. 40, No. 8, (2017), 659-668. doi: 10.1080/02533839.2017.1384327.
16. Wong, C. C., Feng, H. M., Lai, Y. C., and Yu, C. J. "Ant Colony Optimization and image model-based robot manipulator system for pick-and-place tasks." ***Journal of Intelligent & Fuzzy Systems***, Vol. 36, No. 2, (2019), 1083-1098. doi: 10.3233/JIFS-169883.
17. Karami, M., Tavakolpour-Saleh, A. R., and Norouzi, A. "Optimal Nonlinear PID Control of a Micro-Robot Equipped with Vibratory Actuator Using Ant Colony Algorithm: Simulation and Experiment." ***Journal of Intelligent & Robotic Systems***, Vol. 2020, No. 99, (2020), 1-24. doi: 10.1007/s10846-020-01165-5.
18. Yu, Y., Zhang, K., Yang, L., and Zhang, D. "Fruit detection for strawberry harvesting robot in non-structural environment based on Mask-RCNN." ***Computers and Electronics in Agriculture***, Vol. 2019, No. 163, (2019), 104846. doi: 10.1016/j.compag.2019.06.001.
19. Shahbakhsh, Mostafa Balouchzehi, and Hamid Hassanpour. "Empowering Face Recognition Methods Using a GAN-based Single Image Super-Resolution Network." ***International Journal of Engineering, Transactions A: Basics***, Vol. 35, No. 10, (2022). doi: 10.5829/ije.2022.35.10a.05
20. Wang, W., and Fu B. "Target Recognition Method of Eggplant's Picking Robot under Natural Environment." ***Journal of Anhui Agricultural Sciences***, Vol. 2019, No. 18, (2019), 64.
21. Chen, W., Xu, T., Liu, J., Wang, M., and Zhao, D. "Picking robot visual servo control based on modified fuzzy neural network sliding mode algorithms." ***Electronics***, Vol. 8, No. 6, (2019), 605. doi: 10.3390/electronics8060605.
22. Liu, W., Anguelov, D., Erhan, D., Szegedy, C., Reed, S., Fu, C., Y., and Berg, A., C. "SSD: Single shot multibox detector." European Conference on Computer Vision, Cham, September, (2016), 21-37. doi: 10.1007/978-3-319-46448-0_2.
23. Jin, Z., Sun, W., Zhang, J., Shen, C., Zhang, H., and Han, S. "Intelligent Tomato Picking Robot System Based on Multimodal Depth Feature Analysis Method." ***E&ES***, Vol. 440, No. 4, (2020), 042074. doi: 10.1088/1755-1315/440/4/042074.
24. Howard, A. G., Zhu, M., Chen, B., Kalenichenko, D., Wang, W., Weyand, T., and Adam, H. "MobileNets: Efficient convolutional neural networks for mobile vision applications." arXiv preprint, (2017), 1704.04861.
25. Zhang, X., Zhou, X., Lin, M., and Sun, J. "Shufflenet: An extremely efficient convolutional neural network for mobile devices." Proceedings of the IEEE Conference on Computer Vision and Pattern Recognition, (2018), 6848-6856.
26. Bloch, V., Bechar, A., and Degani, A. "Development of an environment characterization methodology for optimal design of an agricultural robot Industrial Robot." ***An International Journal***, Vol. 44, No. 1, (2017), 94-103. doi: 10.1108/IR-03-2016-0113.
27. Taheri, E. "Any-time randomized kinodynamic path planning algorithm in dynamic environments with application to quadrotor." ***International Journal of Engineering, Transactions A: Basics***, Vol. 34, No. 10, (2021), 2360-2370. doi: 10.5829/ije.2021.34.10a.17
28. Kumar, P., and Chaudhary, S., K. "Stability and robust performance analysis of fractional order controller over conventional controller design." ***International Journal of Engineering, Transactions B: Applications***, Vol. 31, No.2, (2018), 322-330. doi: 10.5829/ije.2018.31.02b.17


## Persian Abstract


**چکیده**

در این مقاله، یک روش ادراک بیونیک موقعیت کندن پرتقال ناف بر اساس Fmincon و کنترل زاویه متناسب -دیفرانسیل (PD) برای حل مشکلات آشفتگی باد و شاخه‌های سبز در محیط بدون ساختار پویا پیشنهاد شده است که باعث ایجاد اختلال بزرگ در فضای فضایی می‌شود .درک و کنترل پرتقال ناف در مرحله اول، یک مدل راه حل بهینه از زاویه چرخش هدف جهانی سیستم کنترل مبتنی بر Fminconبرای حل مشکل بهینه سازی زاویه حرکت رویکرد هدف ربات ایجاد شده است .ثانیا، یک سیستم ادراک بیونیک از موقعیت چیدن بر اساس کنترل زاویه PD برای حل مشکلات ادراک خاص ساخته شده است .در نهایت، یک پلت فرم شبیه‌سازی مشترک برای انتخاب ربات‌ها بر اساس Solidworks، Adamsو Simulinkتوسعه داده می‌شود و اعتبار و دقت الگوریتم تأیید می‌شود .نتایج تجربی نشان می‌دهد که میزان دقت برداشت 95درصد است، خطای زاویه هر مکانیزم بیش از 0.5درجه نیست، خطای جابجایی کمتر از 10میلی‌متر است و کل زمان از محاسبه زاویه بهینه تا پایداری سیستم فقط در حدود است 0.33 .ثانیه این روش برای درک سریع موقعیت چیدن و کنترل زاویه فعال ربات‌های چیدن در محیط بدون ساختار پویا مناسب است.

## AIMS AND SCOPE

The objective of the International Journal of Engineering is to provide a forum for communication of information among the world's scientific and technological community and Iranian scientists and engineers. This journal intends to be of interest and utility to researchers and practitioners in the academic, industrial and governmental sectors. All original research contributions of significant value focused on basics, applications and aspects areas of engineering discipline are welcome.

This journal is published in three quarterly transactions: Transactions A (Basics) deal with the engineering fundamentals, Transactions B (Applications) are concerned with the application of the engineering knowledge in the daily life of the human being and Transactions C (Aspects) - starting from January 2012 - emphasize on the main engineering aspects whose elaboration can yield knowledge and expertise that can equally serve all branches of engineering discipline.

This journal will publish authoritative papers on theoretical and experimental researches and advanced applications embodying the results of extensive field, plant, laboratory or theoretical investigation or new interpretations of existing problems. It may also feature - when appropriate - research notes, technical notes, state-of-the-art survey type papers, short communications, letters to the editor, meeting schedules and conference announcements. The language of publication is English. Each paper should contain an abstract both in English and in Persian. However, for the authors who are not familiar with Persian, the publisher will prepare the latter. The abstracts should not exceed 250 words.

All manuscripts will be peer-reviewed by qualified reviewers. The material should be presented clearly and concisely:

- *Full papers* must be based on completed original works of significant novelty. The papers are not strictly limited in length. However, lengthy contributions may be delayed due to limited space. It is advised to keep papers limited to 7500 words.
- *Research* notes are considered as short items that include theoretical or experimental results of immediate current interest.
- *Technical notes* are also considered as short items of enough technical acceptability with more rapid publication appeal. The length of a research or technical note is recommended not to exceed 2500 words or 4 journal pages (including figures and tables).

*Review papers* are only considered from highly qualified well-known authors generally assigned by the editorial board or editor in chief. Short communications and letters to the editor should contain a text of about 1000 words and whatever figures and tables that may be required to support the text. They include discussion of full papers and short items and should contribute to the original article by providing confirmation or additional interpretation. Discussion of papers will be referred to author(s) for reply and will concurrently be published with reply of author(s).

## INSTRUCTIONS FOR AUTHORS

Submission of a manuscript represents that it has neither been published nor submitted for publication elsewhere and is result of research carried out by author(s). Presentation in a conference and appearance in a symposium proceeding is not considered prior publication.

Authors are required to include a list describing all the symbols and abbreviations in the paper. Use of the international system of measurement units is mandatory.

- On-line submission of manuscripts results in faster publication process and is recommended. Instructions are given in the IJE web sites: www.ije.ir-www.ijeir.info
- Hardcopy submissions must include MS Word and jpg files.
- Manuscripts should be typewritten on one side of A4 paper, double-spaced, with adequate margins.
- References should be numbered in brackets and appear in sequence through the text. List of references should be given at the end of the paper.
- Figure captions are to be indicated under the illustrations. They should sufficiently explain the figures.
- Illustrations should appear in their appropriate places in the text.
- Tables and diagrams should be submitted in a form suitable for reproduction.
- Photographs should be of high quality saved as jpg files.
- Tables, Illustrations, Figures and Diagrams will be normally printed in single column width (8cm). Exceptionally large ones may be printed across two columns (17cm).

## PAGE CHARGES AND REPRINTS

The papers are strictly limited in length, maximum 8 journal pages (including figures and tables). For the additional to 8 journal pages, there will be page charges. It is advised to keep papers limited to 3500 words.

| **Page Charges for Papers More Than 8 Pages (Including Abstract)** | |
|---|---|
| For International Author *** | **$55 / per page** |
| For Local Author | **100,000 Toman / per page** |

## AUTHOR CHECKLIST

- Author(s), bio-data including affiliation(s) and mail and e-mail addresses).
- Manuscript including abstracts, key words, illustrations, tables, figures with figure captions and list of references.
- MS Word files of the paper.

**I**nternational **J**ournal of **E**ngineering, P.O. Box 13145-1659, Tehran, I.R. Iran
Materials and Energy Research Center, 5 Ahuramazda St., Alvand Ave., Argentina Sq., Tehran, Islamic Republic of Iran
www.merc.ac.ir - www.emerc.ac.ir


THOMSON REUTERS

WEB OF SCIENCE


Scopus®

CAS®
A DIVISION OF THE
AMERICAN CHEMICAL SOCIETY




Google
Scholar